Fausto Minelli

PLAIN AND FIBER REINFORCED CONCRETE BEAMS UNDER SHEAR LOADING: STRUCTURAL BEHAVIOR AND DESIGN ASPECTS

Relatori
Prof. Ezio Giuriani
Prof. Giovanni A. Plizzari
Prof. Frank J. Vecchio

Starrylink Editrice

SYNOPSIS

The behavior and design of r.c. members subjected to shear remain an area of much concern, even though, after the collapse of the U.S. Air Force hangars in 1955, thousands of experiments have been conducted to assess the shear capacity of structural concrete members.

Several proposals for predicting the shear capacity of beams without transverse reinforcement were published year by year: they are usually empirical formulations, designed to fit the limited set of shear test results that are most familiar to the researchers.

Design codes are continually changing and generally becoming more stringent, so that structures that were designed several decades ago typically do not comply with the requirements of current codes.

A total agreement on the mechanisms of shear transfer and on the interpretation of the collapse mode, for members without web reinforcement failing in shear, is still missing, in spite of the huge database of scientific papers published on shear strength and design, especially in the last two decades.

It remains a pressing need to establish design and analysis methods that provide realistic assessments of the strength, stiffness and ductility of structural elements subjected to shear loading.

The present thesis is intended to be a further contribution to the knowledge of shear behavior in beams without transverse reinforcement.

Different materials are herein considered, in addition to plain concrete: special emphasis is devoted to fiber reinforced concrete materials, increasingly used in the practice and promising with respect to their possible application to shear-critical beams.

This report is focused firstly on a detailed and critical review of the state of the art on shear, with particular attention to the mechanism of shear transfer and to several analytical models predicting the shear strength of members.

An extensive experimental campaign on twenty-seven full-scale beams is thus shown, with emphasis on the effect of steel-to-concrete bond, steel fiber content (if provided), prestressing and concrete grade on the shear response of members.

The extension of a FE routine based on the Modified Compression Field Theory and on the Disturbed Stress Field Model to fiber reinforced concrete is evaluated and corroborated against the available test results.

An analytical model for member made of plain concrete and without web reinforcement is then proposed, based on an assumed shear-critical crack pattern

consisting into two branches. A new distribution of shear stresses along the critical section is assumed, and the abrupt development of the second branch of the shear-critical crack is assumed to be generated once the transverse tensile strength of concrete is achieved.

Two numerical parametric studies are also presented, aiming at the evaluation of the effect of steel-to-concrete bond in guiding the collapse and of the effect of steel fibers in reducing the domain of shear diagonal failure.

Finally, an adaptation of the current EC2 equation for shear in members without transverse reinforcement is discussed and suitably adapted to elements containing steel fibers.

SOMMARIO

Il comportamento strutturale e il progetto di elementi in calcestruzzo armato soggetti ad azioni taglianti resta a tutt'oggi una materia di forte dibattito all'interno della comunità scientifica, nonostante le centinaia di test sperimentali eseguiti dopo il rovinoso crollo, nel 1955, di due hangars negli Stati Uniti, verificatosi per collasso a taglio di travi portanti prive di armatura d'anima.

Tra le molte formulazioni analitiche per il calcolo della resistenza ultima a taglio proposte negli anni si sono evidenziate notevoli discrepanze, sia nell'interpretazione fisica del fenomeno che porta al collasso per taglio, sia in termini di calcolo della capacità limite. Questo è essenzialmente dovuto al fatto che molte formulazioni sono state proposte in base a una serie limitata di prove sperimentali, che non tengono propriamente conto di tutti i fattori che influenzano la resistenza a taglio.

Inoltre, le diverse normative nazionali hanno spesso modificato le loro formulazioni a taglio e tendono a divenire via via più restrittive, per cui strutture progettate qualche decennio fa ora devono essere oggetto di adeguamento alla nuove disposizioni.

In sostanza non c'è ancora accordo, all'interno della comunità scientifica, sui meccanismi resistenti a taglio e sull'interpretazione fisica delle modalità di collasso, nonostante gli enormi sforzi compiuti specialmente negli ultimi due decenni, testimoniati dai molti articoli scientifici apparsi su rivista.

Resta la necessità di stabilire metodologie di analisi strutturale e progetto in grado di apportare affidabili interpretazioni della resistenza, rigidezza e duttilità di elementi strutturali soggetti ad azioni taglianti.

Il presente lavoro di ricerca intende costituire un ulteriore contributo alla conoscenza del taglio in elementi strutturali privi di armatura d'anima. Questo studio viene esteso, dal solo calcestruzzo bianco, ai calcestruzzi fibrorinforzati, che si stanno dimostrando particolarmente efficaci in determinate applicazioni strutturali e non, tra cui proprio in presenza di sforzi taglianti preponderanti.

Una dettagliata ricerca bibliografica, criticamente interpretata, sui meccanismi resistenti a taglio, su alcune tra le più note e interessanti formulazioni analitiche e sul taglio nel fibrorinforzato viene presentata nella parte iniziale di questo lavoro. Successivamente, ampio spazio è dedicato a due campagne sperimentali in cui un totale di 27 elementi strutturali full-scale è stato testato, al fine di valutare e studiare gli effetti dell'aderenza, del contenuto di fibre, della pretensione e della resistenza del calcestruzzo sul comportamento a taglio di elementi privi di armatura d'anima.

Questi risultati sperimentali sono stati poi studiati numericamente grazie all'utilizzo di un programma ad elementi finiti basato sulla Modified Compression Field Theory e sulla Disturbed Stress Field Model, che sono state adattate e valutate in presenza di materiali fibrorinforzati.

Una ampia discussione e interpretazione dei risultati sperimentali viene in seguito presentata, con la formulazione di un modello analitico per il calcolo della resistenza ultima a taglio di travi in calcestruzzo bianco privi di armatura trasversale. Tale modello ipotizza una diversa distribuzione di sforzi a taglio lungo la sezione critica rispetto a quella classica alla Jourawski. Tale distribuzione comporta la nascita di sforzi di trazione trasversale che determinano lo sviluppo del secondo ramo instabile della fessura critica.

Due interessanti studi numerici parametrici vengono mostrati, evidenziando l'effetto dell'aderenza e della presenza di fibre di acciaio sul comportamento a taglio. In entrambi i casi, tale effetto può essere determinante e portare ad un collasso flessionale.

Infine, viene formulata una proposta di adattamento della corrente formulazione a taglio dell'Eurocodice 2 (di elementi senza armatura trasversale convenzionale) per elementi strutturali contenenti fibre di acciaio (e privi di staffe).

ACKNOWLEDGMENTS

CONTENTS

x

PLAIN AND FIBER REINFORCED CONCRETE BEAMS UNDER SHEAR LOADING: STRUCTURAL BEHAVIOR AND DESIGN ASPECTS

1. INTRODUCTION

While thousands of experiments have been conducted to assess the shear capacity of structural concrete members, code provisions are usually developed from a limited and somehow arbitrary subset of these test results. Year by year, different proposals are put forward by researchers all over the world for predicting the shear capacity of members without transverse reinforcement. The proposed relationships are usually empirical and designed to fit the limited set of shear test results that are most familiar to the researchers. This state could be really unsatisfactory for two reasons. First, all proposals differ quite considerably in the selected parameters because there is no generally accepted model for the load transfer and the ultimate capacity of members without transverse reinforcement (stated also by the two state-of-the-art reports by Joint ACI-ASCE Committee 445, 1998 and CEB Bulletin 237, 1997). Secondly, the test data used for comparing proposals with tests differ very much from researcher to researcher in the amount and quality of the selected data. This limited amount of information is insufficient for the development of comprehensive and reliable expressions for estimating the shear strength of concrete members.

Talbot, one the first pioneers in the research field of shear in r.c. members, affiliated at the University of Illinois Engineering Experiment Station, conducted 188 tests on reinforced concrete beams under shear loading. In 1907 he stated that *"with this number of tests, one would expect the understanding of the problem to be quite complete. However, this is not the case…, there is still much to be learned before the problems may be considered solved"*.

In fact, when the author tried to collect, from published test reports, a systematic presentation of the influence of the basic parameters, like concrete strength, percentage of reinforcement, shear length, for the whole range of practically important beams, this turned out to be impossible. Specimens described by different authors were, in general, so different with regard to depth, reinforcement, concrete strength etc., that no reliable interpolation was possible.

Mörsch was the first researcher who predicted in 1902 that the shear stress distribution in a reinforced concrete beam containing flexural cracks, would reach its maximum value at the neutral axis and would then remain constant from the neutral axis down to the flexural steel. Those stresses could be calculated under simple equilibrium relationships, provided that the longitudinal flexural stresses at different sections of a beam were known. This German approach was extrapolated from experiments on beams with stirrups.

The community is also indebted to Mörsch and Ritter for the Truss Model they introduced between 1899 and 1902: that was the approach followed for many years, neglecting any concrete contribution to shear resistance.
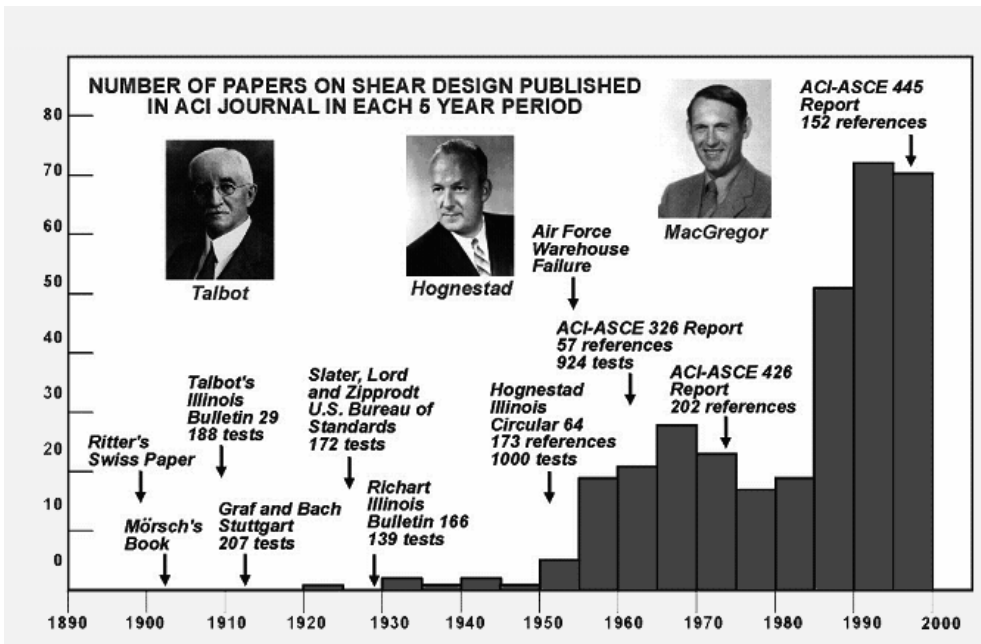
Figure 1.1:Number of papers published in ACI Journal since the beginning of the last Century.

Then, as already mentioned, thousands of experiments followed. Figure 1.1 clearly illustrates the considerable quantity of papers published on shear. The Universities of Stuttgart (Germany), of Illinois (USA), and Toronto (Canada) were basically involved in this filed. The different approaches proved not to sufficiently agree to each other in predicting the shear capacity of simple concrete beams, especially without shear reinforcement. Kani, from the University of Toronto, in 1966 stated, that *"The primary reason for this limited understanding of the problem of diagonal failure is the great number of parameters influencing the beam strength: grade of steel, percentage of steel, grade of concrete, shape of the cross section, shear arm ratio, type of web reinforcement, the quantity, arrangement and location of web reinforcement, the type of loading…, the type of beam.., and prestress in the longitudinal, transverse, and vertical direction which, of course, create additional parameters "*.

Kani is recognized for his effort in clarifying the problem. He postulated the shear-moment domain and investigated the influence of the reinforcement ratio and shear span. He also theorized the *"strut-and-tie action"* as the load bearing capacity for beams having a shear span-to-depth ratio lower than 2.5 and, conversely, the *"beam behavior"* for beams with a shear span-to-depth ratio greater than about 2.5. Moreover, he mentioned the significance of a good anchorage and detailing of the end regions or, more in general, of the disturbed regions. His simple analytical method for predicting shear resistance is still valuable today, even though it does not recognize the quite important influence of the compressive strength (with this respect, it should be recognized that high strength concrete was not extensively used at that time).

Based on a great number of experiments, ACI 318 Building Code was considered quite accurate till 1955, when two warehouses used by the US Air Force dramatically illustrated the unsafe nature of the ACI shear design provisions existing (Figure 1.2 and Figure 1.3). The beams failed in a really hot summer day, under dead load only, at a shear stress around 0.5 MPa, while ACI code permitted a working shear stress of 0.62 MPa, which would correspond to a failure shear stress of about 1.10 MPa. The investigation of this failure led to recommendations for changes to North America design practice, with particular respect to a minimum web reinforcement which should be always provided.
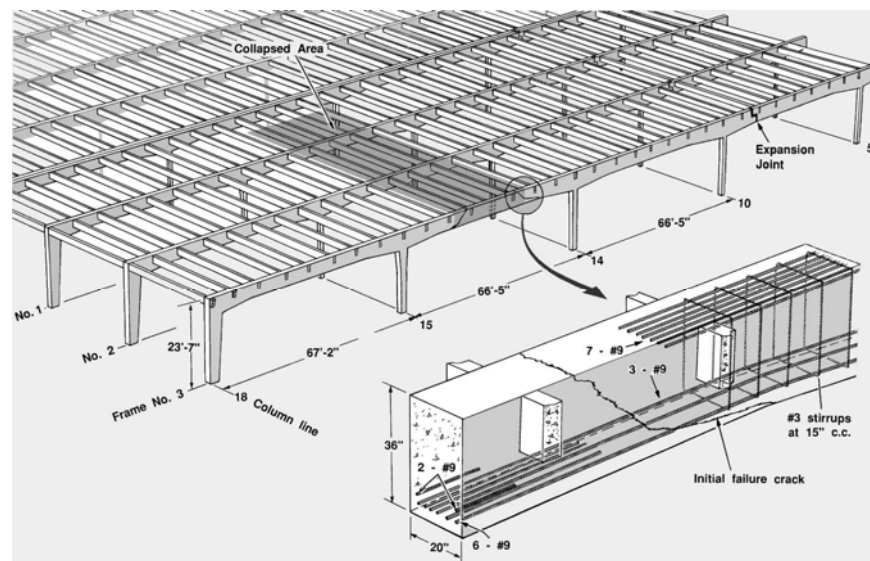
Figure 1.2: Shear failure of roof beams in Air Force Warehouse, Ohio, August 1955.

5

Figure 1.3: Picture of the shear failure of roof beams in Air Force Warehouse, Ohio, August 1955.

A scientific committee established that the failure occurred due to the tension caused by restraint.

Nowadays we know that it was basically a failure due to size effect (Bažant and Carpinteri are the main authors who recognized and studied this important parameter), which was not considered and is really critical for shear. ACI code was in fact calibrated with many experiments of small beams, which exhibited a less brittle behavior than full scale specimens.

We should therefore add, to the parameters influencing shear strength provided by Kani, at least two more: the depth of the beam and the aggregate size. Both parameters proved to fairly influence the shear capacity of a beam.

Further studies have been published after that, but still codes do not agree in predicting the shear capacity of beams without web reinforcement: some of them must be still unsafe.

A recent huge database provided by Reineck et al. (2003), evidenced that current ACI provisions do not adequately capture many trends and become increasingly unsafe as members become larger and more reinforced.

It remains a pressing need to further study and investigate the shear behavior of r.c. members.

This research work is intended to be a further contribution to the knowledge on shear behavior of beams without transverse reinforcement.

In addition to the traditional concrete, many tests were carried out on cementitious composites that are nowadays available in the market and more and more utilized in practice; among these, particular attention was devoted to fiber-reinforced concrete. In particular, the possibility of substituting part of the conventional shear reinforcement (stirrups) with randomly distributed steel fibers was investigated.

The first purpose of this work was to understand the actual failure mechanisms related to shear in conventional reinforced concrete: with this regard, many codes just provide empirical equations based on fitting of a limited series of experiments that do not properly account for all parameters influencing shear capacity. On the contrary, the author strongly believes that, once the phenomenon is known, it is possible to model it so that it can be applicable to a wide range of structural elements.

Full scale beams without web reinforcement were tested in order to reproduce the behavior of real structures: in fact, most of experiments available in literature were carried out on small scale members and, subsequently, code provisions were calibrated on these results, becoming quite unsafe for real structures.

From the experiments carried out by the author and from others published in the literature, it was possible to investigate the crack formation and propagation up to failure. The final crack pattern suggested the formulation of an analytical model aiming at the prediction of the shear capacity of beams without transverse reinforcement.

The proposal basically postulates the occurrence of the shear collapse through the formation of a shear-critical crack, made of two branches. The attainment of the tensile strength of concrete generates the second branch of the crack determining a sudden collapse. Early results are contained in the work of Adami et al. (2003) performed at the University of Brescia.

With regard to fiber reinforced concrete (FRC), the interest in FRC structures is continuously growing due to the improved performance of fiber reinforced concrete after cracking. Steel Fiber Reinforced Concrete (SFRC) is already widely used in structures where fiber reinforcement is not essential for integrity and safety (i.e. slabs on grade).

In the last few years, fibers have been also used as the main reinforcement in structures under bending; early examples are the square slabs of the Heathrow Airport car park in London and the foundation slab of Postdamer Platz in Berlin.

The addition of steel fibers to High Strength Concrete (HSC) results in an optimal composite material, since their presence reduces the well known brittleness of HSC and increases fatigue strength and resistance to impact loading.

In heavy precast industry, where HSC is commonly adopted, diffused fiber reinforcement could be utilized to reduce or substitute conventional transverse reinforcement, with advantages in the production process, and reduction of labor costs in placing and handling rebars. Several SFRC beams were tested to evaluate the effect of fibers on strength, ductility, crack pattern and failure modes of a beam.

After a first review of the state-of-the-art concerning shear in beams with little, no shear reinforcement or with fibers as transverse reinforcement (Chapter 2), this report presents, in Chapter 3 and Chapter 4, the experimental results, pointing out the research significance.

The experimental program consisted on full scale prestressed I-Beams, with and without transverse reinforcement, with and without fibers (Chapter 3), and on full scale shear-critical beams made whether of normal strength or high strength concrete, varying the bond properties and the fiber content, if provided (Chapter 4). All beams were designed without web reinforcement.

The first set of experiments was mainly a practical application in which the effect of fibers, web reinforcement and plain concrete itself was evaluated in terms of overall behavior, ductility and strength. In the shear-critical beams, tests on simpler structures allowed the evaluation and the discussion in details of the shear resistance mechanisms, and especially gave the opportunity to formulate an analytical model predicting the shear capacity of members.

Chapter 5 presents some numerical analyses of several tests performed, with particular emphasis on the FE model adopted (basically a routine implementing the Modified Compression Field Theory and the Disturbed Stress Field Model, MCFT and DSFM respectively), which was adapted for accounting for FRC, namely in terms of different tension softening laws and local conditions at crack.

The validation of the numerical model against the experiments made possible its extension to a wide range of structures, in order to evaluate the shear behavior and rely on the numerical response even without experimental evidence. Parametric studies were conducted by changing the concrete grade, the reinforcing ratio and the fiber content.

8

A new model for predicting the shear capacity of members without transverse reinforcement and without fibers is presented and discussed in Chapter 6. Also its validation against other experiments reported in literature is illustrated.

Moreover, Chapter 6 deals with the influence of steel-to-concrete bond on shear failure of members without web reinforcement and without fibers. Two unbonded specimens were tested to characterize the role of steel-to-concrete bond with respect to shear.

Finally, an adaptation to FRC of the shear design formulation included in Eurocode 2 (EC2) is discussed and compared with several existing proposals.

2.1 Shear in Concrete Members: Concept of Shear Strength.

In any concrete member where the moment over its length is not constant, shear forces have to be considered. In reality almost all flexural members will be subjected to shear stresses and these shear stresses may result in diagonal cracks. Unless appropriate amounts of properly detailed web and longitudinal reinforcement have been provided, these diagonal cracks can result in the premature failure of the member, which is in general a fairly brittle and unstable mechanism [1].

Transverse forces can be derived from a simple consideration of equilibrium. An external shear force acting on a general section should be equilibrated by the shear stresses across that cross-section. The horizontal shear stresses along any fiber of a homogeneous, isotropic, uncracked beam can be easily derived as:

$$v = \frac{VA_i y}{bI} \tag{2.1}$$

where V is the shear force [2], y is the distance of the centroid to the neutral axis and I is the second moment of the area of the section.
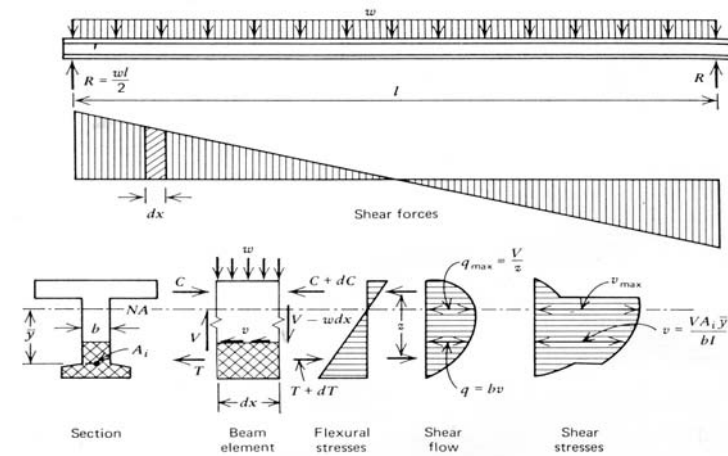
Figure 2.1: Shear force, shear flow, and shear stresses in a homogeneous isotropic elastic beam [1].

In addition, the inner lever arm z and the shear flow q, with respect to the centroidal axis, can be calculated as:

$$z = \frac{I}{A_i y}$$

(2.2)

$$q = v \cdot b = \frac{V}{z}$$

(2.3)

This is normally the location of the maximum shear stress if the width b at that fiber is small enough (Figure 2.1).

The shear stresses so generated can then be combined with the flexural stresses at any fiber. By considering the equilibrium of an infinitesimal element, the magnitude f_1 and f_2 and the inclination ϕ of the principal stresses, resulting from the simultaneous application of a tensile stress f and a shear stress v illustrated in Figure 2.2, can be obtained as follows:

Principal tension
$$f_1 = \frac{1}{2}\left(f + \sqrt{\left(f^2 + 4v^2\right)}\right)$$

(2.4)

Principal compression
$$f_2 = \frac{1}{2}\left(f - \sqrt{\left(f^2 + 4v^2\right)}\right)$$

(2.5)
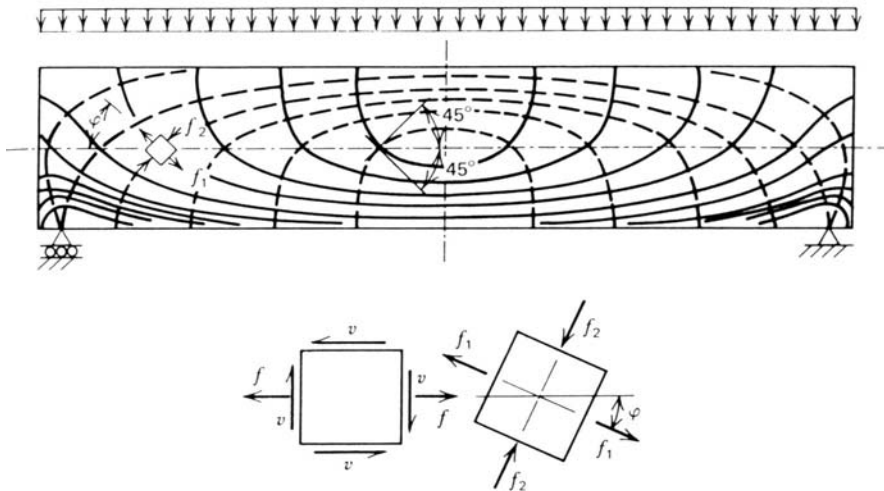
Figure 2.2: Trajectories of principal stresses in a homogeneous isotropic beam [1].

Figure 2.2 also depicts the principal stress trajectories (for a uniformly loaded simply supported beam), which intersect the neutral axis at 45°. When the principal tensile stresses exceed the tensile strength, cracks develop approximately at right angles to these principal tensile stress trajectories.

The inclination of the principal stresses with regard to the axis of the beam is shown in Figure 2.2 and can be obtained using the following relationship:

$$\tan 2\varphi = \frac{2v}{f} \quad \text{or} \quad \tan \varphi = \frac{v}{f_1} \tag{2.6}$$

At the neutral axis location, an angle of 45° is obtained because *f=0* whereas at the boundaries *φ=0* since *v=0*. The trajectories cross each other always with an angle of 90°. Moreover, at the supports, where shear is dominant over the bending moment, the principal tension trajectories are almost 45° inclined to the horizontal while they are horizontal at midspan where shear is equal to zero.

These traditional concepts, based on the elasticity theory, were extended by pioneers of reinforced concrete theory to the idealized section of a cracked reinforced concrete beam. In fact, as the load increases, the principal tensile stress can achieve the tensile strength of concrete causing cracking of the member. Figure 2.3 compares the principal stress trajectories for the same beam in the uncracked (left side) and cracked (right side) state.
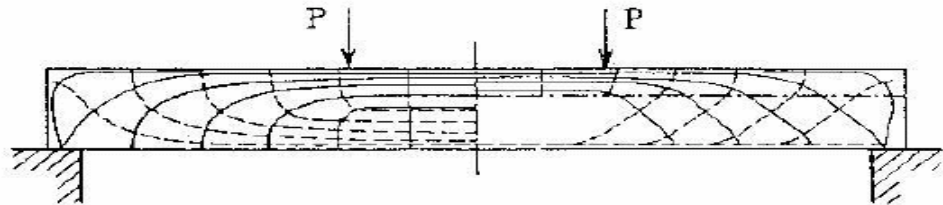
Figure 2.3: Trajectories of principal stresses in a homogeneous isotropic beam (left side) and cracked beam (right side).

Figure 2.4 illustrates the stresses over a cracked concrete cross-section. The horizontal force to be transmitted across the cracked zone of the section remains constant. Using the concepts reported in Figure 2.1, the incremental tension force is *dT=vb_wdx*, and hence we have:

$$v = \frac{1}{b_w} \cdot \frac{dT}{dx} = \frac{dM}{dx} \cdot \frac{1}{b_w \cdot jd} = \frac{V}{b_w \cdot jd} \quad \text{or} \quad q = \frac{V}{jd} \tag{2.7}$$

It is evident that shear stress depends on the width of the beam web, illustrated for a particular example in Figure 2.4. Since the concrete below the neutral axis is assumed to be in a state of pure shear (in fact the shear flow is constant below the neutral axis location; the shear stress would also be constant with a constant width of the web), this equation has been used as the measure of the diagonal tension in the cracked tension zone of a reinforced concrete beam. This also implies that vertical shear stresses are transmitted in this way across section, irrespective of the presence of flexural cracks.

In many countries this traditional shear stress equation is still used. It is a convenient index to measure "shear intensity", but it can not be considered as giving shear stress at any particular location in a cracked reinforced concrete beam. In certain cases the maximum shear stress could occur at a fiber other than at the web of the section. In fact, when the flange of a T section carries a large compressive force, as over the shaded area to the right of section 1 (Figure 2.1), the shear at the web-flange junction may become critical, and horizontal reinforcement in the flange may be needed.
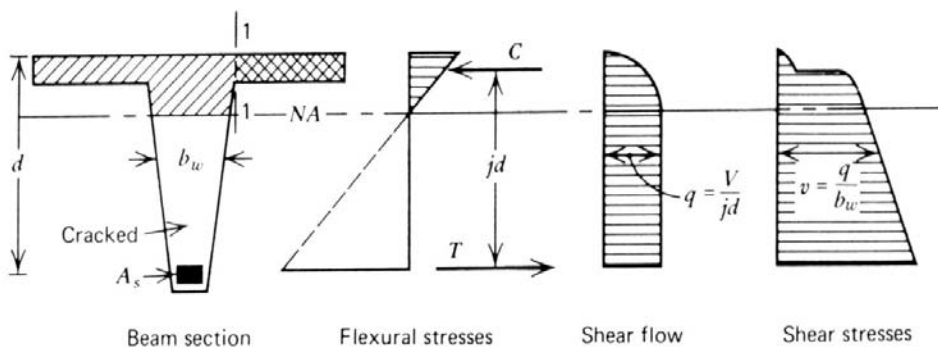
Figure 2.4: Shear stresses across an idealized cracked reinforced concrete section [1].

2.2   Members without Transverse Reinforcement.

2.2.1   Introduction.

Structural concrete members with sufficient reinforcement in both directions (longitudinal and transverse) can be designed using the simple strut-and-tie models [3]. Many structural concrete members are instead constructed without transverse reinforcement (that is, no stirrups or bent-up bars), such as slabs, footings, joints,

and lightly stressed members. The application of a simple strut-and-tie model, as shown in Figure 2.5, may result in an unsafe solution. Assuming that the shear in this slender member without transverse reinforcement is carried by a flat compression strut predicts that failure will be due to yielding of the longitudinal reinforcement whereas, in reality, a brittle shear failure occurred due a diagonal crack.
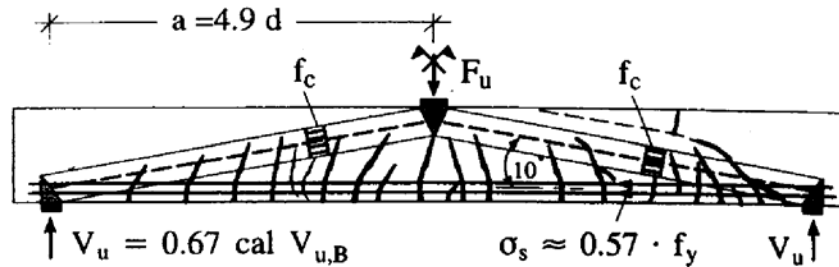
Figure 2.5: Crack pattern at shear failure of beam with unsafe strut-and-tie model [3].

The 1973 ASCE-ACI Committee 426 [4] report gave a detailed explanation of the behavior of beams without transverse reinforcement, including the different shear transfer mechanisms and failure modes. The main parameters influencing shear failure were discussed, and numerous empirical formulas were given. These equations continue to be the basis of shear design rules in many building codes around the world.

The simplest approach, and the first to be proposed (Mörsch 1909) [5], is to relate the average shear stress at failure to the concrete tensile strength (strength criterion). Experimental results have shown that the average principal tensile stress to cause secondary diagonal cracking (that is, flexure-shear cracking) is usually much less than concrete tensile strength. One reason is the stress concentration that occurs at the tip of initial cracks. Another factor is the reduction in cracking stress due to coexisting transverse compression (Kupfer and Gerstle 1973 [6]). Woo and White (1991) [7] have recently suggested that the reason for the low average stress at flexure-shear cracking is a non-uniform shear stress distribution at the outermost flexural crack as a result of a concentration of bond stresses and a reduction of the internal lever arm due to arch action in the flexurally cracked zone.

A simple lower-bound average shear stress at diagonal cracking is given by the following equation (in MPa units):

$$\frac{V_c}{b \cdot d} = v_c = \frac{\sqrt{f'_c}}{6} \qquad (2.8)$$

15

This well-known equation is a reasonable lower bound for smaller slender beams that are not subjected to axial load and have at least 1% of longitudinal reinforcement (Figure 2.6).
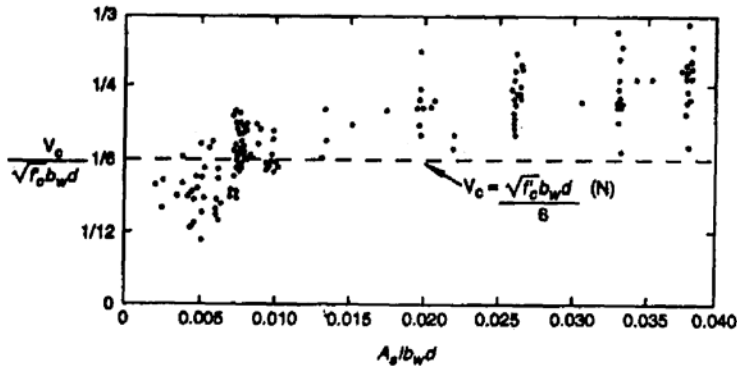
Figure 2.6: Influence of longitudinal reinforcement amount on shear strength of members without transverse reinforcement [3].

Zsutty (1971) [8] presented the following empirical equation:

$$v_c = 59 \cdot \left(f'_c \cdot \rho \cdot \frac{d}{a} \right)^{1/3}$$ (2.9)

with f'_c in psi (1 MPa = 145.03 psi), which proved to be a great improvement over the previous relationships.

Many other empirical equations have been proposed. These equations typically contain the following parameters: the concrete tensile strength, usually expressed as a function of f'_c; the longitudinal reinforcement ratio $p = A_s/b_w d$; the shear span-to-depth ratio a/d or M/Vd; the axial force or amount of prestress; and the depth of the member, to account for size effect.

Bažant and Kim (1984) [9] also included the maximum size of the aggregates in their formula which is based on fracture mechanics (See Section 2.5.2).

The empirical formula by Okamura and Higai (1980) [10] and Niwa et al. (1986) [11] considers all the main parameters as follows:

$$v_c = 0.20 \cdot \frac{\rho^{1/3}}{d^{1/4}} \cdot \left(f'_c \right)^{1/3} \left(0.75 + \frac{1.40}{a/d} \right)$$ (2.10)

with ρ expressed as a percentage, d in meters, and f'_c in MPa. This equation may be considered one of the most reliable empirical formulas as recent test results on large beams were considered for the size effect.

With respect to the various empirical formulas, considerable differences exist as a result of the following factors: the uncertainty in assessing the influence of complex parameters in a simple formula; the scatter of the selected test results due to inappropriate tests being considered (for example, bending failures or anchorage failures); the poor representation of some parameters in tests (for example, very few specimens with a low reinforcement amount or high concrete strength); and finally, the concrete tensile strength often not evaluated from control specimens. These issues limit the validity of empirical formulas and increase the necessity for rational models and theoretically justified relationships.

To predict a shear failure the conditions of shear stress in the web are to be known. Therefore it has to be considered how a cracked concrete member transmits shear (combined with axial load and bending moment).

The shear transfer in a reinforced concrete member is mainly described by five mechanisms (ASCE-ACI Committee 445 on Shear and Torsion, 1998 [3]): (1) shear stresses in uncracked concrete; (2) interface shear transfer, also called as "crack friction" or "aggregate interlock"; (3) dowel action of the longitudinal reinforcement; and (4) arch action.

In the last few decades a new mechanism has been identified, namely (5) residual tensile stresses transmitted directly across cracks. It is difficult to say which mechanism will contribute the most to the shear resistance, because a cracked concrete beam, as a highly indeterminate system, is influenced by many parameters. Different researchers attach various importance to the five mechanisms by using different models to describe the shear transfer. Often the mechanisms are subdivided into two groups of acting, where (1), (2), (3) and, lately, (5) are summarized in *"beam action in the shear spa"'* and the other one (4) is called *"arch action"*.

In a normal reinforced concrete beam in which (owing to slip, cracking, and other causes) the full bond force q required for beam action can not be developed, the two mechanisms will offer a combined resistance against shear forces. The extent at which each mechanism contributes to shear resistance at various levels of external load intensity will depend on the compatibility of deformations associated with these actions. A more detailed discussion about arch action will be provided in Section 2.3; the following consideration will be more focused on the mechanisms related to beam action.

As a result of loading, the beam cracks will divide the tension zone into a number of blocks which can be seen as a cantilever, hold by the compression zone of the

17

concrete (Figure 2.7). At these cantilevers the mechanisms above mentioned will take place to transfer the shear force. At the fix-end support of the cantilever, a horizontal and vertical force as well as a moment will occur and act on it. In the following these mechanisms will be briefly reviewed.
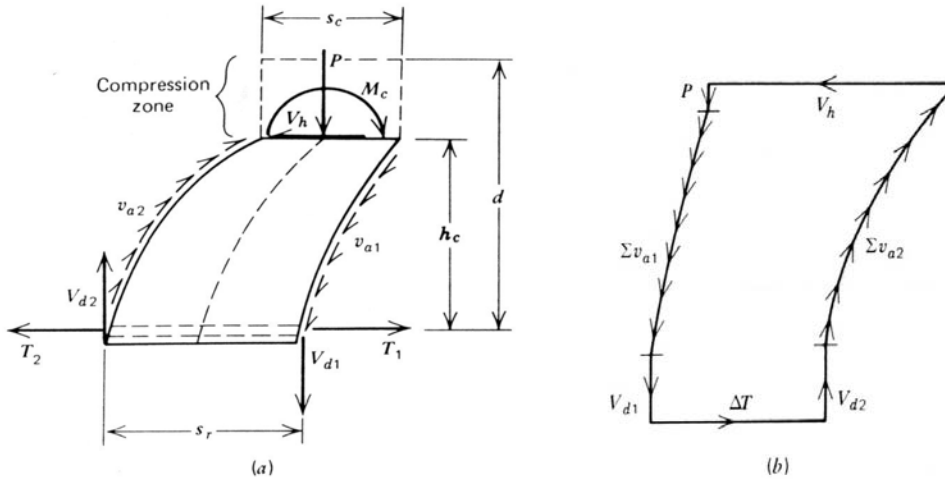
Figure 2.7: Actions on a concrete cantilever in the shear span of a beam (beam action) [1].

2.2.2   Mechanisms of Shear Transfer.

2.2.2.1   Uncracked Concrete Zone.

Schlaich et al. [12] introduced the concept of D and B regions in the uncracked B region of a member, where D stands for discontinuity of disturbed, and B stands for beam or Bernoulli. In D region the distribution of strain is nonlinear, whereas the distribution is linear in B region. A structural concrete member can consist entirely of a D region; however, more often D and B regions will exist within the same member), the shear force is transferred by inclined principal tensile and compressive stresses. In cracked B region, this stress is still valid in the uncracked compression zone, according to Figure 2.2. The integration of the shear stresses over the depth of the compression zone gives a shear force component (see Equation (2.11) and Figure 2.8), which is sometimes thought to be the explanation for the "concrete contribution". This shear force component should not be misinterpreted as a vertical component of an inclined compression strut.

$$V_c = b \cdot \int_0^x \tau_{xy}(k)\, dk$$

<div align="right">(2.11)</div>

In a slender member without axial compression, the shear force in the compression zone does not contribute significantly to the shear capacity because the depth of the compression zone is relatively small (Taylor 1974 [13]; Reineck 1991 [14]). Experiments done by some researchers (Fenwick and Paulay 1968 [15]) have shown that a maximum of 20% of the shear force could be resisted by flexure in this uncracked concrete zone.
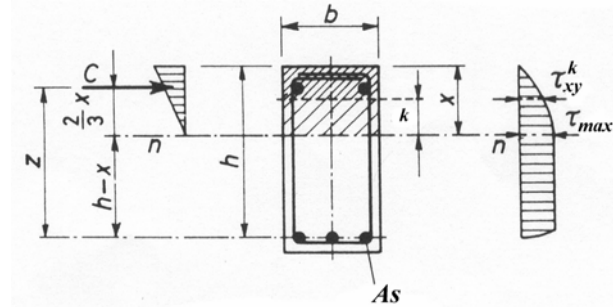
Figure 2.8: Shear stresses over the depth of a cracked beam.

Several tests conducted by a number of researchers [3] evidenced that the concrete contribution decreases as the depth of the members becomes greater. This effect is likely due to the increase (in percentage) of the aggregate interlocking in deep beams. Above 300 mm depth, the concrete contribution seems to become quite constant, if expressed in percentage.

2.2.2.2 *Interface Shear Transfer.*

The interface shear transfer mechanism, as illustrated in Figure 2.9, was clearly described in the 1973 ASCE-ACI Committee 426 report [4], based on work by Fenwick and Paulay (1968) [15], Mattock and Hawkins (1972) [16], and Taylor (1974) [13]. The physical explanation for normal density concrete was "aggregate interlock"; i.e., aggregates protruding from the crack surface provide resistance against slip. Because the cracks go through the aggregate in lightweight and high strength concrete and still have the ability to transfer shear, however, the term "friction" or "interface shear" is more appropriate. These latter terms also indicate that this mechanism depends on the surface conditions and is not merely a material characteristic.

If the first studies on dowel action were basically devoted to the interaction between shear stresses along the crack and the corresponding slip for imposed crack opening values, more recent researches focused even on the significance of the transfer of normal stresses along the two crack surfaces, the latter particularly important for reinforced concrete members, as it arises thanks to longitudinal bars.

The popular relationship for describing the aggregate interlocking proposed by Fenwick and Paulay (1968 [15])

$$v_a = \left(\frac{467}{w} - 8410\right) \cdot \left(0.0225 \cdot \sqrt{f_c} - 0.409\right) \cdot \left(\eta - 0.0436 \cdot w\right) \qquad (2.12)$$

is basically a function of the compressive concrete strength f_c, of the crack width w and of the relative slippage η between the two faces of the crack.
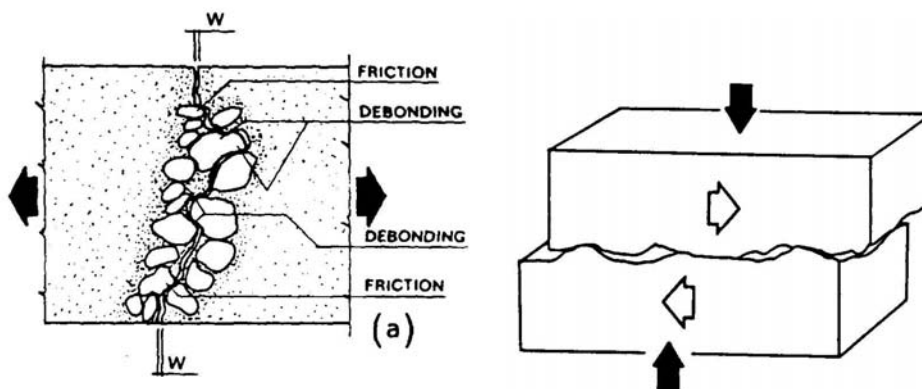
Figure 2.9: Mechanism of interface shear transfer [18].

Typical shear stress-shear displacement relationships, obtained by Paulay and Loeber (1974 [17]) are presented in Figure 2.10.

Significant progress (Gambarova 1981 [18]; Walraven 1981 [19]; Millard and Johnson 1984 [20];) has been made in the last two decades toward understanding this mechanism, which involves the relationships between four parameters: crack interface shear stress, normal stress, crack width, and crack slip.

Bažant and Gambarova [21] determined relationships describing the shear transfer across crack. They considered in-plane forces in concrete elements (wall, slab, plate, shell..) reinforced by a regular net of reinforcing bars (see Figure 2.11). They assumed monotonic loading, failure due to tensile yielding of rebars rather than due to crushing of shearing of concrete. The reinforcement was assumed smeared and carrying only axial force (dowel action across cracks and bar kinking were therefore

neglected) and the cracks were supposed to be parallel and sufficiently densely distributed. The model calculated appeared to be valid for a wide range of concretes. Figure 2.12 shows the comparison of the model with the Paulay and Loeber's [17] test results.
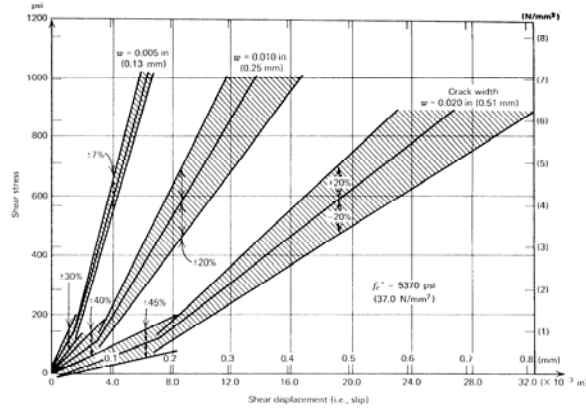
Figure 2.10: Typical mean shear stress-shear displacement relationships for aggregate interlock mechanism.
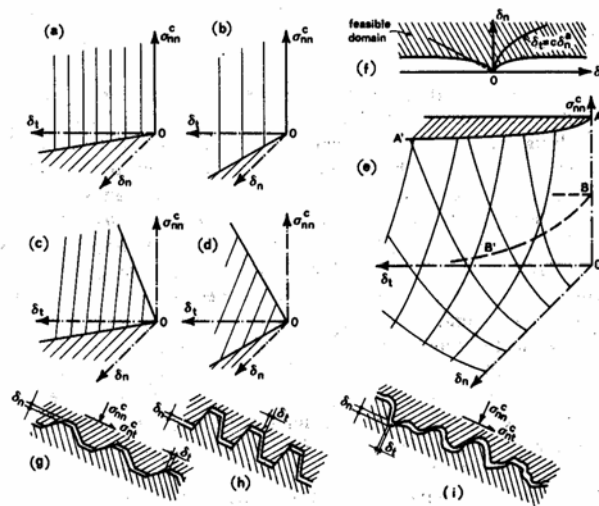
Figure 2.11: Stress-Displacement Surfaces (a)-(f) and crack morphology (g)-(i) [21].

The stress-displacement relationships derived by the authors proved to agree with existing data for plain concrete specimens as well as reinforced specimens. The method developed also allowed the calculation of the width of the cracks of known

spacing as a function of the applied forces, which could allow designing for a maximum crack width.

The latter point was particularly emphasized by the authors [21], who stated that neglecting friction is generally on the unsafe side of the design process: in fact, slip is always accompanied by an increase of the crack opening (relative normal displacement), and if the opening is restrained, then a large compressive stress is induced on the crack surface. The compressive stress, in turn, must be balanced by tensile forces in the reinforcement, which are in addition to those needed to equilibrate the applied tensile forces. Consequently, taking crack friction into account generally leads to a heavier rather than a lighter reinforcement.
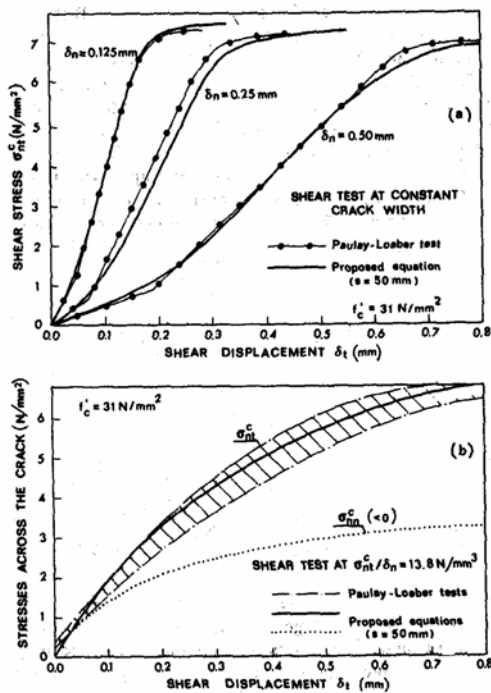
Figure 2.12: Fit of Paulay and Loeber's test results [21].

Walraven (1981 [19]) developed a model that considered the probability that aggregate particles (idealized as spheres) will project from the crack interface.

Concrete matrix was supposed to be made of two different phases, based on the following assumptions:

- Concrete is regarded as a two-phase material, with perfectly stiff spherical inclusions (aggregate) and a perfectly rigid-plastic matrix (paste).

22

- The grading of the aggregate matches Fuller's curve.
- The active contact areas between the inclusions and the matrix are related to interface displacements via geometric relations and take into account the statistics of aggregate distribution.
- The compressive contact strength of the matrix is related to the concrete strength, while the shear contact strength is related linearly to the compressive contact strength via a constant friction coefficient.

Walraven has developed this theoretical model for pure aggregate interlock, i.e., aggregate interlock in cracks which are not intersected by reinforcing bars.

The interlocking is thus modeled as an interaction between the strong aggregate particles and the soft paste, as shown in Figure 2.13. The cracks had to follow aggregate boundaries.

Shear stresses due to the relative slippage were determined then as a simple friction law:

$$\tau_p = \mu \cdot \sigma_p \tag{2.13}$$

$$\mu = \mu\left(f_c, w, D_{\max}, t\right) \tag{2.14}$$

Where σ_p is the normal stress between aggregate and mortar and μ is a friction coefficient, which depends upon the mechanical characteristics of the paste, on the crack width w, on the maximum diameter D_{max} of the aggregate and on the slippage t, as stated by Equation (2.14).

The shear stresses have then to be integrated over a specified area A_i, which depends on the aggregate distribution and can be found through a statistical analysis.

$$V_a = \iint_{Ai} \tau_p dA = \iint_{Ai} \mu(f_c, w, D_{\max}, t) \cdot \sigma_p \, dA \tag{2.15}$$
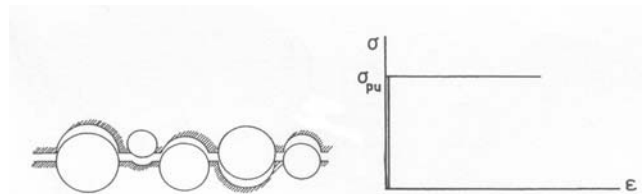
Figure 2.13: Interaction aggregate-mortar and constitutive law of the mortar.

Numerous test results are shown in Figure 2.15, and compared with several experimental evidences obtained by Walraven.
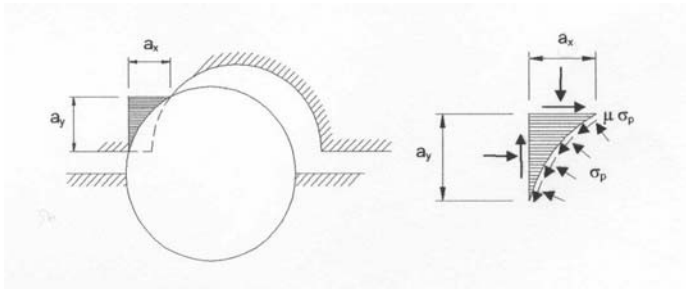
Figure 2.14: Model of the aggregate interlocking.
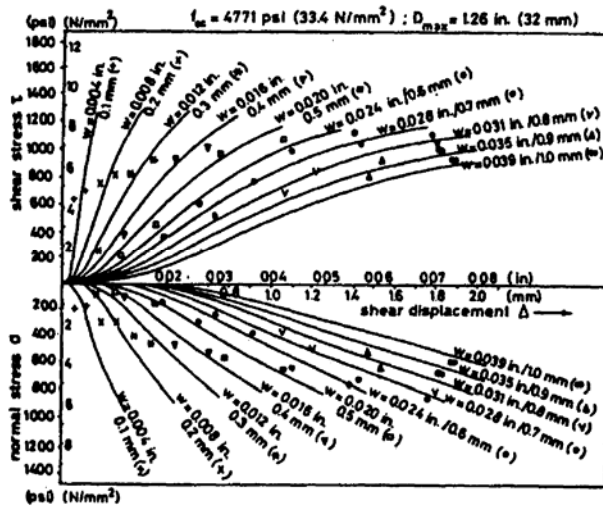
Figure 2.15: Comparison of Walraven's experiments results and predictions for crack interface shear transfer [3].

In Walraven's model, the relationship between stresses and displacements is a function of the concrete compressive strength; however, these relationships were developed for a range of normal (compressive) stresses beyond the range that is relevant for shear transfer in beams without stirrups.

Other relationships have been proposed based on Walraven's experimental data (Kupfer et al. 1983 [22]; Vecchio and Collins 1986 [23]), which assume that the shear that can be transferred is a function of f'_c. Although large differences may still occur between the constitutive laws of different researchers, it may be said that this mechanism is now well known and is widely accepted as an important shear transfer mechanism. The important role of interface shear transfer in the redistribution of diagonal compression fields in beams with stirrups is well known (Collins 1978 [24]; Kupfer et al. 1983 [22]; Dei Poli et al. 1990 [25]).

An interesting state-of-the-art about shear transfer was presented by Vintzileou. [26]. In that paper only the case of rough cracks is considered. It is assumed that a shear slip, s, is imposed to the crack (Figure 2.16). Due to the roughness of the interface, this slip can only occur under simultaneous increase of the crack width, w. A small part of the slip can be attributed to the deformation of the protruding asperities. Due to the increase of the separation between the two faces of the crack, tensile stresses are induced to the reinforcing bars crossing the interface. Thus, the reinforcement imposes compressive stresses to the concrete at their vicinity (clamping effect). The compressive stresses on the interface, multiplied by a friction coefficient (depending on the roughness of the interface, as well as on the magnitude of the normal stress) results to a shear stress which constitutes the resistance of the interface to the imposed slip. In case there is no reinforcement crossing the interface, the mechanism may be mobilized under the favorable effect of an external compressive load acting on the interface or under the action of a prestressing force. It should be noted here that even under zero normal stress, some shear can be transferred across the crack, as illustrated in the schematic profile of an unreinforced crack with zero normal stress on it (Figure 2.17).
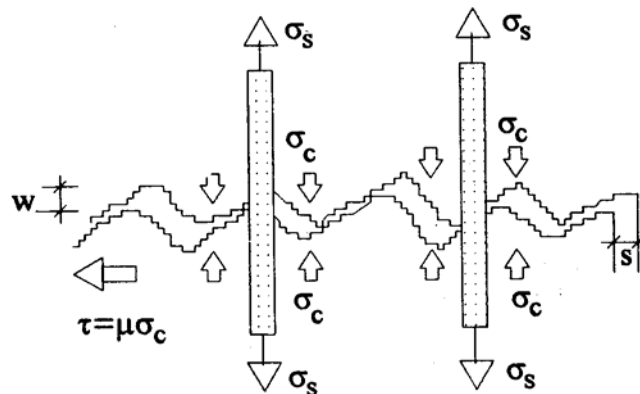
Figure 2.16: Mobilization of concrete to concrete friction in reinforced crack [26].

Figure 2.17: Mobilization of concrete to concrete friction in unreinforced crack [26].

The application of a shear force on the interface gives rise to normal and shear stresses on each protruding asperity which is in contact with an asperity of the

opposite face of the crack. Thus, what was previously described referring to the mean plane of a rough crack is now valid for each individual asperity. Obviously, the (micro) roughness of each asperity being small, a very low resistance is expected to be mobilized in this case.

Now, for the case under consideration (i.e. for cracks crossed by reinforcement; Figure 2.16) supposing that the constitutive laws τ-s of Figure 2.18 are available, one may predict the shear transfer behavior of an interface. In fact, for an applied shear slip, s, curve (b) would allow for the determination of the corresponding crack width. This crack width can be translated into tensile stress of the reinforcement using curve (c) which describes the pullout behavior of the reinforcing bars. Then, the compression force on the interface (which is equal to the tension force in the reinforcement), divided by the area of the crack, gives the mean compressive stress on the interface. For this compressive stress value and for the given shear slip value, the appropriate curve in (a) allows for the calculation of the shear stress which is mobilized to resist the imposed slip.. This procedure, repeated for various s-values, allows for the production of the curve (d), which describes the behavior of a sheared interface.

The above mentioned step by step procedure indicates that (for given pullout characteristics of the reinforcement crossing the crack) the shear stresses to be transferred across the interface are expected to depend on the roughness of the interface (i.e. on the crack width vs. shear slip law). The roughness of the interface (in other words s, the area of the protruding asperities which resists the imposed slip) is expected to affect also the shear force which may be transferred under constant normal stress. On the other hand, it should be checked whether the shear stresses are uniformly distributed along the interface independently of the length of the crack. These major parameters influencing the mechanism of concrete to concrete friction are examined in the following sections.

The Crack width vs. Shear Slip Law.

The relationship between shear slip and crack width is obviously expected to depend on the roughness of the interface. In fact, in the extreme case of very smooth interfaces (concrete blocks cast separately in metallic moulds and then brought together to form an interface), Vintzileou (1986) [27] has measured separations as low as 0.04 mm to 0.08 mm during testing.

On the contrary, in case of natural rough cracks, crack openings as large as 1.5 mm are measured by various researchers. On the other hand, it is reasonably expected that the normal compressive stress acting on the interface would affect the

relationship between crack width and shear slip (higher normal stresses would be expected to cause smaller crack openings). In what follows, experimental evidence related to the parameters affecting the crack width vs. shear slip relationship is presented and commented. The evaluation which follows will be based mainly on the results by Walraven, Vos and Reinhardt (1979) [28], by Daschner (1980) [29] and by Vintzileou (1986) [27].
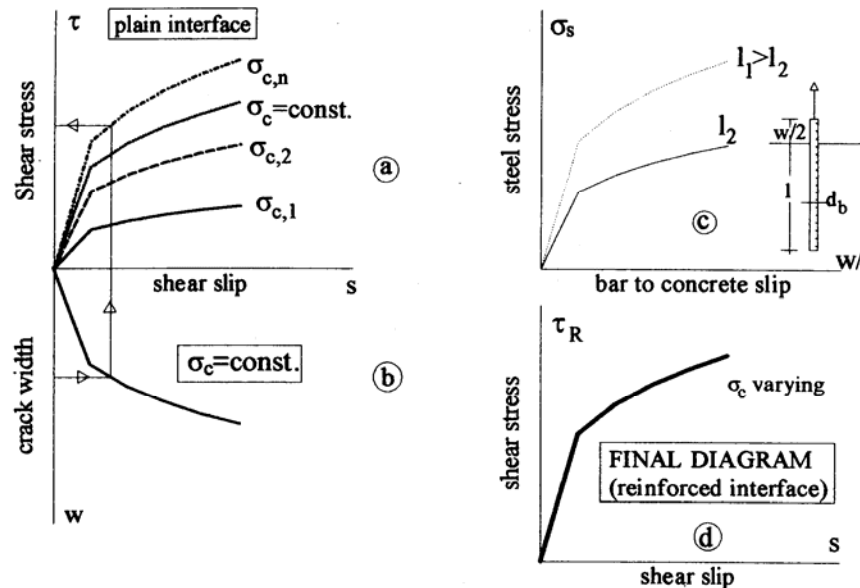
Figure 2.18: Concrete to concrete friction: constitutive laws (schematic) [26].

Roughness of the Interface. The Effect of Aggregate Size.

It is generally recognized that more rough interfaces result into larger crack widths, or that for the same imposed slip, the more rough interface will exhibit a larger crack width. This feature was repeatedly proved by experimental data. Some experimental evidence is presented in Figure 2.19. In Figure 2.19a, crack width vs. slip values are plotted for cracks through a normal concrete, as well as for cracks through a lightweight concrete of the same compressive strength. Since the cracks through lightweight concrete are less rough (the crack crossing both the cement paste and the aggregates), smaller crack widths are recorded.
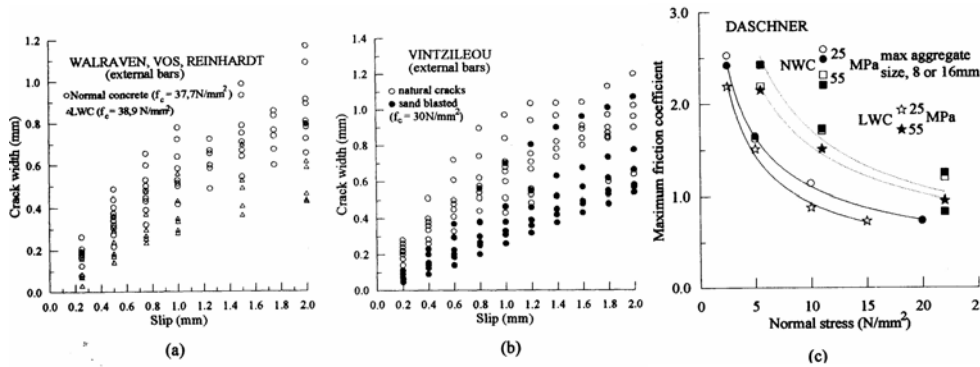
Figure 2.19: Experimental data on the relationship between crack width and shear slip for interfaces of various roughness: (a) Tests by Walraven, Vos and Reinhardt [28], (b) Tests by Vintzileou [30]. Experimental data about the dependence of friction coefficient on the interface roughness: (c)based on results of Daschner [26].

The same holds true for high strength concretes. In fact, the strengths of cement paste and aggregates being comparable, the cracks cross both materials, thus resulting to less rough interfaces. Similarly, the results by Vintzileou (1986) [30] show (Figure 2.19b) that in case of rough interfaces which were sand blasted before testing, smaller crack widths are recorded than in case of natural cracks. This feature is indirectly confirmed also by Daschner (1980) [29], who tested normal and lightweight concrete elements of the same compressive strength. The smaller roughness of the cracks through lightweight concrete (LWC) was responsible for the smaller friction coefficients, compared to those for the normal concrete (Figure 2.19c).

One should now check whether the roughness of a crack is affected by the maximum size of aggregates used for the production of the concrete. It is reasonable to expect that the mean height of asperities protruding from a crack will decrease for decreasing aggregate size. Nevertheless, it is experimentally and repeatedly proved that, at least for the range of aggregate sizes normally used in concrete, it is not possible to detect any significant effect of the aggregates size on the relationship between crack width and slip.

A first, clear -although indirect- indication of this is given by Daschner (1980) [29], as reported in Figure 2.19c. Daschner's experimental results show that the increase of the maximum aggregate size from 8 mm to 16 mm did not result in any increase or the friction coefficient, which constitutes an estimator of the roughness of the interface.

Direct experimental evidence was provided by Walraven, Vos and Reinhardt (1979) [28]. In Figure 2.20 crack width vs. shear slip values are plotted for specimens with maximum aggregate size equal to 16 mm or to 32 mm. It should be noted that the results are expectedly rather scattered, due to the random distribution of both the diameters of aggregates crossed by a crack and the heights of protruding asperities. Nevertheless, for both series of tests (with internal reinforcement crossing the crack or with external restraining bars), it is not possible to distinguish any effect of the maximum aggregate size. This finding seems to be in contradiction with what would be expected, as it is described by Walraven in his model (1980) [31]. However, it seems that for the range of maximum aggregate size, which is normally used in concrete, the roughness (the mean height of protruding asperities) is not characterized by the maximum diameters of aggregates. An indication in this direction is given by roughness measurements effectuated as described in Vintzileou and Tassios (1985) [32]. Measurements on 30 profiles of natural cracks (with maximum aggregate size of 30 mm) have shown that the roughness (i.e. half the height of protruding asperities) was equal to 1.75 mm. The measurements were repeated on the same interfaces after shear testing. The residual roughness was found to be equal to 1.45 mm. This decrease of roughness is due to the deterioration of the interface (fracture of protruding aggregates and particles of cement paste). It seems, therefore, that the roughness of those interfaces depends more on the frequently met smaller diameter aggregates than on the less frequent large diameter ones.
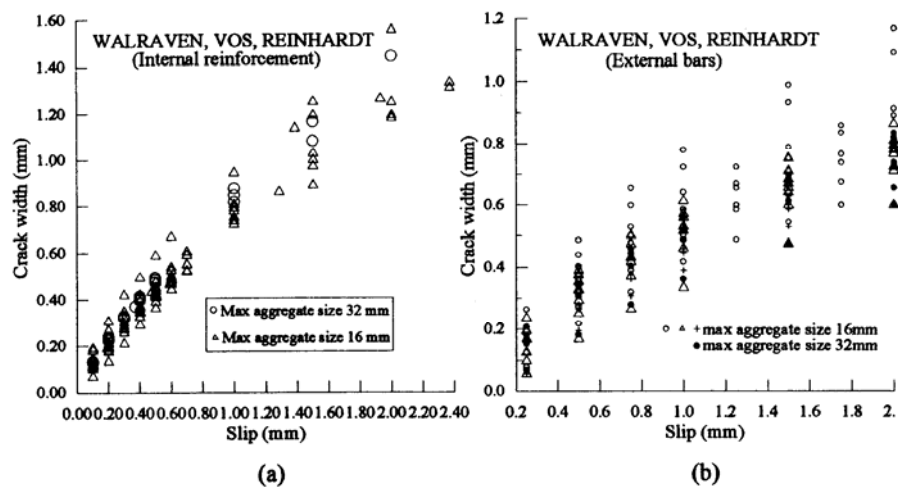
Figure 2.20: The effect of maximum aggregate size on the crack width-shear slip relationship (Based on Walraven, Vos, Reinhardt (1979) [28]).

29

The Effect of Normal Stress on the Interface.

Walraven, Vos and Reinhardt (1979) [28] in their program have tested a series of specimens with reinforced cracks (and with various reinforcement ratios), as well as a series of specimens with external bars (and with various restraint forces applied to the interface). Figure 2.21 shows the crack width vs. shear slip curves for some specimens from these two series. The data plotted on this figure clearly show that the crack width does not depend on the magnitude of the normal stress applied to the interface. The same feature was observed in tests by Vintzileou (1986) [30], in which external bars were provided for the application of compressive stresses on the interface. The normal stress (which was held constant throughout testing) was varying between 0.50 and 2.00 N/mm^2. Although the scatter of the experimental results is rather high (Figure 2.22), no dependence of the *w-s* law on the value of the normal stress was observed.

The Effect of the Length of the Sheared Interface.

The majority of tests for the investigation of the mechanism of concrete to concrete friction were performed on specimens of limited dimensions. To mention some examples, Fenwick (1966) [33] has tested specimens 100 mm high, the sheared area in Loeber's (1970) [34] specimens was 114.3 mm by 190.5 mm, Taylor (1974) [13] has tested cracks of an area of 127 mm by 140 mm, whereas Daschner's (1980) [29] specimens were 350 mm long and 100 mm wide. In Walraven's work (1980) [31] the sheared interface was 120 mm wide and 300 mm long, whereas Vintzileou (1986) [30] has tested interfaces 150 mm wide and 300 mm long. Thus, the question arises whether the experimental results are representative of the behavior of sheared cracks in real structures of considerably larger dimensions or, better, with higher length to width ratios.

Laible (1973) [35] in his work has tested specimens 354 mm wide and 273 mm or 546 mm long. Laible stated, however, that his tests do not allow for any reliable conclusion to be drawn regarding the effect of the length of the interface on the concrete to concrete friction. The only information which is available is offered by two analytical researches (Schwing (1975) [36] and Reineck (1990) [37]). Schwing, in his analytical work, has determined the stresses along joints for a push-off specimen and for various length to width ratios.
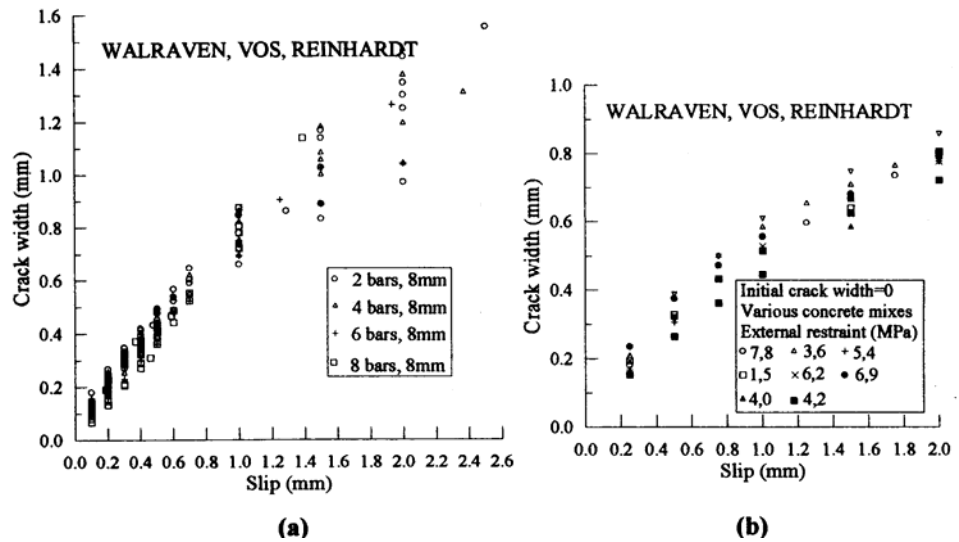
Figure 2.21: Crack width vs. shear slip relationship: (a) Specimens with internal reinforcement (for various concrete mixes), (b) Specimens with external restraining bars (Walraven, Vos, Reinhardt [28]).
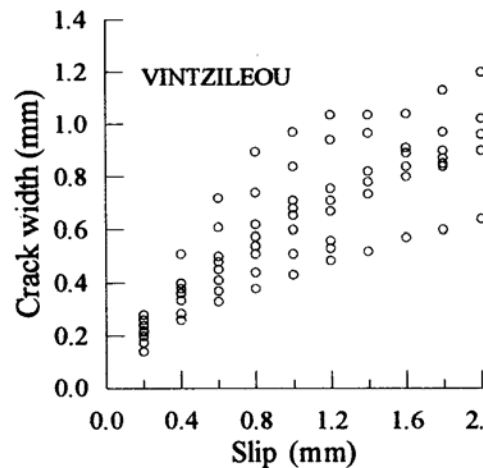
Figure 2.22: The effect of normal stress on the crack width-shear slip relationship (Vintizileou [30]).

As shown in Figure 2.23, for increasing *l/b* ratios, a pronounced concentration of shear stresses is observed close to the end regions of the sheared interface. The same result was found by Reineck who used finite element techniques, as well as strut and tie models to calculate normal and shear stresses in push-off specimen. He found that the concentration of stresses at the ends of the specimen may be

31

responsible for slips as high as 50% of the total slip measured during testing. This result has to be seriously considered, since it clearly shows that the direct use of the available experimental results in the design of R.C. structures may be unsafe. A reliable, quantitative assessment of this effect is needed. Such a work should be based on experimental evidence, which is missing for the time being.
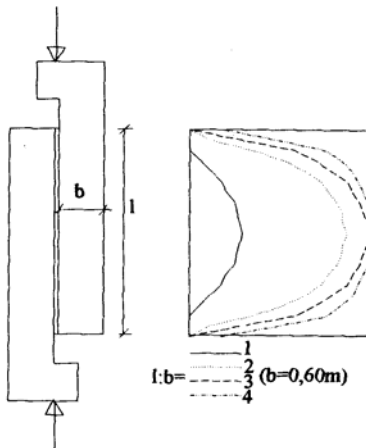
Figure 2.23: Distribution of shear stresses along a sheared joint (Schwing [36]).

2.2.2.3   Dowel Action of Longitudinal Reinforcement.

The well known work done by Baumann and Rüsch (1970) [38] on the resistance of dowels near a surface has been reaffirmed by Vintzeleous and Tassios (1986) [27] and Chana (1987) [39]. In members without transverse reinforcement dowel action is normally not very significant, because the maximum shear in a dowel is limited by the tensile strength of the concrete cover supporting the dowel. Once a splitting crack occurs, the stiffness, hence the effectiveness, of the dowel action is greatly reduced. In several tests (Fenwick and Paulay 1968 [15]; Taylor 1974 [13]) it was shown that the contribution of the dowel action in beams without web reinforcement does not exceed 25% of the total cantilever resistance. However, in members with large amounts of longitudinal reinforcement, the dowel action may be significant, particularly when the longitudinal reinforcement is distributed in more than one layer and a stirrup reinforcement is used (in the latter case, however, the shear contribution will be mostly carried by the transverse reinforcement itself).

Qualitative load-displacement relationships for dowel action are presented in Figure 2.24 [1]: they represent the concepts above presented.
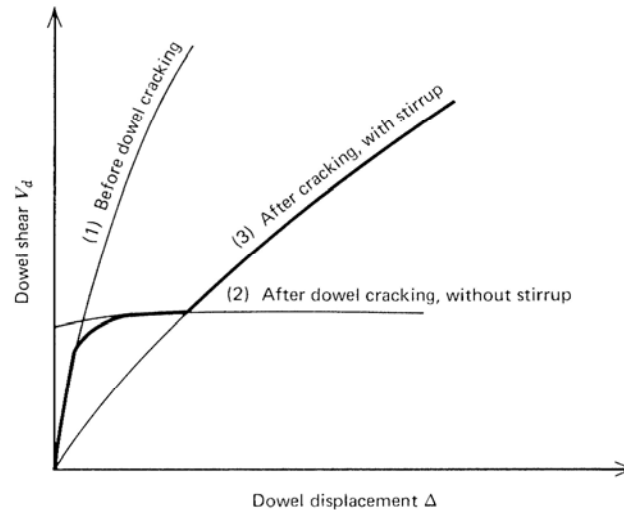
Figure 2.24: General dowel shear-dowel displacement relationships [1].

The shear force that can be transferred across a reinforced concrete interface by means of dowel action depends on various parameters, namely the reinforcement ratio, the bar diameter, the spacing of the bars in-section, the top, side and bottom concrete cover provided to the bars, the material properties for concrete and steel, axial stress on the dowels, etc.., whereas two failure modes of the mechanism may be distinguished (Figure 2.25), namely: splitting failure of the side or/and bottom concrete cover (Failure mode I) or crushing of the concrete under the dowel and yielding of the bar (Failure mode II). The failure mode to occur each time (and, hence, the magnitude of the dowel resistance) depends on parameters which are liable to size effects. Such parameters are the bar diameter, the spacing of bars in-section, the concrete cover, as well as the tensile and compressive strength of the concrete. In the following sections, the size effects related to the above mentioned parameters will be evaluated on the basis of the available literature.
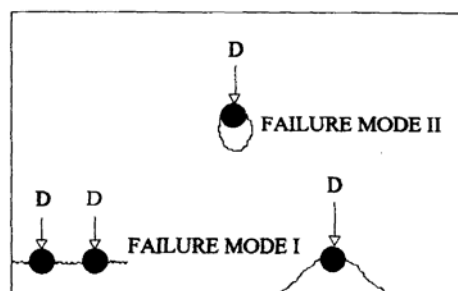
Figure 2.25: Failure modes of dowel mechanisms (schematic)[26].

The Effect of the Bar Diameter.

It is well known that a reinforcing bar surrounded by concrete and subjected to shear force D induces compressive and tensile stresses to the concrete (Figure 2.26). the state of stresses around the bar can be determined using the theory of elasticity. Such analyses were carried out by Stanton (1977) [40] and White and Gergely (1978) [41] and gave the following results (Figure 2.27):

Radial stress
$$\sigma_r = \frac{D}{\pi \cdot R} \cos \varphi \qquad (2.16)$$

Circumferential stress

$$\sigma_\varphi = 0.344 \frac{2 \cdot D}{\pi \cdot R} \quad \text{for } \varphi = 0$$

$$\qquad (2.17)$$

$$\sigma_\varphi = 0.637 \frac{2 \cdot D}{\pi \cdot R} \quad \text{for } \varphi = \pi/2$$

Even such simplified analyses allow for the effect of bar diameter to be qualitatively evaluated: it is assumed that two concrete sections are reinforced with the same percentage of reinforcement but using different bar diameters. The first section is reinforced by means of one bar (bar diameter d_{b1}), whereas the second one is reinforced by means of two bars (bar diameter $d_{b1}/(2)^{1/2}$). The same force, D, is applied to both sections. Using Equations (2.16) and (2.17), one may see that the ratios σ_{r1}/σ_{r2} and $\sigma_{\varphi1}/\sigma_{\varphi2}$ are equal to $(2)^{1/2}$. Thus, it is clearly shown that both compressive and tensile stresses induced to concrete by a dowel are increasing for increasing bar diameter. It is therefore expected that for both failure modes, the maximum force to be transferred by means of dowel action will be negatively affected by increasing bar diameters.
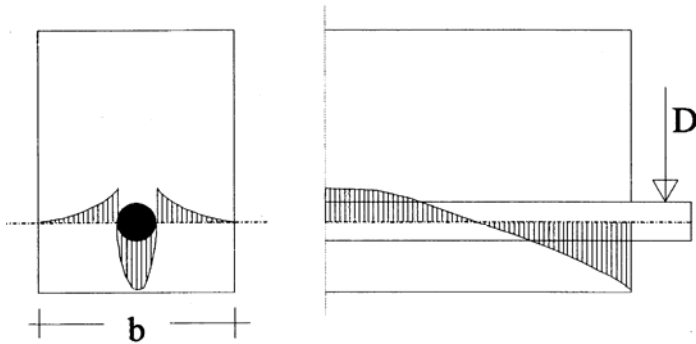
Figure 2.26: Stress distribution along a dowel and within a section (schematic) [26].
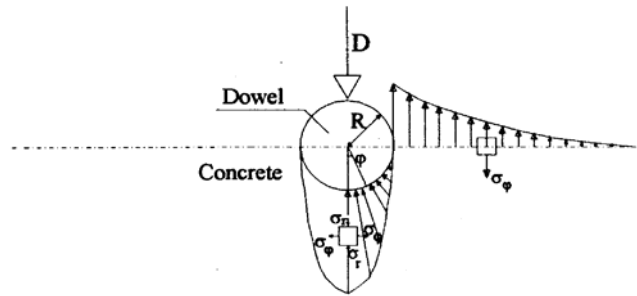
Figure 2.27: Stresses along the perimeter of a loaded dowel (schematic) [26].

In what follows, an attempt is presented to evaluate the effect of bar diameter on the maximum shear force transferred by dowels, on the basis of the available experimental results. It should be noted, however, that such an evaluation is in several cases not possible, since bar diameter was not the only parameter varying from test to test. In cases where the concrete compressive strength was not the same for all specimens, the experimental values were modified to eliminate the effect of varying concrete strength. This correction was made as follows: it was repeatedly proved (see for example Rasmussen (1962) [42], Krefeld and Thurston (1966) [43]) that the maximum dowel resistance is proportional to $(f_c)^{1/2}$ (f_c being the concrete compressive strength). Thus, for each series of test s, the lowest concrete compressive strength (f_{c1}) was selected as reference strength. The dowel resistance for specimens having a higher concrete compressive strength (f_c) was multiplied by $(f_c)^{1/2}/f_{c1}$.

The results of this evaluation are shown in Figure 2.28 and Figure 2.29. Figure 2.28 refers to specimens which failed due to the appearance of (side and/or bottom) splitting cracks in the concrete (Failure mode I). One can see that the maximum dowel resistance is not proportional to the bar diameter, as one might expect for this failure mode. On the contrary, the effectiveness of the mechanism seems to be reduced for increasing bar diameter.

In Figure 2.29, the dowel resistances are plotted against the steel area, since for Failure mode II, the maximum mobilized dowel resistance is expected to be proportional to the percentage of reinforcement. For the experimental results presented in this figure, the increase of the steel area is achieved by increasing the diameter of the bars. Here again, the mobilized dowel resistance is corrected, when necessary, to eliminate the effect of varying concrete compressive strength. The results by Bennett and Banerjee [44], Paschen and Schonhoff [45], as well as the

results by Paulay, Park and Phillips [46] (in Figure 2.30) clearly show the negative effect of increasing bar diameter on the maximum dowel resistance.
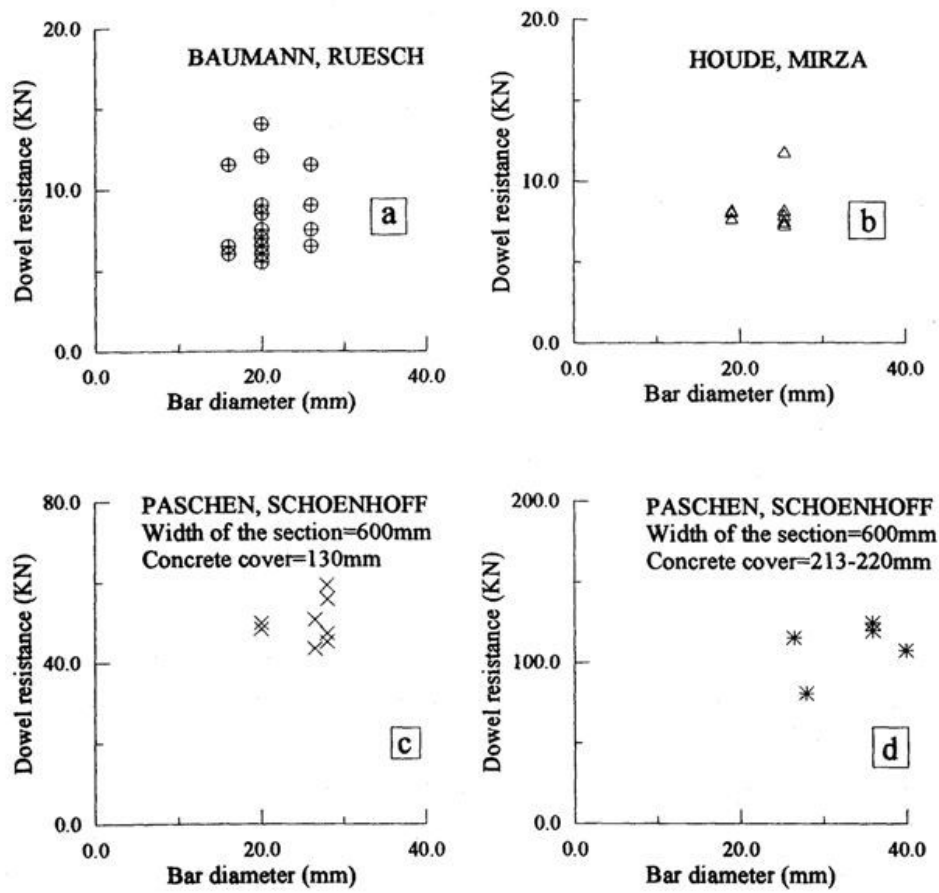
Figure 2.28: The effect of dowel diameter on the shear force transferred by means of dowel action. Evaluation of experimental results by: (a) Baumann and Rüsch [38], Houde and Mirza (1974), (c) and (d) Paschen and Schönhoff [45] for failure mode I.
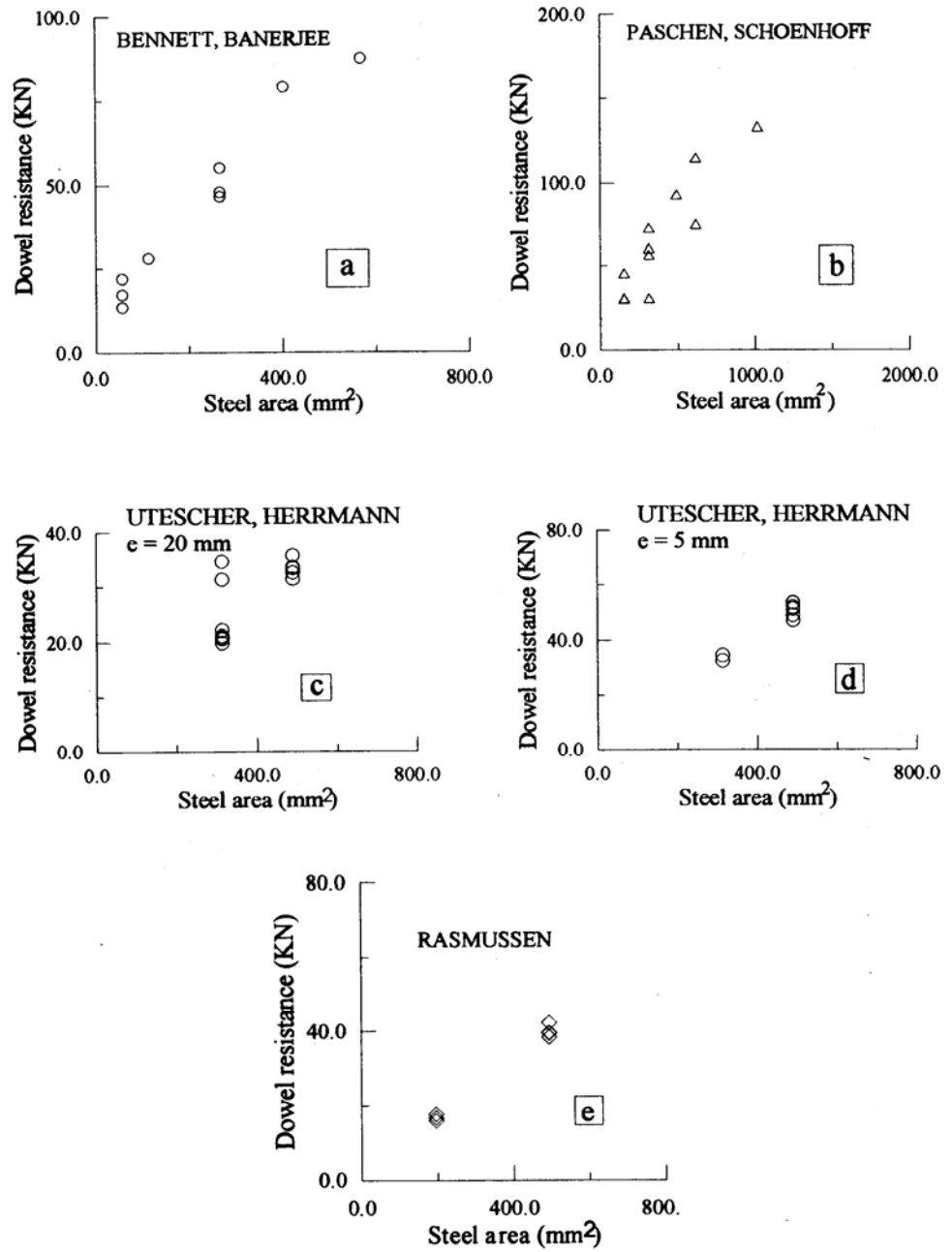
Figure 2.29: The effect of bar diameter on the dowel resistance as evaluated on test results by: (a) Bennett and Banerjee [44], (b), Paschen and Schönhoff [45], (c) and (d) Utescher and Herrmann [47], (e) Rasmussen [42], for failure mode II.

This is not, however, the case for the results by Utescher and Herrmann (1983) [47] and Rasmussen (1962) [42], in which the effect of increasing bar diameter is not that clear. It should be noted that in tests by Utescher and Herrmann [47], the shear force was imposed eccentrically with respect to the interface (e = 20 mm for results in Figure 2.29c and e = 5 mm for results in Figure 2.29d).

On the contrary, the results by Utescher and Hemnann [47] show very clearly the effect of bar diameter on the critical concrete cover value for which a change in the failure mode occurs. As it was already mentioned, for relatively small bottom or side concrete covers, the mechanism of dowel action fails due to the appearance of splitting cracks in the concrete, whereas for large concrete values, crushing of the concrete under the bars is responsible for the failure of the mechanism.
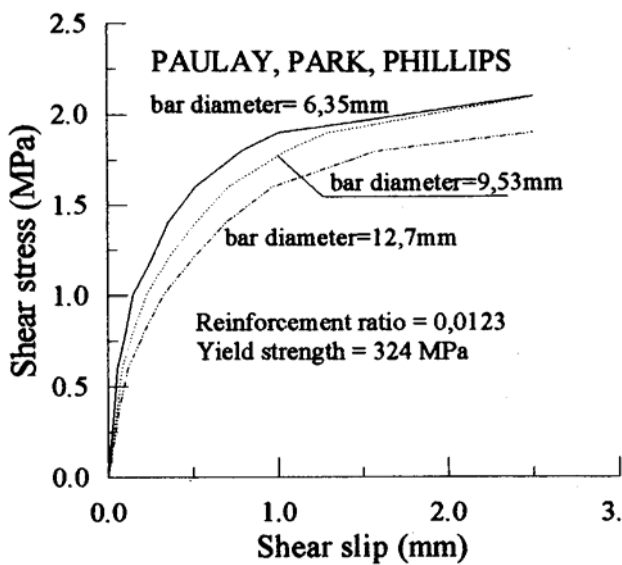
Figure 2.30: The effect of bar diameter on the behavior of dowels, for failure mode II (Paulay, Park, Philips, [46]).

Utescher and Herrman (1983) [47] have studied systematically this parameter. In Figure 2.31a, the specimen used in their research is shown. A large variety of top, bottom and side covers was considered, as well as three bar diameters. Another parameter investigated within the program was the distance from the concrete face, at which the shear force was applied. This distance varied between 5 mm and 50 mm Figure 2.31b, c and d are based on their results and show how the dowel resistance, as well as the failure mode of the mechanism change as a function of the bottom cover provided to the bars. One can easily see on Figure 2.31 that for

38

increasing bar diameter, the concrete cover value needed for the transition to the (favorable) failure mode A (according to the notation of the authors, see Figure 2.31a) is increasing. This result is in agreement with the observation made previously in this section about the higher splitting forces induced to the concrete around a large diameter bar.
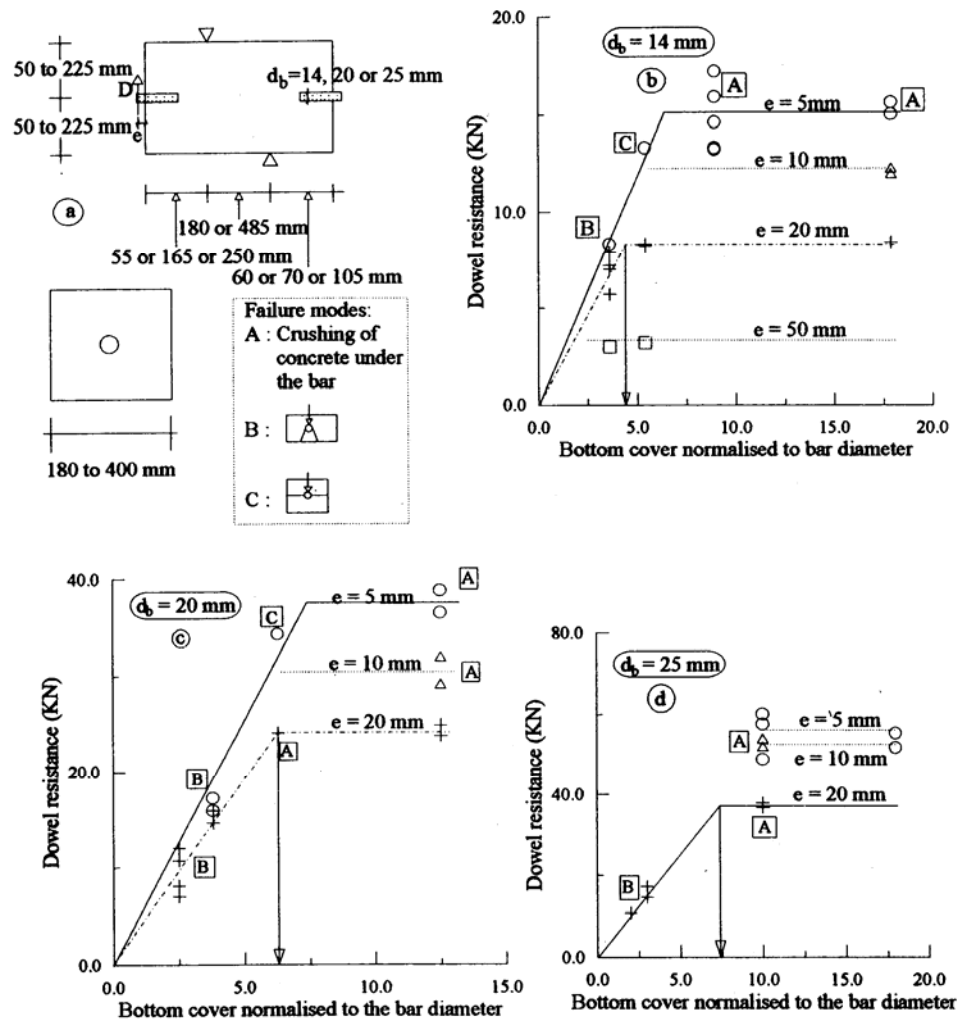
Figure 2.31: The effect of concrete cover on the dowel resistance, as well as the failure mode of the dowel mechanism (based on test results by Utescher and Herrmann [47]).

The Effect of the Concrete Cover.

As shown in Figure 2.32 for a dowel embedded in concrete, three concrete covers may be distinguished, namely: top cover (c_t), side cover (c_s) and bottom cover (c_b), depending on the direction of loading. The effect of each concrete cover on the failure mode, as well as on the mobilized dowel resistance was experimentally investigated.
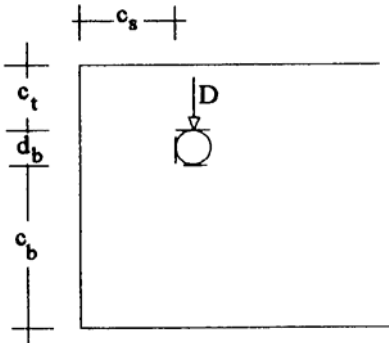
Figure 2.32: Notation for concrete covers provided to a dowel [26].

The effect of top cover on the dowel strength is neglected by most researchers, who are mostly interested on the unfavorable case of dowels loaded towards the concrete cover. Shoroushian et al. (1986) [48] investigated the behavior of dowels loaded against the core. However, in their research top cover was not taken as a parameter. Vintzileou and Tassios (1990) [49] have tested 16 mm deformed bars embedded in concrete blocks. The dowels were loaded against the core and their bottom cover was in all tests equal to 12 times the bar diameter, large enough to ensure failure due to crushing of the concrete under the bar, even after the appearance of horizontal splitting cracks. The investigated parameters were the top and the side concrete cover. Figure 2.33 shows the effect of top cover on the mobilized dowel resistance. It is observed that, for small side cover, the value of the top cover has practically no effect on the mobilized dowel resistance. This may be attributed to the fact that for small side cover, the early appearance of a horizontal splitting crack makes the top cover ineffective. On the contrary, for larger side covers, the dowel resistance is linearly increasing with the top cover. It should be noted, however, that for top covers larger than a certain limit (approximately equal to 5 times the bar diameter), there is no further increase of the dowel resistance.
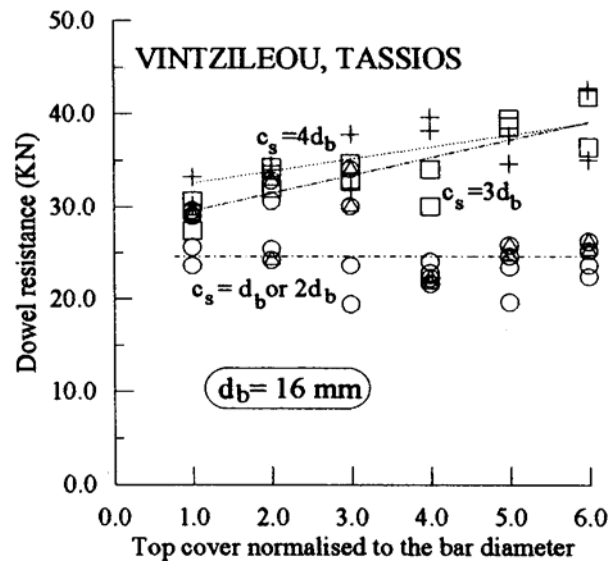
Figure 2.33: The effect of top cover on the mobilized dowel resistance (Vintizleou and Tassios, [49]).

The effect of side and bottom cover on the dowel mechanism was extensively investigated by several researchers. Baumann and Rüsch (1970) [38] have tested beams with preformed cracks at their mid-region. One of the parameters they investigated in their beams without stirrups was the bottom cover provided to the longitudinal reinforcement of the beams. In those tests, the bottom cover was varying from 30 mm to 61 mm (1.5 to 3 times the bar diameter). No significant effect of the bottom cover on the dowel resistance was observed, most probably because the side cover of the bars was very small (15 to 18 mm) and horizontal splitting cracks were appearing at a load practically independent of the bottom cover. Paschen and Schonhoff (1983) [45] have investigated the effect of bottom and side cover on dowel resistance. As shown in Figure 2.34, the dowel resistance increases for increasing bottom cover. This increase is enhanced when associated with increasing side cover. Here again, the increase of concrete covers beyond a certain limit does not lead to further increase of the dowel resistance, since a change in failure mode takes place. This is clearly illustrated in Figure 2.31 (based on results by Utescher, Herrmann (1983) [47]). Unfortunately, the results by Utescher and Herrmann do not allow to assess the effect of bottom and side cover separately, since in their specimens these two parameters vary simultaneously.
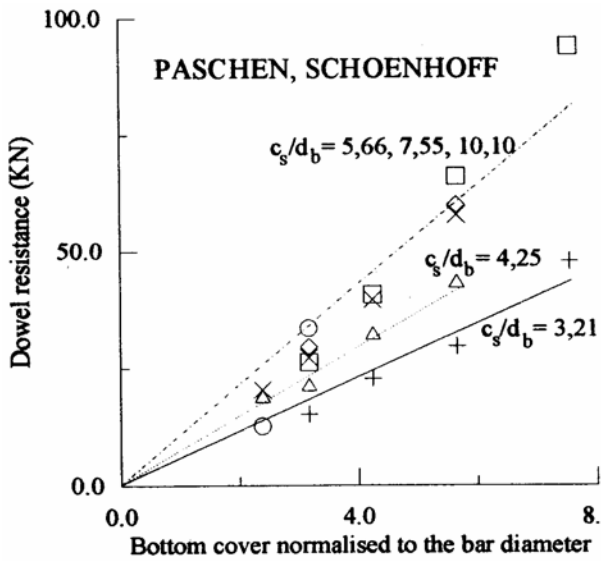
Figure 2.34: The effect of bottom and side cover on the dowel resistance (Paschen, Schönhoff, [45]).

Figure 2.35 shows an evaluation of the test results by Vintizleou and Tassios [49], which allows for the effect of side cover to be illustrated. It may be observed that (for each top cover value) there is a linear increase of the dowel resistance for increasing side cover.
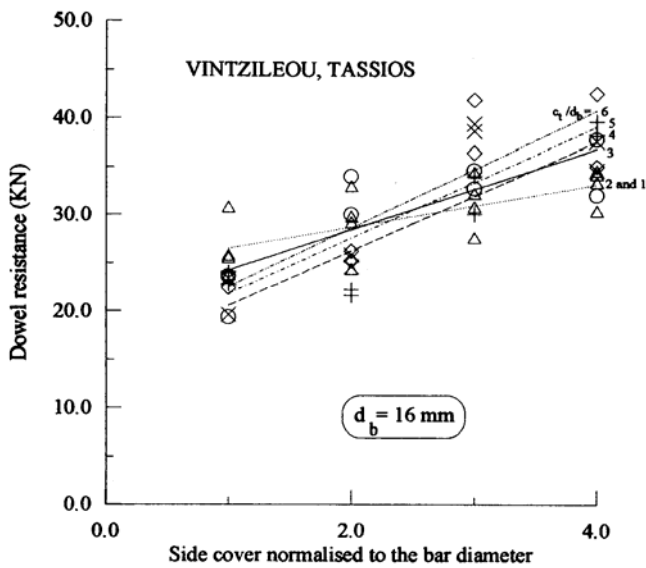
Figure 2.35: The effect of side cover on the dowel resistance (Vintzileou, Tassios, [49]).

42

The Effect of Bar Spacing in-Section.

The failure mode, as well as the magnitude of the dowel resistance are expected to be influenced by the in-section spacing of dowels. Nevertheless, this is a parameter which was not systematically investigated by the numerous researchers who studied the dowel mechanism. In many cases, isolated dowels embedded in concrete blocks were tested. In other cases, even when large concrete blocks with a series of embedded dowels are provided, the dowels are tested one by one (see for example Utescher and Herrmann (1983) [47]), whereas care is taken to have large spacings, in order to avoid any interaction between consecutive dowels. Finally, in beam tests (see, for example, Taylor (1974) [13], Fenwick et al.(1968) [15]), where two or more dowels were simultaneously tested, their spacing was kept constant throughout the program, thus not allowing the effect of this parameter to be evaluated. Baumann and Rüsch (1970) [38], in their research about the dowel action of longitudinal reinforcement in beams, have investigated also the effect of the width of beams.

Based on this study, one may say that, in general, the available experimental evidence on this parameter is not conclusive, although it is reasonably expected that small in-section spacing of dowels lead to premature splitting of the concrete and failure of the mechanism.

Size Effects related to the Fracture Characteristics of Concrete.

Since the failure of the dowel mechanism is due either to splitting or to crushing of the concrete, the dowel resistance is expected to be influenced by the same size effects which affect these two characteristics of the concrete. Nevertheless, in the literature there is no information about tests on dowel action carried out on purpose. However, some researchers (see, for example, Reineck (1990) [37] or Vintzileou and Tassios (1987) [50]), in their effort to develop models for the prediction of the dowel resistance when failure is due to splitting, have taken into account the fracture characteristics of concrete. In Figure 2.36 the equations derived for the calculation of D_u are given, together with a comparison of the predicted dowel resistances with those obtained experimentally by various researchers. It seems that this comparison is quite satisfactory.

43
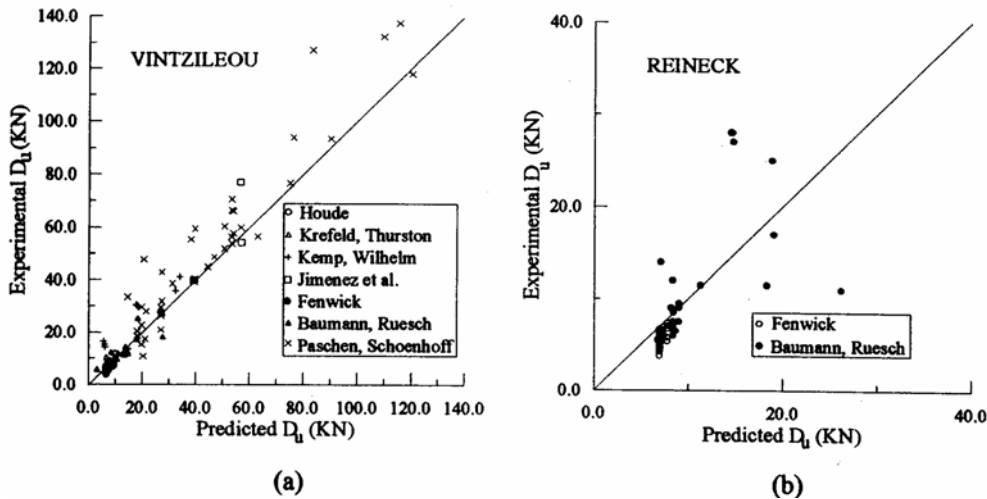
Figure 2.36: Comparison between experimental and predicted values of dowel resistances for failure mode I: (a) Vintzileou [30], (b) Reineck [37].

2.2.2.4 Residual Tensile Stresses across Cracks.

The basic explanation of residual tensile stresses is that when concrete first cracks, a "clean break" does not occur. Small pieces of concrete bridge the crack and continue to transmit tensile force up to crack widths in the range of 0.05-0.15 mm. The fact that there is a significant descending (softening) branch after the peak tensile stress is reached has been known for some time (Evans and Marathe 1968 [51]); however, methods for the reliable measurement of the softening branch have only recently been developed (Gopalaratnam and Shah 1985 [52]; Reinhardt et al. 1986 [53]). Figure 2.37 shows a typical response of concrete loaded in tension. The deformations are localized in a very small region (the fracture process zone); therefore, the response must be expressed in terms of a stress-crack opening relationship and not strain (Evans and Marathe 1968 [51]; Gopalaratnam and Shah 1985 [52]; Reinhardt et al. 1986 [53]; ACI Committee 446 1989 [54]).

The application of fracture mechanics (ACI Committee 446 1989 [54]) to shear design is based on the premise that residual tensile stress is the primary shear transfer mechanism. Other methods consider the contribution from residual tensile stresses such as Reineck's tooth model (1991 [14]), which indicates that residual tensile stresses provide a significant portion of the shear resistance of very shallow members (that is, depths less than about 100 mm) where the width of flexural and diagonal cracks are small (Reineck 1991 [55]).
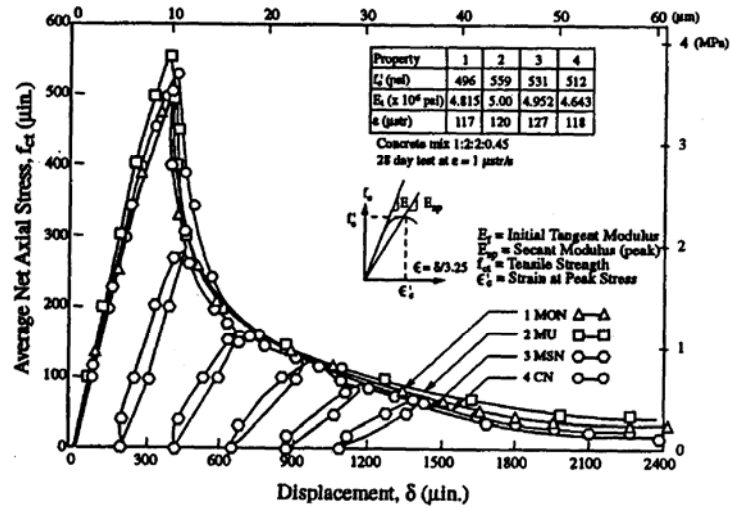
Figure 2.37: Response of plain concrete loaded in uniaxial tension (Gopalaratnam and Shah, [52]).

2.3 "Beam Action" and "Arch Action".

The moment of resistance of a beam can be expressed as:

$$M = x \cdot V = jd \cdot (T + V_d \cdot \cot \alpha)$$ (2.18)

Where V_d is the dowel force transmitted across the crack by the flexural reinforcement, T is the tensile force resisted by the longitudinal reinforcement, jd is the lever arm and α is the angle of the strut with respect to the horizontal (see Figure 2.38). if the contribution of the dowel force toward flexural resistance is ignored (a justifiable step for design purposes, particularly in the absence of stirrups), the moment of resistance simplifies to:

$$M = x \cdot V = T \cdot jd$$ (2.19)

Combining Equation (2.19) with the well known relationship between shear and rate of change of bending moment along a beam, the following modes of internal shear resistance result:

$$V = \frac{dM}{dx} = \frac{d}{dx}(T \cdot jd) = jd \cdot \frac{dT}{dx} + T \cdot \frac{d(jd)}{dx}$$ (2.20)
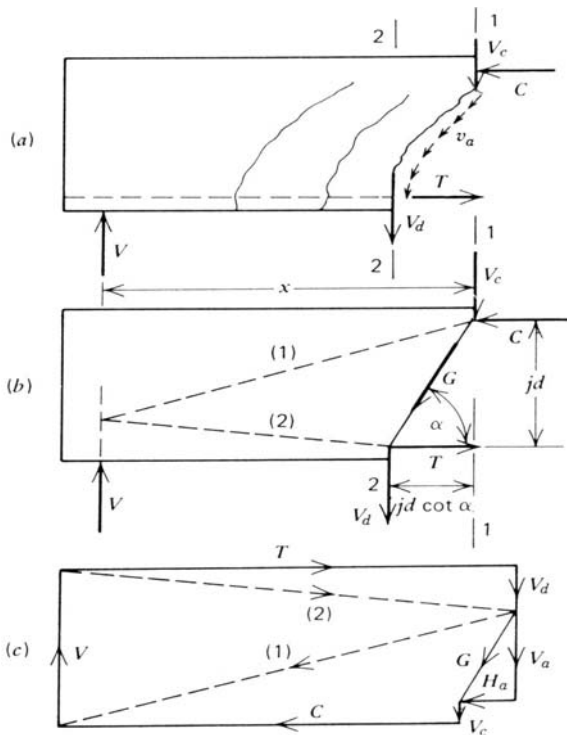
Figure 2.38: Equilibrium requirements in the shear span of a beam [1].

The term *jd/(dT/dx)* expresses the behavior of a true prismatic flexural member in which the internal tensile force *T* acting on a constant lever arm *jd* changes from point to point along the beam, to balance exactly the external moment intensity. The term *dT/dx*, the rate of the change of the internal tension force, is termed the bond force, *q*, applied to the flexural reinforcement per unit length of the beam (see Figure 2.4). Should the internal lever arm remain constant (a normally accepted assumption of the elastic theory analysis of prismatic flexural members) so that *d(jd)/dx=0*, the equation of perfect "beam action" is obtained thus:

$$V = jd \cdot \frac{dT}{dx} = q \cdot jd \qquad\qquad (2.21)$$

The same result was obtained in Equation (2.7), where *q*, the bond force per unit length of the member, at a location immediately above the flexural reinforcement level, was termed shear flow. It is evident that such simplification of behavior is possible only if the shear flow or bond force can be efficiently transferred between the flexural reinforcement and the surrounding concrete. It gives thus rise to the phenomenon of bond.

46

When, for any reason, the bond between steel and concrete is destroyed over the entire length of the shear span, the tensile force T can not change, hence $dT/dx=0$. Under these circumstances the external shear can be resisted only by inclined internal compression. This extreme case may be termed "arch action". Its shear resistance is expressed by the second term on the right-hand side of Equation (2.20), namely:

$$V = T \cdot \frac{d(jd)}{dx} = C \cdot \frac{d(jd)}{dx}$$

(2.22)

Here the internal tension T is replaced by the internal compression force C, to signify that it is the vertical component of a compression force, with constant slope, which balances the external shear force.

In a normal reinforced concrete beam in which (owing to slip, cracking and other causes) the full bond force q required for beam action can not be developed, the two mechanisms, as expressed in Equation (2.20), will offer a combined resistance against shear forces. The extent to which each mechanism contributes to shear resistance at various levels of external load intensity will depend on the compatibility of deformations associated with these actions.

2.3.1   Beam Action.

Cracks induced by load on a simply supported beam divide the tension zone into a number of blocks (see Figure 2.7). each of these blocks may be considered to act as a cantilever with its base at the compression zone of the concrete and its free end just beyond the flexural tension reinforcement. Those blocks will be referred as "concrete cantilevers". On each cantilever, the shear mechanisms reported in Section 2.2.2 will act. Diffuse discussion about that was also provided there.

Starting from the equilibrium in the shear span of a beam (Figure 2.38) it can be seen that the external force V is resisted by the combination of shear force in the compressive zone V_c, the vertical components due to interface V_a and the dowel force V_d. By simplifying the shear stresses transmitted by interlocking of the aggregates as a single force acting in a diagonal direction (Figure 2.38b) the equilibrium can be described by:

$V = V_c + V_a + V_d$

(2.23)

Furthermore, to prevent shear failure, the external moment (given as $M = Vx$) has to be resisted by the internal moment (commonly expressed as $M=jdT$; therefore the

contribution of the dowel force is neglected). By using this moment relationship and assuming a constant internal lever arm, the equation of beam action is obtained as

$$V = qjd \quad \text{and} \quad q = T/x \tag{2.24}$$

As we saw in Equation (2.24) the full bond force q must be resisted so that a perfect beam action takes place. Some explanations regarding the components of the cantilever action (Figure 2.7) are subsequently given. The bond force ($\Delta T = T1 - T2$) is produced by an increase of the tensile force in the flexural reinforcement between the cracks. At the two planes of the crack, shear displacements will occur owing to the shear stresses v_{a1} and v_{a2} which are generated by means of aggregate interlocking. Across the flexural reinforcement the dowel forces V_{d1} and V_{d2} may also induced by these shear displacements. At the end of the uncracked concrete zone, an axial force P, a transverse shearing force V_h, and a moment M_c are induced to equilibrate the abovementioned forces on the cantilever. The resistance of a concrete beam depends largely on the actions of P, V_h, and M_c often quite small, particularly at advanced stages of cracking (Leonhardt 1965) [56].

2.3.2   Arch Action.

The second term of Equation (2.20) signifies that shear can be sustained by inclined compression in beams, as shown in Figure 2.39.

The effect of arch action in the shear span has been investigated by many researchers (Fenwick and Paulay, 1968 [15]). Whenever in a concrete beam an arch action will be developed, a substantial horizontal reaction at the support is required, which in simply supported beams is provided by the flexural reinforcement. This imposes heavy demands on the anchorages, and indeed it accounts for the most common type of arch failure. Figure 2.39 illustrates the arch action taking place in an idealized beam, where full anchorage is assumed: in the bottom reinforcement a constant tensile force can be therefore developed over the full length. A compressed concrete area will thus be formed surrounded by cracks (see shaded area in Figure 2.39).

It was also found, by researchers above mentioned, that arch action can only occur for large values of slip (i.e., of complete loss of bond transfer); however, in actual beams, particularly when rebars are used, no appreciable slip takes place between steel and concrete. Also the translational displacements required for complete arch action increase toward the load point and attain a value approximately equal to the total extension of the steel in the shear span (Figure 2.39). In addition, in the vicinity

of the load point, the line of thrust (hence the neutral axis) rises well above the position predicted by standard flexural theory.
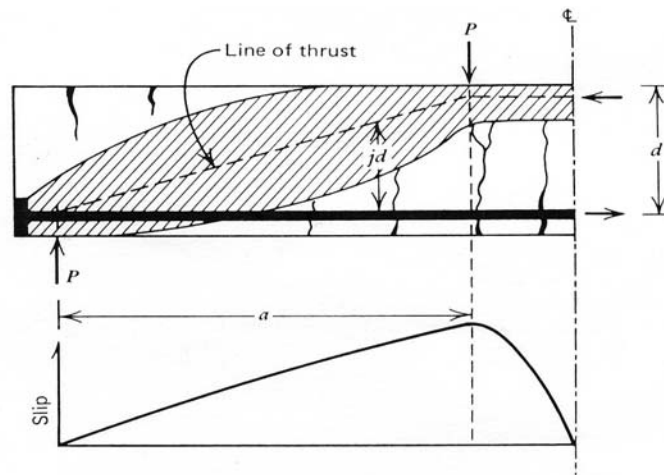
Figure 2.39: Slip associated with arch action in an idealized beam [1].

The available strength from arch action is strongly dependent on the inclination of the line of thrust. The shear span to dept ratio (a/d), which is also equal to *M/Vd*, is a measure of this inclination. Therefore, arch action must be the dominant mode of shear resistance in deep beams.

Excluding loss of anchorages, arch failures may be placed in three groups:

- After the failure of the beam action, the propagation of an inclined crack reduces the compression zone excessively. A slope is reached when the available area of concrete in the vicinity of the load point becomes too small to resist the compression force and it crushes. This is known as a "shear compression" failure.

- The line of thrust may be so eccentric that a flexural tension failure occurs in the compression zone. The failure is very sudden.

- When the line of thrust is steeper (i.e., when a/d is less than 2), considerable reserve strength may be available owing to more efficient arch action. Failure may eventually be due to diagonal compression crushing or splitting, which can be likened to a transverse splitting test performed on a standard concrete cylinder. Frequently the flexural capacity of a beam is attained because the arch mechanism is sufficient to sustain the requires shear force.

Furthermore, it is important to note that arch action in beams without web reinforcement can occur only if loads are applied to the compression zone of the

49

beam. It is evident in fact that effective arch action can not develop in a beam when the external shear force is transmitted to the tension zone. Precautionary measures for such situations should be carefully considered.

2.3.2.1 Extent of the Arch Action Zone in a Beam.

To assess the extent to which arch action may develop simultaneously with beam action the deformations induced must be examined [15].

When arch action acts over the shear span of a beam, the Navier-Bernoulii hypothesis of plane sections remaining plane is no longer valid. Figure 2.40 illustrates a beam where the reinforcement is not bonded to the concrete, but full anchorage is provided by means of a plate at the support. The line of thrust becomes inclined as the load is applied: the diamond shaped block results to be subjected to compression stresses. Concrete is also assumed unable to resist any tensile stress. On the basis of elastic behavior, it can be shown that there is one unique line of thrust which satisfies the compatibility requirement for this beam, namely, the elongation of the reinforcement between anchorages must equal the elongation of the concrete fiber situated at the same level.
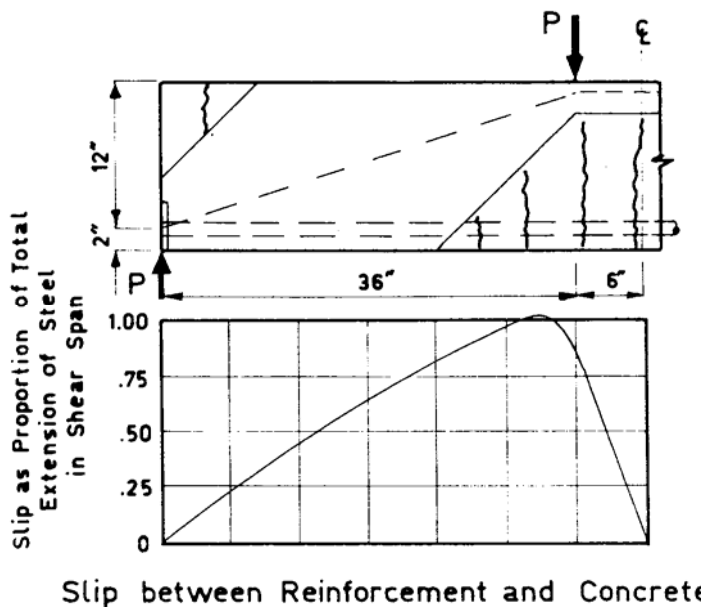
Figure 2.40: Arch action in beam without bond [15].

Where the concrete surrounding the steel is cracked, the elongation is determined by extrapolating the strains from the compression zone of the beam. After the thrust

line is found, the relative movement between compressed concrete and the reinforcement can be determined. The movement, which will be referred to as a translational displacement, occurs in this case as a frictionless slip between concrete and steel, with a distribution depicted in Figure 2.40, as a proportion of the total elongation of the steel.

To assess the distribution and absolute magnitude of such translational displacements, extensive strain measurements were made on the side of several beams, illustrated in Figure 2.41.
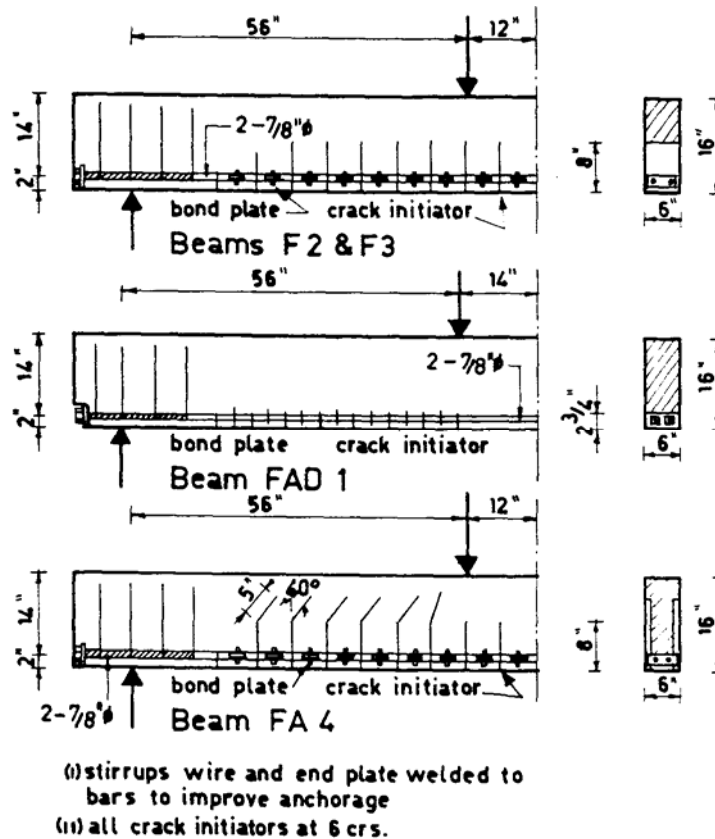
Figure 2.41: Details of the beams tested [15].

These measurements also yielded the strains along the reinforcement from which the bond forces sustained by the cantilever could be found. Thus the extent of shear resistance by arching could be assessed by defining an arching index as follows:

$$\text{Arching Index} = \frac{v - v_t}{v} \tag{2.25}$$

in which $v = V/(b \, j \, d)$ is the nominal shearing stress, and v_t is the average horizontal stress in the tension zone of a beam. This was found in the test beam from the bond forces which acted on the concrete cantilevers. An arching index equal to *1* would indicate that the whole external shear is resisted by arch action. The variation of this index for various load increments of three different beams is also shown in Figure 2.42.
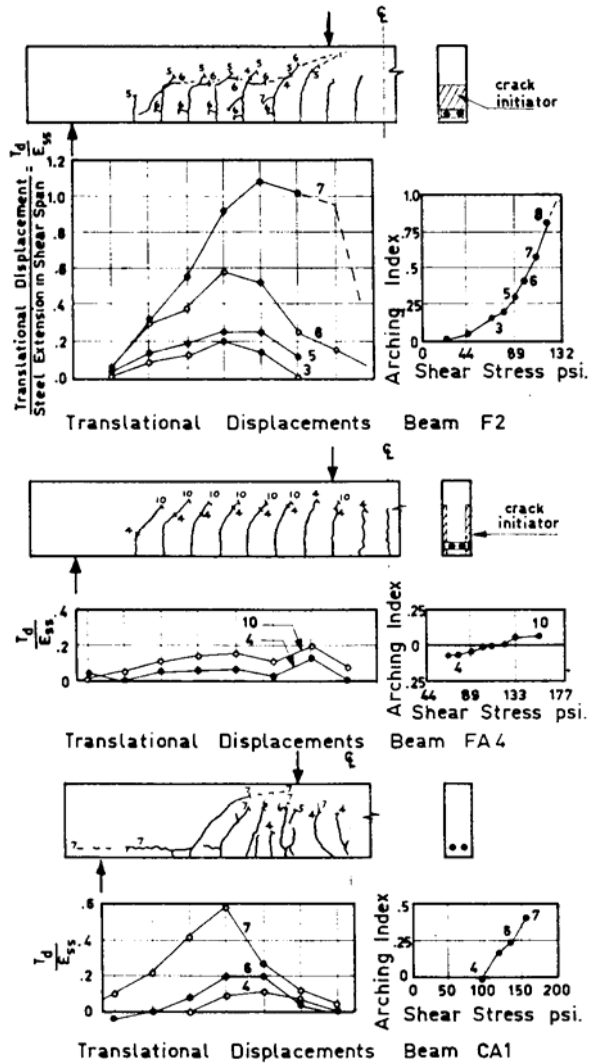
Figure 2.42: Transaltional displacements and arching indexes for test beams [15].

Gage points covered at least half of the symmetrically loaded beams. From these measurements the relative movement of any line of gage points across the beam with respect to the axis of symmetry could be calculated, and consequently the translational displacements could be determined. Figure 2.42 summarizes the test results.

The behavior of beam F2 turned out to be of particular interest. In this beam aggregate interlock and dowel action were eliminated by means of preformed cracks and foam covered bars. At the sixth load increment the diagonal cracks narrowed the depth of the cantilevers at their base so that their resistance against an applied bond force was considerably reduced. The large flexural deformations of the cantilevers resulted in correspondingly large translational displacements. Such displacements could occur in this beam owing to the unusual crack shape determined by the crack initiators. At this stage some 50% of the shear was resisted by arch action. At the next increment most of the bond force sustained by the reduced dowel action had also vanished as a result of the diagonal dowel crack, marked 7, which developed in the cantilevers. Note that the distribution of measured translational displacements at this stage is similar to that obtained from theoretical considerations for the model beam of Figure 2.40.

With respect to beam FA4, in contrast to beam F2, the cracks were partially initiated but not performed (see Figure 2.41). Consequently in this beam aggregate interlock action could contribute towards beam action to a much greater extent. The resulting small translational displacements (Figure 2.42) originated mainly from the bending of the compression zone of the beam above each crack.

The behavior of the third beam CA1, also illustrated in Figure 2.42, evidences that aggregate interlock and dowel action could freely develop in this beam in which cracks formed at random as no initiators were used. The only interference, that may have occurred, was because of the small holes through which welded studs projected from the reinforcement and on which strain measurements were made.

By comparing the results of those three tests, it was possible to note that:

- The magnitude of the arch action in the shear spans, as measured by the arching index, increased with the increase of translational displacement;

- The distribution of translational displacements shows the same pattern which was obtained for a beam with unbonded reinforcement (Figure 2.39);

- Significant translational displacements are confined to those regions of a beam which contain extensive diagonal and horizontal cracks.

- With the formation of wide diagonal cracks in the shear span appreciable arch action occurs. The crack nearest to the support of beam CA1 is a good example

53

of this. The width of this crack, which also happens to be the translational displacement at this point, was 40% of the total measured extension of the reinforcement over the length of the shear span.

A further significant key parameter that characterizes arch behavior is the typology of loading applied on the beam. Figure 2.43 shows a typical pattern of the arch in presence of four point loading set-up or of a uniformly loaded beam [57].
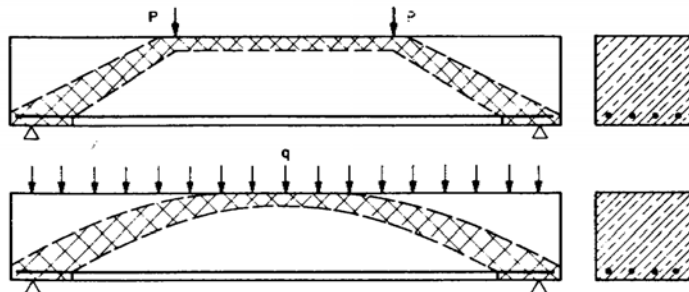
Figure 2.43: Different arch development for two point loaded beam and uniformly distributed loaded beam.

2.4 Members with Transverse Reinforcement.

An old concept to describe the mechanism of shear transfer in concrete structures with transverse reinforcement is the so called truss mechanism, which was already mentioned by Ritter and Mörsch at the beginning of the last century (Ritter 1899 [58], Mörsch 1909 [5]). It is assumed that the shear resistance is related to an analogy between the parallel chord truss and the web-reinforced concrete beam. In this model the web consists of a compression strut, formed by the concrete running parallel to the diagonal cracks (at 45° to the beam's longitudinal axis, in the original formulation of the model) and a tension strut that consists in web reinforcement, usually stirrups.
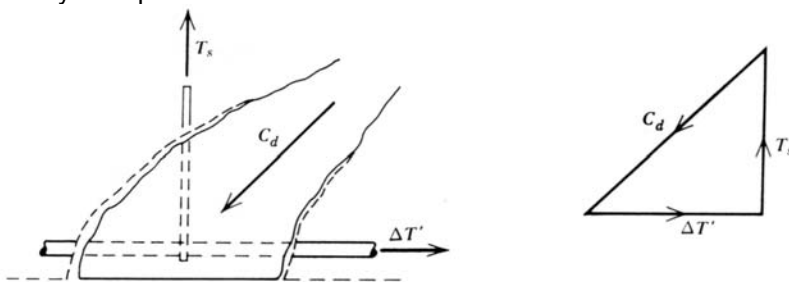
Figure 2.44: Concrete cantilever acting as truss.

The top and the bottom chords are formed by the flexural concrete compressive zone and the flexural reinforcement, respectively. By applying this model the mechanism of shear transfer for members without transverse reinforcement does not change fundamentally. As it can be seen in Figure 2.44, the concrete cantilever will act as tied cantilever. Noticeable is the already mentioned compressive strut which sustains a force C_d and the tension strut formed by the stirrup that sustains a force T_s. In addition, stirrups contribute to the strength of the shear mechanism by improving the dowel action because the flexural reinforcement will be supported by the stirrups. Stirrups limit also the opening of the diagonal cracks, thus the shear transfer by shear interface and residual tensile stresses enhances and prevents a breakdown of bond when splitting cracks develop in the anchorage zone.

The general understanding of the truss mechanism is shown in Figure 2.45 where the web reinforcement is inclined at an angle β to the horizontal axis and α is taken as a general angle of inclination of the concrete strut. The external shear force V_s will be resisted by the truss. Therefore it can be seen that:

$$V_s = C_d \, sin\alpha = T_s \, sin \, \beta \tag{2.26}$$

where T_s is the resultant of all stirrup forces across the diagonal crack. With T_s/s we can describe the web steel force per unit length and the spacing between stirrups can be seen as:

$$s = jd(cot \, \alpha + cot \, \beta) \tag{2.27}$$
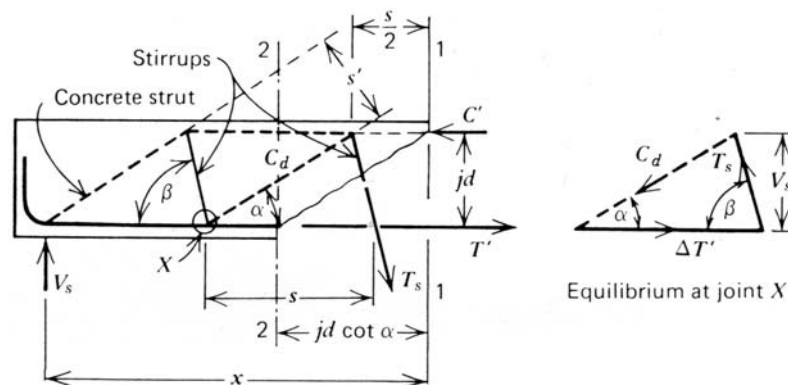
Figure 2.45: Internal forces in an analogous truss.

Therefore the stirrup force per unit length is given by:

55

$$\frac{T_s}{s} = \frac{V_s}{jd \sin \beta \, (\cot \alpha + \cot \beta)} = \frac{A_v f_s}{s} \tag{2.28}$$

where A_v is the area of the web reinforcement spaced at a distance s along the beam and f_s is the stirrup stress. By expressing the shear in terms of nominal stresses the following relation can be expressed:

$v_u = v_c + v_s$ (2.29)

with:

$$v_s = \frac{V_s}{b_w jd} \approx \frac{V_s}{b_w d} \tag{2.30}$$

V_s is the shear resisted by the truss mechanism. The required area of web reinforcement (with $f_s = f_y$) becomes:

$$A_v = \frac{v_s}{\sin \beta \, (\cot \alpha + \cot \beta)} = \frac{s b_w}{f_y} \tag{2.31}$$

The diagonal compression stresses due to the truss mechanism can be determined as:

$$f_{cd} = \frac{C_d}{b_w s'} = \frac{V_s}{b_w jd \sin^2 \alpha \, (\cot \alpha + \cot \beta)} = \frac{v_s}{\sin^2 \alpha \, (\cot \alpha + \cot \beta)} \tag{2.32}$$

Traditionally the slope of the compression diagonals has been assumed to be 45° to the beam axis but in experimental studies (Kupfer and Baumann 1969 [59]) it was detected that the slope of the diagonal cracks varies along the beam and that an optimum angle of the struts is about 38°. In beams having a high concrete strength and low web reinforcement content, the angle of the compressive strut is less than 45°, hence the stirrups are more effective than in a 45° truss. Steep stirrups and flat diagonal compression struts imply larger concrete compression stresses. Therefore, the web steel content can not be increased indefinitely as that would led to a web crushing caused by diagonal compression. Furthermore, it should be observed that the diagonal struts, if participating in a beam action, are subjected to bending moments. The compression forces are not evenly distributed across the web so that transverse tensile stresses and eccentricities may be present. It can be seen that a limit of the diagonal concrete stresses has to be set below the crushing strength of concrete. For that reason the current provisions limit the contribution of the truss mechanism to shear strength by using a factor and the function $(f'_c)^{1/2}$ (Kupfer et al. 1983 [60], Vecchio and Collins 1986 [23]).

56

A stirrup must be able to develop its yield strength over the full extent of its length; hence it has to be anchored adequately. Usually they are bent around larger longitudinal bars. A truss mechanism in beams can function only after the formation of diagonal cracks. The prime role of stirrups is transferring the transverse shear across a potential diagonal failure crack.

2.5   Parameters influencing the Shear Capacity.

2.5.1   Shear Span-to-Depth Ratio (a/d).

As members become deeper (a/d ratio decreases below 2.5) the average shear stress at failure becomes progressively larger than in slender beams, because in deeper members it is easier for shear to be transmitted directly to the support by means of compression struts. The conditions on the supports are therefore important if a direct compression strut will be formed. If a member is loaded on the top face and supported on the bottom face it is more likely to form such a strut (Adebar 1994 [61]).

Members in which a direct compression strut is likely to form should be designed using the strut-and-tie model approach, rather than a sectional design procedure. Collins and Mitchell (1991 [2]) demonstrated how the two methods can be combined to predict the strength of beams without stirrups over a wide range of shear span-to-depth ratios, as shown in Figure 2.46 (the analytical predictions are based on the Canadian Code, CSA A 23.3 M94, see Section 2.7.3).

In the simple strut-and-tie approach, it is assumed that all of the shear will be transmitted by compressive stresses, which suggests anyhow that there will not be a size effect for such members. Thus, refined strut-and-tie models that consider concrete tensile stresses should be used to design deep members, unless minimum distributed longitudinal and transverse reinforcement is provided.

Furthermore, the *a/d* ratio is used to describe a shear failure mechanism of simply supported, plain concrete beams, loaded with point loads. That was the result that Leonhardt and Walter (1966 [62]) observed after testing beams cast with normal strength concrete. It will be distinguished among three types of failure:

- when 3 < *a/d* < 7, failure of the beam mechanism at or shortly after the application of the diagonal cracking load.
- when 2 < *a/d* < 3, a shear compression or flexural tension failure of the compressive zone above diagonal cracking load will appear.
- when *a/d* < 2.5, a failure by crushing or splitting of the concrete will appear.
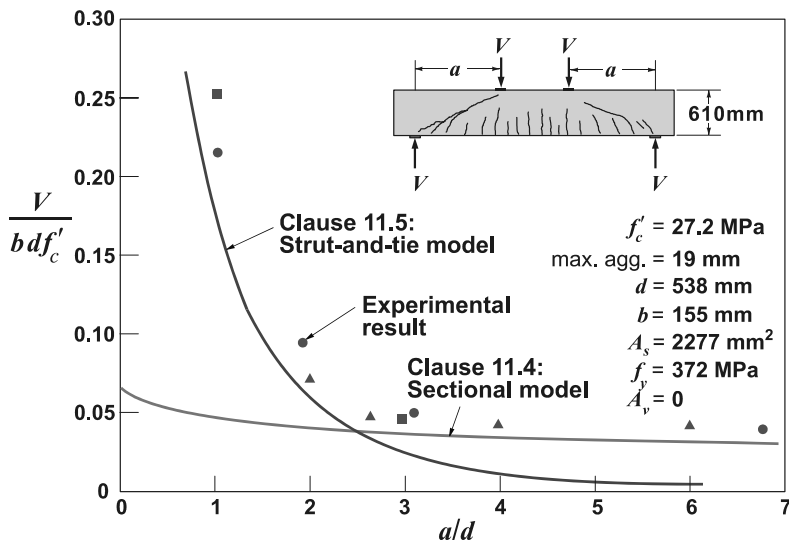
Figure 2.46: Use of strut-and-tie model and sectional models to predict the strength of a series of beams [2].

The failure moments and the ultimate shear forces are plotted against the shear span-to-depth ratio in Figure 2.47. The dashed lines in Figure 2.47 depict the flexural and shear capacities of "beam action" while the discrepancy between the theoretical flexural capacity and the observed shear strength of these beams is indicated by the shadow area.
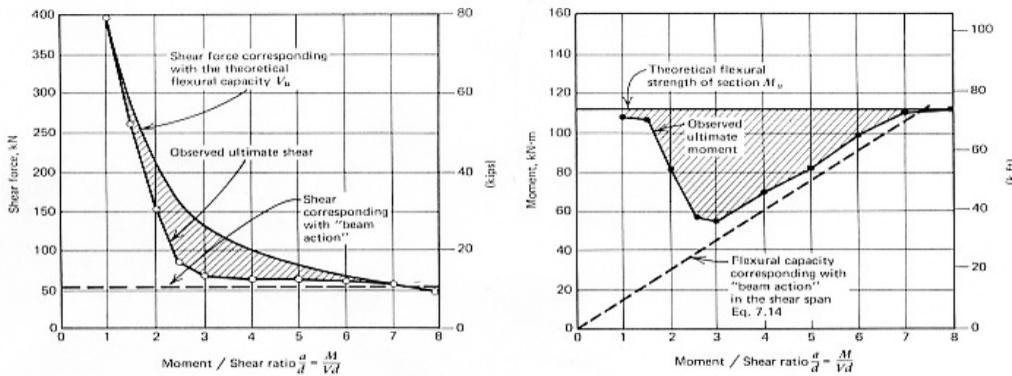
Figure 2.47: Moments and shears at failure plotted against a/d ratio [1].

In 1966, G.N.J. Kani (1964 and 1966, [63] and [64]) conducted a series of 133 experiments on beams at the University of Toronto, Canada. All beams were simply supported and symmetrically loaded in two points, had identical cross section (h = *305 mm and b = 152 mm*) and no transverse reinforcement. The experimental

campaign was conducted to establish not only the influence of the a/d ratio, but even that of the concrete compressive strength (choosing f'_c *of 18 MPa, 26 MPa and 35 MPa*) and the steel percentage ρ (choosing *ρ = 0.5%; 0.8%; 1.88%; 2.8%*). Figure 2.48 presents the test results of four beam series having four different percentages of main reinforcement and shows v_u versus *a/d*. For all four series *f'_c = 26 MPa* is plotted. The values of v_u for *a/d=1.0* are up to 700 % higher than the corresponding values for *a/d=5.0*. In addition to this big difference, a change from ρ = 0.80% to ρ = 2.80% produced a further increase of v_u, of about 100%.

Initially, it was believed, particularly by Mörsch, that v_u was a property constant of concrete and dependent solely on the concrete strength. Therefore v_u was chosen as an indicator of the so-called shear failure. An allowable constant shear stress, depending only on f'_c, is still the accepted basis in most of the building codes. These tests demonstrated however that v_u, for heavily-reinforced short beams, was about 15 times greater than for long beams with a low percentage of reinforcement, although the concrete strength remained constant. v_u is therefore far form being a constant quantity.
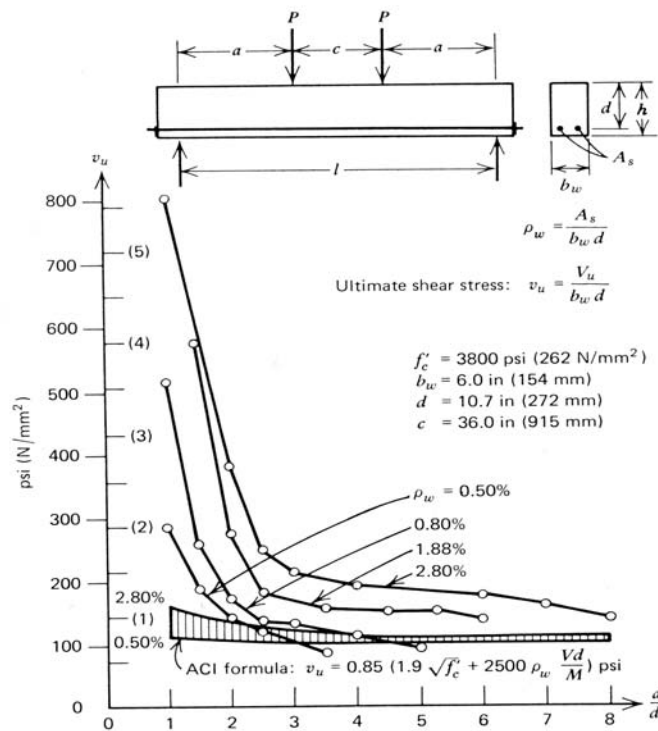
Figure 2.48: Shear stress at failure as a function of the shear span to depth ratio. [1]

The results of all series of beams are plotted in Figure 2.49, Figure 2.50 and Figure 2.51.
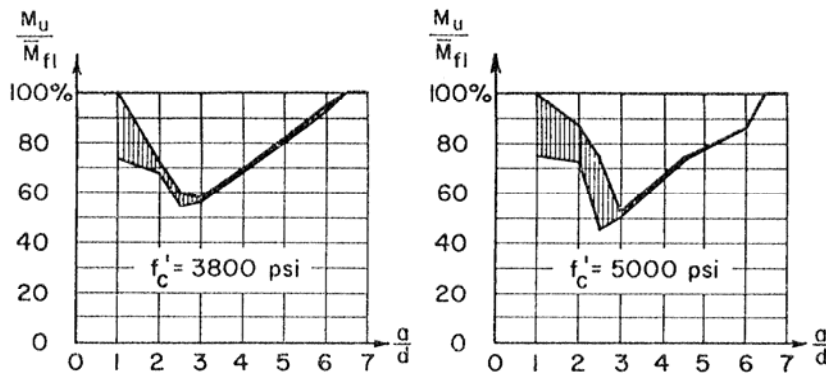
Figure 2.49: Influence of the basic parameters, f'$_c$ and a/d, on the relative beam strength, ρ = 2.80% [64].

Figure 2.49 presents the characteristic variation of beam strength versus *a/d* for the beam series with the highest percentage of reinforcement. At *a/d=1.0*, either full flexural failure was attained with a relative strength of about 100% or, due to high compression in the vicinity of the support, a web compression failure destroyed the beam. With increasing of value of *a/d*, the beam strength decreased and was governed by its diagonal failure capacity, which was as low as 51% of the calculated flexural moment. At *a/d=6.5*, the beam again attained full flexural strength. Between the two high points, *a/d=1.0* and *a/d=6.5*, a *"valley of diagonal failure"* of reduced strength is observed whereas, outside of this region, failure occurs only after the flexural capacity of the cross section has been reached. The two laws governing the strength of a beam for a/d less than 2.5 and for a/d greater than 2.5 are totally different and especially unrelated.

Compressive destruction of the concrete in the vicinity of the supports, which is often observed in T-Beams, was absent in all specimens of the 11 tests series of beams with rectangular cross section except for two beams with ρ = *2.80%* and *a/d=1.0* which had the highest reaction forces at the supports.

Figure 2.50 illustrates the strength diagrams of all the others series.

The behavior exhibited by the first series (Figure 2.50a, ρ = *1.88%*) was essentially the same as the beams with ρ = *2.80%*. However, a shift in the transition point, *T*, from *a/d=6.5* (from the ρ = *2.80%* series), to a lower *a/d=5.5, (*for ρ = *1.88%*) has been observed. This trend was even more obvious for the ρ = *0.80%* series (Figure 2.50b) where the *"valley of diagonal failure"* is greatly reduced to the region of

a/d=1.5 to *a/d=3.5* and the minimum point, which appears here at *a/d=2.5* is not lower than 84% of the maximum calculated flexural load.
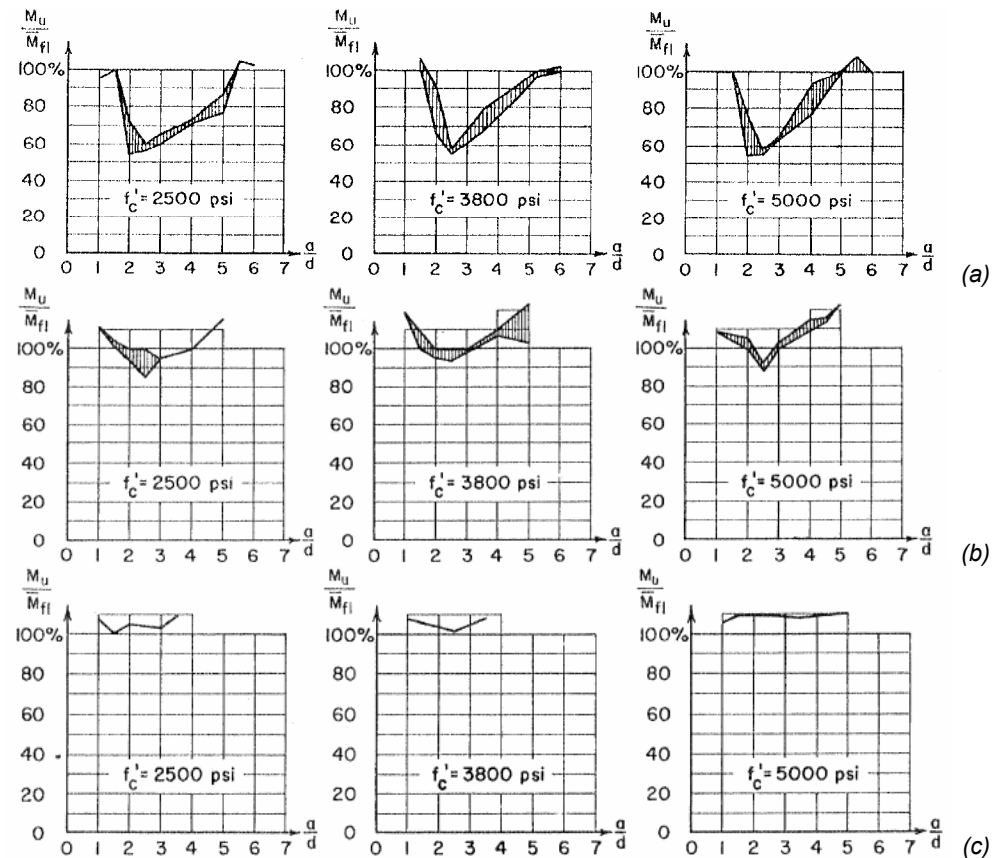
Figure 2.50: Influence of the basic parameters, f'$_c$ and a/d, on the relative beam strength, (a) ρ = 1.88%, (b) ρ = 0.80%, (c) ρ = 0.50% [64].

For the three beams with the lowest steel amount (*ρ = 0.50%*, see Figure 2.50c), the *"valley of diagonal failure"* disappeared completely. In every case, the relative beam strength was 100% or more of the maximum calculated bending capacity of the member.

The region of diagonal failure may be clearly visualized in a three-dimensional coordinate system, with axes *a/d*, *ρ* and *M$_u$/M$_{fl}$*, where the first is *V$_u$d* while the latter is the ultimate moment assumed, as shown in Figure 2.51, in the case of *f'$_c$=26 MPa*. With increasing values of *ρ*, the *"valley of diagonal failure"* deepens rapidly, with its range always limited by the two characteristics boundary points *D* and *T*. if

61

the a/d axis is considered, it can be seen that the reduced beam strength, due to shear failure, occurs only between *a/d=D*, which is nearly a constant equal to 1, and the transition point *T*, which varies with ρ. Therefore all the considerations of web reinforcement should be limited to this region.

Contrary to initial expectations, Kani clearly stated that the shear strength v_u is very remote from being a constant characteristic of a particular grade of concrete. This was a great step toward an adequate understanding of shear in reinforced concrete structures.
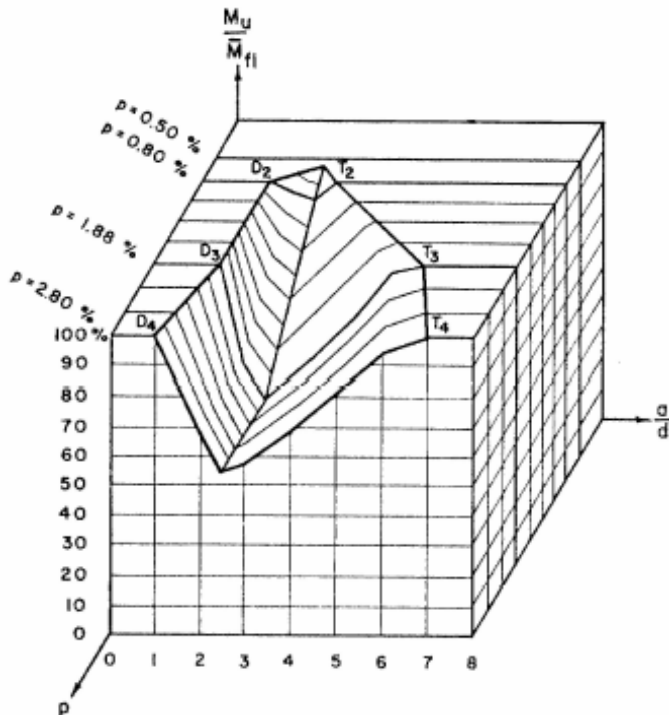
Figure 2.51: Influence of the parameters ρ and a/d for f'$_c$=26 MPa [64].

2.5.2   Depth of Members or Size Effect.

In the last decades many tests on the shear behavior have been carried out on relatively small beams. It was found that the results of these tests can not be directly applied to full size beams. It was shown by Kani (1967 [65]) that there is a very significant size effect on the shear strength of members without transverse reinforcement. The shear strength of these members appears to decrease as the effective depth increases. Shioya et al. (1989 [66]) reaffirmed this fact and extended the available data to beam with depths up to 3000 mm. Figure 2.52 shows that the

average shear stress to cause failure of the largest beam was about one-third the average shear stress to cause failure of the smallest beam.

There is a general agreement that the main reason for this size effect is the larger diagonal crack width that occurs in larger beams. On the other hand there is a disagreement on how to model this phenomenon best.
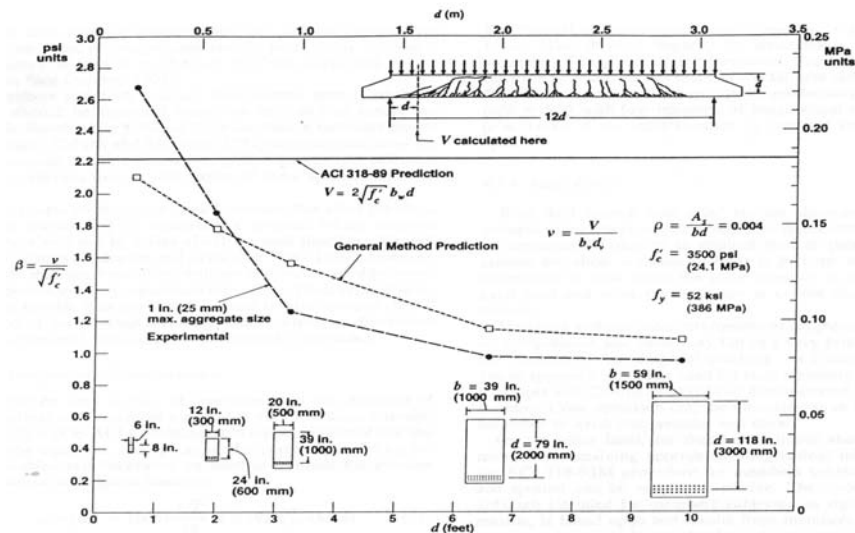
Figure 2.52: Comparison of large Scale Beam Tests by Shioya et al. with predictions from ACI Code and Modified Compression Field Theory (MCFT) [3].

A different approach was proposed by Bažant and Kim (1984 [9]), who stated that the most important consequence of wider cracks is the reduced residual tensile stress and aggregate interlock. Most of current formulas for predicting shear capacity of a member are in fact based on the concept of tensile strength. However, this concept is theoretically justified only in the case of ductile failures governed by the theory of plasticity. For failures in which the stress decreases after reaching the strength limit, as in the case for tensile cracking, the strength concept is inconsistent when applied in a continuum analysis. However, new approaches do not treat fracture like a point phenomenon, but recognizes that in brittle heterogeneous materials such as concrete, the fracture propagates with a relatively large fracture process zone in which progressive microcracking gradually reduces the tensile stress to zero. The authors investigated than the consequences of this nonlinear fracture mechanics approach for diagonal shear failure and proposed a size reduction factor for shear members as follows:

$$\sigma_N = f'_t \cdot \phi(\lambda); \quad \phi(\lambda) = \frac{1}{\sqrt{1 + \dfrac{\lambda}{\lambda_0}}} \quad \lambda = \frac{d}{d_0}$$

<div align="right">(2.33)</div>

In which d_0 is the maximum aggregate size, λ is a relative structure size, and λ_o is an empirical constant. For structures of a small size relatively to the size of the aggregate (i.e., for small λ), the value of λ/λ_0 in Equation (2.33) may be neglected in comparison to unity, and then we have $\varphi(\lambda)=1$ and $\sigma_N=f'_t=constant$. This indicates that the strength criterion (horizontal line in Figure 2.53) is correct for small size structures, which happens to be the case for most structures tested in laboratories. For structures of a very large size compared to the size of aggregate, *1* may be neglected in comparison with λ/λ_0 in Equation (2.33), and then $\sigma_N=f'_t(\lambda/\lambda_o)^{-1/2}$, which is the size effect of linear elastic fracture mechanics described by the inclined straight line in Figure 2.53. Obviously, Equation (2.33) represents a gradual transition from the strength criterion for small structures to the linear elastic fracture mechanics for very large structures. For $\lambda<\lambda_0$ the strength criterion dominates while for $\lambda>\lambda_0$ the fracture mechanics aspect of failure dominates.
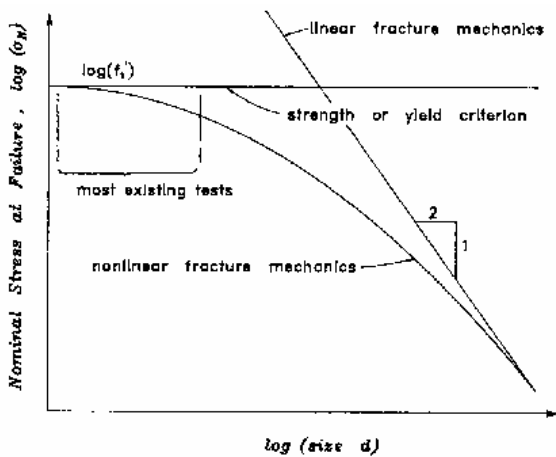
Figure 2.53: Size effect phenomenon [9].

Bažant and Cao (1986) [67] and Bažant and Kazemi (1991) [68] confirmed the significant agreement between nonlinear fracture mechanics and experimental evidence for prestressed concrete beams and a wide series of tests on reinforced concrete beams, with a size range being 1:16 (Figure 2.54). They also suggested

64

important adjustments for the current design codes accounting for size effect coefficients.

(I) Unanchored bars (f'_c = 6790 psi)				(II) Anchored bars (f'_c = 6700 psi)			
d, in.	P_u, kips	$\frac{v_u}{v'}$	Observed failure mode	d, in.	P_u, kips	$\frac{v_u}{v'}$	Observed failure mode
0.8	0.65 / 0.66 / 0.71	1.53 / 1.55 / 1.67	Bar pullout and bending	13/16	0.94 / 1.09 / 1.05	2.19 / 2.54 / 2.45	Diagonal shear and bending
1.6	1.46 / 1.33 / 1.39	1.72 / 1.56 / 1.63		1.625	1.32 / 1.21 / 1.43	1.54 / 1.41 / 1.67	
3.2	2.47 / 2.51 / 2.33	1.45 / 1.48 / 1.37	Diagonal shear (single main peak, failure at one side only)	3.25	2.43 / 2.26 / 2.00	1.42 / 1.32 / 1.17	Diagonal shear (single main peak, failure at one side only)
6.4	4.08	1.20		6.5	3.28 (3.76)	0.96	Diagonal shear (two peaks, major cracks at both sides)
	4.40 (4.63)	1.29	Diagonal shear (two peaks)		3.77 (5.44)	1.10	
	4.56	1.34	Diagonal shear (single peak)		3.69	1.08	
Not tested				13.0	4.62 / 5.06 / 4.16	0.67 / 0.74 / 0.61	Diagonal shear (single main peak)

1 in. = 25.4 mm, 1 kip = 1000 lb = 4448 N, 1 psi = 6895 Pa.
$v_u = \sigma_{tv} = P_u/2bd$, $v_r = 1.222$ and 1.212 MPa (177.2 and 175.8 psi) for the first and second series, respectively [see Eq. (3)].

(a)   (b)

Figure 2.54: (a) Test-specimen geometry (1 in. = 25.4 mm) and (b) results of diagonal shear tests [9].

Other researchers believe that wider cracks reduce the ability to transmit crack interface shear stresses. The crack width is scaled like any other dimension of the member. The crack opening in the middle of the web is controlled by the strain of the longitudinal reinforcement, but this reinforcement is too far away to control the crack spacing. With a larger crack width, the friction of the shear forces is reduced and, consequently, also the ultimate capacity goes down.

As the crack spacing used to determine the limiting crack interface shear stress is a function of the specimen depth, no special factor is required to account for the size effect. Perhaps the strongest argument for this latter approach is that it leads to a consistent treatment of members with different arrangements of longitudinal reinforcement.

Experimental tests (Collins et al. 1993 [69], Frosch 2000 [70]) have demonstrated that the size effect is not significant in beams with web reinforcement and in beams

without stirrups containing well distributed longitudinal reinforcement (all along the depth).

Figure 2.55 compares the predictions of different formulas for the influence of size effect. The proposals by Okamura [10] and Reineck [14] consider the tests in Shioya et al. (1989) [66] and, therefore, represent reasonable lower bound, whereas the predictions using Zsutty's approach (1971) [8] and the US Code ACI 318-95M do not account for size effect.
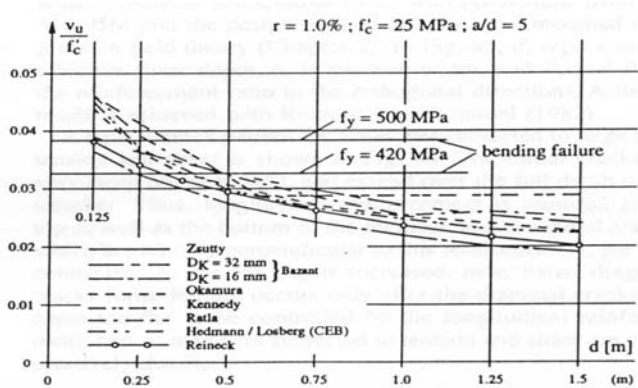
Figure 2.55: Decrease of ultimate shear force (dimensionless value) with increasing depth of member size according to different proposals (Reineck 1991).

The analysis of Zararis (2001) [71] shows that the diagonal shear failure in slender beams is due to a splitting of concrete, which takes place in a certain region of the beam. It was realized that, in this section, the problem of size effect on diagonal shear failure can be reduced to the problem of size effect on split-tensile failure. Tests on cylindrical disks of constant thickness, done by many researchers (Bažant et al. 1991 [68], Hasegawa et al. 1985 [72], Sabnis and Mirza 1979 [73]) confirmed the existence of size effect on split-tensile failure, and showed that, up to a certain critical diameter, the split-cylinder strength decreases as the diameter increases.

Recently, an interesting campaign was carried out at The University of Toronto with the purpose of investigating the safety of the shear design of large, wide beams [74].

A practical design case was considered, which referred to the Bahen Center, an engineering building of The University of Toronto. A wide, large beam was designed to carry loads from the eight upper levels across a 278-seat lecture hall on the ground floor. The beam was made from 35 MPa concrete with a maximum aggregate size of 20 mm, an overall depth of 1800 mm. It spans 12 m and it is 2500

mm wide. According to the actual ACI Standard, as an alternate design, the engineer might have considered increasing the width of the member until stirrups were no longer required. Figure 2.56 shows the actual design (bottom left) and the alternate one (bottom right).
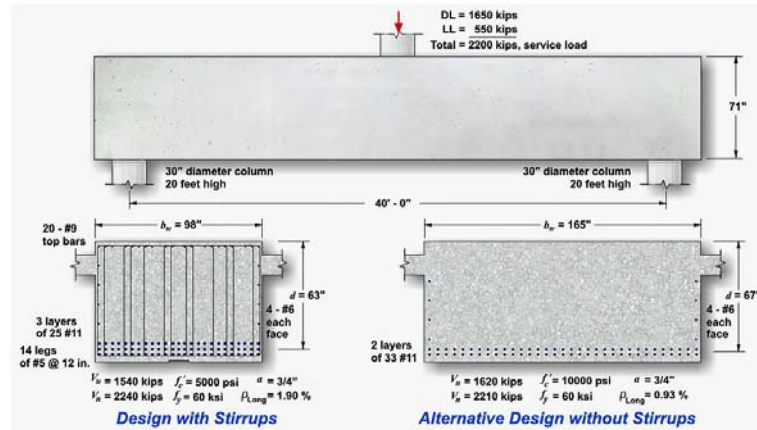
Figure 2.56. Shear design of transfer beams at the Bahen Center (1 in= 2.54 mm; 1 ksi = 6.89 MPa; 1 psi = 6.89 kPa, 1k= 4.45 kN) [74].
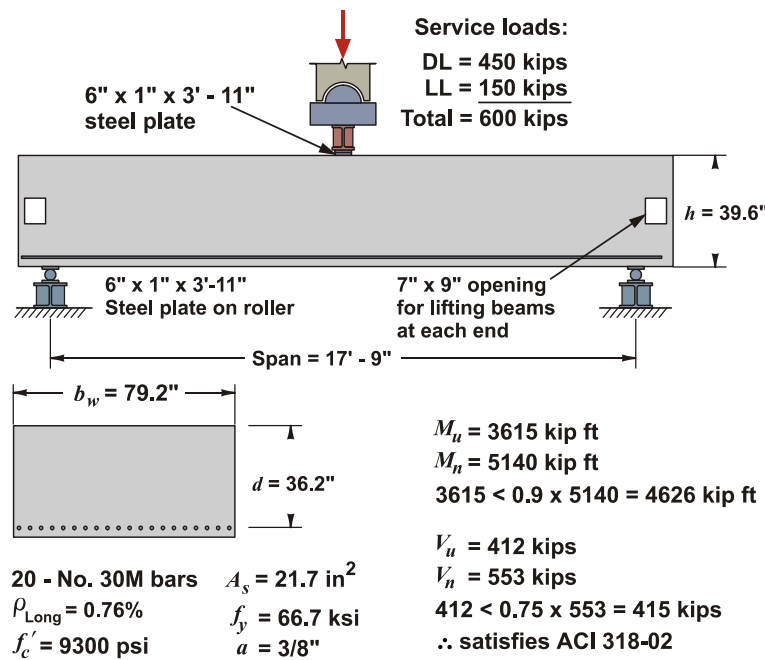
Figure 2.57: Design of test beam [74].

An experimental program was therefore conducted to study the safety of this alternate design. A beam, being about half the size of the alternate design beam for the Bahen Center, was cast and tested, as shown in Figure 2.57.

Figure 2.58 shows the load-deflection response recorded as the Beam was loaded to failure. At nine load stages during the tests, the loading was stopped while cracks were marked and their widths measured. Note that at 90% of the failure load, the maximum crack width measured was only 0.25 mm. In an actual building, such a narrow crack would probably not be noticed and, if it was, would not be a cause of concern. This beam exhibited a brittle shear failure, typical for high-strength concrete beams, with a loud noise as the central load reached 2440 kN. This failure load is only 52% of the failure load predicted by the ACI shear provisions and means that the beam would fail under the actual service loads. The midspan deflection at failure was only 9.5 mm, which is less than 1/500 of the span.
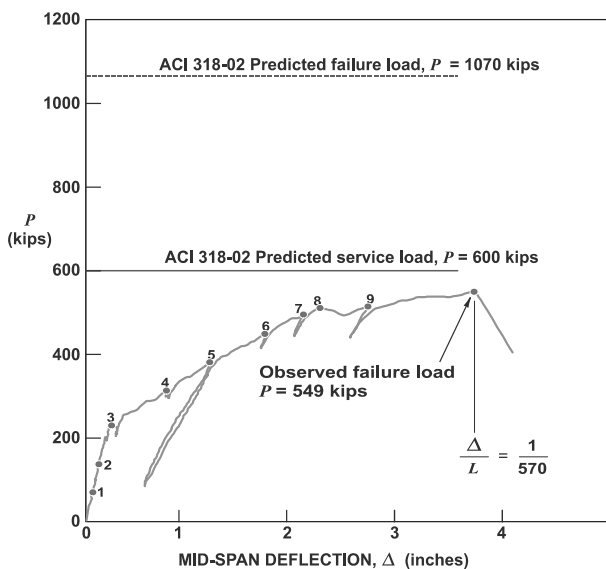
Figure 2.58: Observed Load-Deformation response of the Beam tested [74].

At failure, the central portion of the beam moved downwards. The shape of the crack is the same across the width of the beam, supporting the observation that the failure shear stress is independent on the width of the beam. The shear failure surface was relatively smooth.

The authors concluded that the ACI design procedure is totally unsafe, as neglects the size effects in shear, assuming therefore that if the depth of a member is doubled, the shear capacity will be doubled. On the contrary, the Modified

Compression Fiedl Theory (MCFT; See Section 2.6.7) design procedures predicts that, if the depth of a member is doubled, the shear capacity will be less than double and that this strength ratio will become smaller as the size of the beam increases and as the aggregate size decreases.

Figure 2.60 compares the shear strengths predicted by ACI and MCFT for a range of member depths and aggregate sizes. The predictions of the two equations begin to seriously diverge for depths greater than about 500 mm, for members made from moderate-strength concrete, and greater than about 300 mm for members made from high strength concrete. For a high strength concrete member as deep as the Bahen Center alternate design beam, ACI 318 predicted that the beam's shear strength was 3.4 times as much as the MCFT-based prediction.

The experimental results plotted in Figure 2.58 follow the MCFT-based predictions reasonably well and, hence, diverge strongly from ACI 318-02 predictions as the member depth increases and as the aggregate size decreases. For high-strength concrete members, dangerously unconservative results (for example, a failure shear less than 70% of the predicted value) can be expected for beams more than 450 mm deep. For members made from moderate-strength concrete, dangerously unconservative results can be expected for beams more than 700 mm deep if 10 mm aggregate is used, and more than 1500 mm deep if 40 mm aggregate is used.

Figure 2.59: Shear failure of a deep beam tested at the University of Toronto.

The ACI 318-02 shear design expression for members without stirrups can be very unconservative not only because it was based on test results from beams that had

rather small depths, but also because those test beams typically had very large amounts of longitudinal reinforcement ($\rho > 2\%$) to avoid any possibility of flexural failures.
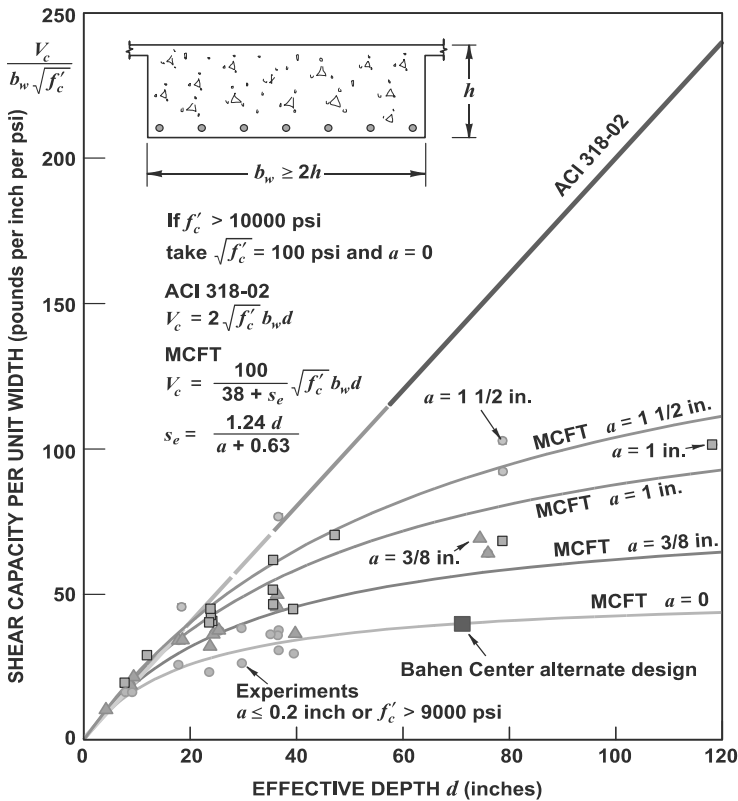
Figure 2.60: Safety of ACI shear design procedure for large, wide beams [74].

Figure 2.61 shows predictions for the critical reinforcement ratio (which represents the transition between flexure and shear failure) for different beam depths and concrete strengths for simply supported beams subjected to point loads that have a shear span-to-depth ratio of 3.0 [74]. Thus, if the beam depth is 300 mm and the concrete strength is 30 MPa, a shear failure is predicted if the area of longitudinal reinforcement is more than 0.77% of the effective cross-sectional area of the beam. For a beam in a building, it is desirable to use somewhat less than the critical amount of longitudinal reinforcement to ensure a ductile flexural failure. For a laboratory investigation of shear, it is desirable to use somewhat more than the critical amount to ensure a brittle shear failure. If unrealistically large amounts of longitudinal reinforcement are used, however, unrealistically large values of shear

strength will be observed. Increasing the amount of longitudinal reinforcement reduces the strain in this reinforcement at a given load and, hence, decreases the crack widths. This makes it possible to resist higher shear stresses.

The MCFT-shear-based design calculates the strain in the longitudinal reinforcement at a stage where they are close to the yield strain (taken as 0.002) at failure and, hence, this expression will give conservative predictions for members that have amounts of longitudinal reinforcement greatly in excess of that required to prevent flexural yielding. Conversely, the equation may give unconservative predictions for members where the reinforcement has a yield strain significantly higher than 0.002. If it is desired to evaluate the shear strength of such members more accurately, more comprehensive MCFT-based procedures have been given by Angelakos, Bentz and Collins [75], and Collins et al. [76].
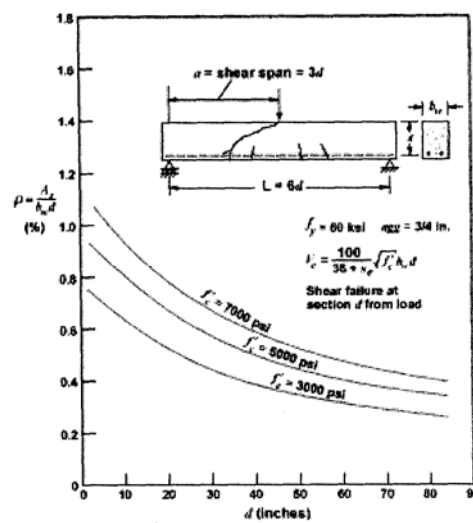
Figure 2.61: Percentage of longitudinal reinforcement above which a beam without stirrups will fail in shear.

2.5.3 Axial Force.

It is well known that the shear strength of members without transverse reinforcement is dependent on axial force. While an axial tension decreases the shear strength of members, an axial compression, due to an applied load or prestressing, increases the shear resistance. But how much an axial force influences shear capacity and what the influence is on the ductility of the member is still a matter of debate in the research community.

71

If a member without shear reinforcement is subjected to large axial compression and shear it may fail in a very brittle manner at the instance of first diagonal cracking. For such members a more conservative approach should be used. It was shown by Gupta and Collins (1993 [77]) that the recent ACI Building Code approach may be not conservative for members subjected to shear and axial compression. Axial load affects the magnitude of shear at the onset of flexural cracking, which was found by Mattock (1969 [78]). But apparently it does not affect the increment of shear between flexural cracking and the onset of diagonal tension cracking. The diagonal cracks in members tend to be flatter than 45° in the presence of axial compression. It is therefore conservative using the design approach for web reinforcement based on the truss analogy with 45° struts, provided that care is devoted to longitudinal reinforcement as its demand for flexure becomes higher when using the actual inclination.

For members without shear reinforcement, but containing appropriate longitudinal reinforcement, the ACI 318-02 procedure for members subjected to shear and tension can be very conservative. The code procedure, although intended for structural elements subjected to significant axial tension, is based upon test results from specimens that did not contain appropriate longitudinal reinforcement to resist axial tension (Bhide and Collins 1989 [79]). Figure 2.62 compares the results from a series of beams without stirrups subjected to shear and tension (Adebar and Collins 1996 [80]) with predictions from ACI 318-02 and the design method based on the MCFT. In Figure 2.62, d_v represents the effective shear depth, b_v is the web width, P_x and P_z are the reinforcement ratio in the orthogonal directions. A similar result is achieved with Reineck's tooth model (1982 [81]).

A typical crack pattern for a member subjected to large axial tension and shear is shown in Figure 2.63. The initial cracks are very steep (close to 90°), and extend over the full depth of the member. Thus, longitudinal reinforcement is required at the top as well as the bottom of the member, and the initial cracks, which are initially perpendicular to this reinforcement, are well controlled. As the loading is increased, new, flatter diagonal cracks form. Failure occurs only after the diagonal cracks become too flat to be controlled by the longitudinal reinforcement; hence, members subjected to tension and shear are comparatively ductile.

72
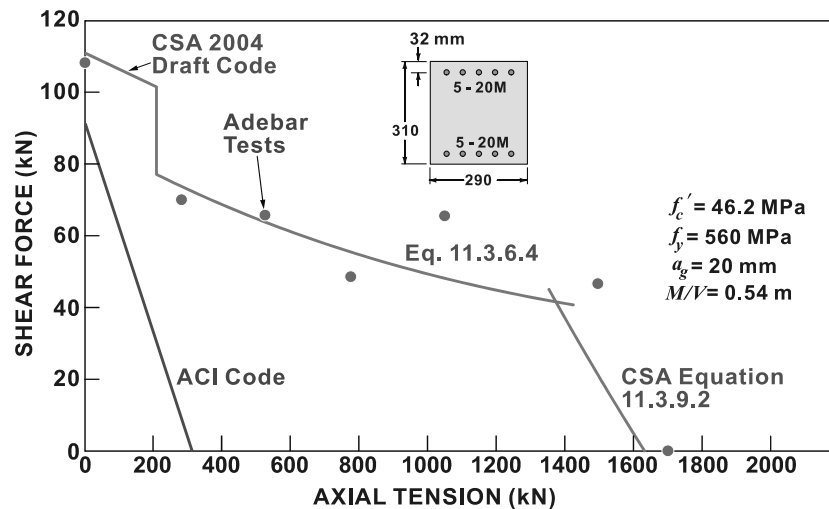
Figure 2.62: Influence of axial load on shear strength of members without stirrups [80].

Figure 2.63: Typical crack pattern of a member without transverse reinforcement subjected to Axial tension and Shear.

2.5.4 Longitudinal Reinforcement.

As can be seen in Figure 2.64, members with low amounts of longitudinal reinforcement may fail at very low shear stresses. The 1973 ASCE-ACI Committee 426 [4] report suggested that the following equation, incorporating the percentage of longitudinal tension reinforcement, be used to estimate the average shear stress at diagonal cracking:

$$v_c = \left(0.8 + 100 \cdot \rho\right) \cdot \frac{\sqrt{f'_c}}{12} \leq 0.192 \cdot \sqrt{f'_c} \quad \text{(MPa)} \tag{2.34}$$

The report further suggested that the reduction in shear capacity can be explained by an increased crack width, resulting in lower interface shear transfer, correspondingly longer flexural cracks that reduce the size of the compression zone, and reduced dowel action.

In the Canadian Design Method (based on MCFT [23]), the influence of the area of longitudinal reinforcement, A_s is reflected in the calculation of the strain at middepth, and predicts larger tensile strains (and larger crack widths) in members with less longitudinal reinforcement and, as a result, lower shear strengths. The design method also requires that additional longitudinal reinforcement be provided to resist the large tensile force due to shear in diagonally cracked members without stirrups. Also the current Eurocode [82] and many other standards contain the effect of the steel amount in their design approaches.

Figure 2.64 compares the predicted influence of the quantity of longitudinal reinforcement from a number of empirical formulas. The flexural capacity is also shown for different strengths of longitudinal reinforcement.
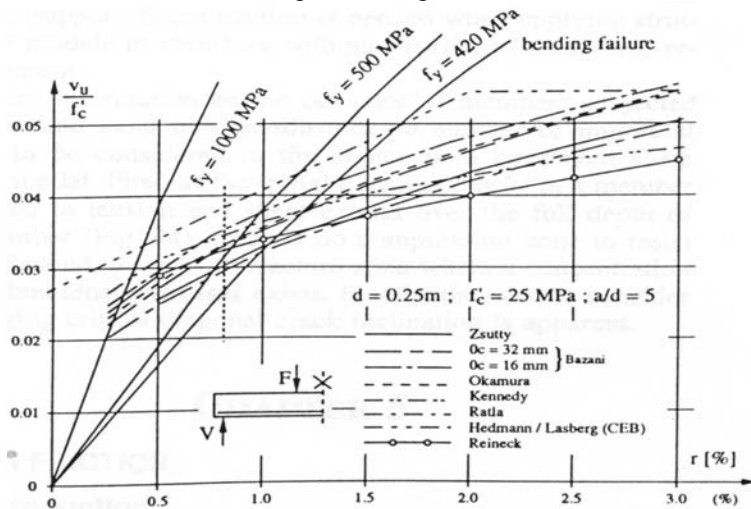
Figure 2.64: Increase in ultimate shear capacity (dimensionless value) with increasing reinforcing ratio according to different proposals (Reineck 1991).

The influence of steel percentage in shear response of members was diffusely investigated even by Kani [64], whose results were reported in Section 2.5.1.

It should finally be noticed that, even though a high steel amount improve the response of a member under shear, it definitely makes the failure more brittle and sudden. The "valley of diagonal failure" results in fact deeper leading to a shear failure for a wider range of a/d ratios (See Section 2.5.1).

74

Out of this, the capacity of moderately long beams ($a/d \geq 5$) with low amounts of longitudinal reinforcement ($\rho < 1\%$) will be governed by a flexural failure rather than a shear failure, which is a favorable mechanism as it is more ductile and predictable than the shear collapse.

It is definitely worthy remarking that, under a structural design point of view, there is a need of balancing a good reinforcement ratio ρ taking into account both mechanisms related to shear and flexure.

2.5.5   Concrete Compressive Strength.

Kani [64] concluded his 11 test series of rectangular reinforced concrete beam by stating than the shear strength does not depend on concrete strength. It should be noticed that Kani tested beams having compressive strength ranging from 18 to 36 MPa. He did not therefore investigate any high strength concrete, where the effect of compressive strength is quite noticeable.

Nowadays, it is given that concrete compressive strength fc' has a significant effect on the ultimate shear strength of concrete members, since shear forces, as already mentioned, are resisted by concrete and transverse reinforcement. It is not theoretical possible to assess the individual components which describe the concrete contribution to shear. Some researchers (e.g. Taylor 1970 [83]) have attempted to determine experimentally each of these components for Normal Strength Concrete (NSC). They have shown that the compressive strength of NSC is usually lower than the crushing strength of the aggregates. Therefore, the crack skirts across the aggregates. This means that, due to the uneven and jagged surface of the crack, the aggregate interlock component of shear resistance is enhanced.

Some researchers and designers are doubting that HSC may not be strong in shear because of the aggregate interlock mechanism, which may be absent in HSC. Due to the smaller difference in the strength of aggregates and the concrete matrix, the crack surfaces are smoother compared to NSC (König et al. 1993 [84]), which means that the aggregate interlock between the fracture surfaces will be reduced, as illustrated in Figure 2.65.

Some tests done by Pendyala and Mendis (2000 [85])) showed that the shear strength of concrete beams does not increase significantly in the range of 30 to 70 MPa (Figure 2.66).

In Figure 2.67 the shear resistance value v_c of a series of tests is compared with an extrapolating of some recent provisions up to 100 MPa. The shear strength

increases, however, from 70 MPa up to approximately 90 MPa. But above 90 MPa the shear strength of HSC either levels off, or its increase is insignificant. The graphic shows that it could be clearly unsafe if extrapolating some of the code provisions up to 100 MPa through the 50 to 80 MPa range.

(a) through aggregate crack   (b) Intergranular crack
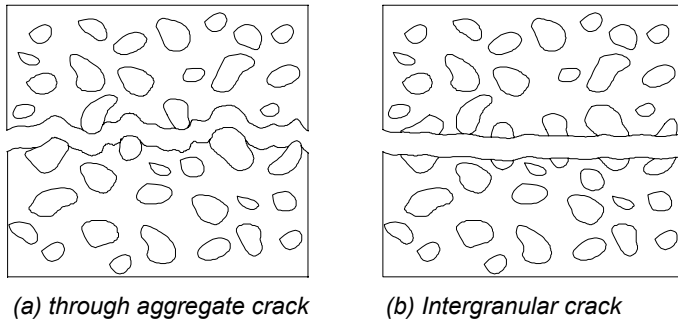
Figure 2.65: Different crack formation and development for (a) NSC and (b) HSC.
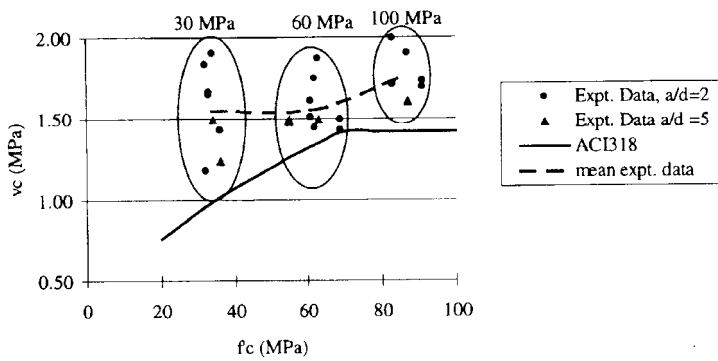
Figure 2.66: Comparison of experimental determined shear strength of beams with the prediction by the American Code (Pendyala and Mendis [85]).

Kuchma and al. [26] demonstrated that lightly reinforced concrete that does not contain either transverse or longitudinal web reinforcement, does not show a reliable gain in shear strength with increasing concrete strength. In that study, beams made with 100 MPa concrete failed at about the same shear stress as beams made from 35 MPa concrete.
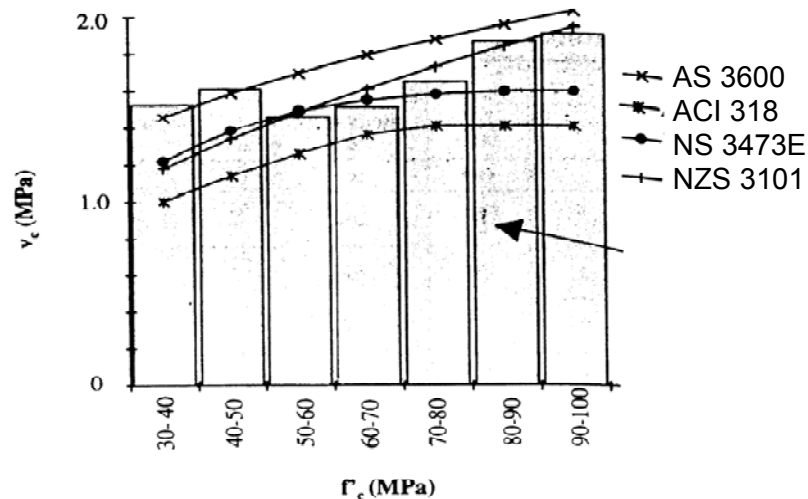
Figure 2.67: Comparison of experimental determined Shear strength of beams with the predictions by recent Codes –Summary of tests (Pendyala and Mendis [85]).

2.5.6 Other Parameters.

Besides all the discussion presented above, other parameters can affect the shear resistance of a member, even though they are not so crucial to deserve a separate and detailed discussion. A brief explanation of some of them will follow.

2.5.6.1 Load Condition.

Leonhardt and Walther (1962 [62]) conducted several tests on specimens similar to the ones tested by Kani (1966 [64]) and discussed in Section 2.5.1. The definition of a shear arm ratio could not be used for a uniformly distributed load, so it was modified.

A simple method to identify a sort of shear arm is shown in Figure 2.68. Starting with two-point loading at the quarter point, the load is gradually distributed until the uniformly distributed load (UDL) is obtained (Figure 2.68c). The resultants of the distributed load remain, in all three cases, at $a=l/4$. Thus, it appears that a uniformly distributed load compares best with a point loading arrangement of two point loads at the quarter points. Consequently, the shear arm with a beam with a uniformly distributed load has been defined by $a=l/4$. This definition has the important advantage that a critical cross section for diagonal failure, which can not be reliably determined, is eliminated. Also, the otherwise suggested definition of $a = M/V$ agrees with the proposed definitions of M_{max} and V_{max}.

77

$$a_{UDL} = \frac{M_{max}}{V_{max}} = \frac{l}{4} \tag{2.35}$$

With this definition for the shear arm a, the "valley of diagonal failure" has been plotted as illustrated in Figure 2.69. The behavior of reinforced concrete beams under a uniformly distributed load appears to be essentially the same as under point loadings, including the observation that a minimum point in the relative strength diagram exists. Thus, the relative strength of short beams, which increases as the a/d ratio goes up, can not be attributed to high pressure under point load since the same effect is observed under a uniformly distributed load.
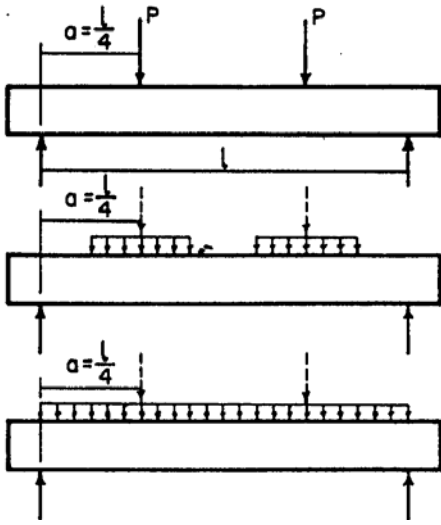
Figure 2.68: Definition of a shear arm for beam under uniformly distributed load [4].
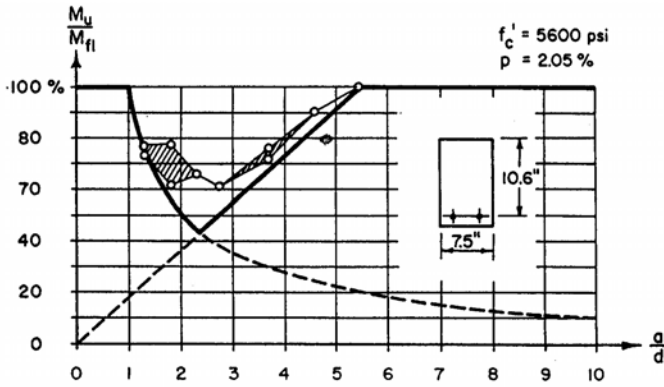
Figure 2.69. "The valley of diagonal failure" for beams under uniformly distributed load [64].

Figure 2.69 evidences anyhow that, as could be expected, a uniformly distributed load produces somewhat more favorable results. Thus, it is slightly conservative if the design requirements for beams under point loadings are extended to beams under uniformly distributed loads.

2.5.6.2 Cross Section Shape.

The ratio between the flange and web widths turned out to be an important parameter for evaluating the shear capacity of a member. This parameter can be defined as b/b_0, where b is the width of the compressed flange while b_0 of the web.

In presence of a behavior mainly governed by arch action, the thrust line tend to be flatter and to run along the compressed flange. Only in the vicinity of the supports the strut concentrates into the web towards the supports (Figure 2.70).
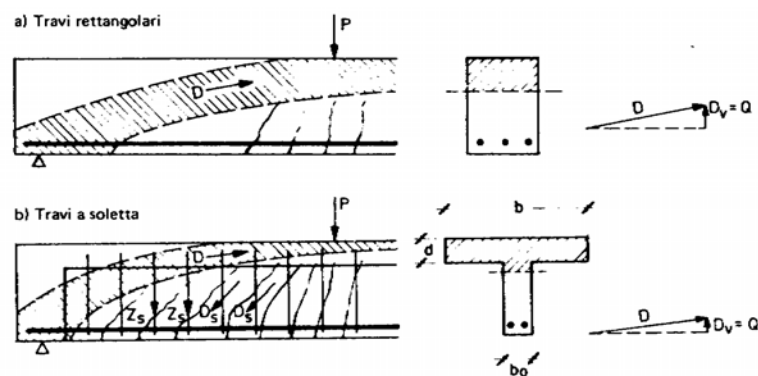
Figure 2.70: The different arch behavior in presence of a flange.

The ASCE-ACI task Committee 426 on Shear and Diagonal Tension (1973 [4]) illustrated the effect of the web width b_0 (Figure 2.71) and the flange width b (Figure 2.72) on the shear capacity of a member. In the first case, crushing of concrete is the main reason of the collapse. Note, moreover, the beneficial effect of the uniform load, as a further proof of the discussion in the previous Section.
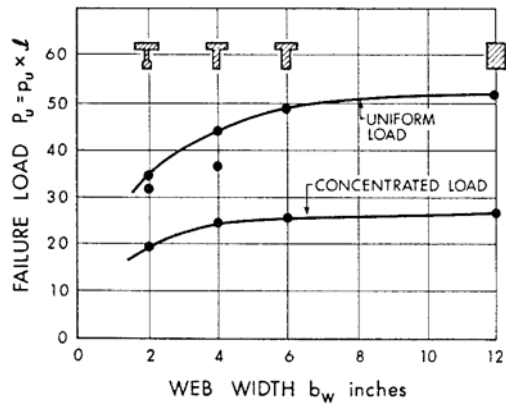
Figure 2.71: Effect of the web width on shear capacity [4].
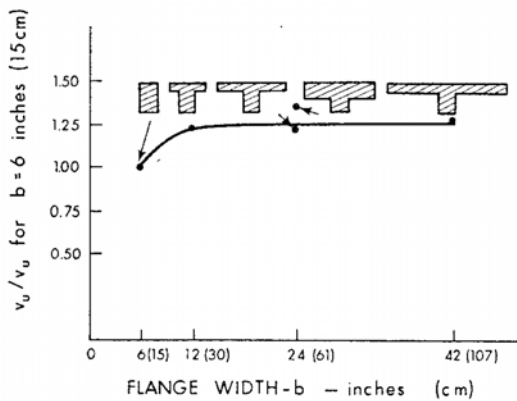
Figure 2.72: Effect of the flange width on shear capacity [4].

2.5.6.3 Distribution of Longitudinal Reinforcement.

A well distributed longitudinal reinforcement over the depth of the member is beneficial for shear capacity of a member as it controls the crack width by bridging the two faces of a crack. This beneficial effect is particularly evident as beams become deeper, since the reinforcement bars at the bottom and top face are too far to resist the opening of any shear critical crack.

Figure 2.73 illustrates a test conducted by Kuchma et al. ([26]) on a member 1 meter deep. The two beams were reinforced with the same steel amount both at the top and bottom face. Moreover, while no further longitudinal reinforcement was added to the member SE100-45A, 6 20 mm bars were added to the SE100-45B beam, at a spacing of 195 mm. These 6 bars, uniformly distributed over the depth, proved to be crucial for the shear strength and the crack pattern of the member. The increase in strength was greater than 50% (312 kN over 200 kN) while the

crack pattern in the second member turned out to be much more diffused, without showing the critical crack localization that always happens in case of shear failure of a member without transverse reinforcement. This brittle and sudden collapse can therefore be avoided even by adding some extra longitudinal bars over the depth of the member.

In the same experimental campaign, other tests on deep beams were conducted. It was found that beams without distributed reinforcement typically failed abruptly after the main diagonal shear crack opened to about 0.5-0.7 mm. Beams with distributed reinforcement had more closely spaced shear cracks and exhibited significantly more ductility prior to failure, as shown in Figure 2.74.
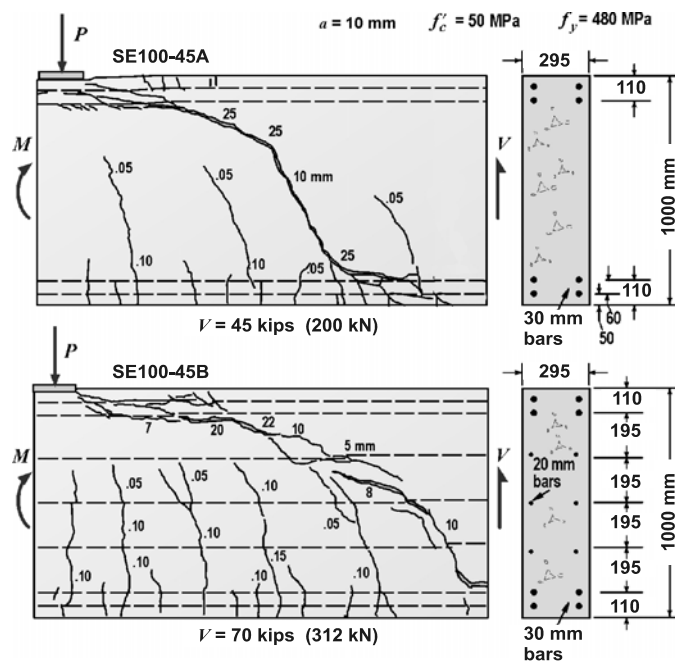
Figure 2.73: Influence of distribution of longitudinal reinforcement on cracking pattern and shear strength [26].

Figure 2.75 shows a comparison between experimental results and predictions using the MCFT. The MCFT (see Section 2.6.6) can be used to predict several important events for a beam including when transverse reinforcement yields, when shear slip occurs, and when diagonal crushing occurs.
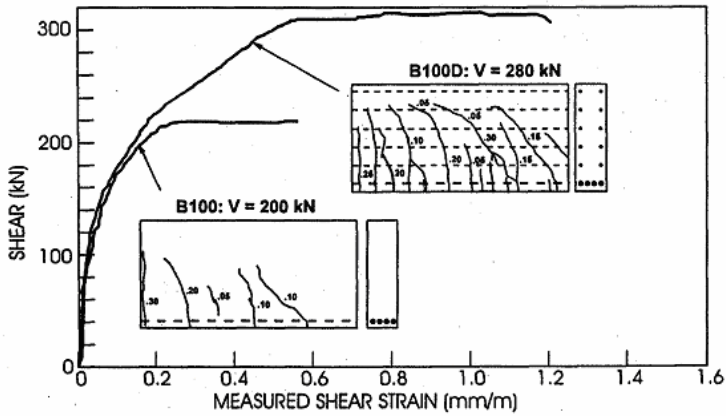
Figure 2.74: Influence of longitudinal reinforcement on the ductility of the shear response [26].
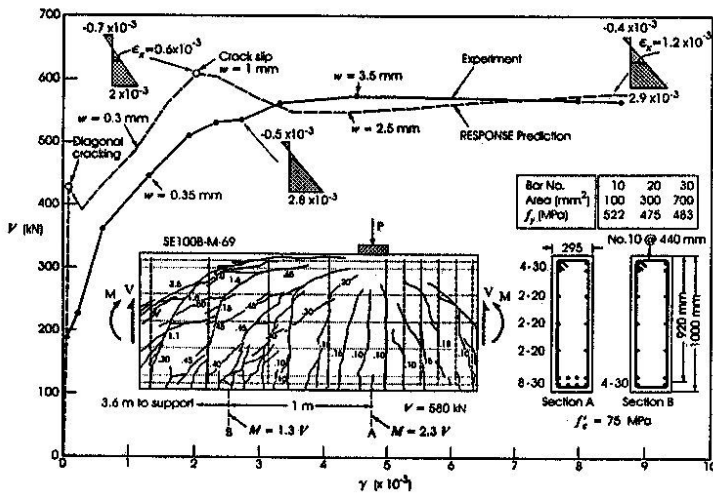
Figure 2.75: Measured versus predicted (RESPONSE Program) shear response of Beam SE100B-M-69 [26].

The main conclusion of this work was that distributed longitudinal reinforcement decreases the crack spacing, decreases the crack width and significantly increases the shear capacity of beams that do not contain transverse reinforcement. For the 1 m deep high strength concrete beams tested in that investigation, adding distributed longitudinal reinforcement increased the shear strength by an average of 72%.

Moreover, the distance between the layers of longitudinal reinforcement is a more appropriate indicator of the size effect in shear than is the overall depth of the

82

member. Members of different sizes, which contain equally spaced layers of longitudinal reinforcement, fail at about the same shear stress. That is such members do not display a size effect (see Section 2.5.2).

2.5.7 Conclusions.

An interesting database on shear tests of beams without transverse reinforcement was published recently to assess the influence of key parameters on shear strength [86]. The purpose of that research was to provide a basis for the development of more unified and reliable provisions. A sanctioned set of criteria was developed for accepting and then considering a test. Examples of these criteria include a minimum compressive strength, a minimum overall height and width, and a check against flexural failure.

To describe the influence of dominant parameters, the shear capacity is expressed in term of the dimension free shear force:

$$v_u = \frac{V_u}{b_w \cdot d \cdot f_{1c}}$$
(2.36)

where f_{1c} is the uniaxial compressive strength (care must have been devoted to make all compressive strength measurements consistent to each other).

Figure 2.76 shows the plot of the test value v_u versus the uniaxial compressive strength f_{1c}. Most tests were carried out with low concrete strength, i.e. 41% of tests were below 30 MPa. The dimensional-free shear force clearly decreases with increasing concrete strength, which means that the shear force V_u itself increases less than in proportion to increasing concrete strength. That confirms many experimental evidences reported in Section 2.5.5.

In Figure 2.77, the test values for the dimension-free shear force v_u are plotted versus the effective depth d. Overwhelming number of tests were carried out for low depths, i.e. 78% of tests were less than 300 mm deep. There are few tests with large depth: only 12% of all tests were in fact deeper than 500 mm. The trend of the curve is anyway significant as it emphasizes and further confirms the size effect, which was already discussed in Section 2.5.2.

In Figure 2.78, the test values for the free-dimensional shear force v_u are plotted versus the reinforcement percentage $\rho_{lw}=A_{sl}/(b_w d)$ (%). Most beams have been tested for large value of ρ_{lw}. For example, more than 50% of the tests contain steel amount greater than 2%, which is mostly unrealistic for normal practice. Only 13% of tests have a ρ_{lw} below 1%.

83
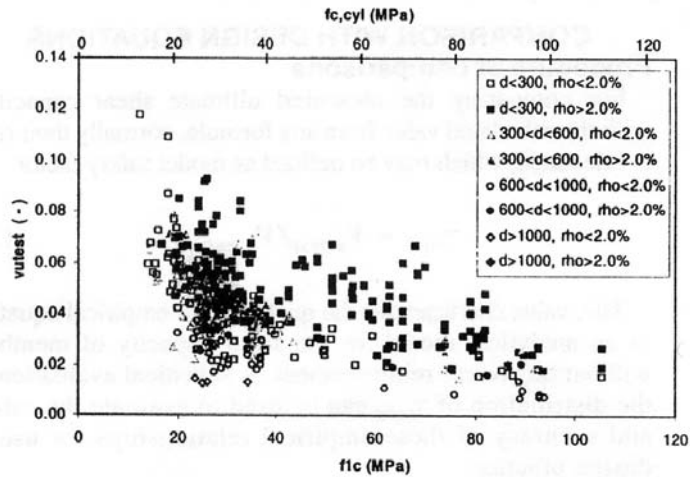
Figure 2.76: Influence of concrete compressive strength on dimension-free shear force for 439 tests of the database [86].
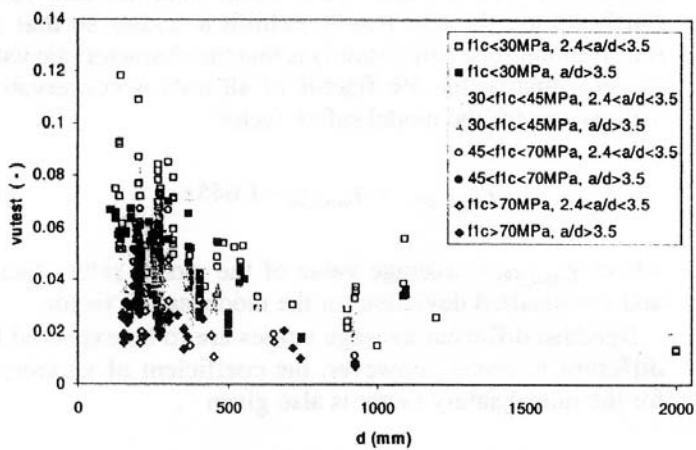
Figure 2.77: Influence of depth on dimension-free shear force for 439 tests of the database [86].

In Figure 2.79, the test values for the free-dimensional shear force v_u are plotted versus the moment–shear ratio a/d. Almost half of all tests were carried out for values a/d less than 3, due probably to the strong influence of Kani. Moreover, it is confirmed that higher values of the shear strength are attained for small values di a/d, where the beneficial effect of supports, in carrying part of the load, should be considered.

All these plots evidence a huge scatter for values of v_u ranging from 0.05 to 0.1.

Based on those huge database, a comparison between experiments and the current ACI formulation for shear was conducted. ACI 318-02 states that the shear strength of a member should be in accordance with:

$$V_u = 0.166 \cdot \sqrt{\frac{f_{1c}}{0.95} - 2.40} \cdot b_w \cdot d \quad \text{(SI Units)} \tag{2.37}$$
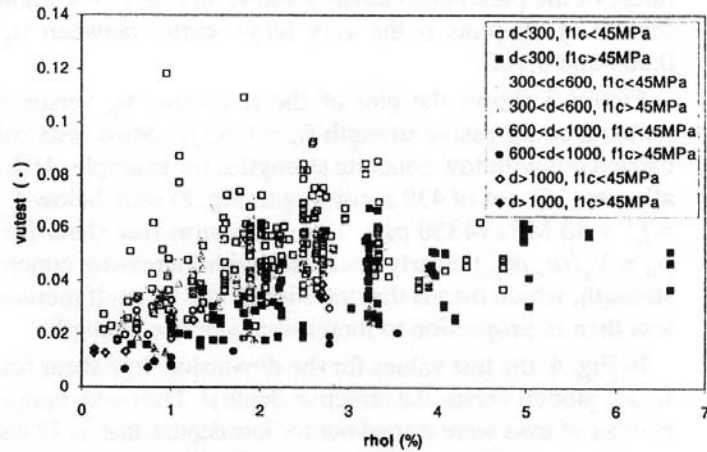
Figure 2.78: Influence of longitudinal reinforcement on dimension-free shear force for 439 tests of the database [86].
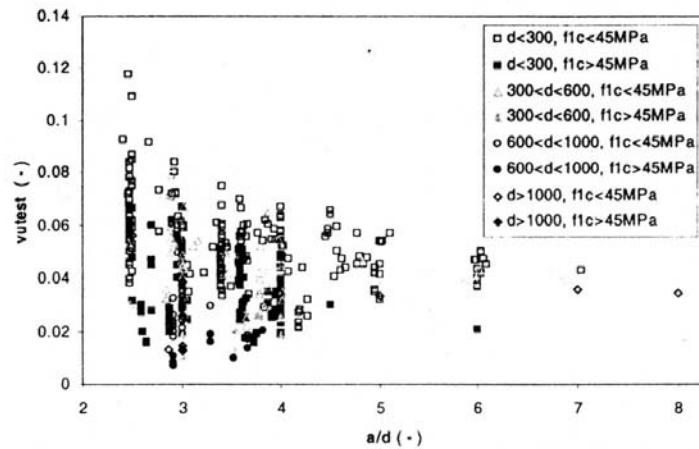
Figure 2.79: Influence of shear pan-to-depth ratio on dimension-free shear force for 439 tests of the database [86].

85

For comparing the measured ultimate shear capacities with the one predicted by the Equation (2.37), a model safety factor was defined as:

$$\gamma_{\mathrm{mod}} = \frac{V_{u,test}}{V_{u,cal}} \tag{2.38}$$

A statistical valuation of the coefficient γ_{mod} was used to evaluate the safety and accuracy of the empirical equation, which is the basis of the current design US approach. If γ_{mod} is greater than *1*, this means that the formula is conservative, assuming that in this calculation the actual material properties are assumed rather than the reduced ones as specified by the code.

In Figure 2.80, the model safety factor γ_{mod} is plotted versus the compressive strength, the only parameters considered in Equation (2.37). The horizontal lines are used to illustrate the average, upper (95% fractile) and lower (5% fractile) for all of the selected tests. The overall distribution of the results suggest that the ACI prediction formula is equally unsafe throughout the whole range of concrete strength. The statistical values of groups of tests with respect to the compressive strength are shown to illustrate the difference between tests with normal strength concrete (NC) and high strength concrete (HSC). A much larger scatter was obtained when considering HSC, owing to fewer tests that were carried out in this respect.
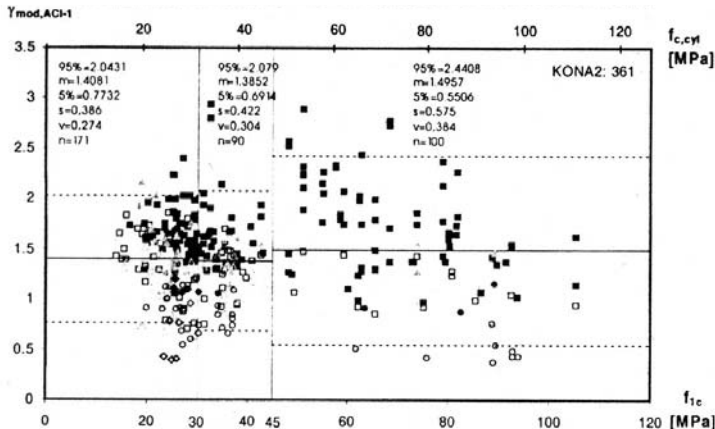
Figure 2.80: Model safety factor γ_{mod} plotted versus concrete strength and statistical results for different groups [86].

In Figure 2.81, the model safety factor γ_{mod} is plotted versus the longitudinal reinforcement ratio, which is not considered in Equation (2.37), conversely to many

other codes. The trend of the results is such that members with low reinforcement ratios appears to be unsafe, and the overall safety of the Equation (2.37) is achieved by the tests with high values of ρ_{lw}. This is more clearly illustrated by examining the different group of tests within small ranges of ρ_{lw}. For the tests with $\rho_{lw} \leq 0.55\%$ as well as for the tests in the range $0.55\% < \rho_{lw} \leq 1.10\%$ the ACI approach is particularly unconservative. Even for $1.10\% < \rho_{lw} \leq 1.50\%$ the accuracy of Equation (2.37) is not good. The agreement between experiments and the ACI model increases steadily with higher reinforcement ratios, and this demonstrates that there is a pronounced influence of the reinforcement ratio on the ultimate load of shear force of members without transverse reinforcement.
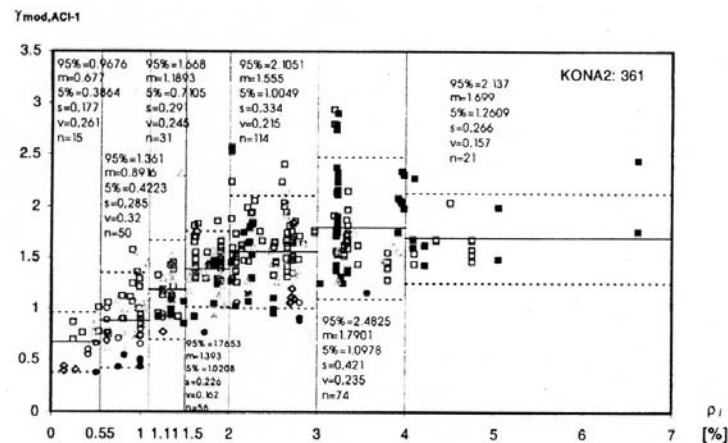
Figure 2.81: Model safety factor γ_{mod} plotted versus reinforcement ratio and statistical results for different groups [86].

In Figure 2.81, the model safety factor γ_{mod} is plotted versus the effective depth d, which is also not considered in Equation (2.37). The trend of the results illustrates the distinct influence of the depth *d* on the ultimate shear force as well as the unsafe results for high depths. These results clearly demonstrate the danger of Equation (2.37) if applied to members of depths larger than approximately 200 mm. In conclusion, Equation (2.37) proved in fact to be unsafe for members with reinforcement ratios lower than about 1.50% and with effective depth *d* larger than 200 mm, which is the case of most of actual structures. These results should lead the research community to reconsider the use of Equation (2.37) and to include the important and obvious parameters *d* and ρ_l.
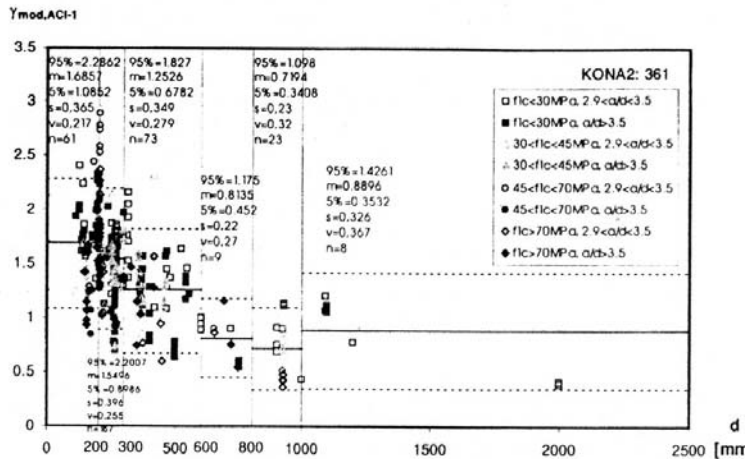
Figure 2.82: Model safety factor γ_{mod} plotted versus effective depth and statistical results for different groups [86].

2.6 Models for Members without Transverse Reinforcement.

2.6.1 Introduction.

The different models that can be used to design members without transverse reinforcement were classified by the ASCE-ACI Committee 445 into the following groups: (1) mechanical or physical models for structural behavior and failure; (2) fracture mechanics approaches; and (3) nonlinear finite element analysis.

In recent decades, the importance of developing relatively simple physical models to explain empirical trends has become increasingly realized.

As already mentioned, the shear resistance of a concrete member can be divided into two separate modes: beam action, where the tension force in the longitudinal reinforcement acting on a constant lever arm changes to balance the external moment; and arch action, where the internal lever arm (location of longitudinal compression stress resultant in concrete) changes to balance the moment (see Section 2.3). The method of choice for cases dominated by arch action is the strut-and-tie model. Regarding beam action, the physical/mechanical models can be classified further into tooth models, which begin with an assumed arrangement of cracks, and truss models with (smeared) concrete tension fields or concrete ties. In the following, fracture mechanics approaches are briefly discussed first. The

nonlinear finite-element method is not discussed in this report: information on this approach can be found elsewhere (Isenberg 1993 [87]). Particular attention will therefore be devoted to physical/mechanical models.

2.6.2   *Fracture Mechanics Approaches.*

Fracture mechanics approaches account for the fact that there is a peak tensile stress near the tip of a crack and a reduced tensile stress (softening) in the cracked zone. For the case of a beam that fails in shear due to the propagation of a single critical diagonal crack, fracture mechanics can be considered a more rational approach than empirical methods. This approach offers a possible explanation for the size effect in shear.

A number of different fracture mechanics models have been proposed over recent years. Among them, two well known studies are the fictitious crack model, by Hillerborg et al. (1976) [88], and the crack band model, by Bažant and Oh (1983) [89]. A survey of fracture mechanics applications was given by Reinhardt (1986) [90]. Further information on fracture mechanics can be found in the 1989 ACI Committee 446 state-of-the-art report.

Fracture mechanics approaches are usually numerically demanding because of the complexity of the tensile stress-crack displacement relationships. As a result, empirical formulas are sometimes developed in terms of fracture mechanics parameters, like that initially proposed by Bažant and Kim (1984) [9]. These equations give little explanation of structural behavior, so the final outcome is often very similar to empirical formulas, as was pointed out by Walraven (1987) [91].

Concerning the model of Bažant and Kim, it was based on a nonlinear fracture mechanics approach, partially already presented in Section 2.5.2. The authors came up with the following relationship:

$$v_u = 8 \cdot \xi \cdot \sqrt[3]{\rho_s} \cdot \left(\sqrt{f_c'} + 3000 \sqrt{\frac{\rho_s}{(a/d)^5}} \right) \text{ (psi)} \tag{2.39}$$

where $\xi = \dfrac{1}{\sqrt{1 + \dfrac{d}{25 \cdot d_a}}}$ and d_a is the maximum aggregate size.

The corroboration against several experimental results demonstrated that this formula was adequate, even for large size elements, since it incorporated the size effect phenomenon. However, in some respect, it proved to be too conservative.

2.6.3   Simple Strut-and-Tie Models.

The application of strut-and-tie models, which has its theoretical basis from the lower-bound theorem of plasticity (Drucker 1961 [92]; Nielsen et al. 1978 [93]; Marti 1985 [94]), requires a minimum amount of distributed reinforcement in all directions (including transverse reinforcement) to ensure sufficient ductility for redistribution of internal stresses after cracking. In the elastic stress distribution of deep members, significant shear is transmitted directly to the support by diagonal compression. This means that less redistribution is required after cracking, and it would seem reasonable to apply strut-and-tie models (cautiously) to deep members without transverse reinforcement. When members are very deep, all of the shear will be transferred directly to the support by compression stresses; however, premature failure of a compression strut without minimum distributed reinforcement may result from transverse splitting due to spreading of compression stress (Schlaich et al. 1987 [12]). Walraven and Lehwalter (1994) [95] carried out tests to investigate the capacity increase beyond that due to spreading of the compression stress; in a bottle-like shape, they proposed a failure criterion for the compression strut that included a size effect.

The simple strut-and-tie approach has also been suggested for more slender members without transverse reinforcement; however, this may result in an unsafe solution, as already discussed (see Section 2.2.1 and Figure 2.5). Solutions have been suggested using a reduced compressive strength of the strut. One method (Collins and Mitchell 1986 [96]) for accomplishing this involves considering strain compatibility between the concrete strut and tension tie. As the strut becomes flatter (i.e., the member becomes slender), the transverse tensile strain in the strut increases, which reduces the diagonal "crushing" strength of concrete (Vecchio and Collins, 1986 [23]). An alternate approach is that of Braestrup (1990) [97], where the maximum diagonal compressive stress is not related to the strut inclination, but the shear capacity reduces with increasing shear span because of the geometry of the nodal zone, which depends on the support dimension, the cover-to-longitudinal reinforcement, and an assumed hydrostatic stress in the nodal zones.

2.6.4   Tooth Model for Slender Members.

2.6.4.1   Kani's Model.
An early attempt to develop a rational model to explain flexure-shear cracking was Kani's tooth model (1964) [63], in which the secondary diagonal cracks were

believed to result from bending of concrete "teeth." The concrete between two adjacent flexural cracks was considered to be analogous to a tooth in a comb (Figure 2.83).
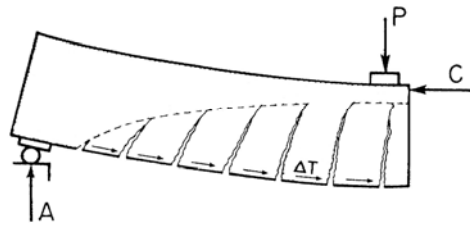
Figure 2.83: Kani's Tooth Model (1964) [63].

The concrete teeth were assumed to be free cantilevers (free body) fixed in the compression zone of a beam and loaded by the horizontal shear ΔT generated by bond in reinforcement. As long as the concrete teeth are capable of carrying the ΔT forces, the comb-like structure is essentially a beam with a distinctive compressive zone, with the highest compressive strain at the top fiber.

In doing so, Kani evidenced first the inefficiency of the fundamental hypothesis of "plane cross section remain plane", which is inaccurate because it leads to an inconsistent shear strength theory. Concrete teeth being short cantilevers loaded by horizontal ΔT forces are subjected to bending. An originally straight axis of a concrete tooth will become therefore a curved line due to the bending action of the ΔT forces. Assuming the axis of the concrete tooth to remain straight would correspond to a condition of "no bending", which on the other hand means $\Delta T=0$. However, without ΔT forces our comb-like beam can not even be in equilibrium. Since the existence of ΔT forces is the main difference between a reinforced concrete beam with and without bond, it can be said that, for the reinforced concrete beam the assumption that plane section remain plane is a contradiction.

To confirm this point, as illustrated in Figure 2.84, Kani measured the horizontal displacement of the points indicated in the picture. The results, shown in Figure 2.85, demonstrated that the displacement of the teeth is almost zero at midspan while it increases around the two load points and at the supports, reaching an average value of about 0.1 mm.

Besides that, Kani proved the validity of the tooth model by applying the linear elastic theory to each cantilever (Figure 2.86). By calculating the horizontal displacements in that way, he obtained appreciable results, if compared to the experimental values.
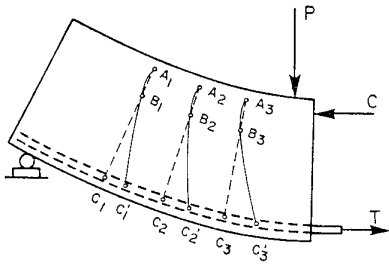
Figure 2.84: Indications of points where horizontal displacements were measured [63].

Using the tooth schematization and the usual beam theory, the maximum moment at the cantilever fixed end is governed by the maximum tensile force, hence:

$$f'_{ct} = \frac{M}{S} = \frac{\Delta T \cdot s}{b \cdot \Delta x^2 / 6} \tag{2.40}$$

where S is the Sectional Modulus and b is the width of the member.
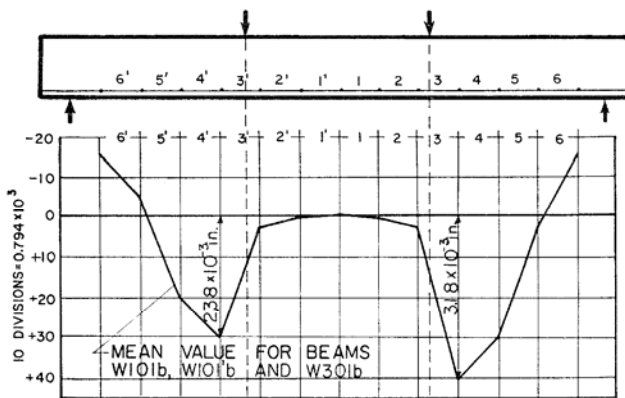
Figure 2.85: Horizontal displacements at the free end of each cantilever [63].
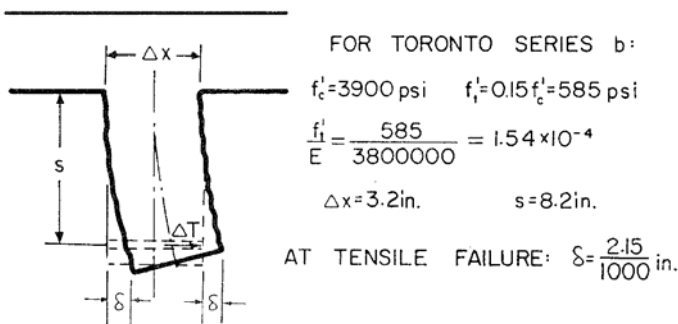
Figure 2.86: Scheme of a single tooth, treated as a cantilever [63].

92

The maximum resistance of concrete teeth per unit length will then be:

$$\overline{T} = \frac{\Delta T}{\Delta x} = \frac{f'_{ct}}{6} \cdot \frac{\Delta x}{s} \cdot b \qquad (2.41)$$

This force, which varies along the shear span according to the external moment variation, can be expressed as the average of the maximum force, at the load point location (maximum moment), and of the force at support, which is almost equal to zero. Therefore, the average bond load between concrete and reinforcement will be:

$$\overline{T} = \frac{T_{max}}{a} \qquad (2.42)$$

where a is the shear span. The maximum bending moment existing in the central section of the beam, assuming that the reinforcement will yield, will be as:

$$M = 0.9 \cdot d \cdot T_{max} \qquad (2.43)$$

where d is the effective depth of the member. Therefore:

$$T_{max} = A_s \cdot f_{sy} \qquad (2.44)$$

The ultimate moment, at which the concrete teeth break away, can be expressed as:

$$M_u = 0.9 \cdot \frac{f'_{ct}}{6} \cdot \frac{\Delta x}{s} \cdot b \cdot a \cdot d \qquad (2.45)$$

while the first cracking moment, herein indicated as M_o, is:

$$M_o = 0.9 \cdot \frac{f'_{ct}}{6} \cdot b \cdot d^2 \qquad (2.46)$$

By combining the previous equation it is possible to come up with an expression of the ultimate moment, which is a function of the crack spacing Δx, the depth of the cantilever s and the a/d ratio:

$$M_u = M_0 \cdot \frac{\Delta x}{s} \cdot \frac{a}{d} \qquad (2.47)$$

Note that the ultimate moment generally increases with an increase of a/d until the maximum flexural capacity is attained, eventually determining a flexure failure. Beyond this point there is no danger of the concrete teeth breaking away.

Kani also observed that after the cracking of the teeth, the ΔT force becomes zero and the beam action can not take place anymore. The behavior turns out to be governed by arch action, as shown in Figure 2.87. In other words, the concrete teeth disappear and the active cross section is reduced and only a tied arch remains (we know today that this is a simplification). A certain amount of tensile stresses are transmitted even in cracked regions.

This further resistance proved to happen just for a/d ratios less than 2.5 whereas for a/d ratios greater than 2.5 a brittle and sudden collapse occurs without any additional arch action.
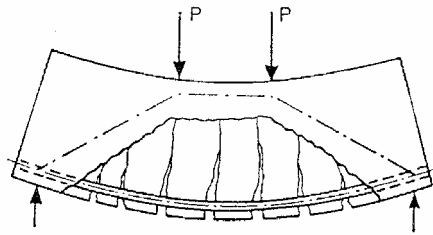
Figure 2.87: Instauration of arch behavior as the final collapse mechanism [63].

For members with a/d lower than 2.5, by considering Figure 2.88, it can be written, simply by assuming that point *O* represents the intersection of all compressive trajectories just prior to failure, the following geometrical relation:

$$\frac{y}{y_0} = \frac{d}{a - s + y_0} \tag{2.48}$$

where *s* is the distance between the closest crack and the support, *y* and y_0 are the depths of the compression zone at flexural failure and at collapse respectively, *d* is the effective depth and *a* the shear span. If it is assumed that $s \sim y_0$, the Equation (2.144) reduces into:

$$\frac{y}{y_0} = \frac{d}{a} \tag{2.49}$$

Assuming that the average stress at failure in the compressive zone *y* is the same as in flexural failure, i.e., over y_0, and neglecting the small difference in the internal lever arm, it is possible to obtain the relationship of the critical moment of arch failure to the moment of flexural failure as:

$$\frac{M_u}{M_{FL}} = \frac{y}{y_0} = \frac{d}{a}$$

(2.50)
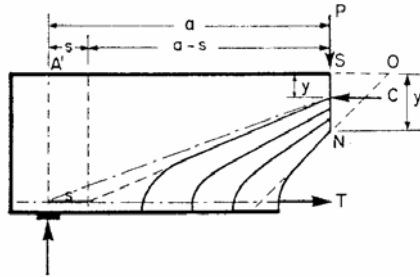
Figure 2.88: Thrust line and schematic crack development for a beam prior to collapse under arch action [63].

The critical cross section is located in a region of biaxial compression underneath the load point. Higher stresses are therefore needed to bring a member up to failure compared to the case of uniaxial compression. To reflect this experimental evidence, Kani modified the last equation as follows:

$$M_u = M_{FL} \cdot \frac{d}{a} \cdot \frac{1}{k}$$

(2.51)

The factor *k* depends largely on the distribution of stresses in the vicinity of the critical cross section. Therefore the width of the plate under the loading point may be of great influence on the load-carrying capacity of the remaining arch. Kani, based on the Toronto test results, proposed an increment of about 10%, which means that *k=0.9*.

The two models presented (the first related to beam action, the second to arch action) turned out to be quite accurate if compared to the experiments carried out at The University of Toronto by Kani, as illustrated in Figure 2.89.

Two points of the two theoretical lines (describing beam and arch action) were also calculated by Kani: firstly the transition point, which corresponds to the transition between shear diagonal failure and flexural failure. The estimation can be done by imposing the identity between the ultimate moment, given in Equation (2.47), and the flexural moment, as follows:

$$M_{FL} = M_u = M_0 \cdot \frac{\Delta x}{s} \cdot \frac{a}{d} \quad \text{and} \quad \alpha_{TR} = \frac{M_{FL} \cdot s}{M_0 \cdot \Delta x}$$

(2.52)

$$\alpha_{TR} = \frac{0.9 \cdot d \cdot A_s \cdot f_{sy}}{0.9 \cdot f'_{ct} / 6 \cdot b \cdot d^2} \cdot \frac{s}{\Delta x} = \frac{6 \cdot \rho_s \cdot f_{sy} \cdot s}{f'_{ct} \cdot \Delta x} \qquad (2.53)$$
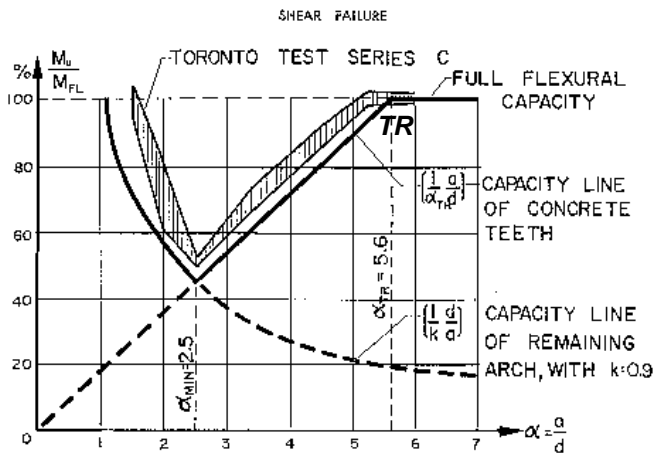
Figure 2.89: Comparison between the experiments of Toronto and the two models proposed by Kani [63].

Applying this formulation could be tedious as much care has to be devoted in choosing proper values of Δx and s: the first one turned out to vary significantly in the different tests conducted. For the second value, as the breaking away of the concrete tooth is indicated by a sharp turn of the crack in the direction of the load point, only the length of the crack up to this turning point should be taken into account.

With this relationships $\alpha_{TR} = 5.6$ was obtained whereas the experimental was equal to 5.2.

A relation for the α corresponding to the point of minimum load-carrying capacity, was also proposed, simply as the intersection of the two lines describing the two different mechanisms (beam and arch):

$$\frac{M_{FL} \cdot a}{\alpha_{TR} \cdot d} = M_{FL} \cdot \frac{d}{a} \cdot \frac{1}{k} \qquad \text{and} \qquad \alpha_{min} = \sqrt{\frac{\alpha_{TR}}{k}} \qquad (2.54)$$

A summary of the Kani's approach can be outlined as follows:

- For $\frac{a}{d} \leq 2.5$ the collapse of a member under shear is gradual, through a progressive transition between beam and arch action;

96

- For $2.5 \leq \dfrac{a}{d} \leq \alpha_{TR}$ a sudden and brittle collapse is observed as soon as the tensile strength of the cantilever is attained.

- For $\dfrac{a}{d} \geq \alpha_{TR}$ a flexure failure is generally observed.

Kani also included some consideration on the influence of bond in the tooth resistance mechanism. Good bond creates closely spaced cracks, while poor or nonexistent bond results in only a few cracks or no cracks at all in the end section of the beam, i.e., in the part where a shear force exists. That means that, under conditions of poor bond, the crack distance Δx will be relatively large. For two beams, identically in every respect except bond resistance, the one with poor bond, and therefore large Δx, will have a higher load-carrying capacity than the beam with good bond. The better the bond the lower the diagonal load-carrying capacity.

Kani's model was evaluated by Fenwick and Paulay (1968) [15] as well as Taylor (1974) [13], who pointed out that the teeth are restricted from bending freely by the friction of the crack faces and the dowel action of the longitudinal reinforcement.
Tooth models have been developed further to include these mechanisms (MacGregor and Walters 1967 [98]; Hamadi and Regan 1980 [99]; Reineck 1991 [14]). With his tests, Chana (1987) [39] confirmed the basic mechanisms of the tooth model by extensive measurements of the deformations prior to failure.

2.6.5 Truss Models with Concrete Ties.

Although it may be possible to extend the simple strut-and-tie model approach to more slender members, clearly a different procedure is needed to capture the shear failure of very slender members without transverse reinforcement, where therefore the concrete tensile stresses have the major role. Marti (1980) [100] extended the plasticity approach by using a Coulomb-Mohr yield criterion for concrete that includes tensile stresses. Schlaich et al. (1987) [12] suggested a refined strut-and-tie approach that includes concrete tension ties. Al-Nahlawi and Wight (1992) [101] proposed a truss model with concrete compression struts inclined at either 45° or 35° and concrete tension ties perpendicular to the struts (Figure 2.90).
An empirical rule was used for limiting the tension tie force based on the geometry of the truss. Muttoni (1990) [102] proposed a truss model for less slender members (Figure 2.91) in which, rather than going directly from the load point to the support, the inclined compression is bent around the initial flexural compression zone.

Truss model with concrete tension member for
beams with shear span-to-depth ratio ≤ 2

Truss model with concrete tension member for
beams with shear span-to-depth ratio > 2
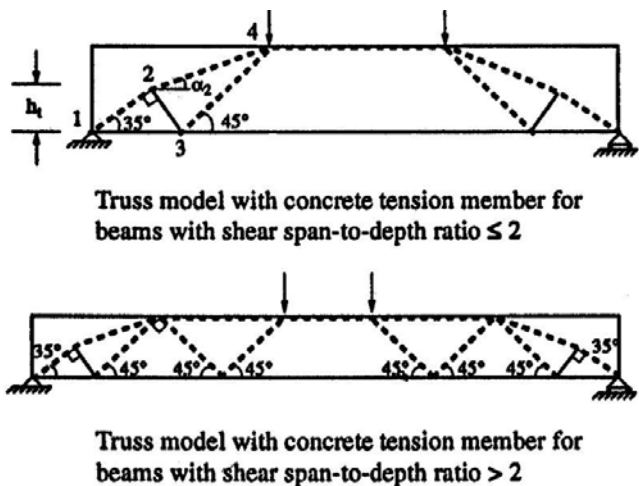
Figure 2.90: Refined strut-and-tie models proposed by Al-Nahlawi and Wright (1992) [101].

This model is based on the tooth model and comprises all shear transfer mechanisms. These are in the cracked tension zone, i.e. the web, the dowel action of the longitudinal reinforcement, the friction of crack surfaces and shear transfer of residual tensile stresses (tension softening of concrete) across cracks. The magnitude of the different shear transfer mechanisms is determined by means of a non-linear analysis employing compatibility conditions in the web.

A more detailed discussion will follow with regards to the most popular truss model with concrete ties, i.e. the Reineck's model.
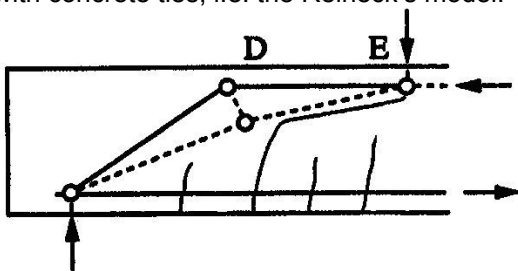
Figure 2.91: Refined strut-and-tie models proposed by Muttoni (1990) [102].

2.6.5.1   Reineck's Model.

The basic assumption of this model [14] is that the crack pattern of a member without transverse reinforcement is discrete. The concrete between the cracks is called "tooth", and the whole member is then represented by a series of teeth, as shown in Figure 2.92.

Teeth are supposed to belong to a *B* region. That consequently means that this theory can not apply to deep beams having small *a/d* ratios (where *D* regions prevail).

The following shear transfer mechanisms can be discerned along the cracks, i.e. in the tension zone of the member:

- dowel-force of the longitudinal reinforcement embedded in the concrete cover;
- friction stresses along the crack resulting in the force T_f with a vertical shear force component V_f; the term friction refers to all concrete types, either normal weight or light weight or high strength concrete;
- cantilever action of tooth clamped into the compression zone;
- residual tensile stresses across cracks in fracture zone near crack tip.

In the compression zone the shear stresses result in a vertical component of the shear force, which however does not contribute significantly to the shear capacity.
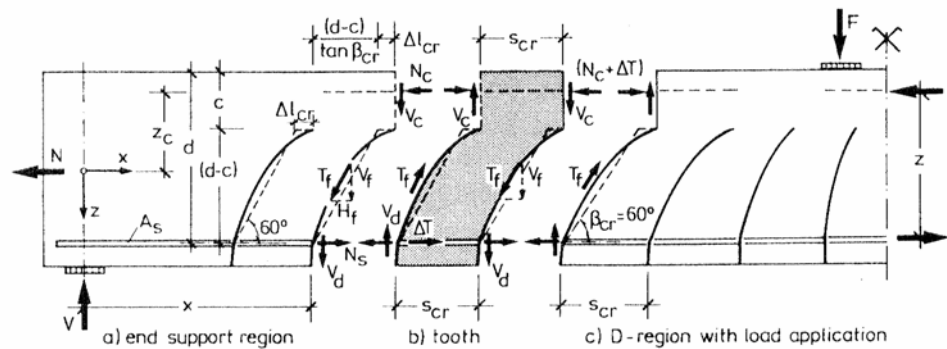
Figure 2.92: Tooth model for a structural concrete member without transverse reinforcement.

The failure of a member without transverse reinforcement is characterized by a crack further propagation into the compression zone and breaking off the tooth from it. It is therefore necessary to model the tooth phenomenon with a discrete crack approach. A value for the spacing, according to other researches, was derived as follows:

$$s_{cr} = 0.70(d - c) \tag{2.55}$$

where *c* is the depth of the compression zone.

For low-load stages, the crack shape is well represented by a straight crack at $\beta_{cr}=60°$, which propagates horizontally by the length Δl_{cr}, all illustrated in Figure 2.92 after the early breakdown of the cantilevering action.

Equilibrium Conditions.

The shear force components are considered and the vertical equilibrium of the end-support region gives:

$$V = V_c + V_f + V_d \tag{2.56}$$

Examining the free-body diagram for the beam element "tooth", the equilibrium of moments gives the basic relation for beams, which relates the shear force and the decrease ΔT of the tension chord force within the element:

$$V \cdot s_{cr} = \Delta T \cdot z \tag{2.57}$$

hence

$$\frac{\Delta T}{b_w \cdot s_{cr}} = \frac{V}{b_w \cdot z} = v_n \tag{2.58}$$

This equation shows that the nominal shear stress v_n has the typical relevance of an average "tooth-bond" stress over the beam width b_w due to ΔT. It is by equilibrium related to the bond stress τ_b at the bar surface:

$$v_n = 4 \cdot \tau_b \cdot \rho_s \cdot \frac{d}{d_b} \tag{2.59}$$

Therefore, as already showed by Kani [64], the bond may basically limit the possible transfer of ΔT to the tooth, and consequently also the ultimate shear force.

The stress distribution in the compression zone is well known, if it is isolated from the tension zone and results from integrating the shear stresses over the depth c, leading to the following relationship (Figure 2.93):

$$V_c = \frac{2}{3} \cdot c \cdot b_w \cdot v_n = \frac{2 \cdot c}{3 \cdot z} \cdot V \tag{2.60}$$

with $z = d - \frac{1}{3} \cdot c$.
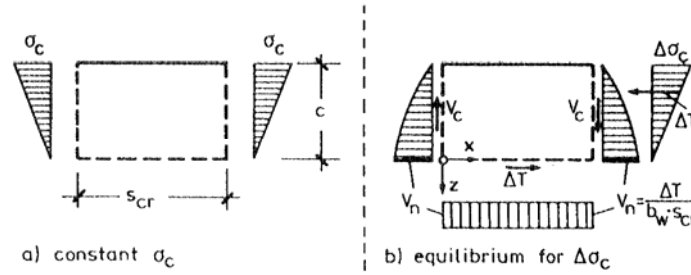
Figure 2.93: Stresses and forces in compression zone of a tooth [14].

At most a maximum of about 30% of the total shear force will be transferred in the compression zone, since the maximum value for the depth of the compression zone is about *0.4 d* (for $\rho=0.02$). Consequently, the major part must be carried in the tension zone of the beam by friction and dowel action. It is possible to rearrange Equation (2.56) as:

$$V = \frac{z}{d-c} \cdot \left(V_f + V_d\right) \tag{2.61}$$

The force in the tension chord is derived from the moment equilibrium of the free-body diagram of Figure 2.92, and this gives the following equation for the steel strain:

$$\varepsilon_s = \frac{1}{E_s \cdot A_s \cdot z}\left[V \cdot \left(x + \frac{d-c}{\tan \beta_{cr}}\right) + N \cdot z_c - V_d + \frac{d-c}{\tan \beta_{cr}} + V_f \cdot \frac{2 \cdot c}{3 \cdot \tan \beta_{cr}}\right]. \tag{2.62}$$

With $\Delta x = \frac{d-c}{\tan \beta_{cr}} \cdot \left(1 + \frac{2}{3} \cdot \frac{c}{z}\right)$ the previous equation becomes:

$$\varepsilon_s = \frac{1}{E_s \cdot A_s \cdot z}\left[V \cdot (x + \Delta x) + N \cdot z_c - V_d \cdot \frac{z}{\tan \beta_{cr}}\right] \tag{2.63}$$

Similarly, the strain in the compression zone may be derived.

Stresses in Tooth.
The dowel force V_d follows directly from the concrete tensile strength, and the component V_f must be determined from integrating the friction stresses along the crack. Since the τ_f distribution and the shear-carrying actions are interrelated and

depend on the shear crack shape, a distribution of τ_f, as shown in Figure 2.94, is assumed. The τ_f distribution is split into a constant part τ_{f1} and a part τ_{f2} with a parabolic distribution. The latter is connected with the dowel action since this causes negative slip in the lower part of the tooth and thus reduces the possible friction transfer over the cracks. From equilibrium and from condition of equal shear stresses from an element at the neutral axis it follows that:

$$\tau_{f2} = 2 \cdot v_{n,d} \quad \text{with} \quad v_{n,d} = \frac{V_d}{b_w \cdot (d - c)} \tag{2.64}$$
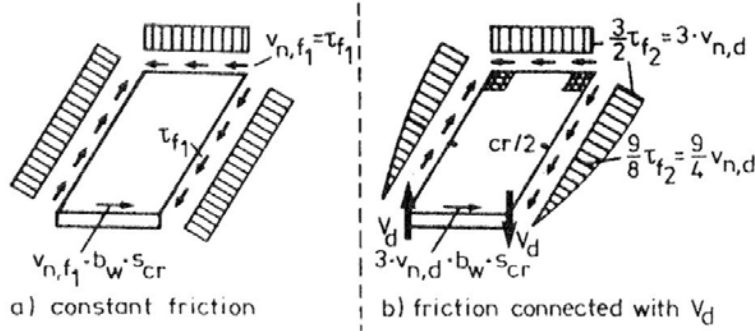
Figure 2.94: Assumed shear stress distribution due to friction along cracks [14].

The resultant friction force V_f may now be expressed in terms of the representative shear stress $\tau_{f,cr/2} = \tau_f$ at mid-depth of the crack and substituting V_f in Equation (2.61) gives:

$$\tau_{f,cr/2} = \tau_f = \tau_{f1} + \frac{9}{8} \cdot \tau_{f2} \tag{2.65}$$

$$V_f = b_w \cdot (d - c) \cdot (\tau_{f1} + \tau_{f2}) = b_w \cdot (d - c) \cdot \left(\tau_f - \frac{1}{8} \cdot \tau_{f2} \right) =$$
$$= b_w \cdot (d - c) \cdot \tau_f - \frac{1}{4} \cdot V_d \tag{2.66}$$

$$V = b_w \cdot z \cdot \tau_f + \frac{3 \cdot z}{4 \cdot (d - c)} \cdot V_d \tag{2.67}$$

The stress field between the cracks follows from the shear stresses along the crack. For the constant part of friction (τ_{f1}) along the crack the stress field in Figure 2.95a is an exact solution, which is shown for a straight crack for simplicity. The

compression field is inclined at $\beta_{cr/2}$ and it is crossed perpendicularly by a constant tension field.

The dowel-force stress field is equilibrated by friction stresses along the crack, so that the bending stresses in the tooth due to the dowel forces superimpose with a biaxial tension-compression stress field as before (Figure 2.95b). The concentrated dowel forces are spread out in the tooth and are basically converted into inclined tension and compression, to maintain equilibrium with the forces due to friction.
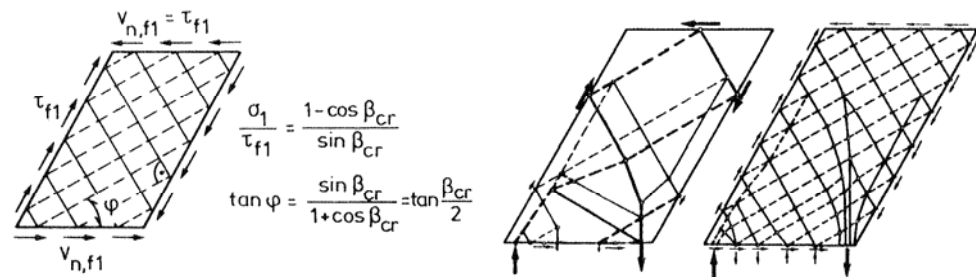
| (a)stress field due to constant part of friction stress | (b) strut-and-tie model in tooth due to dowel forces combined with friction |

Figure 2.95: Strut-and-tie model representing the principal stress fields in tooth [14].

Truss Model.

The calculations confirmed the well known and experimentally verified fact that the dowel forces contribute not much to shear transfer, unless for members with high reinforcing ratios and several layers of bars. Therefore, the state of stress in Figure 2.95a prevails, and this leads to the simple truss model shown in Figure 2.96, which clearly shows that the tensile strength of the concrete is utilized in members without transverse reinforcement. The forces in the member can be calculated from the truss analogy, like e.g. the force in longitudinal reinforcement as follows:

$$N_s = V \cdot \left(\frac{x}{z} + 0.577 \right) = \frac{M_x}{z} + 0.577 \cdot V \tag{2.68}$$

This means that the longitudinal reinforcement may be staggered, unlike in the strut-and-tie model of Figure 2.5.

However, the shear failure is not explained by the tie failing at the tensile strength of concrete, since prior to that it is explained by the limiting capacities of the friction transfer over the crack and of the dowel action reached. Therefore, constitutive relations and limiting capacities for these actions are needed.
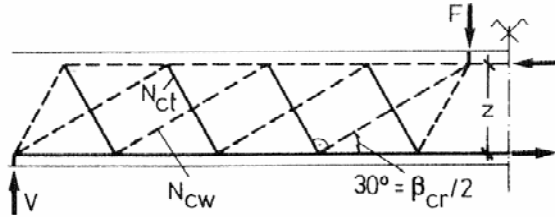
Figure 2.96: Truss model with biaxial tension-compression stress field in concrete of web [14].

Constitutive Laws for Shear Transfer Mechanism.

For determining the contribution of the different mechanisms, deformations and compatibility have to be considered. This requires the constitutive laws to be formulated for all these mechanisms.

The behavior of concrete in tension is shown in Figure 2.97, as taken from the work of Reinhardt et al. (1986). The average concrete tensile strength for calculating the ultimate capacity of test beams is taken as:

$$f_{ct} = 0.246 \cdot f_c^{\frac{2}{3}} \tag{2.69}$$

where $f_c = 0.95 f_c'$ (equation that relates the concrete strengths as defined in the Eurocodes and in the North American Codes, respectively).

The dowel action depends directly on the concrete tensile strength. The limiting value was derived with a simplified procedure which considers the above behavior, and it corresponds well with the values derived from Baumann (1970) [38], later confirmed by Vintzelou and Tassios (1986) [27]. This value may be taken independently from the dowel slip within the range of deformations occurring at failure.

The proposed friction law (Figure 2.98) is based on research by Walraven (1981) [31] as well as Gambarova (1981) [18] and it comprises all the deformations (slip and crack width) and stresses (normal and shear stresses). For members without transverse reinforcement it is assumed that no normal stresses can be activated on the crack face.
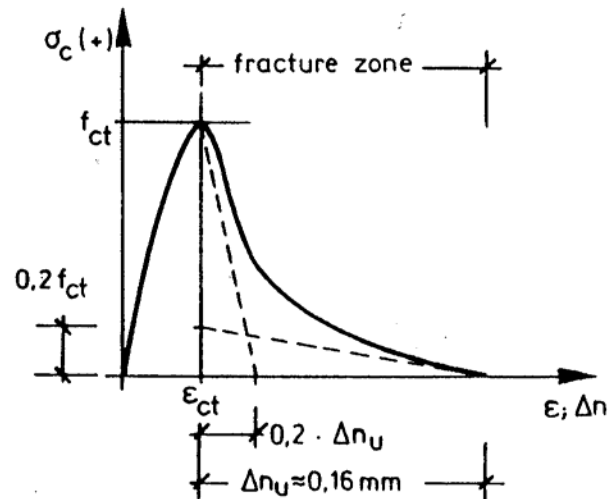
Figure 2.97: Behavior of concrete in tension according to Reinhardt et al. (1986).
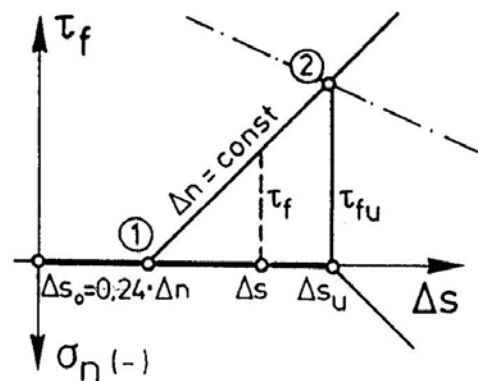
Figure 2.98: Friction law [14].

The simple law for friction is assumed that the maximum value decreases linearly with increasing crack width down to zero at the crack width Δn_u = 0.90 mm:

$$\tau_{fu} = 0.45 \cdot f_{ct} \cdot \left(1 - \frac{\Delta n}{\Delta n_u}\right) \qquad (2.70)$$

This maximum value occurs for the following critical slip of:

$$\Delta s_u = 0.336 \cdot \Delta n + 0.01 \, \text{mm} \qquad (2.71)$$

Beyond this stage of a critical deformation of the tooth, the crack further propagates into the compression zone and the tooth rotates without further restraint.

Crack Pattern and Kinematic Conditions.

The crack pattern of members without transverse reinforcement is characterized by a large crack spacing among the teeth. These primary cracks in the middle of the web are decisive for the transfer of shear forces. There are more cracks in the effective zone near the reinforcement, but these are not decisive for the shear transfer.

The rotation of the tooth is around a point on the neutral axis of strains (Figure 2.99), and the opening is governed by the elongation Δu_L at the level of the longitudinal reinforcement. The simplified crack shape with a horizontal branch Δl_{cr} along the neutral axis (see Figure 2.92 and Figure 2.99) clearly demonstrates that at crack mid-height this crack opening results in a crack width and a slip. Therefore these can be related to the strain ε_s in the longitudinal reinforcement, and the crack width is:

$$\Delta n_{r/2} = 0.71 \cdot \varepsilon_s \cdot s_{cr} \tag{2.72}$$

By considering the above mentioned Equation (2.55), it follows:

$$\Delta n_{r/2} = 0.50 \cdot \varepsilon_s \cdot (d - x) \tag{2.73}$$
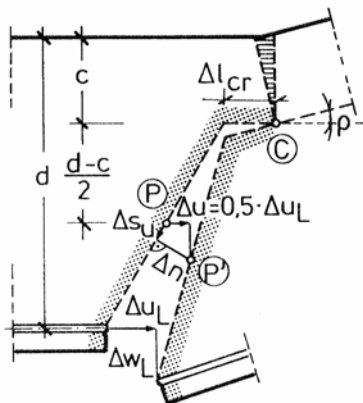
Figure 2.99: Kinematic condition for the crack opening [14].

For example, a member with a medium reinforcing ratio has a depth of the compression zone of about $x = 0.3\,d$, so that Equation (2.73) yields the following crack width at midheight of the crack:

$$\Delta n_{r/2} = 0.35 \cdot \varepsilon_s \cdot d \tag{2.74}$$

106

Thus the size effect is very obvious: doubling e.g. the depth results also in a double crack width, whereby the strain does not change very much. Since the shear transfer mechanisms decrease with increasing crack width (according to Figure 2.97 and Figure 2.98), consequently also the shear capacity is reduced.

Determination of Ultimate Shear Force.
All equilibrium conditions have of course to be considered for solving the problem at any load stage and for deriving the ultimate shear force. The capacity may be determined at any section, but the largest steel strains and thus the largest crack widths occur near the load in a member with point loads only. For the decisive section at the end of the D-Region in a distance of about *1.5 d* from the point load the following explicit equation for the shear force was derived:

$$V_u = \frac{0.4 \cdot b_w \cdot d \cdot f_{ct} - 0.16 \cdot \dfrac{f_{ct}}{f_c} \cdot \lambda \cdot \dfrac{z_c}{d} \cdot N + V_{du}}{\left[1 + 0.16 \cdot \dfrac{f_{ct}}{f_c} \cdot \lambda \cdot \left(\dfrac{a}{d} - 1\right)\right]} \tag{2.75}$$

with:
- N = axial Force (positive for tension);
- z_c= distance between N and N_c (see Figure 2.92);
- $V_{du} = \dfrac{6}{f_c^{1/3}} \cdot b_n \cdot d_b \cdot f_{ct}$ = dowel action, where $b_n = b_w - \sum d_b$

where d_b is the bar diameter. The parameter λ is defined as:

$$\lambda = \frac{\varepsilon_{sy} \cdot d}{\omega \cdot \Delta n_u} = \frac{f_c \cdot d}{E_s \cdot \rho_s \cdot \Delta n_u} \quad \text{with } \omega = \rho \cdot \frac{f_y}{f_c} \tag{2.76}$$

This parameter λ is a dimension-free value for the crack width and thus, according to Equation (2.74), comprises the reinforcing ratio as well as the depth of the member. It physically may be explained as a value for the critical crack width at yielding of the longitudinal reinforcement. For practical use the Equation (2.75) may be plotted in a simple dimension-less diagram (Figure 2.100), since the only ratio of concrete tensile strength to the compressive strength remains a parameter.

$$v_u = \frac{V_u}{b_w\, d\, f_c}$$

$$\frac{f_{ct}}{f_c} = 0{,}086 \; ; \; f_c = 25 \text{ MPa}$$

$$\frac{f_{ct}}{f_c} = 0{,}068 \; ; \; f_c = 50 \text{ MPa}$$

$$\lambda = \frac{\varepsilon_{sy}}{\omega} \cdot \frac{d}{\Delta n_u} = \frac{f_e}{E_s\, \varrho} \cdot \frac{d}{\Delta n_u}$$
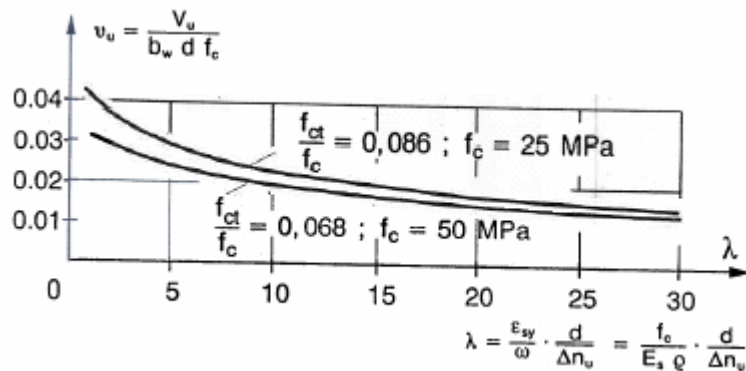
Figure 2.100: Dimension-free dimensioning diagram for the ultimate shear force [14].

Influence of Parameters.

The main parameters influencing the ultimate load or shear force, according to Equation (2.75) are:

- the friction capacity, which is directly related to the concrete tensile strength;
- the dowel action of the longitudinal reinforcement, which mainly depends on the tensile strength of the concrete as well;
- the axial tensile or compressive force;
- the *a/d* ratio or the moment-shear-force ratio;
- the parameter λ for the critical crack width, which takes into account the influence of the reinforcement ratio as well as of the depth of the member (accounting for size effect).

The influence of the a/d ratio is illustrated in Figure 2.101, which represents the well known *"valley of shear diagonal failure"*. The influence of the depth of the member, as expressed by the parameter λ for the critical crack width, is more pronounced. In Figure 2.101 it is especially noteworthy that the *a/d* ratio for the transition point from a shear to bending failure strongly depends on the depth of the member (as well as generally on the reinforcement ratio, both equally included in the parameter λ). For high values of λ, this point does not exist and therefore should not be taken as a reference point for evaluating code equations. For small *a/d* ratios, the failure of the tooth according to this model does not determine the ultimate load of the member, but an increase of the capacity is possible by virtue of a direct load transfer to the supports by an inclined strut.

The ultimate shear capacity of a prestressed member may also be derived with this model.
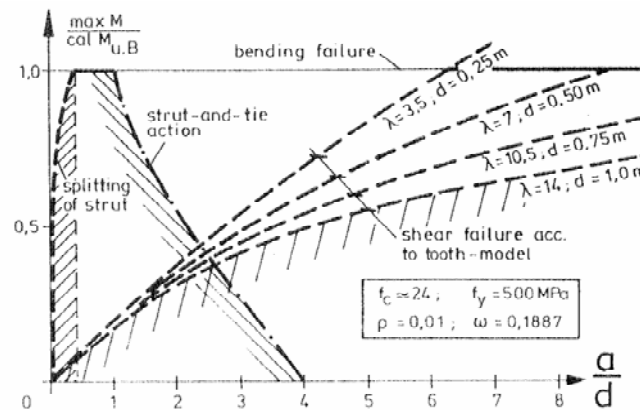
Figure 2.101: Shear valley according to Kani [64] derived from model for a member with ρ=0.01 [14].

Comparison with Tests and Empirical Equations.

Reineck (1990) [37] carried out an extensive comparison with tests, whereby the test results were critically reviewed, so that only 200 tests remained from the available more than 400.

Those tests were separately treated where the tensile strength of the concrete was actually determined, which is the decisive material characteristic here. It is disappointing to state that these were only 40 tests, and even nowadays tests are reported and carried out without testing control specimens for the concrete tensile strength. Furthermore it is noteworthy, that the different control specimens could yield differences in the tensile strengths of more than 20% and up to 30%. It is therefore futile to demand more from a prediction of the ultimate load than this scatter.

The result of this comparison was that this mechanical model was as "accurate" as the best empirical formula by Niwa et al (1988) [11]. Thereby it must be noted that, in the own comparisons, special attention was paid to the crucial tests with low reinforcing ratios and tests with high depths, which constitute the more common structures designed in practice.

2.6.6 Other Models.

2.6.6.1 Russo, Zingone and Puleri's Model.
Russo, Zingone and Puleri [103] developed a model for shear design which extended the Kani's model accounting for other parameters. Such a model is based

on an analytical formulation of the shear-moment domain, taking into account both beam and arch behavior.

One of the bases of the model is respect for the equilibrium in the shear span of the beam at ultimate state: if shear governs the failure, the ultimate moment M_u, for a beam loaded with two concentrated loads, is given by:

$$M_u = V_u \cdot a \tag{2.77}$$

where V_u is the shear force at failure and a is the shear span length (as already mentioned, beams under uniformly distributed loads behave essentially the same as under point loadings, see Section 2.6.4.1).

The second basis is the assumption of the simultaneous occurrence of both the arch action and beam action mechanisms of shear resistance.

At a distance x from the support, the relationship between the external and the internal moment of resistance is:

$$M = T \cdot j \cdot d \tag{2.78}$$

being $T=T(x)$ the tensile force resultant acting at the centroid of the longitudinal reinforcement, and $j=j(x)$ the internal variable lever arm.

The shear force may be expressed, using Equation (2.78) as:

$$V = \frac{\partial M}{\partial x} = j \cdot d \cdot \frac{\partial T}{\partial x} + T \cdot d \cdot \frac{\partial j}{\partial x} \tag{2.79}$$

The first term is usually indicated as the "beam action" and the second one "arch action". The simultaneous occurrence of both actions requires the compatibility of the deformation within the beam. It is implicitly taken into account by the expression of the nominal concrete shear strength provided by the ACI Building Code:

$$\left[v_c = 1.9 \cdot \sqrt{f_c'} + 2500 \cdot \frac{\rho_s \cdot V \cdot d}{M} \right] \tag{2.80}$$

And also by the Bažant and Kim's model:

$$\left[v_u = 10 \cdot \xi \cdot \sqrt[3]{\rho_s} \cdot \left(\sqrt{f_c'} + 3000 \sqrt{\frac{\rho_s}{(a/d)^5}} \right) \right] \tag{2.81}$$

where:

$$\xi = \frac{1}{\sqrt{1 + \frac{d}{25 \cdot d_a}}} \tag{2.82}$$

110

in which d_a the maximum aggregate size.

Analogous to previous models, the flexure-shear interaction is studied by assuming M_u/M_{fl} as the main parameter.

Equation (2.77) can be written as:

$$M_u = b \cdot d^2 \cdot v_u \cdot \frac{a}{d} \qquad (2.83)$$

where:

$$v_u = \frac{V_u}{b \cdot d} \qquad (2.84)$$

By utilizing for v_u a two-term expression distinguishing the two actions, we have:

$$v_u = v_{ub} + v_{ua} \qquad (2.85)$$

where the first and the second term are the main ultimate shear strength provided respectively by beam and arch mechanism.

Using the Bažant and Kim's model (*1 psi = 6.895 10^{-3} MPa*), we can write:

$$v_{ub} = 0.83 \cdot \xi \cdot \rho_s^{\frac{1}{2}} \cdot f'^{\frac{1}{2}}_c \qquad (2.86)$$

$$v_{ua} = 206.9 \cdot \xi \cdot \rho_s^{\frac{5}{6}} \cdot \left(\frac{a}{d}\right)^{-\frac{5}{2}} \qquad (2.87)$$

with all quantities now expressed in SI units.

By means of Equation (2.84), Equation (2.83) can be written as:

$$M_u = M_{ub} + M_{ua} \qquad (2.88)$$

where M_{ub} is the moment contribution of the beam mechanism to the ultimate moment and M_{ua} is the moment contribution of the arch mechanism to the ultimate moment:

$$M_{ub} = b \cdot d^2 \cdot v_{ub} \cdot \frac{a}{d} \qquad (2.89)$$

$$M_{ua} = b \cdot d^2 \cdot v_{ua} \cdot \frac{a}{d} \qquad (2.90)$$

To normalize the ultimate moment, the nominal moment strength, according to ACI Building Code, was adopted:

111

$$M_{FL} = b \cdot d^2 \cdot \rho_s \cdot f_{sy} \left(1 - \frac{\rho_s \cdot f_{sy}}{1.7 \cdot f_c'} \right)$$ (2.91)

where f_y is the yield strength of rebars. Combining these Equations the following expression can be obtained:

$$\frac{M_u}{M_{FL}} = \xi \cdot \frac{0.83 \cdot \rho_s^{1/3} \cdot f_c'^{1/2} \cdot \frac{a}{d} + 206.9 \cdot \rho_s^{5/6} \cdot \left(\frac{a}{d} \right)^{-3/2}}{\rho_s \cdot f_{sy} \cdot \left(1 - \frac{\rho_s \cdot f_{sy}}{1.7 \cdot f_c'} \right)}$$ (2.92)

This Equation clearly shows that, in addition to the parameters ρ and a/d indicated by Kani (Section 2.6.4.1), f'_c, f_y and d/d_a also influence the relative flexural capacity. Figure 2.102 shows the proposed analytical models against some experimental results of Kani, Ahmad-Lue and Krauthammer [14]. The comparison shows that neither model adequately takes into account the influence of ρ on the moment-shear domain diagram, while the proposed one is in fairly good agreement with the experiments.

The aggregate size effect on the relative flexural capacity is shown in Figure 2.103. It can be noticed that the proposed model agrees well with the experimental evidence regarding both the maximum reduction in flexural capacity and extension of the a/d range for which some moment reduction occurs. The Krauthammer model does not take into account the size effects and leads to unconservative predictions in all cases.

Equation (2.92) allows for a simple calculation for the critical a/d ratio, which is the minimum of the function proposed:

$$\frac{\partial M_u}{\partial \left(\frac{a}{d} \right)} = 0$$ (2.93)

which leads to the following formulation:

$$\left(\frac{a}{d} \right)_c = 10.69 \cdot \left(\frac{\rho_s}{f_c'} \right)^{1/5}$$ (2.94)

112
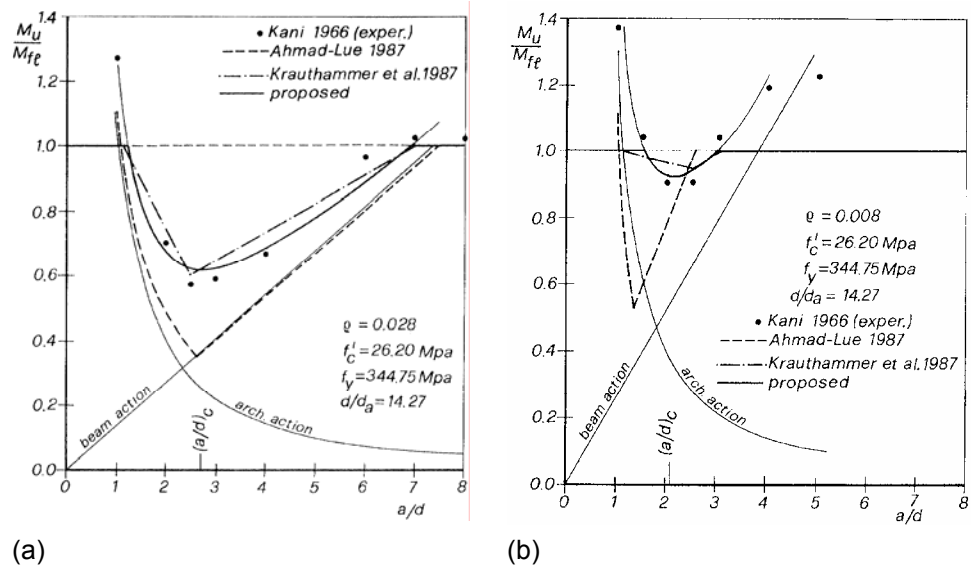
(a)   (b)

Figure 2.102: Relative flexural capacity versus a/d for ρ= 0.028 (a) and for ρ=0.008 [103].
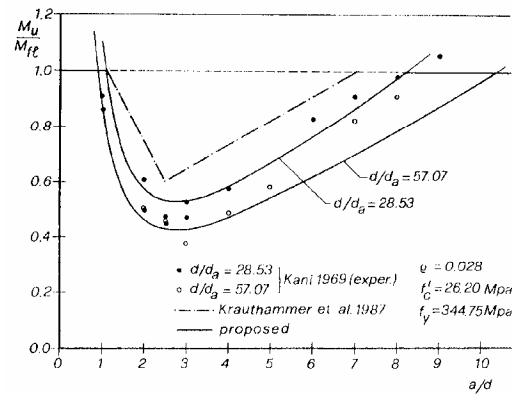
Figure 2.103: Relative flexural capacity versus a/d for ρ=0.028 and different d/d$_a$ values [103].

For usual reinforcement ratios, the last Equation gives *(a/d)$_c$* values falling in the range *2 ≤ a/d ≤3* and also provides an increase of the critical ratio with ρ, as reported in Figure 2.104.

The variation of *(a/d)$_c$* with *f'$_c$* is low and has not been experimentally demonstrated.

The minimum relative flexural capacity, for *(a/d)$_c$*, can be obtained as follows:

$$\left(\frac{M_u}{M_{FL}}\right)_{\min} = \frac{14.79 \cdot \xi \cdot \rho_s^{8/15} \cdot f_c'^{3/10}}{\rho_s \cdot f_{sy} \cdot \left(1 - \frac{\rho_s \cdot f_{sy}}{1.7 \cdot f_c'}\right)} \qquad (2.95)$$

whose trend is shown in Figure 2.105 versus the reinforcement ratio. The agreement between several experimental results is quite relevant.

At the critical condition, the moment contribution of the beam mechanism can be expressed as follows:

$$\left(M_{ub}\right)_c = 8.87 \cdot b \cdot d^2 \cdot \xi \cdot \rho_s^{8/15} \cdot f_c' \qquad (2.96)$$
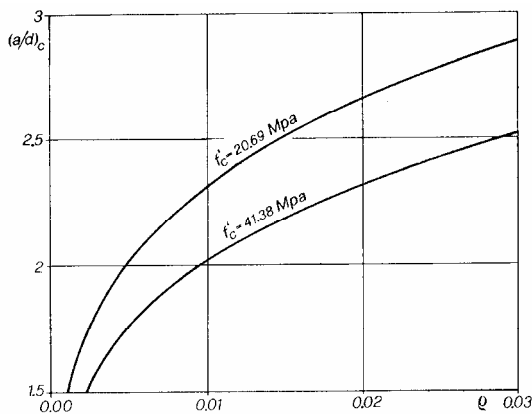
Figure 2.104: Critical shear-span to depth ratio versus ρ for different f'c values [103].

With some calculations it can be derived that:

$$\left(M_{ub}\right)_c = \frac{3}{5} M_{u,\min} \qquad (2.97)$$

This underlines that, whatever ρ and f'c values, at the critical condition the influence of each mechanism is constant and therefore:

$$\left(M_{ub}\right)_c = \frac{3}{5} M_{u,\min}; \qquad \left(M_{uc}\right)_c = \frac{2}{5} M_{u,\min} \qquad (2.98)$$

Figure 2.106 illustrates the two transition points ((a/d)l1 and (a/d)l2) of the diagonal shear failure valley, as a function of the reinforcement amount ρ. Such critical points are analytically obtained by imposing that:

114

$$\frac{M_u}{M_{FL}} = 1 \qquad\qquad (2.99)$$

As proved by many researchers, the difference between these two points decreases with increase of ρ, up to a $\rho = 0.00614$ (in the case of $f'_c = 26.2$ MPa), where the valley of diagonal tensile failure completely disappears.

Figure 2.107 illustrates the domain of failure modes, which varies with f'_c, f_y, and with the function ξ. The characteristic point can fall in one of the three regions (FL, SC or DT) determining the failure mode.
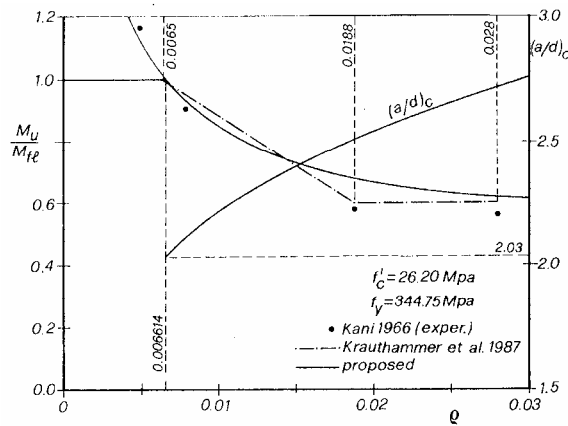
Figure 2.105: Minimum relative flexural capacity and corresponding a/d values [103].
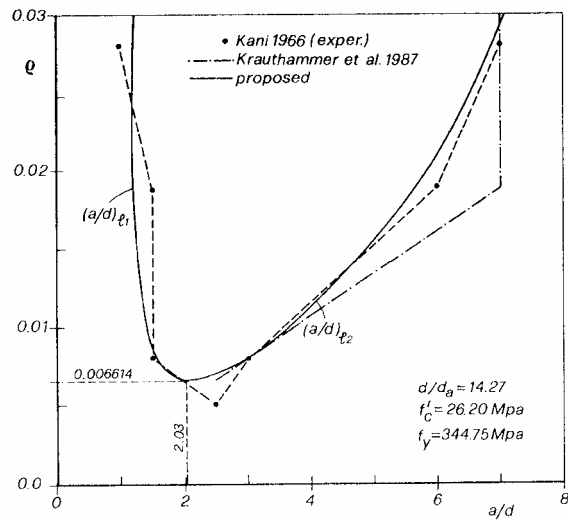
Figure 2.106: Limiting curve of shear influence [103].

115
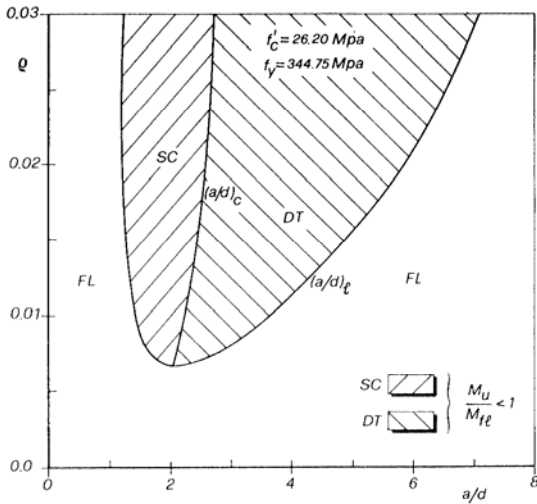
Figure 2.107: Domain of failure modes (SC= shear compression; DT= diagonal tension; FL= flexural) [103].

2.6.6.2 Kim-Kim-White's Model.

Kim and White [7] developed a rational model for shear by first calculating the average shear stress in the region of the member that surrounds the rebar, as shown in Figure 2.108 and expressed in the following Equation, by imposing the horizontal equilibrium of the forces on the element *pp'm'n'*:

$$v = \frac{T}{b \cdot a_c} \tag{2.100}$$
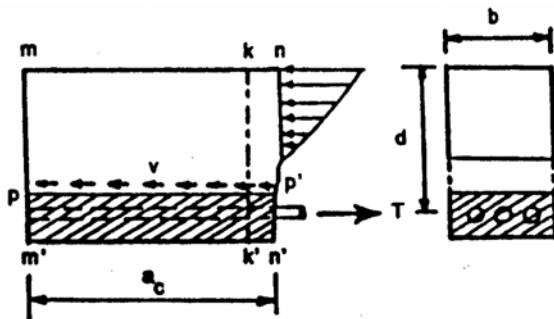
Figure 2.108: Shear stresses in reinforced concrete beam [7].

This shear stress is to be intended as average stress along the face *pp'*. *T* is the force due to bond, which develops along the face *pp'*.

According to several pull-out tests conducted, as depicted in Figure 2.109 (the element *pp'm'n'* is in fact analogous to a simple pullout bond test specimen having special boundary conditions), it was shown that, if the stress level in the embedded rebar is below the yield, the maximum bond stress occurs near the loaded end (n'p' in the present case), with a ratio of maximum bond stress to average bond stress of much more than 2. The bond phenomenon leads to highly concentrated shear stress in the zone above the reinforcement and adjacent to the crack. Prior to flexural cracking, the variation of *T* and the associated bond stress along the length of the element are both quite uniform. The occurrence of the flexural crack *n'p'* produces a dramatic change, leading to a shear-stress concentration and incipient inclined-shear cracking near the flexural crack. For these reasons the flexural crack *n'p'* was termed a *critical flexural crack* and the zone a *critical zone*.

(a)   *(b)*
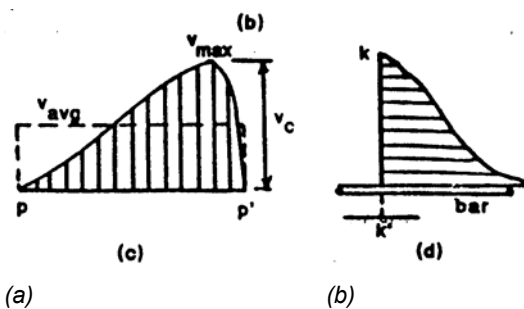
Figure 2.109: Bond stresses in reinforced concrete beam [7].

Based on this evidence, a more refined expression can be assumed for the shear stress, as:

$$v_c = m_b \cdot \frac{T}{b \cdot a_c} \qquad\qquad (2.101)$$

where m_b is a magnification factor defined by v_{max}/v_{avg}, which assumes values close to 2.

In the shear span, as the flexural cracks extend, the compressive stress distribution becomes more uniform and the neutral axis shifts downward (Figure 2.110). This is attributed to the development of arch action. The values of *z* reduce substantially, and the measured *T* in the shear span is consistently higher than the calculated value (Figure 2.111). The authors measured a tension in a rebar, near the middle of the shear span, 1.5 as much as the calculated value. The increased value of *T* due to the reduction of *z* is accounted for in the following relation:

$$\frac{z_0}{z_m} = \frac{T_m}{T_0}$$ (2.102)

where z_0 is the internal moment arm length calculated with the beam theory, z_m the actual lever arm, T_0 the tensile strength acting on the rebar according to the beam theory, and T_m the actual steel force.
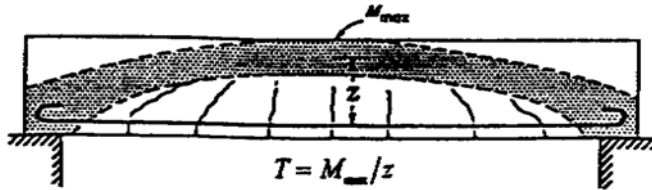
Figure 2.110: Tied-Arch action in beam [7].
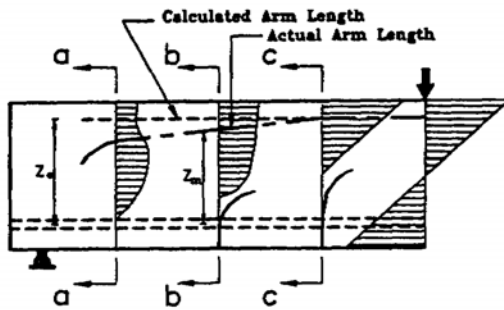
Figure 2.111: Reduction of internal moment arm length due to development of arch action by flexural cracking [7].

The relation of variation of the internal lever arm along the beam was assumed (Figure 2.112):

$$z(x) = \left(\frac{x}{a}\right)^r \cdot z_o$$ (2.103)

where:

$r = k \cdot \left(\dfrac{d}{a}\right)^{n_1} \cdot \left(\rho_s\right)^{n_2} \leq 1$, in which d is the effective depth, ρ_s is the reinforcement ratio, k, n_1 and n_2 are empirical constant (respectively equal to 1.0, 0.6 and -0.1), x is the distance between the support and the section considered and a is the shear span (see Figure 2.112).

Therefore, the tensile force acting on the rebar results:

118

$$T_m = \left(\frac{z_o}{z_m}\right) \cdot T_0 = \left(\frac{x}{a}\right)^{-r} \cdot T_m = m_a \cdot T_0 \tag{2.104}$$
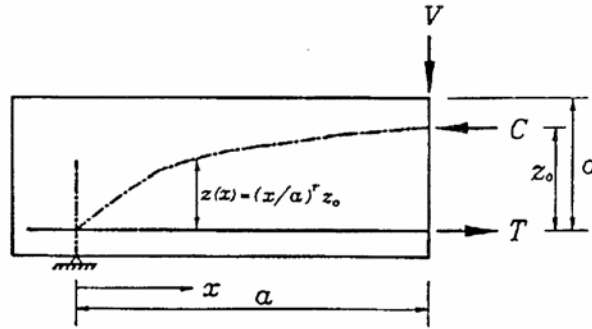
Figure 2.112: Assumed variation of internal lever arm along a beam [7].

The last Equation introduces a further coefficient to be incorporated in the expression of the average shear stress, such as:

$$v_c = m_a \cdot m_b \cdot \frac{T_0}{b \cdot a_c} \tag{2.105}$$

When dealing with simple supported beams loaded by two concentrated loads, the tensile force on the rebar, at the critical section, is:

$$T_0 = \frac{V \cdot a_c}{z} \tag{2.106}$$

The maximum shear stress in the critical zone is therefore:

$$v_c = m_a \cdot m_b \cdot \frac{V}{b \cdot z} \tag{2.107}$$

The shear load representing the onset of the diagonal shear crack corresponds to the achievement of the tensile stress:

$$V_{cr,s} = \frac{1}{m_a \cdot m_b} f_t' \cdot b \cdot z \tag{2.108}$$

The factor m_a*m_b is generally equal to 3 and explain well the reason why the shear collapse occurs for load level equal to about 1/3 of the value predicted with the beam theory (assuming flexural failure). A restriction of the present formulation is that the first cracking moment has to be achieved, otherwise the coefficients m_a and

119

m_b would not have any sense, according to their definition and calculation. So, $V_{cr,s}$ has to be greater than $V_{cr,f}$ as expressed in the following Equation:

$$V_{cr,f} = \frac{M_{cr}}{a_c}$$ (2.109)

Figure 2.113 shows the variation of V_{cr} as the position of an assumed critical section varies along the shear span. Curve I represents the shear cracking load $V_{cr,s}$, which tends to decrease as the assumed critical section approaches the support (taking into account the arch action mechanism). Curve II represents $V_{cr,f}$. The intersection point, A, meets all necessary requirements for inclined-shear cracking. The corresponding V_{cr} and distance a_c of point A can be defined as actual inclined shear cracking load and crack location for a given beam. By imposing the two functions to be equal, an expression of the location of the critical crack is obtained as follows:
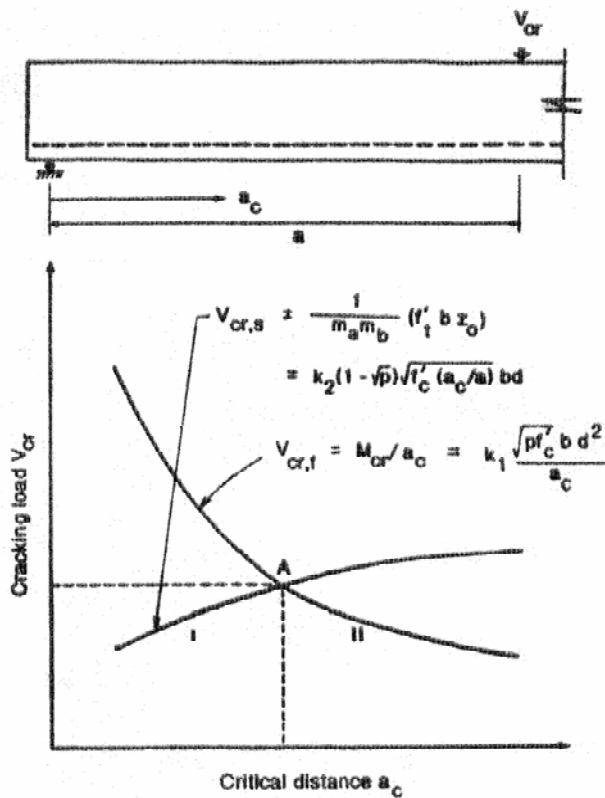
Figure 2.113: Schematic variation of cracking load along shear span: $V_{cr,s}$ and $V_{cr,f}$ versus the distance a [7].

120

$$a_c = 3.3 \cdot \left[\frac{\rho_s \cdot \left(d/a \right)^2}{\left(1 - \sqrt{\rho_s} \right)^2} \right]^{1/3} \cdot a \tag{2.110}$$

D. Kim, W. Kim and White [104] published a further proposal predicting the ultimate shear loading capacity and taking into account both beam and arch action, based on an extensive database of shear tests carried out by the authors.

The shear due to beam action can be expressed as follows:

$$V_1 = z \cdot \frac{dT}{dx} \tag{2.111}$$

where the rate of change of the tensile force in steel (the bond force applied to the flexural reinforcement per unit length of the beam), can be expressed, according to many investigators, as:

$$\frac{dT}{dx} = k_1 \cdot \left(f_c' \right)^{0.5} \tag{2.112}$$

Assuming *x = d* e $z_0 = \left(1 - \sqrt{\rho}_s \right) \cdot d$, the composite beam action contribution to shear becomes:

$$V_1 = k_2 \cdot \left(1 - \sqrt{\rho_s} \right) \cdot \left(f_c' \right)^{0.5} \cdot \left(\frac{d}{a} \right)^r \cdot b \cdot d \tag{2.113}$$

where $k_2 = \dfrac{k_1}{b}$ and

$$r = \left(\frac{d}{a} \right)^{0.6} \cdot \left(\rho_s \right)^{-0.1}$$

The component V_2 expresses shear resistance by inclined internal compression and represents the arch action:

$$V_2 = T \cdot \frac{dz}{dx} \tag{2.114}$$

Being $T = f_s \cdot \rho_s \cdot b \cdot d$, it can be written that:

$$V_2 = \rho \cdot \left(1 - \sqrt{\rho_s} \right) \cdot \left(\frac{r}{a} \right) \cdot \left(\frac{x}{a} \right)^{r-1} \cdot f_s \cdot b \cdot d^2 \tag{2.115}$$

Assuming $x = d$, f_s as a constant and $r = \left(\dfrac{d}{a}\right)^{0.6} \cdot \left(\rho_s\right)^{-0.1}$, the shear contribution due to arch action becomes:

$$V_2 = k_3 \cdot \rho_s \cdot \left(1 - \sqrt{\rho_s}\right) \cdot r \cdot \left(\frac{d}{a}\right)^r \cdot b \cdot d =$$
$$= k_3 \cdot \rho_s^{0.9} \cdot \left(1 - \sqrt{\rho_s}\right) \cdot r \cdot \left(\frac{d}{a}\right)^{r+0.6} \cdot b \cdot d$$

$$(2.116)$$

The internal shear resistance can therefore be expressed as a sum of beam action contribution and arch action contribution; thus:

$$V_u = V_1 + V_2 = k_2 \cdot \left(1 - \sqrt{\rho_s}\right) \cdot \left(\frac{d}{a}\right)^r \cdot \left[(f_c')^{0.5} + k_4 \cdot \rho_s^{0.9} \cdot \left(\frac{d}{a}\right)^{0.6} \right] \cdot b \cdot d \quad (2.117)$$

where $k_4 = k_3 / k_2$.

The range of validity of this equation was, for $\dfrac{a}{d} = 0.98 \div 9.74$, $f_c' = 6.1 \div 109$ MPa and $\rho_s = 0.001 \div 0.066$: A statistical analysis gave values of $k_2 = 0.2$ and $k_4 = 1020$. Thus, the ultimate shear strength equation is obtained as follows:

$$v_u = \frac{V_u}{b \cdot d} = 0.2 \cdot \left(1 - \sqrt{\rho_s}\right) \cdot \left(\frac{d}{a}\right)^r \cdot \left[(f_c')^{0.5} + 1020 \cdot \rho_s^{0.9} \cdot \left(\frac{d}{a}\right)^{0.6} \right] \quad (2.118)$$

in which all quantities are in SI metric units.

The proposed equation depends on the concrete compressive strength, on the amount of longitudinal reinforcement and on the shear span-to-depth ratio and reflects the shear resistance mechanism from combined beam action and arch action in reinforced concrete beams without transverse reinforcement. The proposed equation proved to be in good agreement with many test results and proved to predict particularly well the trend of test data with variation of *a/d*, all in a single equation.

2.6.6.3   Zararis' Model.

In ordinary (or slender) beams without shear reinforcement under two-point loading, the critical crack (leading to collapse) typically involves two branches (Figure 2.114). Normally, these two branches are formed at different time instants and are

122

due to different causes. The first branch is an inclined shear crack, which develops after the onset of nearby flexural cracking. While this first branch is usually formed at the end of the flexural cracks (close to the support), often it is formed between flexural cracks. The height of the first branch is similar to that of the flexural cracks (Figure 2.114). The failure is caused by the formation of the second branch of the critical crack, which initiates from the tip of the first branch and propagates, abruptly or gradually, toward the load point crossing the compression zone. This mode of failure is conventionally called diagonal tension failure, and it occurs only in slender beams (i.e., in beams with a shear span to depth ratio (a/d) > 2.5).

Based on this assumption, analytical expressions are derived by the authors [71] describing the characteristics of these two branches, as well as the mechanism of shear failure based on the following considerations.

The opening of an inclined shear crack (first branch of critical crack) is assumed to be orthogonal (perpendicular to its direction) and is the result of a rotation around its tip. This assumption seems to be realistic in this case, where a compression zone exists above the tip of the first branch of the critical crack. This solid zone essentially acts as a buffer preventing any meaningful contribution of shear slip along the crack interface. As a result of this, no aggregate interlock and dowel forces develop. In this case, as has been shown in previous works (Zararis [105] and [106]), from a tensoral consideration of strains at the crack location, the longitudinal steel bars of the beam undergo an elongation ε_s, and a shear strain γ_s which are expressed as follows:

$$\varepsilon_s = \varepsilon_{cr} \cdot \cos^2 \varphi \tag{2.119}$$

$$\gamma_s = \varepsilon_{cr} \cdot \sin \varphi \cdot \cos \varphi \tag{2.120}$$

where ε_{cr} is the strain perpendicular to the crack strain at the level of reinforcement; and φ = angle between crack and vertical direction (Figure 2.116).
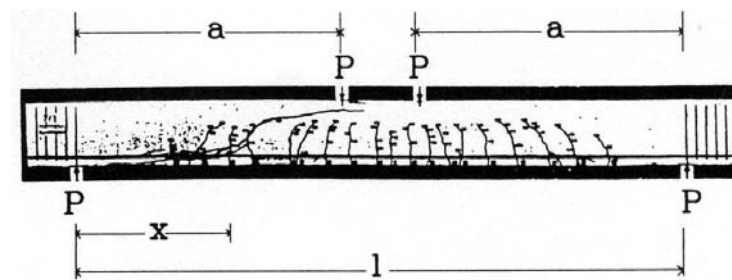
Figure 2.114: Crack Pattern of simply supported test beam under two-point loading (Leonhardt and Walther [62]).

123

These steel strains have corresponding steel stresses, an axial stress σ_s. and a shear stress τ_s. Taking into account that:

$$\sigma = E \cdot \varepsilon ; \quad \tau = G \cdot \gamma ; \quad G_s = \frac{E_s}{2 \cdot (1 + v)} \cong 0.4 \cdot E_s \qquad (2.121)$$

one obtains:

$$\tau_s = 0.4 \cdot \sigma_s \cdot \tan \varphi \qquad (2.122)$$

Equation (2.122) indicates that, on a diagonal crack, the longitudinal reinforcement carries a shear force V_d, connected with its axial force T and the angle φ of the crack by the relation:

$$V_d = 0.4 \cdot T \cdot \tan \varphi \qquad (2.123)$$

This analysis implies that the shear force of steel bars at a crack location is caused by a pure shearing deformation of the bars and is not due to a kinking or a slip of crack faces (as is the case when the well-known dowel force is produced).

Due to the assumption of orthogonal crack opening, the normal force T and shear force V_d of steel bars are the only forces acting on the faces of the first branch of the critical diagonal crack, as shown in Figure 2.115(a) (where the normal and shear concrete forces in the compression zone, C and V_c respectively, are also depicted).

The angle of the crack rotation around the tip of an inclined crack is assumed to be equal to the angle of rotation of the concrete compression zone (Figure 2.116), as has been previously proposed (Leonhardt and Walther 1962, [107]). An element of the beam with a unit length, including an inclined shear crack (first branch of critical crack) and the part of the compression zone above its tip, is shown in Figure 2.116. Taking into account Equation (2.119), from geometrical relations of Figure 2.116, one obtains:

$$\frac{\varepsilon_c}{\varepsilon_s} = \frac{c}{d - c} \qquad (2.124)$$

where c = depth of compression zone above the tip of the diagonal crack; d = effective depth to reinforcement; and ε_c = compressive strain in concrete at extreme fiber.

From the equilibrium of forces acting on the triangular concrete element below the tip of an inclined shear crack, as shown in Figure 2.115 (b), it can be seen that

124

concrete normal compressive stresses are also involved below the tip of the inclined crack on the vertical section of the beam. These stresses are transferred from the top fiber of the beam to the area below the tip of the diagonal crack; this has been experimentally confirmed (Kani 1964, [63]). This explains the presence of compressive force ΔT in Figure 2.115 (b).
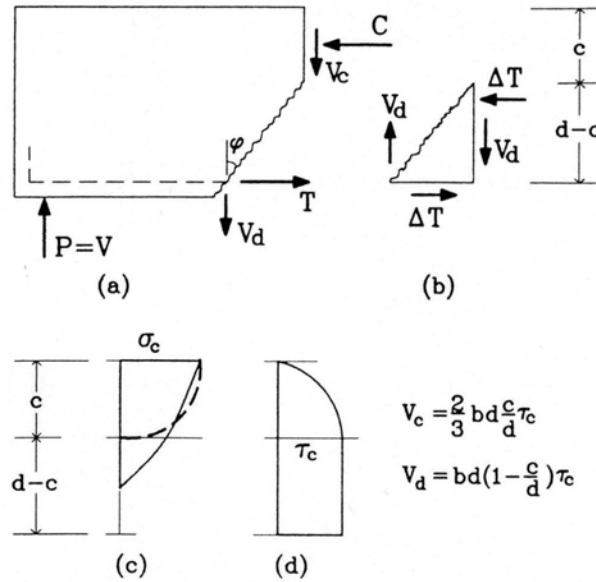
Figure 2.115: Forces and stresses at the inclined crack: (a) Free-Body diagram with inclined crack; (b) Forces on triangular concrete element with inclined crack; (c) Distribution of Concrete Compressive stresses along depth of beam; (d) Distribution of concrete shear stresses along depth of beam [71].

$$V_c = \frac{2}{3} bd\frac{c}{d}\tau_c$$

$$V_d = bd(1-\frac{c}{d})\tau_c$$
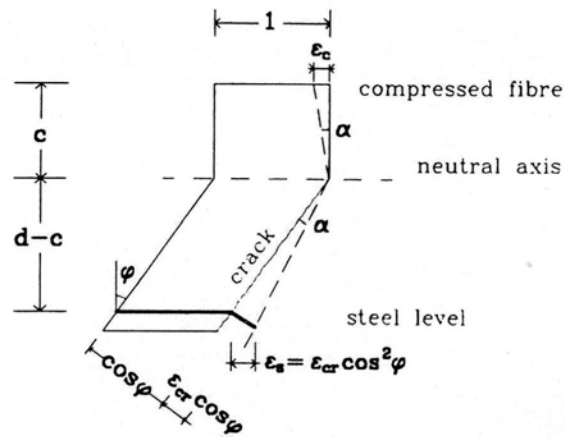
Figure 2.116: Deformation of unit element of beam including Inclined shear crack [71].

In this case, the concrete compressive stresses above the tip of the diagonal crack form a trapezoid block, which can be equivalently approximated as a parabolic (see dashed line in Figure 2.115 (c)). The sum of the concrete compressive stresses of this block is equal to the normal steel force T at the diagonal crack. Therefore, the problem appears to be similar to that of the pure bending of the beam. In this case, the variation of c/d with ε_c is very small (Regan and Yu 1973, [108]), and it is reasonable to use a single value of c/d for all values of ε_c. For convenience, this value can be taken as the one corresponding to the strain, ε_{c0}, at maximum stress. According to Eurocode 2 (CEN 1992, [82]) the value of ε_{c0} is equal to 0.002, and the corresponding resultant of concrete stresses in a compression zone with width b is $C = (2/3)bcf'_c$. Then, equating the normal steel force T with the normal concrete force C in the compression zone above the tip of the diagonal crack and taking into account Equation (2.124) and that $E_s = 2 \times 10^5\ MPa$, one obtains:

$$\left(\frac{c}{d}\right)^2 + 600 \cdot \frac{\rho}{f_c'} \cdot \frac{c}{d} - 600 \cdot \frac{\rho}{f_{c'}} = 0 \tag{2.125}$$

where ρ = steel ratio, and f'_c = strength of concrete in MPa. If a different value of ε_c is used, the analysis is exactly identical, with a different distribution of stresses, yielding an equivalent but somewhat more involved expression.

Equation (2.125) implies that the depth of the compression zone above the tip of the inclined cracks is the same to the depth above the tip of the flexural cracks, as has also been observed in the pattern of cracking of test beams (Figure 2.114).

Assuming that adjacent inclined cracks are about parallel and that only the forces shown in Figure 2.115 (a) act on an inclined crack, then the distribution of concrete shear stresses τ_c along the depth of the beam, at the vertical section passing through the tip of an inclined crack, can be approximated to the one shown in Figure 2.115 (d).

The steel shear force V_d, corresponding to the rectangular part of this distribution along the height $d\text{-}c$, can be easily derived as a function of the total shear force V of the beam as follows:

$$V_d = V \cdot \frac{\left(1 - \dfrac{c}{d}\right)}{\left(1 - \dfrac{c}{3d}\right)} \tag{2.126}$$

Figure 2.117 (a) shows the straight line of compressive action of the resultant of the concentrated load P and the normal concrete force C_f in the region of pure bending, which passes diagonally the shear span of the beam.
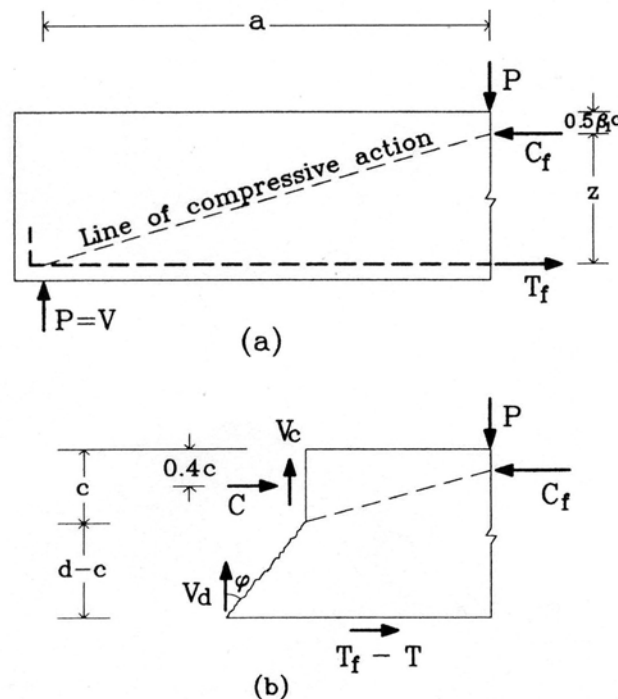
Figure 2.117: Diagonally compressed concrete areas: (a) line of diagonal compressive action; (b) Forces on portion of beam where splitting occurs [71].

If the tip of an inclined shear crack is on this diagonal line, the resultant of the concrete forces (except P and C_f) acting on the portion of the beam between this inclined crack and the load point, as shown in Figure 2.117 (b), will also be lying on this line of compressive action, as the equilibrium of forces acting on this portion requires (in Figure 2.117 (b), T_f -T = difference of steel forces, which is transferred to concrete through bond, and V_d = shear force of steel bars at the crack, which is also transferred to the concrete). Due to these forces, a type of splitting of concrete occurs along this line, featuring a crack that initiates from the tip of the inclined crack and propagates along this line of compressive action toward the area of the load point. This can be analytically explained based on the theory of elasticity. The inclined crack and the crack of splitting are the first and second branches of the critical diagonal crack.

The above consideration constitutes a necessary condition for the shear failure of the beam. This condition requires that the sum of the moments (about the tip of the inclined crack) of the forces acting on the portion of the beam shown in Figure 2.117(b) be equal to zero.

The distance of the normal concrete force C_f from the upper compressed fiber in the region of pure bending, according to ACI 318-02 is $0.5\beta_1 c$, where $\beta_1 c$ = depth of the equivalent rectangular stress block. The factor β_1 varies in the range $0.65 \div 0.85$ and depends on the strength of concrete f'_c. Taking for simplicity a mean value $\beta_1 = 0.72$ for all values of f'_c, from the equilibrium of forces acting on the portion of beam shown in Figure 2.117(a), the steel force T_f in the region of pure bending can be easily derived as $T_f = P(a/d)/(1-0.36c/d)$. By also taking into account Equation(2.123) and that $C = T$, the above condition yields:

$$V_d = \frac{V(a/d)(1-c/d)\tan\varphi}{[2.5 - c/d + (1-c/d)\tan^2\varphi](1 - 0.36c/d)} \qquad (2.127)$$

Rearranging the last two equations and considering that $1-0.36\ c/d \approx 1-1/3\ c/d$, it results that:

$$\tan^2\varphi - \frac{a/d}{1-c/d}\tan\varphi + \frac{2.5 - c/d}{1-c/d} = 0 \qquad (2.128)$$

The angle φ of the first branch of the critical crack corresponds to the positive root of Equation (2.128). For typical values of c/d, Equation (2.128) has real solutions for values of $a/d \geq 2.5$ (approximately), i.e., for the case of ordinary, slender, beams. If $a/d < 2.5$ (case of short beams), Equation (2.128) has imaginary solutions.

Since the tip of the first branch of the critical diagonal crack is on the straight line of the compressive action, the distance x of the initiation of the critical diagonal crack from the support can be obtained by geometrical relations from the scheme shown in Figure 2.118:

$$\frac{x}{d} = \left(1 - \frac{c}{d}\right) \cdot \left(\frac{a/d}{1 - 0.36c/d} - \tan\varphi\right) \qquad (2.129)$$

Based on the above geometrical characteristics of both branches of the critical diagonal crack, as given by Equation (2.125), (2.127) and (2.128), the critical crack can be depicted on a beam.

The equilibrium of forces acting on the portion of beam shown in Figure 2.117(b) implies that no force acts on the line along which the second branch of the critical crack is to be formed. In this case, it could be argued that only normal stresses exist

along this line of the second branch, which compose a group of forces acting in self-equilibrium (i.e., forces not balancing any external load). Such a stress distribution implies a failure due to splitting of concrete in this area.
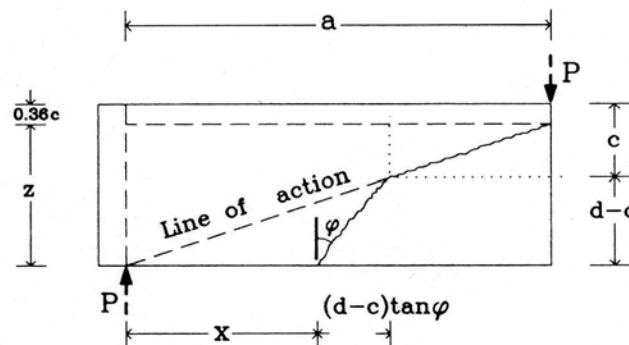
Figure 2.118: Geometrical representation of critical diagonal crack [71].

A possible arrangement of the concrete forces acting in the region of the beam where the splitting of concrete occurs is shown in Figure 2.119. The resultant of forces P and C_f is analyzed in two components F_1 and F_2, each of which represents the resultant of concrete stresses acting above and below the second branch of the critical crack, respectively. The force F_1 balances the resultant of forces C and V_c in the compression zone, while the force F_2 balances the resultant of forces T_f - T (bond force) and V_d (steel shear force transferred to concrete). Thus, as a first approximation, the region of the beam where the splitting occurs with the corresponding forces (of Figure 2.119), can be represented by a circular disk, as shown in Figure 2.120(a), at which, unlike the common split cylinder test, two pairs of equal and apposite forces are acting on the cylinder. The circular disk has a diameter d_{sp} equal to the length of the second branch of the critical crack, whereas its thickness is equal to the width b of the beam, taken equal to unity (i.e., $b = 1$). The force F at the top of the disk represents the resultant of forces P and C_f. This balances the forces F_1 and F_2, which represent the resultants of forces C and V_c and forces T_f -T and V_d, respectively.

According to the theory of elasticity (Timoshenko and Goodier [109]) on the analogy of the case of two equal and opposite forces acting along a chord of a disk, a simple radial distribution of stresses produced by each of the four forces acting on the circular disk (two pairs of two equal and apposite forces acting along the chords AB and AC) can be considered. To obtain the state of stress of the disk with its boundary free from uniform compression, it is necessary and sufficient to superpose

on the above four simple radial distributions a uniform tension with an intensity σ_r given by:

$$\sigma_t = \frac{2 \cdot F_1}{\pi \cdot d_{sp}} \cdot \sin\delta + \frac{2 \cdot F_2}{\pi \cdot d_{sp}} \cdot \sin\gamma \qquad (2.130)$$
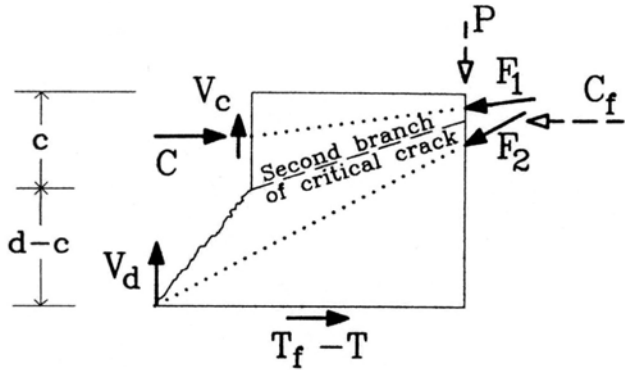
Figure 2.119: Proposed filed of concrete forces [71].

(a)

(b)
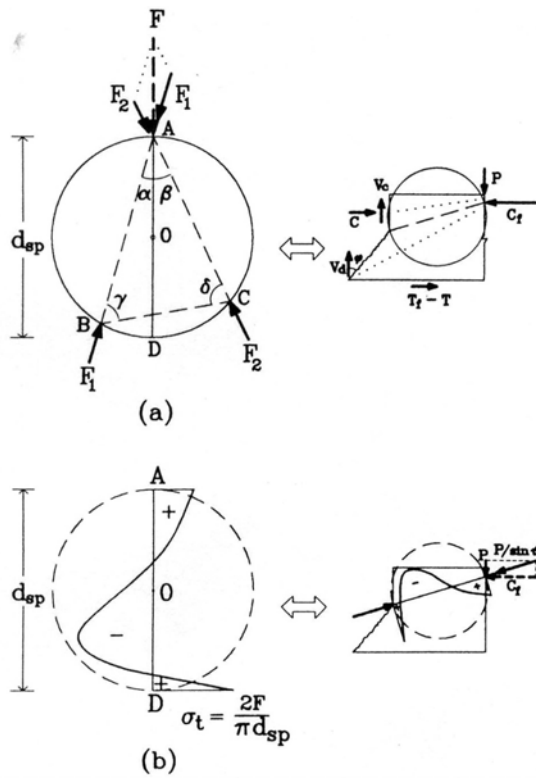
Figure 2.120: Splitting of concrete in circular disk: (a) pairs of equal and opposite forces acting on circular disk; (b) Diagram of normal stresses along diameter [71].

Taking into account that $\sin\delta = \cos\alpha$ and $\sin\gamma = \cos\beta$ (Figure 2.120 (a)), and also that $F_1\cos\alpha + F_2\cos\beta = F$, the uniform normal tension applied to the circumference of the disk yields the following simple expression:

$$\sigma_r = \frac{2 \cdot F}{\pi \cdot d_{sp}}$$

(2.131)

Therefore, the stress at any point of the circular disk can be obtained by superposing the uniform tension of $2F/\pi d_{sp}$ on the radial distributions of the four forces shown in Figure 2.120(a). Following this procedure, the distribution of the normal to the diameter AD stresses has a shape similar to the one shown in Figure 2.120 (b). Note that the normal stress at D is always tensile with a constant value σ_t = $2F/\pi d_{sp}$. This value is in fact identical to the corresponding uniform tensile stress in cylinder specimens during the common splitting test.

Furthermore, it can be easily proven that Equation (2.131) is valid for any number of pairs of two equal and opposite forces. This, in turn, implies that Equation (2.131) is valid for equal and opposite distributed forces, as is the case of forces on the portion of Figure 2.119.

The direct application of this theoretical model to the case here of slender beams implies that the distribution of normal stresses along the line of the second branch of the critical diagonal crack has a shape similar to the one shown in Figure 2.121. These stresses compose a group of forces in self-equilibrium (i.e., forces not balancing any external load). The normal stress at the beginning of the second branch (i.e., at the tip of the first branch) is always tensile with a value:

$$\sigma_t = \frac{2 \cdot P/\sin\theta}{\pi \cdot b \cdot l_{cr}}$$

(2.132)

where l_{cr} = length of second branch of critical diagonal crack; and θ = angle between diagonal line of action and horizontal direction (Figure 2.121). Equation (2.132) results from the value of normal stress at D (Figure 2.120(b)) by substituting the force F by $P/\sin\theta$, the diameter d_{sp} of the disk by the length l_{cr} and the unit thickness of the disk by the width b of the beam.

When the value of the normal tensile stress given by Equation (2.132) exceeds the splitting tensile strength f_{ct} of concrete, an initial crack forms at this area. As the length l_{cr} becomes smaller and therefore the tensile stress σ_t larger, this initial crack propagates to the area of the load point, forming the second branch of the critical diagonal crack. Taking into account that $\sin\theta = c(1-0.5\beta_1)/l_{cr}$ and P = total shear force

V, one can obtain the shear force of the beam, which corresponds to the formation of the second branch of the critical diagonal crack, as follows:

$$V_u = \frac{1}{2} \cdot \pi \cdot b \cdot d \cdot \frac{c}{d} \cdot (1 - 0.5\beta_1) \cdot f_{ct}$$ (2.133)

By substituting $\beta_1 = 0.72$ (as discussed earlier), from Equation (2.133) a simplified nominal shear stress can be calculated, corresponding to the formation of the critical diagonal crack:

$$v_u = \frac{V_u}{b \cdot d} = \frac{c}{d} \cdot f_{ct}$$ (2.134)
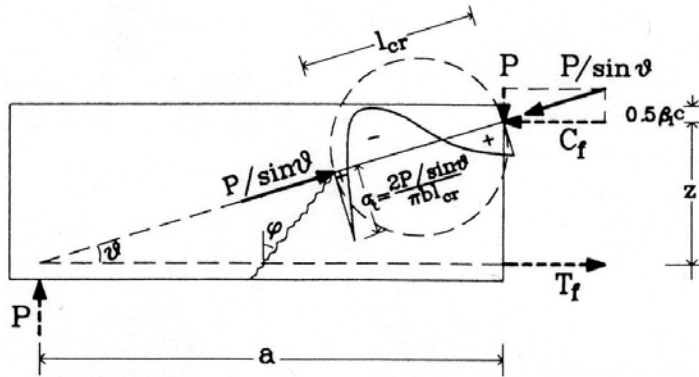
Figure 2.121: Distribution of normal stresses along line of second branch of critical crack [71].

The shear force V_u in Equation (2.133) and the shear stress v_u in Equation (2.134) represent the ultimate shear force and the ultimate shear stress of a slender beam, respectively. Immediately after the formation of the second branch of the critical diagonal crack, the shear force V_d of steel bars is significantly increased due to a significant increase of the angle φ, as can be directly derived from Equation (2.123). This increase of force V_d in turn results in a horizontal cleavage of the concrete cover along the reinforcement, which eventually causes the loss of force V_d. As a result, the whole shear force *V* is transferred to the thin concrete zone above the second branch of the critical diagonal crack. This then behaves as a cantilever eventually failing due to either shear or, more commonly, negative bending forming the well known pattern of failure.

It is important to note that the shear strength of a slender beam, as Equation (2.134) shows, depends primarily on the splitting tensile strength of concrete and

secondarily on the factors affecting the depth c of compression zone, given by Equation (2.125) (i.e., the steel ratio ρ and the concrete strength f'_c).

According to the previous analysis, the diagonal shear failure in slender beams is due to a splitting of concrete, which takes place in a certain region of the beam. In this section, it is argued that the problem of the size effect on diagonal shear failure can be reduced to the problem of size effect on split-tensile failure.

Tests of broad size ranges have been conducted on cylindrical disks of constant thickness by many researchers (Bažant et al. 1991 [68]; Hasegawa et al. 1985 [72]; Sabnis and Mirza 1979 [73]). The results confirm the existence of size effect on split-tensile failure, and show that up to a certain critical diameter the split-cylinder strength decreases as the diameter increases.

In the splitting of concrete occurring in slender beams, the tensile part of the length l_{cr} of the second branch of the critical diagonal crack is considered to play the role of the diameter in split-cylinder tests. The length l_{cr} and its tensile part can be accurately calculated from the relations previously shown. An approximate estimate of l_{cr} and its tensile part can be further derived using geometrical arguments, as shown in Figure 2.121, where l_{cr} is equal to *0.4a* and its tensile part is equal to *0.16a*. Therefore, the size effect on the shear failure of slender beams seems to depend on the size of the shear span a. Taking into account that $a = (a/d)d$, the size effect in beams appears to depend not only on the size of the depth d, as it is commonly believed, but also on the ratio (a/d).

Split-cylinder tensile tests reported by Hasegawa et al. (1985) [72] had a very broad size range (diameter = 100-3000 mm and constant thickness of 500 mm). In spite of the large scatter of these test results, it seems that the normal split-cylinder strength σ_n of a disk with a diameter D approximately satisfies the relation $\sigma_n = $ *(1.20 - 1.30D)f_{ct}* (D in meters), where f_{ct}= nominal split-cylinder strength of a disk with a diameter of 150 mm. This relation is valid up to a certain critical diameter, after which the split-cylinder strength does not decrease any more, but remains about constant at a minimum value. From the test results it seems that min $\sigma_n = 0.65f_{ct}$.

Substituting in the above relation the diameter D with *0.16a* (estimated length of the tensile part of l_{cr}) yields $\sigma_n = $ *(1.20 –0.20a)f_{ct}*. Therefore, one can consider the factor *(1.20 -0.20a)* as the parameter that determines the size effect on the diagonal shear failure of slender beams, with a minimum value of 0.65.

Based on this correlation, Equation (2.134) can be rearranged to take into account the size effect as follows:

133

$$v_u = \frac{V_u}{b \cdot d} = \left(1.2 - 0.2 \cdot \frac{a}{d} \cdot d\right) \cdot \frac{c}{d} \cdot f_{ct} \tag{2.135}$$

where:

$$\left(1.2 - 0.2 \cdot \frac{a}{d} \cdot d\right) \geq 0.65 \quad (d \text{ in meters}) \tag{2.136}$$

The theory is applied as follows for the prediction of the ultimate shear strength of RC slender beams without web reinforcement. 166 test results extracted from the literature were examined at various strengths of concrete (low and high), steel ratios, shear span to depth (a/d) ratios, and geometrical sizes (of length and depth). The experimental and the theoretical results proved to be in an excellent agreement for all the sets of tests.

When applying Equation (2.135) to predict the shear capacity of beams, the depth of compression zone (c/d) has been taken from Equation (2.125), while the splitting tensile strength of concrete has been taken as:

$$f_{ct} = 0.30 \cdot (f_c')^{2/3} \tag{2.137}$$

To further demonstrate the change of the shear strength of slender beams with the shear span, the nominal shear stress at failure is plotted in Figure 2.122(a) as a function of the shear span for all the test beams of Kani (1967) [65]. Figure 2.122 (b) further depicts the same plots for the test beams of Collins and Kuchma (1999) (BN series) [110], Bhal (1968) [111], and Leonhardt and Walther (1962) (C series) [107]. The graph of the proposed formula (Equation(2.135)), for each group of tests, is also depicted in Figure 2.122. Note that the fit with the experimental results is fairly good.
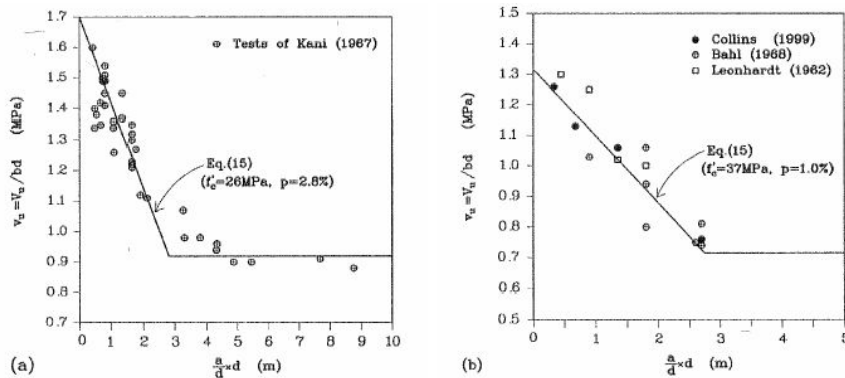
Figure 2.122: Shear strength plotted versus shear span for test results of: (a) Kani; (b) Collins and Kuchma; Bhal and Leonhardt and Walther [71].

134

2.6.7   Modified Compression Field Theory (MCFT).

The MCFT (Vecchio and Collins 1986, [23]) is an analytical model for predicting the load-deformation response of reinforced concrete membrane elements subjected to shear and normal stresses, as shown in Figure 2.123. The MCFT determines the average and local strains and stresses of concrete and reinforcement, and the widths and orientation of cracks throughout the load-deformation response of the element. Based on this information, the failure mode of the element can also be determined.
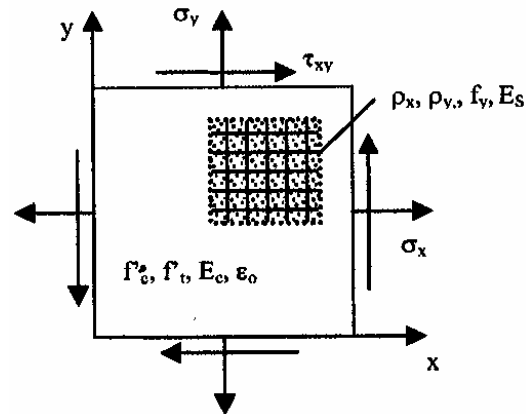
Figure 2.123: Reinforced concrete membrane element subject to in-plane stresses.

The MCFT models cracked concrete as an orthotropic material using a smeared rotating crack approach. Cracked concrete is treated as a solid continuum with cracks distributed over the membrane element, as opposed to a solid interrupted by discrete physical discontinuities. The smeared cracks freely reorient, remaining coaxial with the changing direction of the principal concrete compressive stress field. As well as being computationally convenient, the smeared rotating crack approach is consistent with the distributed and meandering crack patterns observed in many reinforced concrete structures.

The theory is comprised of three sets of relationships: compatibility relationships for concrete and reinforcement average strains; equilibrium relationships involving average stresses in the concrete and reinforcement; and constitutive relationships for cracked concrete and reinforcement. The constitutive relationships for cracked concrete result from tests of reinforced concrete panels using a purpose-built Panel Element Tester at the University of Toronto. As such, the formulation of the MCFT incorporates realistic constitutive models for concrete based on experimentally observed phenomena. While cracks are smeared and the relationships are

formulated in terms of average stresses and strains, a critical aspect of the MCFT is the consideration of local strain and stress conditions at cracks.

2.6.7.1 Assumptions.

The MCFT utilizes the following assumptions:

- Uniformly distributed reinforcement;
- Uniformly distributed and rotating cracks;
- Uniformly applied shear and normal stresses;
- Unique stress state for each strain state, without consideration of strain history;
- Strains and stresses are average over a distances including several cracks;
- Orientations of principal strain, θ_ε, and orientations of principal stress, θ_σ, are the same;
- Perfect bond between reinforcement and concrete;
- Independent constitutive relationships for concrete and reinforcement;
- Negligible shear stresses in reinforcement.

2.6.7.2 Compatibility Relationships.

The compatibility relationships pertain to the average strains in the concrete and reinforcement components as shown in Figure 2.124.
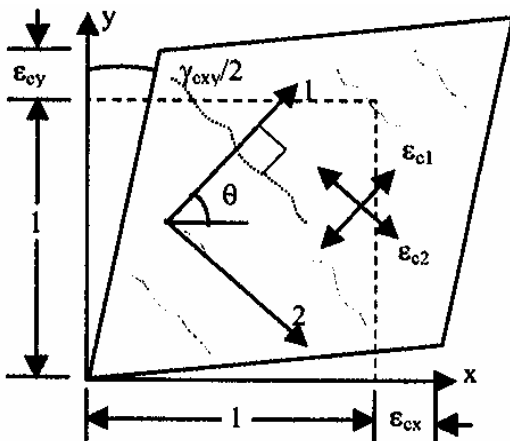
Figure 2.124: Average concrete strains due to average stress-strain response of concrete.

With the perfect bond assumption, it follows that average strains experienced by the concrete are equally experienced by the reinforcement. Therefore, for non-prestressed reinforcement, the average strains in the concrete, ε_c, and reinforcement, ε_s, will be the same. Although the MCFT can address any number of

reinforcement components and orientations, consider the orthogonally reinforced membrane element of Figure 2.123. The strains of the reinforcement parallel to the x and y directions are denoted by ε_{sx} and ε_{sy}, respectively. The compatibility relationships are expressed by the following equations:

$$\varepsilon_x = \varepsilon_{cx} = \varepsilon_{sy} \tag{2.138}$$

$$\varepsilon_y = \varepsilon_{cy} = \varepsilon_{sy} \tag{2.139}$$

With a value for the shear strain, γ_{xy}, relationships from Mohr's circle of strain determine the average principal concrete tensile strain, ε_{c1}, and the average principal concrete compressive strain, ε_{c2} as follows:

$$\varepsilon_{c1}, \varepsilon_{c2} = \tfrac{1}{2}\left(\varepsilon_x + \varepsilon_y\right) \pm \tfrac{1}{2}\left[\left(\varepsilon_x - \varepsilon_y\right)^2 + \gamma_{xy}^2\right]^{\tfrac{1}{2}} \tag{2.140}$$

Relationships from Mohr's circle also determine the orientations of the average principal tensile strain axis, $\theta\varepsilon$, and stress axis, $\theta\sigma$, with respect to the x-axis:

$$\theta = \theta_\varepsilon = \theta_\sigma = \tfrac{1}{2}\tan^{-1}\left(\frac{\gamma_{xy}}{\varepsilon_x - \varepsilon_y}\right) \tag{2.141}$$

2.6.7.3 Equilibrium Relationships.
Consider the free body diagram of the membrane element, in Figure 2.125.
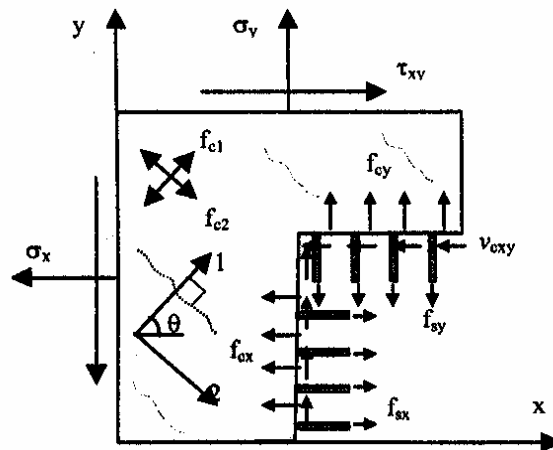
Figure 2.125: Free body diagram of reinforced concrete element showing average stresses.

Equilibrium of forces in the x and y-directions requires that the resultants of the applied normal stresses, σ_x and σ_y, be balanced by the resultants of the average

137

concrete stresses, f_{cx} and f_{cy}, and the reinforcement stresses f_{sx} and f_{sy}. Equilibrium of moments requires that the applied shear stresses, τ_{xy}, are entirely resisted by average shear stresses in the concrete, v_{cxy}, (assuming the reinforcement does not exhibit dowel action). These equilibrium relationships for average stresses may be summarized as follows:

$$\sigma_x = f_{cx} + \rho_{sx} f_{sx} \tag{2.142}$$

$$\sigma_y = f_{cy} + \rho_{sy} f_{sy} \tag{2.143}$$

$$\tau_{xy} = v_{cxy} \tag{2.144}$$

where ρ_{sx} and ρ_{sy} are the reinforcement ratios in the x and y directions, respectively. As cracked concrete is orthotropic with respect to the principal stress directions, Mohr's circle of stress can be used to relate the average concrete stresses, f_{cx}, and, f_{cy}, to the average principal concrete tensile stress, f_{c1}:

$$f_{cx} = f_{c1} - v_{cxy} \cdot \cot(90 - \theta_\sigma) \tag{2.145}$$

$$f_{cy} = f_{c1} - v_{cxy} \cdot \tan(90 - \theta_\sigma) \tag{2.146}$$

2.6.7.4   Constitutive Relationships.

Constitutive models are necessary to relate the strains in the compatibility relationships with the stresses in the equilibrium relationships. As described by Vecchio and Collins (1986), thirty panels measuring 890x890x70mm were subjected to in-plane stress conditions by the Panel Element Tester at the University of Toronto. The test results were analyzed to develop constitutive models for cracked concrete in compression and tension. It should be noted that other relationships have been implemented in VecTor2.

With regards to concrete in compression, the constitutive relationship relates the principal compressive stress, f_{c2}, to the principal compressive strain, ε_{c2}. Panel test results indicate that the compressive strength and stiffness decrease as coexisting principal tensile strains, ε_{c1}, increase. This phenomenon, known as compression softening, is incorporated by softening the stress-strain response of concrete in uniaxial compression. The proposed relationship is as follows:

$$f_{c2} = \frac{f'_c \left[2(\varepsilon_{c2}/\varepsilon_o) - (\varepsilon_{c2}/\varepsilon_o)^2 \right]}{0.8 - 0.34(\varepsilon_{c1}/\varepsilon_o)} \tag{2.147}$$

The term in the numerator is the Hognestad parabolic relationship for concrete in uniaxial compression, often used for normal strength concrete. The value ε_o is the

138

concrete cylinder strain (a negative value) corresponding to the peak compressive stress, f'$_c$, as determined from uniaxial compression tests of concrete cylinders. The term in the denominator reflects the softening effect of principal tensile strains.

With regards to concrete in tension, the constitutive relationship relates the principal tensile stress, f$_{c1}$, to the principal tensile strain, ε_{c1}. It is first necessary to determine the uniaxial cracking strength, f'$_t$, and corresponding cracking strain, ε_{cr}. In the absence of information, they may be estimated as follows:

$$f'_t = 0.33\sqrt{f'_c} \qquad \left(in\ MPa\right) \tag{2.148}$$

$$\varepsilon_{cr} = \frac{f'_t}{E_c} \tag{2.149}$$

where E$_c$ is the initial tangent stiffness of the concrete, estimated as:

$$E_c = 5000\sqrt{f'_c} \quad \left(in\ MPa\right) \tag{2.150}$$

Before cracking, the concrete behaves linear-elastically in tension as follows:

$$f_{c1} = E_c \cdot \varepsilon_{c1} \quad for\ 0 < \varepsilon_{c1} < \varepsilon_{cr}$$
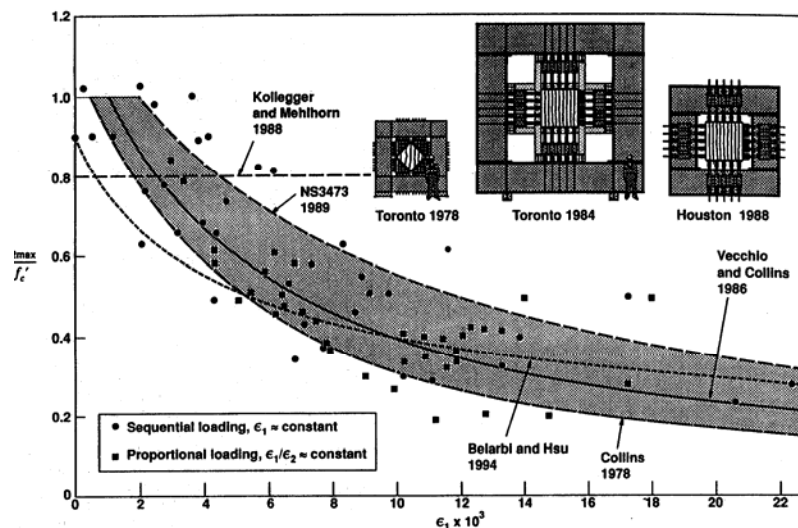
Figure 2.126: Maximum concrete compressive stress as a function of principal compressive stress [2].
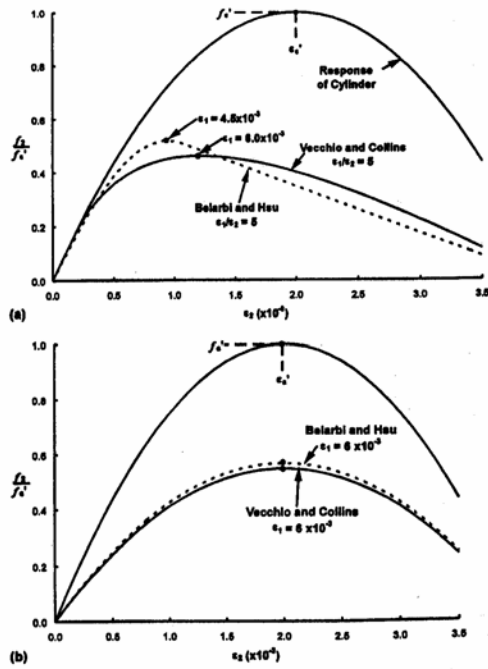
Figure 2.127: Compressive stress-compressive strain relationships for diagonally cracked concrete: (a) proportion loading, ε_1 and ε_2 increased simultaneously; (b) Sequential loading, ε_1 applied first, then ε_2 increased [2].

After cracking, tensile stresses may continue to exist in the concrete between cracks in reinforced concrete due to bond interactions between the concrete and reinforcement. To model this phenomenon, known as tension stiffening, the concrete tensile stress decays from the tensile strength as the principal concrete tensile strain increases. The MCFT proposed relationship is as follows:

$$f_{c1} = \frac{f'_t}{1 + \sqrt{200\varepsilon_{c1}}}$$
(2.151)

As for the reinforcement in compression and tension, the MCFT uses a bilinear relationship between the average stress, f_s and average strain, ε_s. An initial ascending linear-elastic branch is followed by a yield plateau, as described by the following equations:

$$f_{sx} = E_s \cdot \varepsilon_{sx} \leq f_{sxyield}$$
(2.152)

$$f_{sy} = E_s \cdot \varepsilon_{sy} \leq f_{syyield}$$
(2.153)

140

where E_s is the elastic modulus of the reinforcement, and $f_{sxyield}$ and $f_{syyield}$ are the yield stress of the reinforcement in the x and y-directions, respectively.

2.6.7.5   Consideration of Local Crack Conditions.

Given a compatible average strain condition, the preceding relationships can determine the average stresses in the concrete and reinforcement and the applied shear and normal stresses that they equilibrate. However, it would be unconservative to disregard the possibility that the element response is governed by local yielding of the reinforcement at the crack or sliding shear failure along a crack. To address these possibilities, the MCFT limits the local stresses at the crack and the average concrete tensile stress.

Stresses fields in reinforced concrete vary from the average condition between cracks to the local condition at the crack. Consider Figure 2.128a, which depicts the average stresses at a section between cracks perpendicular to the principal tensile stress direction, and Figure 2.128b, which depicts the local stresses at the free surface of the crack.

At a free surface of a crack, the average concrete tensile stresses diminish to virtually zero. To transmit the average tensile stress across the crack, the reinforcement stress and strain must increase locally at the crack. Static equivalency of the average and local stresses in the direction normal to the crack surface results in the following equation:

$$f_{c1} = \rho_x \left(f_{scrx} - f_{sx} \right) \cos^2 \theta_{nx} + \rho_y \left(f_{scry} - f_{sy} \right) \cos^2 \theta_{ny} \tag{2.154}$$

where f_{scrx} and f_{scry} are the local reinforcement stresses at a crack, and θ_{nx} and θ_{ny} are the angles between the normal to the crack and the reinforcement. Considering the above equation, it is apparent that the average tensile concrete stress is limited by the yielding of the reinforcement at the crack. If the reinforcement yield strength is substituted for the local reinforcement stresses, the terms in parentheses define the reserve capacity of the reinforcement, which limits the post-cracking concrete tensile stress as follows:

$$f_{c1} \le \rho_x \left(f_{sxyield} - f_{sx} \right) \cos^2 \theta_{nx} + \rho_y \left(f_{syyield} - f_{sy} \right) \cos^2 \theta_{ny} \tag{2.155}$$

As a principal plane, shear stresses are absent from the section in Figure 2.128a. However, as the reinforcement generally crosses the crack at a skew angle, local shear stresses, v_{ci}, are present on the crack surface. Static equivalency of average and local stresses in the direction tangential to the crack determines the local shear stresses as follows:

$$v_{ci} = \rho_x \left(f_{s\,crx} - f_{s\,x} \right) \cos\theta_{nx} \cdot \sin\theta_{nx} + \rho_y \left(f_{s\,cry} - f_{s\,y} \right) \cos\theta_{ny} \cdot \sin\theta_{ny} \qquad (2.156)$$
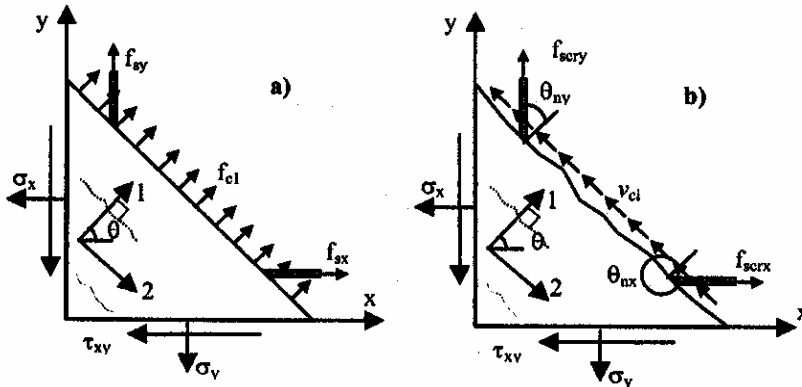
Figure 2.128: Comparison of average and local stresses at a crack a) average stresses between crack, b) local stresses at crack free surface.

Independently of the above equation, local shear stresses can only become so large before sliding shear failure occurs. The shear stress is limited by aggregate interlock mechanisms, which decrease in efficacy as the crack width, w, increases and the maximum aggregate size, a, decreases. Based on the analysis of aggregate interlock by Walraven (1981), the MCFT limits the shear stress on the crack as follows:

$$v_{ci} \leq \frac{\sqrt{f'_c}}{0.31 + 24w/\left(a + 26\right)} \qquad \left(\text{in mm, MPa}\right) \qquad (2.157)$$

The average crack width, w, is the product of the principle concrete tensile strain and the average crack spacing perpendicular to the crack, s_θ:

$$w = \varepsilon_{c1} s_\theta \qquad (2.158)$$

$$s_\theta = \frac{1}{\dfrac{\cos\theta}{s_{mx}} + \dfrac{\sin\theta}{s_{my}}} \qquad (2.159)$$

The average crack spacing in the x-direction, s_{mx}, and y-direction, s_{my}, may be estimated from the bond properties and layout of the reinforcement. For further details, refer to Collins and Mitchell, (1997).

142

If either the maximum permitted average concrete tensile stress or local shear stress at a crack is exceeded, then the strain state of the element is modified to result in a lower average concrete tensile stress.

A summary of the MCFT is given in Figure 2.129 and Figure 2.130.

Equilibrium:

Average Stresses:

$$\rho_x f_{sx} = f_x + v\cot\theta - f_1$$

$$\rho_y f_{sy} = f_y + v\tan\theta - f_1$$

$$f_2 = v(\tan\theta + \cot\theta) - f_1$$

Stresses at Cracks:

$$\rho_x f_{sxcr} = f_x + v\cot\theta + v_{ci}\cot\theta$$

$$\rho_y f_{sycr} = f_y + v\tan\theta - v_{ci}\tan\theta$$

Geometric Conditions:

Average Strains:

$$\epsilon_x = (\epsilon_1\tan^2\theta + \epsilon_2)/(1 + \tan^2\theta)$$

$$\epsilon_y = (\epsilon_1 + \epsilon_2\tan^2\theta)/(1 + \tan^2\theta)$$

$$\gamma_{xy} = 2(\epsilon_x - \epsilon_2)/\tan\theta$$

$$\tan^2\theta = (\epsilon_x - \epsilon_2)/(\epsilon_y - \epsilon_2)$$

Crack Widths:

$$w = s_\theta \epsilon_1 \quad \text{where}$$

$$s_\theta = 1/\left(\frac{\sin\theta}{s_x} + \frac{\cos\theta}{s_y}\right)$$

Average Stress-Average Strain Relationships:

Reinforcement:

$$f_{sx} = E_s\,\epsilon_x \le f_{x\,yield}$$

$$f_{sy} = E_s\,\epsilon_y \le f_{y\,yield}$$

Concrete:

$$f_2 = \frac{f_c'}{0.8 + 170\epsilon_1}\left[2\,\frac{\epsilon_2}{\epsilon_c'} - \left(\frac{\epsilon_2}{\epsilon_c'}\right)^2\right]$$

$$f_1 = \frac{f_{cr}}{1 + \sqrt{500\,\epsilon_1}}$$

Allowable Shear Stress on Crack

$$v_{ci} \le \frac{0.18\sqrt{f_c'}}{0.31 + \frac{24\,w}{a + 16}}$$

Figure 2.129: Summary of MCFT.
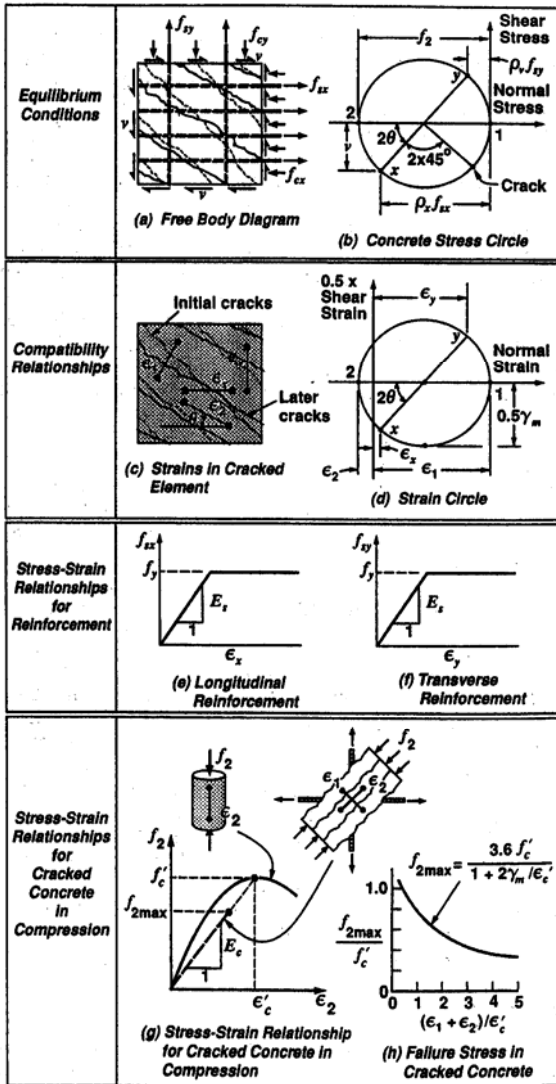
Figure 2.130: Aspects of the Modified Compression Field Theory [3].

2.6.8 Disturbed Stress Field Model (DSFM).

The Disturbed Stress Field Model (DSFM; [112], [113] and [114]) addresses systematic deficiencies of the MCFT in predicting the response of certain structures and loading scenarios. In lightly reinforced elements, where crack shear slip is significant, the rotation of the principal stress field tends to lag the greater rotation of the principal strain field. For such elements, the shear stiffness and strength are generally overestimated by the MCFT, which assumes the rotations are equal.

Conversely, in elements that exhibit limited rotation of the principal stress and strain fields, the MCFT generally underestimates the shear stiffness and strength, partly because the concrete compression response calibrated for the MCFT is overly softened for the effect of principal tensile strains.

The DSFM is conceptually similar to the MCFT, but extends the MCFT in several respects. Most importantly, the DSFM augments the compatibility relationships of the MCFT to include crack shear slip deformations. The strains due to these deformations are distinguished from the strains of the concrete continuum due to stress. As such, the DSFM decouples the orientation of the principal stress field from that of the principal strain field, resulting in a smeared delayed rotating-crack model. Moreover, by explicitly calculating crack slip deformations, the DSFM eliminates the crack shear check as required by the MCFT. Constitutive relationships for concrete and reinforcement are also refined. The following discussion presents the compatibility, equilibrium and constitutive relationships of the DSFM, with an emphasis on differences from the MCFT.

2.6.8.1 Compatibility Relationships.

While the MCFT assumes that principal strain and principal stress axes remain coaxial, panel tests results indicate that this assumption is not always true after the cracking. The evidence demonstrates that the principal strain field generally changes inclination at a larger rate than the principal stress field, resulting in a differential lag between the principal strain and principal stress axes.

The phenomenon is attributable to the manner in which the strain and stress fields are determined. The measured strains are total strains, which are attributable to straining of the concrete continuum in response to applied stresses as shown in Figure 2.124 and discontinuous shear slip as shown in Figure 2.131. Meanwhile, concrete stresses are attributable only to the continuum straining in response to applied stresses.

To reconcile this behavior, the DSFM expresses the total strains, ε_x, ε_y, and γ_{xy}, as the sum of net concrete strains, ε_{cx}, ε_{cy}, and γ_{cxy}, and strain due to shear slip, ε_x^s, ε_y^s and γ_{xy}^s :

$$\varepsilon_x = \varepsilon_{cx} + \varepsilon_x^s \tag{2.160}$$

$$\varepsilon_y = \varepsilon_{cy} + \varepsilon_y^s \tag{2.161}$$

$$\gamma_{xy} = \gamma_{cxy} + \gamma_{xy}^s \tag{2.162}$$

145
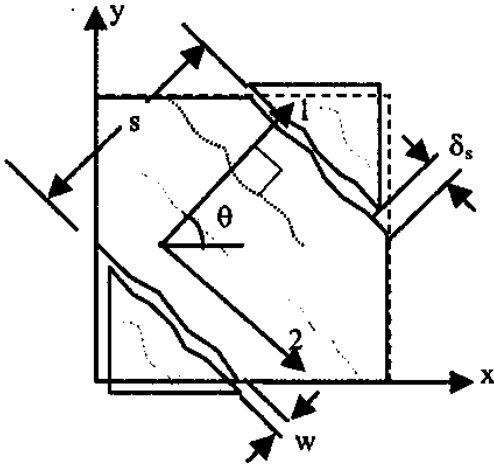
Figure 2.131: Deformation due to crack shear slip.

Relationships from Mohr's circle determine the principal net concrete tensile strain, ε_{c1}, and the principal net concrete compressive strain, ε_{c2}, as follows:

$$\varepsilon_{c1}, \varepsilon_{c2} = \tfrac{1}{2}\left(\varepsilon_{cx} + \varepsilon_{cy}\right) \pm \tfrac{1}{2}\left[\left(\varepsilon_{cx} - \varepsilon_{cy}\right)^2 + \gamma_{cxy}^2\right]^{\frac{1}{2}} \tag{2.163}$$

The crack slip shear strain components, ε_x^s, ε_y^s and γ_{xy}^s, are calculated from the average crack slip shear strain γ_s. This quantity is defined as the crack slip, δ_s, divided by the average crack spacing, s, as follows:

$$\gamma_s = \frac{\delta_s}{s} \tag{2.164}$$

Relationships from Mohr's circle resolve γ_s into the components ε_{sx}, ε_{sy} and γ_{sxy}:

$$\varepsilon_x^s = -\tfrac{1}{2}\gamma_s \sin(2\theta) \tag{2.165}$$

$$\varepsilon_y^s = \tfrac{1}{2}\gamma_s \sin(2\theta) \tag{2.166}$$

$$\gamma_{xy}^s = \gamma_s \cos(2\theta) \tag{2.167}$$

The orientation of the principal net concrete strains, θ, and orientation of principal concrete stresses, $\theta\sigma$, with respect to the x-axis are determined from Mohr's circle relationships involving the net concrete strain components as follows:

$$\theta = \theta_\sigma = \tfrac{1}{2}\tan^{-1}\left(\frac{\gamma_{cxy}}{\varepsilon_{cx} - \varepsilon_{cy}}\right) \tag{2.168}$$

146

Likewise, the orientation of the principal total strain field, θ_ε, is determined from the total strain components:

$$\theta_\varepsilon = \tfrac{1}{2}\tan^{-1}\left(\frac{\gamma_{xy}}{\varepsilon_x - \varepsilon_y}\right) \tag{2.169}$$

The difference between the orientation of total strains and the orientation of the principal concrete stresses defines the rotation lag, $\Delta\theta$:

$$\Delta\theta = \theta_\varepsilon - \theta_\sigma \tag{2.170}$$

Although the DSFM can address any number of reinforcement components and orientations, consider the orthogonally reinforced membrane element of Figure 2.123. Assuming perfect bond, the average strains of the reinforcement components in the x- and y-directions are equal to the total strains:

$$\varepsilon_{sx} = \varepsilon_x \tag{2.171}$$

$$\varepsilon_{sy} = \varepsilon_y \tag{2.172}$$

2.6.8.2 Equilibrium Relationships.

Again, consider the orthogonally reinforced membrane element of Figure 2.123. The average stress equilibrium relationships of the DSFM are the same as those of the MCFT. They are summarized as follows:

$$\sigma_x = f_{cx} + \rho_{sx} f_{sx} \tag{2.173}$$

$$\sigma_y = f_{cy} + \rho_{sy} f_{sy} \tag{2.174}$$

$$\tau_{xy} = v_{cxy} \tag{2.175}$$

Additionally, the DSFM incorporates the equilibrium relationships for local stresses at the crack:

$$f_{c1} = \rho_x \left(f_{s\,crx} - f_{s\,x} \right)\cos^2\theta_{nx} + \rho_y \left(f_{s\,cry} - f_{s\,y} \right)\cos^2\theta_{ny} \tag{2.176}$$

$$v_{ci} = \rho_x \left(f_{s\,crx} - f_{s\,x} \right)\cos\theta_{nx}\cdot\sin\theta_{nx} + \rho_y \left(f_{s\,cry} - f_{s\,y} \right)\cos\theta_{ny}\cdot\sin\theta_{ny} \tag{2.177}$$

Equilibrium of stress resultants normal to the crack surface results in the following equations:

$$f_{c1} = \rho_x \left(f_{s\,crx} - f_{s\,x} \right)\cos^2\theta_{nx} + \rho_y \left(f_{s\,cry} - f_{s\,y} \right)\cos^2\theta_{ny} \tag{2.178}$$

$$v_{ci} = \rho_x \left(f_{s\,crx} - f_{s\,x} \right)\cos\theta_{nx}\cdot\sin\theta_{nx} + \rho_y \left(f_{s\,cry} - f_{s\,y} \right)\cos\theta_{ny}\cdot\sin\theta_{ny} \tag{2.179}$$

The average concrete tensile stress is subject to the limits of the yield strength of the reinforcement traversing the crack:

$$f_{c1} \leq \rho_x \left(f_{sxyield} - f_{sx} \right) \cos^2 \theta_{nx} + \rho_y \left(f_{syyield} - f_{sy} \right) \cos^2 \theta_{ny} \tag{2.180}$$

Unlike the MCFT, however, the tensile stress is not subject to the limitation of shear stresses at a crack, since the DSFM explicitly incorporates deformations due to shear slip rather than ascribing a limiting stress corresponding to shear slip failure.

2.6.8.3 Constitutive Relationships.

Between the development of the MCFT and the DSFM, the constitutive models for cracked concrete were revised and refined. Although a variety of alternative models are available, the following discussion presents the models of the DSFM.

As previously discussed, the response of concrete in compression depends on both the principal compressive strain and coexisting principal tensile strain. Analyses of additional test panels led to the reduction factor, β_d, to reflect the softening effect of the coexisting principal tensile strains:

$$\beta_d = \frac{1}{1 + C_s C_d} \leq 1.0 \tag{2.181}$$

The factor, C_d, accounts for the softening effect of transverse tensile strains:

$$C_d = 0.35 \left(-\varepsilon_{c1} / \varepsilon_{c2} - 0.28 \right)^{0.8} \tag{2.182}$$

The factor C_s recognizes whether or not the analysis accounts for element slip deformations. If the analysis couples the inherent softening effect of shear slippage with the softening effect due to tensile strains (as in the MCFT), then C_s = 1.0. Conversely, if the analysis considers elements slip distortion, as in the DSFM, then the softening effect appears to be less for the same value of $\varepsilon_{c1}/\varepsilon_{c2}$ since the softening effect is attributable only to the tensile strains. In this case, C_s = 0.55.

To soften the compressive strength and stiffness of the concrete, the concrete cylinder strength, f'$_c$, and corresponding peak strain, ε_o, are both reduced by the reduction factor to determine the peak compressive stress, f_p, and corresponding peak strain ε_p:

$$f_p = -\beta_d f'_c \tag{2.183}$$

$$\varepsilon_p = -\beta_d \varepsilon_o \tag{2.184}$$

148

Using the softened parameters, the following relationship determines the relationship between the principal concrete compressive stress, f_{c2}, and the principal net compressive strain, ε_{c2}:

$$f_{c2} = f_p \frac{n(\varepsilon_{c2}/\varepsilon_p)}{(n-1) + (\varepsilon_{c2}/\varepsilon_p)^{nk}} \tag{2.185}$$

where

$$n = 0.80 - f_p/17 \quad (in\ MPa) \tag{2.186}$$

$$k = \begin{cases} 1.0 & for\ \varepsilon_p < \varepsilon_{c2} < 0 \\ 0.67 - f_p/62 & for\ \varepsilon_{c2} < \varepsilon_p < 0 \end{cases} \tag{2.187}$$

With regards to concrete in tension, the response before cracking is linear-elastic, as follows:

$$f_{c1} = E_c \cdot \varepsilon_{c1} \quad for\ 0 \leq \varepsilon_{c1} \leq \varepsilon_{cr} \tag{2.188}$$

For cracked concrete, average concrete tensile stresses, f^a_{c1}, due to tension stiffening, can be generally modeled by the nonlinearly decaying relationship (but must not exceed the bound imposed by Equation (2.178)):

$$f^a_{c1} = \frac{f'_t}{1 + \sqrt{c_t \varepsilon_{c1}}} \quad for\ \varepsilon_{cr} < \varepsilon_{c1} \tag{2.189}$$

The coefficient, c_t, proposed by Bentz (1999) incorporates the influence of reinforcement bond characteristics and is computed as follows:

$$c_t = 2.2m \tag{2.190}$$

$$\frac{1}{m} = \sum_{i=1}^{n} \frac{4\rho_i}{d_{b_i}} |\cos \theta_{n_{ii}}| \quad (in\ mm) \tag{2.191}$$

where d_{bi} is the bar diameter and ρ_i is the reinforcement ratio of each of the n reinforcement components.

In addition to tension stiffening, post-cracking tensile stresses, f_{c1b}, arise in plain concrete due to fracture mechanisms – a phenomenon known as tension softening. Tension softening effects may be significant in lightly reinforced concrete structures. The cracking tensile stress due to tension softening may be calculated by the following linear relationship:

149

$$f_{c1}{}^{b} = f'_t \left[1 - \frac{(\varepsilon_{c1} - \varepsilon_{cr})}{(\varepsilon_{ts} - \varepsilon_{cr})}\right] \qquad \text{for } \varepsilon_{cr} < \varepsilon_{c1} < \varepsilon_{ts} \qquad (2.192)$$

The terminal strain, ε_{ts}, (the strain at which tensile stresses in plain concrete reduce to zero) is determined from the fracture energy parameter, G_f, (the area under the stress-strain curve of plain concrete, assumed to be 75 N/m), and the characteristic length, L_r (assumed to be half the crack spacing):

$$\varepsilon_{ts} = 2.0 \frac{G_f}{f'_t \cdot L_r} \qquad (2.193)$$

Finally, the post-cracking principal tensile stress in the concrete is taken as the largest of the values predicted by the tension stiffening and tension softening phenomena:

$$f_{c1} = max\left(f_{c1}{}^{a}, f_{c1}{}^{b}\right) \qquad (2.194)$$

The DSFM constitutive model for reinforcement in tension or compression is trilinear to account for strain-hardening phenomenon:

$$f_s = \begin{cases} E_s \cdot \varepsilon_s & \text{for } 0 < \varepsilon_s < \varepsilon_{syield} \\ f_{syield} & \text{for } \varepsilon_{syield} < \varepsilon_s < \varepsilon_{sh} \\ f_{syield} + E_{sh}(\varepsilon_s - \varepsilon_{sh}) & \text{for } \varepsilon_{sh} < \varepsilon_s < \varepsilon_u \\ 0 & \text{for } \varepsilon_u < \varepsilon_s \end{cases} \qquad (2.195)$$

where E_s is the elastic modulus of the reinforcement, f_{syield} is the yield strength of the reinforcement, ε_{syield} is the yield strain of the reinforcement, ε_{sh} is the strain at the onset of strain hardening, ε_u is the ultimate strain of the reinforcement.

2.6.8.4   Shear Slip Relationships.

Having defined the compatibility, equilibrium and constitutive relationships, it remains necessary to model the crack slip, δ_s, to determine the crack slip shear strain, γ_s. One approach is to relate the crack slip to the local shear stresses, v_{ci}, at the crack. Based on the analysis of aggregate interlock by Walraven (1981), the following relationship may be used to determine the crack-slip and shear slip strain:

$$\delta_s{}^{a} = \frac{v_{ci}}{1.8w^{-0.8} + (0.234w^{-0.707} - 0.20) \cdot f_{cc}} \qquad (2.196)$$

$$\gamma_s{}^a = \frac{\delta_s{}^a}{s} \tag{2.197}$$

where f_{cc} is the concrete cube strength, w is the average crack spacing and s is the average crack spacing.

However, the above approach is problematic in two respects. First, the equilibrium Equation (2.177) predicts that the shear stress at a crack, and hence the crack slip, are always zero for unreinforced elements. This is equivalent to ignore crack shear stresses arising from aggregate interlock – the sliding friction between the exposed aggregate and cement paste at the crack and the plastic deformation of the cement paste due to contact stresses. Secondly, the slip relationship does not account for the initial crack slip that occurs before contact areas develop between the rough crack surfaces.

To address these deficiencies, a second approach for modeling the shear slip is to specify a constant rotation lag, θ_l, between the inclination of the principal total strain axis, θ_ε and the inclination of the principal stress axis, θ_σ. Indeed, results of panel tests indicate that the lag is established soon after cracking, and generally falls in the range of 5° to 10° until the yielding of a reinforcement component, whereupon the lag increases. To implement this approach, it is necessary to define the post-cracking rotation, $\Delta\theta_\varepsilon$, of the principal total strain axis, relative to the orientation of the principal strains and stresses at initial cracking, θ_{ic}:

$$\Delta\theta_\varepsilon = \theta_\varepsilon - \theta_{ic} \tag{2.198}$$

The post-cracking rotation, $\Delta\theta_\sigma$, of the principal stress field is then related to $\Delta\theta_\varepsilon$, by the constant rotation lag as follows:

$$\Delta\theta_\sigma = \begin{cases} \Delta\theta_\varepsilon & for \; |\Delta\theta_\varepsilon| \le \theta^l \\ \left(\Delta\theta_\varepsilon - \theta^l\right) & for \; |\Delta\theta_\varepsilon| > \theta^l \end{cases} \tag{2.199}$$

The orientation of the principal stress field is determined as the sum of its orientation at initial cracking, and its post-cracking rotation:

$$\theta_\sigma = \theta_{ic} + \Delta\theta_\sigma \tag{2.200}$$

Finally, relationships from Mohr's circle determine the shear slip strain, γ_s^b:

$$\gamma_s^b = \gamma_{xy} \cdot cos2\theta_\sigma + \left(\varepsilon_y - \varepsilon_x\right) \cdot \sin 2\theta_\sigma \tag{2.201}$$

Further, it is possible to combine the two approaches in a hybrid model for shear slip. The shear slip strain is computed by both approaches and the largest value is utilized:

$$\gamma_s = max\left(\gamma_s{}^a, \gamma_s{}^b\right) \qquad (2.202)$$

When the concrete element is unreinforced or when the local shear stress on the crack is small, the constant rotation lag governs the shear slip, reflecting the initial slip occurring prior to development of shear stresses at a crack. Conversely, when the shear stresses on the crack are large, the shear slip is predicted by the stress-based formulation. As such, using the both approaches collectively is consistent with the actual determinants of the shear slip.

2.6.9   Summary of further Models.

Many other analytical models were developed for predicting the shear strength of beams with little or no shear reinforcements. Among those, it is worthy to report some of them, which are fairly popular and often referenced in the scientific community.

These models will not be explained in details. Only the formula predicting the ultimate shear load is herein reported, while full details can be found in the references mentioned.

Denomination	Formula	
ACI-ASCE Committee 426 (1973) [4]	$v_c = \left(0{,}8 + 100 \cdot \rho_s\right) \cdot \sqrt{f'_c} \le 2.0 \cdot \sqrt{f'_c}$	(2.203)
Mattock and Zsutty (1968) [4]	$v_u = 59 \cdot \sqrt[3]{f'_c \cdot \rho_s \cdot \dfrac{d}{a}}$ $\qquad$ a/d ≥2.5 $v_u = \left(\dfrac{2.5}{a/d}\right) \cdot 59 \cdot \sqrt[3]{f'_c \cdot \rho_s \cdot \dfrac{d}{a}}$ $\quad$ a/d<2.5	(2.204)
Okamura and Higai (1981) [10]	$v_c = 64 \cdot \left(f'_c \cdot \rho_s\right)^{1/3} \cdot d^{-(1/4)} \cdot \left(0.75 + 1.4 \cdot \dfrac{d}{a}\right)$	(2.205)

Denomination	Formula	
Bažant and Kim (1984) [9]	$v_u = 10 \cdot \xi \cdot \sqrt[3]{\rho_s} \cdot \left(\sqrt{f'_c} + 3000 \sqrt{\dfrac{\rho_s}{(a/d)^5}} \right)$ where $\xi = \dfrac{1}{\sqrt{1 + \dfrac{d}{25 \cdot d_a}}}$	(2.206)
Japanese Code (JSCE) (1986) (from [116])	$v_c = 61.13 \cdot \left(f'_c \cdot \rho_s \right)^{1/3} \cdot d^{-(1/4)}$	(2.207)
CEB-FIP Model Code (1993) (from [116])	$v_c = 27.67 \cdot \left(f'_c \cdot \rho_s \cdot \dfrac{d}{a} \right)^{1/3} \cdot \left(1 + \sqrt{\dfrac{8}{d}} \right)$	(2.208)
Collins and Kuchma (1999) [110]	$v_c = \dfrac{115}{50 + s_e} \sqrt{f'_c}$ where $s_e = s_x \cdot \dfrac{1.38}{a + 0.63}$	(2.209)
Rebeiz (1999) [115]	$v_u = \dfrac{V_u}{b \cdot d} = 57 + \sqrt{f'_c \cdot \rho_s \cdot \left(\dfrac{d}{a} \right)} \cdot \left(120 - 36 \cdot A_d \right)$ where A_d = shear shape adjustment factor = a/d for 1.0 < a/d < 2.5, or 2.5 for a/d ≥ 2.5	(2.210)
Khuntia and Stojadinovic (2001) [116]	$\nu_c = 28.7 \cdot \rho^{0.37} \cdot \left(\dfrac{V_{cr} \cdot d}{M_u} \right)^{0.13} \cdot (f'_c)^{0.18}$	(2.211)

Table 2.1: Summary of proposed shear strength equations for beams without stirrups.

2.7 Design Aspects: a Standard Overview.

In the following section, a brief review on the prescriptions concerning shear design of beams containing little or no shear reinforcement is provided, especially focusing on three international well known Codes:

- EUROCODE 2;
- ACI Building Code;
- Canadian Code CSA.

Their prescriptions on shear design differ quite a lot to each other, leading to considerably different design procedures, amount of stirrups and definitely to significant scatter in safety.

2.7.1   Eurocode 2 (prEN 1992-1-1, draft December 2003).

For the verification of the shear resistance the following symbols are defined:

$V_{Rd,c}$ is the design shear resistance of the member without shear reinforcement.

$V_{Rd,s}$ is the design value of the shear force which can be sustained by the yielding shear reinforcement.

$V_{Rd,max}$ is the design value of the maximum shear force which can be sustained by the member, limited by crushing of the compression struts.

The main specifications on shear design provided are:

- In regions of the member where $V_{Ed} \leq V_{Rd,c}$ no calculated shear reinforcement is necessary. V_{Ed} is the design shear force in the section considered resulting from external loading and prestressing (bonded or unbonded).

- When no shear reinforcement is required, minimum shear reinforcement should nevertheless be provided. The minimum shear reinforcement may be omitted in members such as slabs (solid, ribbed or hollow core slabs) where transverse redistribution of loads is possible. Minimum reinforcement may also be omitted in members of minor importance (e.g. lintels with span ≤ 2 m) which do not contribute significantly to the overall resistance and stability of the structure.

- In regions where $V_{Ed} > V_{Rd,c}$, sufficient shear reinforcement should be provided in order that $V_{Ed} \leq V_{Rd}$.

- The longitudinal tension reinforcement should be able to resist the additional tensile force caused by shear.

- For members subject to predominantly uniformly distributed loading the design shear force need not to be checked at a distance less than d from the face of the support. Any shear reinforcement required should continue to the support. In addition it should be verified that the shear at the support does not exceed $V_{Rd,max}$.

- Where a load is applied near the bottom of a section, sufficient vertical reinforcement to carry the load to the top of the section should be provided in addition to any reinforcement required to resist shear.

For members not requiring design shear reinforcement, the design value for the shear resistance is given by:

$$V_{Rd,ct} = \left[C_{Rd,c} \cdot k \cdot (100 \cdot \rho_1 \cdot f_{ck})^{\frac{1}{3}} + k_1 \cdot \sigma_{CP} \right] \cdot b_w \cdot d \qquad (2.212)$$

with a minimum of:

154

$$V_{Rd,ct} = (v_{min} + k_1 \cdot \sigma_{cp}) \cdot b_w \cdot d \qquad (2.213)$$

where:

$$k = 1 + \sqrt{\frac{200}{d}} \; (k \leq 2.0, \, d \text{ in mm})$$

f_{ck} is the characteristic compressive strength (MPa)

$$\rho_1 = \frac{A_{s1}}{(b_w \cdot d)} \leq |0.02| \text{ where } A_{sl} \text{ is the area of the tensile reinforcement, which}$$

extends ≥ *(l_{bd} + d)* beyond the section considered (see Figure 2.132).

$$\sigma_{cp} = \frac{N_{Ed}}{A_c} \leq 0.2 \cdot f_{cd}$$

N_{Ed} is the axial force in the cross-section due to loading or prestressing [in N] ($N_{Ed}>0$ for compression). The influence of imposed deformations on N_E may be ignored;

A_C is the area of concrete cross section [mm^2];

b_w is the smallest width of the cross-section in the tensile area [mm];

d is the effective depth of the member.

The values of $C_{Rd,c}$, v_{min} and k_1 for use in a Country may be found in its National Annex. The recommended value for $C_{Rd,c}$ is *0.18/γ_c* , that for v_{min} is given by Equation (2.214) and that for k_1 is 0.15.

$$v_{min} = 0.035 \cdot k^{3/2} \cdot f_{ck}^{1/2} \qquad (2.214)$$
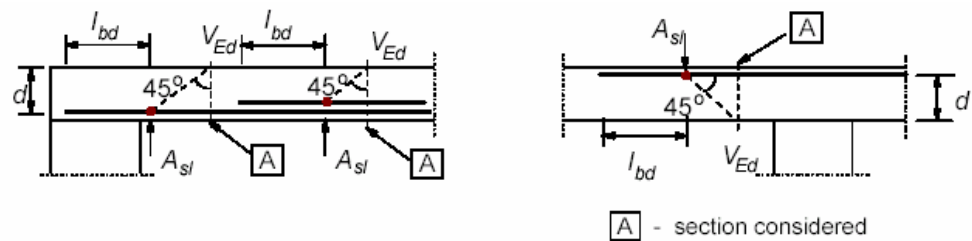
Figure 2.132: Definition of A_{sl}.

For members with loads applied on the upper side within a distance *0.5d ≤ a_v ≤ 2d* from the edge of a support (or center of bearing where flexible bearings are used), the contribution of this load to the shear force V_{Ed} may be reduced by *β = a_v/2d*. This reduction may be applied for checking $V_{Rd,c}$ in Expression (2.212). This is only

155

valid provided that the longitudinal reinforcement is fully anchored at the support. For $a_v ≤ 0.5d$ the value $a_v = 0.5d$ should be used (see Figure 2.133).

The shear force V_{Ed}, calculated without reduction by $β$, should however always satisfy the condition

$$V_{Ed} \le V_{Rd,\max} = 0.5 \cdot b_w \cdot d \cdot v \cdot f_{cd} \qquad (2.215)$$

where v is a strength reduction factor for concrete cracked in shear, whose recommended value is:

$$v = 0.6\left[1 - \frac{f_{ck}}{250}\right] \quad (f_{ck} \text{ in MPa}) \qquad (2.216)$$
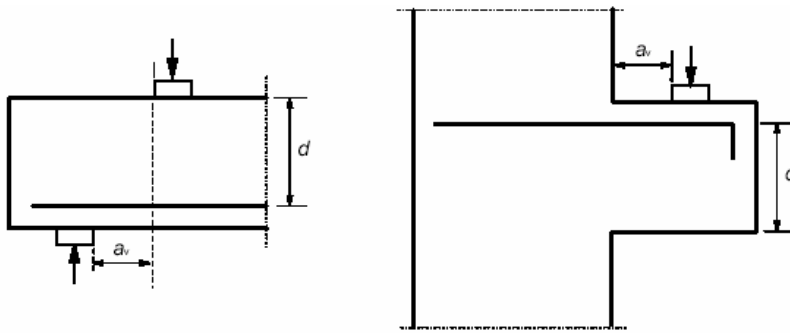
Figure 2.133: Load near supports (beam with direct support and corbel).

Beams with loads near the supports and corbels may alternatively be designed with strut and tie models.

The first issue of the European code (UNI-ENV 1992-1-2, 1993, [82]) was based on the following equation for member without shear reinforcement:

$$V_{Rd1} = \left[\tau_{Rd} \cdot k \cdot (1.2 + 40 \cdot \rho_1) + |0.15| \cdot \sigma_{CP}\right] \cdot b_w \cdot d \qquad (2.217)$$

where:

- $\tau_{Rd} = \dfrac{(0.25 \cdot f_{ctk0.05})}{\gamma_c} \approx 0.0525 \cdot f'^{2/3}_c$;
- $k = |(1.6 - d)| \ge 1$, with d in meters.

2.7.2 ACI 318-02.

The ACI 318-02 Building Code provides shear and torsion provisions for both non prestressed and prestressed members. Special provisions are included for deep flexural members, bracket and corbels, and shear walls. Slabs and footings are also included with special statements.

A consistent number of different equations, basically extrapolated by fitting of experimental data, governs shear design of members, unlike the European and the Canadian Codes, the latter based on a rational model applicable to several typologies of structures.

Among this quite considerable amount of equations (some of them are reported in Figure 2.134), it is worthy discussing the following relationships.

A simplified design method is first provided. For members subject to shear and flexure only, the maximum allowable shear force carried by concrete itself, is:

$$V_c = \left(\frac{\sqrt{f'_c}}{6} \right) \cdot b_w \cdot d \qquad (2.218)$$

For members subject to axial compression:

$$V_c = \left(1 + \frac{N_u}{14 \cdot A_g} \right) \cdot \left(\frac{\sqrt{f'_c}}{6} \right) \cdot b_w \cdot d \qquad (2.219)$$

Quantity N_u / A_g shall be expressed in MPa.

A more detailed calculation is also permitted, distinguishing several cases and member typologies.

For members subject to shear and flexure only,

$$V_c = \left(\sqrt{f'_c} + 120 \cdot \rho_w \cdot \frac{V_u \cdot d}{M_u} \right) \cdot \frac{b_w \cdot d}{7} \qquad (2.220)$$

but not greater than $0.3(f'_c)0.5\ b_w d$. M_u and V_u are factored moment and shear, respectively. Quantity V_{ud}/M_u shall not be taken greater than 1.0 in computing V_c by the last Equation, where M_u is factored moment occurring simultaneously with V_u at section considered.

For members subject to axial compression, it shall be permitted to compute V_c using Equation (2.220) with M_m substituted for M_u and V_{ud}/M_u not then limited to 1.0, where:

$$M_m = M_u - N_u\left(\frac{4h-d}{8}\right) \tag{2.221}$$

However, V_c shall not be taken greater than:

$$V_c = 0.3\sqrt{f'_c}\, b_w \cdot d \cdot \sqrt{1 + \frac{0.3 \cdot N_u}{A_g}} \tag{2.222}$$

Quantity N_u/A_g shall be expressed in MPa. When M_m as computed by Equation (2.221) is negative, V_c shall be computed by Equation (2.222).

For members subject to significant axial tension,

$$V_c = \left(1 + \frac{0.3 \cdot N_u}{A_g}\right) \cdot \frac{\sqrt{f'_c}}{6} b_w \cdot d \tag{2.223}$$

but not less than zero, where N_u is negative for tension. Quantity N_u/A_g shall be expressed in MPa.
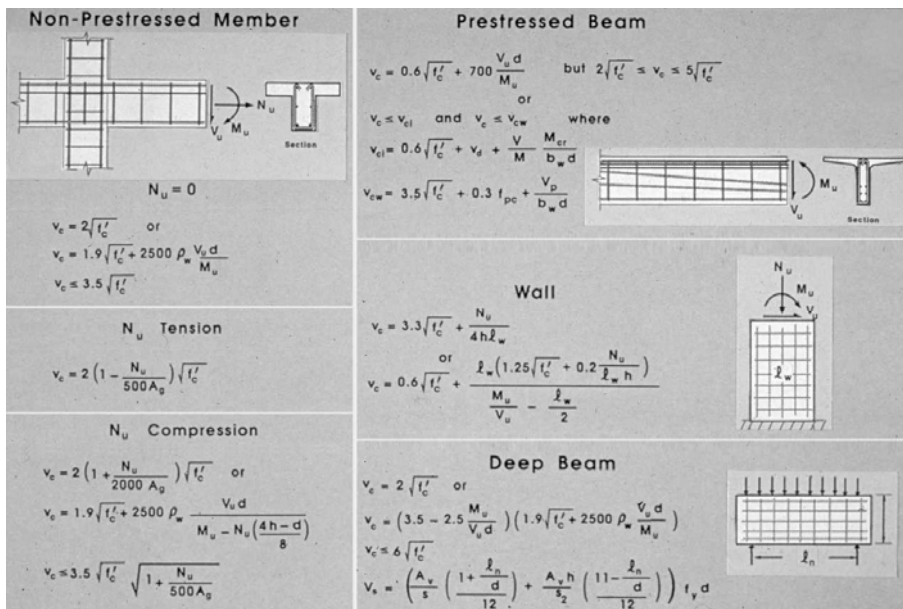
Figure 2.134: Shear design equations for different members, ACI 318-02.

2.7.3 CSA-Canadian Code.

The Canadian Code provisions for shear are based on The Modified Compression Field Theory (see Section 2.6.7), which proved to be highly effective in representing the non-linear behavior of a wide range of reinforced concrete cracked members.
Based on this theory, a simplified analytical calculation was derived and incorporated into the Canadian design Code (CSA A 23.3 M94), as described in the following.
Members subjected to shear shall be proportioned so that:

$$V_r \geq V_f \tag{2.224}$$

Sections located less than a distance d_v from the face of the support may be designed for the same shear, V_f, as that computed at a distance d_v provided that both of the following conditions are satisfied:

- the reaction force in the direction of applied shear introduces compression into the member.
- No concentrated load that causes a shear force greater than:

$$0.3\lambda\phi_c\sqrt{f_c'}\,b_w d_v \tag{2.225}$$

is applied within distance dv from the face of the support.
The factored shear resistance shall be determined by:

$$V_r = V_c + V_s + V_p \tag{2.226}$$

but V_r shall not exceed:

$$V_{r,max} = 0.25\phi_c f_c' b_w d_v + V_p \tag{2.227}$$

The value of V_r shall be computed from:

$$V_c = \phi_c \lambda \beta \sqrt{f_c'}\, b_w d_v \tag{2.228}$$

In the determination of V_c the term $\sqrt{f_c'}$ shall not be taken greater than 8 MPa.

For members with transverse reinforcement perpendicular to the longitudinal axis, V_s shall be computed from:

$$V_s = \frac{\phi_s A_v f_y d_v \cot\theta}{s} \tag{2.229}$$

For members with transverse reinforcement inclined at an angle α to the longitudinal axis, V_s shall be computed from:

159

$$V_s = \frac{\phi_s A_v f_y d_v (\cot\theta + \cot\alpha)\sin\alpha}{s} \tag{2.230}$$

2.7.3.1   Determination of β and θ.

The value of β shall be taken as 0.21 and θ shall be taken as 42° for any of the following member types:

- Slabs or footings with an overall thickness not greater than 350 mm;
- Footings in which the distance from the point of zero shear to the face of the column, pedestal or wall is less than 3 times the effective shear depth of the footing;
- Beams with an overall thickness not greater than 250 mm;
- Concrete joist construction defined by *Clause 10.4*;
- Beams cast integrally with slabs where the depth of the beam below the slab is not greater than one-half the width of web nor 350 mm.

Simplified Method.

In lieu of more accurate calculations, provided that the specified yield strength of the longitudinal steel reinforcement does not exceed 400 MPa and the design concrete strength does not exceed 60 MPa, θ shall be taken as 35° and β shall be determined as follows:

- If the section contains at least minimum transverse reinforcement then β shall be taken as *0.18*;
- If the section contains no transverse reinforcement and the specified nominal maximum size of coarse aggregate is not less than 20 mm then:

$$\beta = \frac{230}{(1000 + d_v)} \tag{2.231}$$

- Alternatively, the value of β for sections containing no transverse reinforcement may be determined for all aggregate sizes by replacing the parameter d_v in Equation (2.217) by the equivalent crack spacing parameter s_{ze} where

$$s_{ze} = \frac{35 s_z}{15 + a_g} \tag{2.232}$$

The crack spacing parameter, s_z, shall be taken as d_v or as the maximum distance between layers of distributed longitudinal reinforcement, whichever is less. Each

layer of such reinforcement shall have an area at least equal to *0.003b_ws_z*, see Figure 2.135.
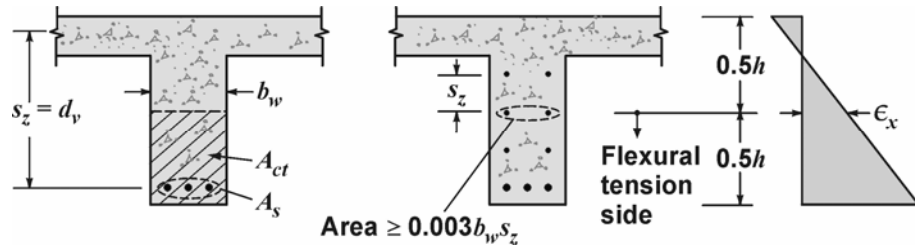
Figure 2.135. Terms in shear design equation.

General Method.

The values of *β* and *θ* shall be determined from the following equations:

$$\beta = \frac{0.40}{(1+1500\varepsilon_x)} \cdot \frac{1300}{(1000 + s_{ze})} \tag{2.233}$$

For sections containing at least minimum transverse reinforcement, the equivalent crack spacing parameter, *s_ze* in Equation (2.233) shall be taken equal to 300 mm, otherwise *s_ze* shall be computed by Equation (2.232). If *f'_c* exceeds 70 MPa the term *a_g* shall be taken as zero in Equation (2.232). As *f'_c* goes from 60 MPa to 70 MPa, *a_g* shall be linearly reduced to zero.

The angle of inclination θ of the diagonal compressive stresses shall be calculated as:

$$\theta = 29 + 7000\varepsilon_x \tag{2.234}$$

In lieu of more accurate calculations, the longitudinal strain, *ε_x*, at mid-depth of the cross-section shall be computed from

$$\varepsilon_x = \frac{M_f / d_v + V_f - V_p + 0.5N_f - A_p f_{po}}{2(E_s A_s + E_p A_p)} \tag{2.235}$$

In evaluating this equation the following conditions apply:

- *V_f* and *M_f* shall be taken as positive quantities and *M_f* shall not be taken less than *(V_f-V_p)d_v*.

- In calculating A_s the area of bars which are terminated less than their development length from the section under consideration shall be reduced in proportion to their lack of full development.
- If the value of ε_x calculated from Equation (2.235) is negative it shall be taken as zero or the value shall be recalculated with the denominator of Equation (2.235) replaced by $2(E_sA_s + E_pA_p + E_cA_{ct})$; however ε_x shall not be taken as less than -0.20×10^{-3}.
- For sections closer than d_v to the face of the support, the value of ε_x calculated at d_v from the face of the support may be used in evaluating β and θ.
- If the axial tension is large enough to crack the flexural compression face of the section, the resulting increase in ε_x shall be taken into account. In lieu of more accurate calculations, the value calculated from Equation (2.235) shall be doubled.
- It is permissible to determine θ and β from Equation (2.233) and Equation (2.234) using a value of ε_x which is greater that that calculated from Equation (2.235); however ε_x shall not be taken greater than 3.0×10^{-3}.

Further prescriptions are also reported in the code concerning proportioning and detailing of transverse and longitudinal reinforcement.

Figure 2.136 and Figure 2.137 provide useful tables containing values of β and θ for members having at least the minimum amount of transverse reinforcement or less than the minimum, respectively.

$\dfrac{v}{f_c'}$		ϵ_x x 1000										
		≤ -0.20	≤ -0.10	≤ 0	≤ 0.25	≤ 0.50	≤ 0.75	≤ 1.00	≤ 1.50	≤ 2.00	≤ 5.00	≤ 10.0
≤ 0.075	θ	22.3°	20.4°	21.8°	26.6°	30.5°	33.7°	36.4°	40.8°	43.9°	53.1°	60.4°
	β	6.32	4.75	3.75	2.94	2.59	2.38	2.23	1.95	1.67	1.00	0.63
≤ 0.100	θ	18.1°	20.4°	22.5°	27.1°	30.8°	34.0°	36.7°	40.8°	43.1°	52.4°	60.0°
	β	3.79	3.38	3.14	2.75	2.50	2.32	2.18	1.93	1.69	1.02	0.64
≤ 0.125	θ	19.9°	21.9°	23.7°	27.9°	31.4°	34.4°	37.0°	41.0°	43.2°	52.0°	59.7°
	β	3.18	2.99	2.87	2.62	2.42	2.26	2.13	1.90	1.67	1.02	0.64
≤ 0.150	θ	216°	23.3°	25.0°	28.8°	32.1°	34.9°	37.3°	40.5°	42.8°	51.7°	-
	β	2.88	2.79	2.72	2.52	2.36	2.21	2.08	1.82	1.62	1.02	-
≤ 0.175	θ	23.2°	24.7°	26.2°	29.7°	32.7°	35.2°	36.8°	39.7°	42.2°	51.7°	-
	β	2.73	2.66	2.60	2.44	2.28	2.14	1.96	1.71	1.54	1.01	-
≤ 0.200	θ	24.7°	26.1°	27.4°	30.6°	32.8°	34.5°	36.1°	39.2°	41.7°	51.4°	-
	β	2.63	2.59	2.51	2.37	2.14	1.94	1.79	1.61	1.47	0.98	-
≤ 0.250	θ	26.1°	27.3°	28.5°	30.8°	32.3°	34.0°	35.7°	38.8°	41.4°	-	-
	β	2.53	2.45	2.40	2.14	1.86	1.73	1.64	1.51	1.39	-	-
≤ 0.250	θ	27.5°	28.6°	29.7°	31.6°	32.8°	34.3°	35.8°	38.6°	41.2°	-	-
	β	2.39	2.39	2.33	1.93	1.70	1.58	1.50	1.38	1.29	-	-

Figure 2.136. Values of θ and β for sections containing at least the minimum amount of transverse reinforcement.

s_{xe} (in)		ϵ_x x 1000										
		≤ -0.20	≤ -0.10	≤ -0.05	≤ 0	≤ 0.125	≤ 0.25	≤ 0.50	≤ 0.75	≤ 1.00	≤ 1.50	≤ 2.00
≤ 5	θ	25.4°	25.5°	25.9°	26.4°	27.7°	28.9°	30.9°	32.4°	33.7°	35.6°	37.2°
	β	6.36	6.06	5.56	5.15	4.41	3.91	3.26	2.86	2.58	2.21	1.96
≤ 10	θ	27.6°	27.6°	28.3°	29.3°	31.6°	33.5°	36.3°	38.4°	40.1°	42.7°	44.7°
	β	5.78	5.78	5.38	4.89	4.05	3.52	2.88	2.50	2.23	1.88	1.65
≤ 15	θ	29.5°	29.5°	29.7°	31.1°	34.1°	36.5°	39.9°	42.4°	44.4°	47.4°	49.7°
	β	5.34	5.34	5.27	4.73	3.82	3.28	2.64	2.26	2.01	1.68	1.46
≤ 20	θ	31.2	31.2°	31.2°	32.3°	36.0°	38.8°	42.7°	45.5°	47.6°	50.9°	53.4°
	β	4.99	4.99	4.99	4.61	3.65	3.09	2.46	2.09	1.85	1.52	1.31
≤ 30	θ	34.1°	34.1°	34.1°	34.2°	38.9°	42.3°	46.9°	50.1°	52.6°	56.3°	59.0°
	β	4.46	4.46	4.46	4.43	3.39	2.82	2.19	1.84	1.60	1.30	1.10
≤ 40	θ	36.6°	36.6°	36.6°	36.6°	41.1°	45.0°	50.2°	53.7°	56.3°	60.2°	63.0°
	β	4.06	4.06	4.06	4.06	3.20	2.62	2.00	1.66	1.43	1.14	0.95
≤ 60	θ	40.8°	40.8°	40.8°	40.8°	44.5°	49.2°	55.1°	58.9°	61.8°	65.8°	68.6°
	β	3.50	3.50	3.50	3.50	2.92	2.32	1.72	1.40	1.18	0.92	0.75
≤ 80	θ	44.3°	44.3°	44.3°	44.3°	47.1°	52.3°	58.7°	62.8°	65.7°	69.7°	72.4°
	β	3.10	3.10	3.10	3.10	2.71	2.11	1.52	1.21	1.01	0.76	0.62

Figure 2.137: Values of θ and β for sections containing less than the minimum amount of transverse reinforcement.

2.8   Fiber Reinforced Concrete (FRC).

2.8.1   Significance of FRC.

The idea to reinforce concrete with fibers is quite old. Fibers have been used to reinforce brittle materials from time immemorial, dating back to the Egyptian and Babylonian eras. Straws were used to reinforce sun-baked bricks and mud-hut walls, horsehair was used to reinforce plaster and asbestos fibers (no longer utilized today) have been used to reinforce Portland cement mortars.

Most recently, in 1874, it was patented [117] the idea to strengthen the concrete behavior by adding metallic waste. But after that steel fiber reinforced concrete (SFRC) was not often used. In the beginning of the 1960s this old idea of adding fibers to the concrete revived. Research by Romualdi and Batson [118] and Romualdi and Mandel [119] on closely spaced random fiber in the late 1950s and early 1960s primarily on steel fiber heralded the era of using fiber composite concretes as we know them today. By the 1960s, steel fiber concretes started to be used especially in pavements. From the 1970s to the present, the use of steel fiber has been well established as a complementary reinforcement to increase the cracking resistance, flexural and shear strength, and impact resistance of reinforced concrete elements both situ-cast and precast.

163

Plain, unreinforced cementitious materials are characterized by low tensile strengths, and low tensile strain capacities; that is, they are brittle materials: they thus require reinforcement before they can use extensively as a construction material. Historically, this reinforcement has been in the form of continuous reinforcing bar, which could be placed in the structure at the appropriate locations to withstand the imposed tensile and shear stresses. Fibers, on the other hand, are discontinuous, and are most commonly randomly distributed throughout the cementitious matrix. They are, therefore, not as efficient in withstanding tensile stresses. However, since they are more closely spaced than conventional reinforcing bars, they tend to act better at controlling cracking. Thus, conventional reinforcing bars are used to increase the load-bearing capacity of concrete whereas fibers are more effective for crack control.

Due to these differences, there are certain applications in which fiber reinforcement is better than conventional reinforcing bars. These include:

- Thin sheet materials, in which conventional reinforcing bars cannot be used, and in which fibers therefore constitute the primary reinforcement. In thin sheet materials, fiber concentrations are relatively high, typically exceeding 5% by volume. In such applications, fibers act at increasing both the strength and the toughness of the composite.

- Components which must withstand locally high loads or deformations, such as tunnel linings, blast resistance structures, or precast piles which must be hammered into the ground.

- Components in which fibers are added primarily to control cracking induced by humidity or temperature variations, as in slabs and pavements. In these applications, fibers are often referred to as secondary reinforcement.

It is important to emphasize that, up to now, fiber reinforcement is not a substitute for conventional reinforcement. Fibers and steel bars have basically different role to play in modern concrete technology, and there are many applications in which both fibers and continuous reinforcing bars should be used together.

In the two last above mentioned applications, fibers are not used to improve the strength (either tensile or other) of concrete, even though a small improvement in strength may sometimes be observed from their use. Rather, the role of fibers is to control the cracking of FRC composites, and also to alter the behavior of concrete once the matrix has cracked. Fibers therefore improve the ductility of the material, or, more properly, its energy absorption capacity. In addition, there is often an improvement in impact resistance, fatigue properties and abrasion resistance.

164

The applications of FRC are as varied as the types of fibers that have been used. Asbestos fibers have long been used in pipes and corrugated or flat roofing sheets. Glass fibers are primarily used in precast panels (non-structural). Steel fibers have been used in pavements, in shotcrete, in dams, and in a variety of other structures. Increasingly , fibrillated polypropylene fiber are used as a secondary reinforcement, to control plastic shrinkage cracking. Vegetable fibers have been used in low cost building materials.

As far as the production is concerned, new production technologies have evolved as new fibers have been developed and new applications found. Clearly, in order to produce useful FRC, the production techniques must be compatible with the particular fibers and matrix. This depends not only upon the fiber type, but also on the fiber geometry. In particular, there is an inherent contradiction between the fiber geometry required to allow easy handling of the fresh FRC, and that required for maximum efficiency in the hardened composite. Longer fibers of smaller diameter will be more efficient in the hardened FRC, but will make the fresh FRC more difficult to handle [120].

This Ph.D. thesis and the following discussion will deal only with steel fiber reinforced concrete, which proved to be more effective, and therefore reliable, for structural applications.

For steel fibers only, the fiber length varies from 10 to 60 mm. They are either round, produced by cutting or chopping wire, or flat, having typical cross section of 0.15-0.40 mm in thickness and 0.25-0.90 mm in width, and produced by shearing sheets or flattering wires. The most common diameter of the round wires are 0.45-1.0 mm. Wires are usually crimped or deformed or have small heads on them for achieving better bond within the matrix, and some are crescent-shaped in cross-section.

The fiber content in a mixture, where steel fibers are used, usually varies from 0.25 to 2% by volume, i.e. from 20 to 160 kg/m^3. The lowest end of the range applies to slab on grade while the upper, more difficult to achieve, is used for security applications such as vaults, safe and impact-resisting structures [121].

2.8.2 Mixture Proportioning.

Mixing of fibers with the other mixture constituents can be done by several methods. The method selected depends on the facilities available and the job requirements: plant batching, ready-mixed concrete, or hand mixing in the

laboratory. The most important factor is to ensure uniform dispersion of fibers and prevention of segregation or balling of fibers during mixing. Segregation or balling during mixing is affected by many factors that can be summarized as follows:

- Aspect ratio l/d_f (most important);
- Volume percentage of fiber;
- Coarse aggregate size, gradation, and quantity;
- Water/cementitious ratio and method of mixing.

A maximum aspect ratio of l/d_f and a steel fiber content in excess of 2% by volume make difficult to have a uniform mixture. While conventional mixing procedures can be used, it is advisable to use a 10 mm maximum aggregate size. The water requirement will vary from concrete without fibers, depending also on the type of cement replacement cementitious pozzolans used and their percent by volume of the matrix. Table 2.2 and Table 2.3 give typical mixture proportions for normal-weight fibrous-reinforced concrete and fly ash fibrous concrete mixtures.

A workable method for mixing in a step-by-step chronological procedure can be summarized as follows:

1) Blend part of the fiber and aggregate before charging into the mixer;
2) Blend fine and coarse aggregate in the mixer, then add more fibers at the mixing speed. Last, add cement and water simultaneously or cement followed immediately by water and additives;
3) Add the balance of the fiber to the previously charged constituents. Add the remaining cementitious materials and water;

Cement	550-950 lb/yd^3
W/C ratio	0.4-0.6
Percent of sand to aggregate	50-100%
Maximum Aggregate	3/8 in.
Air Content	6-9%

Fiber Content	0.5-2.5 vol % of mixture
	    Steel: 1% = 132 lb/yd^3
	    Glass: 1% = 42 lb/yd^3
	    Nylon: 1% = 19 lb/yd^3

Table 2.2: Typical proportions for normal-weight fiber-reinforced Concrete. (1 lb/yd^3 = 0.5933 kg/m^3) [121].

Cement	490 lb/yd^3
Fly Ash	225 lb/yd^3
W/C ratio	0.54
Percent of sand to aggregate	50%
Maximum size coarse aggregate	3/8 in.
Steel Fiber Content	1.5%
Slump	5-6 in.

Table 2.3: Typical fly ash fibrous concrete mixture (1 lb/yd^3 = 0.5933 kg/m^3; 1 in = 25.4 mm) [121].

4) Continue mixing as required by normal practice;

5) Place the fibrous concrete in the forms. Fibrous concrete requires more vibration than nonfibrous concrete. Although internal vibration is acceptable if carefully applied, external vibration of the formwork and the surface is preferable to prevent segregation of fibers.

2.8.3   Mechanics Of Fiber Reinforcement.

2.8.3.1   First Cracking Load.

Fiber-reinforced concrete in flexure essentially undergoes a trilinear deformation behavior, as shown in Figure 2.138. Point A on the load-deflection diagram represents the first cracking load that can be termed the first-cracking strength [122]. Normally, this is the same load level at which a non-reinforced element cracks. Hence, segment OA in the diagram would be the same and essentially have the same slope for both plain and fiber-reinforced concrete.

Once the matrix is cracked, the applied load is transferred to the fibers which bridge and tie the crack from further opening. As fibers deform, additional narrow cracks develop and continued cracking of the matrix takes place until the maximum load reaches point B of the load-deflection diagram. During this stage, debonding and pull-out of some fibers occur. But the yield strength in most of fibers is not reached.

In the falling branch BC of the load-deflection diagram, matrix cracking and fiber pull-out continue. If fibers are long enough to be able to maintain their bond with the surrounding gel, they may fail by yielding or by fracture of the fiber element, depending on their size and spacing.

167
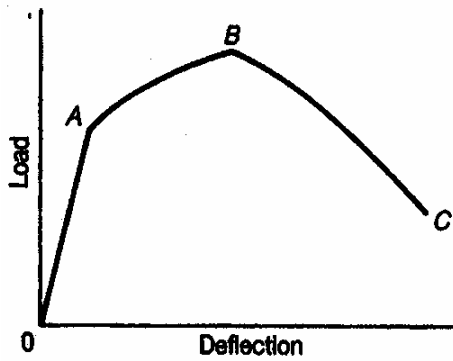
Figure 2.138: Schematic load-deflection relationship of fiber-reinforced concrete [121].

2.8.3.2 Critical Fiber Length: Length Factor.

If l_c is the critical length of a fiber above which the fiber undergoes fracture rather than pull-out when the crack intersects the fiber at its midpoint, it can be approximated by [122]:

$$l_c = \frac{d_f}{2 \cdot v_b} \cdot \sigma_f \tag{2.236}$$

where:

- d_f = fiber diameter;
- v_b = interfacial bond strength;
- σ_f = fiber strength.

Bentur and Mindess [123] developed an expression to relate the average pull-out work and the fiber matrix interfacial bond strength in terms of the critical fiber length, demonstrating that the strength of a composite increases continuously with the fiber length. This is of significance as it indicates that pull-out work may go through a maximum and decrease as bond strength increases over a critical value. This loss of pull-out work would be reduced to a typical range of *l=10 mm* in cement-based composites.

If a critical v_b value of 1.0 MPa is used and a fiber diameter $d_f=20\mu m$, the increase in bond may result in reduced toughness.

2.8.3.3 Critical Fiber Spacing: Space Factor.

The spacing of fibers considerably affects cracking development in the matrix. The closer the spacing, the higher is the first cracking load of the matrix. This is due to the fact that fibers reduce the stress intensity factor that controls fracture. The approach followed by Romualdi and Batson [118] to increase the tensile strength of

168

the mortar consisted of enhancing the stress intensity factor through decreasing of the spacing of fibers as crack arresters. Figure 2.139 relates the tensile cracking stress to the spacing of fibers for various volumetric percentages. Figure 2.140 compares the theoretical and experimental values to the ratio of the first cracking load to the cracking strength of plain concrete (strength ratio). Both diagrams demonstrate that the closer the spacing of fibers, the higher is the strength ratio, that is, the higher is the tensile strength of the concrete, up to the practical workability and cost-effectiveness limits.

Several expressions to define the spacing of fibers have been developed. If s is the spacing of the fibers, one expression [118] gives:

$$s = 13.8 \cdot d_f \cdot \sqrt{\frac{1.0}{\rho}} \tag{2.237}$$

where d_f is the diameter of fiber and ρ is the fiber percentage by volume of the matrix. Another expression, due to Mindess and Young [122], also taking the length of fiber into account, gives:

$$s = 13.8 \cdot d_f \cdot \frac{\sqrt{l}}{\rho} \tag{2.238}$$
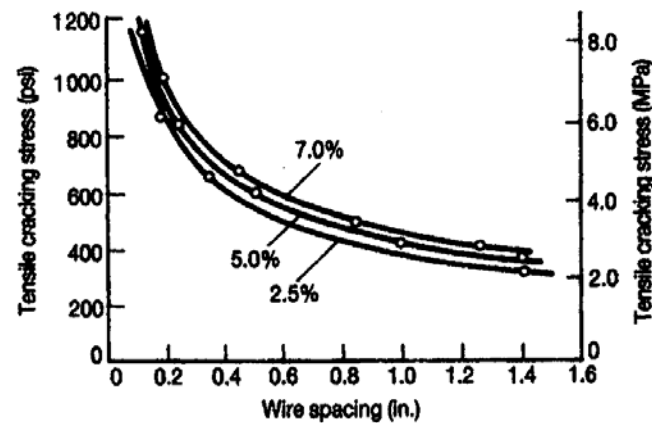
Figure 2.139: Effect of steel fiber spacing on the tensile cracking stress in fibrous concrete for ρ= 2.5, 5.9 and 7.5 % [118].
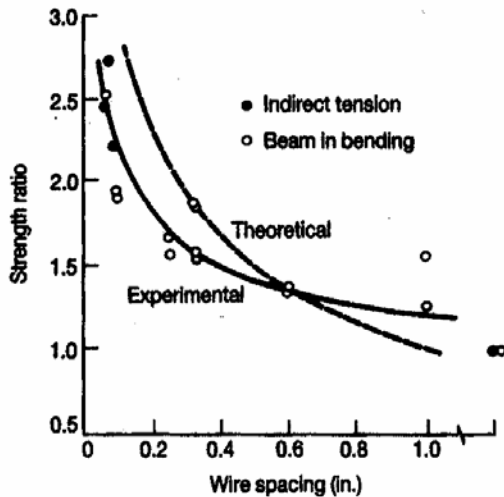
Figure 2.140: Effect of the fiber spacing on the strength ratio (first cracking load of fibrous concrete divided by strength of plain concrete). ([119])

2.8.3.4   Fiber Orientation: Fiber Efficiency Factor.

The orientation of fibers with respect to load determines the efficiency through which the randomly oriented fibers can resist the tensile forces in their direction. This is similar to the contribution of bent bars and vertical shear stirrups in beams provided for resisting the inclined diagonal tension stress. If one assumes perfect randomness, the *efficiency factor* is equal to *0.41l*, but can vary between *0.33l* and *0.65l* close to the surface of the specimen, as troweling or leveling can modify the orientation of fibers [122].

2.8.3.5   Static Flexural Strength Prediction: Beams with Fibers only.

For predicting the flexural strength, several methods could be applied depending on the type of fiber, the type of matrix, using empirical data from laboratory experiments or basing the design on the bonded area of the fiber, or using the law of mixtures. An empirical expression for the composite flexural strength based on a composite material approach can be [123]:

$$\sigma_c = A\sigma_m\left(1 - V_f\right) + BV_f\,\frac{l}{d} \tag{2.239}$$

where:
- σ_c = composite flexural strength;
- σ_m = ultimate strength of the matrix;

170

- V_f = volume fraction of fibers adjusted for the effect of randomness;
- A, B = constants;
- l/d = aspect ratio of the fiber, where l is the length and d is the diameter of the fiber.

The constants A and B obtained from 100 x 100 x 305 mm model beam tests by Swamy et al, adopted and reported by ACI Committee 544 [124] produced the following results. The first crack composite flexural strength (psi) is:

$$\sigma_f = 0.843 \cdot f_r \cdot V_m + 425 \cdot V_f \cdot \frac{l}{d_f} \qquad (2.240)$$

where:

- f_r = stress in the matrix (modulus of rupture of the plane mortar or concrete), psi;
- V_m = volume fraction of the matrix = $l - V_f$;
- V_f = volume fraction of the fibers = $l - V_m$;
- l/d_f = ratio of the length to diameter of fibers (i.e., aspect ratio).

The ultimate composite flexural strength (psi) is:

$$\sigma_{cu} = 0.97 \cdot f_r \cdot V_m + 494 \cdot V_f \cdot \frac{l}{d_f} \qquad (2.241)$$

2.8.4   Characterization of FRC: the Italian Standard.

It is nowadays believed that a proper characterization of fibers should be undertaken by considering the post-cracking behavior itself, rather than considering the geometry and the amount of fibers provided in the matrix. In fact, the same amount of fiber in different concretes results in a quite different post-cracking behavior of the composite. The appropriate fracture mechanics test, according to local national Standard, should be performed in order to find out the actual post-cracking properties. A brief discussion will follow concerning the Italian Standard UNI 11039 [125], which is based on fracture mechanics CMOD-controlled tests on notched beams loaded with a four point system.

The specimen geometry, the loading conditions and the position where the LVDTs had to be placed are shown in Figure 2.141 and Figure 2.142. The first cracking point has to be identified testing the specimen made of plain (reference) concrete, as it is a parameter not affected by fibers and only dependent on the cementitious matrix. The value of the CTOD at the peak load is conventionally assumed as the

first cracking point $CTOD_0$ for plain concrete, as depicted in Figure 2.143, even if the cracking onset actually starts before that point (Figure 2.144). Furthermore, it is assumed that the first cracking point for the same material with fibers corresponds to the crack tip opening displacement $CTOD_0$ previously determined on the reference concrete.
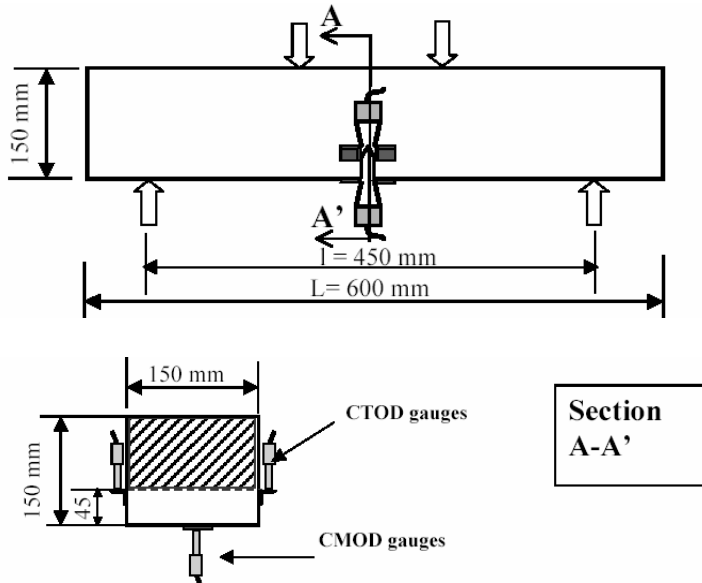
Figure 2.141: Geometry of the specimen and layout for the application of the gauge-holders and the relevant CMOD and CTOD gauges [125].
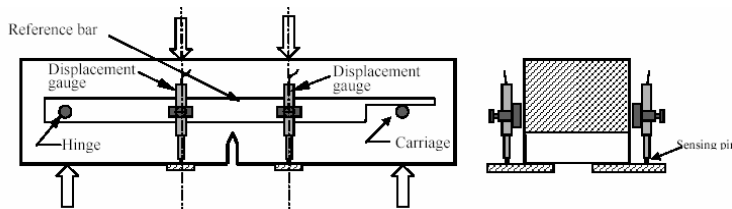
Figure 2.142: Layout for the application of the gauge-holders and the gauges for the measurement of the displacement of the load application points [125].

When the reference concrete test is not available, the Italian Standard assumes a $CTOD_0$ equal to 25 μm, based on a statistical investigation on hundreds of specimens of concrete with compressive strength ranging from 25 to 80 MPa, which showed that there is 95% of probability that the experimental value of $CTOD_0$ be equal to 24 ± 8 μm.

172
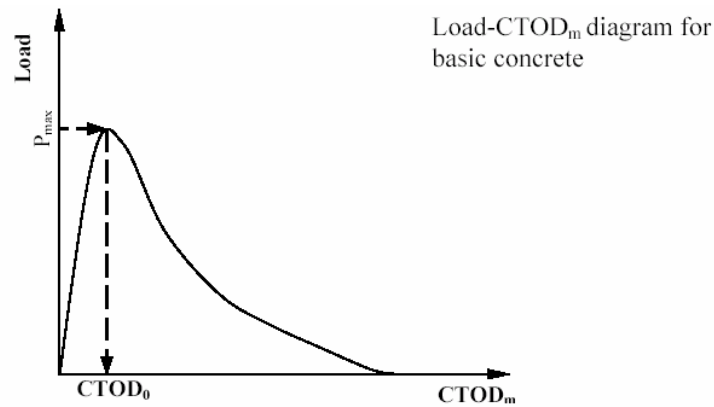
Figure 2.143: Direct detection of CTOD$_0$ [125].

The Italian Standard characterizes the post-cracking strength of a FRC material by 3 independent parameters: the former is correlated to the first cracking strength and the two others are toughness indexes respectively for serviceability and ultimate limit state, defined as:

$$D_0 = \frac{f_{eq,(0-0,6)}}{f_{If}} \qquad (2.242)$$

$$D_1 = \frac{f_{eq,(0.6-3)}}{f_{eq,(0-0,6)}} \qquad (2.243)$$
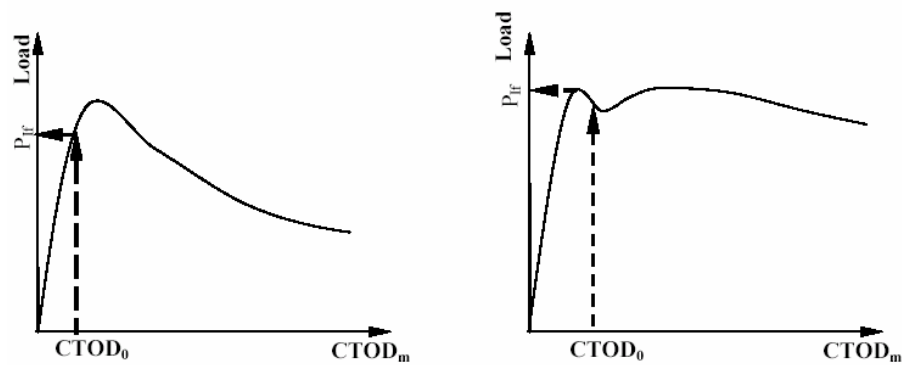
Figure 2.144: Example of first crack load P$_{if}$ detection [125].

Where f_{lf} is the first cracking strength, given by the following formula:

$$f_{lf} = \frac{P_{lf} \cdot l}{b \cdot (h - a_o)^2}$$ (2.244)

and $f_{eq(0\text{-}0.6)}$ and $f_{eq(0.6\text{-}3)}$ are respectively the equivalent stress in the CTOD ranges of 0-0.6 and 0.6-3.

$$f_{eq,(0-0.6)} = \frac{l}{b(h - a_0)^2} \cdot \frac{U_1}{0.6}$$ (2.245)

$$f_{eq,(0.6-3)} = \frac{l}{b(h - a_0)^2} \cdot \frac{U_2}{2.4}$$ (2.246)

where b is the thickness of the specimen, h the height of the specimen, a_0 is the notch length, U_1 and U_2 the areas under the curves *P-CTOD* between 0-0.6 mm and 0.6-3 mm respectively (Figure 2.145), which can be calculated as:

$$U_1 = \int_0^{0.6} P(CTOD) \cdot d(CTOD)$$ (2.247)

$$U_1 = \int_{0.6}^{3} P(CTOD) \cdot d(CTOD)$$ (2.248)
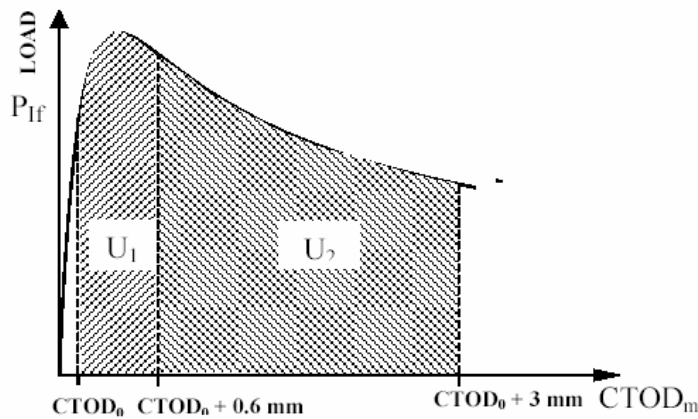
Figure 2.145: Definition of U_1 and U_2 in a given experimental curve [125].

These three parameters proved to be effective in characterizing FRC composites and also can be easily included in structural design guidelines.

2.8.5 Mechanical Properties Of Fibrous Concrete Structural Elements.

Fibers have a negligible influence on the modulus of elasticity, Poisson's ratio, compressive strength, electrical conductivity and porosity, as it was found by Vondran (1991) [126]. Therefore, the behavior of concrete before cracking is not remarkably modified by fibers. In fact, fibers are together with the concrete matrix. The advantage of using fibers is that they can prevent microcracks from propagating and consequently they protect concrete members from external attacks and aggressive environments, such as those containing nitrate and chloride.

Crack widths, as a result of load independent factors, are generally smaller than in plain concrete, thanks to the more uniform stress distribution in the cross section of the structure, being the strength of aggregates and the strength of the matrix more similar to each other. This becomes more important with increasing concrete strength and under fatigue loading, taking into account the increasing brittleness of concrete.

Fibers therefore mainly influence the ductility of the concrete: after concrete cracking fibers bridge the crack and so the concrete is able to transmit higher forces between the crack planes. Fibers take effect and start resisting further deformations once microcracks emerge. The contribution of fibers acts until they are either pulled out or broken.

2.8.5.1 Controlling Factors.

From Section 2.8.3 it can be seen that the mechanical properties of fiber-reinforced concretes are influenced by several factors. The major properties are:

- Type of fiber (i.e., the fiber material and its shape);
- Aspect ratio l/d_f;
- Amount of fiber in percentage by volume, ρ;
- Spacing of the fiber, s;
- Strength of the concrete or mortar matrix;
- Size, shape, and preparation of the specimen.

Hence, it is important to conduct laboratory tests to failure on the mixtures using specimen models similar in form to the elements being designed. As the fibers affect the performance of the end product in all material resistance capacities, such as in flexure, shear, direct tension, and impact, it is important to evaluate the test specimen performance with regard to those parameters [121].

The contribution of fibers to tensile strength, as discussed in Section 2.8.2, is due to its ability as a randomly distributed reinforcement to assume the stress from the matrix when it cracks through interface shear friction interlock between the fiber and the matrix. Hence, deformed or crimped fibers would have a greater influence than smooth and straight ones. The pull-out resistance in zone AB of Figure 2.138 is proportional to the interfacial surface area [124]. The non-round fiber cross sections and the smaller diameter round fibers induce a larger resistance per unit volume than the larger diameter fibers.

This is also analogous to the crack control behavior in traditionally reinforced structural members. There, a larger number of smaller-diameter bars, more closely spaced, are more effective than a smaller number of large diameter for the same reinforcement volume percentage [127]. One reason is the larger surface interaction area between the fibers and the surrounding matrix, resulting in a higher bond and shear-friction resistance.

2.8.5.2 Strength in Compression.

The effect of the contribution of fibers to the compressive strength of the concrete seems to be minor as seen in Figure 2.146 for tests using steel fibers. However, the ductility and toughness are considerably enhanced as a function of the increase in the volume fractions, aspect ratios and post-cracking characteristics of fibers used. Hsu and Hsu [128] shows in Figure 2.146 the effect of the increase in volume fraction on the stress-strain relationship of the fibrous concrete through increasing the fiber volume from 0 to 1.5% for concretes having a compressive strength of 90 MPa.

Figure 2.147 and Figure 2.148 from Fanella and Naaman [129] depict a similar trend with respect to both a volume fraction ratio up to 3% and an aspect ratio of 47-100. Figure 2.149 also demonstrates the influence of the increase in fiber content on the relative toughness of reinforced concrete members.

Toughness is a measure of the ability to absorb energy during deformation. It can be estimated from the area under the stress-strain or load-deformation diagrams. A toughness index (TI) expression proposed by Hsu and Hsu [128] gives:

$$TI = 1.421 \cdot RI + 1.035 \tag{2.249}$$

where:

- RI = reinforcing index = $V_f(l/d_f)$;
- V_f = volume fraction;
- l/d_f = aspect ratio.

176
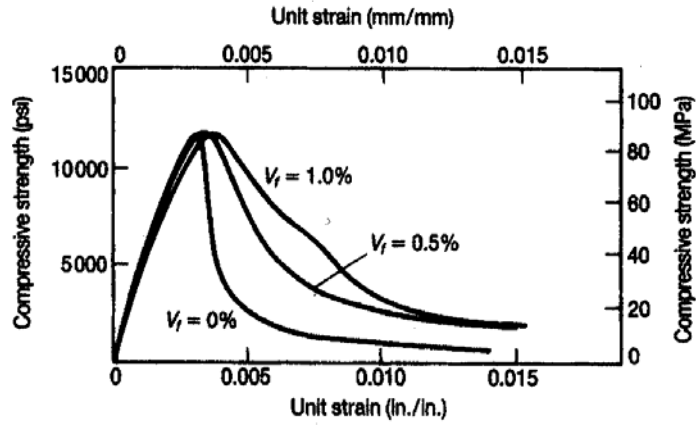
Figure 2.146: Influence of volume fraction of steel fibers on stress-strain behavior for 13000 psi concrete [128].
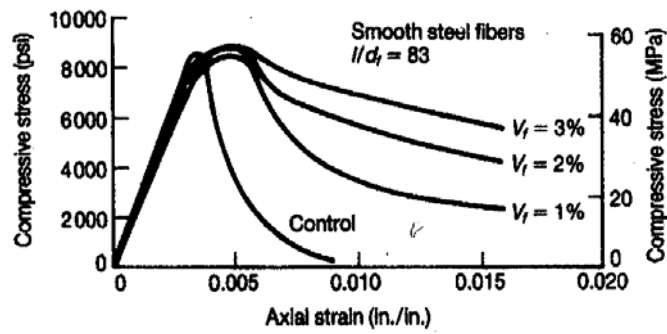
Figure 2.147: Influence of volume fraction of steel fibers on stress-strain behavior for 9000 psi concrete [129].
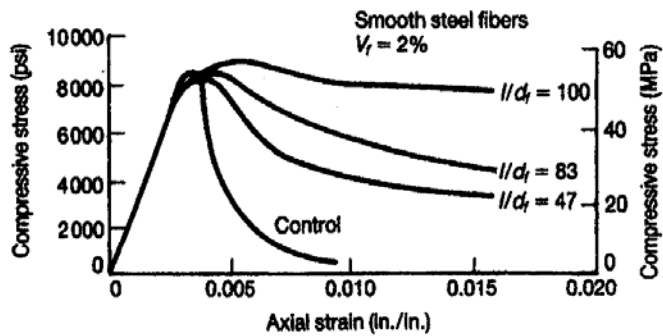
Figure 2.148: Influence of aspect ratio for steel fibers on stress-strain behavior [129].

177

Figure 2.150 gives the relationship of the toughness index to the reinforcing index of fibrous high-strength concretes within the limitation of the type, aspect ratio, and volume fractions of the steel fibers used in those tests.

By increasing the volume fraction, both ductility and toughness have been shown to increase significantly within the practical limits of workable volume content of fiber in a concrete mixture.
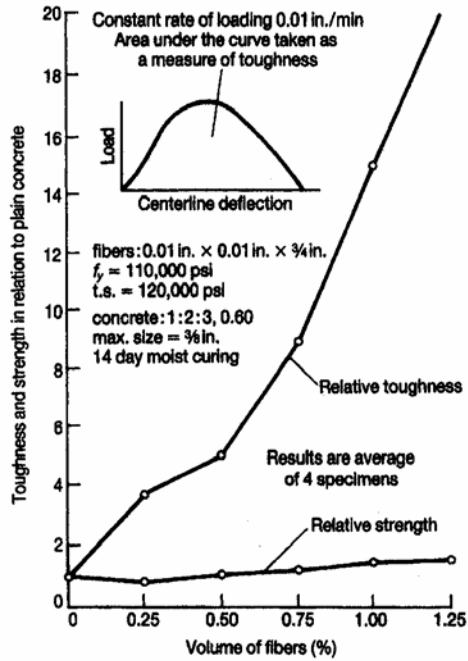
Figure 2.149: Relative toughness and strength vs. fiber volume ratio [130].
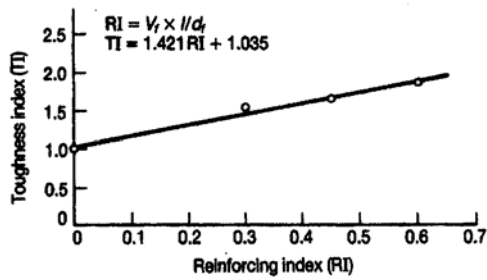
Figure 2.150: Toughness index vs. reinforcing index of fibrous concrete. [128].

In Figure 2.151, which depicts the experimental results of Wafa and Ashour (1992) [131], it is further evidenced that the peak load and the post peak behavior is dependent on the fiber content. According to the fiber amount it was distinguished between a hypercritical, critical and undercritical fiber content. The term critical fiber content is used if the maximum load by cracking can be retained while the strain increases. The critical value can be determined by using following equation:

$$v_{fcrit} = \frac{f_{tm}}{\eta_0 \cdot \eta_v \cdot f_{tf}}$$
(2.250)

with:

- f_{tm} and f_{tf} tensile strength of the matrix and the fiber, respectively;
- η_v is a bond coefficient, which is < 1;
- η_0 is a direction coefficient, which takes into account that not all fibers are orientated to the direction of the principal stresses. The value is given in the literature with $\eta_{02} = 0.78$ for the case of a two dimensional orientation of the fibers and $\eta_{03} = 0.66$ for a not orientated fiber formation (Schönlin 1988 [132]).
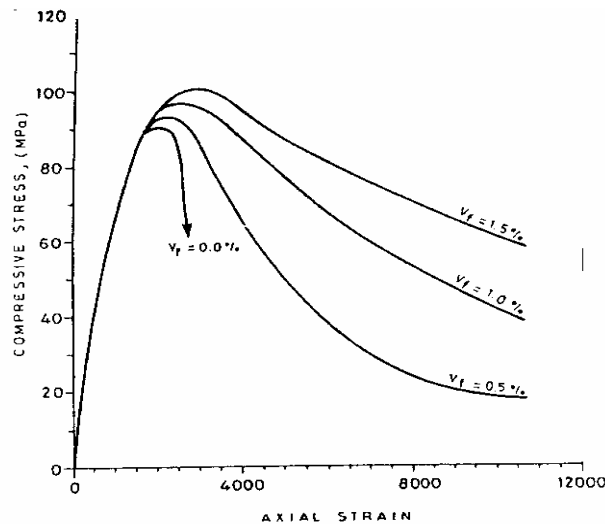
Figure 2.151: Effect of the fiber content on the compressive stress-strain curve (Wafa and Ashour 1992 [131]).

A stress-strain curve in compression for fiber reinforced concrete was proposed by Mansur and Ong [133], who adapted the stress-strain curve proposed by Kent and Park [134] for reference concrete, in which the strain-softening effect prevalent in cracked concrete in compression has been incorporated using Vecchio and Collins'

179

proposal [135]. As reported in Figure 2.152, it consists of an initial parabolic portion up to the peak stress level that corresponds to a strain of ε_p followed by a straight descending branch up to $\varepsilon_d = \varepsilon_{cf}$. Thereafter, the stress remains constant with increasing strain. The three branches can be represented by the following equations:

$$|\varepsilon_d| \le |\varepsilon_p| \quad \Rightarrow \quad \sigma_d = f_c' \left[2\left(\frac{\varepsilon_d}{\varepsilon_o}\right) - \lambda\left(\frac{\varepsilon_d}{\varepsilon_o}\right)^2 \right] \tag{2.251}$$

$$|\varepsilon_p| < |\varepsilon_d| \le \varepsilon_{cf} \quad \Rightarrow \quad \sigma_d = \frac{f_c'}{\lambda} \left[1 - \left(\frac{\varepsilon_d - \varepsilon_p}{\varepsilon_{cd} - \varepsilon_p}\right)(1 - k') \right] \tag{2.252}$$

$$|\varepsilon_d| \ge \varepsilon_{cf} \quad \Rightarrow \quad \sigma_d = k' \frac{f_c'}{\lambda} \tag{2.253}$$
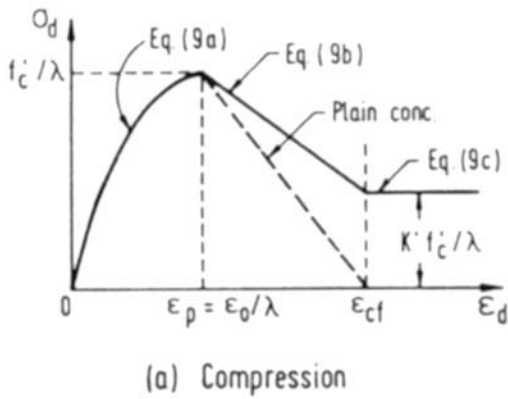
Figure 2.152: Assumed stress-strain relationship for FRC in compression [133].

where:

- $\varepsilon_o = -0.002$;
- $\lambda = \sqrt{0.7 - \varepsilon_r / \varepsilon_d}$;
- $\varepsilon_{cf} = \dfrac{0.041 - 2\varepsilon_o f_c'}{f_c' - 6.896} + \varepsilon_o$;

180

- $k' = 0.38 V_f \dfrac{l_f}{\phi_f}$ where l_f e ϕ_f are the length and the diameter of fibers,

  respectively.

2.8.5.3 Strength in Direct-Tension.

The effect of different shapes of fiber filaments on the tensile stress behavior of steel fiber-reinforced mortars in direct tension is demonstrated in Figure 2.153. The descending portion of the plots shows that fibers with greater anchorage quality increase the tensile resistance of the fiber concrete beyond the first cracking load.

Among the quite huge amount of research on this topic, it is worthy briefly summarizing the work zone by Meda et al. (2004) [136], which investigated the tensile and flexure behavior of different FRC materials, including also some considerations on hybrid fibers, obtained by combining different typologies of fibers.

Figure 2.154 depicts the experimental behavior of specimens made of plain concrete, micro fibers, macro fibers, and hybrid fibers, the last by combining both micro and macro fibers and with the same overall fiber amount.

Hybrid combination of short and long steel fibers improves concrete toughness for both small and large crack opening displacements; these enhanced properties can be useful for serviceability and ultimate limit states. In addition, other synergic effects from the combination of micro and macro fibers, such as the reduction of cracking due to shrinkage and the enhanced resistance to fatigue loading, can be effective for short term and long term behavior of structures.

The authors [136] also developed suitable non-linear analyses which basically confirmed the evidence and proposed tension softening relationships for the different material investigated, as reported in Figure 2.155, which illustrates the enhancement in the response of the material due to the combination of micro and macro fibers.
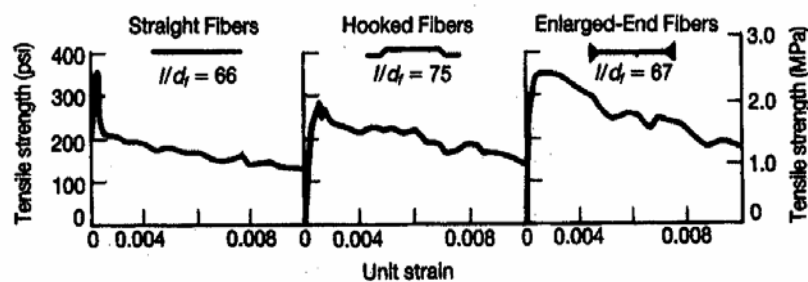
Figure 2.153: Effect of shape of steel fiber on tensile stress in mortar specimens in direct tension [130].
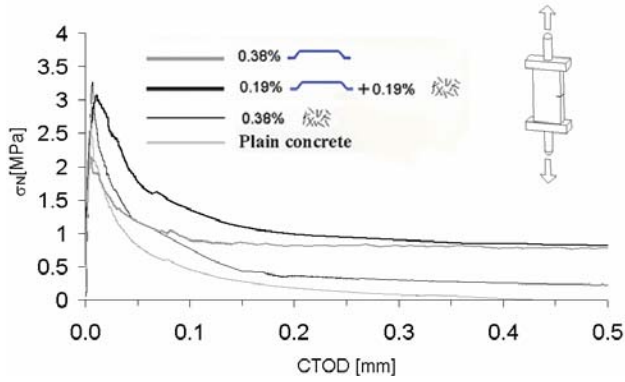
Figure 2.154: Nominal stress-CTOD for different FRC material under uni-axial tensile test.
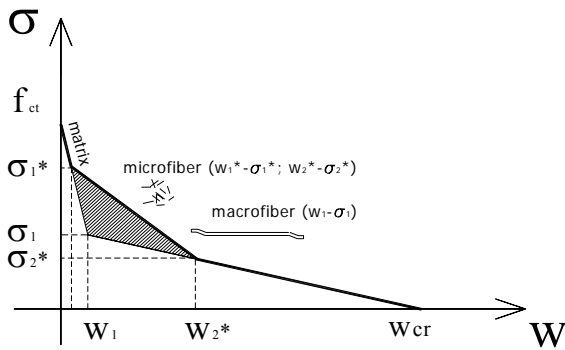
Figure 2.155: Approximation of the softening law by bi-linear or tri-linear curves [136].

Mansur and Ong [133] derived a stress-strain relationship for FRC in tension, similarly to the formulation discussed in the previous Section for FRC in compression.

The relationship also consists of three branches, as shown in Figure 2.156.
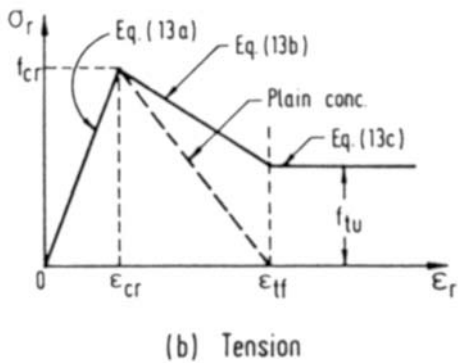
Figure 2.156: Assumed stress-strain relationship for fiber reinforced concrete in direct tension [133].

182

For the ascending branch, it is assumed that the effect of fiber addition on the cracking strength f_{cr} and the modulus of elasticity E_c of concrete can be translated from its influence on the cylinder compressive strength f'_c using the corresponding expressions for plain concrete. The three branches can be expressed as:

$$for \quad \varepsilon_r \le \varepsilon_{cr} \qquad \Rightarrow \quad \sigma_r = \varepsilon_r E_c \tag{2.254}$$

$$for \quad \varepsilon_{cr} < \varepsilon_r \le \varepsilon_{tf} \Rightarrow \quad \sigma_r = (f_{cr} - f_{tu})\left[\frac{\varepsilon_r - \varepsilon_{cr}}{\varepsilon_{cr} - \varepsilon_{tf}}\right] + f_{cr} \tag{2.255}$$

$$for \quad \varepsilon_r \ge \varepsilon_{tf} \qquad \Rightarrow \quad \sigma_r = f_{tu} \tag{2.256}$$

where:

- $f = 0.33\sqrt{f'_c}$;

- $E_c = \dfrac{-2f'_c}{\varepsilon_o}$;

- $\varepsilon_{cr} = \dfrac{f_{cr}}{E_c}$;

- $\varepsilon_{tf} = 2(f_y)_t\left[\dfrac{1}{E_s} + \dfrac{\rho_t}{E_c}\right]$;

- $f_{tu} = 2\eta_l\eta_o\tau_{uf}V_f\dfrac{l_f}{\phi_f}$

being η_l the length efficiency factor for fibers, η_o the fiber orientation factor and τ_{uf} the ultimate bond strength of fiber. The last two expressions were suggested by Bargezar and Schnobrich [137] and Lim et al. [138], respectively.

2.8.5.4 Flexural Strength.

Fibers seem to affect the magnitude of flexural strength in concrete and mortar elements to a much greater extent than it affects the strength of comparable elements subjected to direct tension or compression [124]. Two stages of loading portray the behavior. The first controlling stage is the first cracking load stage in the load-deflection diagram, and the second controlling stage is the ultimate load stage. Both the first cracking load and the ultimate flexural capacity are affected as a function of the product of the fiber volume concentration, ρ, and the aspect ratio, l/d_f. Fiber concentrations less than 0.5% of volume of the matrix and aspect ratios of

less than 50 seem to have a small effect on the flexural strength, although they can still have pronounced effect on the toughness of the concrete element as seen in Figure 2.149.

The flexural strength of plain concrete beams containing steel fibers was defined in Section 2.8.3.5, Equations (2.240) and (2.241). For structural beams reinforced with both normal reinforcing bars and added fibers to the matrix, a modification of the standard expression for the nominal moment strength, $M_n = A_s f_y (d - a/2)$, has to be done in order to account for the shear-friction interaction of fibers in preventing the flexural macro-cracks from opening and propagating in the tensile zone of the concrete section, as seen in Figure 2.158. In this diagram, the standard hypothesis of neglecting the area of concrete in the tensile zone is, therefore, modified so that an additional equilibrium tensile force, T_{fc} is added to the section. That moves the neutral axis downwards, leading to a higher nominal moment strength, M_n. The resulting expression ([124] and [139]) for M_n becomes:
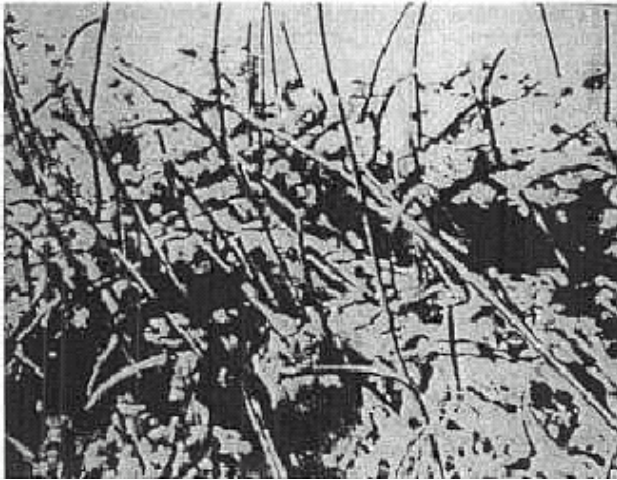
Figure 2.157: Fracture surface of steel fiber-reinforced concrete [121].

$$M_n = a_s \cdot f_y \cdot \left(d - \frac{a}{2}\right) + \sigma_t \cdot b \cdot (h - e) \cdot \left(\frac{h}{2} + \frac{e}{2} - \frac{a}{2}\right) \qquad (2.257)$$

$$2 = [\varepsilon(fibers) + 0.003] \cdot \frac{c}{0.003} \qquad (2.258)$$

$$\sigma_t (MPa) = \frac{0.00772 \cdot l}{d_f \cdot \rho_f \cdot F_{bc}} \qquad (2.259)$$

184
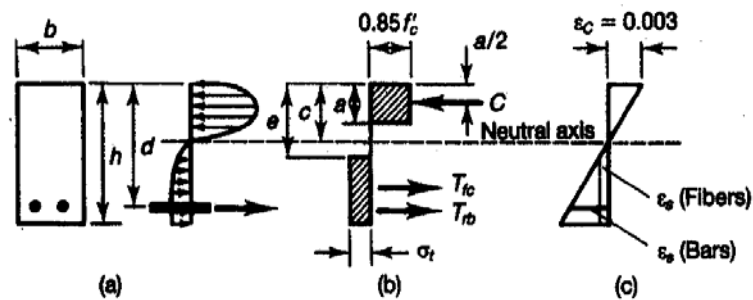
Figure 2.158: Stress and strain distribution across depth of singly reinforced fibrous concrete beams: (a) assumed stress distribution; (b) equivalent stress block distribution; (c) strain distribution. [140].

where:

- l = fiber length;
- d_f = fiber diameter;
- ρ_f = percentage by volume of fibers;
- F_{be} = bond efficiency of the steel fiber depending on its characteristics; varies from *1.0 to 1.2*;
- a = depth of the equivalent rectangular block;
- b = width of beam;
- c = depth to the neutral axis;
- d = effective depth of the beam to the center of the main tensile bar reinforcement;
- e = distance from the extreme compression fibers to the top of the tensile stress block of the fibrous concrete;
- $\varepsilon_s = f_y/E_s$ of the bar reinforcement;
- $\varepsilon_f = \sigma_f/E_f$ of the fibers developed at pull-out at a dynamic bond stress of 333 psi;
- σ_t = tensile yield stress in the fiber;
- T_{fc} = tensile yield of the fibrous concrete = $\sigma_t\, b(h\text{-}e)$;
- T_{rb} = tensile yield forte of the bar reinforcement = $A_s f_y$.

Further proposals of the ultimate moment of FRC structural members were reported in the literature: among them the Imam's formulation [158] will be explained in Section 2.8.9.3.

2.8.5.5 Shear Strength.

A combination of vertical stirrups and randomly distributed fibers in the matrix enhances the diagonal tension capacity of concrete beams. The degree of increase

in the diagonal tension capacity is a function of the shear span-to-depth ratio of a beam. This ratio determines the mode of failure in normal beams that do not fall in the category of deep beams and brackets as detailed by Nawy [140]. Williamson [141] found that when 1.66% by volume of straight steel fibers were used instead of stirrups, the shear capacity increased by 45% over beams without stirrups. When steel fibers with deformed ends were used at a volume ratio of 1.1%, the shear capacity increased by 45-67% and the beams failed by flexure. Using crimped-end fibers increased the shear capacity by almost 100%.

In general, as the shear span-to-depth ratio *a/d* decreases and the fiber volume increases, the shear strength increases proportionally. Tests by Sharma [142] resulted in the following expression in the ACI 544 report [124] for the average shear stress, v_c, for beams in which steel fibers are added:

$$v_{cf} = \frac{2}{3} \cdot f'_t \cdot \left(\frac{d}{a} \right)^{1/4}$$

(2.260)

where

- f'_t = tensile splitting strength;
- d = effective depth of a beam;
- a = shear span = distance from the point of application of the load to the face of the support when concentrated loads are acting or the clear beam span when distributed loads are acting.

There is still no standardized test method in Europe or North America to measure the material properties of FRC in shear, such as shear strength or shear toughness. More recently, the Japan Society of Civil Engineering (JSCE) has proposed a standard method, SF-6 [143], in that, during the test, the stress field remains essentially that of pure shear. Mirsayah and Banthia [144] studied the applicability and feasibility of this test method, and then applied it to FRC composites.

Even though the authors outlined some concerns about the test set up, they concluded that such a test can be used effectively to obtain shear characteristics of FRC. Both types of fibers tested were seen to provide significant improvements in shear strength as well as shear toughness, and these improvements were greater at higher fiber dosage rates. Moreover, when toughness indexes in shear are compared with those in flexure, there appeared to be a direct correlation, which anyhow was not yet brought to light by the authors. Further studies are therefore needed.

2.8.6 Mode of Action of SFRC.

SFRC is a two-composite material whose properties are mainly influenced by the cement matrix and the fibers. According to Schnütgen (1975) [145] the bond strength between the surface of the fibers and the matrix is of huge importance. To describe the behavior of SFRC two different approaches can be used:

- Composite concept
- Spacing concept

By using the composite concept the load will be prorated to each component of the composite according to the volumetric content and the appropriate stiffness matrix. Therefore, the length and the orientation of fibers as well as the bond between the cement matrix and the steel fibers are important for this approach. By means of pertinent equations adopting the Hook law, the behavior of SFRC can be described both before cracking and after cracking, when it transmits the load between the crack planes. The mechanism of bond between the fibers and the surrounding concrete has been investigated by Naaman (2000) [146]. He named four phases of the bond mechanism such as:

- Mechanical interaction;
- Friction;
- Physical and chemical bond (if existing);
- Fiber to fiber interaction.

The mechanical interaction is one of the most important phase of the bond mechanism. It takes place after failure of the chemical bond and remains until fiber pull out or fiber failure by reaching the tensile strength. Mechanical interaction is dependent on the fiber geometry. Friction is mostly influenced by the interface between fiber and matrix. Physical and chemical bond is usually very weak in comparison to the other phases of bond. Fiber to fiber interaction occurs if a high content of fibers is used, which means that a relatively high volume percentage of fibers is provided in the mixture, so that fibers are in contact with each other. It usually happens in SIFCON (Slurry Infiltrated Concrete) or SIMCON (Slurry Infiltrated Mat Concrete), which anyhow are out of the interest in the present research investigation.

The aim to keep fiber influence as high as possible determines a high research interest in the field of cracking because it will be fulfilled if the anchorage to the matrix is as good as possible. If fibers are long, strong and embedded enough, they can be strained until their tensile strength is attained. Otherwise, fiber pull out occurs. The length of anchoring is also called adhesive bond length l_a and depends

187

on the possible bond stresses, on the diameter and the perimeter, respectively. For circular fibers with diameter d and a tensile strength f_{ft} is obtained:

$$l_a = \frac{f_{ft}}{4\tau_m} \cdot d \qquad (2.261)$$

with:

τ_m mean bond strength depending on the type of fiber between 1 and 10 MPa. The critical length of fibers l_{crit} is equivalent to the minimum length by applying the tensile strength by bond. It is at least the double adhesive bond length l_a multiplied by a factor α, which takes into account that a crack in the matrix doesn't occurs always in the middle of the fiber. The coefficient α has to be >1. Under a statistical point of view α should be 2, which means that the length of the fibers is four times the adhesive bond length l_a:

$$l_{crit} = \alpha \cdot 2 l_a = \alpha \cdot \frac{f_{ft}}{2\tau_m} \cdot d \qquad (2.262)$$

After the crack initiation in the matrix it has to distinguish between different cases regarding the strength behavior.

2.8.6.1 Case 1.

Assume that fibers will be pulled out of the matrix before reaching their tensile strength because the anchoring length is smaller than the required adhesive bond length (Figure 2.159). The pull out, however, is hindered by friction. The result is an energy consumption. Such a FRC matrix has a great work capacity and shows a quasi ductile behavior.
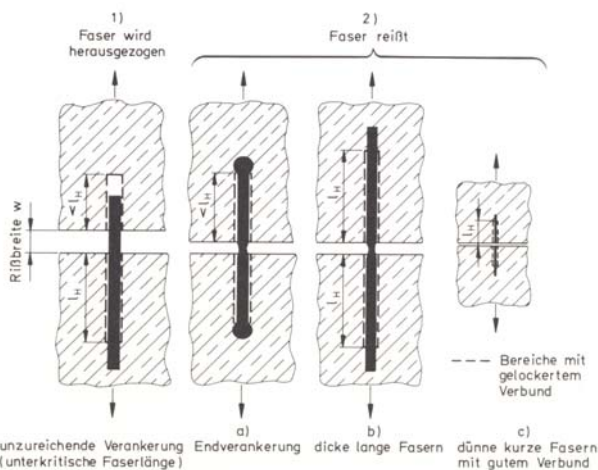
Figure 2.159: Anchorage and failure possibilities of fibers [145].

2.8.6.2   Case 2.

Assume that fibers are strongly anchored in the matrix and can be strained until their tensile strength is attained. Consequently, they can be fully utilized with regard to the enhancement of the tensile strength of the concrete. However, higher tensile strength of fibers is not as critical as high ductility and work capacity. Therefore, the deformation process after crack initiation can develop quite a lot depending on the strain property, bond behavior and the anchorage of fibers. A more ductile fracture behavior of concrete is only possible if fibers can elongate themselves in the fracture zone. An unclip of the bond in a certain length has to be possible without loosing the whole bond. This can be attained by using hooked or paddled fibers (Figure 2.159 case 2a).

The spacing concept was derived from the fracture mechanic approach, developed by Griffith (1920 [147]) for solid materials with imperfections. In concrete such imperfections could be pores and cracks due to shrinkage. Stress concentrations arise during loading at these imperfections, leading to further deformations in the material. By adding fibers to a brittle matrix, the deformations at the crack tip will be reduced and therefore the expansion of microcracks will be delayed. The effectiveness of fibers depends on the spacing among themselves. The smaller the spacing the higher the resistance against cracks. With this approach the behavior of SFRC can be explained until the strength of cracking is achieved. The ability of SFRC to transmit forces between crack planes can not be described using this approach.

2.8.7   Different Fiber Geometry.

There are many different types of available fibers that are produced by certain companies. Fibers differ in their shape as well as in their materials. For FRC predominantly fibers made of steel, glass and plastic are used. Asbestos fibers are especially suitable for fiber-cement products, such as roof plates or pipes. But they are no longer used because of the their insalubrious dust which arises during processing.

Since fibers bridge a crack and control the crack propagation in the first phase of cracking, it is important to select the right fiber in shape and material that can fulfill this task. Many types of fibers have been investigated in the last decades. The geometry is spread from straight to irregular forms and all have their advantages as well as disadvantages. A selection of steel fibers tested by Soroushian and Bayasi (1991) [148] is shown in Figure 2.160.

189
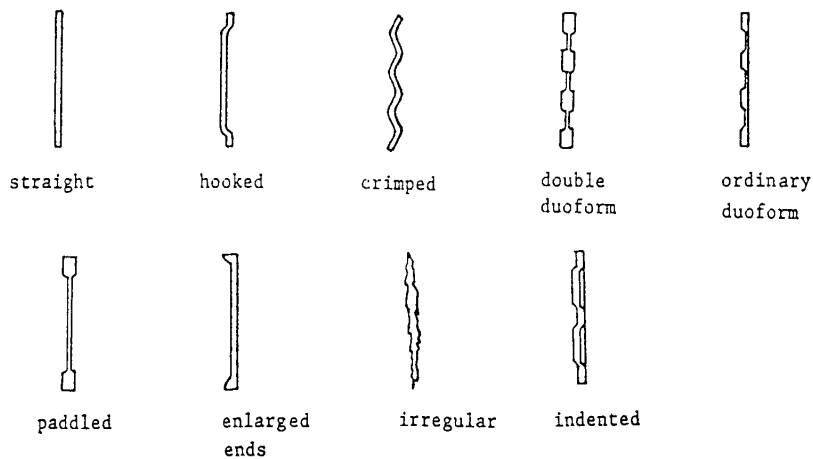
Figure 2.160: Different steel fiber types investigated by Soroushian and Bayasi (1991).

Figure 2.161 shows different fibers in material, shape and geometry, often used nowadays in combination, to enhance both micro and macro cracking, and therefore to have benefit from an improved performance in short-term deformations, such as shrinkage.
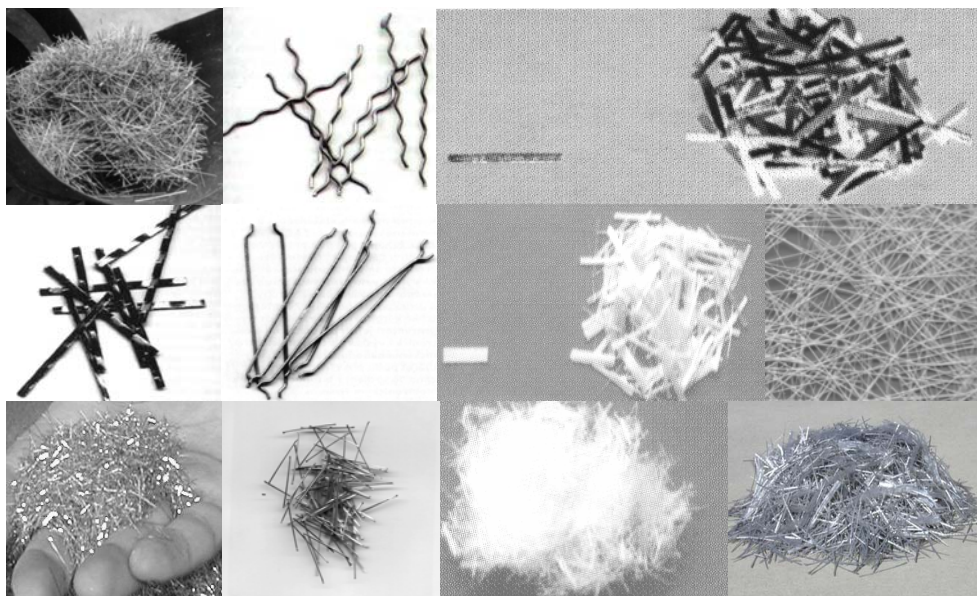
Figure 2.161: Different typologies of fibers in material and geometry.

The most often used fibers are the straight, hooked, crimped and enlarged end fibers. While the straight fiber is only anchored in the matrix by friction and chemical adhesion, all other fibers, which have a deformation along their axis, develop greater bond properties. In order to utilize the usually high tensile strength of fibers it is important that fibers are well anchored in the concrete matrix.

Figure 2.162 shows the stress-strain diagram of different steel fiber concretes under compression loading.

The work done by Hughes and Fattuhi (1976) [149] indicates that crimped fibers show a better workability compared to straight or other forms of fibers for a similar fiber aspect ratio. Furthermore, it was found for most of fibers tested that with increasing fiber aspect ratio the influence on the material parameters increases.

By using the same fiber content a higher aspect ratio affects the post peak behavior in a positive way, the slope of the declining branch of the stress-strain curve decreases with an increase of the aspect ratio, as already shown in Figure 2.148.
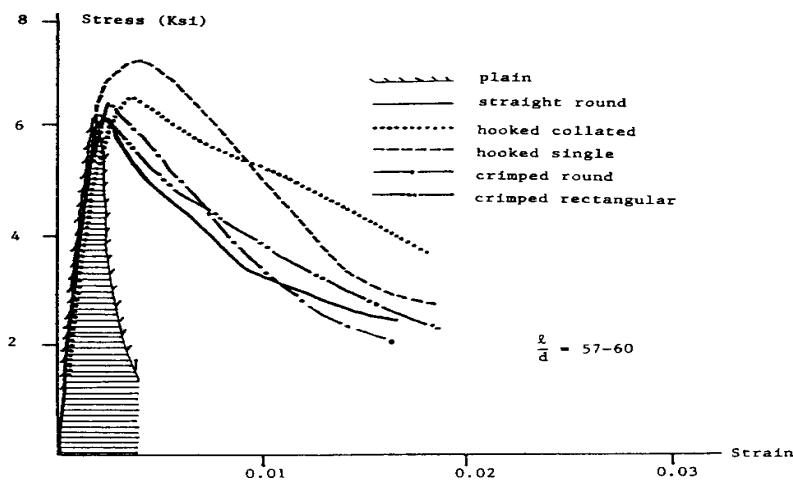
Figure 2.162: Compressive stress-strain diagram for concrete with different steel fiber types (Hughes, Fattuhi 1976).

2.8.8   Structural Application of SFRC.

Steel fiber reinforced concrete is becoming more and more appealing in structural and non structural applications, thanks to its improved knowledge and previous successful experiences.

Due to its properties SFRC, is used mainly (if necessary with additional reinforcement) for:

Industrial pavements [150], airport fixations and bridge screeds. Here, especially a favorable influence of crack initiation on the fresh concrete is expected (shrinkage), where a conventional reinforcement wouldn't be so effective. Instead of some main wide cracks small hairline cracks emerge. Further advantages are a better behavior on impact loading and the possibility of reducing the thickness of slabs by a predetermined loading.

Structural elements (especially precast) where secondary reinforcement (shear, transverse, torsion reinforcement) is substituted by fibers [151]; [152] and [153].

Non-structural precast elements such as culverts, panel and tanks, where sometimes fibers are the only reinforcement provided.

Dynamic stressed structures, such as structures in earthquake areas and structures with explosion or impact risk, for bank fixations, for engine foundations.

Thin-walled devices, where the placement and the corrosion protection of a conventional reinforcement could be problematical. Examples are shells, pipes, elements of facades and tribunes, containers and noise barriers.

Manufacturing of precast elements such as beams, pipes, sills, container because of the possibility to combine automation and quality control.

Shotcrete in mining and tunneling; restoration of reinforced and prestressed concrete structures.

The fact that fibers are becoming extensively utilized in the practice and often in structural application lead to the mandatory necessity to define guidelines or specifications that could allow engineers to incorporate SFRC in their design procedures. It is noticeable that no design code contains any statement or guidance on SFRC up to now.

2.8.9   Shear Tests and Analytical Models of SFRC Beams.

In the following paragraphs some test reports, concerning experiments investigating the shear behavior of SFRC beams taken from the literature are summarized.

Attention was especially devoted to the experimental results and their interpretation toward rational and feasible design procedures for shear in structural elements made of SFRC.

This review will just focus on steel fibers, the only typology studied in this thesis. Moreover, it does not mean to be exhaustive. However, it shows a survey of the most important ongoing investigations and the derived approaches for calculating the shear strength of SFRC beams.

192

Many reports published over the past 25 years confirm the effectiveness of steel fibers as shear reinforcement. Fiber are used to boost the shear capacity of concrete or to replace, in part, the vertical stirrups in RC structural members. This relieves reinforcement congestion at critical section such as beam-column junctions. Fiber reinforcement may also significantly reduce construction time and costs, especially in areas of high labor costs and possibly even labor shortages, since conventional stirrups require relatively high labor input to bend and fix in place. Fiber concrete can also be easily placed in thin or irregularly shaped sections, such as architectural panels, where it may be very difficult to place stirrups.

Several equations based on test data and theoretical analyses have been proposed for calculating the shear capacity of SFRC beam. These equations can be divided into two categories.

First category considers the steel fibers to directly influence the shear capacity of the concrete, determined by split tensile cylinder or modulus of rupture tests, and does not explicitly consider fiber characteristics.

Second category of equations considers that steel fibers provide shear strength in excess of the shear strength of plain concrete and that they may eliminate stirrups. This category of design equations incorporates fiber properties, which generally is expressed as fiber factor, F.

The concept of fiber factor was introduced to account for the fiber aspect ratio, volume fraction of fibers and a bond factor (Narayanan & Kareem- Palanjian 1984 [154]).

$$F = \left(\frac{L}{D}\right) \cdot V_f \cdot D_f \tag{2.263}$$

where:
- L is the length of fiber;
- D is the diameter of fiber;
- L/D is the aspect ratio of fiber;
- V_f is the fiber volume percentage;
- D_f is the fiber bond factor, which may vary form 0.5 to 1.0 depending on the fiber geometry and on the concrete matrix.

The existing shear equations of SFRC beams are usually generated by a regression analysis of SFRC beam test data for a few fiber types and volume percentages, but the number of beam tests does not cover a wide enough range of fiber types and volume percentages. There is not at the present time sufficient

number of reported tests to generate a comprehensive empirical shear equation as a function of all the relevant important parameters of SFRC, such as fiber volume, fiber geometry, range of a/d ratios and concrete strengths.

2.8.9.1   RILEM TC 162-TDF: First Approach.

The model for representing the beam behavior of shear critical beam by Rilem [155] was undertaken based firstly on the experimental results of Vandewalle and Dupont [156], who performed experiments of 43 full-scale beams. The investigated parameters were the fiber dosage, the shear span-to-depth ratio, the amount of longitudinal reinforcement and stirrups.

The Rilem Design Method is based on the European pre-standard ENV 1992-1-1 [82]. This method calculates the shear capacity V as consisting of 3 separate contributions:

$$V = V_c + V_w + V_f \qquad \text{[N]} \qquad\qquad (2.264)$$

The first term is calculated in the same way as in Eurocode 2 and takes into account the shear resistance of the member without shear reinforcement:

$$V_c = 0.12 \cdot k \cdot \left(100 \cdot \rho_l \cdot f_{ck}\right)^{\frac{1}{3}} \cdot b \cdot d \qquad \text{[N]} \qquad\qquad (2.265)$$

with:

- $k = 1 + \sqrt{\dfrac{200}{d}} \leq 2$;

- f_{ck} = characteristic cylinder compressive strength [N/mm²];
- b = width of the beam [mm];
- d = effective depth of the beam [mm];

- $\rho_l = \dfrac{A_{sl}}{b \cdot d} \leq 0.02$;

- A_{sl} = tensile reinforcement in the critical section.

The second term is also identical as in Eurocode 2 and takes account of the contribution of the stirrups and/or inclined bars:

$$V_w = \frac{A_{sw}}{s} \cdot 0.9 \cdot d \cdot f_{ywd} \qquad \text{[N]} \qquad\qquad (2.266)$$

with:

194

$$\frac{A_{sw}}{s} = \frac{\textit{Area of stirrups}}{\textit{spacing between stirrups measured along the longitudinal axis}}$$

The third term is the contribution of the steel fibers:

$$V_f = k_f \cdot k_l \cdot \tau_{fd} \cdot b \cdot d \qquad \text{[N]} \tag{2.267}$$

with:

- k_f = factor for taking into account the contribution of the flanges in a T-section; it is equal to 1 for rectangular sections;
- k_l = factor for taking into account the size effect of the member = (1600-d)/1000 ≥ 1;
- τ_{fd} = 0.12 $f_{eq,3}$ [N/mm^2].

A refinement of the previous sets of equations was also suggested by the Rilem Committee TC 162-TDF [155].

Equation (2.264) remains unchanged. In Equation (2.265) the factor 0.12 takes into account the influence of the shear span-to-depth ratio, which is replaced by its original formula:

$$0.15 \cdot \sqrt[3]{\frac{3d}{a}} \tag{2.268}$$

Also the average value of the cylinder compressive strength is used instead of the characteristic one. As a result Equation (2.265) becomes:

$$V_c = 0.15 \cdot \sqrt[3]{\frac{3d}{a}} \cdot k \cdot \left(100 \cdot \rho_l \cdot f_{cm}\right)^{\frac{1}{3}} \cdot b \cdot d \qquad \text{[N]} \tag{2.269}$$

with:

- a = shear span [mm];
- f_{cm} = average cylinder compressive strength [N/mm^2].

In Equation (2.266) only the design value of the yield strength of the stirrups is changed into the average yield strength f_{ywm}, giving:

$$V_w = \frac{A_{sw}}{s} \cdot 0.9 \cdot d \cdot f_{ywm} \qquad \text{[N]} \tag{2.270}$$

A real ultimate steel fiber contribution is calculated using following equation:

$$V_f = k_f \cdot k_l \cdot 0.5 \cdot \frac{d}{a} f_{eqm,3} \cdot b_w \cdot d \qquad \text{[N]} \tag{2.271}$$

195

2.8.9.2 RILEM TC 162-TDF: Final Recommendation.

The technical Committee 162-TDF recently issued Final Recommendation [157] for steel fiber reinforced concrete. Provisions for shear slightly changed, affecting the fiber contribution to shear, which can now be expressed as:

$$V_f = 0.7 \cdot k_f \cdot k_l \cdot \tau_{fd} \cdot b_w \cdot d \qquad \text{[N]} \tag{2.272}$$

with:

k_f = factor for taking into account the contribution of the flanges in a T-section; it is equal to 1 for rectangular sections, whereas, for general shapes, can be calculated as:

$$k_f = 1 + n \cdot \left(\frac{h_f}{b_w} \right) \cdot \left(\frac{h_f}{d} \right) \quad \text{and} \quad k_f \leq 1.5 \tag{2.273}$$

being h_f the height of the flange, b_f the width of the flange, b_w the width of the web and:

$$n = \frac{b_f - b_w}{h_f} \leq 3 \quad \text{and} \quad n \leq \frac{3 \cdot b_w}{h_f} \tag{2.274}$$

k_l = factor for taking into account the size effect of the member, given by:

$$k_l = 1 + \sqrt{\frac{200}{d}} \leq 2 \tag{2.275}$$

τ_{fd} = design value of the increase in shear strength due to fibers, given by:

$$\tau_{fd} = 0.12 \cdot f_{Rk,4} \tag{2.276}$$

where

$$f_{R,4} = \frac{3 \cdot F_{R,4} \cdot L}{2 \cdot b \cdot h_{sp}^2} \tag{2.277}$$

In the last equation, referred to fracture mechanics test on specimens under a three point bending loading system [157], the parameters are:

- $F_{R,4}$ is the load corresponding to a CMOD of 3.5 mm in the three point bending tests performed;
- L is the span of the specimen, 500 mm;
- h_{sp} is the distance between the tip of the notch and the top of the cross section (125 mm);

196

- *b* is the width of the specimen (150 mm).

2.8.9.3   Imam et al.

This model [158] does not split the contributions of concrete, stirrups and fibers into three separate terms, but it combines the actions of concrete and fibers, according to many experimental evidences that clearly showed the fiber contribution as an improved toughness provided to the matrix.

The contribution of stirrups is derived with Equation (2.270) according to Rilem Recommendation.

The equation for predicting the ultimate shear capacity for steel fiber reinforced high strength concrete is:

$$v_u = 0.6 \cdot \psi \cdot \sqrt[3]{\omega} \cdot \left[f_c^{0.44} + 275 \cdot \sqrt{\frac{\omega}{(a/d)^5}} \right] + v_w \qquad \text{[N]} \qquad (2.278)$$

where:

- *ω = ρ (1+4F);*

with:

- $F = \left(\dfrac{L_f}{D_f} \right) \cdot V_f \cdot d_f$;

- L_f / D_f = aspect ratio of the fiber (=length/diameter);
- V_f = volume fraction of fibers;

- *Ψ* = size effect factor = $\psi = \dfrac{1 + \sqrt{(5.08/d_a)}}{\sqrt{1 + d/(25 \cdot d_a)}}$;

- d_a = *maximum aggregate size, in mm;*
- d_f = bond efficiency coefficient
    = 1 for hooked fibers;
    = 0.9 for deformed fibers;
    = 0.5 for straight fibers.

The authors found out that the Rilem method (first provision) is a conservative approach. Especially the contribution of the stirrups and the influence of the shear span-to-depth ratio are underestimated. For SFRC beams containing longitudinal reinforcement a calculation with the equation of Imam approximates the experimental values fairly good.

Based on the model above mentioned, Imam et al. [159] derived interesting considerations about the shear domain of fiber reinforced high strength concrete beams. The use of steel fibers is in fact a possible solution to overcome the shear failure, since they are capable of increasing the beam strength up to its full flexural capacity.

Figure 2.163 shows the effect of fiber factor, F, on both the ultimate moment and the flexural moment (M_u and M_{fl}, respectively), given by:

$$M_{fl} = \frac{1}{2} \cdot \rho \cdot f_y \cdot b \cdot d^2 \cdot (2-\eta) + 0.83 \cdot F \cdot b \cdot d^2 \cdot (0.75-\eta) \cdot (2.15+\eta) \quad (2.279)$$

$$M_u = V_u \cdot a = 0.6 \cdot b \cdot d^2 \cdot \psi \cdot \sqrt[3]{\omega} \cdot \left[f_c^{0.44} \cdot \left(\frac{a}{d} \right) + 275 \cdot \sqrt{\frac{\omega}{(a/d)^3}} \right] \quad (2.280)$$

where all parameters where above reported except:

- $\eta = \dfrac{\rho \cdot f_y + 2.32 \cdot F}{0.85 \cdot f_c + 3.08 \cdot F}$.

It can be observed that the ultimate moment is strongly affected by increasing F, while the flexural moment is only slightly influenced. That means that the improvement of shear capacity by the effect of fibers is more significant than the improvement of nominal flexural capacity.
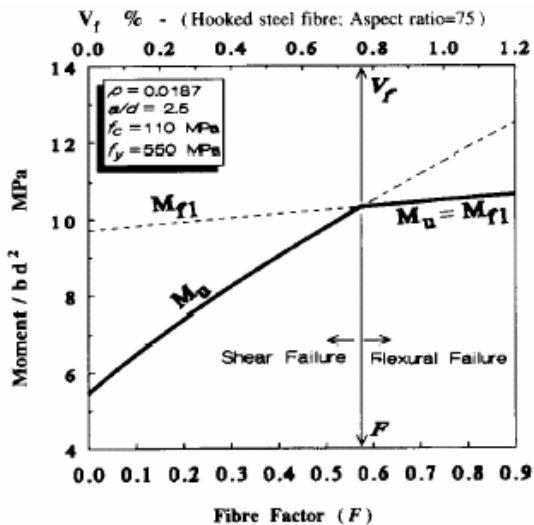
Figure 2.163: Fiber effect on both ultimate and nominal flexural moments [158].

Steel fibers can therefore successfully replace the shear reinforcement, but it is senseless to use steel fibers as a complementary reinforcement of longitudinal bars.

The solid lines of Figure 2.163 present the border of the beam strength, which consists in two parts. In the first portion, steel fibers are not influential enough to increase the beam strength up to its full flexural capacity. Shear failure is therefore expected, whereas in the right hand part, fibers are effective enough to provide a beam without stirrups with full flexural capacity and safety in shear. The point at which the two parts meet indicates the minimum percentage of fibers which is capable of increasing the beam strength up to 100 % M_{fl}. This point can be denoted as the optimum fiber factor at a give span-to-depth ratio, which can also be observed in the representation M_u/M_{fl} versus F in Figure 2.164. Note that the increase of F results in an appropriate increase of M_u/M_{fl}. Furthermore, the percentage of steel fibers to be added to a beam with a lower ρ to reach its full flexural capacity, is less than that required for the same beam with a higher ρ.
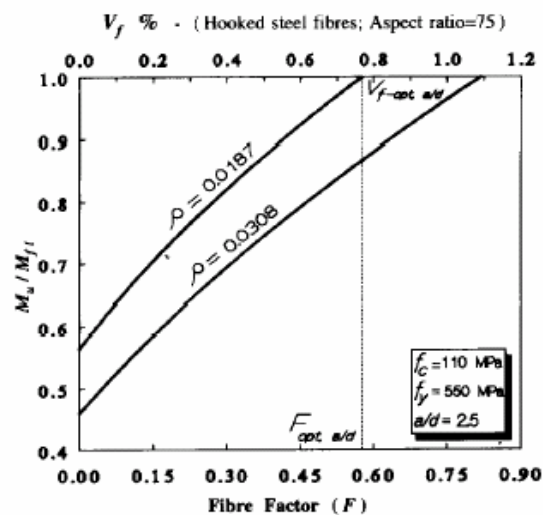
Figure 2.164: Fiber factor (F) versus relative flexural capacity [158].

By analytically combining the Equations (2.279) and (2.280), the authors were able to determine a shear domain, as a function of many crucial parameters, such as the reinforcing ratio, the fiber factor, the *a/d* ratio, the compressive concrete strength, the reinforcement tensile strength, the depth of the member and the maximum aggregate size.

Figure 2.165 illustrates the shear domain as a function of *a/d* and the fiber factor *F*, given the other parameters as constants. By increasing F, the region of diagonal failure disappears completely.

The shear domain exhibits three different important values of *a/d*: two limiting values at which the shear effect starts to appear and a third value at which the effect of shear becomes maximum, indicated as critical shear span-to-depth ratio *(a/d)$_c$*. The authors analytically determined an expression for defining such a value, as:

$$(a/d)_c = 11.12 \cdot \omega^{0.2} \cdot f_c^{-0.176} \tag{2.281}$$
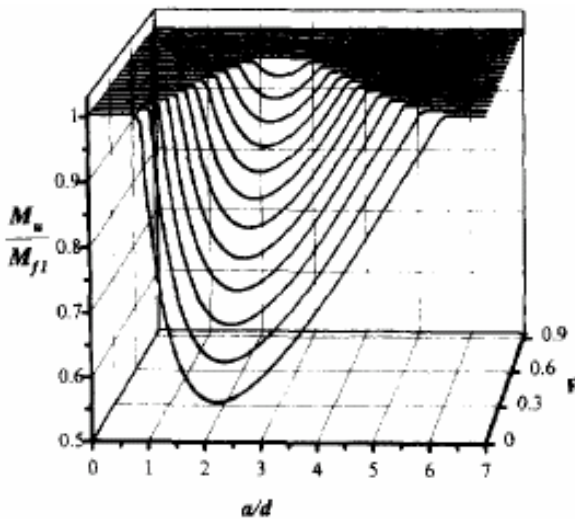
Figure 2.165: Domain of diagonal shear failure varying the fiber factor F (f$_c$ = 100 MPa, f$_y$ = 550 MPa, ρ = 1.87%, d = 300 mm, and d$_a$ = 14 mm) [158].

The last equation indicates that *(a/d)$_c$* depends on ρ, *F* and *f$_c$*, being directly proportional two the first two parameters and inversely proportional to the latter. However, the authors reported that *f$_c$* does not influence significantly this ratio.

The relationship between *(a/d)$_c$* and *F* is depicted in Figure 2.166.
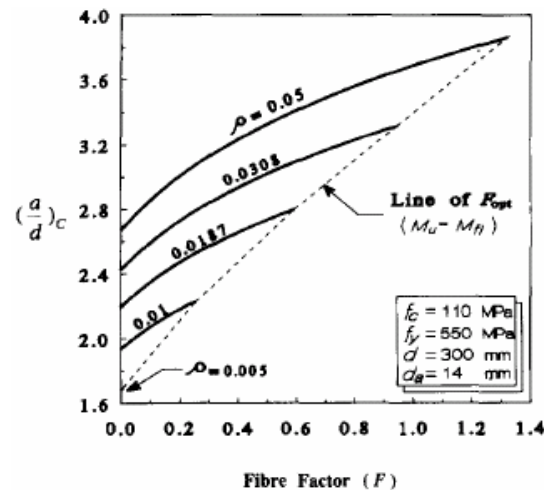
Figure 2.166: Critical shear span-to-depth ratio (a/d)$_c$ versus fiber factor F [158].

For a given ρ, the value of F is limited by and optimum value F_{opt}, for which the ultimate flexural capacity is fully attained ($M_u = M_{fl}$). Again, it can be noted that an increase in the longitudinal reinforcement ratio determines an increase in *(a/d)$_c$* and especially a greater amount of F to reach the full flexural capacity of a beam without conventional transverse reinforcement.

2.8.9.4 Casanova, Rossi, and Schaller.

In this work, both large scale double T-girders and small rectangular beams were tested [160]. With stereophotogrammetry cracking was monitored. Mainly a Mode I crack opening was determined and also a scale effect linked to the height of the beam was suggested.

Concerning the first step of tests carried out, a normal strength concrete of 35 MPa was utilized for casting five double-T girders failing in shear. Attention was paid in choosing the shear span (set greater than three times the depth of the member to limit eventual diffusion effect towards supports), the depth of the members (800 mm, representative of full scale beams), and in avoiding yielding of the longitudinal reinforcement and failure of concrete in compression. These constraints led to a beam 6.2 m long, as shown in Figure 2.167.

Various beams, without transverse reinforcement (PC), with stirrups having two different spacings (RC1 and RC2,130 mm and 500 mm spacing respectively) and two different fiber lengths using the same volume percentage of 1,25% each (FRC1 and FRC2; 60 mm and 30 mm long, respectively) were tested.

As a result, a globally similar behavior between the RC2 and the FRC1 specimens was observed, confirming the capacity of fibers to replace stirrups (Figure 2.168).

The PC girder, without any transverse reinforcement, first developed a network of fine cracks inclined at around 45°, which suddenly merged together in a single large crack that rapidly grew along the tension and compression flanges, separating the beam into two blocks. Only the longitudinal reinforcement served to knit this crack together.

While the RC1 girder showed, according to its design, the best performance failing under failure, RC2, FRC1 and FRC2 specimens proved to behave similarly and made possible a comparison between conventional transverse reinforcement and fibers. The FRC2 diagram shows that vigilance is necessary concerning ductility, because the drop in force experimentally observed is directly related to the drop in the post-cracking plateau in tension beyond a certain opening. That makes necessary to specify a maximum opening corresponding to an ultimate limit state to ensure a completely safe design. This maximum opening should depend on the height of the beam, since a remarkable scale effect on the crack opening at failure was recognized .
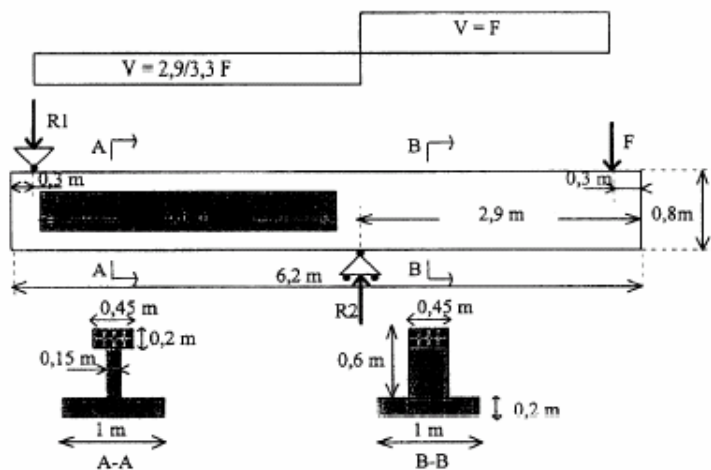
Figure 2.167: Geometry of T girder and testing device [160].
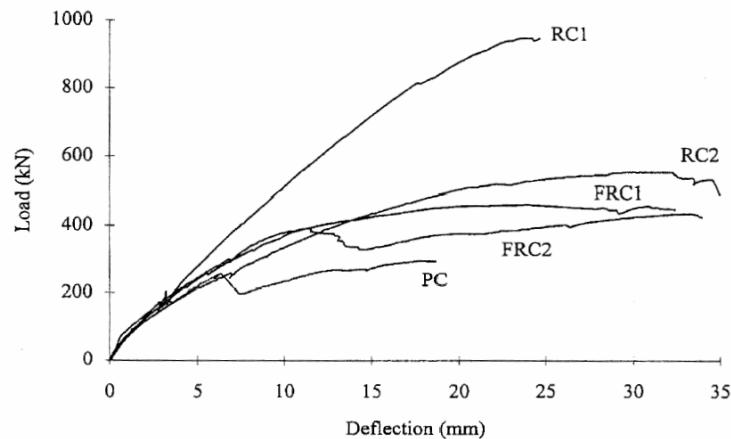
Figure 2.168: Experimental load-deflection curves of the T-girders [160].

The onset of a block mechanism is observed just before the maximum load. Prior to this step, cracks mainly open in mode I-normal displacement.

These tests have shown that the post-cracking tensile behavior is an adequate parameter to quantify the part due to SFRC in the shear-loading capacity of a beam. The fiber-matrix interface is greater in a good matrix and leads to a higher post-cracking residual stress. Furthermore, a good bond limits crack openings and, so, risks of corrosion.

After a material study, five further beams, having a rectangular cross section, made of HSC, were tested: two beams made of classical reinforced HSC while three beams cast with HSFRC (with hooked end drawn steel fibers, 30 mm long). Concrete compressive strength was around 90 MPa.

The effect of steel fibers in a high strength matrix resulted in a even improved post-cracking strength, ductility and crack control.

Under a design point of view, the authors developed a rational method for predicting the ultimate shear capacity of a beam, using the block mechanism approach. As already mentioned, it was proved the necessity that a maximum opening corresponding to an ultimate limit state has to be specified to ensure a completely safe design.

The shear load capacity V_u of a beam with classical longitudinal reinforcement may be divided into two terms:

$$V_u = V_s + V_t \qquad [\text{N}] \qquad\qquad (2.282)$$

where V_s is the structural part (due to the compression zone, longitudinal reinforcement, aggregate interlocking…) and V_t is the part directly carried by the transverse reinforcement. The structural part shows the same V_s as for plain concrete.

The difference between a regular beam and a SFRC beam is therefore in the transverse part V_t, which is substituted by V_f. This part is determined by integrating the post-cracking residual stress [$\sigma_f(w)$] of SFRC along the crack and projecting it vertically to equilibrate a part of the shear load, according to Figure 2.169.
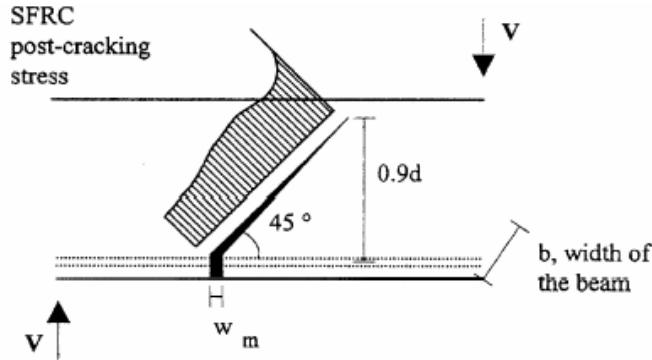
Figure 2.169: Block mechanism at failure [160].

$$V_f = \int_0^{0.9d\sqrt{2}} \sigma_f\left(\frac{s}{0.9d \cdot \sqrt{2}} \cdot w_m\right) \cdot b \cdot \frac{\sqrt{2}}{2} \cdot ds \tag{2.283}$$

$$= 0.9b\,d \cdot \frac{1}{w_m} \int_0^{w_m} \sigma_f(w)\,dw \tag{2.284}$$

$$V_f = 0.9b\,d \cdot \overline{\sigma}_p(w_m) \tag{2.285}$$

$$\overline{\sigma}_p(w_m) = \frac{1}{w_m} \int_0^{w_m} \overline{\sigma}_f(w)\,dw \tag{2.286}$$

$\overline{\sigma}_p(w_m)$ is called the equivalent post-cracking residual stress of SFRC at the crack width w_m. The latter is in fact a mean value of the post-cracking residual stress between zero and w_m. The last equation evidences that uni-axial tensile test is necessary to quantify the part due to fibers.

Moreover, the ultimate limit state in tension is defined by the value of w_m. The ultimate crack opening is experimentally shown to be proportional to the height of the beam. As the average crack spacing is roughly similar to the inner lever arm, *0.9 d*, and the crack opening is controlled by the longitudinal reinforcement, the authors proposed a definition of w_m as:

$$w_m = \varepsilon_s \cdot 0.9d \tag{2.287}$$

where ε_s is the strain of the longitudinal reinforcement.

A mean value of the structural part is proposed by Kordina (1987) [161] as:

$$V_s = 0.85 \cdot h \cdot b \cdot k_c \cdot k_L \cdot \Delta\tau \tag{2.288}$$

with:

- h = height;
- b = width;
- $\Delta\tau$ = corrective factor of the structural part;
- k_c = concrete factor;
- k_L = longitudinal reinforcement factor;
- $\Delta\tau$ = 0,24 (mean value);
- $k_c = (f'_c)^{1/2}$ (f'_c, compressive strength);
- $k_L = \rho_L^{1/3}$ (ρ_L, longitudinal reinforcement).

This second series of tests showed that a combination of HSC with drawn steel fibers provides ductility, a high post-cracking residual stress and small crack openings. The same global behavior was obtained using a volume of 1.25% of fibers or 1.1% of conventional steel (stirrups and compression bars). Furthermore, HSFRC leads to a better durability in the structure than HSRC, because of a smaller crack opening.

2.8.9.5 *Khuntia, Stojadinovic, and Goel.*

Based on experimental investigations of different researchers, a design equation for predicting the shear strength of normal and high strength fiber reinforced concrete with compressive strength up to 100 MPa is suggested [162]. In addition to concrete strength, the influence of other variables such as fiber factor, shear span-to-depth ratio, longitudinal reinforcement ratio, and size effect are considered.

The authors consider first the equation given by the ACI Building Code (Equ. 11-5 of ACI 318-02) for conventional RC beams for computing the shear strength of beams without web reinforcement:

$$V_c = \left(0.157 \cdot \sqrt{f_c'} + 17.2 \cdot \rho \frac{Vd}{M} \right) b_w \cdot d \leq \left(0.29 \cdot \sqrt{f_c'} \right) b_w \cdot d \qquad (2.289)$$

By using a factor suggested by Zsutty (1971) [8], which is based on elaborate statistical study (aiming at improving the ACI equation particularly for short beams), a formula to calculate the shear strength of short beams is derived as:

$$V_c = 2.5 \frac{d}{a} \cdot \left(0.167 \sqrt{f_c'} \right) b_w \cdot d \leq 0.5 \cdot \sqrt{f_c'} \ b_w \cdot d \qquad (2.290)$$

Equation (2.290) shows that the main parameters influencing the shear strength of FRC beams are compressive strength of concrete, shear span-to-depth ratio (as for conventional RC members), and post-cracking tensile strength. The latter depends, amongst other factors, on the volume fraction, shape, aspect ratio, surface characteristics of the fiber, and on the properties of the concrete matrix, and can be expressed as:

$$\sigma_{pc} = A \beta \tau V_f \frac{l_f}{d_f} = A \tau F_1 \qquad (2.291)$$

where:
- A = nondimensional constant depending on the orientation factor and length efficiency factor of fibers, taken as 0,41 (Swamy et al., 1993) [163];
- τ = fiber-matrix interfacial bond stress;
- β = factor for fiber shape and concrete type;
- V_f = volume percentage;
- l_f = fiber length;
- d_f = diameter of fiber;
- F_1 = fiber factor expressed as:

$$F_1 = \beta V_f \frac{l_f}{d_f} \qquad (2.292)$$

The post-cracking tensile strength of FRC can be conservatively and more easily expressed as a function of the fiber factor and the compressive strength of concrete as follows:

$$\sigma_{pc} = 0.41 F_1 \cdot 0.68 \sqrt{f_c'} = 0.28 F_1 \sqrt{f_c'} \qquad (2.293)$$

Considering the forces acting at a diagonal crack in FRC beams without stirrups (Figure 2.170) and assuming a crack inclination of 45°, it can be shown that the

206

total shear resistance of FRC beams is the sum of shear contribution from concrete and shear contribution from fibers.
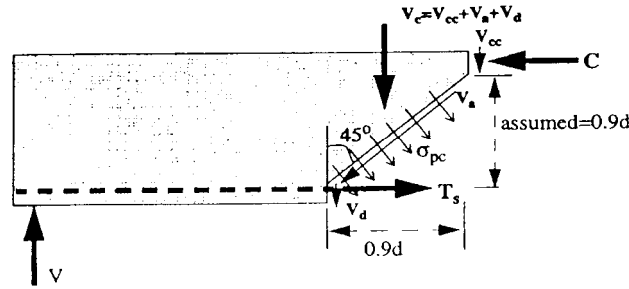
Figure 2.170: Contribution of fibers to shear resistance of FRC beam without stirrups [162].

As it has seen in Figure 2.170, the fiber contribution can be expressed as:

$$V_{fr} = 0.9 \, d \, b_w \cdot \sigma_{pc} = 0.25 F_1 \cdot \sqrt{f_c'} \cdot d \, b_w \tag{2.294}$$

The concrete contribution can be assumed equal to that given by the following ACI Code equation:

$$V_c = 0.167 \, d \, b_w \sqrt{f_c'} \tag{2.295}$$

Thus the ultimate shear resistance of FRC beams can be expressed as:

$$V_{frc} = V_c + V_{fr}$$

or (2.296)

$$V_{frc} = 0.167 \, d \, b_w \sqrt{f_c'} + 0.25 F_1 \cdot \sqrt{f_c'} \cdot d \, b_w$$

The authors also highlighted that, by including steel fibers the shear strength of RC beams tends to change the mode of failure from brittle shear to ductile flexure. The addition of steel fibers is more beneficial for high strength concrete in comparison with normal strength concrete. The ultimate shear strength of FRC beams without stirrups can be conservatively computed by using the following simplified equation:

$$V_{frc} = \left(0.167 \, \alpha + 0.25 F_1\right) \sqrt{f_c'} \tag{2.297}$$

being α = arch action factor.

It may be noted that the above simplified equation for ultimate shear strength resembles those presented by Swamy [163] and Mansur [174]. The major and significant difference lies in the fact that their expressions did not consider

application to high strength FRC. Moreover, they suggest no explicit relation between concrete strength and post-cracking tensile strength of FRC. The proposed equation seems therefore applicable to all practical ranges of concrete strengths.

The authors conducted an extensive corroboration of the model against many experiments, demonstrating that the experimental strength is almost always higher than that predicted analytically, being too conservative for deep beams. In such cases, however, the authors suggested using a strut-and-tie model, which should be more reliable.

Figure 2.171 shows the comparison of the proposed equation with other expressions, such as that of Swamy [163] and that of Narayanan [175]. It demonstrates the improvement achieved by the new model, especially for high strength concrete.
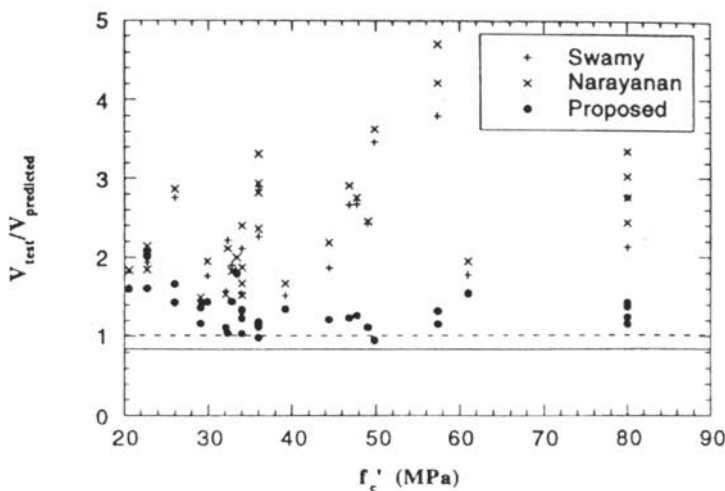
Figure 2.171: Comparison of different equations for normal and high strength concrete [162].

2.8.9.6 *Swamy, Jones and Chiam.*

Swamy, Jones and Chiam (1993 [163]) carried out an experimental program which consisted of 18 simply supported 3-5 m long I-Beams tested under a symmetrical four-point loading system. A thin web was chosen as it is in such beams that conventional shear reinforcement will be difficult to place. A thin section insures a more efficient fiber orientation to arrest the shear crack. Three major parameters, which significantly affect the shear strength of reinforced concrete beams, were considered, namely:

208

- The amount of the shear reinforcement in the form of steel fibers, 0 to 1 % by volume (in the entire depth of the member);
- The amount of longitudinal tension reinforcement, at 1.55, 2.76 and 4.31 %;
- Shear span-to-depth ratio of 2.0, 3.43 and 4.91.

Lightweight concrete mixtures were adopted for all beams, resulting in a compressive strength of around 40 MPa.

The authors reported that the most significant effect of the presence of steel fibers in the concrete was reflected in the cracking behavior of the beams. All the fiber concrete beams displayed an increased number of both flexural and shear cracks at closer spacing than the corresponding concrete beams without fibers. The shear crack also spread further toward the supports. Several inclined cracks formed in the fiber concrete beams, and these were much narrower; there was also greatly reduced spalling and bond cracking. The cracking behavior clearly showed the ability of steel fibers in mobilizing the tension zone of the beam in resisting the shear forces to produce smaller deformations at equivalent loads and to sustain higher loads at failure compared to the concrete beams without fibers.

All the concrete beams without fibers failed in shear in the classical way, by tensile splitting along the level of the main tensile reinforcement and simultaneous instability of the compression flange. The failure occurred along a single shear crack in a sudden and very brittle manner. In the fiber concrete beams failing in shear, on the other hand, steel fibers held the cracked compression flange in place and, at failure, reduced substantially the bond cracking along the tension reinforcement and the spalling in the vicinity of supports. In many FRC beams, failure occurred along an inclined crack running across several other active shear cracks. Many FRC beams failed under flexure, showing therefore a much enhanced ductility and a controlled mechanism.

A simple method based on a truss model with variable inclination of compression diagonals or struts was proposed for the analysis of FRC beams. The shear resistance, in doing so, consists of the contribution V_w of the web reinforcement and of the inclined compression chord V_c, which takes into account the reduction in tension forces in the web due to strut inclinations less than 45°. Since the addition of steel fibers was considered to have a little effect on the concrete compressive strength, this analogy was assumed to be valid both for plane and fiber reinforced concrete.

As in the case of conventional stirrups, the contribution of steel fibers to shear after the formation of shear cracks is approximated by assuming strut inclinations of 45° in the web. V_w is then given by (according to Figure 2.173):

209

$$V_w = 0.9 \sigma_{cu} b_w d \qquad (2.298)$$

where:

- σ_{cu} is the post-cracking tensile strength of fiber concrete;
- b_w is the breadth of the web or rib of the member;
- d is the effective depth of the member.

The post-cracking tensile strength of fiber concrete was defined based on the composite mixture rule [164]. Neglecting the contribution of the matrix, this is given by:

$$\sigma_{cu} = \eta_o \, \eta_L \, \sigma_{fu} \, V_f \qquad (2.299)$$

where:

- η_0 = orientation factor of fibers;
- η_l = length efficiency factor of fibers;
- σ_{fu} = fiber fracture stress;
- V_f = volume percentage of fibers.
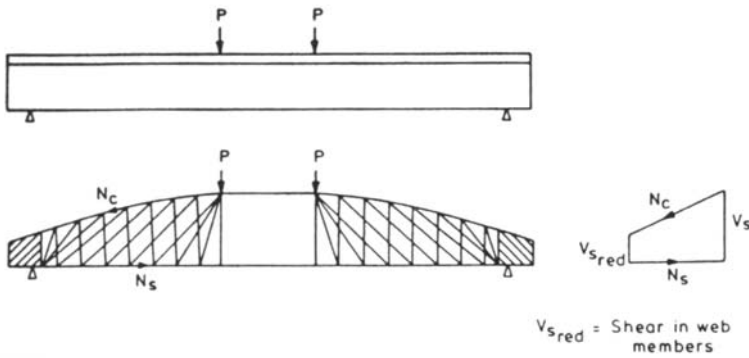
Figure 2.172: Generalized truss model with variable inclination of compression chord and of struts [163].
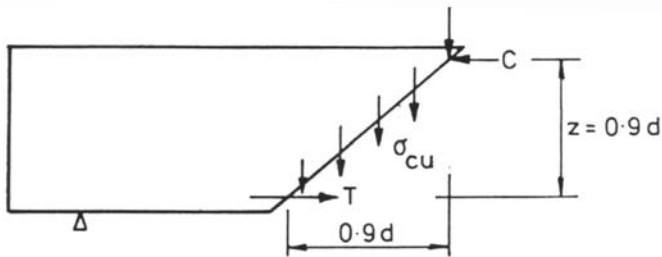
Figure 2.173: Contribution of steel fibers to shear [163].

The orientation factor for randomly oriented fibers is taken as 0.41. In members with thin web, this factor may be higher, but this possible increase is neglected. The length efficiency factor can be expressed based on other parameters, among them the diameter of the fibers d_f and the fiber-matrix interfacial bond stress τ.

The final predicting formula can be expressed as following:

$$v_{frc} = v_w + v_c = 0.37 \cdot \tau \cdot V_f \cdot \frac{l_f}{d_f} + v_c \qquad (2.300)$$

An extensive comparison against experimental results was conducted. The proposed model proved to be quite effective in predicting the ultimate shear load for lightweight concrete beams. However, it turned out to generally underestimate the ultimate load of deep beams (a/d lower than 2) while overestimate the shear strength of beams having a fiber content greater than 1.5 % by volume.

2.8.9.7 *Lim and Oh.*

Lim and Oh [165] carried out an experimental program consisting of testing three series of reinforced concrete beams having identical rectangular cross sections of 100 x 180 mm. The span length of the members was 1300 mm with a shear span length of 400 mm (Figure 2.174). A total of nine beams were tested to investigate the influence of fiber reinforcement on the mechanical behavior of reinforced concrete beams in shear. The major test variables were the volume fraction of steel fibers and the contents of shear stirrups. The volume fraction of steel fibers were varied from 0% to 2% and the ratios of stirrups from 0% to 100% of the required shear reinforcement.
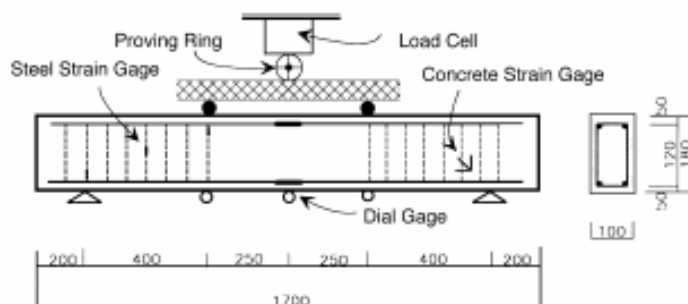
Figure 2.174: Test set up and geometry of the beams tested [165].

Round straight steel fibers of 0.7 mm diameter, 42 mm length, and ultimate strength of 1784 MPa were used.

The aspect ratio of steel fibers is 60. The mix was designed to obtain a compressive strength of 35 MPa at 28 days.

From the experimental results, the authors highlighted that the addition of steel fibers increases the compressive strength, flexural strength and tensile splitting strength, and the increase is greatest in tensile splitting strength. Steel fibers can greatly enhance the tensile properties of concrete and improve resistance to cracking. The mode of failure changed from shear to flexure when the volume fraction of steel fibers used exceeded a certain amount, namely about 1% in this study. The use of fiber reinforcement can reduce the amount of shear stirrups required and a combination of fibers and stirrups may satisfy strength and ductility requirements.

An analytical method to predict the shear strength of reinforced concrete beams containing steel fibers was developed.

To formulate the equilibrium condition for a loaded fiber reinforced concrete beam, it is necessary to identify all external and internal actions that may be present. Figure 2.175 shows the free body diagram of a part of the shear span of a simply supported fiber reinforced concrete beam. From this figure, the total shear forces can be written as follows:

$$V = V_c + V_a + V_d + V_f \tag{2.301}$$

where V_c is the shearing force across the compression zone; V_a is the interlocking force; V_d is the dowel action force; and V_f is the vertical components of the fiber pull out force along the inclined crack.
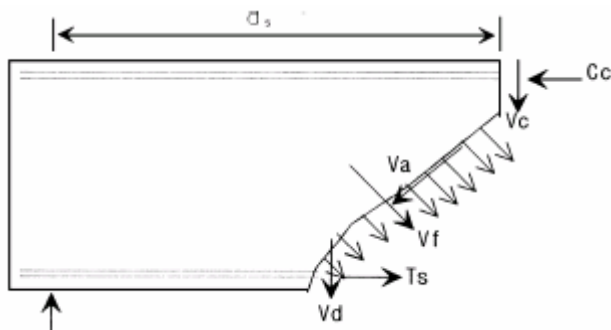
Figure 2.175: Free body diagram of a part of shear span of a simply supported fiber reinforced concrete beam [165].

Considering the shear resistance of concrete without web reinforcement, the equation for ultimate shear strength in MPa can be written as suggested by Zsutty [8], as follows:

$$V_{uc} = \begin{cases} \left(160 \cdot \rho \cdot f_c{}'\right)^{1/3} \left(\dfrac{d}{a_s}\right)^{4/3} & for \dfrac{a_s}{d} < 2.5 \\[4mm] \left(10 \cdot \rho \cdot f_c{}' \cdot \dfrac{d}{a_s}\right)^{1/3} & for \dfrac{a_s}{d} \geq 2.5 \end{cases} \qquad (2.302)$$

where ρ is the longitudinal reinforcement ratio; f_c' is the compressive strength of concrete (MPa); d is the effective depth (m); and a_s is the shear span (m). For beams with web reinforcement, the equation of ultimate shear strength in MPa may be written as follows:

$$V_{uc} = \begin{cases} \left(160 \cdot \rho \cdot f_c{}'\right)^{1/3} \left(\dfrac{d}{a_s}\right)^{4/3} + \dfrac{A_v f_y}{s\,b} & for \dfrac{a_s}{d} < 2.5 \\[4mm] \left(10 \cdot \rho \cdot f_c{}' \cdot \dfrac{d}{a_s}\right)^{1/3} + \dfrac{A_v f_y}{s\,b} & for \dfrac{a_s}{d} \geq 2.5 \end{cases} \qquad (2.303)$$

where A_v is the area of stirrups; f_y is the yield strength of stirrup; and s is the spacing of stirrups.

To estimate the contribution of steel fibers to the total shear resistance, the neutral axis depth c has to be calculated first. The external moment ($V_u\,a_s$) must be equal to internal ultimate resisting moment M_u.

$$M_u = V_u a_s = 0.85\, f_c{}' \cdot a \cdot b \left(d - \frac{a}{2}\right) + A_s{}' \cdot f_y (d - d') \quad for \frac{a_s}{d} \geq 2.5 \qquad (2.304)$$

where d' is the distance from the compression fiber to the centroid of compression steel.

From Equation (2.304), we can determine a (stress block depth), and the neutral axis depth is calculated as $c = a/\beta$.

Referring to Figure 2.175, the length of the inclined shear crack is equal to $(h-c)\sin\alpha$, and the area through which the steel fibers contribute to shear resistance of the beam is $b(h-c)/\sin\alpha$. The number of fibers crossing a unit area of the crack may be taken, as proposed by Hannant [166],

213

$$N = 0.5 \frac{V_f}{\pi r_f^2}$$ (2.305)

where V_f is the volume fraction of fiber and r_f is the radius of fiber.

At failure, fiber pull-out invariably occurs, since the fiber length (l_f) is usually less than the critical length necessary to develop the ultimate tensile strength of fiber, and also due to displacement of two faces of the crack. Since failure is by fiber pull-out, it has been shown that the mean fiber pull-out length is $l_f/4$. The average pull-out force, f, is given by:

$$f = \tau \cdot \pi \cdot d_f \frac{l_f}{4}$$ (2.306)

where τ is the average bond strength; and d_f is the diameter of steel fiber.

The ultimate shear stress sustained by a unit area of crack at failure is therefore given by:

$$\sigma_{cu} = Nf = N\tau\pi d_f \frac{l_f}{4}$$ (2.307)

Substituting Equation (2.305) into Equation (2.307), the following equation is obtained for σ_{cu}:

$$\sigma_{cu} = 0.5 V_f \tau \frac{l_f}{d_f}$$ (2.308)

The total force (F) perpendicular to the crack is therefore:

$$F = \sigma_{cu} b(h - c)/sen\alpha$$ (2.309)

The vertical component of this force is equal to the increase in shear resistance of the beam due to the presence of steel fibers and is equal to:

$$V_{uf} = Fsen\alpha = \sigma_{cu} b(h - c)$$ (2.310)

The total shear strength of fiber reinforced concrete beams can be calculated as the sum of V_{uc} and V_{uf}, i.e.:

$$V_u = V_{uc} + V_{uf}$$ (2.311)

Figure 2.176 represents the results of the comparison between the experimental ultimate shear strength V_{uo} with predicted ultimate shear strength V_{up} given by the method herein. The method proposed gives acceptable results.

214
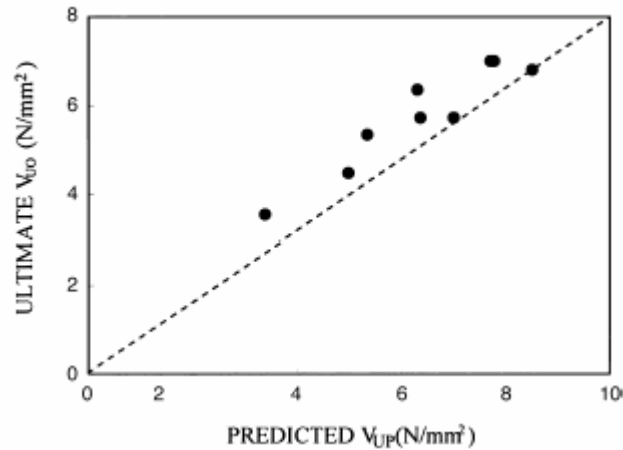
Figure 2.176: Comparison of the experimental ultimate shear strength V_{u0} with the predicted ultimate shear strength V_{up} [165].

2.8.9.8 Gustafsson and Noghabai.

In this research project [167] , a total of twenty reinforced beams of a relatively high strength concrete were tested. In order to study the effect of an increasing size on the shear capacity, beams of three different dimensions were produced. Moreover, various types and amounts of steel fibers were added to the concrete in order to find an optimal fiber-concrete mixture. Material strength parameters were obtained from uni-axial tensile and compressive tests. As fibers are known to primarily contribute to the post cracking behavior of the concrete, tensile tests were performed in displacement control. In this way a measurement of the fracture toughness, or residual strength, of the concrete was supplied.

The beams were divided into three series with respect to the geometrical dimensions, *S*, *M* and *L* (small, medium and large respectively), see Figure 2.177.

One beam in each series contained stirrups as shear reinforcement. The beams contained a substantial amount of longitudinal reinforcement to avoid undesired flexural failures. Three different types of fibers were adopted (DRAMIX 6/0.15; 30/0.6; 60/0.7, where the first number indicated the length whereas the second the diameter. Fibers 6 mm long were straight while the other two typologies had hooked ends).

Also, to prevent an equally undesired anchorage failure, the end zones were provided with relatively high ratios of stirrups, as reported in Figure 2.177.

The concrete mix was designed in order to reach an average cube compressive strength of about 120 MPa at 28 days of age.
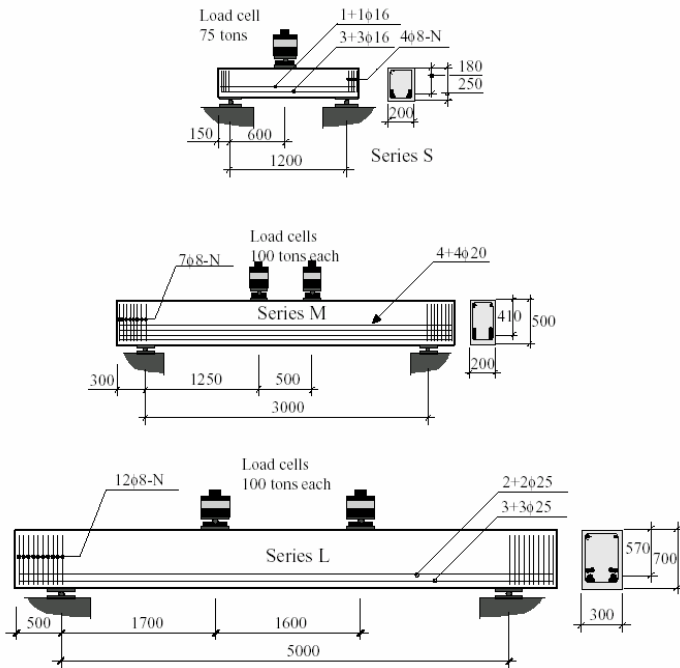
Figure 2.177: Load set up and geometrical configurations of tests [167].

The authors found out that beams reinforced with fibers had the same or even a higher shear capacity as beams with a conventionally web reinforcement in terms of stirrups.

The different fibers acted in different ways. Longer fibers, which are better anchored to the concrete, are needed if the beam size increases. This is to carry the relative higher load that occurs if a larger beam cracks. Moreover, for the small beam series, the short straight fibers were as effective as the long fibers, while they proved to be too short in the large size beams, resulting in a complete pull-out of all fibers at early stages of loading.

The failures of the smaller beams were considerably more ductile as compared to the larger beams, bringing to light the size effect issue, which seems to act even in presence of fibers. An indication of the difference in brittleness was easily found by comparing the crack patterns of the beams tested. The large number of visible diagonal shear crack occurred in the smallest beam gives an indication of the greater ductility of this beam. For the biggest beam, on the contrary, one only shear diagonal crack appeared, even though the same amount and typologies of fibers were provided into the matrix. This means that the residual strength of fiber concrete was not sufficient to resist the large impulse load that was released as the

216

crack started developing. As a consequence the beam failed in a considerably more brittle fashion.

Gustafsson pointed out that with a fracture mechanics approach, it might be possible to explain how an increasing beam size influences the ability of the fibers to contribute to the shear resistance. A brittleness number, which is commonly defined as the ratio between stored elastic energy and dissipated fracture energy was used to prove that the brittleness increases if the structural size increases too, if the material characteristics are kept constant:

$$Brittleness = \frac{Elastic\ Energy}{Fracture\ Energy} = \frac{f_{ct}^2 \cdot L}{2E \cdot G_f} \tag{2.312}$$

In other words, the size effect is due to the release of strain energy from the structure into the fracture zone as the cracking zone extends. The larger the structure the greater is the energy release and the more fracture energy is needed to avoid a sudden failure. This point should be kept in mind especially when designing real structures, very often bigger in size than the specimens tested in laboratories.

The authors then made a comparison between tests results and some of the available shear predicting formula. The best predictions were obtained by the Imam [158] formula, probably owing to the fact that Imam's model was developed for high strength concrete mixtures.

Looking at Figure 2.178, which shows the ratio of the calculated over the experimental shear force, it is quite clear that the predictive formulas do not describe the shear capacities with great accuracy. In general, it seems that all predicting formulas tend to underestimate the shear capacities of the smaller beams, make fairly good predictions for the beam series M and slightly overestimate the capacities of the largest beams. Such a development is quite dangerous considering that beams with depths of up to 1000 mm and above are frequently used in design.
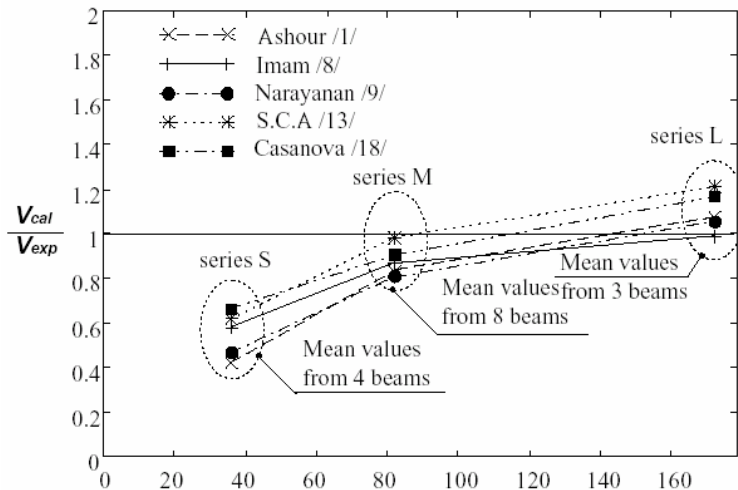
Figure 2.178: Ratio between the predicted and experimental shear force, for some models available in literature [165].

2.8.9.9 Further Proposals predicting Shear Strength of SFRC Beams.

There are some other approaches to calculate the shear strength of SFRC beams which can be found in the literature. Some equations are summarized in Table 2.4. Another summary and debriefing of more than 400 tested beams during the past 25 years can be found by Adebar et al. (1997 [168]). Investigations by Tan et al. (1993) [169] showed that the behavior of SFRC beams could be modeled well using the principle stress-strain relationships. In another test series done by Tan et al. (1995) [170] with partially prestressed beams, the results indicated that stirrups may be replaced by an equivalent amount of steel fibers without affecting the stiffness, shear strength, and cracking behavior of the beam. The equivalence of steel fibers to stirrups was determined from the consideration of equilibrium of a cracked element. Similar results were noticed during the tests of 18 high strength fiber reinforced concrete beams surveyed by Ashour et al. (1992) [171]. Some aspects of shear capacity of SFRC beams based on experiments with beams and plates are given by Kützing (1998) [172], whereas Kovács and Balázs [151] investigated SFRC behavior of prestressed and reinforced concrete beams under shear through an extensive experimental program.

Unfortunately, most of these formulas were extrapolated for a limited series of experimental tests, which therefore did not take into account all parameters influencing shear behavior. As a result, some of these can not be used for a wide

218

range of structural elements or material properties, which are too different from the ones that form the basis of the model.

Moreover, the comparison of these models give a huge scatter, which means that some formulas are unsafe whereas some other are too conservative.

The important issue of size effect is not properly considered, or even neglected, by many proposals.

The following chapters aim at clarifying at least some of those critical issues.

Investigator	Predictive equation for ultimate shear strength [MPa]	Application
Ashour et al. (1992) [171]	$v_{frc} = \left(0.7\sqrt{f_c'} + 7F\right)\dfrac{d}{a} + 17.2\,\rho\dfrac{d}{a}$	High strength FRC.
Li et al. (1992) [173]	$v_{frc} = 1.25 + 4.68\left[\left(f_f\,f_{sp}\right)^{3/4}\left(\rho\dfrac{d}{a}\right)^{1/3}(d)^{-1/3}\right]^{1/3}$ $for\ a/d > 2.5$ $v_{frc} = 9.16\left[\left(f_f\right)^{2/3}(\rho)^{1/3}\left(\dfrac{d}{a}\right)\right] for\ a/d < 2.5$	Normal strength fiber reinforced concrete.
Mansur et al. (1986) [174]	$v_{frc} = \left(\tau\,V_f\,\dfrac{l_f}{d_f}\right) + \left(0.16\sqrt{f_c'} + 17.2\dfrac{\rho V d}{M}\right)$	Normal strength fiber reinforced concrete.
Narayanan et al. (1987) [175]	$v_{frc} = e\left[0.24\left(f_{sp}\right) + 80\,\rho\dfrac{d}{a}\right] + 0.41\,\tau\,F$ $e = 1\ for\ a/d > 2.8;\ otherwise\ e = 2.8d/a$ τ = average fiber matrix interfacial bond stress, 4.15 MPa	Normal to medium strength fiber reinforced concrete.
Sharma (1986) [142]	$v_{frc} = k\,f_t\left(\dfrac{d}{a}\right)^{0.25}$ k = 1 if f_t is obtained by direct tension test; k = 2/3 if f_t is obtained by indirect tension test; k = 4/9 if f_t is obtained using modulus of rupture.	Normal strength fiber reinforced concrete.
Shin et al. (1994) [176]	$v_{frc} = 0.22\,f_{sp} + 217\,\rho\dfrac{d}{a} + 0.34\,\tau\,F\ \ for\ a/d < 3$ $v_{frc} = 0.19\,f_{sp} + 93\,\rho\dfrac{d}{a} + 0.34\,\tau\,F\ \ for\ a/d \geq 3$	High strength fiber reinforced concrete.

219

Investigator	Predictive equation for ultimate shear strength [MPa]	Application
S.C.A. 1995 [177]	$$v_{frc} = \left[\xi(1 + 50\rho_s) \cdot 0.30 \cdot f_{ct} + 1.7 \cdot F_f \right]$$	Normal to medium high concrete strength.
Kwak et al. 2002 [178]	$$v_{frc} = 3.7 \cdot e \cdot f_{spfc}^{2/3} \cdot \left(\rho \cdot \frac{d}{a} \right)^{1/3} + 0.8 v_b$$ $e = 1 \ for \ a/d > a/d_{trans};$ $otherwise \ e = a/d_{trans} \cdot d/a$ f_{spfc} is the computed value of split-cylinder strength of fiber concrete.	Normal to medium high concrete strength.

Table 2.4: Summary of proposed shear strength equations for FRC.

2.9   REFERENCES.

[1]   **Park, R. and Paulay T.**, *"Reinforced Concrete Structures", Wiley-Interscience Publication, New York, 1975.*

[2]   **Collins, M.P., and Mitchell, D.**, *"Prestressed Concrete Structures", Response Publication, Toronto and Montreal, Canada, 1997.*

[3]   **ASCE-ACI Committee 445 on Shear and Torsion**, *"Recent Approaches to Shear Design of Structural Concrete", Journal of Structural Engineering, Vol. 124, No 12, 1998, pp. 1375-1417.*

[4]   **ASCE-ACI Committee 426**, *"the Shear Strength of Reinforced Concrete Members", Journal of Structural Division, Vol. 99, No 6, 1973, pp. 1091-1187.*

[5]   **Mörsch, E.**, *"Concrete-Steel Construction", McGraw-Hill, New York (English translation by E.P. Goodrich).*

[6]   **Kupfer, H. B., and Gerstle, K.**, *"Behavior of Concrete under Biaxial Stresses", Journal Engrg. Mech. Div., Vol 99, No 4, 1973, pp. 853-866.*

[7]   **Kim, W., and White, R. N.**, *"Initiation of Shear Cracking in Reinforced Concrete Beams with no Web Reinforcement", ACI Structural Journal, Vol. 88, No 3 , 1991, pp. 301-308.*

[8]   **Zsutty, T. C.**, *"Shear Strength Prediction for Separate Categories of Simple Beams Tests", ACI Journal, Vol. 68, No 2, 1971, pp. 138-143.*

[9]   **Bažant, Z. P., and Kim, J,-K.**, *"Size Effect in Shear Failure of longitudinally Reinforced Beams", ACI Journal, Vol. 81, No 5, 1984, pp. 456-468.*

[10]   **Okamura, H., and Higai, T.**, *"Proposed Design Equation for Shear Strength of R.C. Beams without Web Reinforcement", Proc., Japan Soc. Civ. Engrg., 300, 1981, pp. 131-141.*

[11]   **Niwa, J., Yarnada, K., Yokozawa, K., and Okarnura, M**, *"Re-evaluation of the Equation for Shear Strength of R.C.-Beams without Web Reinforcement", Translated from Proc., Japan Soc. Civ. Engrg., Vol 372, No 5, 1986, pp. 1986-1988.*

[12]   **Schlaich, J., Schäfer, I., and Jennewein, M.**, *"Towards a Consistent Design of Structural Concrete", Journal Prestressed Concrete Inst., Vol. 32, No 3, 1987, pp. 74-150.*

[13]   **Taylor, H. P. J.**, *"The Fundamental Behavior of Reinforced Concrete Beams in Bending and Shear", ACI SP-42, Detroit, 1974, pp. 43-77.*

[14]   **Reineck, K.-H.**, *"Ultimate Shear Force of Structural Concrete Members without Transverse Reinforcement derived from a Mechanical Model", ACI Structural Journal, Vol. 88, No 5, 1991, pp. 592-602.*

[15]   **Fenwick, R. C., and Paulay, T.**, *"Mechanisms of Shear Resistance of Concrete Beams", Journal Structural Division, ASCE, Vol. 94, No 10, 1968, pp. 2325-2350.*

[16]   **Mattock, A. H., and Hawkins, N. M.**, *"Research on Shear Transfer in Reinforced Concrete", PCI Journal, Vol. 17, No 2, 1972, pp. 55-75.*

[17]   **Paulay, T. and Loeber, P.J.**, *"Shear Transfer by Aggregate Interlock", Shear in reinforced Concrete, ACI Special Publication 42, V. 1, Detroit, 1974, pp. 1-15.*

[18] **Gambarova, P. G.**, "On Aggregate Interlock Mechanism in Reinforced Concrete Plate with Extensive Cracking", Transactions, IABSE Colloquium Delft, 1981, on "Advanced Mechanics of Reinforced Concrete", International Association for Bridge and Structural Engineering, Zurich, pp. 99-120.

[19] **Walraven, J.C.**, "Fundamental Analysis of Aggregate Interlock", Journal of Structural Division, ASCE, V. 108, pp. 2245-2270.

[20] **Millard, S. G., and Johnson, R. P.**, "Shear Transfer in Cracked Reinforced Concrete", Magazine Concrete Research, Vol. 37, No 130, 1974, pp. 3-15.

[21] **Bažant, Z. P., and Gambarova, P.**, "Rough Crack in Reinforced Concrete", Journal of the Structural Division, Vol 106, No 4, 1980, pp. 819-842.

[22] **Kupfer, H., Mang, R., and Karavesyrouglou, M.**, "Failure of the Shear-Zone of R.C. and P.C. Girders - An analysis with consideration of interlocking of cracks", Bauingenieur, Vol. 58, 1983, pp. 143-149 (in German).

[23] **Vecchio, F. J., and Collins, M. P.**, "The Modified Compression Field Theory for Reinforced Concrete Elements Subjected to Shear", ACI Journal, Vol. 83, No 2, 1986, pp. 219-231.

[24] **Collins, M. P.**, "Toward a Rational Theory for RC Members in Shear", Journal Structural Division, ASCE, Vol. 104, No 4, 1978, pp. 649-666.

[25] **Dei Poli, S., di Prisco, M. D., and Gambarova, P. G.**, "Stress Field in Web of RC Thin-webbed Beams Failing in Shear", Journal Structural Engineering, ASCE, Vol. 116, No 9, 1990, pp. 2496-2515.

[26] **CEB Bulletin 237**, "Concrete Tension and Size Effect", 1997, CEB, Lausanne, 258 pp.

[27] **Vintzeleou, E. N., and Tassios, T. P.**, "Mathematical Models for Dowel Action under Monotonic Conditions", Magazine Concrete Research, Vol 38, 1986, pp. 13-22.

[28] **Walraven, J.C., Vos, E., Reinhardt, H.W.**, "Experiments on Shear Transfer in Cracks in Concrete; Part I: Description of Results (Report 5-79-3, 89 pp.); Part II: Analysis of Results (Report 5-79-10, 132 pp.)", Stevin Laboratory, 1979, Delft University of Technology, The Netherlands.

[29] **Daschner, F.**, "Schubkraftübertragung in Rissen von Normal- und Leichtbeton", Preliminary Report, 1980, Technical University of Munich, 93 pp.

[30] **Vintzileou, E.**, "Mechanisms of Load transfer along Reinforced Concrete Interfaces under Monotonic and Cyclic Actions, Dr Thesis, Faculty of Civil Engineering, 1986, Nat. Tech. Univ. of Athens, 549 pp.

[31] **Walraven, J.C.**, "Aggregate Interlock: A Theoretical and Experimental Analysis", PhD Thesis, 1980, Delft university of Technology, The Netherlands.

[32] **Vintzileou E., Tassios T.P.**, "Mechanisms of Load Transfer along Interfaces in Reinforced Concrete: Prediction of Shear Force vs. Shear Displacement Curves", Studi e Ricerche, Corso di Perfezionamento per le costruzioni in cemento armato, Vol. 7, 1985, Italcementi S.p.A, Bergamo Editrice, pp. 121-161.

[33] **Fenwick, R.C.**, "The Shear Strength of Reinforced Concrete Beams", PhD Thesis, University of Canterbury, 1966, Christchurch, New Zeeland.

[34]   **Loeber, J.P.**, "Shear Transfer by Aggregate Interlock", MSc Thesis, University of Canterbury, 1970, Christchurch, New Zealand.

[35]   **Laible J.P.**,   "An Experimental Investigation of Interface Shear Transfer and Applications in the Dynamic Analysis of Nuclear Containment Vessels", PhD Thesis, 1973, Cornell University, Ithaca.

[36]   **Schwing H.**, "Zur wirklichkeitsnahen Berechnung von Wandscheiben aus Fertigteilen", Dissertation, 1975, Technical University of Darmstadt, Germany.

[37]   **Reineck K.-H.**, "Ein Mechanisches Modell fiir den Querkraftbereich von Stahlbetonbauteilen" ("Mechanical Model for the Behavior of Reinforced Concrete Members in Shear"), Dr Thesis, 1990, University of Stuttgart, 1990, 273 pp.

[38]   **Baumann Th., Rusch H.**, "Versuche rom Studium der Verdubelungswirkung der Biegezugbewehrung eines tahlbetonbalkes" ("Test on the Dowel-Action of the Longitudinal Reinforcement of a Reinforced Concrete Beam"), Deutscher AusschuB fur Stahlbeton, Heft 210, 1970, Berlin, Germany, pp. 42-83.

[39]   **Chana, P. S.**, "Investigation of the Mechanism of Shear Failure of Reinforced Concrete Beams", Mag. Concrete Res., Vol. 39, No 12, 1987, pp. 196-204.

[40]   **Stanton J.F.**, "An Investigation of Dowel Action of the Reinforcement of Nuclear Containment Vessels and their non-linear Dynamic Response to Earthquake Loads", MSc Thesis, Cornell University, 1977, Ithaca.

[41]   **White R.N., Gergely P.**, "Final Report on Shear Transfer in Thick Walled Reinforced Concrete Structures under Seismic Loading", Report 7-2, Dept. of Structural Engineering, Cornell University, 1978, Ithaca.

[42]   **Rasmussen, B.H.**, "Strength of Transversely Loaded Bolts and Dowels Cast into Concrete", Laboratoriet for Bygningastatik, Denmark Technical University, 1962, Meddelelse, Vol. 34, No 2.

[43]   **Krefeld W., Thurston C.W.**, "Contribution of Longitudinal Steel to Shear Resistance of Reinforced Concrete Beams", ACI Journal, Vol. 63, No 3, 1966, pp. 325-344.

[44]   **Bennett E.W., Banerjee S.**, "Strength of Beam-Column Connections with Dowel Reinforcement", The Structural Engineer, Vol. 54; No 4, 1976, pp. 133-139.

[45]   **Paschen H., Schönhoff, T.**, "Untersuchungen tiber in Beton eingelassene Sherbolzen aus Betonstahl", Deutscher AusschuB fur Stahlbeton, Heft 346, Berlin, 1983, pp. 105-149.

[46]   **Paulay T., Park R., Phillips M.H.**, "Horizontal Construction Joints in Cast in Place Reinforced Concrete", ACI Special Publication SP42 «Shear in reinforced concrete», Vol. 2, 1974, pp. 599-616.

[47]   **Utescher G., Herrmann H.**, "Versuche zur Errnittlung der Tragfahigkeit in Beton eingespannter Rundstahldollen aus nichtrostendem austenitischem Stahl", Deutscher AusschuB fiir Stahlbeton, Heft 346, 1983, Berlin, pp. 49-104.

[48]   **Shoroushian P., Obaseki K., Rojas M.C., Sim J.**, "Analysis of Dowel Bars acting against Concrete Core, ACI Journal, July-August, 1986, pp. 642-649.

[49]   **Vintzileou E., Tassios T.P.**, "Eccentric Dowels Loaded against Core of concrete Sections", Journal of Structural Engineering, ASCE, Vol. 116, No 10, 1990, pp. 2621-2633.

[50] **Vintzileou E., Tassios T.P.**, *"Behavior of Dowels under Cyclic Deformations"*, ACI Structural Journal, Vol. 84, No 1, 1987, pp. 18-30.

[51] **Evans, R. H., and Marathe, M. S.**, *"Microcracking and Stress-Strain Curves for Concrete in Tension"*, Mat. and Struct., Res. and Testing, RILEM, Paris, 1(1), 1968, pp. 61-64.

[52] **Gopalaratnam, V. S., and Shah, S. P.**, *"Softening Response of Plain Concrete in Direct Tension"* ACI J. Proc., Vol 82, No 3, 1985, pp. 310-323.

[53] **Reinhardt, H. W., Cornelissen, H. A. W., and Hordijk, D. A.**, *"Tensile Tests and Failure analysis of Concrete"*, Journal of Structural Engineering., ASCE, Vol 112, No 11, 1986, pp. 2462-2477.

[54] **ACI Committee 446**, *"Fracture Mechanics of Concrete: Concepts, Models and Determination of Material Properties"*, ACI 446.I R-9I, American Concrete Institute, 1989, Detroit.

[55] **Reineck, K.-H.**, *"Model for Structural Concrete Members without Transverse Reinforcement"*, IABSE Colloquium Struct. Concrete, IABSE Rep., IABSE, Zurich, Vol 62, 1991, pp. 643-648.

[56] **Leonhardt, F.**, *"Reducing the Shear Reinforcement in Reinforced Concrete Beams and Slabs"*, Mag. Concrete Res., Vol 17, No 53, 1965, pp. 187-198.

[57] **Leonhardt, F.** *"C.A.&C.A.P.- Calcolo di Progetto e Tecniche Costruttive; Le Basi del Dimensionamento nelle Costruzioni in Cemento Armato"*, Vol 1, Edizioni di Scienza e Tecnica, Milano, 1978 (available also in German).

[58] **Ritter, W.**, *"Die bauweise bennebique"*, Schweizerische Bauzeitung, Vol 33, No 7, 1899, pp. 59-61.

[59] **Kupfer, H., Baumann, T.**, *"Staffelung der Biegezugbewehrung bei hohen Schubspannungen in schlanken Stahlbetonträgern mit I-Querschnitt"*, Beton-und Stahlbetonbau, Vol. 64, 1969, pp. 278-283 (in German).

[60] **Kupfer, H., Mang, R., Karavesyrouglou, M.**, *"Failure of the shear-zone of R.C. and P.C. girders- An analysis with consideration of interlocking of cracks"*, Bauingenieur, 58, 1983, pp. 143-149 (in German).

[61] **Adebar, P.**, *"Testing Structural Concrete Beam Elements"*, RILEM: Mat. And Struct., Vol 27, No 172, 1994, pp. 445-451.

[62] **Leonhardt, F., and Walther, R.**, *"Wardetiger Trager,"* Deutscher Ausschuss fur Stahlbeton, Bulletin No. 178, 1966, Wilhelm Ernst und Sohn , Berlin, Germany.

[63] **Kani, G.N.J.**, *"The riddle of Shear Failure and its Solution"*, Journal ACI, Vol. 61, No 4 1964, pp. 441-467.

[64] **Kani, G.N.J.**, *"Basic Facts Concerning Shear Failure"*, Journal ACI, Vol. 63, June 1966, pp. 675-692.

[65] **Kani, G.N.J.**, *"How Safe are our Large Reinforced Concrete Beams?"*, Journal ACI, Vol. 64, March 1967, pp. 128-141.

[66] **Shioya, T., Iguro, M., Nojiri, Y., Akiayma, H., Okada, T**., *"Shear Strength of Large Reinforced Concrete Beams, Fracture Mechanics: Application to Concrete"*, SP-118, ACI, Detroit 1989, pp. 259-276.

[67]   **Bažant, Z.P., and Cao, Z.**, *"Size Effect of Shear Failure in Prestressed Concrete Beams"*, ACI Journal, Vol 83, No 2, 1986, pp 260-268.

[68]   **Bažant, Z.P., and Kazemi, M. T.**, *"Size Effect on Diagonal Shear Failure of Beams without Stirrups"*, ACI Structural Journal, Vol 88, No 3, 1991, pp 268-276.

[69]   **Collins, M.P., Mitchell, D., MacGregor, J. G.**, *"Structural Design Considerations for high-Strength Concrete"*, ACI Concrete Int., 1993, pp. 27-34.

[70]   **Frosch, R.J.**, *"Behavior of Large-Scale Reinforced Concrete Beams with Minimum Shear Reinforcement"*, ACI Structural Journal, Vol 97, Nov. 2000, pp. 814-820.

[71]   **Zararis, P. D., Papadakis, G. Ch.**, *"Diagonal Shear Failure and Size Effect in RC Beams without Web Reinforcement"*, Journal of Structural Engineering, Vol 127, No 1, 2001, pp. 733-742.

[72]   **Hasegawa, T., Shioya, T., Okada, T.**, *"Size Effect on Splitting Tensile Strength of Concrete"*, Proc., Japan Concrete Inst. 7th Conf., 1985, pp. 309-312.

[73]   **Sabnis, G.M., Mirza, S.M.**, *"Size Effect in Model Concretes"*, J. Struct. Div., ASCE, Vol 106, No 6, 1979, pp. 1007-1020.

[74]   **Lubell, A., Sherwood, T., Bentz, E., and Collins. M. P.**, *"Safe Shear Design of Large, Wide Beams"*, Concrete International, Vol 26, No 1, 2004, pp. 67-78.

[75]   **Angelakos, D., Bentz, E. C., and Collins, M. P.**, *"Effect of Concrete Strength and Minimum Stirrups on Shear Strength of Large Members,"* ACI Structural Journal, Vol 98, No. 3, 2001, pp. 290-300.

[76]   **Collins, M. P., Mitchell, D., Adebar, P. E. and Vecchio, F. J.**, *"A General Shear Design Method,"* ACI Structural Journal, Vol 93, No 1, 1996, pp. 36-45.

[77]   **Gupta, P., Collins, M.P.**, *"Behavior of Reinforced Concrete Members Subjected to Shear and Compression"*, Report, Department of Civil Engineering, University of Toronto, Canada, 1993.

[78]   **Mattock, A.H.**, *"Diagonal Tension Cracking in Concrete Beams with Axial Forces"*, Journal of Structural Division, ASCE, Vol. 95, September 1969, pp. 1887-1900.

[79]   **Bhide, S. B., and Collins, M. P.**, *"Influence of Axial Tension on the Shear Capacity of Reinforced Concrete Members"*, ACI Structural Journal, Vol 86, No 5, 1989, pp. 570-581.

[80]   **Adebar, P., Collins, M.P.**, *"Shear Strength of Members without Transverse Reinforcement"*, Can. J. Civ. Engrg., Vol. 23, No 1, 1996, pp. 30-41.

[81]   **Reineck, K.-H.**, *"Models for the Design of Reinforced and Prestressed Concrete Members"*, CEB Bull. 146, Paris, 1982, pp. 43-96.

[82]   **EUROCODE 2, "**Design of Concrete Structures*"*, UNI-ENV 1992-1-2, 1993.

[83]   **Taylor, H.P.J.**, *"Investigation of the Forces Carried Across Cracks in Reinforced Concrete Beams in Shear by Interlock of Aggregate"*, Cement and Concrete Association, London, 1970, 22 pp.

[84]   **König, G, Grimm, R., Remmel, G.**, *"Shear Behavior of Longitudinally Reinforced Concrete Members of HSC"*, Darmstadt Concrete, Vol. 8, 1993, pp. 27-42.

[85]   **Pendyala, R.S., Mendis, P.**, *"Experimental Study on Shear Strength of High-Strength Concrete Beams"*, ACI Structural Journal, Vol. 97, No4, 2000, pp. 564-571.

225

[86] **Reineck, K.-H., Kuchma, D., Kim, K.S., and Marx, S.**, "Shear Database for Reinforced Concrete Members without Shear Reinforcement", ACI Structural Journal, Vol 100, No 2, 2003, pp. 240-249.

[87] **Isenberg, J.**, "Finite Element Analysis of Reinforced Concrete Structures II", Proc., Int. Workshop, 1993, New York.

[88] **Hillerborg, A., Modéer M., and Petersson, P. E.**, "Analysis of Crack Formation and Crack Growth in Concrete by means of Fracture Mechanics and Finite Elements", Cement and Concrete Res., 6, 1976, pp. 773-782.

[89] **Bažant, Z. P., and Oh, B. H.**, "Crack Band Theory for Fracture of Concrete", RILEM, Vol 16, No 93, 1991, pp. 155-177.

[90] **Reinhardt, H. W.**, "The Role of Fracture Mechanics in Rational Rules for Concrete Design", IABSE Survey S-34/86 in IABSE Per. 1/1986, IABSE, 1986, Zurich.

[91] **Walraven, J. C.**, "Shear in Prestressed Concrete Members" A State-of-the-Art Report; CEB Bull. 180, 1987, Paris.

[92] **Drucker, D. C.**, "On structural Concrete and the Theorems of Limit Analysis", IABSE Report 2, Zurich, EC2, 1991, Eurocode No. 2." Design of concrete structures, Part 1: General rules and rules for buildings, Thomas Telford, London.

[93] **Nielsen, M. P., Braestrup, M. W., Jensen, B. C., and Bach, F.**, "Concrete Plasticity, Beam Shear-Shear in Joints-Punching Shear", Special Publication, Danish Society for Structural Science and Engineering, Lyngby, Denmark, Final Ed, 1978.

[94] **Marti, P.**, "Basic Tools of Reinforced Concrete Beam Design", ACI Journal, Vol 82, No 1, 1985, pp. 46-56.

[95] **Walraven, J., and Lehwalter, N.**, "Size Effects in Short Beams Loaded in Shear", ACI Structural Journal, Vol 91, No 5, 1994, pp. 585-593.

[96] **Collins, M. P., and Mitchell, D.**, "A Rational Approach to Shear Design-The 1984 Canadian Code Provisions." ACI Journal, Vol 83, No 6, 1986, pp. 925-933.

[97] **Braestrup, M. W.**, "Shear Strength Prediction-Plastic Method," Reinforced Concrete Deep, F. K. Kong, ed., Blackie and Son, London, Van Nostrand Reinhold, New York, 1990, pp. 182-203.

[98] **MacGregor, J. G., and Walters, J. R. V.**, "Analysis of Inclined Cracking Shear in Slender R.C. Beams", ACI Journal, Vol 64, 1967, pp. 644-653.

[99] **Hamadi, Y. D., and Regan, P. E.**, "Behavior in Shear of Beams with Flexural Cracks", Mag. Concrete Res., Vol 32, No 1, 1980, pp. 67-77.

[100] **Marti, P.**, "Zur Plastischen Berechnung von Stahlbeton (On Plastic Analysis of Reinforced Concrete)", Rep. No 104, Institute of Structural Engineering, ETH, 1980, Zurich.

[101] **Al-Nahlawi, K. A., and Wight, J. K.**, "Beam Analysis using Concrete Tensile Strength in Truss Models" ACI Journal, Vol 89, No 3, 1992, pp. 284-289.

[102] **Muttoni, A.**, "Applicability of the Theory of Plasticity for Dimensioning Reinforcing Concrete", PhD Thesis, ETH Zurich Birkhauser, 1990, Basel, pp. 1-180 (in German).

[103] **Russo, G., Zingone, G., and Puleri, G.**, "Flexure-Shear Interaction Model for Longitudinally Reinforced Beams", ACI Structural Journal, Vol 88, No 1, 1991, pp. 60-68.

[104]   **Kim, D., Kim, W., and White, R.N.**, "Arch Action in Reinforced Concrete Beams – A Rational Prediction of Shear Strength", ACI Structural Journal, Vol 96, No 4, 1999, pp. 586-593.

[105]   **Zararis, P. D.**, "Failure Mechanism in Concrete Plates Reinforced in only one Direction", J. Structural Engineering, ASCE, Vol 121, No 8, 1995, pp. 1161-1169.

[106]   **Zararis, P. D.**, "Aggregate Interlock and Steel Shear Forces in the Analysis of RC Membrane Elements", ACI Structural Journal, Vol. 94, No 2, 1997, pp. 159-170.

[107]   **Leonhardt, F., and Walther, R.**, "Schubversuche an einfeldrigen Stahlbetonbalken mit und ohne Schubbewehrung zur Ennittlung der Schubtragfahigkeit und der oberen Schubspannungsgrenze," DAfStb, Heft 151, W. Ernst u. Sohn, Berlin (in Gennan), 1962.

[108]   **Regan, P. E., and Yu, C. W.**, "Limit State Design of Structural Concrete", Chatto & Windus, London, 1973.

[109]   **Timoshenko, S., and Goodier, J. N.**, "Theory of Elasticity", McGraw-Hill, New York, 1951.

[110]   **Collins, M. P., and Kuchma, D.**, "How Safe are our Large, Slightly Reinforced Concrete Beams, Slabs, and Footings?", ACI Structural Journal, Vol 96, No 4,1999, pp. 482-490.

[111]   **Bhal, N. S.**, "Uber den Einfluss den Balkenhohe auf Schubtragfahigkeit von einfeldrigen Stahlbetonbalken mit und ohne Schubbewehrung", PhD dissertation, Universität Stuttgart, Stuttgart, Germany (in German), 1968.

[112]   **Vecchio, F.J.**, "Disturbed Stress Field Model for Reinforced Concrete: Formulation", Journal of Structural Engineering, V. 126, No 9, 2000, pp. 1070-1077.

[113]   **Vecchio, F.J.**, "Disturbed Stress Field Model for Reinforced Concrete: Implementation", Journal of Structural Engineering, V. 127, No 1, 2001, pp. 12-20.

[114]   **Vecchio, F.J., Lai, D., Shim, W. and Ng, J.**, "Disturbed Stress Field Model for Reinforced Concrete: Validation", Journal of Structural Engineering, V. 127, No 4, 2001, pp. 350-358.

[115]   **Rebeiz, K. S.**, "Shear Strength Prediction for Concrete Members", Journal of Structural Engineering, Vol 125, No 3, 1999, pp. 301-308.

[116]   **Khuntia, M., and Stojadinovic, B.**, "Shear strength of Reinforced Concrete Beams without Transverse Reinforcement", ACI Structural Journal, Vol 98, No 5, 2001, pp. 648-656.

[117]   **Bedard, C., Aïtcin, P.-C.**, "A la recherche d'un béton de 150 MPa", Canadian Journal Civ. Engineering, Vol 10, No 4, 1983, pp. 600-613 (in French).

[118]   **Romualdi, J.P., and Batson, G.B.**, "Mechanics of Crack Arrest in Concrete", ASCE Engineering Mechanics Journal, Vol 89, No 3, 1963, pp. 147-168.

[119]   **Romualdi, J.P., and Mandel, J. A.**, "Tensile Strength of Concrete Affected by Uniformly Distributed Closely Spaced Short Lengths of Wire Reinforcement", ACI Journal, Vol 61, No 6, 1964, pp. 657-671.

[120]   **Bentur, A., and Mindess**, S., "Fibre Reinforced Cementitious Composites", Elsevier Science Publishers LTD, New York, 1990.

[121] **Nawy, E.G.**, "Fundamental of High-Performance Concrete", 2nd Edition, John Wiley and Sons, Inc., New York.

[122] **Mindess, S., and Young, J. F.**, "Concrete", Prentice Hall, Upper Saddle River, N.J., 1981.

[123] **Bentur, A., and Mindess, S.**, "Fiber Reinforced Cementitious Deposits", Elsevier Applied Science, London, 1990.

[124] **ACI Committee 544**, "Guide for Specifying, Proportioning, Mixing, Placing and Finishing Steel Fiber Reinforced Concrete, ACI Report 544.3R-93, American Concrete Institute, Farmington Hills, Mich., pp. 1-10.

[125] **UNI 11039**, "Steel Fiber Reinforced Concrete - Part I: Definitions, Classification Specification and Conformity - Part II: Test Method for Measuring First Crack Strength and Ductility Indexes", Italian Board for Standardization, 2003.

[126] **Vondran, G.L.**, "Applications of Steel Fibre Reinforced Concrete", Concrete International, Vol. 13, No 11, 1991, pp. 44-49.

[127] **Nawy, E.G., and Blair, K.**, "Further Studies on Flexural Crack Control in Slab Systems", Proceedings, International Symposium on Cracking, Deflection and Ultimate Load of Concrete Slab System, ACI SP-30, ed. E.G. Nawy, American Concrete institute, Farmington Hills, pp. 1-28, 1971.

[128] **Hsu, L.S., and Hsu, T.C.T.**, "Stress-Strain Behavior of Steel-Fiber High-Performance Concrete Under Compression, ACI Structural Journal, Vol 91, No 4, 1994, pp. 448-457.

[129] **Fanella, D.A., and Naaman, A.E.**, "Stress-Strain Properties of Fiber Reinforced Concrete in Compression", ACI Journal, Vol 82, No 4, pp. 475-483.

[130] **Shah, S.P., and Rangan, B.V.**, "Fiber Reinforced Concrete Properties", ACI Journal, Vol 68, No 2, 1971, pp. 126-135.

[131] **Wafa, F.F., Ashour, S.A.**, "Mechanical Properties of High Strength Fibre Reinforced Concrete", ACI Materials Journal, Vol 89, No. 5, 1992, pp. 449-455.

[132] **Schönlin, K.**, "Ermittlung der Orientierung, Menge und Verteilung der Fasern in faserbewehrtem Beton", Beton und Stahlbetonbau 83, 1988, pp. 168-171 (in German).

[133] **Mansur, M.A., and Ong, K. C. G.**, "Behavior of Reinforced Concrete Deep Beams in Shear", ACI Structural Journal, Vol 88, No 1, 1991, pp. 98-105.

[134] **Kent, D. C., and Park, R.**, "Flexural Members with Confined Concrete", Proceedings, ASCE, Vol 97, ST7, 1971, pp. 1969-1990.

[135] **Vecchio, F J., and Collins, M. P.**, "Stress-Strain Characteristics of Reinforced Concrete in Pure Shear", Final Report, IABSE Colloquium on "Advanced Mechanics of Reinforced Concrete", (Delft, 1981), International Association for Bridge and Structural Engineering, Zurich, pp. 211-225.

[136] **Meda., A., Plizzari, G.A., and Sorelli, L.**, "Uni-Axial and Bending Test for the Determination of Fracture Properties of Fiber Reinforced Concrete", Proceedings, 5th International Symposium on Fracture Mechanics of Concrete Structures, Vail, Colorado, 12-16 April 2004, Vol 2, 1163-1170.

228

[137] **Bargezar. F., and Schnobrich, W.C.**, "Modeling Tension Stiffening in Finite Element Analysis of R.C. Panels, Proceedings, Canadian Society for Civil Engineering (Montréal), Vol 3, 1998, pp. 277-303.

[138] **Lim, T.Y., Paramasivan, P., Mansur, M.A.**, and Lee, S.L., "Tensile Behavior of Steel Fibre Reinforced Concrete Composites", Proceedings, 3rd RILEM International Symposium on Developments in Fiber Reinforced Cement and Concrete, University of Sheffield, 1986, pp. 7-16.

[139] **Henager, C.H., and Doherty, T.J.**, "Analysis of Fibrous Reinforced Concrete Beams", ASCE Structural Journal, Vol 12, No ST1, 1976, pp. 177-188.

[140] **Nawy, E.G.**, "Reinforced Concrete: A Fundamental Approach", 4th ed., Prentice Hall, Upper Saddle River, 2000, N.J.

[141] **Williamson, G.R.**, "Steel Fibers as Web Reinforcement in Reinforced Concrete", Proceedings, U.S. Army Service Conference, West point, N.Y., Vol 3, 1978, pp. 363-377.

[142] **Sharma, A.K.**, "Shear Strength of Steel Fiber Reinforced Concrete Beams", ACI Journal, Vol 83, No 4, 1986, pp. 624-628.

[143] **Valle, M., and Buyukozturk, O.**, "Behavior of Fiber Reinforced High-Strength Concrete under Direct Shear", ACI Material Journal, Vol 90, No 2, 1993, pp. 122-133.

[144] **Mirsayah, A. A., and Banthia, N.**, "Shear Strength of Steel Fiber-Reinforced Concrete", ACI Material Journal, Vol 99, No 5, 2002, pp. 473-479.

[145] **Schnütgen, B.**, "Das Festigkeitsverhalten von mit Stahlfasern bewehrtem Beton unter Zugbeanspruchung", Ruhr-Universität Bochum, PhD Thesis, 1975 (in German).

[146] **Naaman, A.E., Harajli, M.H.**, "Mechanical Properties of High Performance Concrete", SHRP-C/WP-90-004, Strategic Highway Research Program, National Research Council, 1990.

[147] **Griffith, A.A.**, "The Phenomena of Rupture and Flow in Solids", Philosophical Transaction, Royal Society of London, 1920, pp. 163-198.

[148] **Soroushian, P., Bayasi, Z.**, "Fibre Type Effects on the Performance of Steel Fibre Reinforced Concrete", ACI Materials Journal, Vol. 88, 1991, pp. 129-134.

[149] **Hughes, B.P., Fattuhi, N.I.**, "Assessing the Workability of Steel Fibre Reinforced Concrete", Magazine of Concrete Research, V. 28, No. 96, 1976, pp. 157-161.

[150] **Meda, A. and Plizzari, G. A.**, "New Design Approach for Steel Fiber-Reinforced Concrete Slabs-on-Ground Based on Fracture Mechanics", ACI Structural Journal, V. 101, No 3, 2004, pp. 298-303.

[151] **Kovács, I., and Balázs, G.L.**, "Structural Behavior of Steel Fibre Reinforced Concrete", FIB Structural Concrete Journal, Vol 4, No 2, 2003, pp. 57-63.

[152] **Roshanisefat, S.**, "Shear Capacity of Steel Fiber Reinforced Concrete Beams", Master Thesis 96:5, Chalmers University of Technology, Division of Concrete Structures, 1996, Göteborg, Sweden, pp. 127.

[153] **Nordlund, M.**, "Steel Fibres as Secondary Reinforcement in Prestressed Concrete Beams", Master Thesis 04:8, Chalmers University of Technology, Division of Concrete Structures, 2004, Göteborg, Sweden, pp. 90.

[154] **Narayanan, R., and Kareem- Palanjian, A.S.**, *"Effect of Fiber Addition on Concrete Strengths", Indian Concrete Journal, April 1984, pp. 100-103.*

[155] **RILEM RECOMMENDATION TC-162-TDF,** *"Test and Design Methods for Steel Fibre Reinforced Concrete; σ–ε Design Method", Materials and Structures, Vol 33, March 2000, pp. 75-81.*

[156] **Vandewalle, L., and Dupont, D.**, *"Recommendations for Design of SFRC", Report of subtask 7.2 from Test and Design Methods for Steel Fibre Reinforced Concrete. EU Contract-BRPRCT98-0813.*

[157] **RILEM FINAL RECOMMENDATION TC-162-TDF,** *"Test and Design Methods for Steel Fibre Reinforced Concrete; σ–ε Design Method", Materials and Structures, Vol 36, October 2003, pp. 560-567.*

[158] **Imam, M., Vandewalle, L. and Mortelmans, F.**, *"Shear-Moment Analysis of Reinforced High Strength Concrete Beams Containing Steel Fibers", Canadian J. Civil Eng., Vol 22, No 3, 1995, pp. 462-470.*

[159] **Imam, M., Vandewalle, L. and Mortelmans, F., and Van Gemert, D.**, *"Shear Domain of Fibre-Reinforced High-Strength Concrete Beams", Elsevier Engineering Structures Journal, Vol 19, No 9, 1997, pp. 738-747.*

[160] **Casanova, P., Rossi, P., Schaller, I.**, *"Can Steel Fibers Replace Transverse Reinforcement in Reinforced Concrete Beams?", ACI Material Journal, Vol.94, No 5, 1997, pp. 341-354.*

[161] **Kordina, K., Hegger, J.**, *"Zur Schubtragfähigkeit von Stahlbeton- und Spannbetonbalken", Beton- und Stahlbetonbau, 1, 1987, pp. 5-9 (in German).*

[162] **Khuntia, M., Stojadinovic, B., Goel, S.**, *"Shear Strength of Normal and High-Strength Fibre Reinforced Concrete Beams without Stirrups", ACI Structural Journal, Vol 96, 1999, pp. 282-289.*

[163] **Swamy, R.N., Jones, R., Chiam, A.**, *"Influence of Steel Fibres on the Shear Resistance of Lightweight Concrete T-Beams", ACI Structural Journal, Vol 90, No 1, 1993, pp. 103-114.*

[164] **Swamy, R.N., and Mangat, P.S.**, *"Theory for the Flexural Strength of Steel Fiber Reinforced Concrete", Cement and Concrete Research, Vol 4,1974, pp. 313-325.*

[165] **Lim, D.H., and Oh, B.H.**, *"Experimental and Theoretical Investigation on the Shear of Steel Fibre Reinforced Concrete Beams", Elsevier Engineering Structures, Vol 21, 1999 pp. 937-944.*

[166] **Hannant, DJ.**, *"Fibers cements and fibers concretes", New York, John Wiley & Sons, 1978..*

[167] **Gustafsson, J., Noghabai, K.**, *"Steel Fibres as Shear Reinforcement in High Strength Concrete Beams", Luleå University of Technology, Division of Structural Engineering, 1999, pp. 1-18.*

[168] **Adebar, P., Mindess, S., St.-Pierre, D., Olund, B.**, *"Shear Tests of Fiber Concrete Beams without Stirrups", ACI Structural Journal, Vol 94, No 1, 1997, pp. 68-76.*

[169] **Tan, K.H., Murugappan, K., and Paramasivan, P.**, *"Shear behavior of Steel Fiber Reinforced Concrete Beams", ACI Structural Journal, Vol 90, No 1, 1993, pp. 3-11.*

[170] **Tan, K.H., Paramasivan, P., and Murugappan, K.**, *"Steel Fibers as Shear Reinforcement in Partially Prestressed Beams", ACI Structural Journal, Vol 92, No 6, 1995, pp. 643-652.*

[171] **Ashour, S., Hasanain, G., Wafa, F.**, *"Shear Behavior of High-Strength Fiber Reinforced Concrete Beams", ACI Structural Journal, Vol 89, No 2, 1992, pp. 176-184.*

[172] **Kützing, L.**, *"Shear Strength of Steel Fibre Reinforced Concrete Beams and Plates", LACER No 2, University of Leipzig, 1997, pp. 263-272.*

[173] **Li, V., Ward, R., Hamza, A.**, *"Steel and Synthetic Fibers as Shear Reinforcement", ACI Material Journal, Vol 89, No 5, 1992, pp. 499-508.*

[174] **Mansur, M., Ong, K., Paramasivam, P.**, *"Shear Strength of Fibrous Concrete Beams without Stirrups", Journal of Structural Engineering, ASCE, Vol 112, No 9, 1986, pp. 2066-2079.*

[175] **Narayanan, R., Darwish, I.**, *"Use of Steel Fibers as Shear Reinforcement", ACI Structural Journal, Vol. 85, No. 2, 1987, pp. 216-227.*

[176] **Shin, S., Oh, J., Ghosh,S.**, *"Shear Behavior of Laboratory-Sized High-Strength Concrete Beams Reinforced with Bars and Steel Fibers", Fiber Reinforced Concrete Developments and Innovations, SP-142, ACI, 1994, pp. 181-200.*

[177] **Swedish Concrete Association**, *"Stalfiberbetong – "Recommendationer for konstruktion, utforande och provning" (Steel Fiber Reinforced Concrete – Recommendations for Design, Construction and Testing), Betongrapport nr 4, Stockholm. June 1995.*

[178] **Kwak, Y.-K, Eberhard, M. O., Kim, W. S., and Kim, J.**, *"Shear Strength of Steel Fiber-Reinforced Concrete Beams without Stirrups", ACI Structural Journal, Vol 99, No 4, 2002, pp. 530-538.*

3. EXPERIMENTS ON PRESTRESSED I-BEAMS

3.1 Introduction.

In this chapter, the results of an experimental research program on prestressed beams are presented. Six full scale beams, two made of plain concrete and four made of fiber reinforced concrete, were tested primarily to evaluate the possibility of substituting the minimum conventional transverse reinforcement required by Eurocode 2 (EC2) [2.82] with steel fibers. The shear behavior of the beams was analyzed both in the prestressing transfer zone (with the acronym TZ where, usually, reinforcement is required to provide shear strength) as well as in a zone where the prestressing force is completely diffused (acronym DZ where, usually, the minimum shear reinforcement is sufficient). Particular attention was paid to the shear contribution offered by fibers, either in addition to stirrups or in substitution of conventional shear reinforcement.

Furthermore, the effect of prestressing diffusion on shear behavior, the interaction between fibers and stirrups, the contribution of concrete itself and the mechanism of slippage of cables were in depth studied.

Shear behavior was analyzed both at Service Limit State, with particular attention to fiber effects on crack pattern, and at Ultimate Limit State, where steel fibers may influence the shear failure mechanism.

3.2 Materials and Specimen Geometry.

In order to investigate the effect of fibers on shear strength, six prestressed concrete beams were cast by adopting a concrete having a compressive strength (target characteristic value from cubes) $f_{ck,cube}$ = 75 MPa (C60/75) and the composition reported in Table 3.1.

In the following discussion, each specimen will be indicated as I-Beam # (from 1 to 6).

Table 3.2 shows the average compressive strength $f_{c,cube}$ (measured from 100x100x100 mm cubes), the tensile strength f_{ct} (measured from cylinders with diameter equal to 80 mm and height equal to 240 mm) and the Young's modulus of concrete E_c (measured from cylinders with diameter of 80 mm and height of 240 mm). All these quantities were measured on at least 3 specimens immediately before testing the beams. It can be noticed that the materials adopted for five out of six beams (I-Beam 1, 2, 3, 5 and 6) have almost the same mechanical properties,

while the concrete of I-Beam 4 has a compressive strength approximately 10% higher.

CEMENT TYPE	CEM I - 52.5R
CEMENT CONTENT	380 kg/m^3
MAXIMUM AGGREGATE SIZE	15 mm
WATER-CEMENT RATIO	0.31
PLASTICIZER	2.75 l/m^3 in beams without fiber; 3.67 l/m^3 in beams with fiber
FIBER CONTENT	50 kg/m^3 (V$_f$=0.64%) only in Beam 3 and Beam 4

Table 3.1: Concrete composition.

SPECIMEN	$f_{c, cube}$ [MPa]	f_{ct} [MPa]	E_c [MPa]
I-BEAM 1	84.9	4.43	41400
I-BEAM 2	86.1	3.69	41600
I-BEAM 3	82.3	4.65	44200
I-BEAM 4	92.8	5.18	43100
I-BEAM 5	83.6	4.43	42300
I-BEAM 6	84.2	4.72	43500

Table 3.2: Mechanical properties of concrete.

Table 3.3 shows the yielding (f_{sy}) and tensile (f_{st}) strength of the traditional steel reinforcement (cold formed welded mesh fabric and Tempcore rebars).

TRANSVERSE REINFORCEMENT	f_{sy} [MPa]	f_{st} [MPa]
STIRRUPS Φ6	480	575
MESH Φ5	610	660

Table 3.3: Mechanical properties of transverse reinforcement steel.

Two beams (I-Beam 1 and I-Beam 2) were cast with plain concrete, while 50 kg/m^3 of steel fibers (V$_f$ = 0.64 %) were added to the remaining beams. Two types of fibers were used: a normal strength fiber (45/30) having a length of 30 mm and an aspect ratio (length/diameter) equal to 45 and a high carbon fiber (80/30) having a length of 30 mm and an aspect ratio of 80 (see Figure 3.1). Fibers 45/30 were used in I-Beam 3 and in I-Beam 5 while fibers 80/30 were used in I-Beam 4 and I-Beam 6. The mechanical properties of the hooked steel fibers adopted in the present research are presented in Table 3.4.

STEEL FIBERS	RC-45/30-CN (Beam 3/5)	RC-80/30-BP (Beam 4/6)
TYPE OF STEEL	Low carbon	High carbon
SHAPE	Hooked	
SECTION	Circular	
LENGTH [mm]	30	
DIAMETER [mm]	0.62	0.38
ASPECT RATIO [l/ϕ]	48	79
MINIMUM TENSILE STRENGTH [MPa]	1250	2300

Table 3.4: Characteristics of the two types of fibers adopted.

As mentioned above, the shear behavior in both transfer and diffused zones was investigated. First, four beams (I-Beams 1-4) were cast and tested in each zone. Secondly, in order to confirm the results obtained from the first four beams, two other beams (I-Beams 5 and 6) were cast, but tested only in diffused zones to better verify the possibility of substituting the minimum conventional reinforcement with steel fibers (the main goal of this research).

All beams were designed according to EC2 [2.82] provisions in order to have a shear failure in either of the two testing areas. For this reason, the flanges and web out of the experimental zones (the collapse location) were stiffened: the section of the beam along the zones chosen for the shear collapse had therefore the typical geometry of a precast beam with a panel-web thickness equal to 120 mm (see Figure 3.2 and Figure 3.3).

A detailed discussion concerning the design procedure of all beams is reported in Section 3.3.
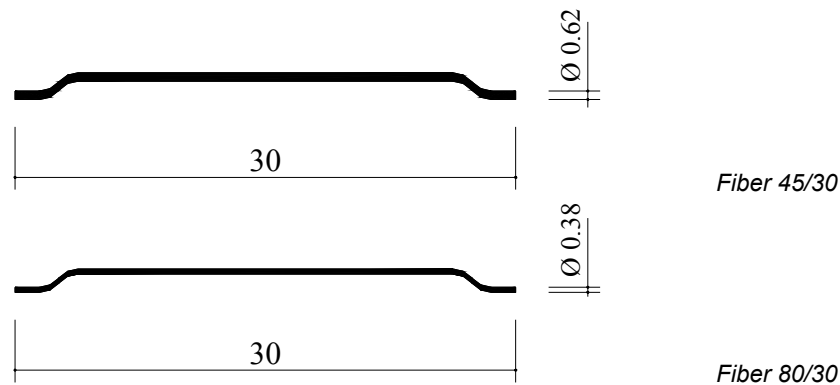
Figure 3.1: Geometry of fibers adopted: 45/30 fiber is shown above, 80/30 fiber below.

TEST "T" - BEAMS 1-4

F

A ▲
3225   3450   2200   125
B ▲
9000

TEST "D" - BEAMS 1-4

F

A ▲
2325   3450   2200   1025
B ▲
9000

TEST "D" - BEAMS 5-6

F

A ▲
3225   3450   2200   1025
B ▲
9900
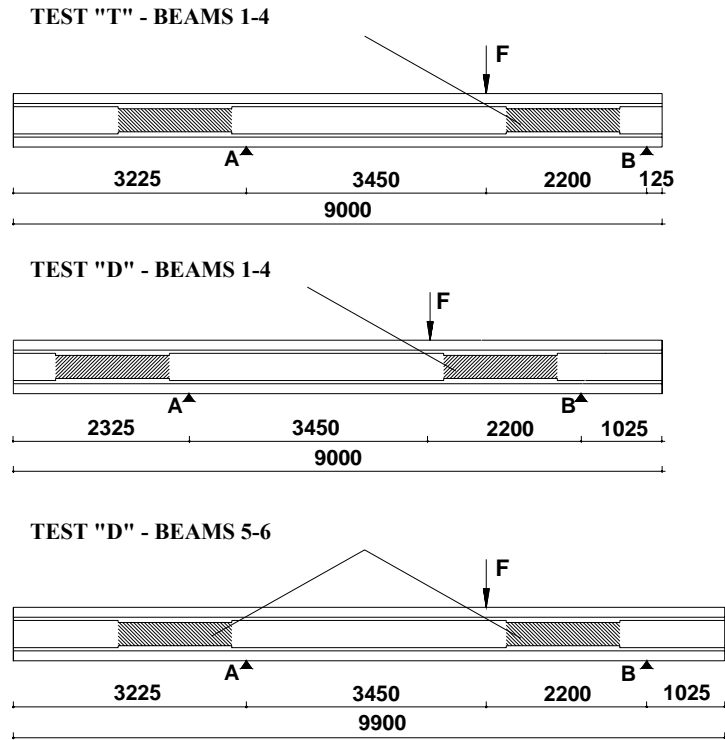
Figure 3.2: Scheme of the loading phases.

The test area was 1.75 m long (5 times the web depth) while the overall beam length was 9 m for I-Beams 1-4 and 9.9 m for I-Beams 5-6 (Figure 3.3: the greater length in the two latter specimens was set to allow the complete diffusion of prestressing in both test areas). All beams were simply supported with a span of 5.65 m and a point load was applied 2.2 m away from support "B" (Figure 3.2), in order to have a constant shear force along the testing zone (neglecting dead load).

Two shear tests were performed on each beam, adopting the configuration shown in Figure 3.2.

For I-Beams 1-4, the first test concerned zone TZ, while the second was devoted to zone DZ. Concerning I-Beams 5-6, both tests were carried out in a zone of diffused prestressing (DZ). The tests in zone TZ was representative of the beam behavior near supports, where transverse reinforcement is necessary to improve both the strand bond behavior through confinement and the shear strength of the beam, while those in zone DZ represented the behavior of an internal part of the beam,

where usually a minimum reinforcement amount (whose calculation does not come from equilibrium) is required and the prestressing action is completely diffused.

BEAMS 1-4
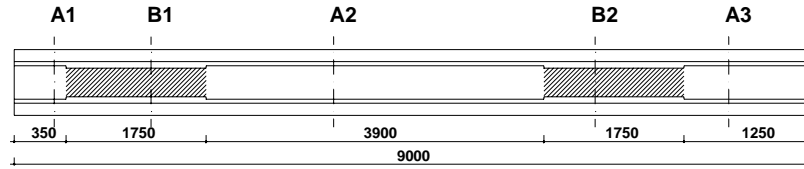
BEAMS 5-6
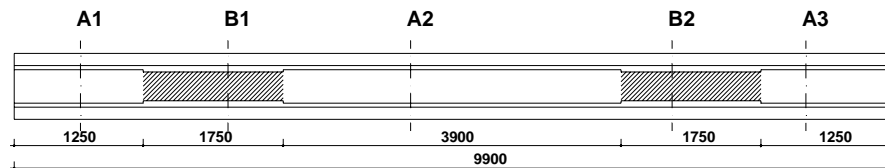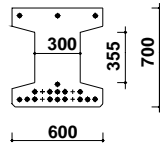
SECTION A1, A2, A3   **SECTION B1, B2**
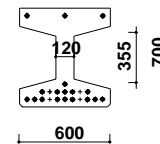
Figure 3.3: Geometry of the full scale beams.

Figure 3.4 represents the mechanism of diffusion of the prestressing action, which needs a certain length to fully develop (i.e. 80 times the tendon diameter), according to the current literature. For the tested beams a diameter of 0.6" (15.24 mm) was used and consequently a distance of about 1220 mm was calculated. Therefore, to allow the complete diffusion of the prestressing forces, a distance of 1250 mm was chosen for the tests DZ whereas the other panel area (test TZ) was located just 350 mm away from the beam end, enabling the complete diffusion of the prestressing force just beyond the middle of the panel.

The different diffusion of the prestressing action over the complete cross-section is described in Figure 3.4 (a), in which a stress field with a constant prestressing over the whole cross-section is achieved before the onset of the panel area (i.e., test DZ). On the contrary, in Figure 3.4 (b) the prestressing is not uniformly distributed over the cross-section of the panel that is to fail under shear loading (i.e., test TZ).
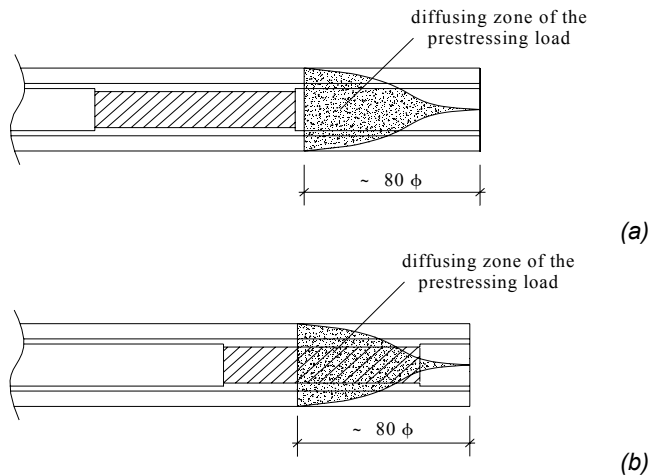
Figure 3.4: Schematic diagram of the prestressing stresses: experimental model with diffused (a) and not diffused (b) prestressing load.

Figure 3.5 illustrates the cross section of the beam and the strand position (note the two different cross sections, the wider is all along the beam except in the two panel area, which have the section indicated in Figure with the dotted line). Eighteen low-relaxation strands having a diameter of 0.6'' were used with an initial tension of 1400 MPa (before prestress losses, which can approximately be accounted in reason of 15%). The initial bending moment due to prestressing, referred to the centroid of the gross cross-section, was about 670 kNm.

In addition, 6 ∅ 22 deformed rebars were placed both at top and bottom flange (50 mm clear cover) in order to provide sufficient ductility and cracking control, for short term loading (camber) and long term loading as well.
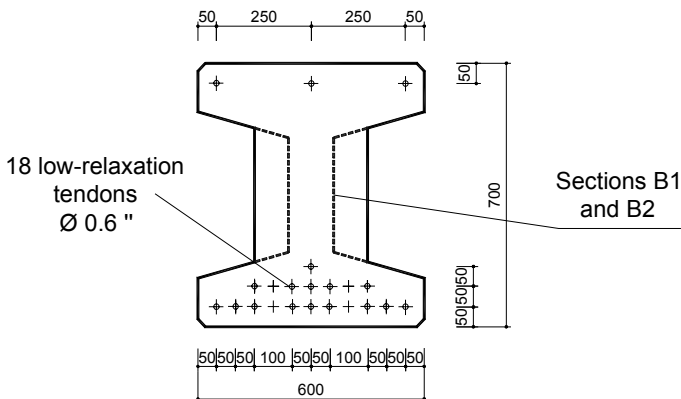
Figure 3.5: Cross-section of the beam specimen with the prestressing reinforcement.

The load set-up allowed for the simulation of the real behavior of a full scale precast beam where secondary beams usually transfer point loads on the main girder (Figure 3.6). Secondary beams could be roof elements, which are usually characterized by thin web cross section and transfer point loads to the principal girder. In the prefabrication practice, most of girders (and in general most of structural elements) are statically determined, so that the design in portions close to the supports (Figure 3.6) might be governed by shear whereas the design along the span is mostly influenced by flexure.
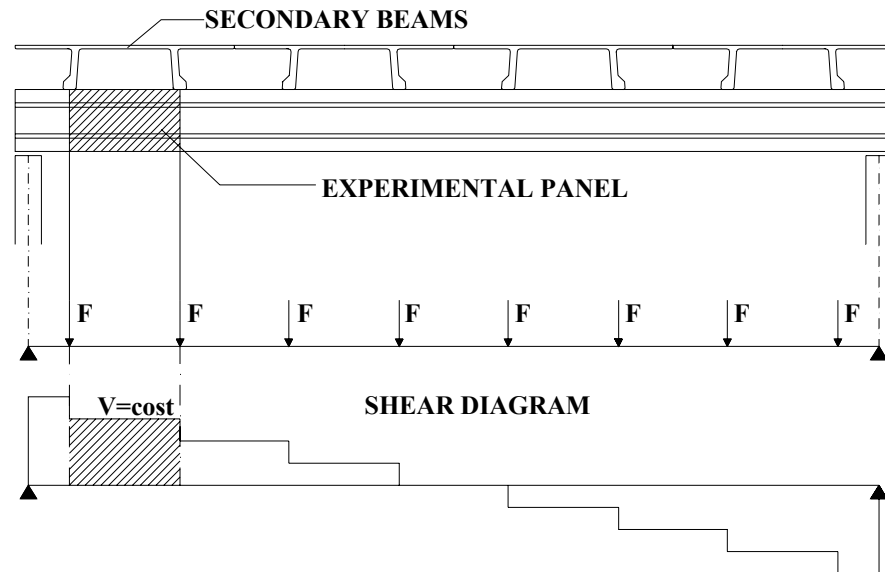
Figure 3.6: Load scheme for a beam subjected to pointed loads from secondary beams.

In TZ and DZ zones different types of transverse reinforcement were adopted:

- I-Beam 1 was made of prestressed concrete without any transverse reinforcement (neither in TZ nor in DZ zones);
- I-Beam 2 was made of prestressed concrete with transverse reinforcement designed according to EC2 [2.82]. In TZ, stirrups (ϕ6@100 mm) were designed on the basis of truss mechanism while in DZ, transverse reinforcement was the minimum required by the code (mesh fabric ϕ5@200x200 mm);
- The TZ zone of I-Beam 3 and I-Beam 4 was made with the same transverse reinforcement of I-Beam 2, while the DZ zone was made without traditional rebars, so that steel fibers were the only reinforcement provided in the beam web;

- I-Beam 5 and I-Beam 6, being copies of the DZ experimental models of I-Beam 3 and I-Beam 4, respectively, were cast with only steel fibers as shear reinforcement;
- In the remaining parts of the beams, stirrups ϕ10@100 mm were adopted.

Table 3.5 summarizes the shear reinforcement adopted in both zones of all the beams tested, and Figure 3.7 summarizes the traditional reinforcement, both longitudinal and transverse, provided in the six specimens.

	TEST	SHEAR REINFORCEMENT (experimental panel)
I-BEAM 1	TZ	*No shear reinforcement*
	DZ	*No shear reinforcement*
I-BEAM 2	TZ	*Stirrups (design reinf.)*
	DZ	*Mesh (minimum reinf.)*
I-BEAM 3	TZ	*Stirrups +45/30 fibers*
	DZ	*45/30 fibers*
I-BEAM 4	TZ	*Stirrups +80/30 fibers*
	DZ	*80/30 fibers*
I-BEAM 5	DZ I	*45/30 fibers*
	DZ II	*45/30 fibers*
I-BEAM 6	DZ I	*80/30 fibers*
	DZ II	*80/30 fibers*

Table 3.5: Shear reinforcement in each experimental test.

3.3 Design of the Beams.

Before testing, a procedure for predicting the ultimate load of the I-Beams was attempted, according to the available European Code [2.82]. Some considerations on the shear carried by the two stiff flanges and by fibers were also included, according to the available literature, since the EC2 does not contain any statement accounting for fibers as shear reinforcement, up to know.

Both the standard method and the variable inclination truss method were considered, where possible. In addition, calculations were performed with respect to three different levels:

- The structural level, where all safety and partial coefficients were neglected. The aim of this calculation was to predict the actual shear resistance of the members tested;
- The design level, where ultimate loads were predicted according to the actual safety coefficients required by the EC2;

- The serviceability level, where service loads were determined by dividing the ultimate loads by a coefficient equal to 1.45, which is an average value between the coefficient for dead loads (1.35) and live loads (1.5).
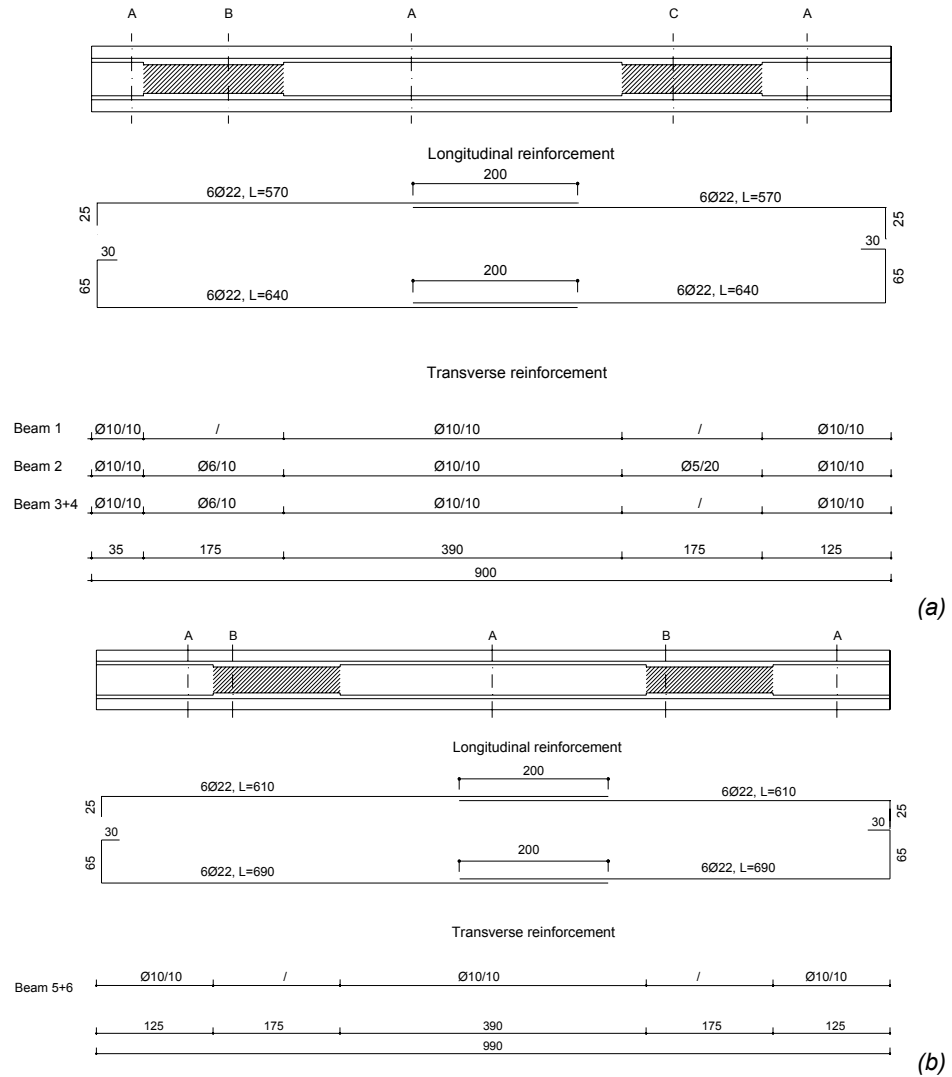
Figure 3.7: Traditional reinforcement (longitudinal rebars and stirrups) placed in the full-scale beams, for I-Beams 1-4 (a) and I-Beam 5 and 6 (b).

It is worthy emphasizing that, if at the structural level a prediction for all beams could be obtained, at ultimate and service loads it was not possible to predict load values in the following cases:

241

- I-Beam 1, without any transverse reinforcement in either of the two panels. In fact, EC2 does not allow such a design;
- I-Beam 3, 4 5 and 6, in which fiber contribution had to be neglected, as EC2 does not take into account it. The design and service loads were therefore the same of I-Beam 2.

The material properties adopted for the design of the beams are reported in Table 3.6-Table 3.8 (See also Section 3.2).

Mean value of cube compressive strength	R_{cm} = 84.4 MPa
Characteristic compressive strength	$R_{ck} = R_{cm}$ -8 = 76.4 MPa
Mean value of cylinder compressive strength	f_{cm} = 0,83 R_{cm} = 70.1 MPa
Characteristic cylinder compressive strength	f_{ck} = 0,83 R_{ck} = 63.4 MPa
Design value of cylinder compressive strength	$f_{cd} = f_{ck} / \gamma_C$ = 63.4/1.5 = 42.3 MPa
Mean value of axial tensile strength	f_{ctm} = 3.9 MPa

Table 3.6: Characteristic values of concrete.

Note that the cubic compressive strength is the average of all experimental values for I-Beam 1-3 (neglecting I-Beam 4, which higher characteristics, and the second series of specimens). The other concrete material properties were determined according to the actual EC2 provisions.

Steel properties were experimental determined before preparing the specimens. The values obtained from the experimental tests from the mesh and the stirrups are reported in Table 3.7 and Table 3.8.

Mean value for the yielding strength	f_{ym} = 610 MPa
Mean value for the tensile strength	f_{tm} = 660 MPa
Characteristic yielding strength	$f_{yk} = f_{ym}$ −34 MPa = 576 MPa
Design yielding strength	$f_{yd} = f_{yk} / \gamma_s$ = 576/1.15 = 500 MPa

Table 3.7: Characteristic values of steel mesh.

Mean value for the yielding strength	f_{ym} = 480 MPa
Mean value for the tensile strength	f_{tm} = 575 MPa
Characteristic yielding strength	$f_{yk} = f_{ym}$ −34 MPa = 446 MPa
Design yielding strength	$f_{yd} = f_{yk} / \gamma_s$ = 446/1.15 = 388 MPa

Table 3.8: Characteristic values of stirrups.

3.3.1 Test TZ.

The forces occurring on the supports of the beam (point A and B, Figure 3.2) consists of the applied load *F* and the self weight of the beam. The weight of the

beams is calculated assuming *p=6.5 kN/m*. By using the equilibrium of the moments the reaction forces subjected to the applied force F can be determined as follows:

A = (3.45/5.65)F + 0.23pL   (3.1)

with:

p=6.5 kN/m

B = (2.20/5.65)F + 0.77pL   (3.2)

3.3.1.1   *Mean Value of Shear Strength of I-Beams without Fibers.*

The shear force was calculated by using these material values:

f_{cm} = 70.1 MPa

f_{ym} = 480 MPa

Section B1 (I-Beam 2, Figure 3.3):

$$\upsilon = 0{,}7 - \frac{f_{cm}}{200} = 0.7 - \frac{70.1}{200} = 0.35 \Rightarrow \qquad \nu = 0.5 \qquad\qquad (3.3)$$

The shear strength considered by EC2 is:

$V_{wd} = \varpi_{st}\, f_c\, b_w\, z\, \lambda$ (3.4)

according to the variable inclination truss method (suitable only in presence of a certain amount of transverse reinforcement), where:

- ρ_w is the shear reinforcement ratio;
- ϖ_{st} is the mechanical ratio of shear reinforcement;
- λ is the slenderness ratio;
- λ_r is the modified slenderness ratio (describes the contribution of shear reinforcement to the crack development);
- b_w is the width of the web;
- z is the internal lever arm;
- $\rho_w = A_{sw} / (s\; b_w \sin \alpha)$;
- A_{sw} is the area of shear reinforcement having a spacing s (ϕ6@100mm);
- α is the angle between the shear reinforcement and the main steel;
- ρ_w = 2*28.3/(120*100) = 0.0047;
- $\omega_{st} = \dfrac{A_s}{sb_w} \cdot \dfrac{f_{ym}}{f_{cm}} = 0.0323$;

- $\lambda_r = \sqrt{\dfrac{v - \varpi_{st}}{\varpi_{st}}} = 3.805$ while $\lambda_{geometrical}$ = 4;

- b_w = 120 mm;
- z = 550 mm;

for $\lambda=\lambda_r$ $\Rightarrow$ **V_{wd}^{I}= 568 kN**

for $\lambda=\lambda_{geometrical}$ $\Rightarrow$ **V_{wd}^{II}= 597 kN** (highest limit)

The contribution of the upper and the lower flange (V_{bnd}) can be considered as (di Prisco and Romero, 1995 [1]):

$\Delta\tau$= $0.012f_c$ (3.5)

V_{bnd}= 49 kN

Therefore: **$V_r=V_{wd}+V_{bnd}$**

for $\lambda=\lambda_r$ $\Rightarrow$ **V_r^{I}= 617 kN**

for $\lambda=\lambda_{geometrical}$ $\Rightarrow$ **V_r^{II}= 646 kN** (highest limit)

For section A2, as a result of the wider cross-section, the shear stresses will be less than in section B1 therefore the resistance in this section will be higher. The reinforcement ratio of shear reinforcement (ρ_w), the mechanical ratio of shear reinforcement (ϖ_{st}) and therefore also the modified slenderness ratio (λ_r) will change because in this section stirrups with a diameter of 10 mm instead of 6 mm were used. In fact:

V_{wd} = $\varpi_{st}\, f_c\, b_w\, z\, \lambda_r$

ρ_w= 0.0053

ω_{st}= 0.0363

λ_r= 3.574

V_{wd}= 1498 kN

Therefore the maximal applied load (F) can be calculated with the minimum obtained shear force, of course in section B1:

A = $V_{r(section\ B)}$

F_1 = (A-0.23pL)/0.61= **989 kN** (for $\lambda=\lambda_r$)

F_2 = (A-0.23pL)/0.61= **1037 kN** (for $\lambda=\lambda_{geometrical}$)

The bending moment at the loading point is determined with:

$V_{r(section\ B)}$=617 kN

$M_{bending} = V_r \, dist_{(B\text{-}point\ load)} = 617*2.20 = 1357$ kNm

3.3.1.2   *Design Value of Shear Strength of I-Beams without Fibers.*

The calculation is the same as before with the difference that the design values of materials will inhere be used. These can be obtained by dividing the characteristic values for safety factor, as follows:

f_{cd} = 42.3 MPa

f_{yd} = 388 MPa

$$\upsilon = 0.7 - \frac{f_{cd}}{200} = 0.7 - \frac{42.27}{200} = 0.488 \qquad \Rightarrow \qquad \nu=0.5$$

Section B:

$V_{wd} = \varpi_{st} \, f_{cd} \, b_w \, z \, \lambda$

where:

- $\rho_w = 0.0047$;

- $\omega_{st} = \dfrac{A_s}{sb_w} \cdot \dfrac{f_{yd}}{f_{cd}} = 0.0432$;

- $\lambda_r = \sqrt{\dfrac{\nu - \varpi_{st}}{\varpi_{st}}} = 3.251$;

- b_w = 120 mm;

- z = 550 mm;

for $\lambda=\lambda_r$ $\qquad \Rightarrow \qquad$ **V_{wd}^{I}= 392 kN**

for $\lambda=\lambda_{geometrical}$ $\qquad \Rightarrow \qquad$ **V_{wd}^{II}= 482 kN** $\qquad$ (highest limit)

The contribution of the upper and the lower flange was not be considered in this calculation, as it is neglected by the European Code for design purpose.

For section A2 as a result of the wider cross-section the shear stresses will be lower than in section B1, as already shown for the mean value of shear strength.

The maximum applied load (F) can be calculated as:

$A = V_{wd(section\ B)}$

$F_1 = (A-0.23pL)/0.61=$ $\qquad$ **620 kN** $\quad$ (for $\lambda=\lambda_r$)

$F_2 = (A-0.23pL)/0.61=$ $\qquad$ **768 kN** $\quad$ (for $\lambda=\lambda_{geometrical}$)

From the design value, an indication of serviceability loads by EC2 can be calculated by using a partial safety factor (γ) for the applied loads of 1.45, giving the following values:

F_1 = 620/1.45=   **427 kN**   (for $\lambda = \lambda_r$)

F_2 = 768/1.45=   **530 kN**   (for $\lambda = \lambda_{geometrical}$)

3.3.1.3   *Mean Value of Shear Strength of FRC I-Beams.*

To take into account the contribution of fibers to the shear strength of the beam, the method of Nielsen and Braestrup [2.93] was used. This is a method based on experimental results but is not provided by the provisions of EC2. The transverse reinforcement contribution remains the same in the beam and, in addition, the influence of fibers is to be considered, through the following factor:

$$\varsigma_{ft} = \frac{\sigma_{tu}}{f_{cm}}$$

where:

- ς_{ft} is a factor for describing fiber contribution;

- σ_{tu} is an equivalent stress, derived from σ-w relationship;

σ_{tu} = 1.07 MPa, on the basis of experimental results on notched beams containing 45/30 fibers, according to the Italian Standard UNI [2.125]. Only 45/30 fibers were considered in the design process, as they were assumed to be the most feasible and applicable in real structures.

$$\varsigma_{ft} = \frac{1.07}{70.1} = 0.015$$

Section B1 (I-Beam 3).

ω_{st}= 0.0323

$$\lambda_r = \sqrt{\frac{v - (\varpi_{st} + \varsigma_f)}{\varpi_{st} + \varsigma_f}} = 3.09$$

$$V_{wd} = (\varpi_{st} + \varsigma_f) f_c b_w z \lambda$$

$$V_{wd} = (0.0323 + 0.015) * 70.1 * 0.12 * 0.55 * 3.09$$

for $\lambda = \lambda_r$ $\Rightarrow$ **V_{wd}= 677 kN**

for $\lambda = \lambda_{geometrical}$ $\Rightarrow$ **V_{wd}= 875 kN**

Furthermore the contribution of the upper and the lower flange (V_{bnd}) according to di Prisco and Romero, 1995 [1] was taken into account as follows:

246

$\Delta\tau = 0.01f_c$ $\Rightarrow$ **$V_{bnd} = 41$ kN**

therefore:

$V_r = V_{wd} + V_{bnd} = 718$ kN (for $\lambda = \lambda_r$)

For section A2, as already mentioned, the shear stresses will be less than in section B1 and therefore the resistance will be higher and will not be decisive.

Therefore the applied Load F can be calculated as:

$A = V_{r(section\ B)}$

$P = (A - 0.23pL)/0.61 =$ **1154 kN** (for $\lambda = \lambda_r$)

Of course, as the Eurocode does not consider any eventual contribution of fibers, it does not make any sense extending this calculation to design values. An engineer, nowadays, would obtain the same load prediction with and without fibers.

3.3.2 Test DZ.

The reaction forces A and B were calculated likewise test TZ. The following expressions were obtained for the forces A and B subjected to the applied force F:

$A = 0.39P + 0.62pL$

with p=6.5 kN/m

$B = 0.61P + 0.38pL$

3.3.2.1 Mean Value of Shear Strength of I-Beams without Fibers.

Only section B2 (Figure 3.3) will be calculated because section A2 is not decisive for the design, as previously discussed.

Both the variable truss inclination and the standard method were used to calculate the value of the shear strength, even though, as a designer, the minimum shear reinforcement should be neglected, and the total shear strength should be provided by concrete only. With this respect, the standard method would be adopted in practice. Moreover, I-Beam 1 (plain concrete only as shear reinforcement) would not be verified and could not be designed.

$$v = 0.7 - \frac{f_{cm}}{200} = 0.35 \qquad \Rightarrow \qquad v=0.5$$

247

The shear strength considered by EC2 with the variable crack inclination is:

$V_{wd} = \varpi_{st} f_c b_w z \lambda$

$\rho_w = 2*19.63/(120*200) = 0.00164$ (steel fabric mesh)

$$\omega_{st} = \frac{A_s}{sb_w} \cdot \frac{f_{ym}}{f_{cm}} = 0.01429$$

$$\lambda_r = \sqrt{\frac{\nu - \varpi_{st}}{\varpi_{st}}} = 5.83 > \lambda_{geometrical} \qquad \Rightarrow \lambda_{geometrical} \text{ is used}$$

V_{wd}= 264 kN

with the contribution of the flanges (V_{bnd}); $\Delta\tau$= 0.008f_c

V_{bnd}= 33 kN

therefore:

$V_r=V_{wd}+V_{bnd}$= 297 kN

According to the standard method, the prestressing will be considered, therefore a higher value can be obtained:

$V_{Rd3} = V_{cd} + V_{wd} \qquad (V_{cd} = V_{Rd1})$ (3.6)

$$V_{Rd1} = \left[0.25 \cdot \frac{f_{ctd}}{\gamma_c} \cdot k \cdot (1.2 + 40 \cdot \rho_l) + 0.15\sigma_{cp} \right] b_w \cdot d$$ (3.7)

where:

- $k=1.6-d \geq 1$ (d in meter)
- $\sigma_{cp}= N_{sd}/A_c$;
- N_{sd} is the axial force in the cross-section due to prestressing;
- $N_{sd} = 18 * 194.6 = 3502$ kN (where 18 is the total number of tendons and 194,6 kN is the prestressing force applied);
- A_c is the total cross-sectional area of the concrete section B2;
- $A_c = 2402000$ mm^2;
- $\sigma_{cp} = 14.6$ MPa;
- ρ_l is the reinforcement ratio for longitudinal reinforcement;
- $\rho_l= A_{sl} / (d\ b_w) \leq 0.02$;
- A_{sl} is the cross-sectional area of the tensile reinforcement;
- b_w is the smallest width of the cross-section in the tensile area.

$\rho_l = 6*380/(120*650) = 0.029 \Rightarrow 0.02$

$f_{ctk} = 0.7* f_{ctm} = 0.7*3.92 = 2.74$

$cotg\psi_l=\lambda_l=\tau/\sigma_l=2.5$

248

(γ_c=1)

$$V_{Rd1} = \left[0.25 \cdot \frac{2.74}{1} \cdot 1 \cdot (1.2 + 40 \cdot 0.02) + 0.15 \cdot 14.6 \right] \cdot 120 \cdot 650 = 278 \text{ kN}$$

This value is an estimation for I-Beam 1. For predicting a value for I-Beam 2, one should take into account the contribution of the fabric mesh as:

$$V_{Rd3} = \frac{A_{sw}}{s} \cdot 0.9 \cdot d \cdot f_{wd} \tag{3.8}$$

which gives V_{Rd3} = 68 kN

The total shear, considering concrete, flanges and fabric mesh, is therefore

V_r= 379 kN

The maximal applied Load F can be calculated:

B = $V_{r(\text{section C})}$

F = (B-0.38pL)/0.61=   **585 kN**   (with the standard method)

3.3.2.2   *Design Value of Shear Strength of I-Beams without Fibers.*

The contribution of the minimum shear reinforcement has to be neglected in the design process, as well as that of flanges, since the minimum shear amount is to be provided only once the concrete itself is able to carry all external shear. The standard method was therefore used.

Section B2:

$$V_{Rd1} = \left[0.25 \cdot \frac{f_{ctd}}{\gamma_c} \cdot k \cdot (1.2 + 40 \cdot \rho_l) + 0.15\sigma_{cp} \right] b_w \cdot d$$

$$V_{Rd1} = \left[0.25 \frac{2,0}{1} (1.2 + 40 \cdot 0.02) + 0.15 \cdot 14.6 \right] \cdot 120 \cdot 650 = 249 kN$$

Therefore the applied Load (F) can be calculated:

B = $V_{Rd3(\text{section C})}$

F = (B-0,38pL)/0,61=   **372 kN**   (Standard method)

By using a partial safety factor (γ) of 1.45, the following service load can be determined:

F_1 = 372/1.45=   **257 kN**   (with the standard method)

3.3.2.3 *Mean Value of Shear Strength of FRC I-Beams.*

The value of this section depends only on the fiber reinforcement because a transverse reinforcement is not included in this part. Therefore the fiber contribution, only for fibers 45/30, was considered by means of the factor ζ_{fiber}. In the recent provisions a calculation of the shear value of fiber reinforced concrete does not exist. Therefore the method of the variable truss inclination and the standard method, given by EC2, were used to determine the shear strength.

Section B2 (I-Beam 3):

ζ_{fiber}= 0,015 (according to the calculation shown for Test TZ)

$$\lambda_r = \sqrt{\frac{\nu - \zeta_{fibre}}{\zeta_{fibre}}} = 5.68 > \lambda_{geometrical}$$

The values can be calculated by using the variable truss inclination method as before with $\lambda = \lambda_{geometrical}$

$$V_{wd} = \varsigma_f f_{cm} b_w z \lambda$$

$$V_{wd} = 0.015 \cdot 70.1 \cdot 0.12 \cdot 0.55 \cdot 4$$

V_{wd}= 278 kN

with adding the contribution of the flanges (V_{bnd});

$\Delta\tau$= 0.008f_c $\Rightarrow$ **V_{bnd}= 33 kN**

consequential:

$V_r = V_{wd} + V_{bnd}$= 311 kN

According to the standard method:

$V_{Rd3} = V_{cd} + V_{wd}$ ($V_{cd} = V_{Rd1}$)

$$V_{Rd1} = \left[0.25 \cdot \frac{f_{ctd}}{\gamma_c} \cdot k \cdot (1.2 + 40 \cdot \rho_l) + 0.15\sigma_{cp} \right] b_w \cdot d =278 \quad \text{kN} \quad \text{as} \quad \text{previously}$$

calculated;

$$V_{fibre} = \zeta_{fibre} f_{cm} b_w z \lambda_I =173 \text{ kN}$$

$\Rightarrow$ **V_{Rd3}= 451 kN**

Therefore the applied Load P can be calculated:

$B = V_{r(section\ C)}$

P = (B-0.38pL)/0.61=   **473 kN**   (with $\lambda = \lambda_r$)

                              702 kN   (with the standard method)

250

All calculated values for the shear strength are summarized in Table 3.9.

	Test TZ (Transfer length zone)			Test DZ (Diffused prestressing zone)		
	Collapse Load	Design Load	Service Load	Collapse Load	Design Load	Service Load
I-Beam 2	989 kN	620 kN	427 kN	585 kN[*]	372 kN	257 kN
I-Beam 3	1154 kN	620 kN	427 kN	702 kN[*]	372 kN	257 kN
[*] Using the Standard Method, more proper in members with minimum transverse reinforcement..						

Table 3.9: Results of the design calculations of I-Beams.

3.4 Set up Description and Loading Modalities.

Shear strength in a beam is initially provided by concrete, which, unfortunately, is weak in tension and therefore cracks at low level of loads. After cracking, if transverse reinforcement is provided, the shear strength can be ensured by a truss mechanism. However, before the truss mechanism activates, an unstable branch may occur in the overall response of a beam, with eventual sudden load decreases and crack propagations. In order to capture this unstable branch, which a standard load controlled procedure would totally skip, a displacement controlled test had to be carried out.

Displacement control was obtained by adopting a worm electro-mechanical screw jack having a maximum load of 1000 kN and a stroke of 350 mm, as reported in Figure 3.8.

The numbers in Figure 3.8 (a) describe the main characteristics of the worm screw jack, which are:

1) Spheroidal cast iron / welded steel;
2) Worm screw in carburized and case hardened steel;
3) Special and anti-friction bronze wheel / nut;
4) Steel screw thread;
5) Spherical or roller thrust bearings;
6) Flange;
7) TECALEMIT grease nipples (UNI 7662);
8) Threaded ring;
9) Protection.

251

By imposing the engine rate it was possible to control the displacement velocity.
The jack was placed below the beam and the load (F) was applied by means of a steel frame (Figure 3.9).
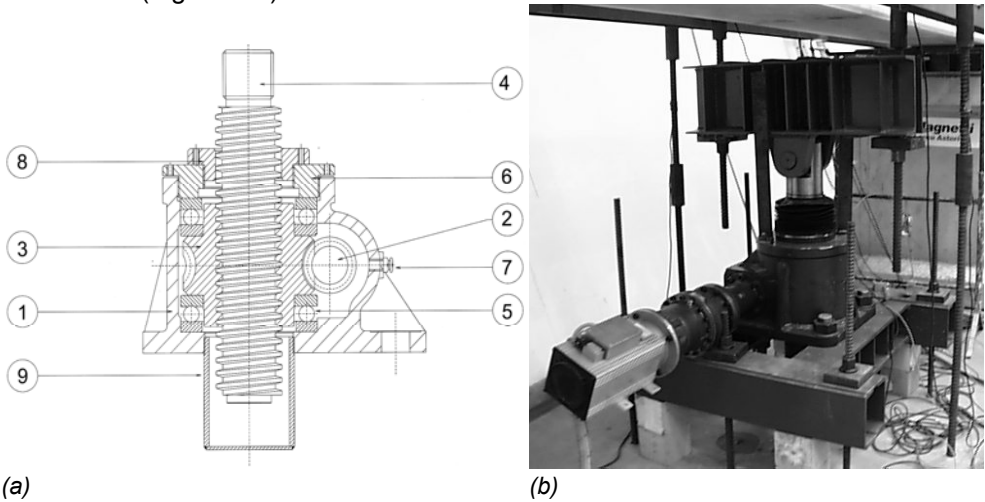
(a)   *(b)*

Figure 3.8: Longitudinal section of the worm screw jack (a) and worm screw jack with the motor, the bottom crossbeam and the support frame (b).
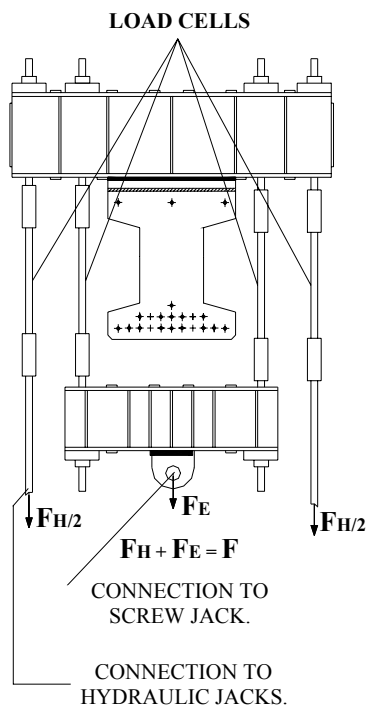
Figure 3.9: Scheme of the steel loading frame adopted.

For the heavily reinforced beams, with a strength higher than 1000 kN (maximum load applicable by the screw jack), two 600 kN hydraulic jacks were used in parallel with the screw jack (Figure 3.9). To ensure a displacement controlled test in the range of interest (especially in the cracked stage), an initial force, smaller than the first cracking load, was applied with the hydraulic jacks and kept constant throughout the test, while the remaining load, up to collapse, was applied by means of the screw jack. The applied loads (both from the screw and the hydraulic jacks) were measured with load cells connecting the top and bottom crossbeams.

The measurement of the load through load cells allowed checking whether the load was applied in the appropriate way, i.e. if it was the same both in the two bars connected to the worm screw jack and in the two bars connected to the hydraulic jacks, within an acceptable tolerance, in order to prevent any torsion into the specimen (Figure 3.9).

The top crossbeam was placed at the top face of the specimen to be tested. Its purpose was to transfer the force produced by the worm screw jack directly into the specimen. It was welded together out of two channel sections with a height of 400 mm, a length of 1500 mm while the total width of the cross beam was 260 mm (Figure 3.10). Ten metal stiffeners were welded symmetrically to the crossbeam in order to improve the shear capacity, particularly at the location where the vertical rebars transferring load had to be placed. At the bottom side a steel cylinder with a diameter of 60 mm and a length of 600 mm (which is the flange width) was welded, turning out to be the only element in contact with the specimen, to make sure that the load be applied along a line only. To prevent unevenness of the surface of the beam and consequently an incorrect loading, between the beam and the cylinder of the crossbeam a thin layer of high strength mortar was placed.

The cross-section of the upper crossbeam is shown in Figure 3.10, together with its placement at the top of the specimen.

The bottom crossbeam was connected by means of a high strength bolt having a diameter of 70 mm with the worm screw jack. For this connection, two plates with a hole of 70 mm were welded at the bottom side of each channel section, being 300 mm high.

The bottom crossbeam, being pulled out by the worm screw jack, allowed the load transfer, through the vertical rebars, to the top crossbeam that loaded the specimen. Suitable load cells were placed along these rebars, made of high strength steel (dywidag), to measure the load.

253
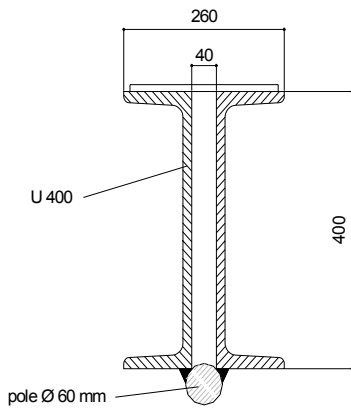
(a)   *(b)*

Figure 3.10: The cross-section of the upper transverse loading beam (a) and its placement on the specimen to be tested (b).

The worm screw jack was anchored to the floor of the laboratory by means of a steel frame and suitable dywidag bars passing through a slab having a thickness of one meter and designed to resist a concentrated load of 1000 kN.

A consistent number of instruments were utilized for monitoring the most important displacements and deformations of the specimens, besides the applied loads.

Figure 3.11 shows the measuring devices: Linear Variable Differential Transformers (LVDTs) allowed the measurement of the vertical displacements of the beam and the supports as well as the strand slips and the flange deformations; potentiometric transducers were placed on both sides (back and front) of TZ and DZ zones (experimental zones in Figure 3.12 and Figure 3.13) to measure crack openings and strut deformations.

These transducers were placed with an inclination of 20° (for the strut deformations) and 70° (for the crack openings) with respect to the horizontal line (Figure 3.13, where the instruments 1-6 measured crack openings while instruments 7-10 recorded strut deformations). Such inclinations were selected by observing that, at collapse, the arch action would have prevailed, with a strut inclination approximately equal to the panel diagonal. This assumption was confirmed during most of tests.
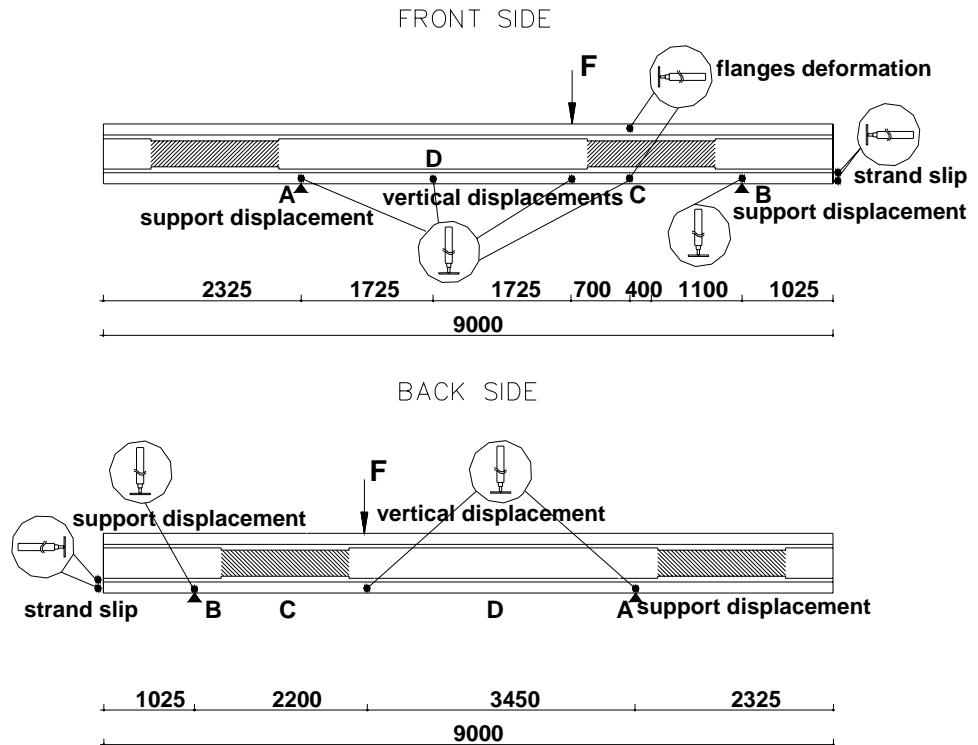
Figure 3.11: Measuring devices on the front and back sides.

A total number of 26 instruments were recorded each test:

- 4 load cells;
- 4 LVDTs for measuring support displacements;
- 4 LVDTs for measuring vertical displacements, 2 at point load, 1 at point C and 1 at point D (Figure 3.11). Point C is in the middle of the panel area while point D is in the middle between the point load and the support A;
- 2 LVDTs for measuring flange deformations;
- 10 potentiometric transducers for measuring strut deformations and crack openings in the panel area;
- 2 LVDTs for measuring slippage of cables.

Figure 3.14 shows the arrangement of the two instruments for measuring the slip of cables, which was expected to be significant, especially in tests TZ.
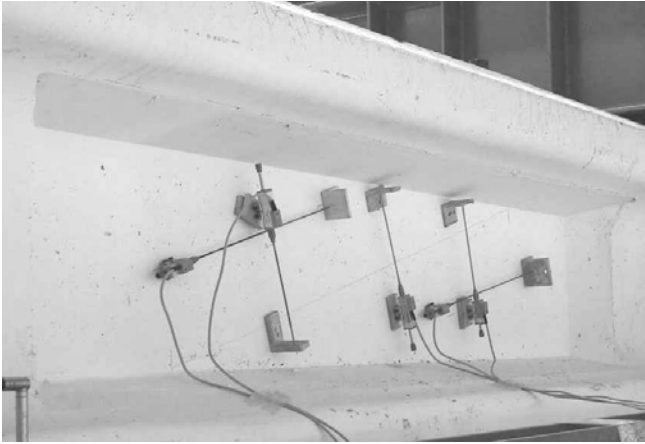
Figure 3.12: Instrumentation in the experimental model.

(a)   *(b)*
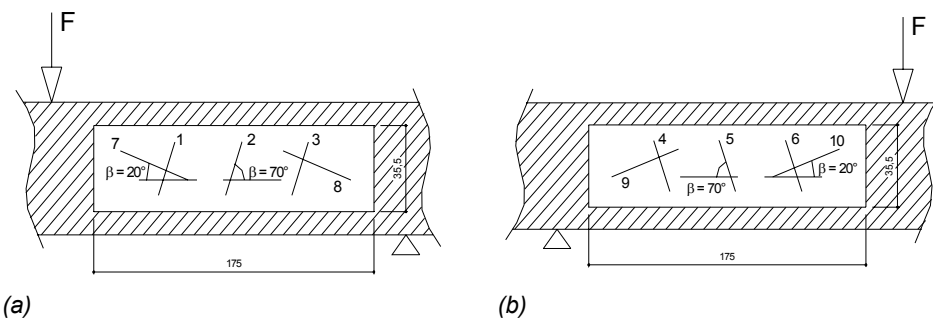
Figure 3.13: Scheme of the instrumentation in the window: front side (a) and back side (b).

Figure 3.14: The instrumentation for measuring the cable movement.

Concerning the loading modalities, few cycles of preloading (generally two loading and unloading cycles), of course in the elastic range, were always done in order to make sure that the instruments were working properly.

For all tests performed without the extension of the two hydraulic jacks (I-Beam 1, Test TZ and DZ, and I-Beam 2, Test DZ), the load was controlled only by the screw jack. The test started by imposing a rate of 100 revolutions per minute to the worm screw jack. After reaching the first cracking point, the rate was reduced to 50 r.p.m. up to the end of the test.

The specimens were not brought to complete collapse in order to prevent failure mechanisms that could have been dangerous for the equipment. Rather, it was decided to stop the test when the load started decreasing at a vertical displacement of a defined value, which was set to be at least three-four times greater than the displacement at first cracking point and, in any case, with a crack pattern really clear and at advanced stages.

The procedure for all tests performed with the two additional hydraulic jacks can be described in a similar way. Figure 3.15 shows a typical load vs. time curve of one of these tests (I-Beam 4, Test DZ) where the different load contributions can be seen. Note that the hydraulic jacks were loaded up to 250 kN each and their pressure was then kept constant during the test. This value was chosen as less as possible, just to obtain a total load sufficient to perform the test. Note, in fact, that the first cracking point was greater than 700 kN, and much higher that the load applied by the two hydraulic jacks.

At the initial stage, the load was therefore produced only by the hydraulic jacks. The worm screw jack started applying the remaining load through an imposed piston rate only after the stabilization of the specimen under 500 kN. With increasing of damage, it was necessary to reload the external hydraulic jacks because the beam's deflection decreased the pressure.

From Figure 3.15 some sudden decreases in the curve of the total load and of the load provided by the screw jack as well can be noticed: they are the result of the crack opening and the progressive damage of the specimens. Note that such leaps could not been captured by a load-controlled system, to further confirm the proper choice of limiting the load applied by hydraulic jacks.
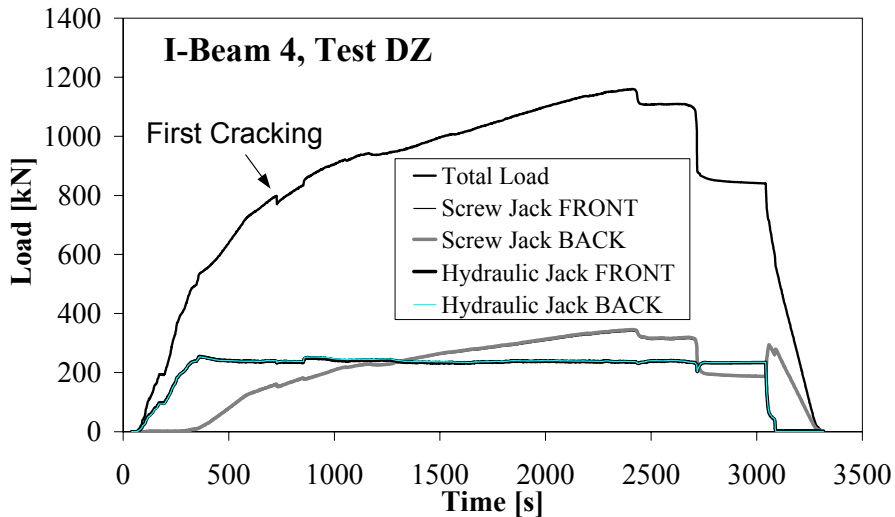
Figure 3.15: Typical load versus time curve of tested beam, I-Beam 4, test DZ.

3.5 Experimental Results and Discussion.

Figure 3.16 and Figure 3.17 show the shear force versus displacement curve for the tested beams both for TZ (I-Beam 1,2, 3 and 4; Figure 3.16) and DZ zones (I-Beam 1, 2, 3 and 6 I; Figure 3.17). In all tests, cracking appeared at the end of the elastic stage, with a shear force approximately equal to 450 kN. Only I-Beam 4 exhibited a higher elastic limit due to a higher concrete strength, already reported in Table 3.2.

In the post cracking stage, some differences were observed in the response of the six beams. I-Beam 1, without transverse reinforcement, exhibited the lowest post cracking strength. In the TZ zone, a brittle behavior occurred after cracking (Figure 3.16). The post cracking load, related to the strength offered by concrete alone, was not able to increase beyond the value reached at the elastic limit. On the contrary, in the DZ zone, the post cracking load exceeded the first cracking load, but only after large deformations and significant damage (Figure 3.17).

The results of I-Beam 2, with traditional reinforcement, and of the fiber reinforced I-Beams 3, 4, and 6, are similar. In the TZ zone, where a constant amount of transverse reinforcement was provided (regardless of the fiber content), fibers allowed a significant increase of the ultimate shear force (up to 20% more than the ultimate load of I-Beam 2). Moreover, the shear-displacement curve showed a more stable, resistant, and ductile post-peak behavior for fiber reinforced beams (Figure 3.16).

258

From Figure 3.16 it can be concluded that fibers interact in a highly positive way with the traditional reinforcement, providing a significant contribution to the tension stiffening mechanism, improving the bond properties of rebars and, of course, providing the bridge effect across cracks.

The additional contribution of both fabric mesh and fibers is significant, especially at the beginning of the nonlinear stage, which is the range of more interest, under a design point of view.
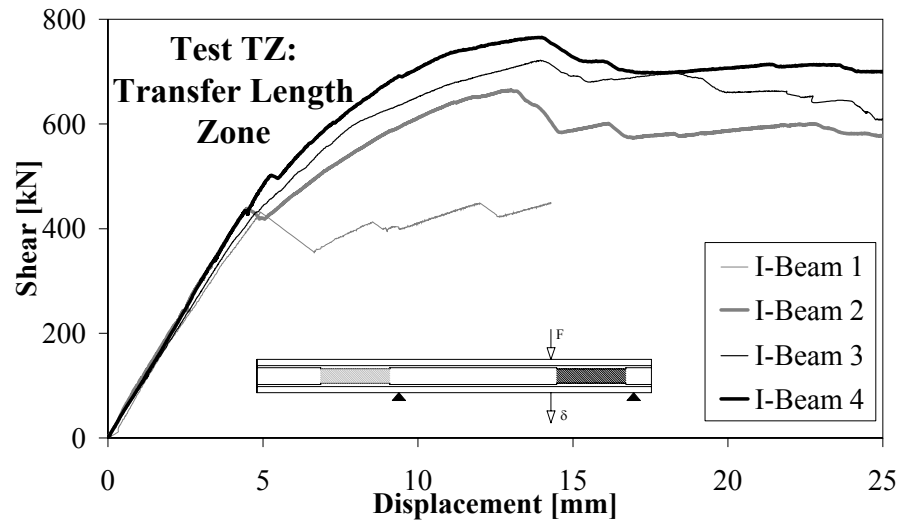
Figure 3.16: Shear-displacement curves for tests TZ.
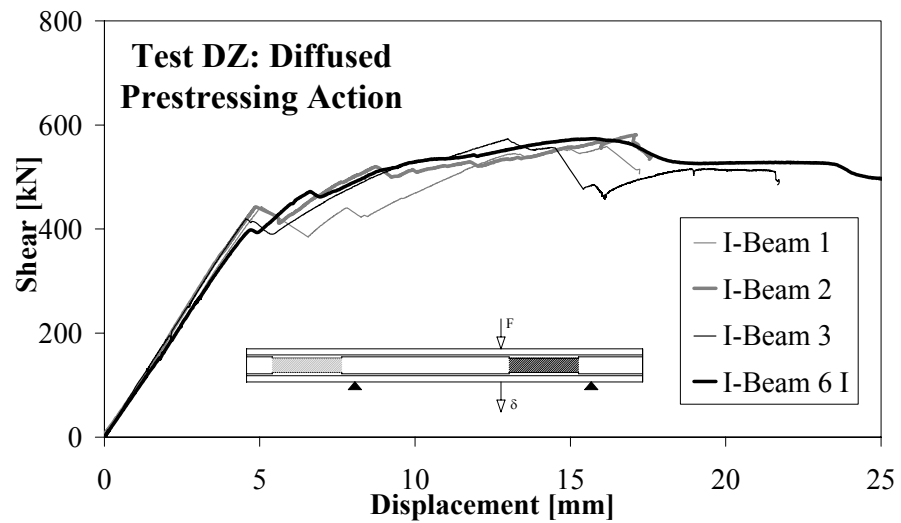
Figure 3.17: Shear-displacement curves for tests DZ.

259

As far as the DZ zone is concerned, the observed behavior of I-Beam 2 (with minimum reinforcement) and I-Beam 3 (with fiber reinforcement only) was similar. Beam 6 showed the best performance: at the crack onset, a small load decrease was observed and the post cracking behavior was stable with an overall ductility considerably enhanced compared to the other specimens.

From Figure 3.17 it is evident that fibers can substitute the minimum shear reinforcement required by the Code (EC2 in the present investigation). This conclusion is particularly important because it applies to real full-scale structures avoiding therefore the consideration of eventual dimension sensitivity, i.e. size effect.

Figure 3.18 and Figure 3.19 report the comparison of the shear-displacement curve of tests DZ with either 45/30 fibers (Figure 3.18) and 80/30 fibers (Figure 3.19). These figures show that the test results present a remarkable consistency.

Note that the two curves of I-Beam 6 are characterized by lower resistance than I-Beam 4, due to the different material properties of I-Beam 4. For this reason, the following comparisons concerning tests DZ will be undertaken, where possible, considering either of the two tests of I-Beam 6 rather than I-Beam 4.

These results confirm that 45/30 fibers ensure at least the same shear resistance offered by the minimum shear reinforcement, while 80/30 fibers can slightly improve the performance of the steel fabric mesh.
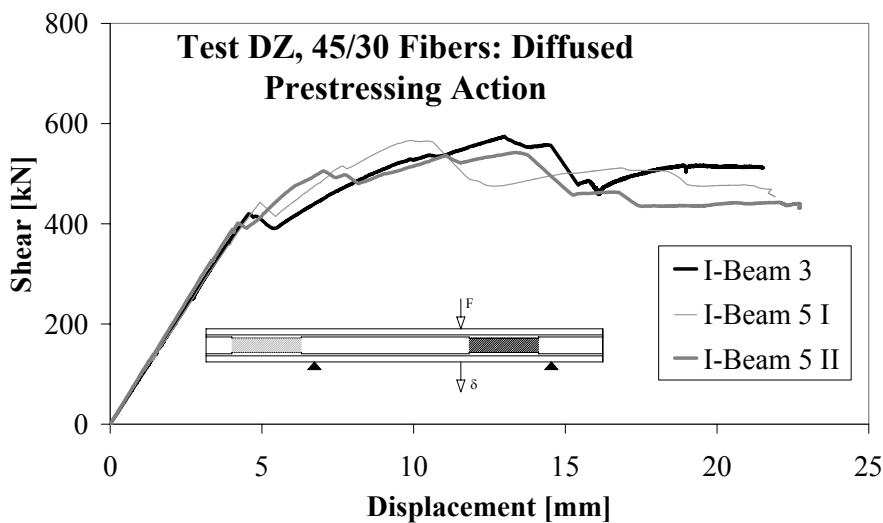
Figure 3.18: Repeatability of results: shear-displacement curves for 45/30 fibers (Beam 3 and Beam 5), test DZ.
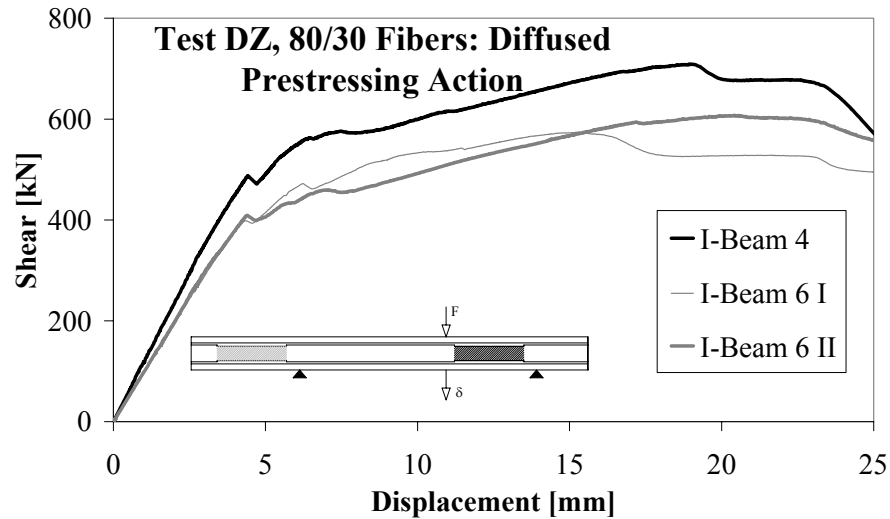
Figure 3.19: Repeatability of results: shear-displacement curves for 80/30 fibers (Beam 4 and Beam 6), test DZ.

Figure 3.20 illustrates all tests in which fibers were the only shear reinforcement provided (tests DZ: I-Beam 3 and I-Beam 5 for fibers 45/30; I-Beam 4 and I-Beam 6 for fibers 80/30). Even if the maximum load attained by the different curves is adequately similar, fibers 80/30 exhibited a greater ductility and capacity to keep cracks smaller for the same load intensity. However, for ranges of load-point displacements up to four times the displacement at first cracking, the two different fibers determined a similar structural behavior; this is the range of more interest in terms of practical applications.

In conclusion, using 80/30 fibers does result in an improvement of strength (slight) and ductility. However, the considerable cost of these fibers (approximately twice as much as 45/30 fibers) and the reduced concrete workability does not seem to justify their use for the common practical applications.

Figure 3.21 and Figure 3.22 report the width of the main cracks versus the shear force for tests TZ and DZ, respectively.

Note that the measurements of I-Beam 1 is not reported just for a small range of loading, as the energy release at first cracking was so high to detach almost all instruments located in the panel area.

The crack widths measured were quite big and grew in a relatively stable fashion, particularly in presence of fibers. By sketching a vertical line on these graphs for a given shear loading value, it is possible to appreciate the fiber contribution. By

assuming a shear value of 600 kN, in Figure 3.21, one can observe that I-Beam 2 is already under a consistent damage in the panel area (the main shear crack is in fact around 3 mm), whereas the main shear crack is 0.4 mm in I-Beam 3 and 0.1 mm in I-Beam 4.
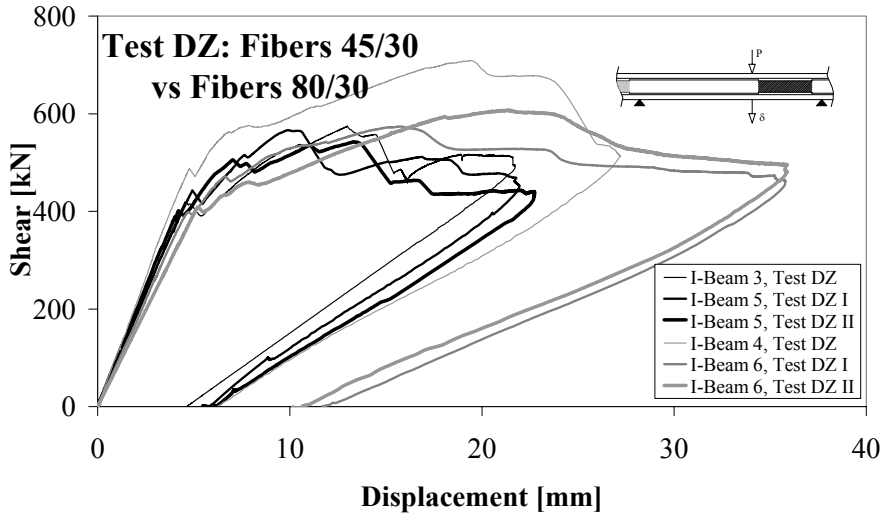
Figure 3.20: Shear-displacement curves for all tests DZ with fibers 45/30 and 80/30.
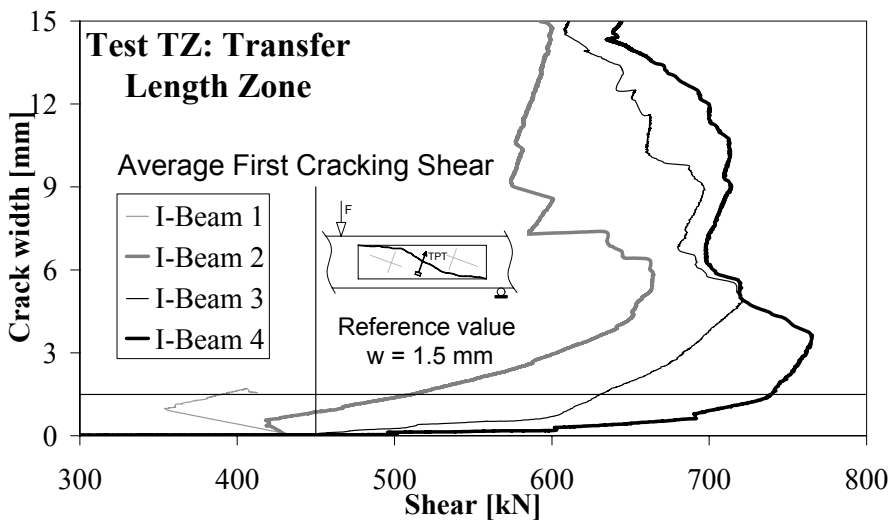
Figure 3.21: Main crack opening-shear curves for tests TZ.

Another way of comparing the shear contribution of the two fiber types adopted is to assume a reference opening value for the main crack, for instance equal to 1.5 mm, which is a value significant for ultimate conditions. At this crack opening value in the TZ zone (Figure 3.21), I-Beam 1 carries a shear force of 380 kN, I-Beam 2 (shear reinforcement according to EC2) carries a shear force equal to 560 kN, I-Beam 3 (same shear reinforcement and 45/30 fibers) a shear force of 620 kN, and I-Beam 4 (same shear reinforcement and 80/30 fibers) a shear load equal to 730 kN. The increase of shear strength due to the use of either 45/30 or 80/30 fibers is approximately equal to 12 % and 32 %, respectively, if compared to I-Beam 2. In the latter case, however, the higher concrete strength of I-Beam 4 should also be accounted for.

Concerning DZ zone (Figure 3.22), the behavior of I-Beams 2, 3 and 6 I was similar, whereas I-Beam 1 was the weakest: after a more brittle crack formation, cracking developed more easily due to the low shear transfer capacity offered by concrete itself. For a shear value of 500 kN, I-Beam 2, 3 and 6 I had a main shear crack width around 2.5 mm while 5 mm was the value measured for the plain concrete beam.
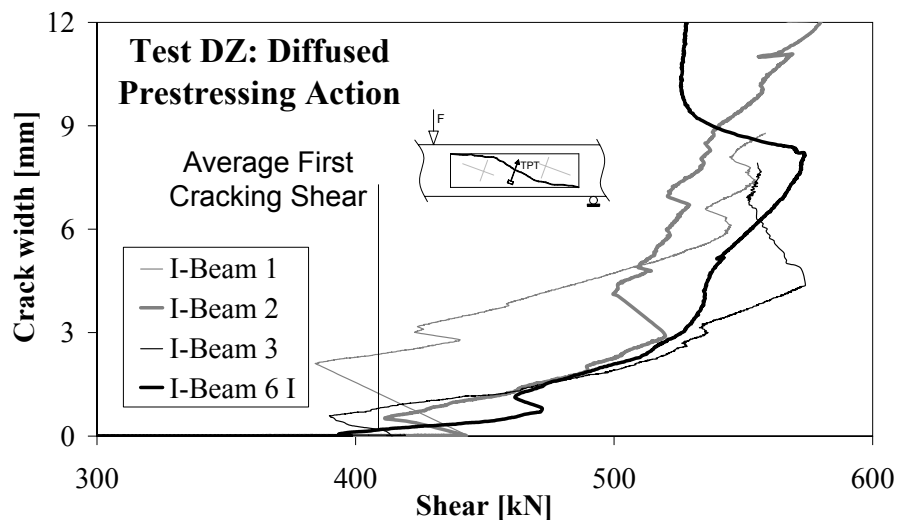
Figure 3.22: Main crack width-shear curves for tests DZ.

The performance of I-Beam 4 (with high carbon steel fibers) is again remarkable, even if it was not reported in Figure 3.22: the crack width increased more slowly, particularly just after first cracking, till a shear force value equal to 480 kN was

reached, after which the crack propagation exhibited a behavior similar to that of the other beams.

Figure 3.23 and Figure 3.24 depict the main compressive displacement- shear force curves, measured in the panel area for tests TZ and DZ, respectively. Again, in both cases it is evident the beneficial effect of fibers in reducing the strain (in this case compressive) for a given load intensity, in comparison with both plain concrete and traditional reinforcement only (I-Beam 2, test DZ). Fibers therefore provide a significant contribution even in compression, which becomes particularly important, in such structures, at ultimate states, where a pronounced arch action takes place (especially for tests DZ).
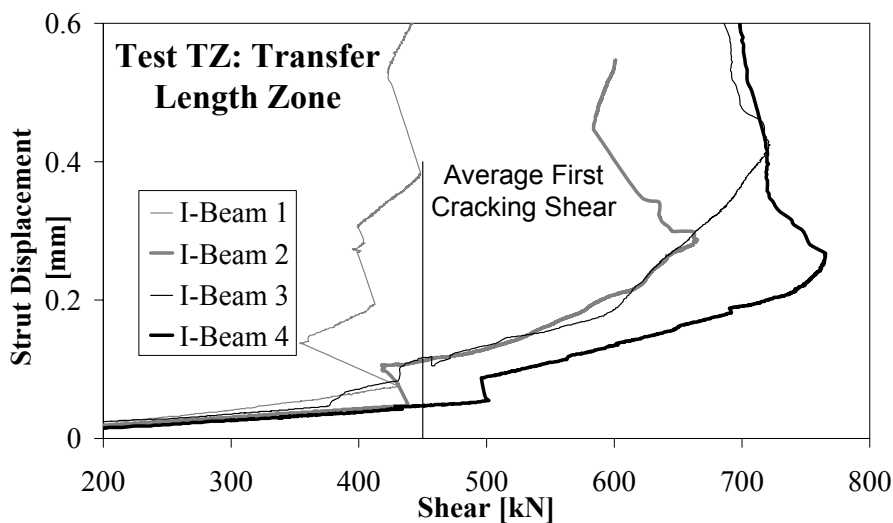
Figure 3.23: Main compression displacement-shear curves for tests TZ.

More in details, I-Beam 1, test TZ (Figure 3.23), evidences that diagonal compressive deformations are quite high and concentrated along the panel diagonal. Moreover, a huge scatter can be noticed between the response of I-Beam 1 and all other specimens. The lack of a completely diffusion of prestressing force seems to be the main reason: transverse reinforcement, either stirrups or fibers, if provided in the panel, help the distribution of prestressing forces, limiting or preventing localization of deformations.

In tests DZ (Figure 3.24) the scatter between plain concrete and the other beams is much lower, due to the completely diffusion of prestressing force. The behavior is

264

different especially at the beginning of cracking while, after the activation of the arch mechanism, all four specimens proved to behave in a similar way.
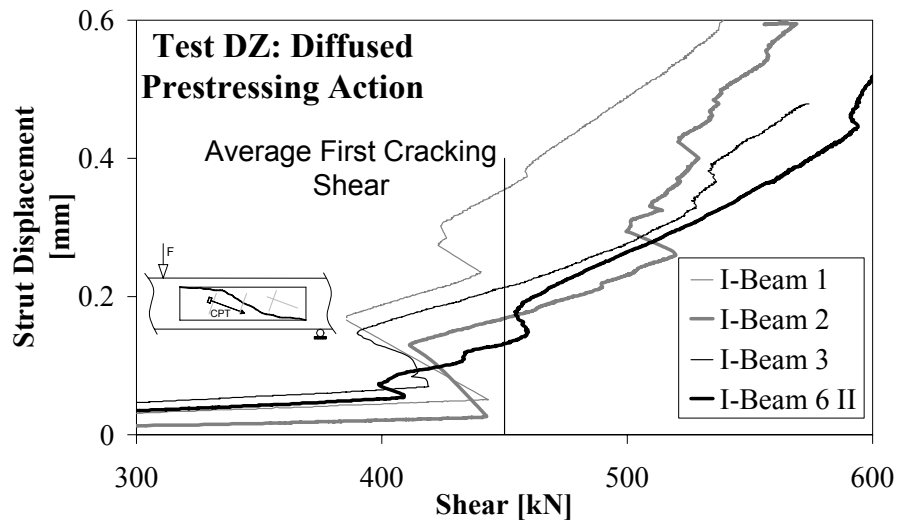
Figure 3.24. Main compression displacement-shear curves for tests DZ.

Figure 3.25 and Figure 3.26 illustrate the slippage in the central bottom cable (see Figure 3.5) for tests TZ and DZ, respectively.
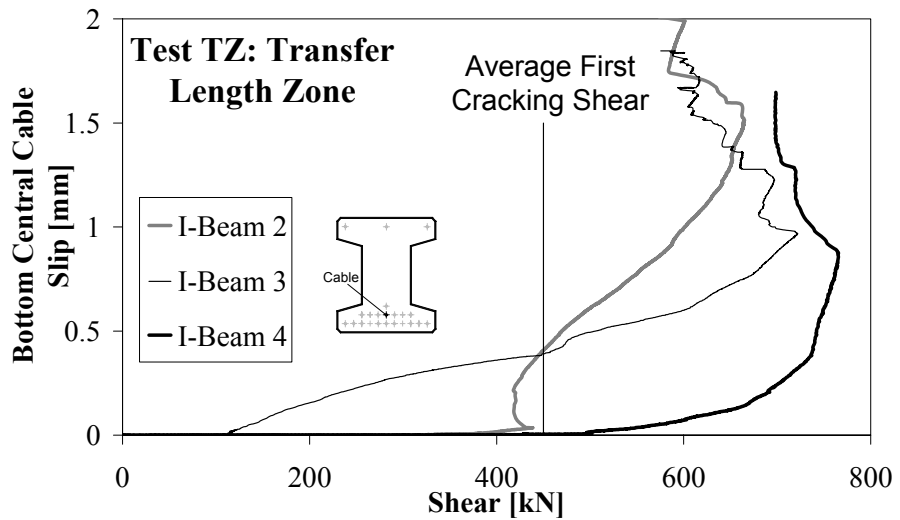
Figure 3.25: Slippage of the central bottom tendon for tests TZ.

In the former case, a significant slippage, up to 2 mm, was measured, even for low degree of damage, both for I-Beam 2 and I-Beam 3. The fact that, in the specimen with 45/30 fibers, slippage started much earlier than the first cracking occurred, is probably due to a local cracking in the transfer length caused by a mistaken positioning of the transverse reinforcement, which is critical in the bursting zone. Fibers seem to help anyway this specimen since, as the overall cracking develops, slippage in I-Beam 3 increases more slowly than slippage in I-Beam 2, which, on the contrary, starts exhibiting a greater slippage after the first cracking point. I-Beam 4 evidences, once again, the best performance.
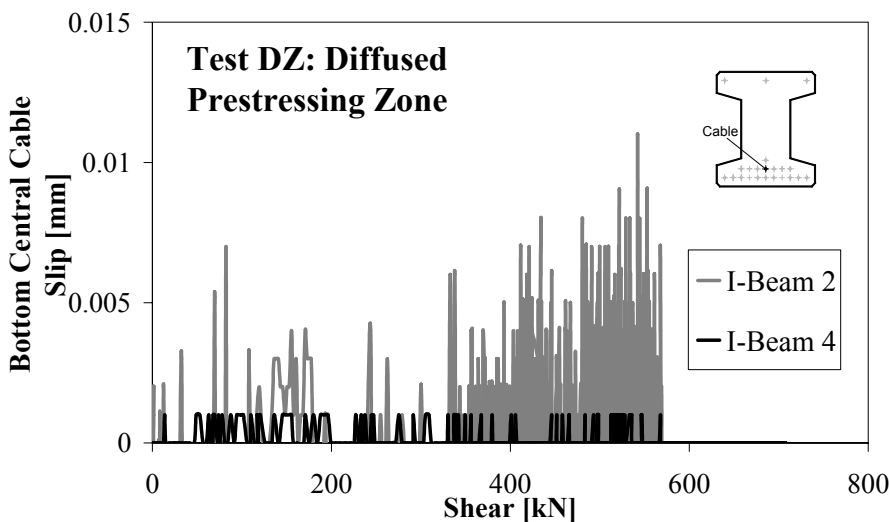
Figure 3.26: Slippage of the central bottom tendon for tests DZ.

Figure 3.27 shows the cross section of I-Beam 4, test TZ, at the end of the test. Noticeable is the slippage occurred during the test, which was measured to be more than 4 mm in some cables.

Concerning tests DZ, it is evident that significant slippage was not measured, according to the expectations, as the concentrated load is applied in a zone where prestressing action is totally diffused.

In conclusion, fibers highly influence the bond properties of concrete [2], determining a reduced slippage of tendons. In other words, fibers reduce the transfer length, i.e. the length of a specimen necessary to fully develop the prestress force and fully distribute it over the entire cross-section. Further studies

should be done in this respect, with possible advantages in practical design applications.
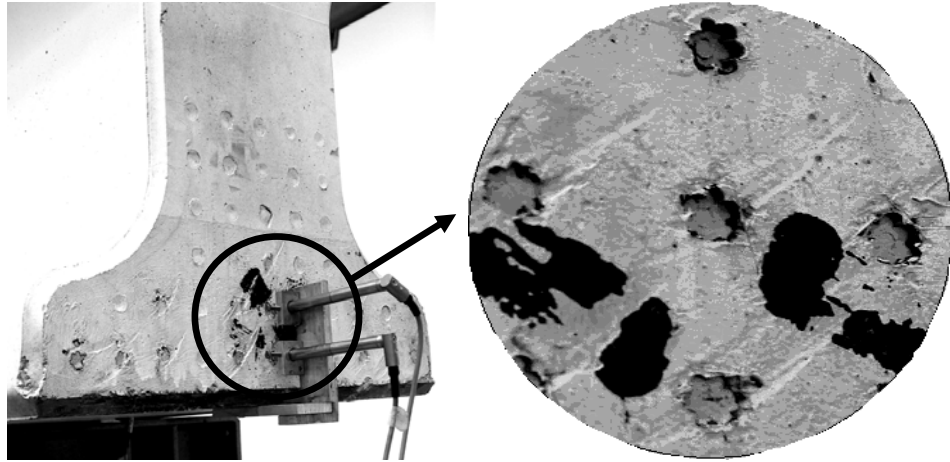
Figure 3.27: Particular of the prestressed cables at the end of test, I-Beam 4, test TZ.

Figure 3.28 and Figure 3.29 show the crack pattern evolution for TZ and DZ zones, respectively. The photographs concern three different load levels: the first corresponds to the crack onset, the second to the maximum load, while the third regards the final crack pattern.

Tests TZ will be discussed first (Figure 3.28). In I-Beam 1, a single wide crack occurs at the beginning of cracking and grows without formation of adjacent cracks. This proofs that there is a strong localization of stresses, leading to the formation of a single macro-crack oriented as the panel diagonal. I-Beam 2 exhibits at the onset of non linearity, a more controlled crack pattern, made of few inclined cracks oriented according to the classical truss mechanism (which differs from the panel diagonal). These cracks, by growing, tend to merge into a single macro-crack, flatter than the original ones and inclined, more or less, as the panel diagonal. Spalling of concrete at the bottom right corner of the experimental area (panel) is also noticeable.

In I-Beam 3 and I-Beam 4 the crack formation arises in a similar way to that shown by I-Beam 2. However, from the classical truss mechanism, cracking develops in a more distributed, even though more difficult to predict, way, leading to smaller cracks for a given load intensity and hence to a greater ductility. The third picture of I-Beam 4 in Figure 3.28 clearly shows the initial development of few inclined parallel

cracks (having a spacing about twice as much as the stirrup spacing) and a wider crack, which developed at the ultimate states.

I-Beam 1

I-Beam 2
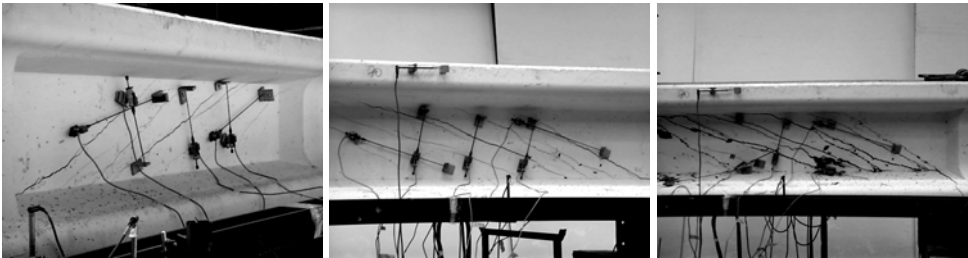
I-Beam 3

I-Beam 4

Figure 3.28: Crack pattern evolution in TZ zone of the four beams.

With regard to test DZ, I-Beam 1 and I-Beam 2 evidences a similar crack onset, again influenced by the panel geometry. The effect of the mesh fabric (I-Beam 2) induces a widening of the resistant compression strut but no evident truss

mechanism is observed as it was in the corresponding test TZ. Spalling is once again observed in I-Beam 2.

I-Beam 1
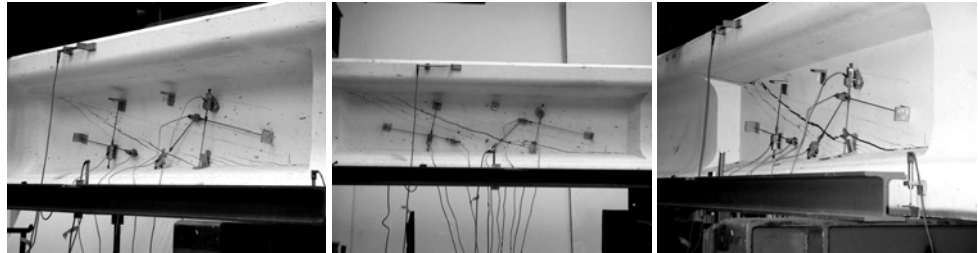
I-Beam 2

I-Beam 3
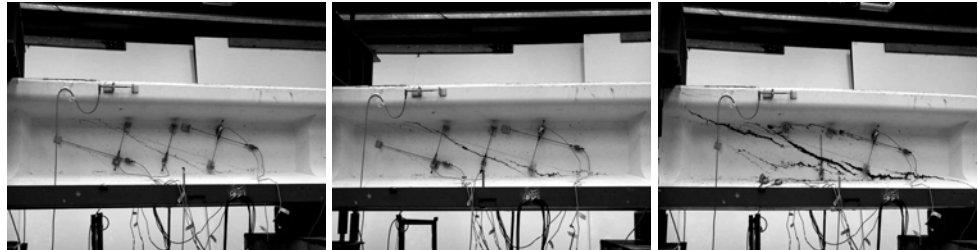
I-Beam 4

Figure 3.29: Crack pattern evolution in DZ zone of the four beams.

A more complex crack development concerns I-Beam 3 and I-Beam 4, which are characterized by a more diffused cracking that, particularly at ultimate limit states, determines a wider strut resistant area (see the central area delimited by the two

wide cracks both in I-Beam 3 and I-Beam 4) with a corresponding increase in bearing capacity. This further confirms the ability of fibers in reducing the damage in tension and therefore in providing a higher residual compressive strength.

Figure 3.30 depicts in details the progressive formation of the strut, governed by arch action, in I-Beam 4, test DZ. Fibers proved to be highly positive in this respect, as they determined a wide resistant area, capable of bearing further loading.
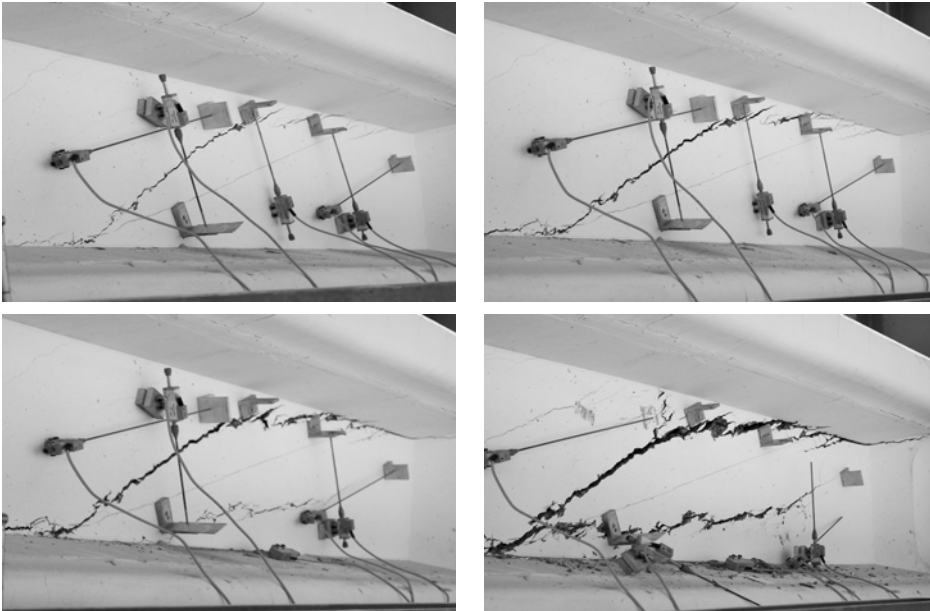
Figure 3.30: Crack development in the panel area with progressive formation of a resistant strut, I-Beam 4, test DZ.

Figure 3.31 illustrates the crack pattern of tests DZ for I-Beam 5 and 6 (two tests DZ in each beam). These crack developments further confirm the capacity of fibers to redistribute stresses in a wider area, thus allowing the structure to resist higher loading. In some pictures, at the ultimate states (third photograph, see especially I-Beam 6 I and I-Beam 4, test DZ, in Figure 3.29) it is possible to notice that cracking tends to move towards both the point load and the nearest support through the stiff flanges, emphasizing that arch action becomes quite influential on the overall response.

It should be noticed that the resisting mechanism for Beams 2, 3, and 4, initially showed a distributed crack pattern in the panel, that eventually developed with a progressive rotation during which the cracks merged, leading to a single macro crack oriented as the diagonal of the panel. This progressive phenomenon is the

270

cause of the several small unloadings observed in the shear-displacement curve (Figure 3.16, Figure 3.17, Figure 3.18 and Figure 3.19).

I-Beam 5 I

I-Beam 5 II

I-Beam 6 I
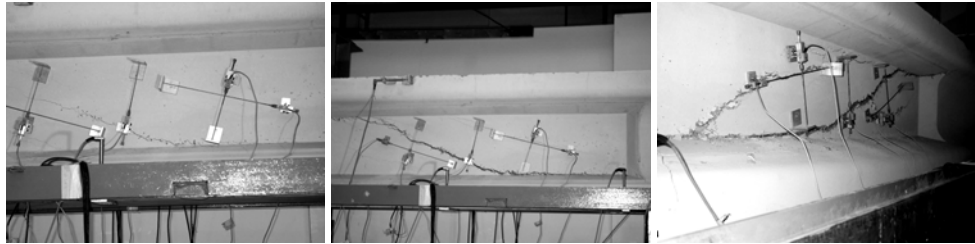
I-Beam 6 II

Figure 3.31: Crack formation and development, tests DZ, I-Beam 5 and I-Beam 6.

The deformations of the upper and lower flange of the specimens were also recorded. That was done by measuring the compression and the tension, respectively over a base length of 115 mm for all beams. Figure 3.32 and Figure 3.33 show the comparison of the measurements in the top flange, for tests TZ and

271

DZ respectively. One should recognize that, after a certain damage, the flange in tests DZ start measuring tension in the top flange, owing to the formation of a crack towards the load point related to the arch action (see Figure 3.34), which takes place especially where prestressing force is completely diffused. In tests TZ, on the contrary, the behavior is linear and then the measurements keep constant for a certain range. Close to the completion of the test, i.e. in presence of a big damage, the measurements tend to decrease, confirming the probable instauration of a different stress field in that region, eventually accompanied by the formation of a crack toward the point load. However, this fact is not totally clear in tests TZ.
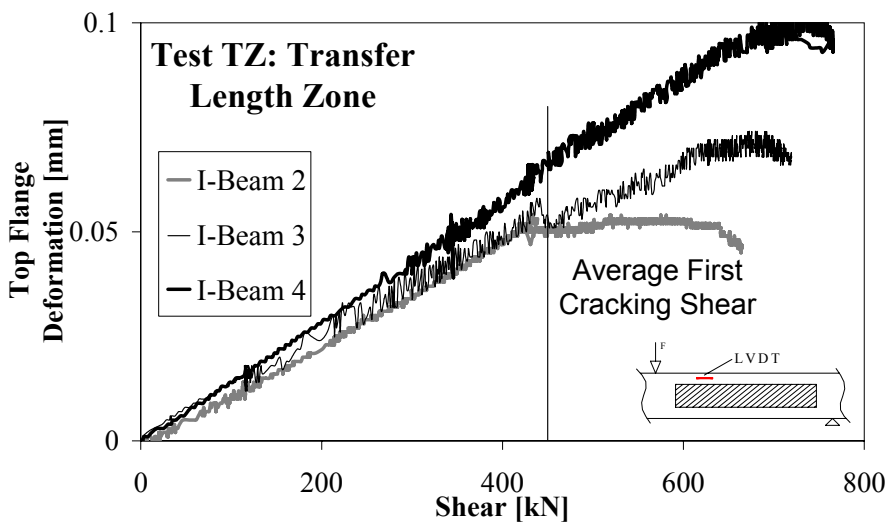
Figure 3.32: Comparison of displacements at the top flange, above the panel area, test TZ (compression is positive).

Figure 3.35 and Figure 3.36 report the comparison of displacements measured at the bottom flange, both in tests TZ and DZ. Here the behavior is totally comparable between the two tests, and agrees to the classical development of deformations in the bottom flange of a member subjected to flexure, according to the beam theory (on the contrary, the deformation in the top flange, especially in tests DZ, were quite influenced by the near point load and by the instauration of arch action, which is not a sectional phenomenon).

Quite small flexure cracks appeared in the bottom flange, according to the design philosophy of those beams. So, in this respect, the overall behavior was almost the same for all beams and no significant influence of fibers could be reported.
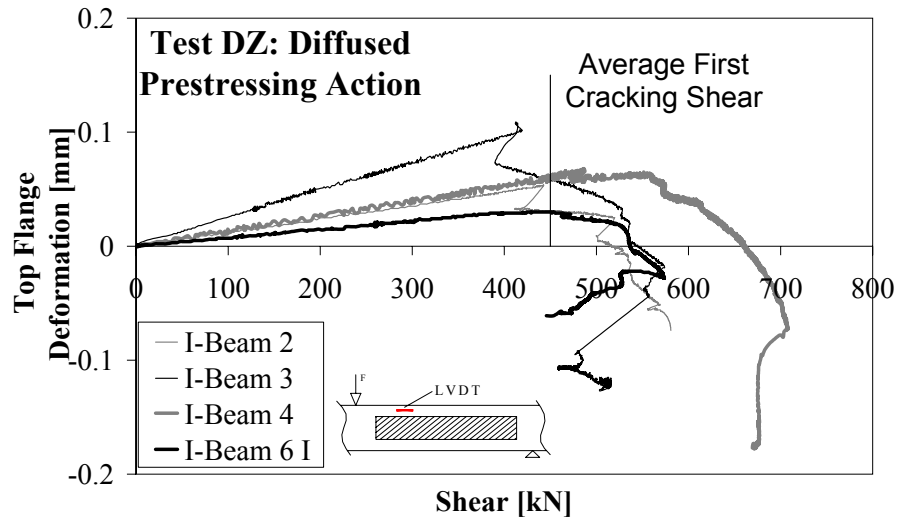
Figure 3.33: Comparison of displacements at the top flange, above the panel area, test DZ (compression is positive).
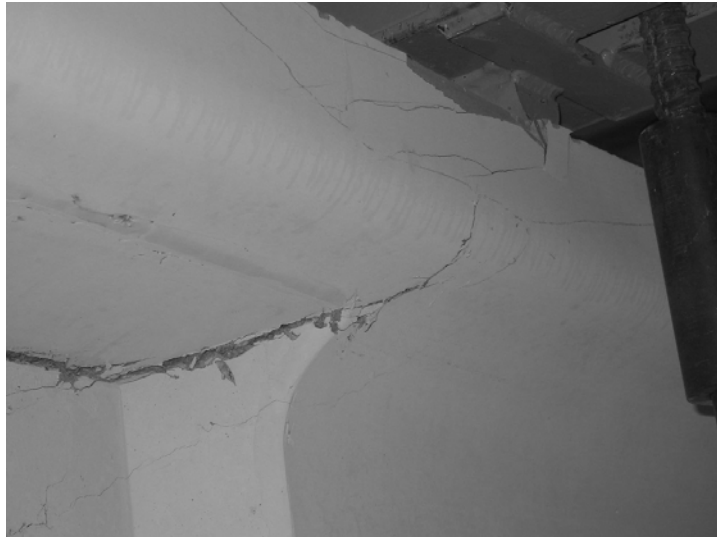
Figure 3.34: Cracking toward the point load, I–Beam 6 I, test DZ.
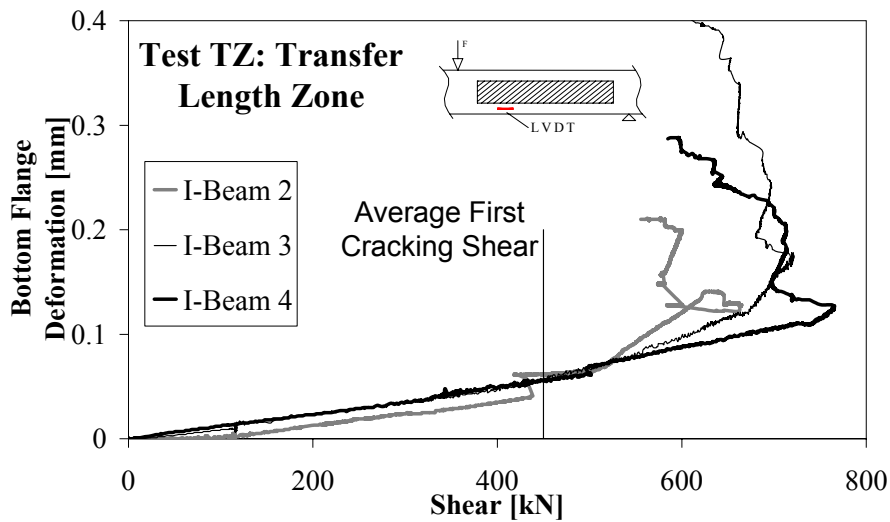
Figure 3.35: Comparison of displacements at the bottom flange, below the panel area, test TZ (tension is positive).
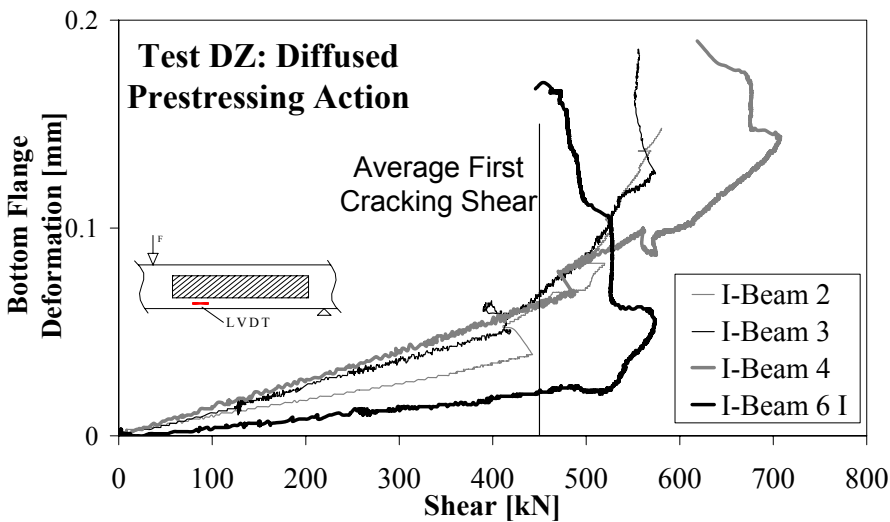
Figure 3.36: Comparison of displacements at the bottom flange, below the panel area, test DZ (tension is positive).

Table 3.10 summarizes the experimental results in terms of load at first cracking, maximum load and values of displacements in different points:

- The *front* and *back* displacements are the vertical displacements at the load point location, measured in both front and back side in order to consider

possible rigid overall displacement of the specimen. The *mean* value is intended to be the average of the two;

- The *right* displacement was measured in the middle between the loading point and the furthest support (point D in Figure 3.11);
- The *left* displacement was measured in the middle of the panel area designed for shear failure (point C in Figure 3.11).

Beam	Test	F_{crack}	F_{max}	F_{max}/F_{crack}	Displacement Beam [mm]				
					Mean	Front	Back	Right	Left
I-Beam 1	TZ	707		1.04	4.93	4.73	5.13	+)	+)
			737		14.28	14.70	13.86	+)	+)
	DZ	727		1.26	5.05	4.83	5.27	4.38	3.63
			916		16.17	16.88	15.47	15.75	9.09
I-Beam 2	TZ	719		1.52	4.49	4.67	4.31	3.13	3.29
			1090		13.00	13.26	12.74	11.70	8.34
	DZ	726		1.31	4.87	4.81	4.93	3.39	3.82
			952		17.07	17.33	16.82	16.82	10.47
I-Beam 3	TZ	708		1.67	4.81	5.04	4.58	3.48	3.51
			1183		13.95	14.27	13.63	12.06	9.21
	DZ	687		1.37	4.55	4.50	4.59	3.04	3.24
			941		12.99	11.26	14.72	9.78	4.52
I-Beam 4	TZ	823		1.53	5.28	5.40	5.15	3.57	3.94
			1255		14.00	13.92	14.07	10.96	9.22
	DZ	798		1.45	4.78	4.89	4.70	3.46	3.49
			1161		19.43	19.12	19.77	18.66	11.53
I-Beam 5	DZ I	725		1.28	4.93	4.82	5.05	3.19	3.50
			927		9.91	9.68	10.14	8.32	6.37
	DZ II	657		1.35	4.22	4.18	4.26	2.79	3.07
			888		13.34	13.07	13.62	12.23	8.07
I-Beam 6	DZ I	652		1.44	4.72	4.91	4.52	3.36	3.56
			939		15.74	15.69	15.80	14.66	9.61
	DZ II	669		1.49	5.21	5.19	5.22	3.47	3.65
			995		21.31	20.67	21.95	20.25	12.07

+) *Not measured.*

Table 3.10: Experimental results with respect to the first cracking load, maximum load and deflections in different points.

Table 3.11 and Table 3.12 summarize the experimental values measured for the potentiometric instruments disposed in the panel area (experimental zone); the

former presents the crack widths values whereas the latter reports the displacements along the strut direction.

| Beam | Test | Load [kN] | | Displacement Tension members [mm] | | | | | | |
		F_{crack}	F_{max}	TPT 1	TPT 2	TPT 3	TPT 4	TPT 5	TPT 6	Max.
I-Beam 1	TZ	707		0.00	0.09	0.07	0.16	0.22	+)	1.72
			737	*)	*)	*)	*)	*)	+)	
	DZ	727		0.01	0.02	0.01	0.03	0.02	0.00	8.79
			916	8.78	*)	*)	*)	*)	8.41	
I-Beam 2	TZ	719		0.01	0.02	0.02	0.03	0.03	0.01	15.86
			1090	3.44	4.38	4.31	5.82	4.29	3.52	
	DZ	726		0.00	0.02	*)	0.00	0.02	0.00	12.58
			952	10.82	12.07	*)	*)	12.09	9.97[1)]	
I-Beam 3	TZ	708		0.03	0.04	0.03	0.01	0.01	0.02	20.28
			1183	4.96	4.93	1.82	4.78	1.55	2.52	
	DZ	687		0.03	0.03	0.03	0.02	0.04	0.03	13.00
			941	0.23	4.38	5.98	6.83	7.83	0.54	
I-Beam 4	TZ	823		0.05	0.05	0.03	0.06	0.02	0.11	19.34
			1255	2.98	3.63	3.05	2.57	3.89	3.02	
	DZ	798		0.03	0,04	0.05	0.05	0.02	0.01	19.15
			1161	*)	12.48	10.98	0.22	12.40	*)	
I-Beam 5	DZ I	725		0.03	0.04	0.03	0.04	0.03	0.01	8.40
			927	2.13	2.51	3.36	0.06	2.47	0.17	
	DZ II	657		0.01	0.02	0.02	0.02	0.02	0.02	6.83
			888	4.99	1.94	1.37	1.30	1.92	4.63	
I-Beam 6	DZ I	652		0.01	0.02	0.04	0.00	0.01	0.01	19.83
			939	7.35	1.64	0.85	0.67	8.12	6.95	
	DZ II	669		0.02	0.01	0.01	0.04	0.01	0.03	23.94
			995	12.62	14.31	11.70	0.24	12.71	9.83	

*) Instrument failed during test.
+) Not measured for this beam.
[1)] Instrument over ranged

Table 3.11: Experimental results with respect to the crack widths measured by means of potentiometric instruments in the panel area.

Beam	Test	Load [kN]		Displacement Compression members [mm]					
		F_{crack}	F_{max}	CPT 1	CPT 2	CPT 3	CPT 4	CPT 5	Max.
I-Beam 1	T Z	707		0.00	0.09	0.07	0.20	0.207	0.62
			737	*)	*)	0.62	*)	*)	
	D Z	727		0.00	0.01	*)	0.05	+)	1.35
			916	0.82	0.48	*)	1.19	+)	
I-Beam 2	TZ	719		0.05	0.06	0.05	0.08	+)	0.55
			1090	0.29	0.42	0.33	0.47	+)	
	DZ	726		0.03	0.04	0.05	0.03	+)	0.77
			952	0.64	0.49	0.57	0.53	+)	
I-Beam 3	TZ	708		0.06	0.15	0.09	0.05	+)	1.17
			1183	0.31	0.52	0.42	0.26	+)	
	DZ	687		0.07	0.06	0.06	0.06	+)	0.72
			941	0.48	0.34	0.39	0.53	+)	
I-Beam 4	TZ	823		0.05	0.08	0.08	0.06	+)	1.66
			1255	0.27	0.39	0.38	*)	+)	
	DZ	798		0.05	0.06	0.06	0.03	+)	0.82
			1161	0.51	0.48	0.50	0.31	+)	
I-Beam 5	DZ I	725		0.06	0.05	0.04	0.05	+)	1.49
			927	0.35	0.21	0.23	0.29	+)	
	DZ II	657		0.04	0.03	0.04	0.06	+)	1.55
			888	0.21	0.55	0.59	0.44	+)	
I-Beam 6	DZ I	652		0.05	0.04	0.04	0.07	+)	1.76
			939	0.55	0.44	0.48	0.37	+)	
	DZ II	669		0.06	0.03	0.05	0.04	+)	2.44
			995	0.53	0.65	0.57	0.58	+)	

*) Instrument failed during test.
+) Not measured for this beam.

Table 3.12: Experimental results with respect to the compressive displacements measured by means of potentiometric instruments in the panel area.

Figure 3.37 reproduces a histogram summarizing all tests performed, giving indication of the load at first cracking, the maximum load attained and the ratio of the two. The latter parameter evidences the post-peak characteristics of the different beams. Once again, one can confirm that fibers at least provides the same

post-peak strength of the fabric mesh, giving in addition more crack control and enhanced ductility.
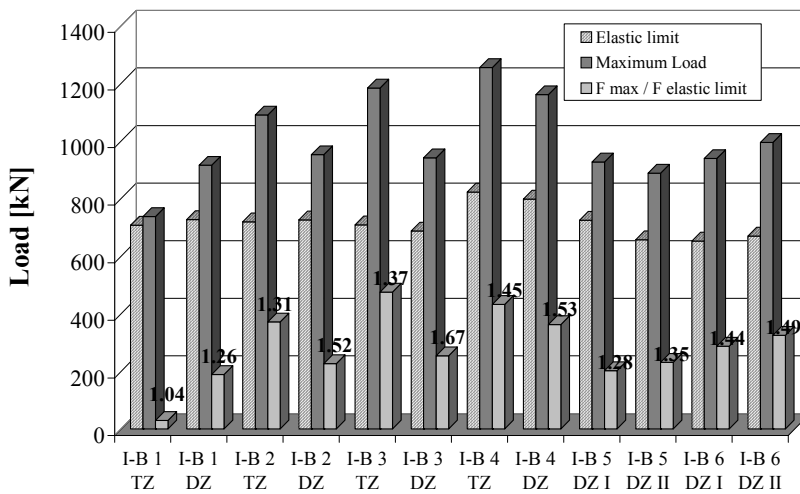
Figure 3.37: Comparison of load values for the different specimens.

3.6   Standard Overview.

A discussion of the experimental results in light of the provisions given by RILEM Recommendation on fiber reinforced concrete design [2.157], and EC2 [2.82] (which is limited to reinforced concrete structures without fibers) and other analytical models is herein presented. First of all, the discussion will be limited on RILEM and EC2 provisions, as the former is intended to be an extension of the actual European Code. The two standards are therefore homogeneous and suitable for an in-depth comparison. The second step of this discussion will focus on other models for predicting the ultimate shear capacity of a beam made of SFRC, as already shown in Chapter 2, Section 2.8.9.

Table 3.13 shows the value of each shear strength contribution (concrete, stirrups, mesh and fibers) calculated according to EC2 Standard Method, EC2 Variable-Angle Truss Model and RILEM Provision. The shear strength is also determined according to a Variable-Angle Truss Model assuming $\lambda = \cot \theta = 4.0$ ($\theta = 14°$), where θ is the inclination of the compression strut on the beam axis (which is the maximum possible value of λ for the given geometry of the panel tested, see Figure 3.3). Note that some values were already calculated in Section 3.3, which dealt with the design aspects of these beams.

278

Contribution	Experiments	EC2 Standard [2.82]	EC2 Var. Inc. $\lambda = 2.5$	RILEM [2.157]	Var. Inc. $\lambda = 4.0$
Transfer Length zone "TZ"					
Shear reinforcement (stirrups ϕ6/100)					
Concrete	443	278	0	274	0
Stirrups	219	152	404	152	646
Total	**662**	**430**	**404**	**426**	**646**
Shear reinforcement (stirrups ϕ6/100)+ 45/30 fibers					
Concrete	443	278	0	274	0
Stirrups	285	152	404	152	646
Fiber		0	0	35	0
Total	**728**	**430**	**404**	**461**	**646**
Shear reinforcement (stirrups ϕ6/100)+ 80/30 fibers					
Concrete	443	278	0	274	0
Stirrups	327	152	404	152	646
Fiber		0	0	163	0
Total	**770**	**430**	**404**	**589**	**646**
Diffused prestressing action "DZ"					
Minimum shear reinforcement (mesh ϕ5/200)					
Concrete	443	278	0	274	0
Mesh	138	68	165	68	264
Total	**582**	**346**	**165**	**342**	**264**
45/30 fibers only (I-Beam 3)					
Concrete	443	278	0	274	0
Fiber	131	0	0	35	0
Total	**574**	**278**	**0**	**309**	**0**
80/30 fibers only (I-Beam 6 II)					
Concrete	443	278	0	274	0
Fiber	165	0	0	163	0
Total	**608**	**278**	**0**	**437**	**0**
NB. All values are in kN					

Table 3.13: Resistance shear contributions.

The experimental shear strength assumed for the comparison represents the mean value of the measured maximum loads of each beam tested. The experimental concrete strength contribution was conventionally assumed as equal (for all beams) to the first cracking load of I-Beam 1 (Figure 3.16 and Figure 3.17) without transverse reinforcement. Note that, since no significant differences were observed between TZ and DZ zones of I-Beam 1 (Figure 3.16 and Figure 3.17), the concrete strength contribution was assumed to be equal for both zones.

An explanation of this could be given by observing that the prestressing action, even in the transfer length zone (test TZ), may be totally diffused in the middle of the experimental zone, where the first crack appeared. Moreover, the rate of diffusion of the prestressing force proved to highly influence the post-peak behavior more than the elastic (see I-Beam 1, test TZ, versus I-Beam 1, test DZ).

The shear strength contribution due to stirrups, mesh fabric, or fibers, was conventionally assumed, for the other beams, to be equal to the difference between the observed maximum shear strength and the shear strength of I-Beam 1.

In order to better compare the experimental results and the code provisions, the partial safety factors for materials (γ_c and γ_s) were assumed to be equal to 1, whereas all other limitations, i.e. the maximum longitudinal reinforcement ratio, were strictly took into account.

For all beams tested, the concrete strength contribution, if estimated according to the "old" edition of EC2 [2.82] provisions, is almost equal to 75% of the experimental value while, if computed according both to RILEM and the "new" edition of EC2 [3], it is approximately equal to 62% of the experimental value.

Moreover, the old EC2 and RILEM underestimate the strength contribution offered by steel reinforcement (mesh fabric or stirrups) when the "Standard Method" is adopted. Assuming the EC2 variable angle truss model, the upper limit for the truss provided by EC2 ($\lambda_{max} = \cot \theta = 2.5$) seems too restrictive; in fact, by assuming $\lambda = 4.0$, a more accurate strength prediction is obtained for tests DZ.

It should be observed that, when the minimum shear reinforcement required by EC2 is provided by mesh fabric alone, the variable angle truss model significantly underestimates the experimental value due the "arch action" that developed for wide opened cracks.

As far as fiber reinforced concrete is concerned, the most recent RILEM provisions account for fiber strength contribution as an addendum that depends on the post-cracking residual tensile strength of the material that is related to the ultimate limit state ($f_{r,4}$) [2.157].

280

In the present research work, SFRC characterization was carried out according to the Italian Standard [2.125], which is based on four point bending tests on a notched beam having a span of 450 mm and a cross section of 150x150mm (see Chapter 5 for details). On the contrary, RILEM provisions are based on three point bending tests on beams having a similar span (500 mm instead of 450 mm) and the same cross section with a shorter notch (25 mm instead of 45 mm). Both test methods refer to residual strengths (named as an equivalent post-cracking strength in the Italian Standard) that, although different, are related to serviceability or ultimate limit states. The equivalent strength significant for the ultimate limit state from the Italian Standard is ($f_{eq(0.6-3.0)}$), whereas the RILEM test refers to $f_{r,4}$ (See Section 2.8.4 for the details concerning the Italian Standard, whereas Section 2.8.9.2 dealt with the RILEM Final Recommendation).

Figure 3.38 shows the experimental load-displacement curves for the four point bending beams tested, 4 cast with 45/30 fibers, and 4 cast with 80/30 fibers. The equivalent strength ($f_{eq(0.6-3.0)}$) was found to be equal to 2.18 MPa and 8.61 MPa for 45/30 fibers and 80/30 fibers, respectively.
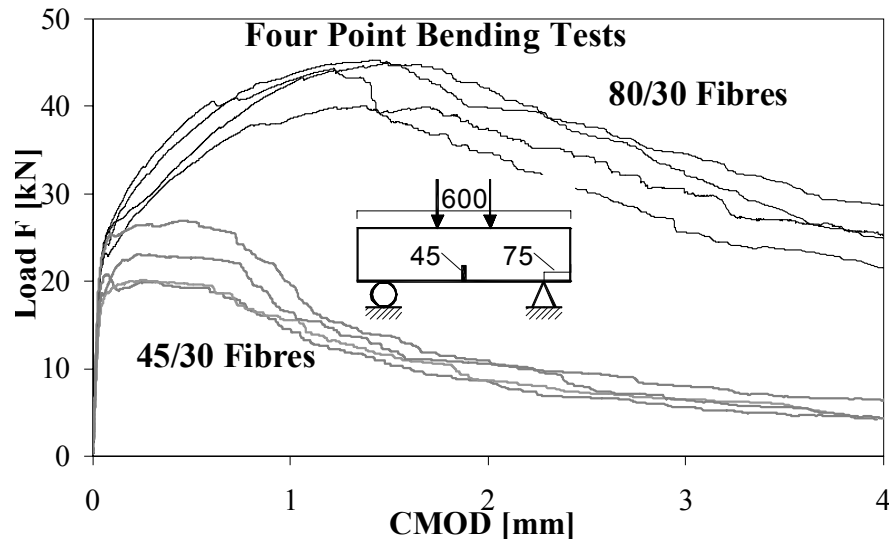
Figure 3.38: Load-CMOD curves from four point bending tests using 45/30 and 80/30 fibers.

An approximate value of the residual tensile strength required by RILEM ($f_{R,4}$) was determined from the results of the four-point bending test by using the procedure suggested by RILEM for the three-point bending test. In doing so, the computed $f_{R,4}$ was equal to 2.36 MPa for 45/30 fibers and to 11.07 MPa for 80/30 fibers. The

considerable differences between the two types of fibers (according to both Recommendations) is not reflected in the full-scale beams because of the presence of other shear resistant mechanisms, which have a greater impact on the beam response (Table 3.13).

By considering the above mentioned approximation, DZ tests show that fiber resistance contribution calculated according to RILEM, is smaller than the experimental one, particularly for 45/30 fibers (35 kN versus 131 kN, equal to 27% of the experimental value, Table 3.13). A quite great estimation was instead obtained when considering 80/30 fibers (163 kN versus 165 kN, equal to 99% of the experimental value).

The experimental results presented in Table 3.13 clearly demonstrate, once again, that fibers may effectively substitute the required minimum shear reinforcement; in fact, the strength contribution provided by the mesh fabric was found to be equal to 138 kN while that of fibers was equal to 131 kN for 45/30 fibers and 163 kN for 80/30 fibers. In addition, as already discussed, a better structural behavior was observed in SFRC beams (Figure 3.17)

Figure 3.39 and Figure 3.40 illustrate the experimental shear-displacement curves in comparison with the prediction of EC2, Standard method, both for tests TZ and tests DZ. All calculations were performed for I-Beam 2, the only specimens that can be verified within the current design provisions. It should be emphasized that the ultimate shear strength for test TZ, if calculated according to EC2 by assuming the actual values of the material partial safety factors (γ_c = 1.5, γ_s = 1.15), is equal to 380 kN (while the value shown in Table 3.13, equal to 430 kN, was calculated neglecting all material coefficients). This shear value is considerably smaller than the first cracking load, similar for all beams and it is equal to 57% of the experimental maximum load (Figure 3.39). Using the variable-angle truss method would have been even more conservative.

Regarding tests DZ, the ratio between the predicted value of EC2 and the maximum experimental shear (I-Beam 2, test DZ) is equal to 0.43.

EC2 is definitely more conservative for test DZ, probably owing to the presence of only a minimum shear transverse reinforcement.

In all cases, it is interesting to notice that all values are below the first cracking point, where no rebar nor transverse reinforcement nor fiber can significantly influence the overall behavior of the specimens.
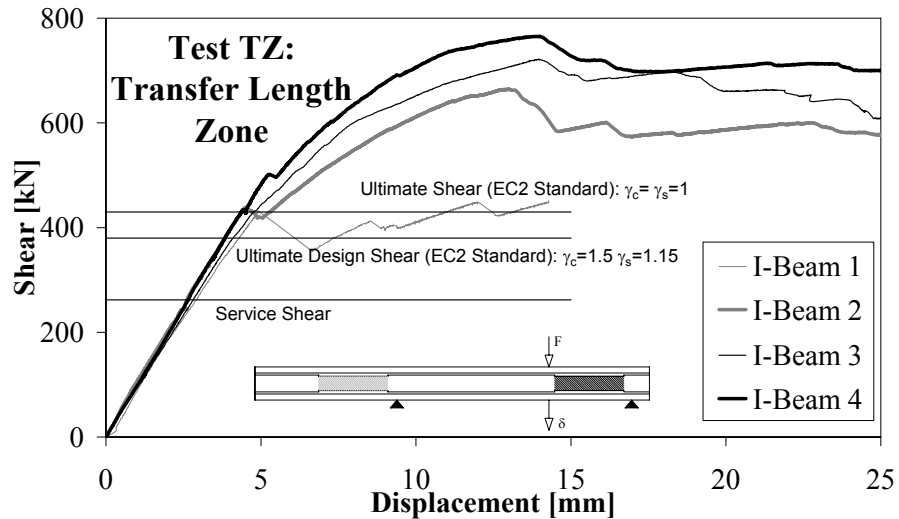
Figure 3.39: Experimental curves against predictions of EC2, tests TZ.
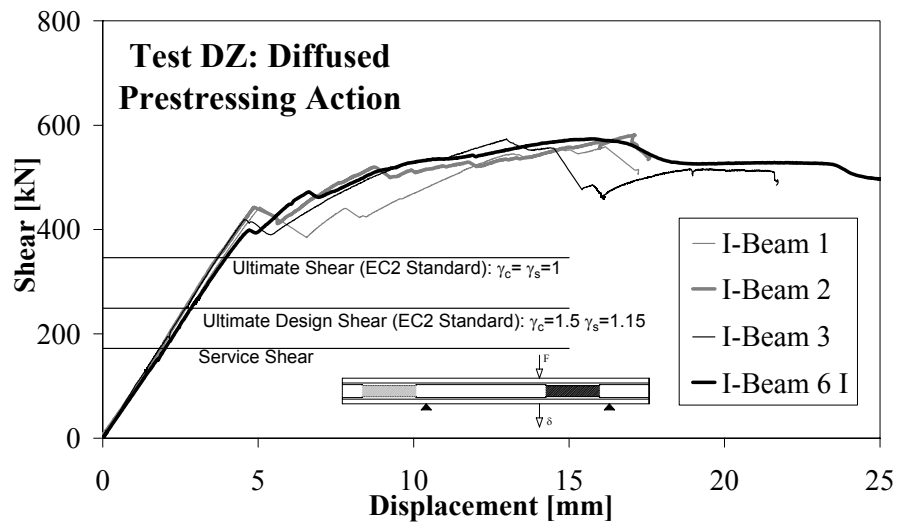
Figure 3.40: Experimental curves against predictions of EC2, tests DZ.

With regards to fibers only, further considerations can be done concerning the ability of the principal analytical methods presented in Section 2.8.9 in predicting the shear capacity of the set of prestressed I-Beams inhere presented.

The models of RILEM [2.157], Ashour et al. [2.171], Imam et al. [2.158], and Narayanan et al [2.175]. will be compared in the following discussion.

With the exception of RILEM, all the other formulations calculate the resistance capacity due to fibers as a component of the concrete contribution, while RILEM identifies a fiber component alone.

If missing, a contribution due to prestress action was added, corresponding to the one prescribed by the latest EC2. The prestress contribution was therefore identical in each model. In addition, all formulations, except RILEM, neglect the effect of the two huge flanges (Figure 3.3), which stiffen the structure and therefore increase the shear resistance.

The calculations were performed assuming the measured mean material properties, without using any partial safety coefficient. Only tests DZ of I-Beam 3, I-Beam 4 and I-Beam 6 II were considered in the calculation (fibers are the only shear reinforcement provided), in order to focus the discussion just on the effect of fibers, without analyzing stirrup contribution or stirrup/fiber interaction.

Table 3.14 reports the results for I-Beam 3, I-Beam 4 and I-Beam 6 II, test DZ, in comparison with the experimental ultimate value.

It can be said the all formulations really underestimate the ultimate shear capacity of these beams.

Even with this respect, RILEM proves to be a quite conservative model, and, moreover, does not give a simple formulation based on fiber and concrete parameters. Rather, it is based on a flexural fracture mechanics three point bending test. However, since numerical modeling of SFRC structures by means of a proper tension softening law proved to be a simple and quite accurate procedure [4], using a post-cracking material property, like an "equivalent post-peak stress", as RILEM does, should be the right design approach of SFRC elements.

Nevertheless, the different post-peak behavior is definitely related to the concrete matrix, hence fiber shear contribution should be incorporated into the concrete one and thus should not appear as a separate addendum.

Designation	Beam 3, DZ Test		Beam 4, DZ Test		Beam 6 II, DZ Test	
Experimental Shear [kN]	574	$V_{experimental}/V_{analytical}$	709	$V_{experimental}/V_{analytical}$	608	$V_{experimental}/V_{analytical}$
RILEM [kN]	309	1.86	437	1.62	439	1.38
Ashour [kN]	348	1.65	389	1.82	383	1.59
Imam [kN]	427	1.34	489	1.45	481	1.26
Narayanan [kN]	354	1.62	395	1.80	388	1.57

Table 3.14: Experimental and predicted shear capacity of Beam 3, Beam 4 and Beam 6 II, DZ test.

284

The best predictions were obtained by Imam formulation, which was developed for SFRC high strength concrete beams using a fracture mechanics approach [2.158].

Further studies on size effect, normal and high strength concrete, in terms of different brittleness and shear contribution of concrete alone, are stringent and should take into consideration in order to find a design or prediction method both feasible and reliable.

No one of the models above mentioned emphasized the effectiveness of fibers in increasing the residual compressive strength, which was one of the main results of the present work. Therefore, further studies are necessary to find a design method that could take into account fibers in the strut resistance check formulas, based on concrete crushing, prescribed by many Codes (i.e. $V_{rd,max}$ in EC2).

3.7 Concluding Remarks.

In this chapter, the experimental results of shear tests on full scale prestressed beams were presented. The aim of the research was to compare beams with transverse reinforcement and/or a low volume fraction (V_f = 0.64 %) of hooked steel fibers, in order to investigate the fiber contribution as a shear reinforcement and the possibility of substituting the minimum shear reinforcement with steel fibers.

The experiments simulated both the beam behavior close to the supports, where stirrups are usually designed to resist shear, and at midspan, where only a minimum shear reinforcement is usually required by building codes.

The experimental results showed that the beams reinforced only with steel fibers have a similar, or even better, post-cracking behavior than the beams with the minimum amount of transverse reinforcement: results from six tests (three specimens, DZ tests, for each of the two types of fibers adopted) confirmed this important evidence.

In prefabrication, this is particularly appealing for facilitating the industrialization of the production and introducing an improvement in the overall characteristics and durability of the products. Moreover, reducing in handling and placing of rebars, with a consequent possibility of saving labor and money, should be considered.

When fibers were used in addition to conventional transverse reinforcement the shear strength significantly increased. Steel fibers also reduced the width of shear cracks, thus improving also durability.

Steel fibers turned out to be really effective even in increasing the residual compressive stress, which governed the experimental behavior when arch action occurred, in tests DZ especially.

The shear strength evaluated according to the EC2 provisions (which do not take into account the contribution of fibers) under the hypothesis of a variable truss inclination model, and with the Standard method as well, proved to be lower than the experimental shear force at crack onset.

Finally, most of available analytical models predicting shear strength of FRC beams gave really conservative estimations of the experimental results.

3.8 REFERENCES.

[1]   *di Prisco, M., and Romero, J.*, *"Diagonal Shear in Thin-Webbed Reinforced-Concrete Beams: Fiber and Stirrup Roles at Shear Collapse", Magazine of Concrete Research, Vol. 48 (174), March 1996, pp. 1-18.*

[2]   *Cairns, J., and Plizzari, G.A.*, *"Bond behaviour of conventional reinforcement in fibre reinforced concrete", in "Fibre-Reinforced Concretes, Befib 2004", Proceedings of the international Conference, Varenna, Italy, 20-22 September 2004 (Edited by M. di Prisco, R. Felicetti and G.A. Plizzari, Published by RILEM Publications s.a.r.l., Bagneux, France), Vol 1, pp. 321-330.*

[3]   *EUROCODE 2*, *"Design of Concrete Structures", prEN 1992 ver. December 2003.*

[4]   *Minelli, F., and Vecchio, F.J.*, *"Compression Filed Modelling of Fibre Reinforced Concrete: Preliminary Numerical Study", in "Fibre-Reinforced Concretes, Befib 2004", Proceedings of the international Conference, Varenna, Italy, 20-22 September 2004 (Edited by M. di Prisco, R. Felicetti and G.A. Plizzari, Published by RILEM Publications s.a.r.l., Bagneux, France), Vol 2, pp. 885-894.*

4. EXPERIMENTS ON SHEAR-CRITICAL BEAMS

4.1   Introduction.

This chapter will present the results of an extensive experimental program on shear-critical beams loaded with a four point loading system and having a shear span-to-depth ratio of 2.5, which is recognized to be the most critical in terms of shear strength (see Section 2.5.1).

A total number of 15 beams were tested to evaluate the effect of several parameters on shear behavior, crack formation and development, and shear strength.

All beams had the same geometry and no stirrups were added anywhere, aiming at the investigation of resistant mechanisms dependent on concrete matrix (i.e. shear transfer, dowel action, residual tensile stresses and compressive resistance, basically).

A first set of tests aimed at studying the effect of loading conditions and the bond characteristics on shear strength. Four beams were tested in this respect, two with embedded deformed bars (reinforcement ratio of 1.04%), and two with the same bars, but placed as unbonded rebars through a smooth plastic pipe that covered them. In addition, two beams (one unbonded, one bonded) were tested with a four point loading system (a/d=2.5) whereas the other two with a uniformly distributed load, by adopting an equivalent span-to-depth ratio of 2.5 (See Chapter 2, Section 2.5.6.1). All four beams were made of identical normal strength concrete.

The second set of experiments concerned 11 shear-critical beams, whose main scope was to analyze the effect of the addition of a randomly distributed fibrous reinforcement to concrete. Different fiber typologies and fiber contents were provided and both normal and high strength concrete were investigated.

The following acronyms will be used to identify the different specimens:

- NSC0: normal strength concrete, series 0 (first set):

    NSC0 BP: specimen with bonded rebars and 4 point loading system;

    NSC0 BD: specimen with bonded rebars and uniformly distributed load;

    NSC0 UP: specimen with unbonded rebars and 4 point loading system;

    NSC0 UD: specimen with unbonded rebars and uniformly distributed load;

- NSC1: normal strength concrete, series 1 (second set):

    NSC1 PC: specimen made of plain concrete (reference concrete);

    NSC1 FRC1: specimen with fiber type and content 1;

    NSC1 FRC2: specimen with fiber type and content 2;

- NSC2: normal strength concrete, series 2 (second set):

    NSC2 PC: specimen made of plain concrete (reference concrete);

    NSC2 FRC1: specimen with fiber type and content 1;

    NSC2 FRC2: specimen with fiber type and content 2;

- NSC3: normal strength concrete, series 3 (second set):

    NSC3 PC: specimen made of plain concrete (reference concrete);

    NSC3 FRC: specimen with fibers;

- HSC: high strength concrete (second set):

    HSC PC: specimen made of plain concrete (reference concrete);

    HSC FRC1: specimen with fiber type and content 1;

    HSC FRC2: specimen with fiber type and content 2.

4.2 Materials and Specimen Geometry.

All 15 shear-critical beams tested (4 belonging to the first set, 11 two the second) had the same geometry and reinforcement content. The dimensions of specimens were mainly governed by the idea of performing tests on full scale element, being size effect a critical point in the shear behavior of reinforced concrete members (see Chapter 2, Section 2.5.2). In fact, it would have been difficult and disputable to extrapolate structural considerations from experiments on small size elements.

A total depth of 480 mm was chosen, with a gross cover of 45 mm. These two values determined the length of the specimen (10 times the effective depth, to achieve the a/d = 2.5 ratio even in case of uniformly distributed load). Being the span equal to 4350 mm, an overall length of the specimen was chosen equal to 4450 mm.

Figure 4.1 illustrates the geometry of the specimens and the reinforcement details. Two deformed longitudinal bars, having a diameter of 24 mm, were added to each specimen, corresponding to a reinforcement percentage equal to 1.04%.

Table 4.1 summarizes the geometrical characteristics of beams.

Only in the case of the two unbonded specimens (NSC0 series) the two reinforcing bars were covered by smooth plastic pipes having a diameter of 30 mm.

Suitable anchorage and support steel plates, as reported in Figure 4.1, were provided to all specimens. Particular attention was devoted to the design of the anchorage plates, in order to avoid local failure prior to the development of the desired shear collapse. The dimensions and stiffness of this plate were, in addition, calibrated to prevent a local failure due to concrete crushing or localization of loads.
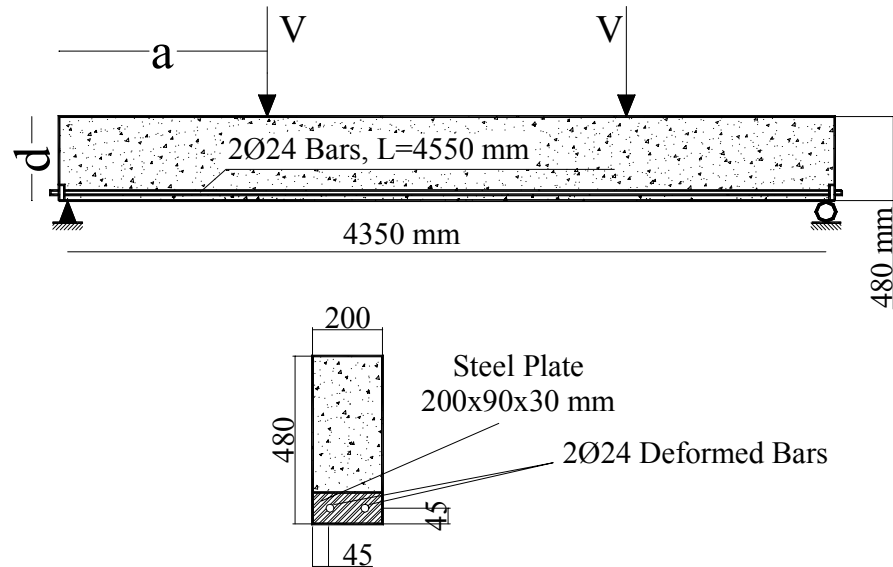
Figure 4.1: Geometry and reinforcement details of specimens.

Geometry Characteristics of Specimens	
Total Length	4450 mm
Span	4350 mm
Shear Span a	1090 mm
Width	200 mm
Total Depth	480 mm
Gross Cover	45 mm
Effective Depth d	435 mm
Reinforcement Area (2ϕ24)	905 mm^2
Reinforcement Ratio	1.04%

Table 4.1: Geometry characteristics of specimens.

The support plates were adequately designed to allow the development of the arch action within the specimen from its external surface. The dimension of such plate

was therefore related to the depth of the anchorage plate and to the slope of the compressive field that takes place in the specimen (Figure 4.2).
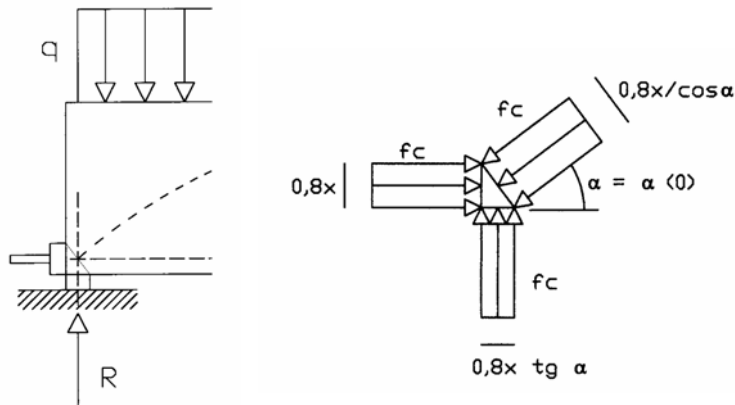
Figure 4.2: Representation of stress field at supports.

The design process brought to anchorage and support steel plates having dimensions of 200x90x30 mm and 200x35x15 mm, respectively.

Steel cylinders were also provided to properly reproduce the support and pin restraints, as reported in Figure 4.3.

Figure 4.3: Pin and supports restraints, with the support steel plate connected to the specimen through a thin layer of high strength mortar.

Table 4.2 reports the composition of concrete mixtures for the different series of specimens cast, giving indication of the main parameters such as the cement content, the maximum aggregate size and the water-cement ratio.

Table 4.3 reports the mechanical properties of concrete for all 5 series of specimens. Note that different measurements are reported for the high strength concrete series, as each specimen was cast separately. On the contrary, all the other specimens belonging to the same series were cast at once, just by adding the eventual fiber content.

	NSC0	NSC1	NSC2	NSC3	HSC
CEMENT TYPE	CEM I - 32.5R	CEM I - 42.5R	CEM I - 32.5R	CEM I - 32.5R	CEM I - 52.5R
CEMENT CONTENT [kg/m^3]	345	345	345	345	380
MAXIMUM AGGREGATE SIZE [mm]	20	20	20	20	15
WATER-CEMENT RATIO	0.55	0.5	0.55	0.55	0.31
PLASTICIZER [l/m^3]	3.8	3.8	3.8	3.8	2.75

Table 4.2: Composition of normal strength concrete for the specimens with or without fibers.

SPECIMEN	f_c [MPa]	f_{ct} [MPa]	E_c [MPa]
NSC0	32.9	3.15	32600
NSC1	24.8	2.30	31400
NSC2	33.5	3.15	32600
NSC3	38.6	2.60	33100
HSC PC	60.5	3.15	34400
HSC FRC1	61.1	3.48	36800
HSC FRC2	58.3	3.20	32700

Table 4.3: Mechanical properties of concrete.

Table 4.4 shows the yielding (f_{sy}) and tensile ultimate (f_{st}) strength of the longitudinal rebars provided.

REINFORCEMENT	f_{sy} [MPa]	f_{st} [MPa]	E_s [MPa]
REBARS $\Phi 24$	512	645	210960

Table 4.4: Mechanical properties of transverse reinforcement steel.

Different steel fibers were added to four concrete mixtures utilized (NSC1, NSC2, NSC3 and HSC). Different combination of fibers (micro and macro), different contents or different aspect ratios were investigated.

Table 4.5 depicts the main characteristics of all 5 typologies of fibers adopted. Note that the designation of the first three types, according to the supplier indications, reports the fiber length as the first number and the fiber diameter as the second,

while the designation of the two last types, as already discussed in Chapter 3, indicates the aspect ratio (first number) and the length (second number).

Designation	50/1.0	30/0.6	12/0.18	45/30	80/30
Type of steel	carbon	carbon	carbon	carbon	high carbon
Shape	hooked	hooked	straight	hooked	hooked
Cross Section	circular	circular	circular	circular	circular
Minimum Tensile Strength [MPa]	1100	1100	1800	1250	2300
Length [mm]	50	30	12	30	30
Diameter [mm]	1.00	0.60	0.18	0.62	0.38
Aspect Ratio l/ϕ	50	50	66.6	48	79
Fibers per kg	3200	15000	417000	14000	37000

Table 4.5: Characteristics of the different types of fibers adopted for the fiber reinforced NSC and HSC series of beams.

Figure 4.4 shows a representation of the different fibers adopted.
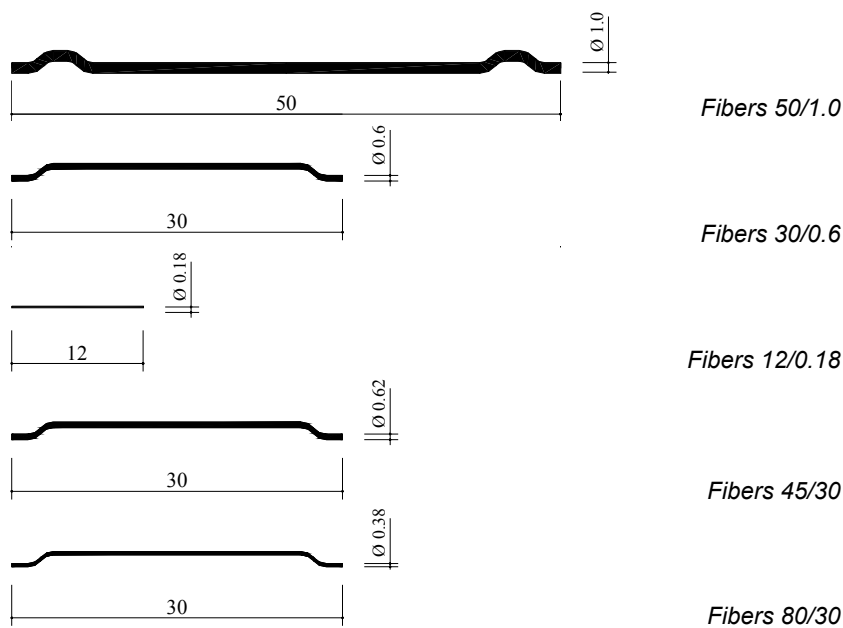
Figure 4.4: Representation of different fibers added to concrete mixtures.

Except the 12/0.18 type, all fibers can be indicated as macro-fibers. All types, except 80/30 and, again, 12/0.18, have a normal tensile strength. The micro fibers were only used in addition to macro fibers, determining therefore a hybrid system that can help both early cracking (controlled by micro fibers) and diffused macro cracking (controlled by macro fibers).

In Table 4.6:, the different fiber contents and combinations are reported. Note that series NSC0 is not reported, as no specimen was cast with steel fibers. The denomination FRC2 always indicates a beam with a greater amount of fibers, compared to the corresponding FRC1 or, limited to HSC series, a beam with fibers having stronger mechanical and fracture properties. This table is particularly significant as it shows the content of fibers, which is the only shear reinforcement provided into these specimens.

Specimen Designation	Volume Fraction of Steel Fibers						
	50/1.0 $[\%]_{vol.}$	30/0.6 $[\%]_{vol.}$	12/0.18 $[\%]_{vol.}$	45/30 $[\%]_{vol.}$	80/30 $[\%]_{vol.}$	$V_{f,tot}$ $[\%]_{vol.}$	$V_{f,tot}$ $[kg/m^3]$
NSC1-PC	-	-	-	-	-	-	-
NSC1-FRC 1	-	0.38	-	-	-	0.38	30
NSC1-FRC 2	-	0.38	0.19	-	-	0.57	45
NSC2-PC	-	-	-	-	-	-	-
NSC2-FRC 1	0.38	-	-	-	-	0.38	30
NSC2-FRC 2	0.38	-	0.19	-	-	0.57	45
NSC3-PC	-	-	-	-	-	-	-
NSC3-FRC 1	-	0.38	-	-	-	0.38	30
HSC-PC	-	-	-	-	-	-	-
HSC-FRC 1	-	-	-	0.64	-	0.64	50
HSC-FRC 2		-	-	-	0.64	0.64	50

Table 4.6: Combination of fiber types and amounts utilized in specimens of Normal Strength Concrete (NSC# series) and High Strength Concrete (HSC series).

Figure 4.5 and Figure 4.6 illustrate pictures of the formworks utilized for casting the specimens: the wood formworks were used at the laboratory of the University of Brescia whereas the steel ones were utilized by a precast concrete industry

(*Magnetti Building, Carvico-Italy*) that provided the high strength concrete specimens (series HSC).
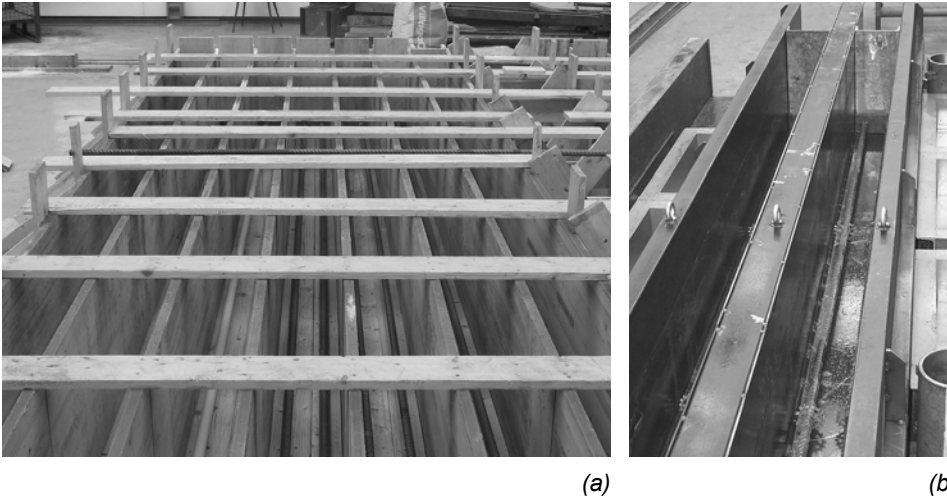
Figure 4.5: Formworks utilized for casting the first series of shear-critical beams (a) and the last series (b).

Figure 4.6 depicts the completion of the casting process for two specimens made of high strength concrete.

Figure 4.6: Completing of casting.

4.3   Set up Description and Loading Modalities.

Likewise the experiments shown in Chapter 3, displacement control had to be insured in order to carry out a proper experiment, especially after cracking. This was obtained by adopting a worm electro-mechanical screw jack having a loading capacity of 1000 kN and a stroke of 350 mm, as reported in Section 3.4.

The load was transferred to the specimen in a similar fashion to the way it was done in the prestressed I-Beams, as shown in Figure 4.7, which illustrates a schematic sketch of the loading frame for the four point loading test.

The top cross beam loaded the longitudinal steel beam at its midspan. The longitudinal beam, in turn, loaded the specimen in the two desired points through steel cylinders.

A front view of this set up is presented in Figure 4.8.

A little different was the set up for the two specimens (NSC0 BU and NSC0 UD) that had to resist a uniformly distributed loading. This was reproduced by interposing, between longitudinal steel beams (carrying one eighth of the total load) suitable square neoprene layers 100 mm wide and 20 mm thick, as shown in Figure 4.9.
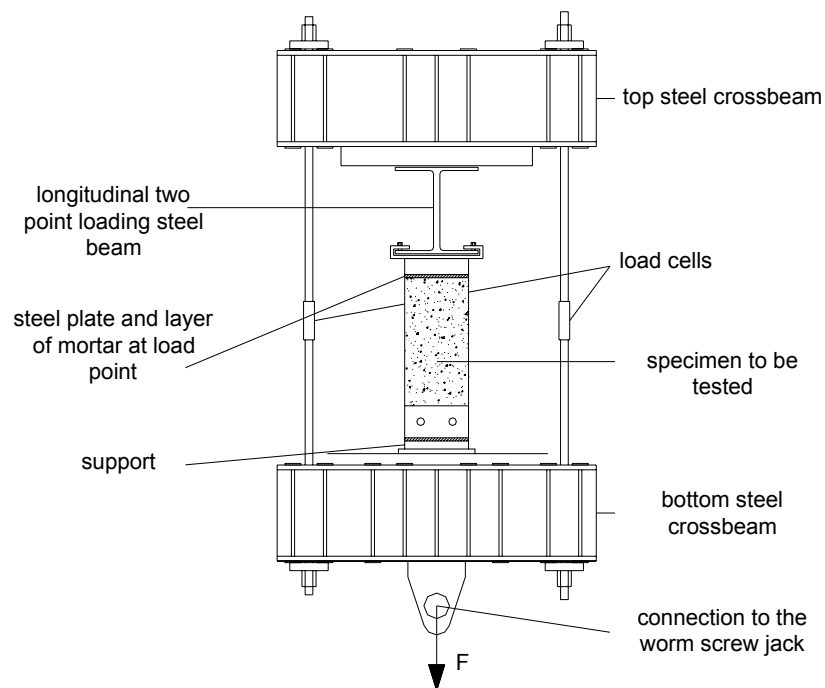
Figure 4.7: Scheme of the frame used for loading the specimens under a four point system.
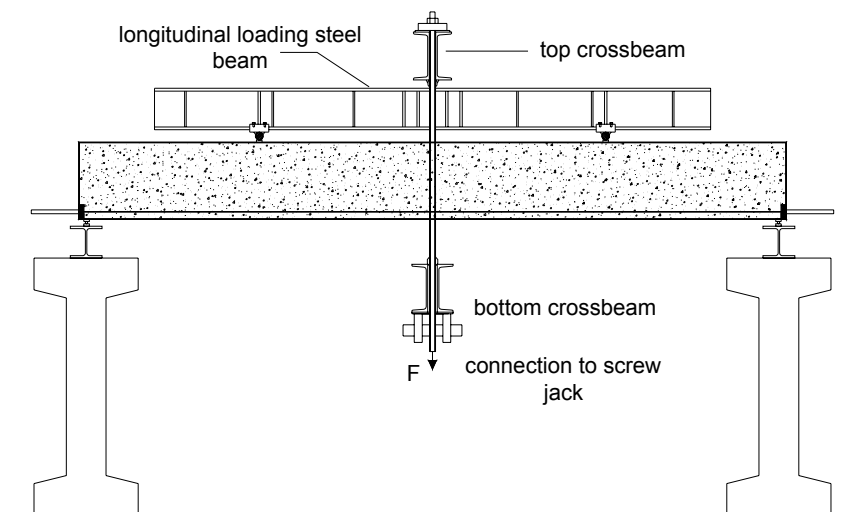
Figure 4.8: Test set up, 4 point loading system.
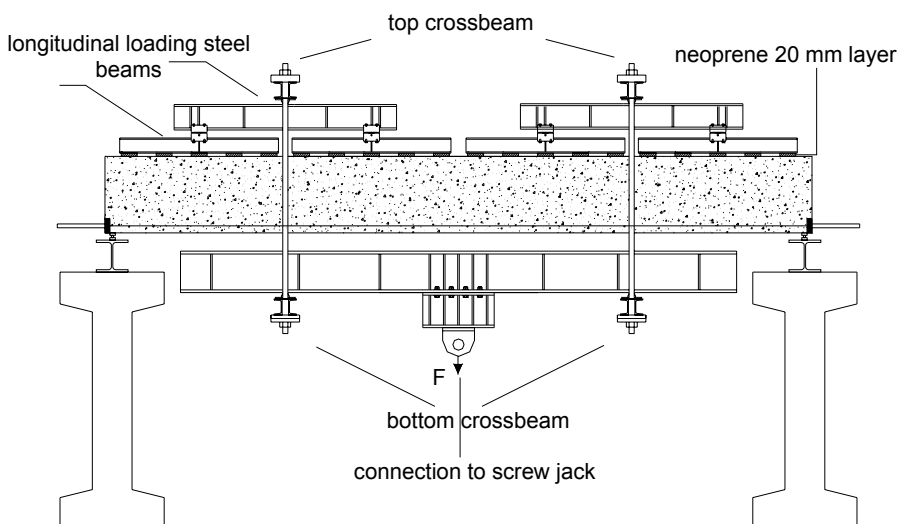
Figure 4.9: Test set up, uniformly distributed loading system.

The loading system for an uniformly distributed load proved to be more complicated and especially time consuming to assess. Moreover, a calculation based on the beam on elastic ground theory was performed to find out the correct spacing

between adjacent neoprene layers that better could reproduce a uniformly distributed load.

Figure 4.10 illustrates the particular of the steel loading system with the neoprene layers, whereas Figure 4.14 shows the set up of the 4 point loading system.

Figure 4.10: Loading system for the representation of a UDL.

A consistent number of instruments were utilized for monitoring the most important displacements and deformations of specimens, besides the applied loads.

Figure 4.11, Figure 4.12 and Figure 4.13 show the measuring devices: Linear Variable Differential Transformers (LVDTs) allowed the measurement of the vertical displacements of the beam and the supports; potentiometric transducers were placed on both sides (back and front) in the area of shear stresses (shear spans) to measure crack openings and strut deformations.
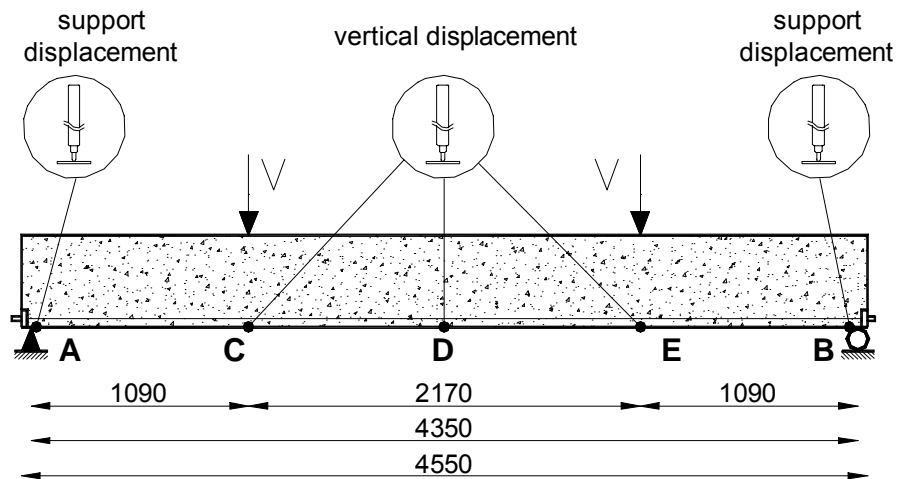
Figure 4.11: Scheme of the instrumentation measuring vertical and support displacements (note that two instruments were placed in point D, one in the front and one in the back side).

These transducers were placed with an inclination of 40° (for the strut deformation) and 140° (for the crack opening) with respect to the horizontal line (Figure 4.12 and Figure 4.13). Such inclinations were selected on the basis of the observation (and on many similar experiments reported in literature) that the collapse mechanism is characterized by a sudden macro crack running from the point load to the bottom reinforcement, at a distance from the support approximately equal to the depth of the member. From that point, a splitting crack develops toward the nearest support. This assumption was confirmed during most of tests carried out in this experimental program.

A total number of 16 instruments were used in each test:

- 2 load cells;
- 2 LVDTs for measuring support displacements;
- 4 LVDTs for measuring vertical displacements, 1 at each point load, and 2 at midspan (one in the front side, the other in the back);
- 7 potentiometric transducers for measuring strut deformations and crack openings in the panel area;
- 1 potentiometric transducer measuring the bottom flange deformation at midspan (Figure 4.12).
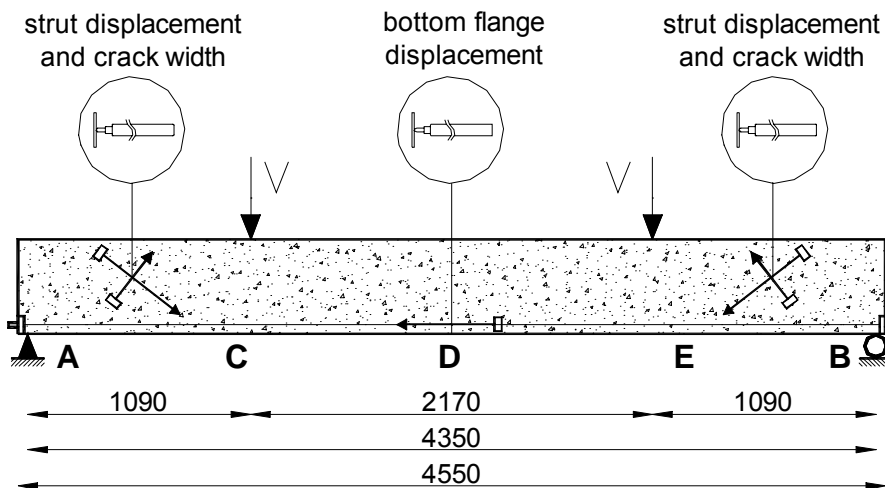
Figure 4.12: Scheme of the instrumentation for measuring crack openings and strut displacements in the front side on the tested beam.

Concerning the loading modalities, few cycles of preloading (generally two loading and unloading cycles), of course in the elastic range, were always done in order to make sure that the instruments were working properly.

The test started by imposing a rate of 100 revolutions per minute to the worm screw jack. After reaching the first cracking point, the loading rate was reduced to 50 r.p.m. When any shear crack appeared, the rate was further reduced to 15 r.p.m. up to failure.

A stabilization procedure was, in addition, performed at certain load levels, significant under a design point of view. These values are the serviceability limit and the ultimate limit, calculated according to the Eurocode 2 [2.82].

Figure 4.14 shows a specimen ready for testing under a 4 point loading system: note the instruments placed in the shear spans for recording both crack widths and strut deformations.
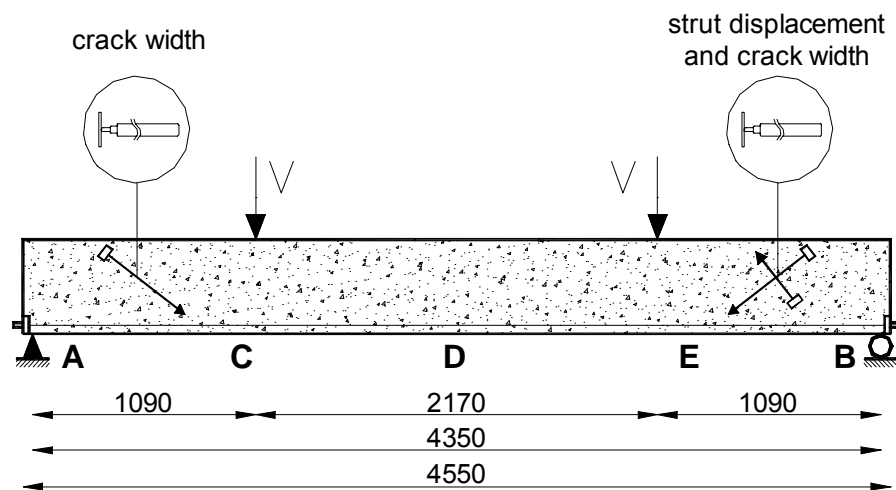
Figure 4.13: Scheme of the instrumentation for measuring crack openings and strut displacements in the back side on the tested beam.

Figure 4.14: Picture of a specimen ready for testing. Note the potentiometric instruments measuring crack widths and strut displacements.

4.4 Experimental Results and Discussion.

4.4.1 First Set of Experiments: the Effect of Bond and Loading Condition.

Figure 4.15 reports the comparison of the load-displacement (at midspan) curves for the four specimens belonging to the first set of experiments (NSC0 series).

Firstly, it can be noticed that the influence of bond is very significant and, by varying, determines a totally different structural behavior. For a range of loading belonging to the serviceability state (around 80 kN), the bonded specimens exhibited a quite stable behavior with a crack onset and propagation highly controlled, and with overall deformations much smaller than those shown by the unbonded specimens at the same load intensity. In addition, the slope of the elastic and the cracked branches of both experimental curves turned out to be in close agreement with the predictions. A consistent tension stiffening effect was also reported.
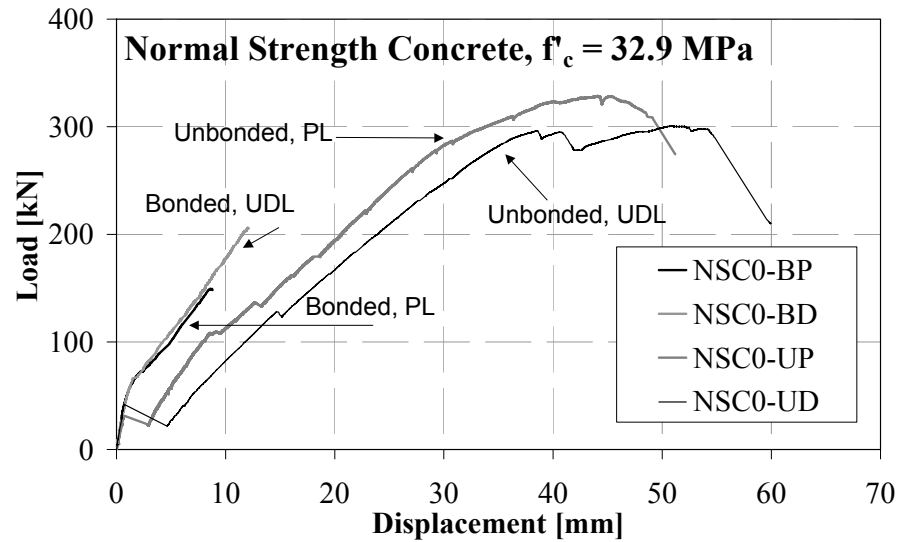
Figure 4.15: Load-midspan displacement curves for NSC0 series.

However, at a very low load level, a sudden and brittle shear failure appeared through a wide crack running from the point load to the bottom reinforcement, toward the support, in the shear span. This brittle collapse occurred for crack widths, measured in the shear span, of about 0.1-0.2 mm, which represents a quite small value (i.e., one would think to be in a safe situation under such a structure). In addition, the midspan deflection at failure was about 1/500 of the span, being therefore almost imperceptible.

These concepts emphasize the dangerousness of shear mechanism in elements without transverse reinforcement: a sudden brittle collapse mechanism arises for a low value of cracking and deflection. The mechanism of shear collapse, which will be explained in details in the following Section, is mainly governed by concrete-to-steel bond. Shear stresses, which act in maintaining the equilibrium along the span of a beam subjected to non constant bending moment, determines the premature collapse of the structure.

On the other hand, the behavior exhibited by the two specimens with unbonded rebars was really different: after the first cracking load, which turned out to be adequately similar for all specimens and in close agreement with the predictions, a single wide flexure crack appeared, in general close to either one of the two load points, accompanied by a considerable energy release and displacement. After that, the cracked stage developed with the formation of a few other flexural cracks,

which were very wide. The specimens proved anyhow to be able to resist further load till a flexure failure was attained through concrete crushing at the top chord.

The maximum deflection was 5-6 times greater that the one exhibited by the bonded specimens, while the bearing capacity turned out to be almost twice as much. No crack in the shear span, or inclined crack elsewhere, were reported.

The overall behavior and the mechanism of collapse were therefore entirely governed by flexure.

The unbonded specimens, however, exhibited a cracking onset unacceptable under a design point of view. The first crack that arose in specimen NSC0-UP was about 2 mm wide and the midspan displacement suddenly dropped from 0.7 to 3.0 mm (from 0.7 to 4.6 mm in the case of the NSC0-UD beam). Moreover, the first vertical crack ran for almost 90% of the depth of the beam. Such a situation would have considered much more dangerous that the one mentioned for the bonded specimens. We know, on the contrary, that after this stage, flexural cracks develop in a fairly stable fashion.

Figure 4.16 reports the comparison of the load-displacement curves for the two bonded specimens only, evidencing the effect of different loading.
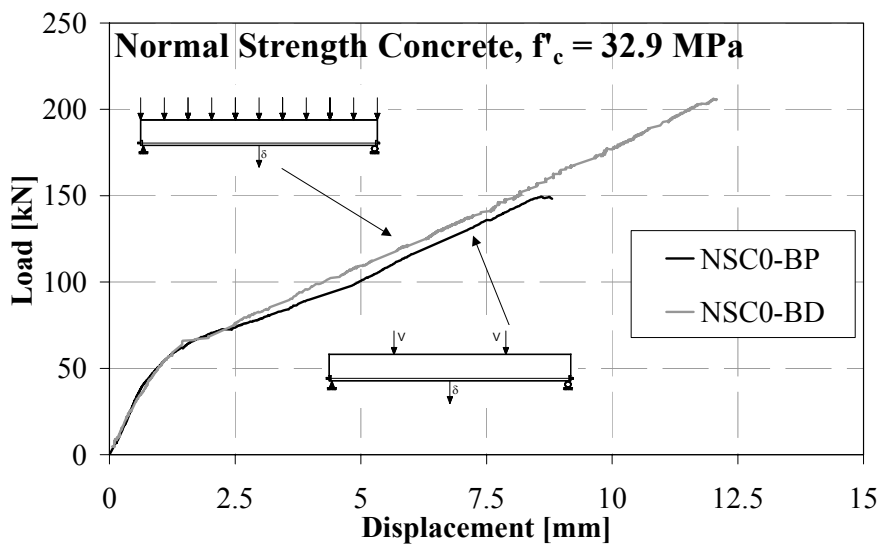
Figure 4.16: Load-midspan displacement of the two specimen with bonded rebars, series NSC0.

The uniformly distributed load tended to delay the brittle mechanism occurring in the shear span, owing to the presence of a uniformly distributed load on the upper face, which resists the rotation of the external block that determined the collapse.

The increase in bearing capacity, due to the uniformly distributed load, was about 38% whereas the maximum displacement was about 37% higher.

Figure 4.17 illustrates the main shear crack width, measured in the shear span, versus the load, for the two specimens with bonded rebars. The different loading condition did not significantly influence the cracking process: in both cases, the collapse arose for very small crack width. The vertical branch in specimen NSC0-BP is only due to two final measurements before collapse (with this respect, tests were conducted recording one measurement per second). This branch, in other words, was already part of the mechanism at collapse. In both tests the maximum crack width before the onset of the collapse mechanism was around 0.19-0.35 mm.
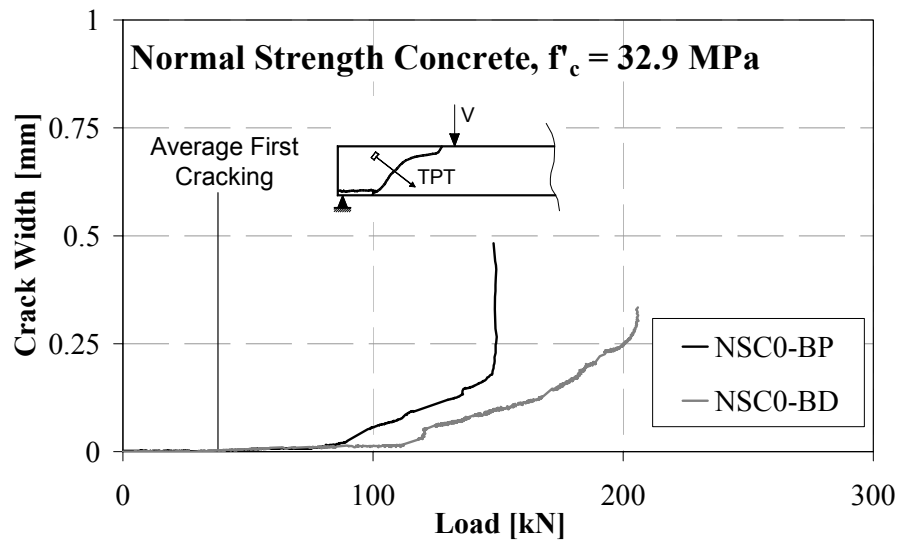
Figure 4.17: Main shear crack-load curves of the two specimens with bonded rebars, series NSC0.

Table 4.7 summarizes the principal measurements recorded for all 4 beams: the maximum load, the maximum displacement at midspan and under the two point loads, and the maximum measurement for the main shear crack. Note that the latter values are missing for the two specimens with unbonded rebars, as no shear crack was reported. In addition, the ratio between the ultimate experimental moment M_U

and the ultimate flexural moment $M_{U,FL}$ (calculated assuming the actual material properties) is also reported.

Designation	Maximum Load	$M_u/M_{u,FL}$	Midspan Displacement	Point Load Displacement I	Point Load Displacement II	Main Shear Crack
	[KN]	[-]	[mm]	[mm]	[mm]	[mm]
NSC0 BP	149	0.44	8.8	6.8	6.7	0.48
NSC0 BD	206	0.62	12.1	8.2	8.0	0.33
NSC0 UP	329	1.00	49.2	29.1	39.6	-
NSC0 UD	302	1.00	55.0	26.1	23.7	-

Table 4.7: Ultimate loads and displacements achieved by experiments of series NSC0.

Figure 4.18 reports the crack patterns for the four specimens at failure. Note the brittle mechanism in the shear span of the two bonded beams and, on the other hand, the concrete crushing at the top of the central part of the specimen in the unbonded beams.

Once again, no very significant influence due to the loading can be reported. For the bonded beams, the collapse mechanism was, in case of the UDL, as brittle and sudden as it was in the beam loaded with 2 point loads. On the contrary, the crushing of concrete in the unbonded beams proved to be more controlled in the specimen under a UDL, whereas this phenomenon was more brittle in the NSC0-UP specimen (see the two pictures on the left, Figure 4.18).

Figure 4.19-Figure 4.22 report the crack patterns of the four specimens at different load stages up to failure. The first pattern concerns an initial stage of cracking, the second is at a load level close to a serviceability limit state, and the final picture illustrates the pattern at failure.

Concerning NSC0-BP specimen, an inclined crack appeared at a load intensity of 96 kN. Before that point, the behavior was totally governed by flexure. After the first cracking point (for a load of around 41.5 kN), a few small vertical cracks developed in the central portion of the specimen. Those cracks, with increasing load, propagated in depth and in number even beyond the two point loads.

The first flexure-shear crack (i.e., inclined crack) appeared at a load intensity of 96 kN, and further developed, until a new inclined crack formed at a load of 130 kN, at a distance from the support of almost 500 mm (similar to the depth of the member), being the critical one along which the block mechanism took place.

NSC0-BP
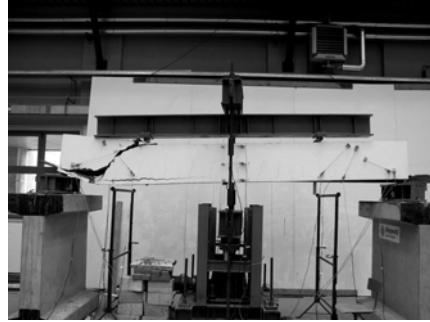
NSC0-BD
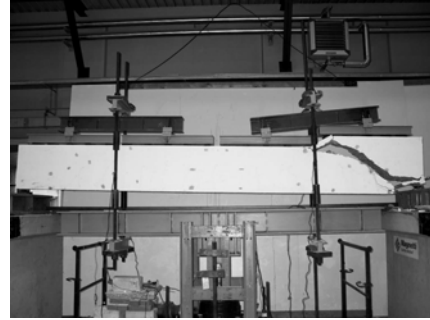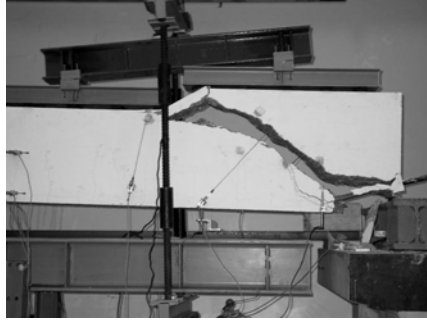
NSC0-UP

NSC0-UD
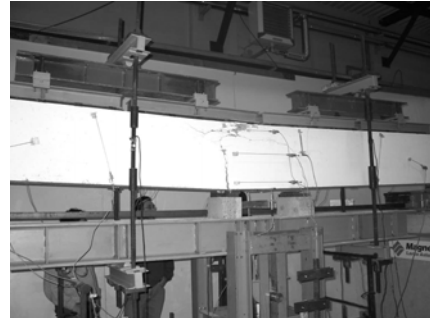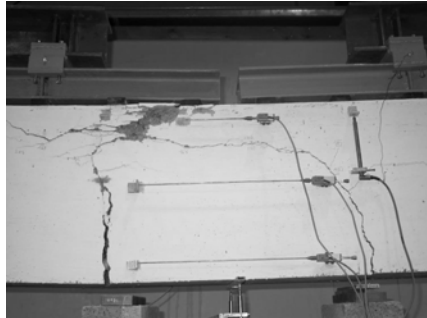
Figure 4.18: Crack patterns at failure for all beams of series NSC0.

The macro crack that determined the collapse of the specimen, as reported in Figure 4.19, had a shape that started with the inclination of the thrust line connecting the point load to the support. It then deviated with an inclination of about 45° with respect to the horizontal. Once it reached the longitudinal reinforcement, due to splitting phenomena, it deviated toward the closest support, showing an almost horizontal branch. This three branch crack is the typical final crack observed in almost all shear-critical beams inhere tested, and it is diffusely reported in the scientific literature as well.
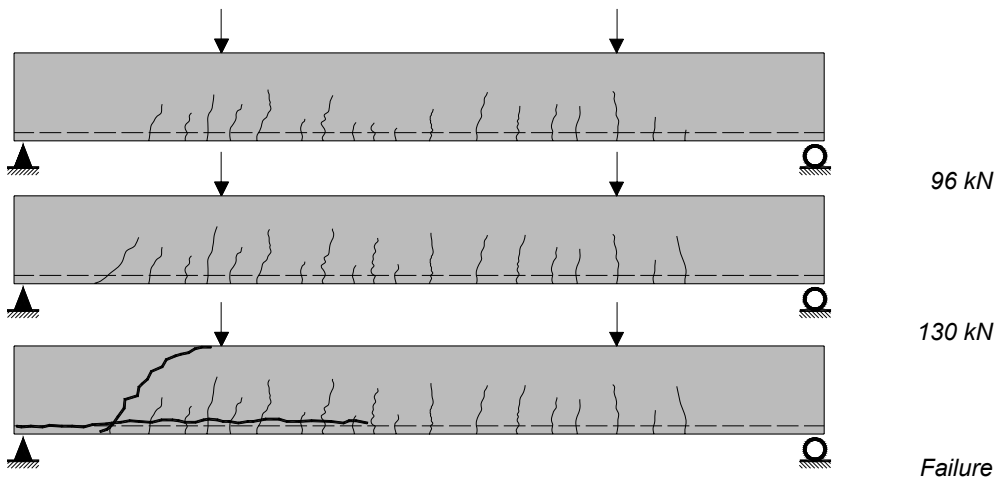
Figure 4.19: Crack pattern evolution, NSC0-BP specimen.

Concerning specimen NSC0-BD (Figure 4.20), the first neat crack appeared at a load of 56 kN. The crack evolution was quite similar to that of specimen NSC0-BP, i.e., the behavior was governed by flexure till a load level of around 120 kN, where in both shear spans the formation of inclined cracks was clearly visible. Another inclined crack then formed, determining the collapse of the specimen, in the same way and shape as reported for the previous specimen. Figure 4.17 confirms the delayed formation of a shear crack in the beam uniformly loaded, compared to the one with four point loading system, according to the crack pattern. The difference is anyhow quite small.

Looking at the crack patterns of the two unbonded specimens, it can be concluded that the beam behavior was governed by the formation of a few wide cracks, which appeared suddenly and determined big increases of vertical displacements and, eventually, load drops.
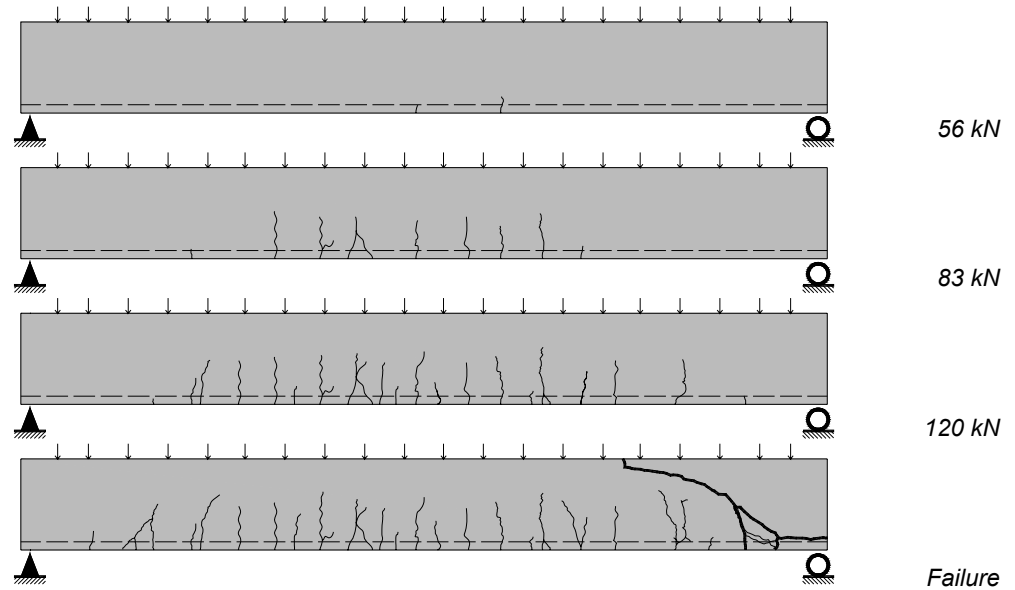
Figure 4.20: Crack pattern evolution, NSC0-BD specimen.

Concerning specimen NSC0-UP, a 2 mm vertical wide crack arose at a load level of 35 kN (first cracking point) with a length of 90% of the depth of the specimen. A second shorter crack developed at midspan for a load intensity of around 110 kN. This second crack tended to bifurcate and become horizontal, clearly showing the arch shape (Figure 4.21).
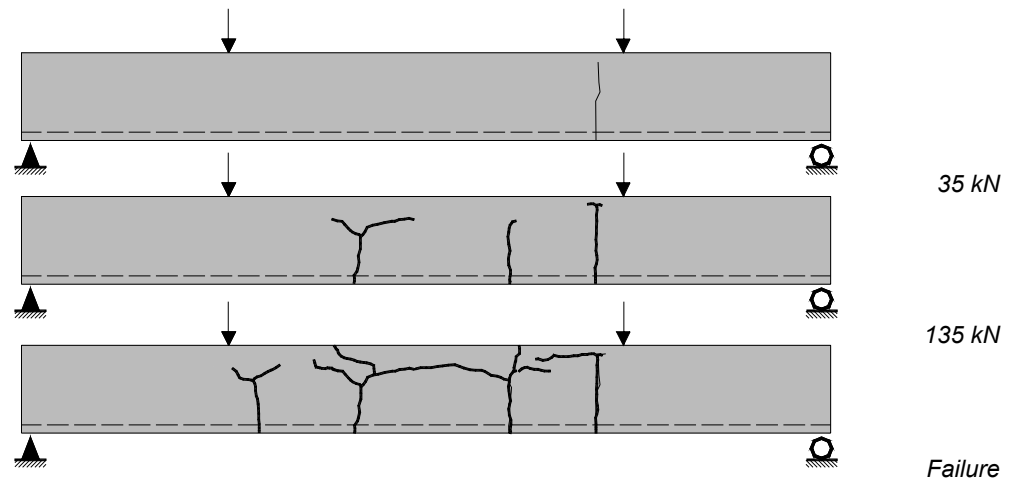
Figure 4.21: Crack pattern evolution, NSC0-UP specimen.

Two other macro cracks formed with increasing load: they also tended to bifurcate and horizontally join to each other. The final collapse occurred at the top chord of the member with crushing of concrete.

Suitable measurements of deformations at the top chord (just set for the two unbonded specimens) showed that concrete exceeded its ultimate compressive strength (while the concrete stress at the same location, in the bonded beam, was about 15 MPa, less then half of the compressive strength, see Table 4.3).

The specimen NSC0-UD exhibited a response similar to the corresponding beam loads with a four point loading system (Figure 4.22). Only two macro cracks developed, bifurcated and horizontally joined together till the maximum compressive strength was reached (about 33 MPa). The concrete crushing proved to be less brittle without any explosion of material, as observed, on the contrary, in specimen NSC0-UP.

40 kN

165 kN

Failure
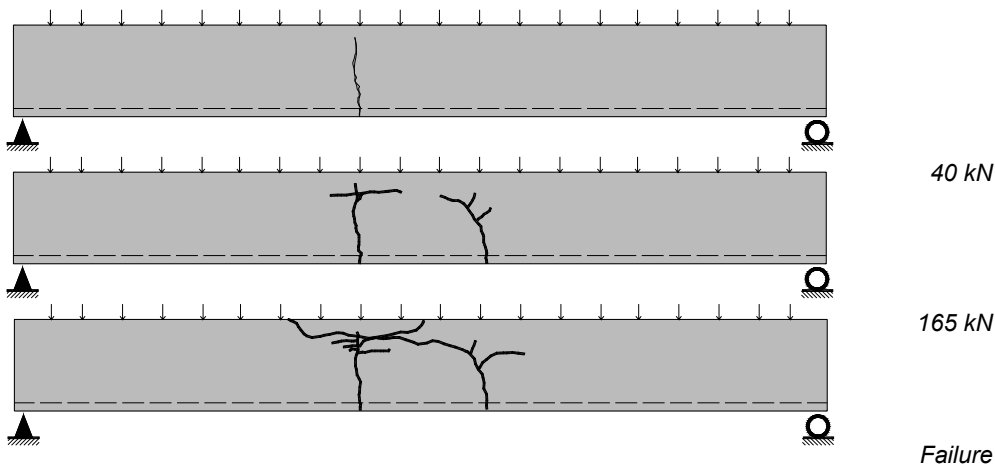
Figure 4.22: Crack pattern evolution, NSC0-UD specimen.

4.4.2   FRC Beams.

Figure 4.23 illustrates the load-displacement curve for the three specimens of series NSC1, all having bonded rebars and all tested under a 4 point loading system.

The NSC1-PC beam (the reference specimen) showed the behavior already reported for the two bonded beams of series NSC0: in other words, a brittle collapse arose for relatively low loading levels, deflections and cracking.

310

The addition of a low content (30 kg/m^3) of hooked steel fibers (fibers 30/0.6, see Table 4.6) allowed the specimen to resist further load (twice as much) and deflection, and to have an enhanced stiffness in the cracked stage.
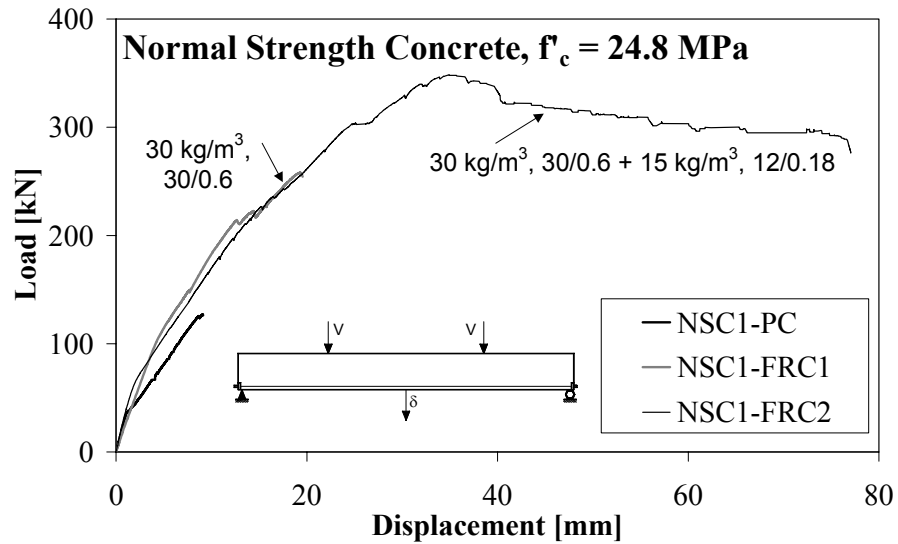
Figure 4.23: Load-midspan displacement curves for NSC1 series.

The shear cracking in the shear span was evident (from a load of around 110 - 120 kN, while the instruments evidenced shear cracking at 70 kN for the reference specimen) and its development was quite controlled till the same brittle mechanism occurred for a load level of 258 kN.

The NSC1-FRC2 specimen, with 30 kg/m^3 of macro fibers (the same used for beam NSC1-FRC1) and 15 kg/m^3 of micro fibers proved to be able to resist enough shear and to achieve a flexure failure with a quite consistent ductility. The midspan deflection and the load resisted were respectively 8.5 and 2.7 times greater than those of the beam made of plain concrete.

Adding a considerably low content of fibers ($V_{f,tot}$=0.57%), which does not significantly influence the costs and the workability of the mixture, can alter the final collapse mode of a specimen, getting rid of shear brittle mechanisms in members without traditional shear reinforcement.

Figure 4.24 and Figure 4.25 report the crack width-load and strut displacement-load curves, respectively, for the three specimens. Particularly significant is the first plot, concerning the crack widths in the shear span. While the specimen made of plain concrete was not able to resist a shear crack greater than 0.2 mm (the vertical

branch of the curve is already part of the failure mechanism, as observed even for beam NSC0-BP), the two specimens with fibers could resist shear cracks at least 10 times greater, due to their bridging action through adjacent crack surfaces. The main shear crack recorded for NSC1-FRC2 specimen reached 3 mm and, in spite of that, the shear cracking developed in a considerably stable fashion until a flexural collapse occurred.

By considering the maximum shear crack value of beam NSC1-PC, one can find out that the corresponding total load resisted by the three specimens was 127 kN (NSC1-PC), 185 kN (NSC1-FRC1) and 177 kN (NSC1-FRC2). If the first value is the load at failure for the reference specimen, beams NSC1-FRC1 and NSC1-FRC2 resisted further 29% and 51% of load, respectively (Figure 4.24).
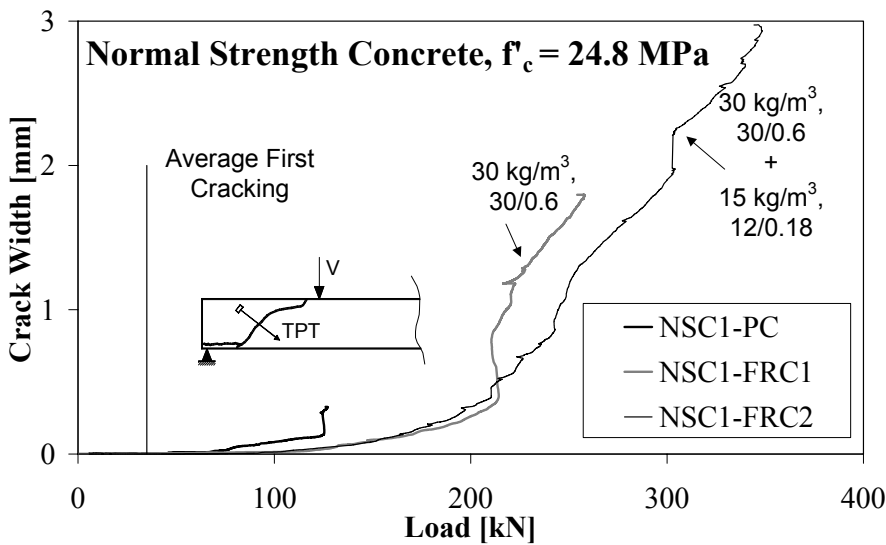
Figure 4.24: Crack width-load curves for NSC1 series.

The strut displacements in the shear span, shown in Figure 4.25, confirms the ability of fibers to provide a significant resistant contribution even in the compression side, especially in terms of residual compressive strength in a cracked zone. Note that the plot concerning specimen NSC1-FRC2 is missing, due to the fact that all instruments crossed the inclined cracks and therefore did not measure properly the compressive deformations.

Figure 4.26-Figure 4.29 represent the experimental results of series NSC2 and NSC3, having a compressive strength slightly higher than that of NSC1 series. In the first case, 45 kg/m³ of fibers (combination of macro and micro fibers, see Table

4.6) were not able to bring beam NSC2-FRC2 to a flexure failure, unlike specimen NSC1-FRC2.
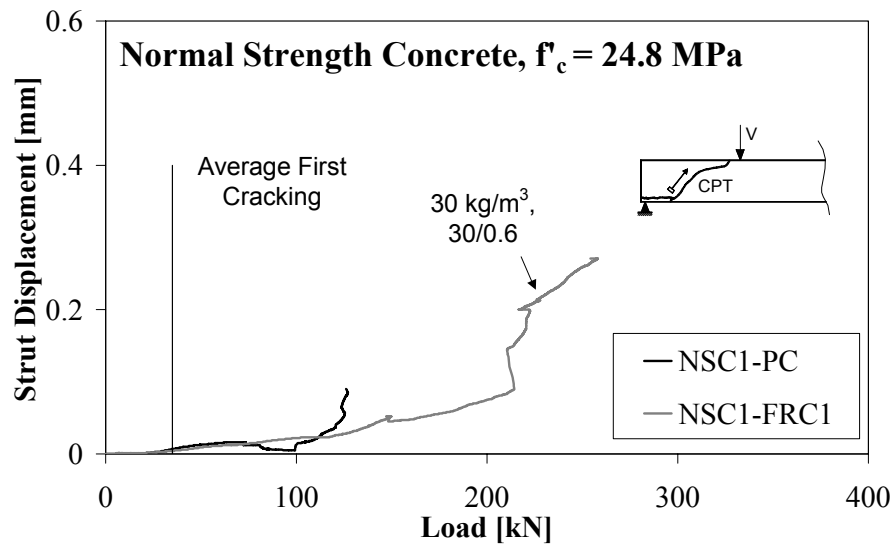
Figure 4.25: Strut displacement-load curves for NSC1 series.
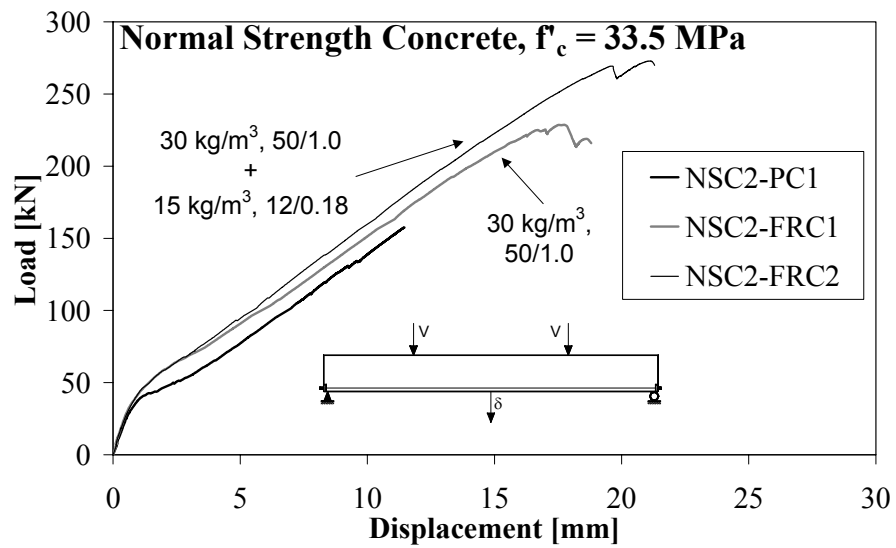
Figure 4.26: Load-midspan displacement curves for NSC2 series.

This is more likely due to the casting process, where a certain amount of concrete without fibers had to be added to the top part of this specimen for completely filling

the formwork. For this reason (simply a mistake during casting operations) the upper part of the shear-critical beam (almost 100 mm out of 480 mm, in depth) turned out to be without fibers. This upper part is well known to be crucial since, as already discussed for series NSC0, is the zone where the collapse shear mechanism starts.

Nevertheless, the specimen NSC2-FRC2 exhibited the best performance showing a load and a midspan deflection respectively 73% and 85% higher than those observed for the corresponding reference specimen (NSC2-PC).

The crack width distribution, shown in Figure 4.27, evidences the stable development of the main shear crack in the FRC specimens (the main shear crack of beam NSC2-FRC2 was around 26.5 times greater than that in beam NSC2-PC). Unfortunately, the instruments for recording the main shear crack in specimen NSC2-FRC1 did not measure the main shear crack, but just one adjacent, secondary in wide. However, it can be said that, at failure, the main shear crack resulted in being around 1.5 mm wide.

In all pictures regarding either crack widths or strut displacements (where provided) in the shear span, there is an indication of the first cracking load: note that it always occurred, as expected, with cracking under flexure in a portion of the specimens within the two load points (rather than in the shear spans).
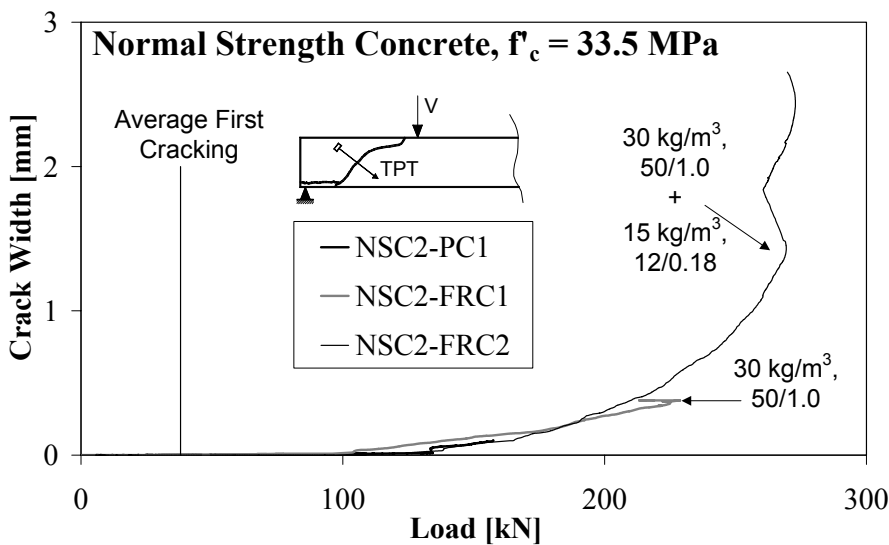
Figure 4.27: Crack width-load curves for NSC2 series.

The NSC3 series, whose main results are plotted in Figure 4.28 and Figure 4.29, consisted only in two specimens, the plain concrete and the one with 30 kg/m³ of 30/0.6 fibers. The two specimens were identical to NSC1-PC and NSC1-FRC1, respectively, except for the concrete compression strength, higher in this case.
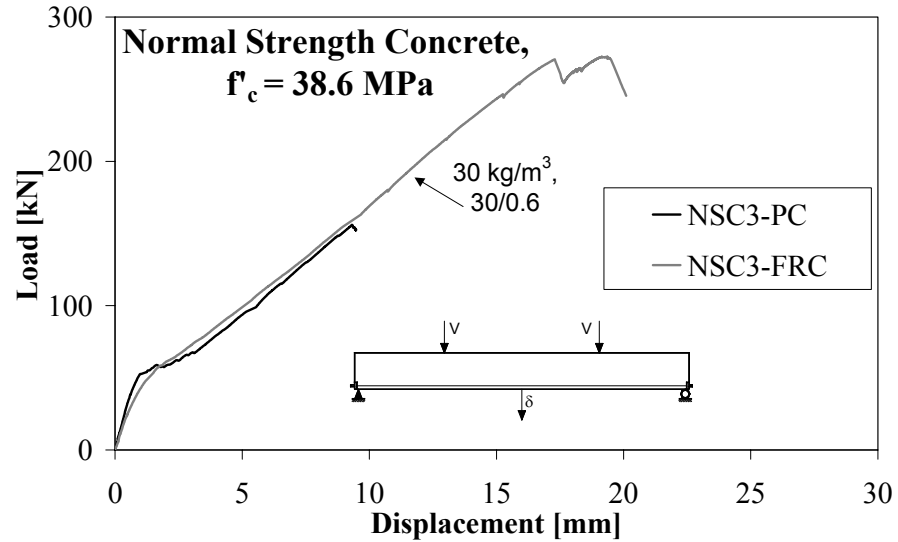
Figure 4.28: Load-midspan displacement curves for NSC3 series.
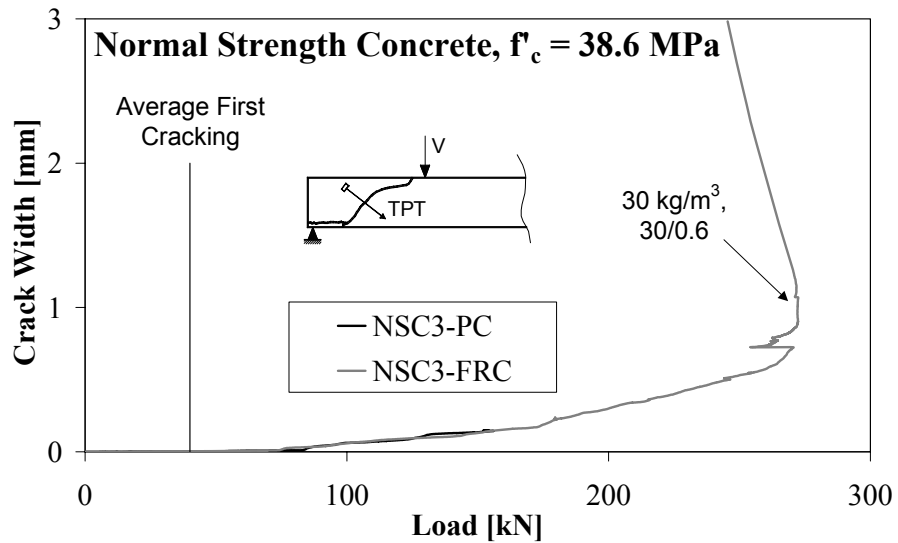
Figure 4.29: Crack width-load curves for NSC3 series.

The addition of 30 kg/m^3 of fibers almost resulted in doubling the total load and the midspan deflection, while the main shear crack (Figure 4.29) was 20 times higher in the FRC specimen. In both specimens failure was determined by the sudden formation of the block mechanism.

Three specimens were also tested with high strength concrete, remaining constant the geometrical and reinforcement properties.

Figure 4.30 illustrates the load-deflection curves for the three beams. Note that the two FRC specimens had the same content of fibers which, however, were characterized by different aspect ratio and ultimate tensile strength (45/30 fibers having normal strength, 80/30 fibers high strength due to high carbon content; see Table 4.6).

HSC-PC specimen showed a behavior similar to that exhibited by the plain concrete beam having normal strength. The increase in the ultimate load (strictly related to the tensile strength of concrete), was just of 37%, if compared to NSC2-PC and NSC3-PC (with a maximum load of 157 and 156 kN, respectively), while the ratio of the different compressive strengths is more than 2. It is evident that high strength concretes are much more brittle than normal strength mixtures, as already discussed in Section 2.5.5.
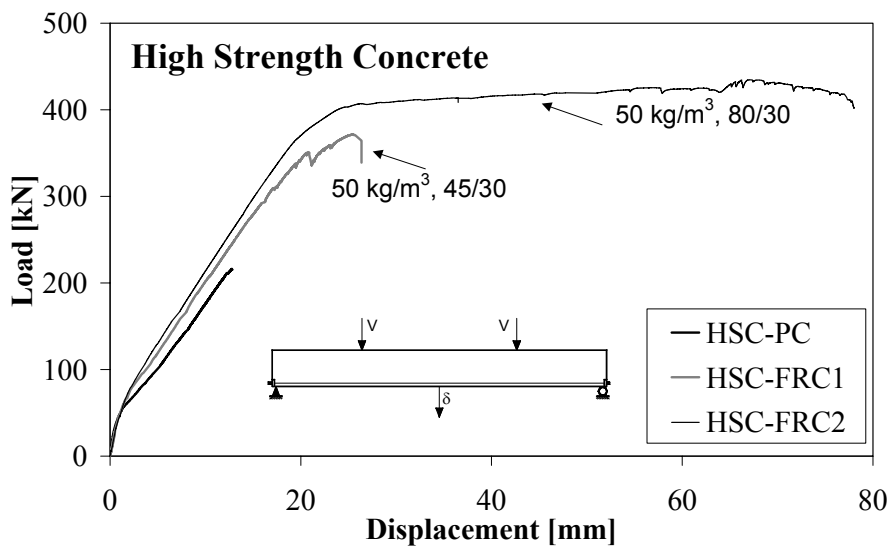
Figure 4.30: Load-midspan displacement curves for HSC series.

HSC-FRC1 exhibited a behavior that was governed by a shear failure, even though not extremely brittle. The main shear crack, which reached 2.2 mm in width,

316

developed in a stable fashion, firstly arising in the left shear span, then developing in the right one where the block mechanism occurred.

However, the total load was quite close to the member full flexural capacity: an alternative loading scheme, i.e., adopting a shear-to-span ratio of 3-3.5, would probably have caused flexural failure with a much higher ductility (Chapter 6 will deal with these considerations).

HSC-FRC2 achieved its full flexural capacity with midspan deflection 6.5 times greater than that of beam HSC-PC. The test was then stopped to prevent brittle and dangerous phenomena. In fact, it was evident that yielding occurred in the longitudinal rebars.

Very interesting is the mean shear crack development, especially for beam HSC-FRC2, which did not show a huge shear crack as one would have expected. On the contrary, many secondary shear cracks developed and no one of them significantly grew toward the point load. The high carbon fibers, with their enhanced bridging action, were able to prevent the growth of such critical cracks.

The main cracks developed within the two loading points, where many flexural cracks were observed and two big cracks, almost at the load point locations, determined local yielding of the rebars.

Conversely, specimen HSC-FRC1 was characterized by a localization of shear cracking, as usually observed in all other specimens.
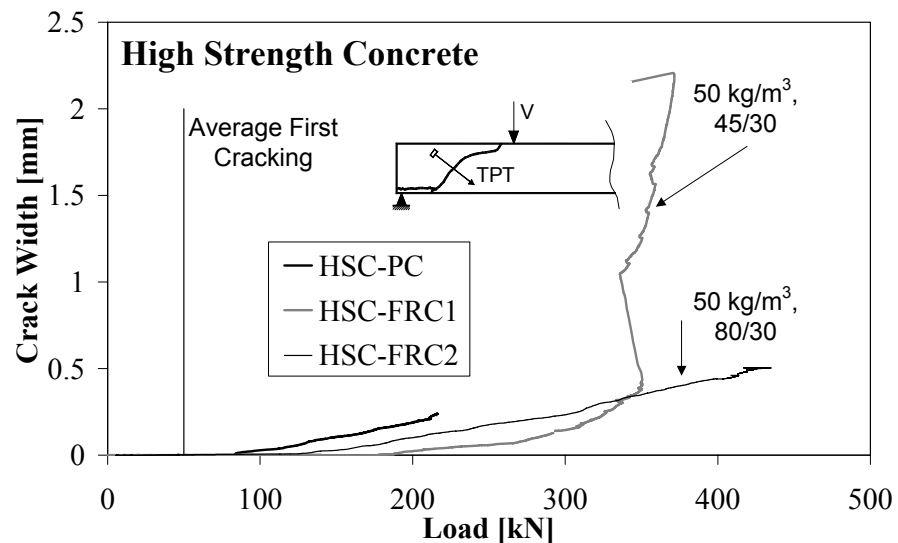
Figure 4.31: Crack width-load curves for HSC series.

The same distribution can be reported for the strut displacements in the shear span: once again, HSC-FRC2 specimen proved to have a local response, in the shear span, much less nonlinear than in the other two specimens of the same series. That is due to the strength provided by the high strength, which keep cracks small as they need a considerable amount of energy to allow further openings.

Next Chapter will show that this fiber typology determines a strain-hardening response in notched beams, for small crack widths.

In conclusion, for shear-critical beams, the maximum value of the shear crack width, in the shear span, before the complete structural collapse, was equal to 0.1-0.2 mm for specimens made of plain concrete, whereas it jumped to 1.5-3 mm, depending on the typology and amount of fibers, for beams made of FRC. This is quite significant under a structural point of view: one would be aware of the dangerousness of the structure due to its evident crack pattern, and its stable development, only possible if fibers are provided in sufficient amount.
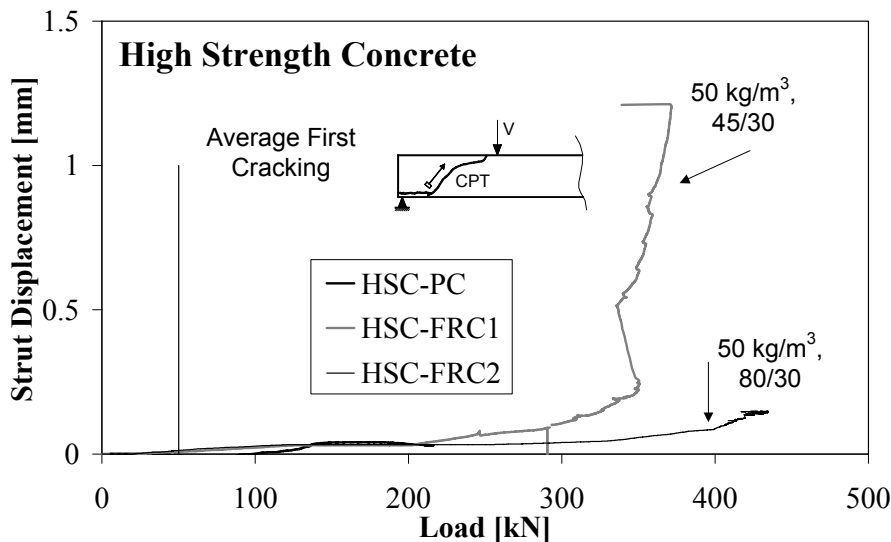
Figure 4.32 : Strut displacement-load curves for HSC series.

Table 4.8 reports the main values of displacements and crack widths at failure, for all series of specimens discussed in this Section.

318

Designation	Maximum Load [KN]	Midspan Displacement [mm]	Point Load Displacement I [mm]	Point Load Displacement II [mm]	Main Shear Crack [mm]
NSC1-PC	127	9.1	6.2	6.1	0.33
NSC1-FRC1	258	19.6	14.3	15.2	1.80
NSC1-FRC2	349	77.1	58.4	59.3	2.99
NSC2-PC	157	11.5	8.6	8.6	0.10
NSC2-FRC1	229	18.8	14.0	15.3	0.38*)
NSC2-FRC2	273	21.3	14.4	17.0	2.65
NSC3-PC	156	9.5	6.6	7.1	0.15
NSC3-FRC	272	20.1	13.4	14.3	2.98
HSC-PC	216	12.8	9.6	9.3	0.24
HSC-FRC1	372	26.4	19.7	17.0	2.21
HSC-FRC2	435	78.0	59.1	58.2	0.50

*) The main shear crack developed out of the instruments bases.

Table 4.8: Ultimate loads and displacements achieved by experiments of series NSC1, NSC2, NSC3 and HSC.

Figure 4.33-Figure 4.37 show some pictures of specimens at failure. Note the block mechanism in most of specimens presented, and the shear crack, visible only if fibers are provided, namely in NSC1-FRC1 and NSC1-FRC2 (left pictures in Figure 4.34 and Figure 4.35), and HSC-FRC1 (left picture in Figure 4.37).

Moreover, note concrete crushing in beam NSC1-FRC2 (right picture in Figure 4.35).
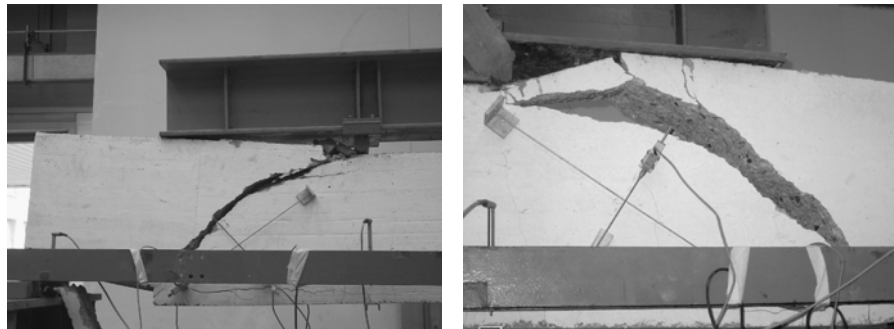
Figure 4.33: Crack patterns at failure for beam NSC1-PC.
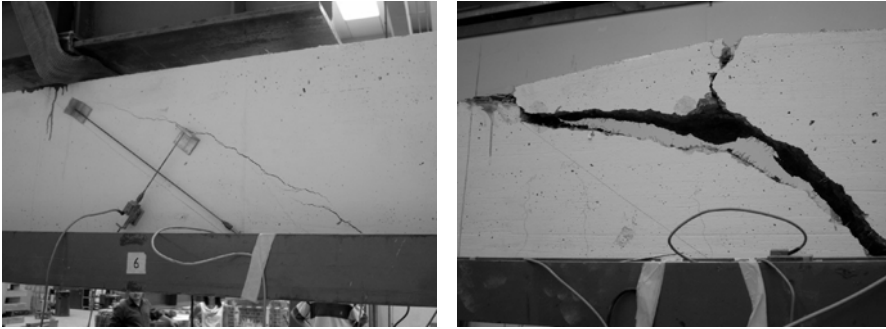
Figure 4.34: Crack patterns at failure for beam NSC1-FRC1.
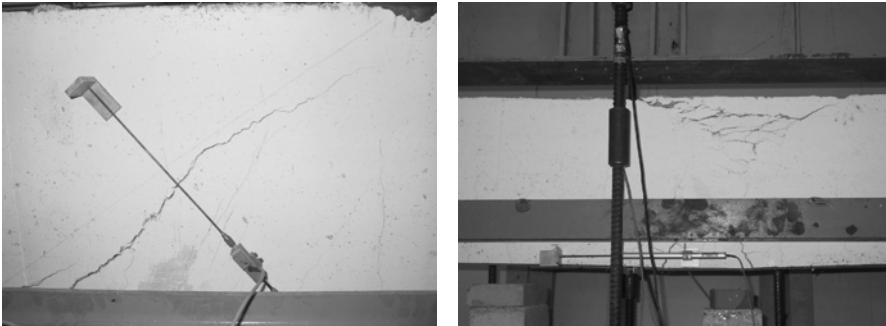
Figure 4.35: Crack patterns at failure for beam NSC1-FRC2.

Because of the presence of fibers, no explosion of materials in compression was reported. This further confirms the beneficial effect of fibers in improving the residual compressive strength (on the contrary, specimens NSC0-UP and NSC0-UD showed a final explosion of the crushed concrete).

Figure 4.36: Crack patterns at failure for beam HSC-PC.
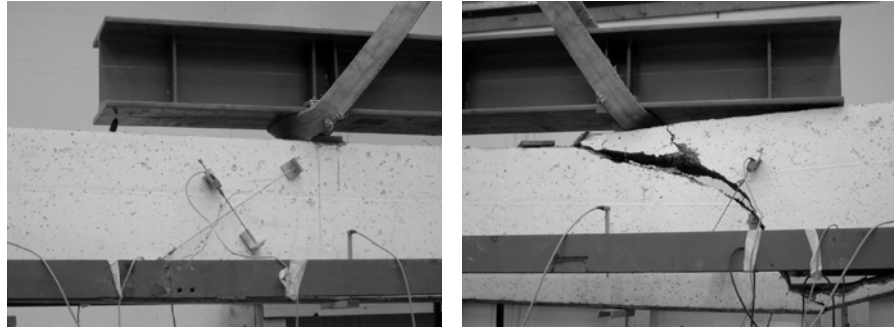
Figure 4.37: Crack patterns at failure for beam HSC-FRC1.

Figure 4.38, Figure 4.39 and Figure 4.40 depict the evolution of crack patterns for specimens of series NSC1 while Figure 4.41, Figure 4.42 and Figure 4.43 for series HSC. In the first case, it is valuable emphasizing that, for low level of loadings (i.e., 40 kN), much less cracks were reported for the FRC specimens (no crack at all was observed for specimen NSC1-FRC2 till a load of 70 kN).

In addition, with increasing loading, FRC specimens showed a more diffused cracking, being the crack spacing quite lower.

In specimen NSC1-PC inclined cracking, in the shear span, arose at a load of 70 kN and began evident at a load of 90 kN, whereas no significant shear cracks were observed, in the FRC specimens, before a load intensity of 120 kN. In the latter beams, shear cracks then developed quite considerably before the collapse.

40 kN

90 kN
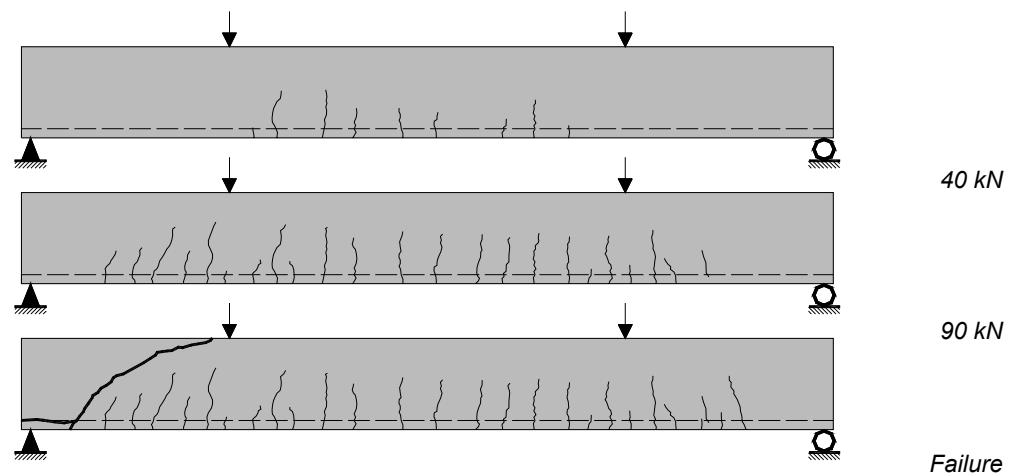
Failure

Figure 4.38: Crack pattern evolution, NSC1-PC specimen.
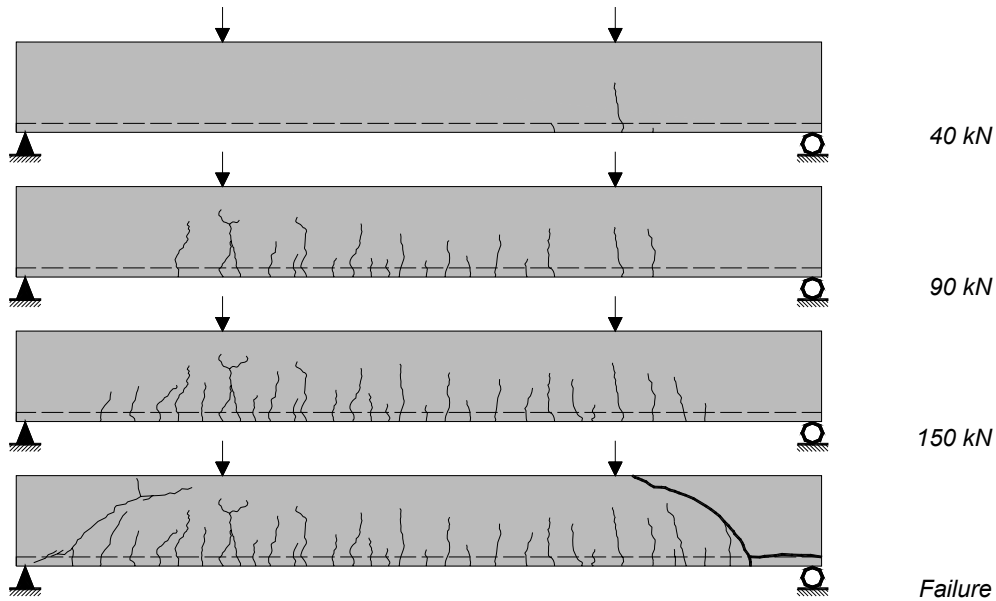
Figure 4.39: Crack pattern evolution, NSC1-FRC1 specimen.

The same considerations can be extended to HSC series. In beam HSC-FRC1 the evident shear failure was accompanied by quite wide flexural cracks, whereas in specimen HSC-FRC2 the crack evolution and its final fashion is governed by flexure and poorly influenced by shear.
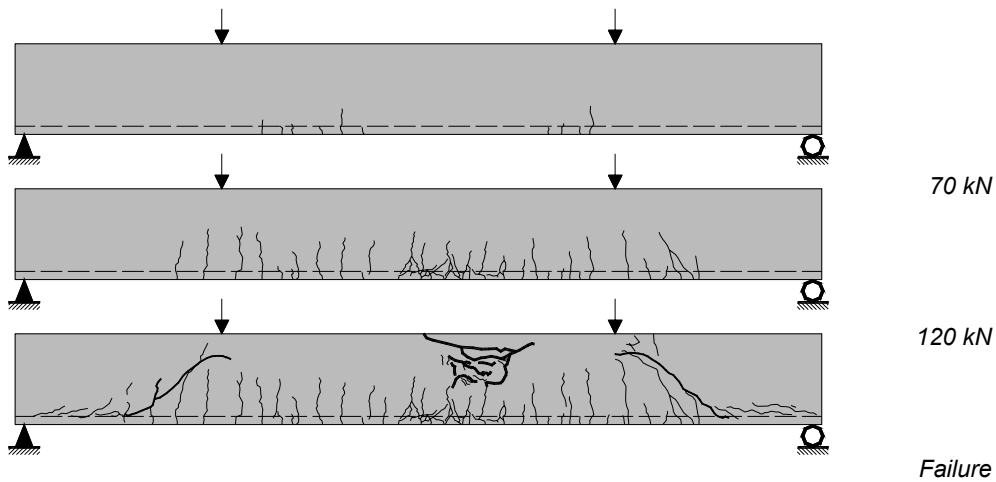
Figure 4.40: Crack pattern evolution, NSC1-FRC2 specimen.

90 kN

135 kN

Failure
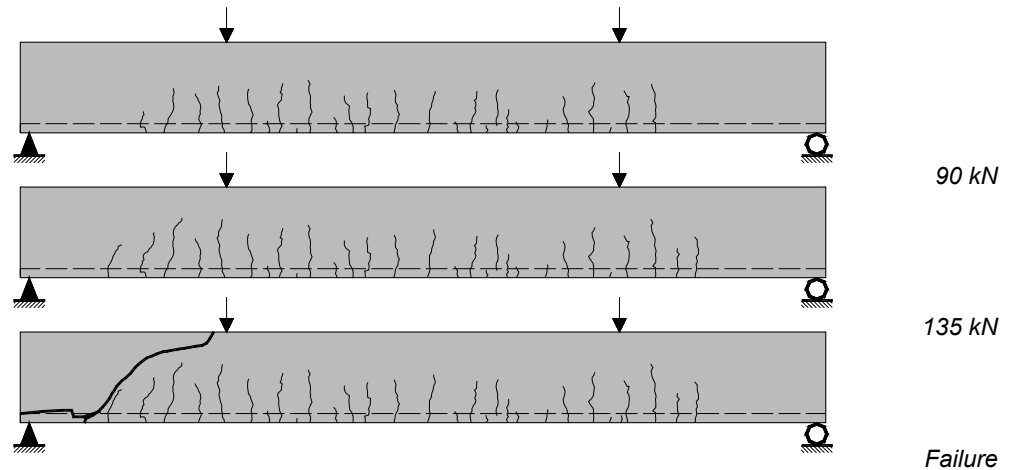
Figure 4.41: Crack pattern evolution, HSC-PC specimen.

For these two sets of experiments (NSC1 and HSC), Figure 4.44 and Figure 4.45 show a picture of the specimens at the end of the tests. Note the considerable irreversible deformations, after complete unloading, exhibited by beams NSC1-FRC2 and HSC-FRC2.

In addition, by comparing only the final crack patterns, noticeable is the higher complexity of cracking in members with fibers.

One should recognize the reduced crack pattern, reported at 90 kN, going from the reference specimen to beam HSC-FRC2. At 150 kN, still a considerable difference can be remarked between specimens HSC-FRC1 and HSC-FRC2.

90 kN

150 kN

Failure
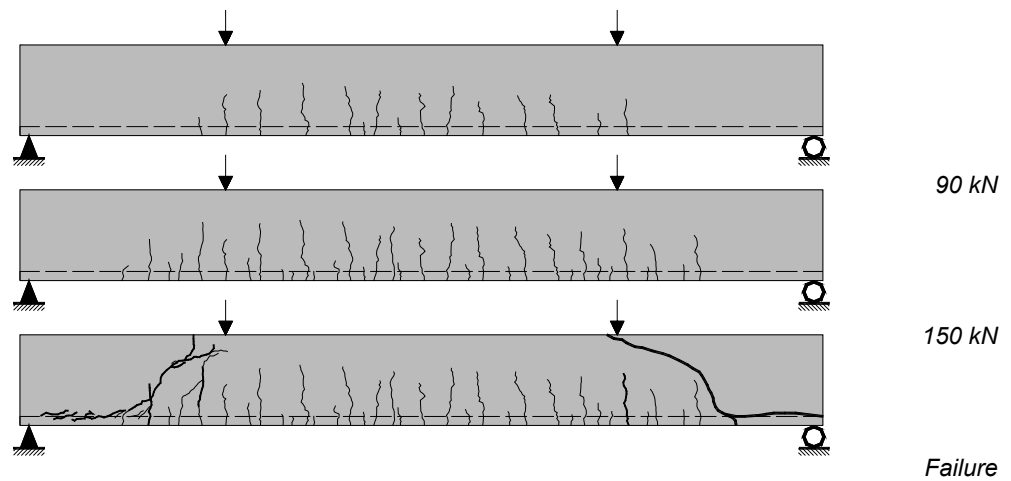
Figure 4.42: Crack pattern evolution, HSC-FRC1 specimen.

323
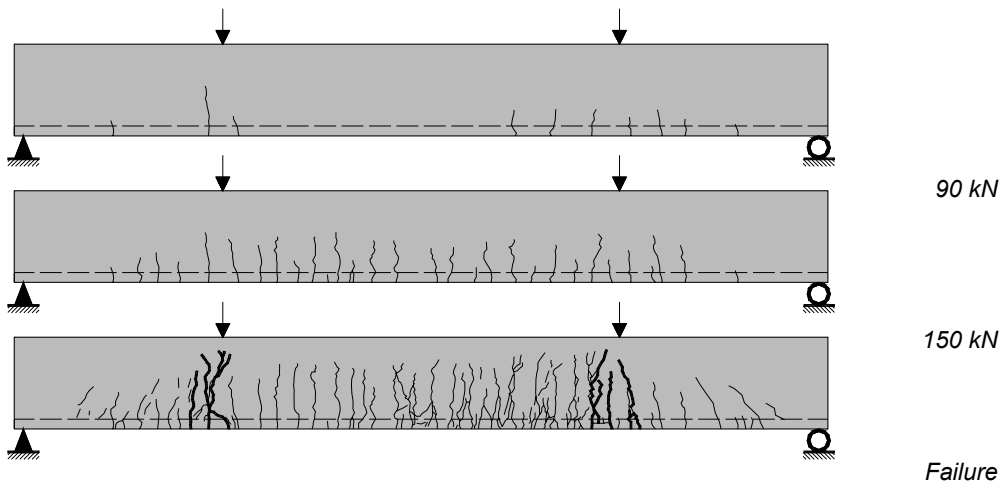
Figure 4.43: Crack pattern evolution, HSC-FRC2 specimen.

NSC1-PC
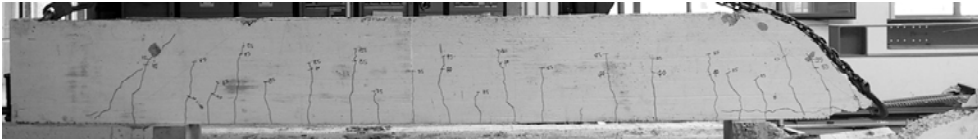
NSC1-FRC1

NSC1-FRC2

Figure 4.44: Comparison of final crack patterns, NSC1 series.

HSC-PC
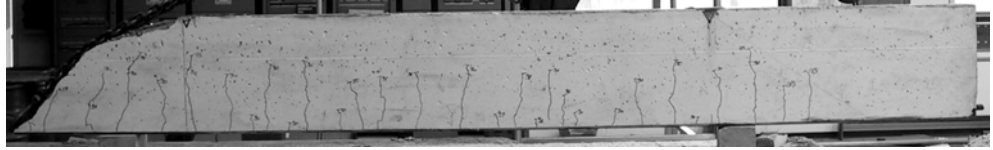
HSC-FRC1

HSC-FRC2

Figure 4.45: Comparison of final crack patterns, HSC series.

4.5   Concluding Remarks.

Fifteen tests on shear-critical beams have been presented in this Chapter.

A first series of four experiments made of normal strength plain concrete demonstrated the crucial effect of steel-to-concrete bond in determining the collapse mode as well as in influencing the post-cracking behavior and the crack formation and evolution. Steel-to-concrete bond tends to anticipate the collapse by determining a critical shear failure at load and displacement levels very low. This is due to the cracking process governed by the compatibility between steel and concrete.

The lack of bond, on the other hand, determines a flexural behavior, even though under considerable deflections and localizations of cracks.

The second series of experiments concerned the comparison of identical beams with different amount of steel fibers, used as the only shear reinforcement in the concrete matrix. Both normal strength and high strength concrete were investigated, whereas only bonded specimens were considered.

Fibers, even though in relatively low amount, turned out to greatly influence the shear behavior of beams, basically by delaying the occurrence of the block mechanism, and eventually by altering the collapse from shear to flexure, with increasing bearing capacity and, especially, ductility.

As it will be shown in Chapter 6, fibers are able to bring a structural member to its full flexural capacity, under certain conditions. In other words, the domain of the

valley of diagonal shear failure in SFRC beams can diminish, or even disappear completely, depending on the toughness and on the residual tensile strength provided by fibers to the matrix.

Finally, fibers can totally substitute the shear reinforcement required to avoid shear failure. Chapter 6 will attempt to transfer this experimental evidence into suitable design guidelines.

5. NUMERICAL ANALYSES

5.1 Introduction.

The behavior and design of reinforced concrete beams in shear remain an area of much concern. Design codes are continually changing and generally becoming more stringent. It remains a pressing need to establish design and analysis methods that provide realistic assessments of the strength, stiffness and ductility of structural elements under shear loading.

Aiming at that, the help of numerical analyses could represent an alternative and meaningful way for studying the behavior of a wide range of structural elements, once the model is verified against suitable experimental evidences.

Numerical modeling of the nonlinear behavior of reinforced concrete materials, eventually with high strength concrete or with addition of fibers requires the use of advanced computer codes, which implement material nonlinearities and allow the correct modeling of concrete fracture phenomena, fundamental when crack development and propagation significantly influence the structural response.

As already discussed in Chapter 2 (Section 2.6.7) the Modified Compression Field Theory (MCFT) is a well known model for representing the nonlinear behavior of reinforced concrete structures. It is essentially a smeared, rotating crack model for cracked reinforced concrete elements. On the basis of a number of panel tests, constitutive relationships were developed describing the behavior of cracked reinforced concrete in compression and in tension. Those models were incorporated into new design procedures (for example, that form the basis for the general method for shear design in the Canadian Code, CSA A 23.3 M94), and into the formulation of various nonlinear finite elements algorithms. The resulting analysis procedures have been shown to provide accurate simulations of response for a wide range of structures including beams in flexure, shear and torsion, deep beams, shear walls, columns, plates and shells.

However, in lightly reinforced elements, where crack shear slip is significant, the rotation of the principal stress field tends to lag the greater rotation of the principal strain field. For such elements, the shear stiffness and strength are generally slightly overestimated by the MCFT, which assumes the rotations are equal. The Disturbed Stress Field Model (DSFM; see Section 2.6.8) was developed to address this and other systematic deficiencies of the MCFT in predicting the response of certain structures and loading scenarios. The DSFM is conceptually similar to the

MCFT, but extends the MCFT in several respects. Most importantly, the DSFM augments the compatibility relationships of the MCFT to include crack shear slip deformations. The strains due to these deformations are distinguished from the strains of the concrete continuum due to stress. As such, the DSFM decouples the orientation of the principal stress field from that of the principal strain field, resulting in a smeared delayed rotating-crack model. Moreover, by explicitly calculating crack slip deformations, the DSFM eliminates the crack shear check as required by the MCFT. Constitutive relationships for concrete and reinforcement are also refined.

In this Chapter, a number of numerical analyses will be presented in order to model and discuss the most significant experiments contained in Chapter 3 and Chapter 4. Numerical analyses were basically performed on:

- The entire I-Beam series (Chapter 3);
- NSC0 series (just NSC0-BP and NSC0-UP, as the loading condition proved not to extremely influence the structural behavior);
- NSC1 series;
- HSC series (the latter three series in Chapter 4).

The numerical analyses of beams were carried out adopting a 2D plane stress FE model based on the MCFT and DSFM. In modeling the different structures, particular attention was devoted to the nonlinear behavior of the materials, especially with regards to FRC. With this respect, the program was modified by adding new tension softening relationships for the fibrous reinforcements used and, without stirrups, considering carefully the crack width limits.

A major objective of the analyses undertaken was to study, in detail, the development of shear resistant mechanisms in beams with and without shear reinforcement. An accurate evaluation of the fiber contribution to shear resistance was also sought. The analyses would also provide a measure of the accuracy and the reliability of the MCFT and DSFM in predicting the actual behavior of reinforced concrete structural elements, with special emphasis on bond mechanisms, shear failure and fiber reinforced concrete softening behavior. Details and results of these studies will be presented in this Chapter.

Further numerical studies on similar structural elements, using different FE codes and material models, can be found in [3.4], [1] and [2].

5.2 Numerical Modeling of Test Specimens.

A 2D plane stress model was developed for both types of test specimens. For the shear-critical beams (specimens of NSC0, NSC1 and HSC series) this was an accurate assumption. In the case of I-Beam specimens, a 2D representation was sufficient enough for adequately simulating the stress distribution, the crack formation and its development even at the abrupt section change (B1 and B2 section of Figure 3.3) where a 3D model could have been more representative of the actual behavior. Conversely, a 2D model was elsewhere totally faithful of the actual behavior.

Table 5.1 summarizes the transverse reinforcement details for all specimens considered.

Figure 5.1 depicts the mesh constructed for the Shear-Critical model.

Specimen	Test	Transverse Reinforcement	Concrete				Transverse Reinforc.	
			$f_{c,cube}$ [MPa]	f'_c [MPa]	f_{ct} [MPa]	E_c [MPa]	f_{sy} [MPa]	f_{st} [MPa]
I-Beam 1	TZ	no shear reinforcement	84.9	70.5	4.43	41400	-	-
	DZ	no shear reinforcement	84.9	70.5	4.43	41400	-	-
I-Beam 2	TZ	Stirrups (design reinf.)	86.1	71.5	3.69	41600	480	575
	DZ	Mesh (minimum reinf.)	86.1	71.5	3.69	41600	610	660
I-Beam 3	TZ	stirrups + 45/30 fibers	82.3	68.3	4.65	44200	480	575
	DZ	45/30 fibers	82.3	68.3	4.65	44200	-	-
I-Beam 4	TZ	stirrups + 80/30 fibers	92.8	77.0	5.18	43100	480	575
	DZ	80/30 fibers	92.8	77.0	5.18	43100	-	-
NSC0-BP		no shear reinforcement	39.6	32.9	3.15	32600	-	-
NSC0-UP		no shear reinforcement	39.6	32.9	3.15	32600	-	-
NSC1-PC		no shear reinforcement	29.9	24.8	2.30	31400	-	-
NSC1-FRC1		30/0.6 fibers	29.9	24.8	2.30	31400	-	-
NSC1-FRC2		30/0.6 and 12/01.8 fibers	29.9	24.8	2.30	31400	-	-
HSC-PC		no shear reinforcement	72.9	60.5	3.15	34400	-	-
HSC-FRC1		45/30 fibers	73.6	61.1	3.48	36800	-	-
HSC-FRC2		80/30 fibers	70.3	58.3	3.20	32700	-	-

Table 5.1: Summary of experimental program.

Table 5.2 and Table 5.3 report the main features of the meshes adopted for the different sets of structural elements considered. Note that four-noded elements with uniform thickness were used in all concrete FE representations, while two-noded truss bars with uniform cross-sectional area were adopted for any reinforcement not embedded.

329
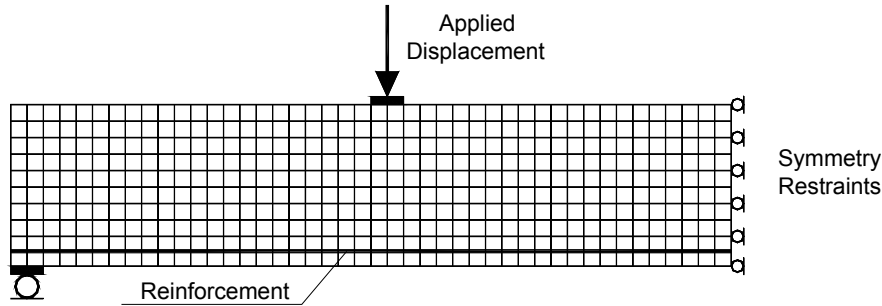
Figure 5.1: FE representation of the shear-critical specimens.

Specimen	Test	Concrete Elements	Reinforcement Elements	Link Elements
I-Beam 1	TZ	1544	440 truss elements for prestressing; longitudinal rebars, stirrups and welded mesh fabric were embedded.	Perfect bond
	DZ			
I-Beam 2	TZ			
	DZ			
I-Beam 3	TZ			
	DZ			
I-Beam 4	TZ			
	DZ			
NSC0-BP		499	45 truss elements for longitudinal rebars;	Perfect bond
NSC0-UP				44 (no bond)
NSC1-PC		499	45 truss elements for longitudinal rebars;	Perfect bond
NSC1-FRC1				
NSC1-FRC2				
HSC-PC		499	45 truss elements for longitudinal rebars;	Perfect bond
HSC-FRC1				
HSC-FRC2				

Table 5.2: Summary of numerical models.

With regard to the reinforcement, different modeling approaches were adopted. Prestressing steel reinforcement (which was provided to the I-Beam model trough 0.6" low-relaxation strands) was modeled by using truss elements, linking nodes having the same coordinates and numbers of concrete nodes. Perfect steel-to-concrete bond was therefore assumed. The pretension loading was simulated by applying a prestrain to the cable. The prestrain was chosen equal to the experimental value (taking into account friction and inelastic losses in the amount of 15% of the total initial value). In the transfer zone a linear development of prestrain was assumed, in order to simulate the transfer phenomenon of the pretensioning from the beam end (no prestrain) to a distance equal to 80 strand diameter

(1200 mm), beyond which the pretension action was assumed to be uniform and completely developed.

Specimen	Test	Loading Stages	MCFT/DSFM	Failure
I-Beam 1	TZ		DSFM	Shear
	DZ		DSFM	Shear
I-Beam 2	TZ	- Prestressing and dead load	MCFT	Shear
	DZ		DSFM	Shear
I-Beam 3	TZ	- Concentrated Load	MCFT	Shear
	DZ		DSFM	Shear
I-Beam 4	TZ		MCFT	Shear
	DZ		DSFM	Shear
NSC0-BP		Concentrated Load	DSFM	Shear
NSC0-UP			DSFM	Flexure
NSC1-PC			DSFM	Shear
NSC1-FRC1		Concentrated Load	DSFM	Shear
NSC1-FRC2			DSFM	Flexure
HSC-PC			DSFM	Shear
HSC-FRC1		Concentrated Load	DSFM	Shear
HSC-FRC2			DSFM	Flexure

Table 5.3: Summary of Loading scheme, model applied and failure predicted.

For the I-Beam model, deformed bars (which were placed to control crack formation and development, and to allow the structure to achieve greater ductility), stirrups and welded wire mesh were modeled as embedded reinforcement in the concrete elements. Perfect steel-to-concrete bond was also assumed in this case. In the shear-critical beam model (NSC0, NSC1 and HSC series), deformed bars, which were the only flexure reinforcement, were modeled with truss elements. Except the element NSC0-UP, where no bond at all was modeled, perfect steel-to-concrete bond was assumed for elements made both of plain concrete and of fiber reinforced concrete. Concerning the latter sets of elements, there are not appropriate shear stress-shear slip laws accounting for FRC that are well accepted in the current literature.

Conversely, Chapter 6, will discuss the effect of bond by presenting different steel-to-concrete models, intermediate between perfect bond and no bond.

In order to avoid unrealistic punching failure and numerical instability problems due to load concentration, point loads and supports were simulated as nodal loads acting on a steel plate having the longitudinal dimension of two finite elements (total of 100 mm) and a thickness of 30 mm (Figure 5.1), perfectly connected to the concrete elements.

While a single load condition was needed to analyze the shear-critical beams, a two load case analysis was defined for the I-Beam model:

- LOAD CASE I: the prestrain loading was applied to the tendons and the dead load to the concrete elements. In order to account for the prestressing losses, a prestrain of 6.1 x 10^{-3} mm/mm (corresponding to a prestress of 1190 MPa) was applied to all cables instead of the original 7.2 x 10^{-3} mm/mm (prestress of 1400 MPa), applied during jacking. At transfer, a prestrain variable from 0 to 6.1 x 10^{-3} mm/mm was applied. By investigating the structure at this step, it was found that the camber calculated by the FE program was similar to the experimental one and the stress along the cable was in good agreement with most of analytical predictions. Moreover, few small cracks at the very beginning of the transfer appeared in the model.
- LOAD CASE II: application of live load. The point load was increased up to failure.

5.3   Modeling of Materials.

5.3.1   Concrete.

Concrete mechanical properties adopted in the numerical analyses, illustrated in Table 5.1, are based on the results of a number of tests performed on the same mixes used in the full-scale elements, as already reported in the two previous chapters.

In this section, it is particularly worthy discussing the assumption regarding the tensile behavior. Concrete in tension was assumed to be linear up to the tensile strength, experimentally measured on cylinders.

The post-peak behavior in tension, if in one hand is well known for plain concrete, on the other hand had to be cautiously evaluated for FRC as it can significantly influence the response of a member.

The identification of the tensile behavior of FRC materials utilized was carried out according to the Italian Standard (see Section 2.8.4), which requires that fracture mechanics CMOD (Crack Mouth Opening Displacement) controlled four-point bending tests (4PBT) be performed on small notched beam specimens (150x150x600 mm) to determine toughness indexes and conventional residual strengths.

Figure 5.2 illustrates a picture of the steel loading frame available at the Laboratory for Testing Materials of the University of Brescia for performing four point bending tests.

Figure 5.2: Top and bottom steel loading frame for performing four point bending test.

Figure 5.3 shows a notched beam ready to be tested, with the instrumentation, consisting in a clip gauge (which controls the rate of increasing CMOD), and LVDTs measuring crack openings (2 CTODs, one in the front and one in the back side) and vertical displacements (at midspan and at the two load point locations).

The beam was notched at midspan; the depth of the notch was set equal to 45 mm, corresponding almost one third of the total depth of the member.

Figure 5.4 illustrates the experimental load-CMOD curves and the geometry of some of the many 4PBTs carried out: four beams were cast both with 45/30 fibers and with 80/30 fibers, whereas only two specimens made of plain concrete are shown. The following discussion will deal only with this kind of fibers (adopted both in I-Beam and HSC series) even though the procedure herein followed applies for all fiber typologies utilized.

Note the highly significant contribution provided by fibers, if compared with plain concrete. Fibers 80/30 proved to be very performing, showing even a hardening behavior under bending, for small values of cracking.

Figure 5.3: Specimen with instrumentation.

Figure 5.5 shows the ligament length of two specimens (the one on the left containing fibers 45/30, the one on the right with fibers 80/30) after completion of test. Recognize the consistent difference in the number of fibers crossing the crack, in spite of the content, which was the same in the two specimens: it is a matter, in fact, of the different aspect ratio (namely, 45 versus 80).
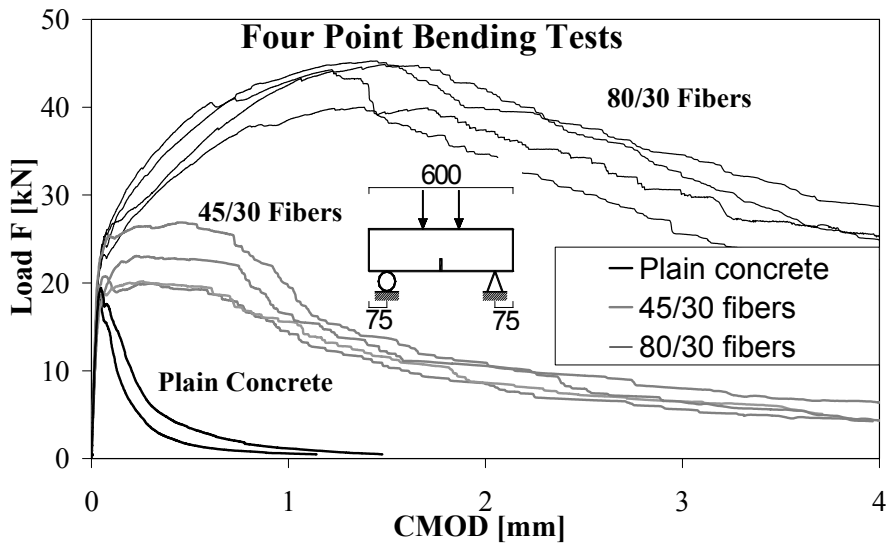
Figure 5.4: Experimental results of 4PBTs in the case of I-Beam series.

In order to find a stress-crack opening constitutive relationship after cracking, numerical analyses were performed using the FE program MERLIN [3], which is based on a discrete crack approach. Program MERLIN considers the structure as many linear elastic sub-domains, linked by interface elements that simulate cracks whose position must be known a priori. Interface elements initially connect the sub-domains (as rigid links) and start activating (i.e. cracks start opening) when the normal tensile stress at the interface reaches the tensile strength of material. The crack subsequently propagates and cohesive stresses are transmitted between the crack faces according to a stress-crack opening (σ-w) law (which is given as an input for the interface elements).

Figure 5.5: Ligament area of two different kinds of concrete mixtures after completion of test.

Figure 5.6 illustrates a FE representation adopted for performing the analyses with MERLIN. Plain stress three-noded elements were adopted with a quite different refinement: the mesh was in fact built in order to be very detailed along the ligament length, and at load point and support locations.

Figure 5.7 shows the numerical response of the 4PBTs, obtained by calibrating suitable σ-w laws, indicating a close agreement with the experimental results.

No softening law was calibrated for plain concrete, as the models that are already available in the VecTor program [4] proved to be accurate enough for a wide range of applications.
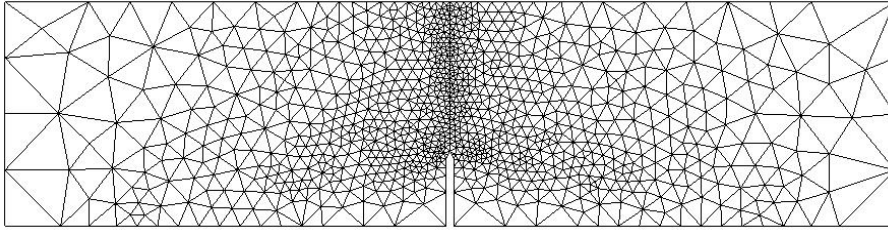
Figure 5.6: Mesh of the tested concrete beams adopted in Merlin.

The cohesive laws calculated with MERLIN had to be reduced into a cohesive stress-strain relationships (VecTor2 [4] is a smeared cracking model) by dividing the crack width by a "characteristic length". Since well acknowledged procedures do not exist for calculating characteristic lengths in presence of fibrous reinforcement (which is actually a matter of debate), a method was used based on the evidence of many 4PBTs carried out at the University of Brescia [5]. In fact, after the peak load, members with low volume fractions of fibers ($V_f<1\%$) generally do not show a strength higher than that offered by plain concrete: fibers, like regular reinforcement, need a certain amount of cracking to start resisting failure. The first branch of the cohesive post-peak law of a fibrous material is thus generally similar to that of the reference material (without fibers). It was therefore chosen to calibrate the characteristic length of the two FRC materials, as illustrated in Figure 5.8, by imposing the first post-peak branch of the $\sigma-\varepsilon$ curve of plain concrete (assuming the bilinear $\sigma-\varepsilon$ softening curve suggested by CEB [6], and imposing a crack spacing of 150 mm, value close to the experimental one) to be equal to the first branch of the two curves of FRC, as shown in Figure 5.8 (line AB). The condition being applied led to a value of characteristic length equal to 125 mm for 45/30 fibers and 1000 mm for 80/30 fibers. Note that the higher the fracture energy G_f, the greater is the characteristic length value, according to many researchers. Note that 80/30 fibers showed a G_f four time greater than 45/30 fibers.

This was a conventional way to find a reliable value of the characteristic length. Further studies, which are out of the interest of the present research, should be done with this respect.

336
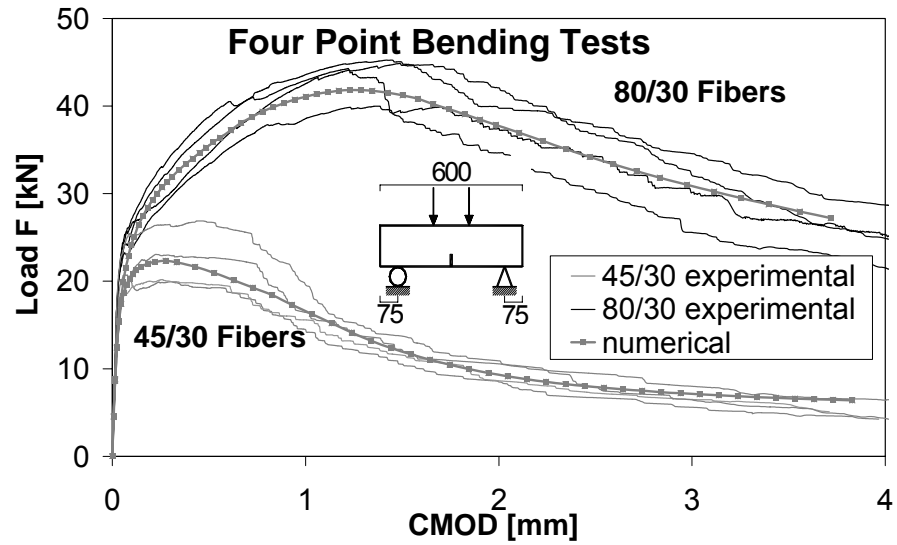
Figure 5.7: Experimental and numerical Load-CMOD curves of 4PBT on beams cast with 45/30 and 80/30 fibers, I-Beam series.

These relationships were then incorporated in the code of VecTor2 [4], and used in performing all elements made of FRC.
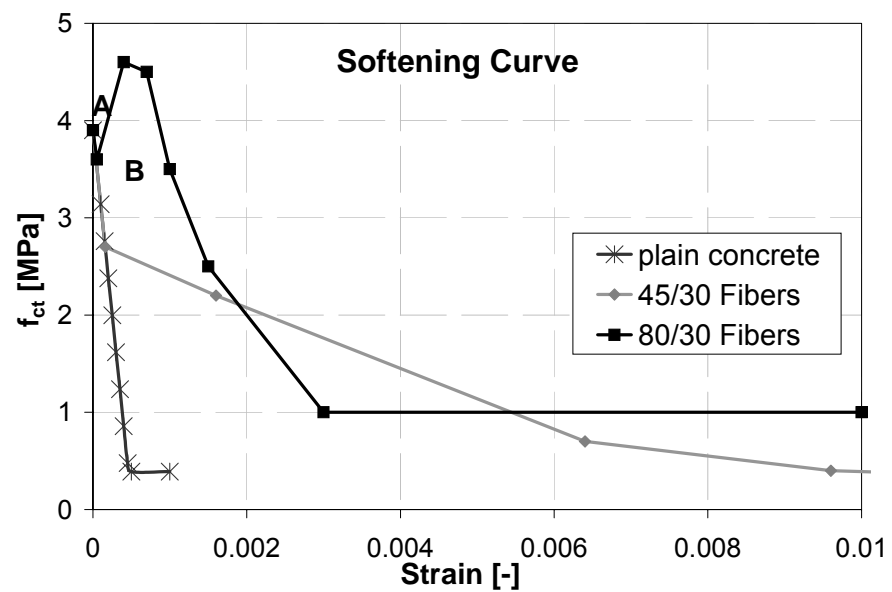
Figure 5.8: Constitutive stress-strain tension softening laws adopted for fibers and plain concrete.

Table 5.4 reports the cohesive laws calibrated with the program MERLIN and the $\sigma-\varepsilon$ laws then incorporated into VecTor.

Fiber Reinforced Concrete Type					
FIBERS 45/30			FIBERS 80/30		
f_{ct} =3.9 MPa			f_{ct} =3.9 MPa		
σ	w	ε	σ	w	ε
[MPa]	[μm]	E-3	[MPa]	[μm]	E-3
3.9	0.0	0	3.9	0.0	0.0
2.7	0.02	0.16	3.6	0.05	0.05
2.2	0.2	1.6	4.6	0.4	0.4
0.7	0.8	6.4	4.5	0.7	0.7
0.4	1.2	9.6	3.5	1.0	1.0
0.15	2.5	20.0	2.5	1.5	1.5
			1.0	3.0	3.0

Table 5.4: Stress-crack opening-equivalent strain relationships for fiber reinforced concrete.

The same procedure was followed for all other fiber typologies utilized (See Figure 4.4. and Table 4.6): firstly, 4PBTs were carried out according to the Italian Standard. By means of the FE program MERLIN, appropriate cohesive laws were calibrated, then turned into $\sigma-\varepsilon$ laws by equating the first branch of the σ-w laws of all specimens having the same concrete matrix. As an example, Table 5.5 reports the softening laws, both in terms of crack width and strain, of specimens of NSC1 series. The characteristic lengths turned out to be equal to 180 mm and 250 mm, respectively for fibers 30/0.6 (specimen NSC1-FRC1) and for the composite containing both kind of fibers (specimen NSC1-FRC2).

Fiber Reinforced Concrete Type					
FIBERS 30/0.6			FIBERS 30/0.6+12/0.18		
f_{ct} =2.70 MPa			f_{ct} =2.70 MPa		
σ	w	ε	σ	w	ε
[MPa]	[μm]	E-3	[MPa]	[μm]	E-3
2.7	0.0	0.0	2.7	0.0	0.0
0.9	0.026	0.14	1.35	0.035	0.14
0.0	10.0	5.55	1.1	0.20	0.8
			0.0	20.0	80.0

Table 5.5: Stress-crack opening-equivalent strain relationships for fiber reinforced concrete.

338

5.3.2   Reinforcement.

The same steel types were utilized in all sets of structures.

Based on experimental results for tendons, a modified Ramberg-Osgood polilinear curve, suitable for low relaxation steel, was defined for the prestressing steel. Stirrups, welded wire mesh, and deformed bars were in all cases defined as an elasto-plastic materials with hardening by means of a multilinear stress-plastic strain curve representing the actual response of several bars tested. Table 5.1 also shows the yield and the ultimate stress of each type of transverse reinforcement utilized. Further details on materials are reported in Chapter 3 and Chapter 4.

5.4   Comparison of Numerical and Experimental Results.

5.4.1   I-Beam Specimens.

As with the laboratory tests, the numerical analyses were performed with a displacement controlled procedure, by imposing an increasing displacement at the nodes located at the middle of the steel transfer plate.

Figure 5.9-Figure 5.12 illustrate the load-displacement curves for the four I-Beam specimens in the TZ and DZ zones, respectively. Displacement were measured at the load location. Note that three experiments were plotted for test DZ of I-Beam 3 (it contains also the two identical tests performed on I-Beam 5, see Chapter 3).

In all cases, the linear behavior is closely captured by the numerical model. The first cracking point, corresponding to the onset of nonlinearity, is adequately similar to the experimental value. Upon formation of the first tensile crack, probably owing to the smeared approach of the MCFT, the behavior is still stable and the numerical model takes slightly more load, compared to the experimental response, before showing a distinct diagonal crack.
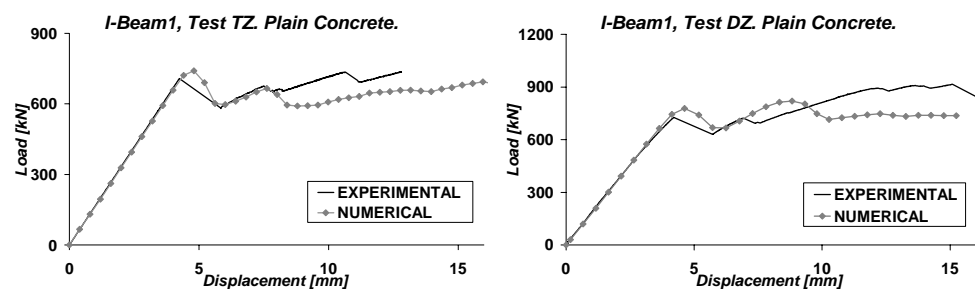
Figure 5.9: Numerical and experimental load-displacement curves, I-Beam 1.
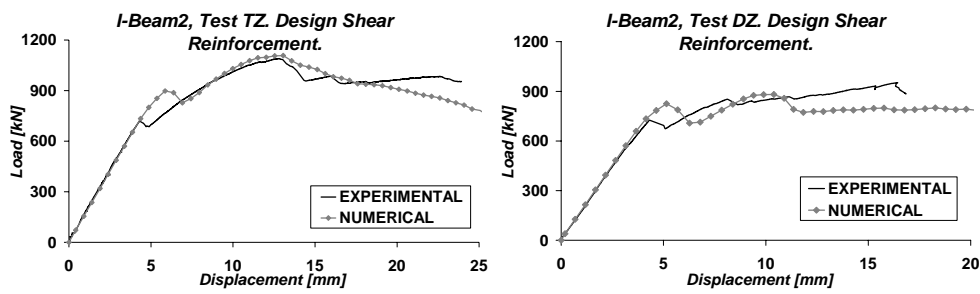
Figure 5.10: Numerical and experimental load-displacement curves, I-Beam 2.

As far as post-cracking phase is concerned, the FE program VecTor2 exhibited very good convergence in every case, although strong instability after the first cracking point was observed in the experiments. Calculated responses for the TZ zones were generally more accurate than for the DZ zones, probably due to the presence, in I-Beam 2, 3 and 4, of stirrups, which produced a more stable post-peak response, both numerically and experimentally. Moreover, the crack pattern consisted of well distributed cracks corresponding to the well known truss model, at least up to the maximum experimental load value, as shown in Figure 5.9-Figure 5.12.
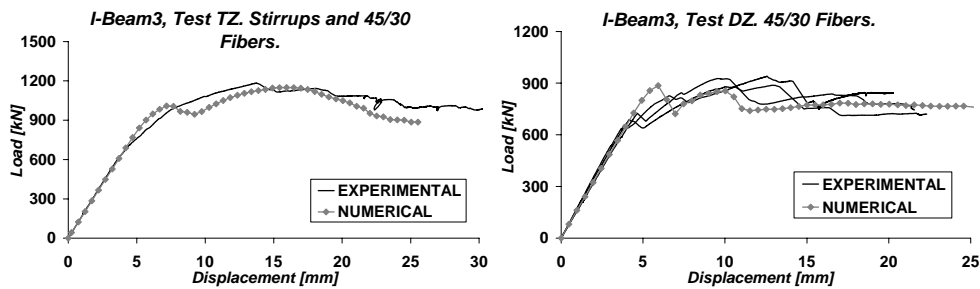
Figure 5.11: Numerical and experimental load-displacement curves, I-Beam 3.
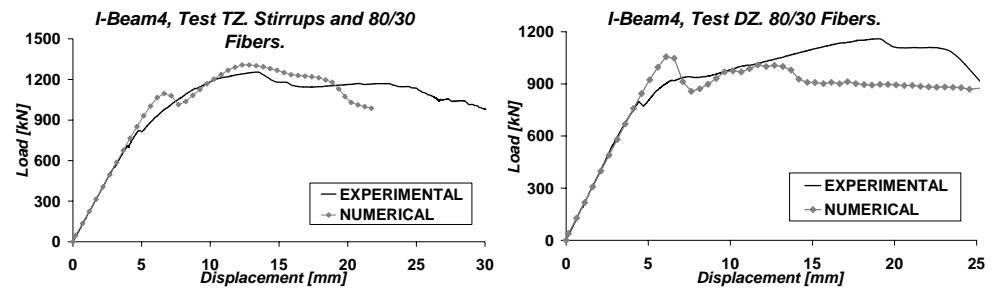
Figure 5.12: Numerical and experimental load-displacement curves, I-Beam 4.

In such a situation, numerical analyses typically provide accurate simulations. However, in lightly or non reinforced shear beams, such as I-Beam 1 (both TZ and DZ model) and I-Beam 2, 3 and 4, DZ model, the behavior was governed soon after cracking by the formation of a dominant shear crack running from the load application point to the support. Here, some considerations on the local behavior, in terms of maximum crack width and local stress conditions adjacent to the crack, were examined in order to perform a proper analysis. The MCFT has been shown to provide a viable and accurate method for analysis of shear-critical beams containing little or no shear reinforcement as long as two minor limits are imposed on the original constitutive relations, one relating to tensile stresses in the concrete and the other to crack widths (leading to the formulation of the DSFM). Concerning the latter aspect, shear slip along the surfaces of wide cracks can result in a divergence between the directions of principal stress and the apparent directions of principal strain (see Section 2.6.7 and 2.6.8). An overestimation of the reorientation of the stress trajectories and, hence, in the ductility of the beam may result. To guard against this, the principal compressive stress was rapidly diminished in elements containing cracks exceeding a limit of 5.0 mm in width. The latter value is greater than the proposed of 2.0 mm [7] due to the huge geometry and the beneficial effect of fibers, which act in reducing the instability of cracks (the measured main crack width reached values up to 20 mm in the fibrous I-Beams). That assumption resulted in a better correlation with the experimental results. In the case of I-Beam 2, 3 and 4 (test TZ) which were cast with design stirrups, the crack width limit had little or no influence, as already known [7] in presence of transverse reinforcement. In those beams, by inputting the experimentally measured average crack spacing of 150 mm, preferred to the program default CEB-FIB [6] code expression, the agreement with the experimental evidence increased somewhat.

The average crack spacing was chosen in all other cases as a value close to the experimental one.

Moreover, it is important to note that the strong correlations achieved in the analytical modeling was in large part due to the rotating crack approach, which is a basis of the MCFT and DSFM. In fact, the experimental beams initially showed a diffused crack pattern in the panel (except in I-Beam 1, made of plain concrete), which later developed through a progressive crack rotation and crack merging together, leading to a single macro-crack oriented diagonally. This rotation led to an ultimate resisting mechanism governed by arch action and concrete residual compressive strength. The numerical model was able to capture this phenomenon, even in presence of fibers.

Fibers increased the residual compressive strength since they effectively reduced damage in tension (i.e., by controlling transverse tensile strains). Examining the experimental and numerical curves for high values of displacement, fibers could not offer any further residual tensile strength, since the main shear crack was very wide. However, the load bearing capacity proved to be significantly greater in the fibrous beams than in the others. This evidence meant that the resisting strut area, in the final arch resisting mechanism, must have been greater with fibers. The latter aspect is significant, particularly in terms of compression strength offered by fibers and in terms of material characterization.

The ability of the model to rotate the principal tensile strain pattern is likely a major reason for the good convergence attained in the numerical analyses, even for point-load displacements 5-6 times greater than the one corresponding to the first cracking point (Figure 5.9-Figure 5.12).

5.4.2   Shear-Critical Beams.

5.4.2.1   The Effect of Steel-to-Concrete Bond (NSC0 series).

Figure 5.13 reports the comparison between the experimental and numerical load deflection curve, whereas Figure 5.14 shows some comparisons of crack patterns at different load stages.

Concerning the first diagram, it can be said that the numerical model, even though carried out considering perfect steel-to-concrete bond, is quite accurate in terms of first cracking point and post-cracking stiffness. The ultimate load is slightly overestimated (166 kN versus 149 kN, differencing of about 10%). The quite important scatter associated with phenomena related to cracking in tension is

anyhow to be considered: to confirm that, the ultimate experimental load exhibited by specimen NSC2-PC, having almost identical mechanical properties with respect to the specimens herein discussed, turned out to be equal to 157 kN. In this case, the difference compared to the numerical prediction is even lower, of around 6%.
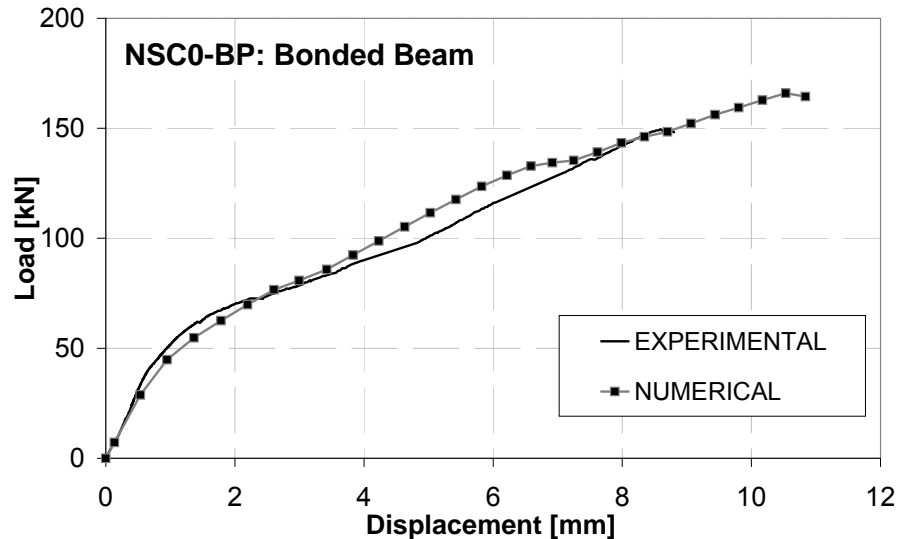
Figure 5.13: Numerical and experimental load-displacement curves, specimen NSC0-BP.

Looking at the cracking phenomena, crack formation and development in the experiments and in the numerical models are quite similar to each other. At a load intensity of 130 kN (Figure 5.14 (b)), cracking in the shear span is noticeable both in the experimental and numerical picture: nevertheless, the critical crack, which brings the specimen to the final collapse, is different in location and inclination. The numerical model locates the critical shear crack at a distance, from the support, around 1.5 times the depth of the member, while in the experiment that distance was around equal to the depth of the beam.

Moreover, while the inclination of the predicted crack is around 45° directly from the load point to the longitudinal bottom reinforcement, a more detailed pattern was experimentally observed, having a first branch inclined as the thrust line running from the load point to the support, then deviating into a crack inclined of 45° to the horizontal till the bottom reinforcement.

The numerical model was anyhow able to model the final block mechanism, accompanied also with an extensive cracking due to splitting along the longitudinal rebars.
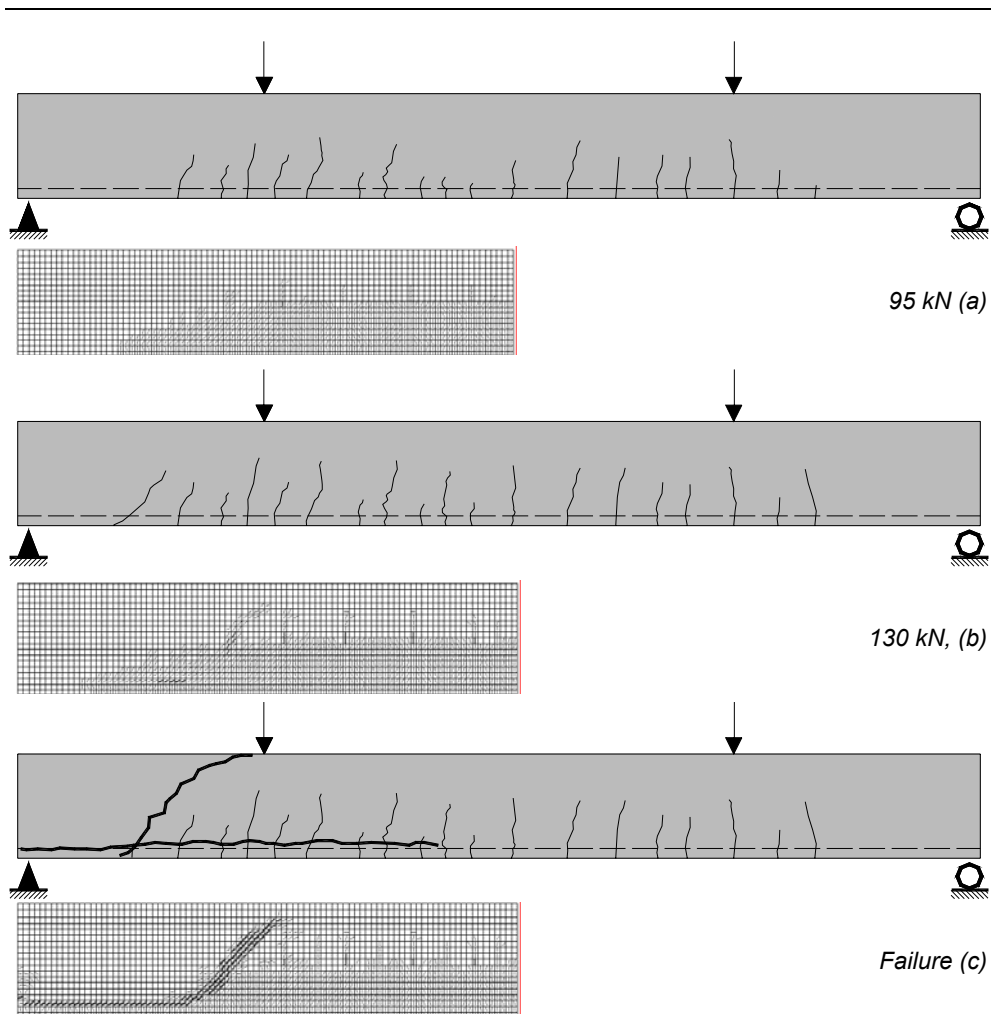
Figure 5.14: Predicted and experimental crack patterns at different load stages, specimen NSC0-BP.

Figure 5.15 reports the predictions of crack pattern and its developments, plotted at the same load levels of the previous Figure (namely, 95 kN, 130 kN and at failure), according to program Response 2000, developed at the University of Toronto, and also based on the MCFT [8].

The program allows analysis of beams and columns subjected to arbitrary combinations of axial load, moment and shear. It also includes a method to integrate the sectional behavior for simple prismatic beam-segments. The assumptions implicit in the program are that plane sections remain plane, that steel-to-concrete bond is perfect, and that there is no transverse clamping stress across

the depth of the beam. For sections of a beam or column a reasonable distance away from a support or point load, these are excellent assumptions. These are the same locations in beams that are usually the critical locations for brittle shear failures.
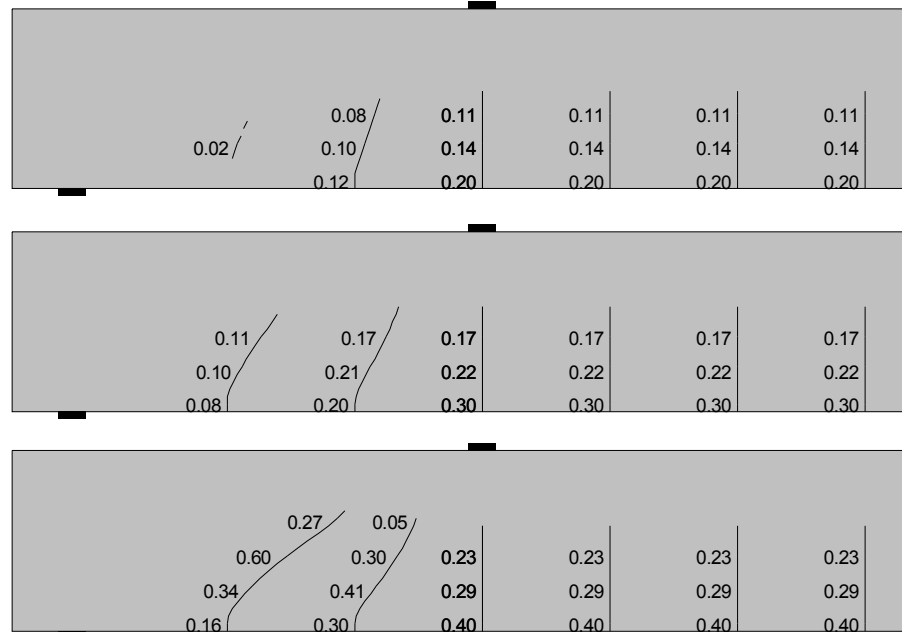
Figure 5.15: Crack pattern and its development predicted by Program Response 2000.

The first plot clearly evidences the occurrence of the first shear crack in the panel area, at a distance of about the depth of the member, from the support. This crack develops till becoming the critical one that determines the shear collapse of the member. Note the rotation of the critical crack at the ultimate loading stage, toward the load point. The final crack pattern seems to be a little closer to the one experimentally observed, if compared to the one observed with Program VecTor 2.

The program calculated the member response as well, giving a maximum load of 166 kN (identical to the value predicted by VecTor 2) and a maximum deflection at midspan of 9.2 mm. The former value is overestimated of about 11%, compared to the corresponding experiment.

The results of the numerical simulations of specimen NSC0-UP turned out to be even in higher agreement with the experimental evidence.

Figure 5.16 shows the experimental and numerical load-deflection curves: the agreement is considerable, even though the numerical model slightly overestimates the post-cracking stiffness, especially for high levels of deformations. The ultimate load is easily predicted by the model (340 kN against the experimental value of 329 kN, with a difference of only 3%) due to the fact that the specimen achieved its full flexural capacity with a consistent ductility.
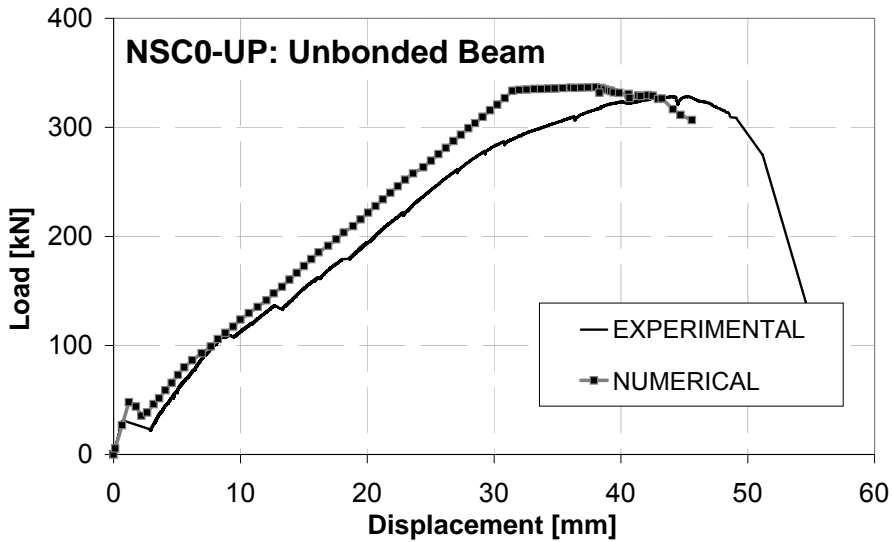
Figure 5.16: Numerical and experimental load-displacement curves, specimen NSC0-UP.

A concentrated huge crack, under the load point location, suddenly generates in the model (Figure 5.17 (a)), according to the experiment. This is accompanied with a huge displacement increase, but not as consistent as the experiment exhibited. Another flexural wide crack then develops, tending to bifurcate and join to the adjacent, in exactly the same fashion as it was observed.

The numerical analyses also accurately model the arch action as well as the final failure due to crushing of concrete at the top face. Moreover, the failure of the numerical model arises for slightly lower levels of deformations, with crushing of concrete at the point load, rather than at midspan, as experimentally observed.
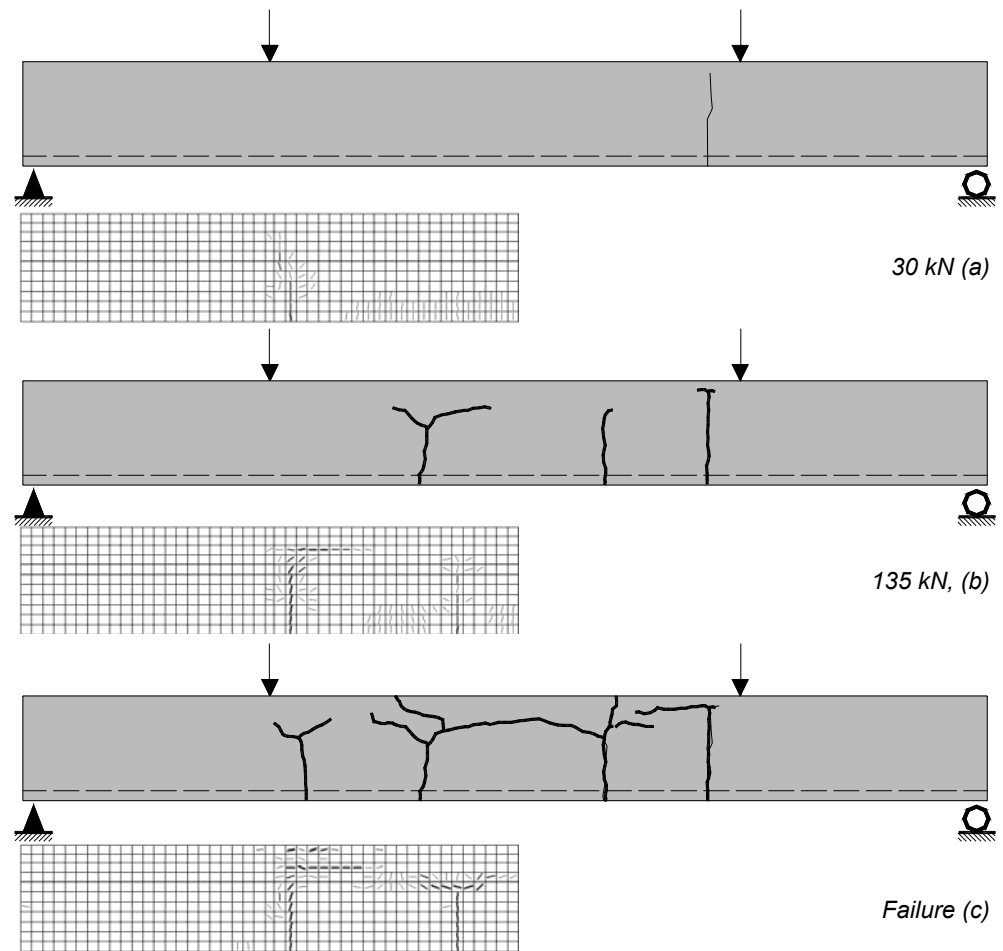
Figure 5.17: Predicted and experimental crack patterns at different load stages, specimen NSC0-UP.

5.4.2.2 The Effect of Fibers (NSC1 and HSC series).

As with the experimental tests, the numerical analyses were performed with a displacement controlled procedure.

Figure 5.18 illustrates the load-displacement experimental and numerical curves for the three specimens of HSC series, with the displacement measured at midspan.

The post-peak behavior is somewhat overestimated by the simulations, particularly at the beginning of the non-linearity. This is probably due to the effects of tension stiffening and tension softening, which play an important role at the onset of cracking, before the complete transition to the cracked stage.

347

The DSFM was applied to all specimens owing to the absence of stirrups everywhere. Different crack limits were set for the specimens, in accordance with the experimental results, which showed different collapse phenomena (namely, for HSC-PC a value of one tenth of the aggregate size was chosen, whereas 2 mm and 10 mm were the values assumed respectively for models HSC-FRC1 ad HSC-FRC2).
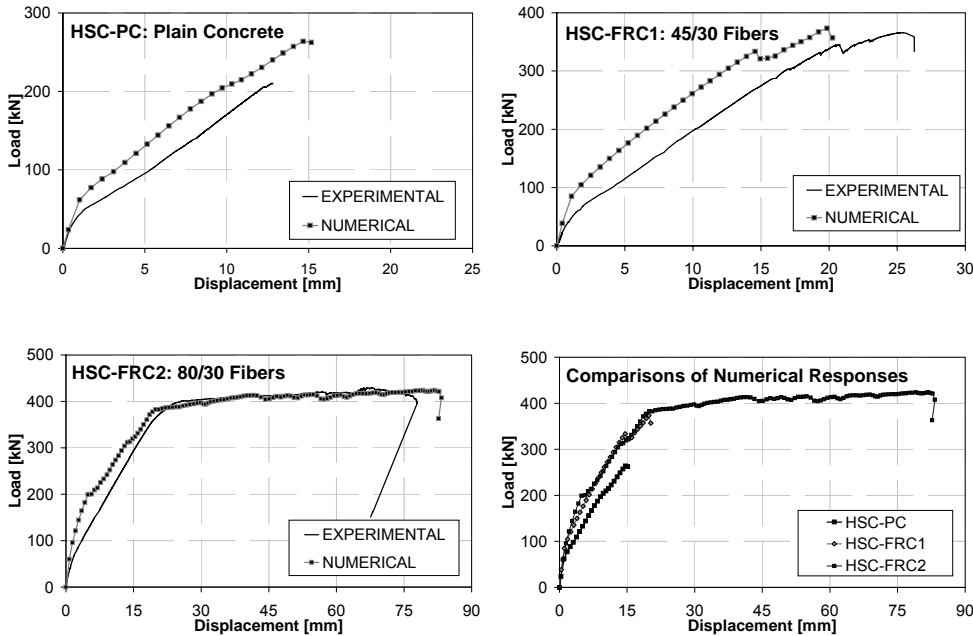
Figure 5.18: Numerical and experimental load-displacement curves, specimen HSC-PC, HSC-FRC1 and HSC-FRC2.

A sudden and very brittle shear failure was observed in beam HSC-PC, with a main shear crack only 0.24 mm wide. HSC-FRC1 showed a shear failure as well, but with a much wider main shear crack and greater overall displacement, the former being 2.2 mm and the latter 26 mm (see Table 4.8). Hence the collapse was more controlled due to the bridging effect provided by fibers, which allowed the transfer of tensile stresses along the shear-critical crack.

HSC-FRC2 exhibited a flexure failure with yielding of the longitudinal deformed bars. A shear-critical crack formed too, but the high carbon fibers (80/30 designation) were able to provide sufficient shear capacity and therefore alter the collapse from shear to bending. This results in considerable structural advantages such as a much grater ductility and a higher load bearing capacity (Figure 5.18) .

Figure 5.19 illustrates the crack pattern at the termination of the tests and the corresponding crack patterns determined from the analyses.

HSC-PC, (a)
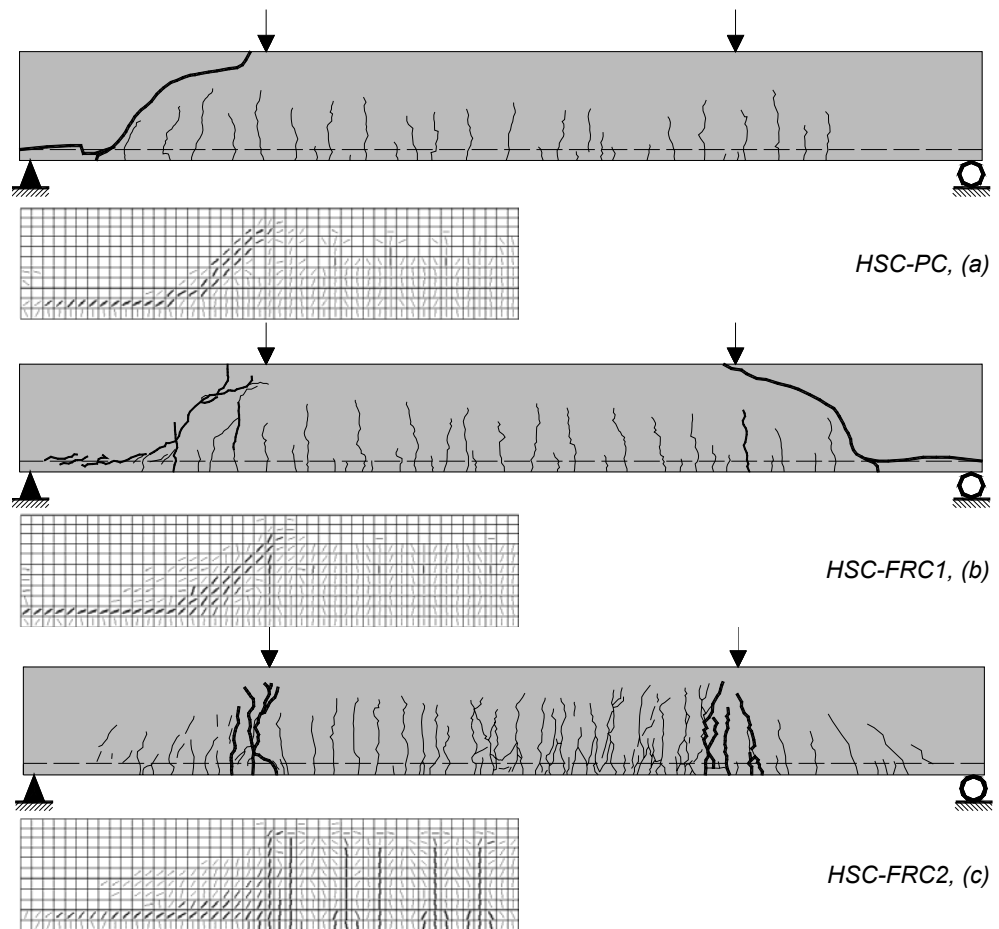
HSC-FRC1, (b)

HSC-FRC2, (c)

Figure 5.19: Predicted and experimental crack pattern at failure, HSC-PC (a), HSC-FRC1 (b), and HSC-FRC2 (c).

An appreciable agreement is seen between experiments and simulations: HSC-FRC1 exhibited a behavior in between the other two tests shown in Figure 5.19: in fact, it was possible to note fairly big cracks even in flexure, while HSC-PC did not exhibit any significant. HSC-FRC2 showed consistent cracks in shear (not crucial anyhow) and wide cracking in bending, likewise the experiment.

The model was also able to predict yielding of the rebars at the point load location.

Figure 5.20 provides all experimental and numerical plots for specimens of NSC1 series, having a compressive strength of about 25 MPa. Even in this case,

numerical results are adequately accurate, particularly in predicting the failure mechanism, that was due to shear in specimens NSC1-PC and NSC1-FRC1, whereas was due to crushing of concrete in member NSC1-FRC2.

In the first case, the maximum load, displacement, and the overall post-cracking stiffness are slightly overestimated, giving however a quite precise fitting (the ultimate load and deflection of the prediction are 7% and 9% higher, respectively).

Concerning the crack patterns, the block mechanism arises in the model, even though the critical crack locates closer to the point load, compared to the experimental, as already shown for specimen NSC0-UP.
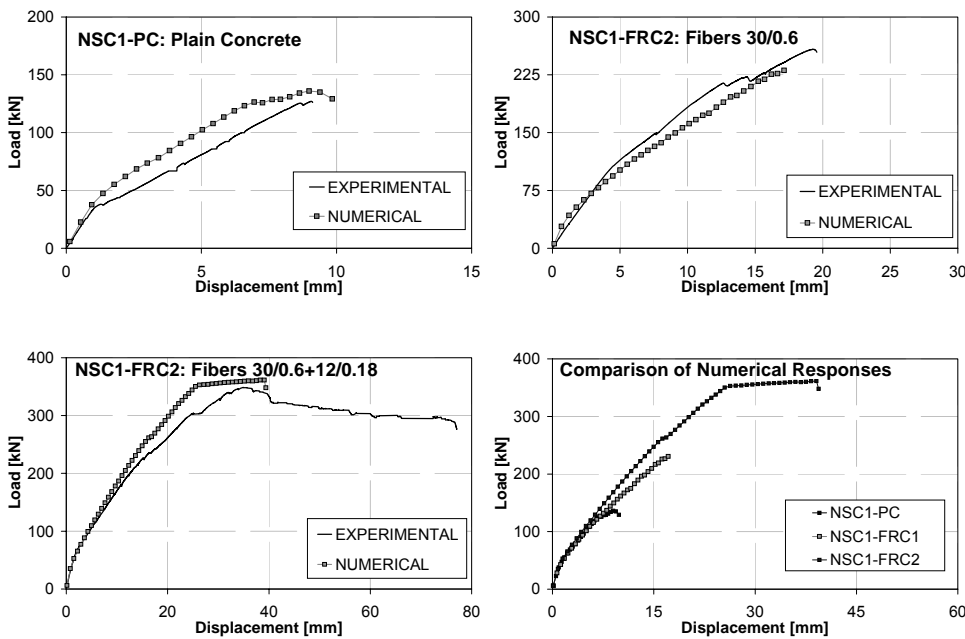
Figure 5.20: Numerical and experimental load-displacement curves, specimen NSC1-PC, NSC1-FRC1 and NSC1-FRC2.

With regards to beam NSC1-FRC1, the tension softening law adopted and implemented into the program proved to be quite accurate, giving a very good fitting of the post-cracking stiffness. The model underestimates both ultimate load and deflection, of about 10% and 14%, respectively. The crack pattern at failure evidences the quite important shear cracking that could developed in the shear span (Figure 5.21 (b)). This is well modeled by the analysis, which also brings the specimen up to failure with a more extensive cracking in the shear span, according to the experiment. This is a situation fairly close to the transition between shear and

flexure failure: cracking is well influenced by both mechanisms and the load is not far to that corresponding to the full flexural capacity of the member.

NSC1-PC, (a)

NSC1-FRC1, (b)
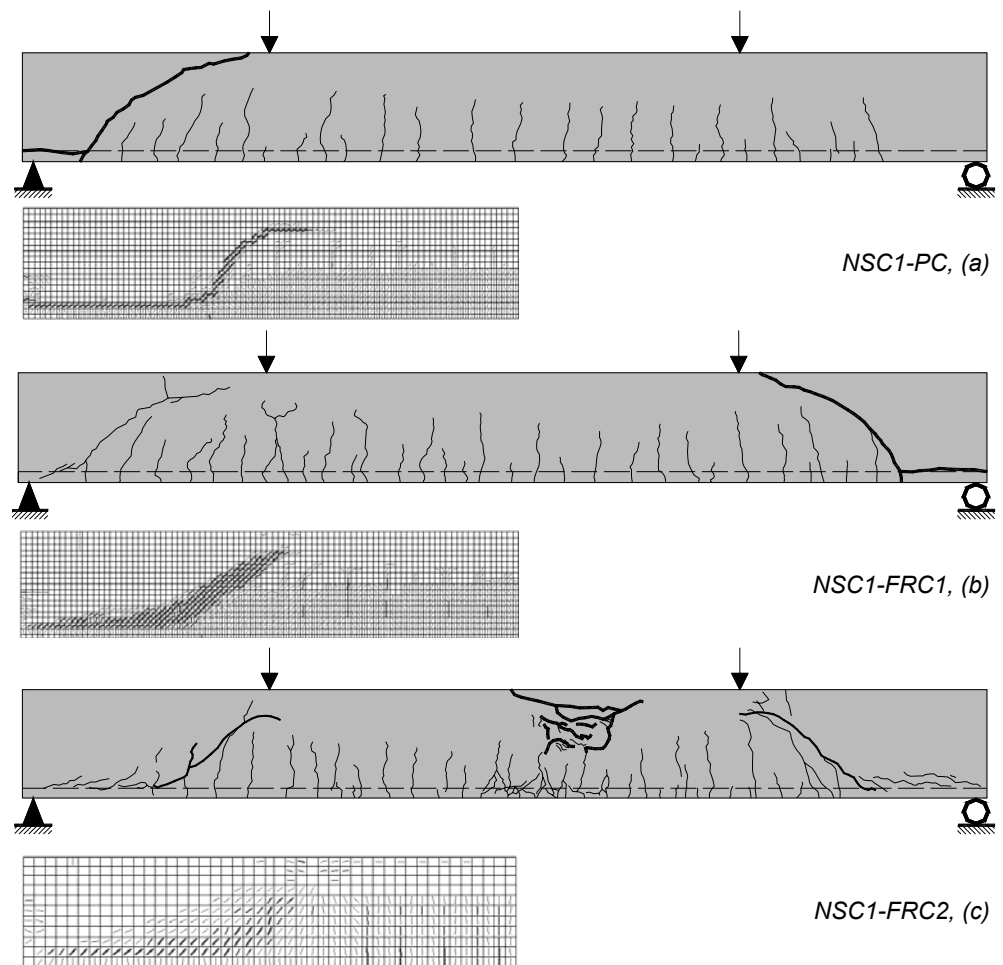
NSC1-FRC2, (c)

Figure 5.21: Predicted and experimental crack pattern at failure, NSC1-PC (a), NSC1-FRC1 (b), and NSC1-FRC2 (c).

The block mechanism is well modeled, with an inclination of the critical crack quite lower (with respect to the horizontal) than that predicted for specimen NSC1-PC and than that experimentally observed.

Beam NSC1-FRC2 is also modeled with sufficient accuracy, even though one can observe that the analysis is not able to entirely simulate the ductility exhibited by the specimen tested. This is surely due to the lack of a good compression softening curve for such a fibrous material. Many investigations have been showing that, with

a similar amount of fibers, the softening in compression is quite enhanced, whereas the compressive strength and the pre-peak load are almost not influenced by the presence of fibers (see Chapter 2, Section 2.8.5.2).

The effect of fibers in compression is out of scope of the present research, even though, once again, it results quite important especially with regards to the residual strength at ultimate limits (see also I-Beam model).

However, this affects only the degree of ductility: the collapse mechanism is well simulated by the model, by crushing of concrete under the point load (whereas the crushing appeared at midspan in the experiment). Cracking in the shear span is also consistent in the model, according to the experiment.

Figure 5.22 and Figure 5.23 show the predictions of crack patterns at failure, according to program Response 2000: the former concerns specimen HSC-PC whereas the second specimen NSC1-PC.
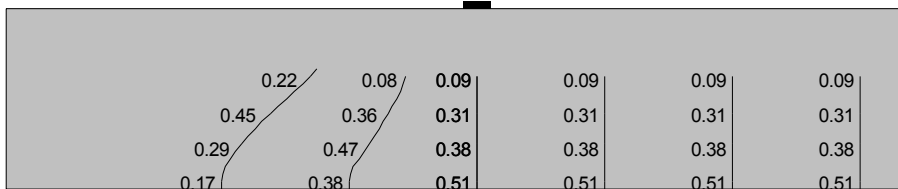
Figure 5.22: Crack pattern at failure predicted by Program Response 2000, specimen HSC-PC.
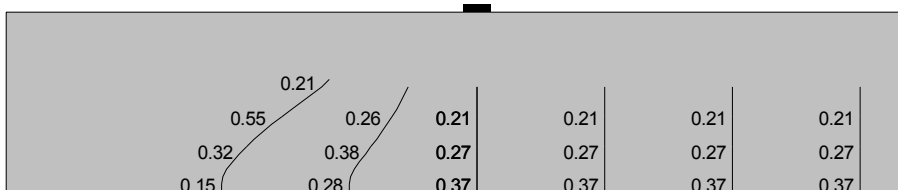
Figure 5.23: Crack pattern at failure predicted by Program Response 2000, specimen NSC1-PC.

Response 2000 does not allow the user to include his own tension softening relationship, so enabling modeling the response of FRC specimens. Therefore, the latter beams cannot be accurately analyzed with this Response 2000. However, it should be recognized that Response 2000 is a really user-friendly FE program.

The same considerations provided for specimen NSC0-UP can be outlined herein as well. The critical shear crack is located in both cases at a distance of around the

depth of the member and deviated toward the load point with increasing load. The very different compressive strength does not influence that much the crack pattern and the crack width (reported in the two Figures at different locations). This was evidenced even in the experiments and in the analyses performed with program VecTor2.

Table 5.6 reports a comparisons between the maximum values of load and displacements at midspan, between experiments and the two FE program considered. One should recognize that the two FE programs, where possible, give similar responses and, in all cases, no significant difference are observed in terms of ductility and bearing capacity.

	P_{exp}	$P_{num, VT2}$	$P_{num,Resp2000}$	δ_{exp}	$\delta_{num, VT2}$	$\delta_{num,Resp2000}$
	[kN]	[kN]	[kN]	[mm]	[mm]	[mm]
NSC0-BP	149	166	166	8.8	10.8	9.2
NSC0-UP	329	337	-	49.2	45.6	-
NSC1-PC	127	136	153	9.1	9.8	8.7
NSC1-FRC1	258	231	-	19.6	17.1	-
NSC1-FRC2	349	361	-	77.1	39.4	-
HSC-PC	216	257	223	12.8	15.2	11.3
HSC-FRC1	372	373	-	26.4	20.5	-
HSC-FRC2	435	424	-	78.0	82.7	-

Table 5.6: Comparison of experimental and numerical values of maximum load and maximum deflection at midspan. Values obtained from Response 2000 are reported only where possible.

5.4.3 Merits of the FE Program adopted.

The numerical modeling approach adopted, based on the MCFT and DSFM, is capable of representing the linear and nonlinear behavior of the different beams tested under shear loading. It is also able to model with sufficient accuracy the fiber contribution to tension softening. Modeling fiber reinforced concrete by inputting an appropriate tension softening behavior is a quite precise and, from a structural design point of view, a simple and effective procedure. The MCFT and DSFM formulations give excellent results in the presence of shear reinforcement: failure mode, postcracking stiffness, ultimate strength and ductility are accurately simulated. For beams containing little or no shear reinforcement or fibers, the

accuracy provided by the DSFM is still quite good, although with the scatter naturally associated with mechanisms highly dependent on concrete tensile strength.

5.5   Concluding Remarks.

In this chapter, a validation of the MCFT and the DSFM, through a comparison between numerical analyses and shear experiments on two sets of full-scale concrete and fiber reinforced concrete beams was presented.

Numerical analyses were performed by using the FE program VecTor2, developed at The University of Toronto and based on the MCFT and the DSFM, suitably adapted to fiber reinforced concrete in terms of different post-cracking behavior and local conditions at cracks. The corroboration of the model was carried out on a wide range of full-scale structures.

The adopted model accurately predicted the post-cracking response of the members in terms of strength, stiffness, ductility, crack patterns and failure modes. It was also able to simulate the post-peak behavior up to failure and to accurately predict the different collapse modes that occurred in the experiments.

The numerical results were accurate in every case, particularly in presence of transverse reinforcing steel or when dealing with specimens which failed under bending.

The rotating crack model proved to be effective in simulating the final collapse mechanism of the I-Beam specimens, which related to arch action, involving crack re-orientation and merging.

The shear contribution due to fibers and regular reinforcement was also modeled with good accuracy.

The numerical analyses, as well as the experimental results, demonstrated that shear reinforcement may be, partially or totally, effectively substituted with steel fibers, resulting in a reduction of labor cost due to the elimination of handling and placing of reinforcement. In shear-critical beams, under certain conditions (e.g., toughness, amount) fibers can post-pone the shear collapse and eventually force a flexural failure, with a significant increase of ductility and load bearing capacity.

These results can be used to further study the behavior of shear-critical beams, in order to better understand the mechanisms governing shear failure especially in fiber reinforced concrete beams and to develop a practical design procedure that accounts for the effects of fibers on beam behavior. In doing so, one must consider the two following key points:

354

- The fiber resistance contribution should be included with the concrete contribution, whereas many researchers suggest a separate fiber shear contribution (see Section 2.8.9). That conclusion is based on the experiments and on the numerical evidence, which demonstrates the ability of simulating FRC structures by just adopting a proper tension softening model.
- Fibers also increase the ultimate strength of the compression strut (see I-Beam model and NSC1 series), which is critical in some structures. The corresponding check formula, prescribed by many Codes, should be adapted to FRC structures.

355

5.6   REFERENCES.

[1]   **Minelli, F.**, *"Toward a consistent Modelling af shear in Fibre Reinforced Concrete Elements", V International Ph. D. Symposium in Civil Engineering, Delft, The Netherlands, 15-19 June 2004, Vol 1, 467-475.*

[2]   **Riva, P., and Minelli, F.**, *"Numerical Modelling of Prestressed fiber reinforced high performance concrete beams subjected to shear"; 5th International Symposium on Fracture Mechanics of Concrete Structures, Vail, Colorado, 12-16 April 2004, Vol 2, 1179-1186.*

[3]   **Reich, R., Cervenka, J., and Saouma, V.E**, *"MERLIN, a Three-dimensional Finite Element Program Based on a Mixed-iterative Solution Strategy for Problems in Elasticity, Plasticity, and Linear and Nonlinear Fracture Mechanics", EPRI, Palo Alto (CA), 1994.*

[4]   **Wong, P.S. and Vecchio, F.J.**, *"VecTor2 and FormWorks User's Manual", Technical Report of the Department of Civil Engineering, University of Toronto, August 2002, pp.217. (available @* http://www.civ.utoronto.ca/vector/ *).*

[5]   **Cangiano, S., Cucitore, R. e Plizzari G.A.**, *"A New Proposal for the Evaluation of Fracture Properties of Steel Fiber Reinforced Concrete", 6th International Symposium on Utilization of High Strength/High Performance Concrete, König, G., Dehn, F., and Faust Eds., Lipsia Germany, 16-20 June 2002, V. 2, pp.873-886.*

[6]   **CEB-FIP, Model Code for Concrete Structures**, *"CEB-FIP International Recommendations, 3rd ed. ", Comité Euro-International du Béton, Paris, 1978, pp. 348.*

[7]   **Vecchio, F.J.**, *"Analysis of Shear-Critical Reinforced Concrete Beams", ACI Structural Journal, Vol 97, No 1, 2000, pp. 102-110.*

[8]   **Bentz, E.C.**, *"Sectional Analysis of Reinforced Concrete", PhD Thesis, Department of Civil Engineering, University of Toronto, 2000, pp 304.*

6. DISCUSSION AND MODELING OF SHEAR

6.1 Introduction.

Modeling of shear (especially in members without web reinforcement), even if attempted by many researchers and increasingly studied, is still today a matter of a strong debate in the scientific community. Many parameters have to be accounted for a proper modeling and, among them, the role of size effect is seen to be crucial in terms of correct applications to real structures; nevertheless, many models still neglect that.

The different proposals and national codes give predictions of shear capacity of members without web reinforcement that considerably differ to each other.

The first part of this Chapter presents a critical review and discussion of the analytical models, limited to beams without web reinforcement and without fibers (those basically considered in Chapter 2) against the experimental results outlined in Chapter 4. Advantages and disadvantages of the different proposals will be discussed.

The second part of the Chapter deals with an analytical formulation for predicting the shear strength of members without transverse reinforcement, and collapsing under shear diagonal failure (namely, for a/d ratio greater than 2.5). This proposal is supported by the experiments on shear-critical beams reported in Chapter 4 and by other experimental results published in the scientific literature.

The influence of the basic parameters on shear behavior are taken into account and someway included in the formulation.

The same approach is then followed for members without web reinforcement containing steel fibers: firstly, a review of current analytical proposals, with pros and cons, will be provided. Secondly, an attempt to include fibers in the available European Code will be suggested, on the basis of the experiments of Chapter 4 and, moreover, on the basis of a wide set of numerical analyses performed.

The effect of fibers in reducing the domain of shear diagonal failure will be clearly outlined, depending on different properties of fibers, concrete strength and reinforcement ratios. A new analytical model will not be proposed at this stage, as the author believes that it is more important, at this level of knowledge (fibers in shear-critical elements need further studies, whereas shear in plain concrete is quite known, even though no agreement is observed between different models), trying to include fibers in the building codes, in order to get designers accustomed

to fiber reinforcement through an existing and generally accepted calculation, and, lastly, get engineers including steel fibers in their design procedures.

Finally, this Chapter presents a numerical study on the effect of steel-to-concrete bond (which proved to be the main cause of the premature collapse of the structure under shear) on the member response. Different available bond models are tested in order to find their merits against the experiments. A parametric study is also conducted on bond properties aiming at the examination of intermediate bond situations, between a perfectly embedded and an unbonded bar (the latter in specimens NSC0-UP and NSC0-UD).

6.2 Discussion on Available Models for Shear Strength of Members made of Plain Concrete without Web Reinforcement.

Several analytical approaches predicting shear capacity of members without web reinforcement were diffusely discussed in Chapter 2.

Table 6.1 reports the comparison between the experimental values of specimens NSC0-BP, NSC1-PC and HSC-PC, against the predictions of some analytical models.

The experimental ultimate shear, to be compared with the values predicted by the different models, was calculated, according to the loading system, as half of the experimental maximum load plus half of the self weight of the beam, which was estimated equal to 10.68 kN.

The first two prediction refer to the Kani's model [2.63] [2.64]: it is a simple formulation, assuming, in the case of diagonal shear failure (a/d ratios greater than 2.5), linear elastic behavior of each tooth formed between two adjacent cracks.

For predicting failure under arch action (a/d ratios lower than 2.5) a number of geometrical considerations on the compressive trajectories and on the biaxial stresses were made.

Since tests carried out in the present research had *a/d=2.5*, both equations were evaluated. However, it is more worthy, in our case, commenting the first formulation, which deals with the diagonal shear failure. Note that, in this calculation, the depth of the cantilever (concrete tooth) was assumed equal to the neutral axis in a standard serviceability state.

Analytical Model	Reference Equation in Chapter 2	V_u [kN]			$V_{u,experiment}/V_{u,prediction}$		
		NSC0-BP	NSC1-PC	HSC-PC	NSC0-BP	NSC1-PC	HSC-PC
Kani	(2.45)	102	75	102	0.78	0.92	1.11
Kani	(2.51)	75	74	79	1.06	0.94	1.44
Reineck	(2.75)	87	78	124	0.91	0.89	0.91
Russo-Zingone-Puleri	(2.92)	106	100	125	0.75	0.69	0.91
Kim-Kim-White	(2.118)	103	99	118	0.77	0.69	0.96
Zararis-Papadakis	(2.135)	97	77	74	0.83	0.89	1.54
ACI-ASCE Committee 426	(2.203)	74	66	103	1.08	1.04	1.10
Mattock-Zsutty	(2.204)	94	87	117	0.85	0.79	0.97
Okamura-Higai	(2.205)	89	83	111	0.90	0.83	1.02
Bazant-Kim	(2.206)	94	87	111	0.85	0.79	1.02
CEB-FIP Model Code	(2.208)	74	69	93	1.08	1.00	1.22
Collins-Kuchma	(2.209)	92	83	129	0.86	0.83	0.88
Rebeiz	(2.210)	112	104	143	0.71	0.66	0.79
Khuntia-Stojadinovic	(2.211)	70	68	79	1.13	1.02	1.43
Code Equation	**Reference Equation in Chapter 2**	V_u [kN]			$V_{u,experiment}/V_{u,prediction}$		
		NSC0-BP	NSC1-PC	HSC-PC	NSC0-BP	NSC1-PC	HSC-PC
Eurocode 2	(2.217)	84	74	133	0.96	0.93	0.86
Eurocode 2 draft	(2.212)	84	78	105	0.95	0.89	1.08
ACI Committee 318	(2.218)	83	75	113	0.97	0.92	1.00
ACI Committee 318 Simplified	(2.220)	81	72	113	0.99	0.95	1.00
Canadian CSA, General method	(2.228)	84	78	102	0.95	0.88	1.12
Japanese Code (JSCE)	(2.207)	65	60	81	1.23	1.14	1.40

Table 6.1: Prediction of several analytical models against the experimental results of shear-critical beams presented in Chapter 4.

The main merit of this model, which gives adequate results against our experiments, is that it is the first rational model including a number of fundamental parameters influencing shear capacity, namely the a/d ratios and the reinforcement

ratio. Nevertheless, it does not recognize any influence of the compressive strength (or, more in general, of the concrete mechanical properties) and of the size of members, which are both quite important.

Moreover, the definition of the comb-like shape of cracks in the shear span is quite arbitrary, especially when one has to predict the shear capacity of a member prior to carry out the test. The crack spacing (Δx) and the depth of the cantilever (*s*) (Figure 2.86) might be difficult to evaluate and might be even more complicated to include in a design procedure. There are many methods for calculating those two parameters, but quite different values can be obtained, giving therefore a significant scatter in the predictions.

The tensile strength, in addition, is not easy to be properly identified, as there is a quite huge scatter in test results. That determines the need of a significant number of tests to obtain a reliable value of tensile strength.

The second Kani's equation, whose predictions are reported in Table 6.1, concerns the arch mechanism. One should recognize that the outcome of the two equations should give the same result, as the *a/d=2.5* ratio was considered as the transition point between arch mechanism and concrete tooth phenomenon, according to the author.

Almost identical values are seen just for specimen NSC1-PC that, with a compressive strength of around 25 MPa, has similar mechanical properties of the specimens of the Toronto series [2.63]. This evidence further confirms the significant contribution of concrete grade and, consequently, the inability of Kani's model to give good accuracy for specimens having concrete strengths much higher than 30 MPa.

The experiments demonstrate that, in case of beam NSC1-PC, the Kani's formulation is a little unconservative. It becomes, on the contrary, quite safe when predicting the specimen with high strength concrete. However, the analytical formula for the concrete-tooth mechanism is strongly dependent on the concrete tensile strength, which often is not properly measured or, sometimes, is not measured at all. In our case, the value of f'_t obtained for HSC-PC was a little lower than what one would have expected.

Finally, the size effect can in part justify the greater prediction for NSC1-PC. Note that the Toronto series specimens were almost 150 mm wide and 300 mm deep. They were therefore quite smaller than those tested in the present research.

An adaptation of this, still valuable model could be done first by including the compressive strength (as attempted by Russo et al. [2.103]) and the size effect.

The Reineck's model [2.14], developed at the beginning of 90's, is much more recent and was studied with a more extensive knowledge of shear in members without web reinforcement. It considers, in the comb-like structure, the presence of all main shear transfer mechanisms (which Kani's model does not: it takes into account just the difference in the tensile force transferred through bond between the two faces of adjacent cracks).

This model is more detailed than the previous one, as it accounts for concrete grade and size effect, in addition to all other parameters also contemplated by Kani's model.

Reineck's model includes also the possible presence of axial force and, through a dimension-free value for the crack width, the reinforcement ratio, the depth of the members and the elastic modulus of rebars. The only concern regards the choice of the friction law, in terms of a maximum crack width of 0.9 mm, whose reason is not totally clear and does not reflect the size effect. The author anyway reported a fairly good agreement between this law and the results from Walraven and Gambarova (See Section 2.2.2.2, Chapter 2). Moreover, the practical application of this equation for design purposes can result in some difficulties due to the many parameters involved.

Concerning the predictions of the experiments carried out at the University of Brescia, the model overestimates the member response of about 10% in all cases. These values were obtained by assuming a default value of the tensile strength. Conversely, using the tensile strength measured from cylinders, brings to ratio, between experimental and analytical, of 0.98, 1.02 and 1.48, respectively for NSC0-BP, NSC1-PC and HSC-PC. The two former values are really good predictions, whereas the latter, for specimen HSC-PC, gives a worse estimation than that calculated with the default value of tensile strength. In fact, as already mentioned, the tensile strength of specimen HSC-PC turned out to be quite lower than the default considered into the model ($f_{ct}=0.246 * f_c^{2/3}$ where $f_c=0.95\, f'_c$).

This fact emphasizes that further studies are stringent for a better understanding of the shear behavior of members made of high strength concrete.

The model of Russo at al. [2.103] is actually a combination of existing models with some improvements. Starting from the Kani's and Bazant's [2.9] models, and from the ACI-318 approach, the authors determined an expression of the domain of shear diagonal failure.

All main parameters influencing shear resistance are clearly reported, with the addition of the aggregate size, included in the size-effect factor, according to Bazant and Kim.

According to Table 6.1, predictions are anyhow quite unconservative, giving a scatter of around 30% for the two specimens with concrete having normal strength, while a better estimation is observed for beam HSC-PC. The main merit of this formulation is that it is quite easy to apply and can be undoubtedly adapted for design purposes.

The model also provides an analytical expression giving the transition point (between arch action and beam action), as a function of the concrete compressive strength and the reinforcement ratio. For specimen HSC-PC this value is 1.89, which seems to be a little low and, moreover, it is not supported by any experimental result.

Kim et al. [2.104] determined an expression for shear capacity by combining both arch and beam action, even though some coefficients and parameters were based on statistical analyses. The model accounts for the main parameters that govern shear behavior, with the exception of the size effect, which is totally neglected.

Once again, predictions considerably overestimate the ultimate shear capacity of the members tested, with a tendency analogous to that reported for the model proposed by Russo et al. [2.103].

Looking at the Zararis model [2.71], it firstly appears that a quite different approach is followed: the model basically investigates the shear failure as the summation of a first shear-flexure crack and an instable second branch, which brings the members to a sudden and brittle collapse.

The first branch is treated with the usual assumptions of the beam theory under elastic behavior. Differently to other models (Kani and Reineck above all) the author assumes that the two faces of a crack rotate around its tip, neglecting any contribution due to slippage along the crack. As a result, no aggregate interlock nor dowel action is considered. The shear force resisted by the longitudinal layer of reinforcement, calculated as a function of the tensile force on them, is considered to be caused by a pure shear deformation of the bars rather than be produced by kinking or slip of crack faces. Each cantilever-tooth is therefore subjected only by a horizontal and a vertical force at the longitudinal steel location.

The shear-flexural crack is treated like a flexural crack, with its tip reasonably assumed at the neutral axis location, which is calculated assuming a stress-block approach, according to Section 2.6.6.3.

The tip of this crack is also assumed to lie along the line of compressive action, directly connecting the support to the closest load point.

362

The second branch of the shear-critical crack develops through a sort of splitting of concrete along the line of compressive strength, starting form the tip of the shear-flexural crack and propagating toward the load point.

Zararis explains his approach on the basis of the theory of elasticity. He theorizes that, along the second branch of the crack, a self-equilibrated system of forces takes place, similar to that occurring into the common split cylinder test. A radial distribution of stresses develops, making the portion of a member above the second branch as a cantilever failing in bending once the radial stress reaches the splitting tensile strength.

The length of the second branch, which corresponds to the diameter of the cylinder in the split cylinder tests, is considered, in addition to the size itself, as a further indication of the size effect (with increasing diameter, a lower tensile strength is observed, in the split cylinder test) (Figure 2.119 and Figure 2.120).

The final formulation is a function of a few parameters, the concrete splitting tensile strength, defined as a function of the concrete compressive strength according to Eurocode 2 [3.3], the *a/d* ratio and the depth of the neutral axis, which includes in it the reinforcing ratio and the concrete grade.

This model is undoubtedly new and offers an original way of thinking to the shear failure phenomenon. It is only applicable for members exhibiting a collapse under shear diagonal failure (i.e., a/d greater than 2.5).

The size effect is also expressed in terms of the shear span length, in addition to the height of the member.

Neglecting both dowel action and shear transfer is quite unusual, especially nowadays, where there is considerable agreement, in the scientific community, about the mechanisms of shear transfer. However, this assumption does not extremely affect the final formulation, which is based on the occurrence of the splitting tensile strength of concrete along the second branch of the shear-critical crack.

The main concern that should be emphasized is that the self-equilibrated system of forces, which determines the shear failure in the second branch, is a little forced, as that region is not characterized by a system of concentrated forces. Rather, in the zone located above the second branch of the shear-critical crack, a diffusion of the external concentrated load should be considered.

Predictions, reported in Table 6.1, are quite satisfactory, even though, once again, the model seems to overestimate the response of members having normal strength concrete and underestimate the one of specimen HSC-PC, having high strength concrete.

Predictions were obtained by calculating the neutral axis according to the model (see Section 2.6.6.3). A comparison between predictions calculated with the measured tensile strength and those calculated assuming a tensile strength according to EC2 (procedure advised by the author) suggests that an acceptable scatter is noticeable for specimens NSC0-BP and NSC1-PC, while a quite different estimation is observed, once again, for member HSC-PC.

In conclusion, the model can be transferred into design procedures quite easily but applies only for members having *a/d* ratios greater than 2.5. Furthermore, no extension is reported to combined axial load and shear, neither for prestressed structures (on the contrary, the formulation of Reineck includes both cases).

All other formulations reported in Table 6.1 were not diffusely discussed in the literature review (Chapter 2), but only summarized in Section 2.6.9.

As a general comment, before the 80's, almost all formulations neglected the size effect in shear (see Table 2.1 in Section 2.6.9).

More recently, Collins and Kuchma proposed a different parameters taking into account this phenomenon through a factor related to the distribution of the longitudinal reinforcement over the depth of the member.

All models combine the concrete grade, the reinforcement ratio and the a/d ratio. Other models include the aggregate size, the dimension, the spacing of longitudinal rebars over the depth, or the neutral axis (which includes in itself both concrete grade and reinforcement ratio).

All formulations give acceptable estimations for some of the specimens, with differences of about 3-30%.

By giving an overall sight to Table 6.1, one can conclude that, among all models, there is a significant difference. Some formulations predict a shear strength twice as much as another model does, making obvious the conclusion that either one of the two equations is unsafe.

The majority of analytical models tends to overestimate the shear capacity of members, especially those made of normal strength concrete, from which, by the way, the models were calibrated. The scatter between predictions becomes higher and unacceptable, even though in the safe side, for specimen HSC-PC. However, it has to be recognized that many models were calibrated only for members having a normal strength concrete.

Table 6.2 summarizes and compares the main features of the analytical models herein discussed, emphasizing whether each model takes into account or neglects each fundamental parameter that affects the shear response of a beam without web reinforcement.

364

Model for Shear Diagonal failure	Concrete Grade	Size Effect	ρ_s	a/d	Other	Predictions
Kani [2.64]	N	N	Y	Y	-	ADEQUATE
Reineck [2.14]	Y	Y	Y	Y	Axial Force Prestressing	ACCURATE
Russo et al. [2.103]	Y	Y	Y	Y	Aggregate size	UNCONSERVATIVE
Kim et al. [2.104]	Y	N	Y	Y	-	UNCONSERVATIVE/ ADEQUATE
Zararis et al. [2.71]	Y	Y	Y	Y	-	ADEQUATE

Table 6.2: Main features of the analytical models discussed.

Bringing the discussion to the design code formulations, the European, American, Canadian and Japanese codes were considered, assuming in all cases all partial safety factors of material equal to the unity. All equations herein discussed are reported as well in Chapter 2, as indicated in Table 6.1.

The two European formulations considered gave results almost similar for normal strength concrete, whereas the old version tended to overestimate the ultimate shear of specimen HSC-PC.

The new formulation of EC2 (Section 2.7.1) is a function of the main parameters that govern shear failure, including the size effect. However, it does not result from a rational model. Rather, it is an empirical formulation based on statistical analysis and fitting of a number of experiments. It is applicable to a wide range of structures, including prestressed structures and members subjected to axial force.

Both the simplified and the more accurate formulas provided in ACI-318-02 predict the shear capacity of all three members considered with high accuracy, in spite of the fact that this easy approach proved to be quite unsafe when dealing with full scale structures ([2.74] and [2.75]).

The only concern for the ACI code is that it provides different formulations for different members typologies or loading conditions. The overall shear provisions result therefore in being fairly heavy, without a rational background behind them.

The Canadian code, based on the MCFT, was herein applied by adopting the general method (Section 2.7.3) as the simplified procedure does not apply to all

specimens, especially to HSC-PC. Moreover, the general method is recognized to be more reliable.

These provisions, only at first glance, can be considered a little redundant and complicated to apply, even though, on the other hand, are very precise and result from a rational model, which proved to give accurate results and appreciable representations of the behavior of a wide range of r.c. structures. Furthermore, the same procedure and formulations can be applied to all members to be designed under shear loading. The size effect is also included in a very efficient way as reported in several studies ([2.74] and [2.75]). Predictions are quite satisfactory in all cases, even if they are fairly conservative for the member cast with high strength concrete.

Finally, the Japanese equation for shear (Section 2.6.9) attributes a huge decrease in shear strength due to size effect. It is, in addition, a simple equation that tend to underestimate the experimental results quite considerably.

Note that all code provisions do not include the shear span-to-depth ratio factor in their formulations, as one would have expected (the Canadian Code requires the moment-to-shear ratio). This is likely due to the fact that members in practice are in general subjected to loads that differ from the simple and useful four point bending loading scheme.

The Canadian provisions seem to be the most precise and proper among the available formulations in the world. Some refinements, basically in terms of size effect, are expected during 2005.

6.3   A new Model for Predicting the Shear Strength of Members without Web Reinforcement.

By analyzing the failure mode of beams with bonded rebars and without steel fibers (NSC0-BP, NSC1-PC, NSC2-PC, NSC3-PC and HSC-PC), it was observed that the same collapse mode occurred, consisting in:

- A first shear-flexural crack, which basically started as a flexural crack and then, running through the depth of the member, tended to assume a certain inclination with respect to the vertical axis;

- A second branch, connecting the top of the first branch to the load point. The appearance of the second branch was almost imperceptible as it brought immediately to a sudden and brittle collapse, characterized by a consistent

release of energy. The occurrence of the second branch arose once the tensile strength of concrete was reached.

The appearance and growth of the main shear-critical crack as well as the stress field in the shear span were analytically studied by means of the D.S. Venant theory [1]. Early results were also previously presented by Adami et al. [2] in a technical report of the Department of Civil Engineering of the University of Brescia.

According to Figure 6.1, which shows the first branch of the shear-critical crack, it is possible to express the tensile stress at the tip of the crack itself, as:

$$\sigma_x = \frac{M}{J} \cdot \overline{\overline{x}}$$

(6.1)

where:

- M is the external moment;
- J is the modulus of Inertia of the section;
- $\overline{\overline{x}} = d - \overline{x} - y$;
- d is the effective depth of the section;
- y is the depth of the crack, measured from the bottom of the member;
- $\overline{x}$ is the neutral axis location, measured from the top of the beam.

In doing so, it is implicitly assumed that concrete can resist tensile stresses.
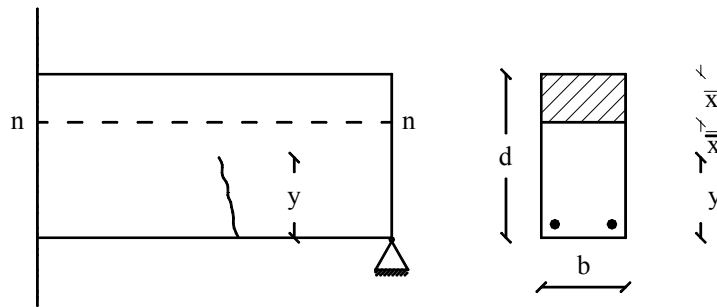
Figure 6.1: First branch of the shear critical crack in bonded beams and notations.

Shear stresses, according to Jourawski [3], can be expressed as:

$$\tau_{xy} = \frac{V \cdot S^*}{J \cdot b}$$

(6.2)

where:

- V is the external shear;
- S^* is the static moment of the section;
- b is the width of the beam.

Figure 6.2 shows a schematic plot of both flexure and shear stresses in a cracked section. Note that tensile stresses σ_y are at the moment neglected, because a region of the beam reasonably far from the influence of the two load points is considered. With this regard, further details will be presented in Section 6.4.

The crack indicated in Figure 6.2 forms once the tensile strength of concrete is reached at the bottom fiber of the beam. At the tip of the crack, the presence of both flexure and shear stresses determines a stress field that can be investigated throughout the Mohr circle and the Mohr-Coulomb failure envelope (suitable for concrete) [4], as reported in Figure 6.3.
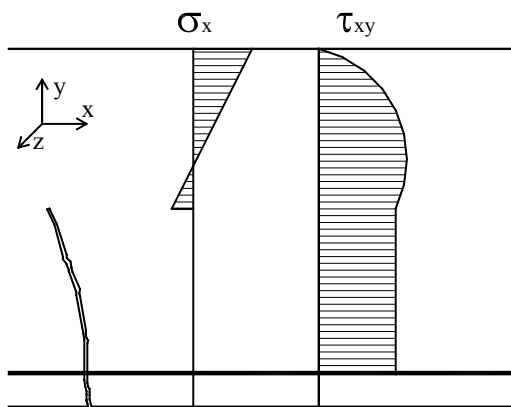
Figure 6.2: Assumed distribution of stresses in a cracked region of the shear span.
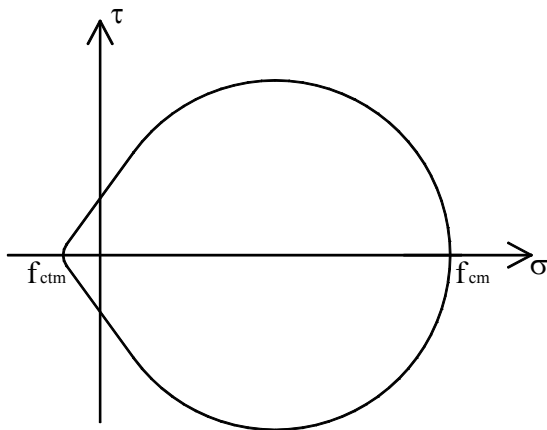
Figure 6.3: Failure envelope by Mohr-Coulomb.

368

The crack develops as the Mohr's circle becomes tangent to the failure envelope, with an inclination given by the following equation:

$$tan\left(2\alpha\right) = \frac{2 \cdot \tau_{xy}}{\sigma_x}$$ (6.3)

This formulation can be rearranged and adapted to specimen NSC0-BP, so that it is possible to define the slope of the first branch of the shear-critical crack as a function of the main parameters that are significant for the shear response.

This specimen is characterized by normal strength concrete (concrete slightly stronger than 30 MPa, according to Table 4.3) and bonded rebars.

Figure 6.4 illustrates a front view of the specimen with the inclined crack that constitutes the first branch of the shear-critical crack.

The external moment and shear acting on the specimen can be expressed as:

$$M = F \cdot a$$ (6.4)

$$V = F$$ (6.5)

where F is the concentrated load and a the shear span.

In the cracked cross section, according to De S. Venant and Jourawski, stresses can be defined as:

$$\sigma = \frac{F \cdot a}{J} \cdot \overline{\overline{x}}$$ (6.6)

$$\tau = \frac{F \cdot S^*}{J \cdot b}$$ (6.7)
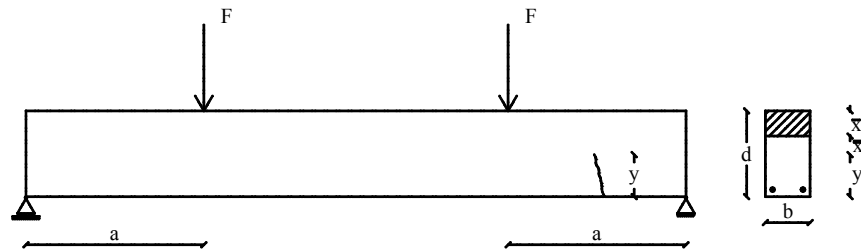
Figure 6.4: Front view if the specimen NSC0-BP, having bonded rebars.

If σ_u e τ_u are assumed as the ultimate flexure and shear stresses at failure, one can write that:

369

$$\frac{\sigma_u}{\tau_u} = \frac{F \cdot a}{J} \cdot \frac{\overline{\overline{x}}}{\dfrac{F}{J} \cdot \dfrac{S^*}{b}} = \frac{a \cdot b \cdot \overline{\overline{x}}}{S^*} \tag{6.8}$$

The shear stress at failure can be determined from the Mohr circle as a function of the tensile strength of concrete f_{ct}, the longitudinal tensile stress σ_u and the angle φ:

$$\tau_u = \left(f_{ct} - \sigma_u \right) \cdot tg\, \varphi \tag{6.9}$$

By calculating σ_u from Equation (6.8) and by substituting it in Equation (6.9), one can obtain that:

$$\tau_u = \left(f_{ct} - \tau_u \cdot \frac{a \cdot b \cdot \overline{\overline{x}}}{S^*} \right) \cdot tg\, \varphi = \frac{f_{ct} \cdot tg\, \varphi}{\left(1 + \dfrac{a \cdot b \cdot \overline{\overline{x}}}{S^*} \cdot tg\, \varphi \right)} = \frac{f_{ct} \cdot tg\, \varphi}{1 + \dfrac{a \cdot b \cdot \overline{\overline{x}} \cdot tg\, \varphi}{\dfrac{b}{2} \cdot \left(\overline{x}^2 - \overline{\overline{x}}^2 \right)}} =$$

$$= \frac{f_{ct} \cdot tg\, \varphi}{1 + 2 \cdot a \cdot \dfrac{\overline{\overline{x}}}{\overline{x}^2 - \overline{\overline{x}}^2} \cdot tg\, \varphi} \tag{6.10}$$

where $S^* = \dfrac{b}{2} \cdot \left(\overline{x}^2 - \overline{\overline{x}}^2 \right)$ is the static moment at the tip of the crack.

From Equation (6.3) it results:

$$tg\, 2\alpha = 2 \cdot \frac{\tau}{\sigma} = 2 \cdot \frac{S^*}{b \cdot a \cdot \overline{\overline{x}}} = \frac{2 \cdot b}{2} \cdot \frac{\left(\overline{x}^2 - \overline{\overline{x}}^2 \right)}{b \cdot a \cdot \overline{\overline{x}}} = \frac{\left(\overline{x}^2 - \overline{\overline{x}}^2 \right)}{a \cdot \overline{\overline{x}}} \tag{6.11}$$

Substituting in Equation (6.10) it is possible to calculate the angle of inclination of the crack α as:

$$tg\, 2\alpha = \frac{2 \cdot tg\, \varphi}{\dfrac{f_{ct} \cdot tg\, \varphi}{\tau_u} - 1} = \frac{2 \cdot tg\, \varphi}{\dfrac{\tau_c}{\tau_u} - 1} \tag{6.12}$$

The shear stress at failure can be expressed as:

$$\tau_u = \frac{F_u \cdot S^*}{J \cdot b} = \frac{M_u}{a} \cdot \frac{S^*}{J \cdot b} \tag{6.13}$$

From the Mohr's circle it can be written that (Figure 6.5):

370

$$\left(f_{ct} + \frac{f_c}{2} \right) \cdot sen\, \varphi = \frac{f_c}{2} \qquad (6.14)$$

By assuming $f_{ct}=f_c/10$ (which is a reasonable estimation in case of normal strength concrete, in agreement with the experimental results on materials shown in Tale 4.3), one can obtain $\varphi=56°$ and $tg\varphi=1.5$. The cohesive shear stress, according to the Mohr-Coulomb envelop, can be calculated as:

$$\tau_c = f_{ct} \cdot tg\varphi \cong 1.5 \cdot f_{ct} \qquad (6.15)$$
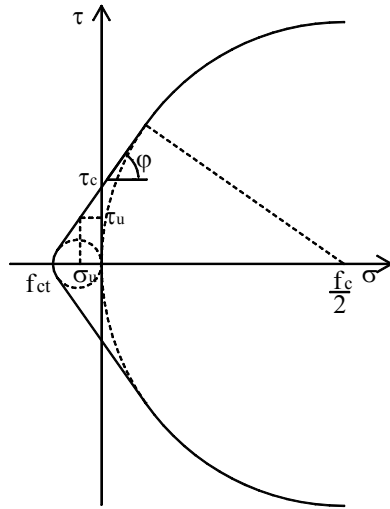
Figure 6.5: Mohr circle with stresses at failure.

The ratio between the cohesive stress and ultimate shear stress can therefore be expressed as (Equation (6.13) and Equation (6.15)):

$$\frac{\tau_c}{\tau_u} = \frac{\tau_c \cdot b \cdot a \cdot J}{M_u \cdot S_A^*} = \frac{1.5 \cdot f_{ct} \cdot b \cdot a \cdot J}{M_u \cdot S_A^*} = 1.5 \cdot f_{ct} \cdot \frac{b \cdot \left(J/S^* \right) \cdot a}{M_u} \qquad (6.16)$$

By indicating the ultimate moment as $M_u=A_s\, f_y\, z$, where A_s is the longitudinal reinforcement, f_y the tensile stress of rebars and z the lever arm, the following equation can be obtained:

371

$$\frac{\tau_c}{\tau_u} = 1.5 \cdot f_{ct} \cdot \frac{a \cdot b \cdot \left(J/S^*\right)}{A_s \cdot f_y \cdot z} = 1.5 \cdot \frac{f_{ct}}{f_y} \cdot \frac{b \cdot d}{A_s} \cdot \frac{a}{d} \cdot \chi = 1.5 \cdot \chi \cdot \frac{f_{ct}}{f_y} \cdot \frac{1}{\rho_s} \cdot \frac{a}{d} \quad (6.17)$$

Where ρ is the reinforcement ratio and $J/S^* = \chi\, z$ being $\chi>1$.

By substituting Equation (6.17) in Equation (6.12), a rearranged expression of the angle of the crack can be written:

$$tg\, 2\alpha = \frac{2 \cdot tg\, \varphi}{1.5 \cdot \chi \cdot \frac{f_{ct}}{f_y} \cdot \frac{a/d}{\rho_s} - 1} \quad (6.18)$$

Close to the final collapse, the last equation assumes the following shape:

$$tg\, 2\alpha = \frac{2 \cdot 1.5}{1.5 \cdot 1 \cdot \frac{1}{170} \cdot \frac{a/d}{\rho_s} - 1} \quad (6.19)$$

where:

- $\chi = J/S^* = 1$;
- $\dfrac{f_{ct}}{f_y} = \dfrac{3}{510} = \dfrac{1}{170}$ (valid for concrete having a compressive strength of about

  30 MPa and rebars with yielding stress of 510 MPa, typical of the Italian production and in agreement with the experimental value of all shear-critical beams tested).

Equation (6.19) is plotted in Figure 6.6. It should be recognized that the inclination of the crack decreases with increasing values of the *a/d* ratio, according to many experimental evidences. Shear effects play in fact a minor role as the a/d ratio increases. Furthermore, there is a consistent effect of the reinforcing ratio, which acts in flattening the main crack with its increase.

In case of critical a/d ratio (a/d=2.5) and reinforcement ratio of 1% (the two latter values apply for all shear-critical beams tested in this research work), the maximum inclination of the first branch of the shear-critical crack is around 32° (see Figure 6.7). This value is lower than the experimental values measured in all tested beam having similar characteristics.
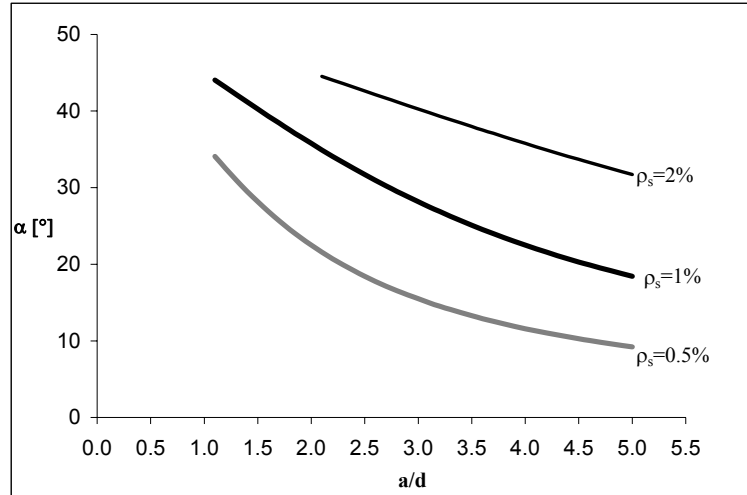
Figure 6.6: Maximum inclination of the first branch of the shear-critical crack as a function of the shear span-to-depth ratio.

Moreover, the approach followed so far, based on the classical theory of beams, predicts a maximum shear stress of about 1 MPa, which is not sufficient for determining a greater inclination of the crack.

Other considerations have to be highlighted in order to completely understand this phenomenon.
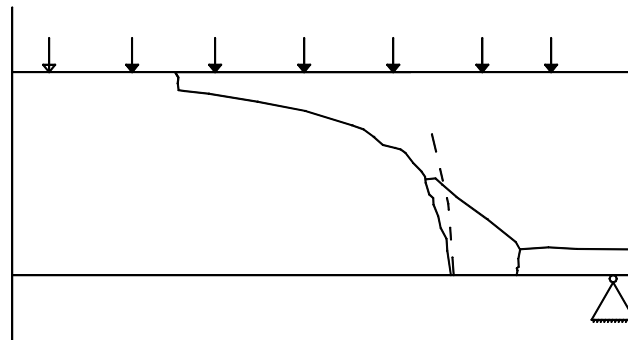
Figure 6.7: Comparison between actual (continuous line)and theoretical (dashed line)crack.

The approach followed up to now, starting from the results of the classical theory, assumes that a different distribution of shear stresses and the occurrence of transverse flexural stresses σ_y have to be accounted for a correct modeling of the failure block mechanism.

Figure 6.8 (a) shows the distribution of shear stresses in a rectangular section of a member, assuming an elastic material.

It is reasonable to consider that, after the formation of a flexure crack, due to the attainment of the tensile strength of concrete, a redistribution of stresses arises, determining a decay of the intensity of shear stresses in the cracked region and an increase in the uncracked portion of the section, as schematically illustrated in Figure 6.8 (b). The redistribution of shear stresses over the depth of the section must of course satisfy the overall equilibrium. Note that Figure 6.8 is only a qualitative representation.

a)   b)
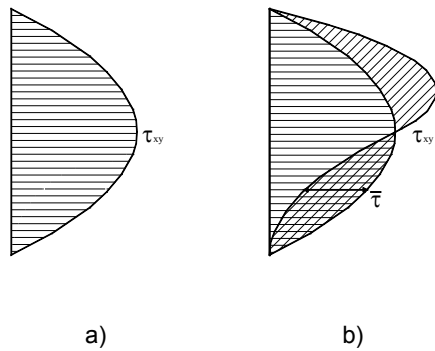
Figure 6.8: Distribution of tangential stresses in a uncracked region (a) and in a cracked region (b).

Such a new distribution can not be easily determined. As a first attempt, a parabolic self-equilibrated distribution of tangential stresses that increases the shear flow in the upper half of the cross section and reduces the shear stresses in the lower part of the same section was considered. This distribution was chosen so that the maximum shear stress could have been achieved at the neutral axis location, according to the classical theory for cracked members.

The location of the neutral axis can be computed at a serviceability limit state, and can be approximated, for normal strength concrete, at about one third of the depth of the member. Therefore, the field of shear stresses can be written, as shown in Figure 6.9, as the summation of two terms as:

$$\tau = \tau_J + \overline{\tau} \tag{6.20}$$

where:

- τ_J are the shear stresses according to the Jourawski theory for uncracked regions;
- $\bar{\tau}$ are the shear stresses coming from the self-equilibrated parabolic distribution.

Figure 6.9 describes this field of shear stresses: note that the maximum stress is located at around one third of the depth of the member, while little total shear stress is observed at the bottom of the cross section, where crack is larger and hence the shear transfer is reduced.
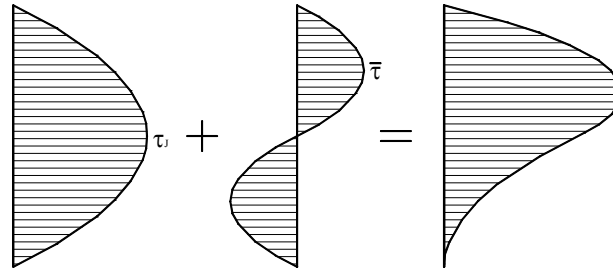
Figure 6.9: Distribution of shear stresses assumed.

The maximum shear stress of the self-equilibrated distribution, $\bar{\tau}$, can be expressed as a function of the corresponding Jourawski stress, according to the following relationship:

$$\bar{\tau} = \chi \cdot \tau_J \tag{6.21}$$

The effect of the parabolic self-equilibrated distribution were examined through an elastic analysis on a panel region representing a portion of the shear span of the beams tested in the present research (Figure 6.10). The panel had a square shape and each side was as long as the height of the shear-critical beams tested (namely, 480 mm). The panel was loaded on the right edge by the parabolic distribution above presented, having a maximum value equal to the unity, which made easy the extrapolation and the interpretation of results.

Four-noded plane stress elements, having a dimension of 1 mm and a thickness of 1 mm, were adopted for the elastic analysis. In addition, suitable restraints were located, according to Figure 6.10, at the top and bottom left nodes to make the structure statically determined (the reaction at the two points were monitored and, as one would have expected, turned out to be equal to zero).

The elastic analyses demonstrated the presence of stresses σ_y in the panel, whose representation, along the line of the horizontal symmetry axis of the panel, is plotted in Figure 6.11.
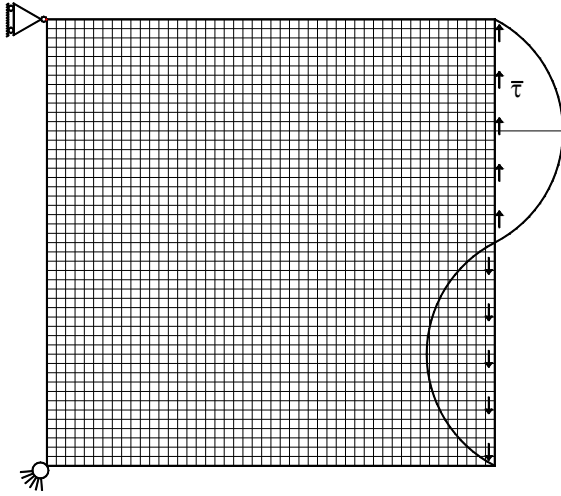
Figure 6.10: FE elastic analysis of a panel element statically determined subjected to a self-equilibrated distribution of shear stresses.
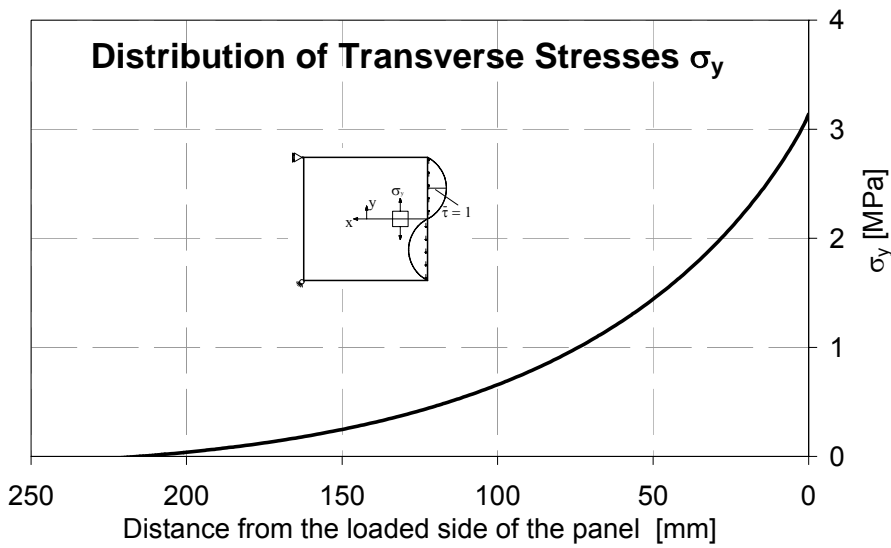
Figure 6.11: Transverse tensile stresses σ_y along the horizontal axis of symmetry of the panel.

From this plot it can be seen that the maximum transverse flexure stress is around 3.15 MPa at the edge of the panel, along the horizontal axis of symmetry.

From this evidence, it is possible to relate the stresses σ_y to the maximum stress of the self-equilibrated distribution assumed, as:

$$\sigma_y = \beta \cdot \overline{\tau} = 3.15 \cdot \overline{\tau}$$ (6.22)

The coefficient β, given a parabolic self-equilibrated field of shear stresses with a maximum stress equal to one, proved to range between 3 and 4 even using the elastic classical solutions of plane stress membranes [5]. The coefficient β was further evaluated by refining the mesh adopted: this procedure brought to similar values of the coefficient β.

As the results of any elastic analysis, no size effect can be modeled, so the coefficient β can definitely be assumed as equal to 3.15.

The coefficient χ of Equation (6.21) can be determined by considering the test data of the experiment NSC0-BP. Firstly, the maximum shear stress, according to Jourawski, occurred in the section where the collapse took place and can be determined as:

$$\tau_J = \frac{V \cdot S^*}{J \cdot b} = 1.29 \, MPa$$ (6.23)

where:
- $V = 84 \, kN$;
- $S^* = 6.31 \cdot 10^6 \, mm^3$;
- $J = 2.053 \cdot 10^9 \, mm^4$;
- $b = 200 \, mm$.

The coefficient χ can therefore be calculated by imposing that the maximum shear stress of the parabolic distribution $\overline{\tau}$ determines a stress σ_y equal to the tensile strength of concrete, as:

$$\chi = \frac{\overline{\tau}}{\tau_J} = \frac{\sigma_y}{3.15 \cdot \tau_J} = \frac{f_{ctm}}{3.15 \cdot \tau_J} = 0.74$$ (6.24)

obtained with the assumption that $\sigma_y = f_{ctm} = 3MPa$.

With this assumption, the maximum shear force $\tau = \tau_J + \overline{\tau}$ is obtained at 155 mm from the top side of the member and its value is 1.80 MPa.

In this modeling, further transverse flexural stresses should have been considered, as, in the top chord, compressive stresses arise. However, in case of beams with

bonded rebars failing under diagonal shear failure, they are almost negligible, because the load intensity attained is considerably smaller than that observed in unbonded rebars. The crack spacing is also small, if compared to the depth of the member. This prevents the diffusion of these stresses, which would determine the formation of significant tensile stresses. With regard to this matter, some details will be provided when dealing with the effect of bond on shear behavior, in Section 6.4.

6.3.1   Application of the Method to different a/d Ratios.

In the previous paragraph, a new explanation of the brittle and sudden collapse that characterizes shear diagonal failure was proposed and examined. It was found that additional flexural stresses σ_y, due to a parabolic self-equilibrated distribution of shear stresses and defined as a function of the shear stresses according to Jourawski, determine the appearance of the second branch of the shear-critical crack that brings the structural member up to failure.

In this section, the model above presented will be applied to a bonded beam of series NSC0, loaded with different a/d ratios, in order to examine the domain in which transverse flexural stresses are critical and anticipate the collapse of a structure under shear.

The case of uniformly distributed loaded (UDL) beam will be considered first, as it is more representative of most of practical applications. The case of a specimen loaded with a four point system will then follow and compared with the previous, even though it is know that only slight differences in behavior are expected.

As the shear diagram, in case of UDL, is linear, it was necessary to assume the location of the shear-critical section. Aiming at that, it was chosen to start from the bending moment diagram with the maximum flexural capacity, of course at midspan. Then the section exhibiting the first cracking moment was selected. A number of calculations then followed:

- Calculation of the shear length for uniformly distributed load (See Section 2.5.6.1) $\dfrac{a^*}{d} = \dfrac{L}{4 \cdot d}$, from which the length of the member was calculated;

- Calculation of the UDL q, based on the ultimate moment (analytically estimated);

- Determination of shear and moment diagram;

- Determination of the section subjected to the first cracking moment, located at a distance x from the nearest support;

- From the shear determined in that section, calculation of shear stresses according to Jourawski;
- Calculation of shear stress $\bar{\tau}$, according to Equation (6.21), with the assumption of $\chi=0.74$, as determined in the previous section;
- Calculation of tensile stresses σ_y according to Equation (6.22).

Table 6.3 reports the calculation for a/d ranging from 1 to 10, whereas Figure 6.12 provides a plot of the same relationship.
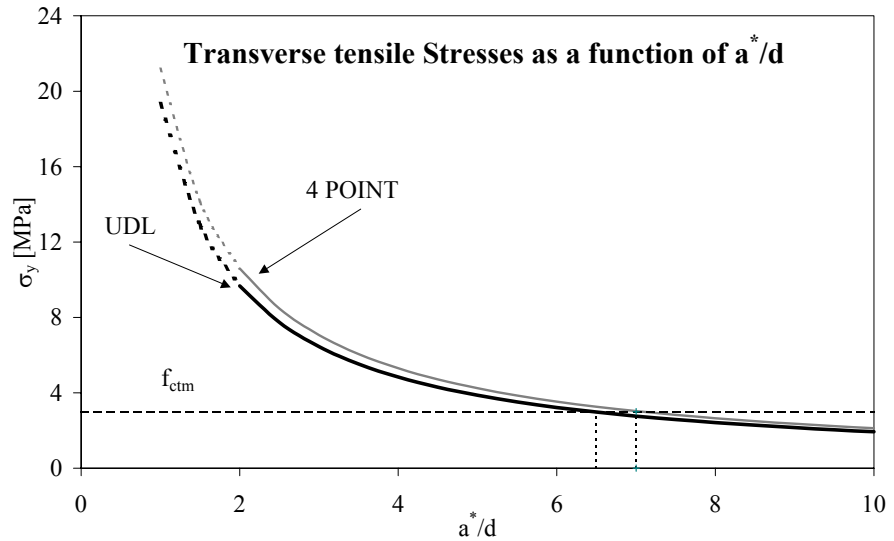
Figure 6.12: σ_y as a function of a/d ratios.

a^*/d	L [m]	q [kN/m]	x [mm]	V [kN]	τ [MPa]	$\bar{\tau}$ [MPa]	σ_y [MPa]
1	1740	487	76	387	5.94	4.40	19.34
1.5	2610	216	114	258	3.96	2.93	12.90
2	3480	122	152	193	2.97	2.20	9.67
2.5	4350	78	190	155	2.38	1.76	7.74
3	5220	54	228	129	1.98	1.47	6.45
3.5	6090	40	266	110	1.70	1.26	5.53
4	6960	30	304	97	1.49	1.10	4.84
4.5	7830	24	342	86	1.32	0.98	4.30
5	8700	19	380	77	1.19	0.88	3.87
5.5	9570	16	418	70	1.08	0.80	3.52

a^*/d	L [m]	q [kN/m]	x [mm]	V [kN]	τ [MPa]	$\bar{\tau}$ [MPa]	σ_y [MPa]
6	10440	14	456	64	0.99	0.73	3.22
6.5	11310	12	494	59	0.91	0.68	2.98
7	12180	10	532	55	0.85	0.63	2.76
7.5	13050	9	570	52	0.79	0.59	2.58
8	13920	8	608	48	0.74	0.55	2.42
8.5	14790	7	646	45	0.70	0.52	2.28
9	15660	6	684	43	0.66	0.49	2.15
9.5	16530	5	722	41	0.63	0.46	2.04
10	17400	5	760	39	0.59	0.44	1.93

Table 6.3: σ_y as a function of a/d ratios, case of UDL.

As expected, transverse tensile stresses remarkably decay with increasing a/d, till becoming lower than the tensile strength of concrete.

In case of the beam under UDL, the value of a/d at which this transition occurs is *a/d=6.5*. This ratio can be considered as the transition point between shear diagonal failure and flexure failure, and it is in agreement with many analytical proposals and experimentations.

For values of a/d lower than 2, this graph tend not to have relevant significance, as the failure mode dramatically changes and, in some case, the full flexural capacity is achieved.

Giving a look at the case of beam subjected to a four point loading system (the same calculation procedure was performed), it can be noticed, as expected, that higher transverse stresses are observed, with a transition point shifting upward, from *a/d=6.5* to *a/d=7.0* (see Figure 6.12), according to Kani's theory (see Section 2.6.5.1).

Table 6.4 reports the main calculations in the latter case. The same consideration previously outlined can be herein reaffirmed.

a/d	Q [kN]	x [mm]	V [kN]	τ [MPa]	$\bar{\tau}$ [MPa]	σ_y [MPa]
1	423	73	423	6.51	4.82	21.19
1.5	282	109	282	4.34	3.21	14.13
2	212	145	212	3.25	2.41	10.60
2.5	169	182	169	2.60	1.93	8.48
3	141	218	141	2.17	1.61	7.06
3.5	121	254	121	1.86	1.38	6.06
4	106	291	106	1.63	1.20	5.30
4.5	94	327	94	1.45	1.07	4.71
5	85	363	85	1.30	0.96	4.24
5.5	77	400	77	1.18	0.88	3.85
6	71	436	71	1.08	0.80	3.53
6.5	65	472	65	1.00	0.74	3.26
7	60	509	60	0.93	0.69	3.03
7.5	56	545	56	0.87	0.64	2.83
8	53	581	53	0.81	0.60	2.65
8.5	50	618	50	0.77	0.57	2.49
9	47	654	47	0.72	0.54	2.35
9.5	45	690	45	0.69	0.51	2.23
10	42	727	42	0.65	0.48	2.12

Table 6.4: σ_y as a function of a/d ratios, case of two concentrated loads.

6.3.2 Towards a New Formulation for Shear.

In order to define e feasible equation predicting the shear strength of members without web reinforcement, Equation (6.21) and Equation (6.22) have to be recalled:

$$\bar{\tau} = \chi \cdot \tau_J \tag{6.21}$$

$$\sigma_y = \beta \cdot \bar{\tau} = 3.15 \cdot \bar{\tau} \tag{6.22}$$

The combination of the two last equations brings to the relationship:

$$\sigma_y = \beta \cdot \chi \cdot \tau_j \tag{6.25}$$

Considering the shear stresses according to Jourawski in an elastic stage, it can be written that:

$$\tau_j = 1.5 \cdot \frac{V}{b \cdot h} \tag{6.26}$$

which does not significantly differ from the more precise for cracked regions. Rearranging the last equation, one can observe that:

$$V = \frac{\tau_j \cdot b \cdot h}{1.5} \tag{6.27}$$

while from Equation (6.25):

$$\tau_j = \frac{\sigma_y}{\beta \cdot \chi} \tag{6.28}$$

By combining the to last relations, an expression of the ultimate shear can be obtained as:

$$V = \frac{\sigma_y}{1.5 \cdot \beta \cdot \chi} \cdot b \cdot h \tag{6.29}$$

Failure of specimens under diagonal shear failure (namely, for a/d ratios greater than 2.5) occurs when the transverse tensile stress σ_y reaches the tensile strength of concrete, so that $f_{ct}=\sigma_y$. The tensile strength of concrete can be determined from the compressive strength, according to the EC2 [3.3], as:

$$f_{ct} = 0.302 \cdot (f_c - 4)^{2/3} \text{ (MPa)} \quad \text{for } f_c \le 50 \text{ MPa;}$$
$$f_{ct} = 2.12 \cdot \ln(1 + \frac{f_c}{10}) \quad \text{(MPa)} \quad \text{for } f_c > 50 \text{ MPa .} \tag{6.30}$$

where:
- f_c is the mean value of concrete cylinder compressive strength;
- f_{ct} is the axial tensile strength of concrete.

the ultimate shear strength of a member can be indicated as:

$$V_u = \frac{0.302 \cdot (f_c - 4)^{2/3}}{1.5 \cdot \beta \cdot \chi} \cdot b_w \cdot d \text{ (MPa)} \quad \text{for } f_c \le 50 \text{ MPa;}$$

$$V_u = \frac{2.12 \cdot \ln(1 + \frac{f_c}{10})}{1.5 \cdot \beta \cdot \chi} \cdot b_w \cdot d \quad \text{(MPa)} \quad \text{for } f_c > 50 \text{ MPa.} \tag{6.31}$$

where, compared to Equation (6.29), *b* and *h* were generalized with b_w (width of the web of a beam) and *d* (effective depth).

An expression related to the cylinder compressive strength rather than to the tensile strength was chosen as the former is a mechanical property always measured and reported in all experimental campaigns.

In addition, there is total agreement on the determination of a cylinder strength from other testing procedures. Conversely, this is not the case for the tensile strength, as many investigations do not report any measure of tensile strength and, on the other hand, there is not agreement on its determination from different testing procedures.

Last but not least, a huge scatter is in general observed in the determination of this property, so a considerable number of tests would be necessary for a proper evaluation.

To make the predicting formula of Equation (6.31) sufficiently general and applicable to a wide range of members, one should mainly discuss the effect of the two factors β and χ. How do these parameters change with increasing or decreasing the dimension of members, the reinforcing ratio, the a/d ratio?

β, as a factor evaluated through elastic analysis, is not affected by any of the above mentioned parameters. Therefore, the main goal of this analytical modeling is trying to discuss the factor χ as a function of the main parameters that influence the shear response of a member.

The formulation presented in Equation (6.31) can be applied for predicting the factor χ to all experiments on shear-critical beams herein presented and to other experiments carried out at the University of Brescia in a different research project [6]. Corroboration against the experiments of Collins and Kuchma, Kani, Leonhardt et al., Aster at al., Niwa et al., Walraven and Yoshida et al. are also considered, according to the shear database published in [2.86] and [7].

Table 6.5 reports the main characteristics of all 57 beams considered and the determination, via inverse analysis, of the factor χ.

Test		a/d	b_w	d	ρ	f_{cm}	f_{ctm}	V_u	χ	χ_{EC2}
		[-]	[mm]	[mm]	[-]	[MPa]	[MPa]	[kN]	[-]	[-]
University of Brescia	NSC0-BP	2.5	200	435	1.04	32.9	3.15	79	0.73	0.66
	NSC1-PC	2.5	200	435	1.04	24.8	2.3	69	0.61	0.61
	NSC2-PC	2.5	200	435	1.04	33.5	3.15	84	0.69	0.63
	NSC3-PC	2.5	200	435	1.04	38.6	2.6	83	0.58	0.71
	HSC-PC	2.5	200	435	1.04	60.5	3.15	113	0.51	0.72
	NSC1-PC-B	4.5	200	435	1.04	24.8	2.3	69	0.61	0.61

383

Test		a/d	b_w	d	ρ	f_cm	f_ctm	V_u	χ	χ_EC2
		[-]	[mm]	[mm]	[-]	[MPa]	[MPa]	[kN]	[-]	[-]
Collins and Kuchma	B 100	2.92	300	925	1.01	36	3.02	225	0.79	-
	B 100-R	2.92	300	925	1.01	36	3.02	249	0.71	-
	B 100 H	2.92	300	925	1.01	98	5.10	193	1.55	-
	B 100 HE	2.92	300	925	1.01	98	5.10	217	1.38	-
	B 100 L	2.92	300	925	1.01	39	3.21	223	0.85	-
	B 100 L-R	2.92	300	925	1.01	39	3.21	235	0.80	-
	B 100 B	2.92	300	925	1.01	39	3.21	204	0.92	-
Kani	63	4	154	543	2.77	26.2	2.37	93	0.45	-
	64	8.1	156	541	2.75	25.7	2.33	79	0.53	-
	66	6.02	156	541	2.75	26.4	2.38	91	0.47	-
	68	9.05	157	539	2.71	27.2	2.44	76	0.58	-
	71	2.99	155	544	2.66	27.4	2.45	102	0.43	-
	74	3.11	152	523	2.84	27.3	2.45	108	0.38	-
	75	3.11	152	524	2.83	27.3	2.45	108	0.38	-
	76	2.62	152	518	2.87	30.8	2.69	115	0.39	-
	79	6.83	153	556	2.72	26.2	2.37	84	0.51	-
	3043	3	154	1092	2.72	27	2.43	185	0.47	-
	3044	3.97	152	1097	2.73	29.5	2.60	159	0.58	-
	3045	5	155	1092	2.7	28.3	2.52	152	0.59	-
	3046	7	155	1097	2.72	26.7	2.41	154	0.56	-
	3047	8	155	1097	2.68	26.7	2.41	147	0.59	-
Leonhardt et al.	D2/1	3	100	140	1.66	31.3	2.72	21	0.38	-
	D2/2	3	100	140	1.66	31.3	2.72	23	0.35	-
	D3/1	3	150	210	1.62	33.8	2.88	46	0.42	-
	D3/2	3	150	210	1.62	33.8	2.88	43	0.45	-
	D4/1	3	200	280	1.67	34.6	2.93	74	0.47	-
	D4/2	3	200	280	1.67	34.6	2.93	71	0.49	-
	C1	3	100	150	1.33	38.3	3.17	22	0.46	-
	C2	3	150	300	1.34	38.3	3.17	65	0.46	-
	C3	3	200	450	1.34	38.3	3.17	102	0.59	-
	C4	3	225	600	1.34	38.3	3.17	152	0.60	-
	5L	3	190	270	2.07	28.9	2.56	60	0.46	-
	5R	3	190	270	2.07	28.9	2.56	77	0.36	-
	6L	4	190	270	2.07	28.9	2.56	61	0.46	-
	6R	4	190	270	2.07	28.9	2.56	68	0.41	-
	7-1	5	190	278	2.01	30.3	2.65	62	0.48	-
	7-2	5	190	278	2.01	30.3	2.65	68	0.44	-

Test		a/d	b_w	d	ρ	f_cm	f_ctm	V_u	χ	χ_{EC2}
		[-]	[mm]	[mm]	[-]	[MPa]	[MPa]	[kN]	[-]	[-]
Leonhardt et al.	8-1	6	190	278	2.01	30.3	2.65	66	0.45	-
	8-2	6	190	274	2.04	30.3	2.65	66	0.44	-
	9-1	7	190	273	2.04	30.6	2.67	60	0.49	-
	9-2	7	190	273	2.04	31.5	2.73	60	0.50	-
	10-1	8	190	272	2.05	28.9	2.56	51	0.55	-
	10-2	8	190	272	2.05	28.9	2.56	56	0.50	-
Aster et al.	16	3.67	1000	750	0.42	30.4	2.66	392	1.08	-
	17	3.67	1000	750	0.42	27.3	2.45	349	1.11	-
Niwa et al.	1	3	600	2000	0.28	27.1	2.43	402	1.54	-
	2	3	600	2000	0.14	26.2	2.37	382	1.58	-
	3	3	300	1000	0.14	24.6	2.25	102	1.40	-
Walraven	A2	3	200	420	0.74	24.1	2.22	71	0.56	-
	A3	3	200	720	0.79	24.4	2.24	101	0.68	-
Yoshida et al.	R	2.86	300	1890	0.74	33.6	2.87	255	1.35	-

Table 6.5: Prediction of factor χ from 57 tests of different researchers ([2.86] and [7]).

Note that in most of tests, no indication of the tensile strength was reported. The default value of this property was selected according to the current EC2 Draft [3.3], as also reported by Reineck et al. [2.86]. In case of the experiments carried out in this research, a comparison between the actual value and the value predicted using the tensile strength according to EC2, is also featured.

Factor χ can be plotted versus the reinforcement ratio, the depth of the member and the *a/d* ratio, as illustrated in Figure 6.13-Figure 6.15.

Concerning the first plot, one can observe that factor χ highly depends on the longitudinal steel percentage, as expected. As the reinforcement ratio increases, the ultimate shear stress enhances and therefore the value of χ diminishes, according to Equation (6.31).

For most of tests, factor χ tends to vary in the range of 0.35-0.90, whereas few tests showed results a little out of this domain. High values of χ can be observed for two specimens carried out by Collins and Kuchma [7] (specimens B100 H and B100 HE), and by specimens performed by Niwa and Yohida [7]. It should be recognized that, in the first case, a high strength concrete was adopted and the test showed an ultimate shear even lower than an identical beam with normal strength concrete (namely, 96 MPa vs. 36 MPa). Concerning tests of Niwa et al. [7], a very

low reinforcement ratio was adopted and members were up to 2000 mm high. The test performed by Yoshida had also a depth of around 2000 mm.

Figure 6.13: Experimental distribution of coefficient χ with variation of reinforcement ratio.

All these tests can be considered a little out of the ordinary: some of them are till matter of a strong debate in the scientific community for their really poor results.

In conclusion, for reinforcement ratios in the range of 0.8-3%, factor χ shows an exponential distribution with tendency of diminishing with increasing ρ_s.

Figure 6.14 features the coefficient χ versus the depth of the member. As the depth get greater, the ultimate shear stress decreases and, accordingly, coefficient χ becomes higher. This is clearly illustrated by the chart, even though the same above mentioned tests, and especially the two performed by Collins and Kuchma, do not fit the other experimental results.

A linear relation between factor χ and the depth of the member can be observed.

The influence of the a/d ratio on factor χ is presented in Figure 6.15. No correlation can be reported in this case. However, it is worthy noticing that, out of the region of critical a/d ratios (namely, *2<a/d<3*) values of χ are stable in the range of 0.40-0.60.

Regarding the influence of the compressive strength of concrete on factor χ, no clear correlation was noticed.

Figure 6.14: Experimental distribution of coefficient χ with variation of depth of members.
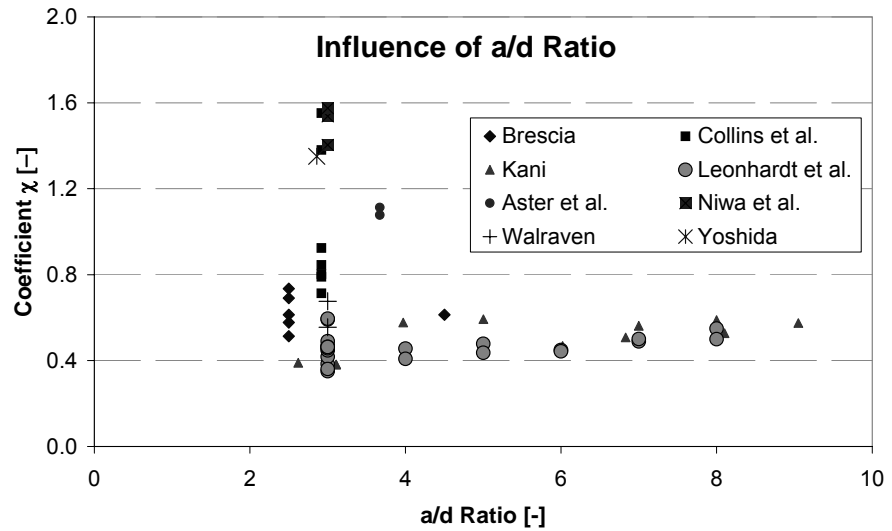
Figure 6.15: Experimental distribution of coefficient χ with variation of a/d ratios.

The results above presented are fairly encouraging toward a reliable formulation predicting the ultimate shear capacity of members.

The proposal is respectful of the actual behavior of a beam without web reinforcement failing under shear loading and especially gives a new interpretation

of the mechanism that generates prior to failure. Such a phenomenon is strictly related to the tensile strength of the material.

One can argue that this model could be somehow similar to the Zararis' approach [2.71]. This is correct only in part. The collapse mechanism constituting in two branches is the basic assumption of both models. However, Zararis postulates a distribution of concentrated forces on the second branch of the shear-critical crack, which is treated in a similar way as the tensile splitting cylinder test. The author does not agree on that, as the stress field, around the region where the second branch takes place, is more likely due to a diffusion of stresses. The interpretation and modeling of the second branch is therefore totally different between the two models, even though both formulation are strongly dependent on the tensile strength of concrete, which is assumed to be the main cause of the instable shear collapse.

To complete this analytical procedure, further studies are essential.

Factor χ should carefully evaluated and expressed in terms of the main parameters plotted in Figure 6.13-Figure 6.15, such as the longitudinal reinforcement, the depth of the member, the a/d ratios and the concrete grade. This non-dimensional factor could be extrapolated from statistical analysis of the significant amount of shear experiments published on the scientific literature. This could be a first possibility. However, the author is currently looking for a rational set of equations and an analytical method that could allow a calculation of factor χ as a function of the parameters above mentioned.

Further considerations can be done on the choice of the self-equilibrated distribution of shear stresses. With this respect, other distributions are in the process of being evaluated: they basically were chosen as non-symmetrical with respect to the centroid of the gross section, and with shear stress equal to zero at one third or one fourth of the depth of the member, measured from the top fiber. However, results are not ready yet.

From this approach a different value of β can be calculated, determining a consequently new evaluation of factor χ.

Finally, an evaluation of β by means of a fracture mechanics approach can also be considered. In doing so, a size effect law could numerically be obtained and corroborated against available experimental results.

All these considerations were provided to address new developments and refinements of the model herein presented.

6.4   Discussion on the Effect of Bond on Shear Behavior.

Steel-to-concrete bond proved to be very influential in the shear response of a members. By simply comparing the crack patterns in bonded and unbonded specimens (see Section 4.4.1), it was possible to remark that in case of bonded rebars many small and well distributed cracks were observed, having a width up to 1 mm. On the contrary, in case of unbonded beams, few wide cracks were reported, having a width of centimeters and a spacing of about 1-1.5 the depth of the beams. In the first case, cracks were observed even in the shear span whereas, in the second, all cracking phenomenon was limited to the portion of the member within the two load points.

With bonded rebars, the top compressive force is balanced by the tensile force at the bottom chord, transmitted through bond. Cracking starts at the bottom of the central portion of the beam once the tensile strength of material is reached. Cracks further grow toward the neutral axis location that, in general, moves upward with increasing external load.

Cracks also develop in the shear span where, due to the presence of shear stresses, tend to rotate toward the point load determining the block mechanism.

Some more considerations can be done for beams with unbonded rebars. Cracking develops mainly according to the moment distribution, and only in the central part of the beam. The first crack generally develops in a sudden and quite instable way, immediately reaching the neutral axis location. Conversely, cracks that develop later tend to grow in a slower fashion.

The first crack is quite big since the total load, firstly carried by concrete itself, suddenly is to be resisted by the bar itself, which has therefore to deform for carrying such a load.

Further cracks form due to the moment determined by an eccentricity *e* of the compressive force acting at the neutral axis location. It is possible to prove that by applying the classical formulas (for combined flexure and axial force) to a cross section of the specimen considered.

The maximum stress at the bottom of the beam in a section at a distance *d* from the existing first crack can be calculated, in case of specimen NSC0-UD, as follows:

$$\sigma = \frac{N}{A} - \frac{N \cdot e}{W} = 2.7 \text{ N/mm}^2 \cong f_{ctm} \tag{6.32}$$

where:

- *N≈150 kN* is the force acting on the compressive chord;

389

- *A=96 10³ mm²* is the gross area of the cross section at a distance *d* from the first crack;
- *e≈220 mm* is the eccentricity of the compressive load (i.e., of the location of the neutral axis) with respect to the centroid of the cross section;
- *W=7.68 10⁶ mm³* is the elastic section modulus of the cross section.

The tensile stress due to combined flexure and axial force is close to the tensile strength of concrete. This determines the growth of a new crack.

As shown in Figure 6.16, the small inclination of the second crack can be related to the combination of flexure and axial actions.
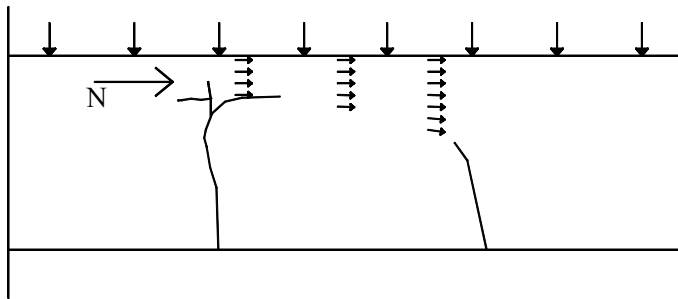
Figure 6.16: Stress field in the top compressive chord determining the occurrence of the second crack, in an unbonded beam.

Another interesting experimental evidence is related to the bifurcation of cracks at the neutral axis location. This can be accurately explained by considering a portion of a beam between two wide crack, as illustrated in Figure 6.17. This "panel" is subjected to compressive stresses that can be approximately modeled as triangular stresses (Figure 6.17 and Figure 6.18), which determine significant transverse tensile stresses. Once the tensile strength of the material is attained, a horizontal crack hence develops joining the two vertical cracks and defines in this way the shape of the resisting arch.

The width of the cracks that form successively are initially equal to the decrease in width of the existing cracks.
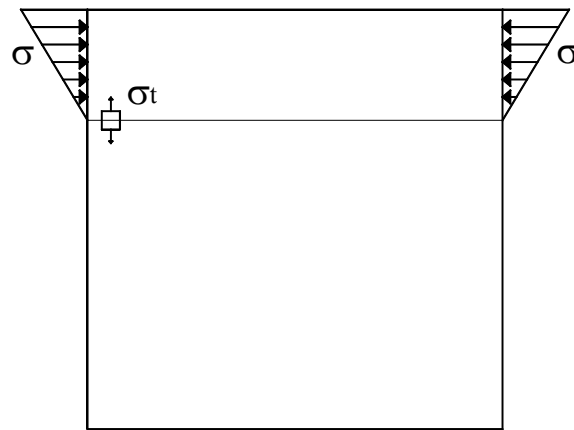
Figure 6.17: Transverse tensile stresses caused by the compressive stresses in a portion of a beam with unbonded rebars.
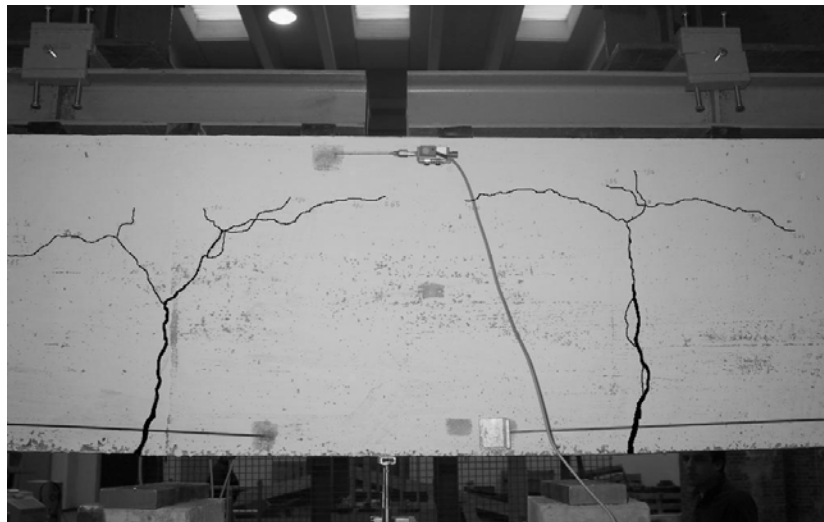
Figure 6.18: Bifurcation of crack in specimen NSC0-UD.

Note that in the shear span no crack is reported. This is likely due to the action of the inclined strut that, according to Figure 6.19, significantly influence the behavior of a broad area in the shear span: the horizontal component of the compressive force of the strut lies, in fact, in the central part of the section, allowing the section itself to be under compression only.
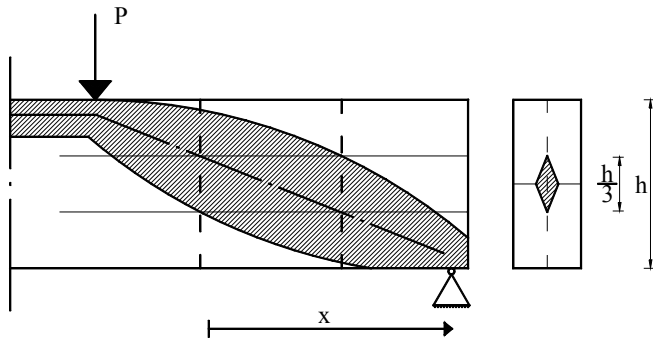
Figure 6.19: Compressive stresses in the shear span of an unbonded member.

6.4.1 Parametric Numerical Study on Steel-to-Concrete Bond.

To further investigate the effect of bond on the shear response of beams without web reinforcement, several steel-to-concrete bond relationships were assumed and numerically studied, by means of the FE Program VecTor2, already diffusely presented and discussed in Charter 5. The same mesh and material properties (according to specimen NSC0-BP) were adopted for all numerical tests.

However, bond-slip elements, which serve as deformable interfaces between reinforced concrete elements and discrete reinforcement elements, had to be added.

Increases of bond stresses are accompanied by bond slip, manifested by relative displacement on the paired nodes of the attached reinforced concrete and the discrete reinforcement element.

Link elements are two-noded non dimensional elements. Prior to any slippage, the paired nodes must have the same coordinates, and the element has therefore a total of 4 degrees of freedom.

Forty-four link elements were defined at any steel-concrete interface, except at the end of the specimen and at midspan, where just one node was defined for both materials, so that concrete and steel had coincident displacements. In the first case, that represents the anchorage of the bar (experimentally obtained by means of a steel plate), whereas in the latter the displacement of concrete and steel must be equal for symmetry.

As the first attempt, the Eligehausen model [8] was adopted. This model is a well known non-local model for representing the bond-slip phenomenon and it is defined by:

392

$$\tau = \tau_1 \cdot \left(\frac{s}{s_1}\right)^{\alpha} \quad \text{for } 0 \leq s \leq s_1$$

$$\tau = \tau_1 \qquad \text{for } s_1 \leq s \leq s_2$$

(6.33)

and by a linear decreasing branch starting from point τ_2-s_2 and leading to the value of the residual bond-resistance τ_3 at a slip value of s_3. These values of bond and slip change depending upon the degree of confinement of concrete, which, in all our cases, was very small as no stirrup was added in any specimen tested. Figure 6.20 shows a plot of the Eligehausen's model for unconfined concrete.

Note that, for unconfined concrete, $s_1=s_2=0.6$ mm, $s_3=10$ mm, $\tau_1=2.0(f_{ck})^{1/2}$, $\tau_3=0.3$ $(f_{ck})^{1/2}$, and $\alpha=0.4$.
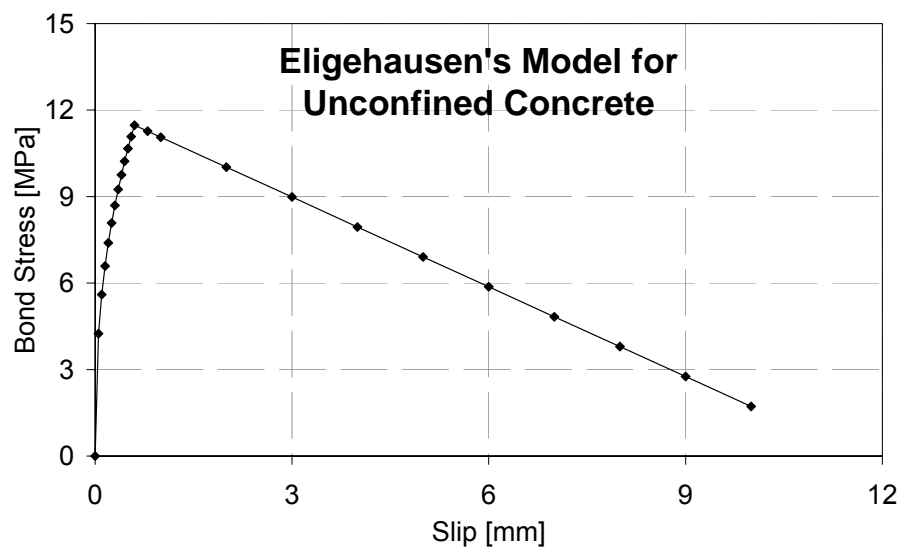
Figure 6.20: Eligehausen's Model for unconfined concrete.

For improving the bond-slip relationship, a local formulation, developed by Giuriani [9] was also investigated. This is a relation very detailed for small slippages between concrete and steel; it should hence be suitable in case of brittle shear failure where no big slippage is in general observed (the main shear crack, in the present experimentation, proved to range between 0.1-0.2 mm prior to failure).

Furthermore, the theoretical analysis performed by Giuriani, from which this bond-slip law was identified, deals with the behavior of the reinforcement during the early second stage, which is characterized by very small values of crack openings and

steel being in the elastic range. A trilateral law was suggested by the author, with a maximum slippage of 0.1 times the diameter of the bar, as depicted in Figure 6.21. According to the notations presented in Figure 6.21, the equation of the proposed relationship is:

$$\tau = \tau_{11} \cdot s \qquad\qquad \text{for } 0 \le s \le s_1$$
$$\tau = \tau_{02} + \tau_{12} \cdot (s - s_1) \qquad \text{for } s_1 \le s \le s_2 \tag{6.34}$$

where:

- $\tau_{02} = 3 \cdot MPa$;
- $\tau_{03} = 6 \cdot MPa$;
- $\tau_{12} / \tau_{11} = 0.1$;
- $\tau_{12} \cdot \phi = 500 \cdot MPa$;
- $s_{max} = 0.1 \cdot \phi$.

The plot of Giuriani's model clearly explains the different approach undertaken, in comparison with the Eligehausen law, in which the slippage can reach values greater than 10 mm.

Note that this model neglects the wedge actions exerted by the ribs of a deformed bars [10].
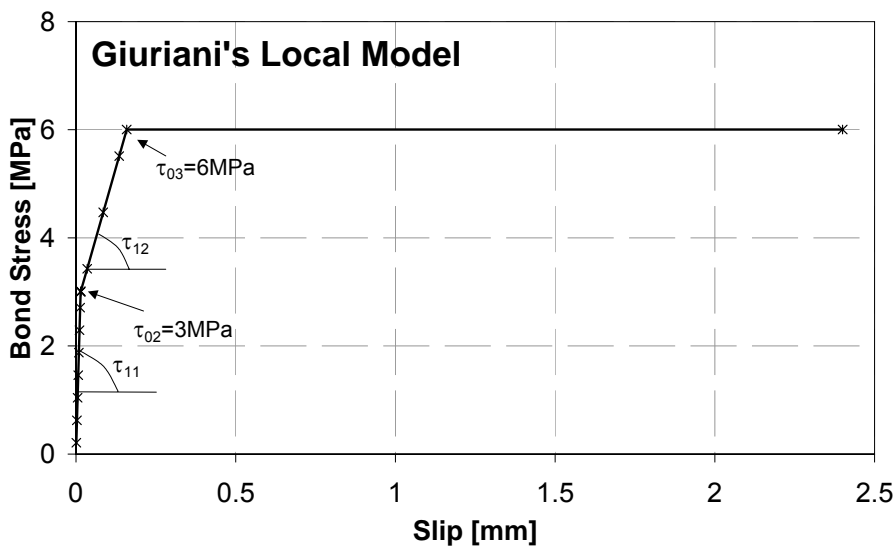
Figure 6.21: Giuriani's model.

In addition to these laws, other simple and arbitrary bond-slip relationships were investigated, namely:

- a constant plateau of 1.5 MPa;
- a constant plateau of 3.0 MPa.

The latter two relations represent bars with low capacity of preventing slippage, and hence were chosen to examine situations close to the no-bond (specimens NSC0-UP and NSC0-UD).

Due to the remarkably different responses numerically obtained, the numerical load-displacement curves are plotted in two different graphs: Figure 6.22 illustrates the comparison among the experimental curve of specimen NSC0-BP and the numerical analyses that modeled perfect bond, bond according to Eligehausen and according to Giuriani. It can be immediately noticed that the analysis with perfect bond is the critical case: the collapse under shear appears first, with lower deformations and loading bearing capacity. Moreover, assuming perfect bond gives the better fitting, compared to the experimental result.

Both Eligehausen's model and Giuriani's model give quite accurate predictions, in terms of post cracking stiffness as well as with regard to the ultimate load and collapse mechanism.
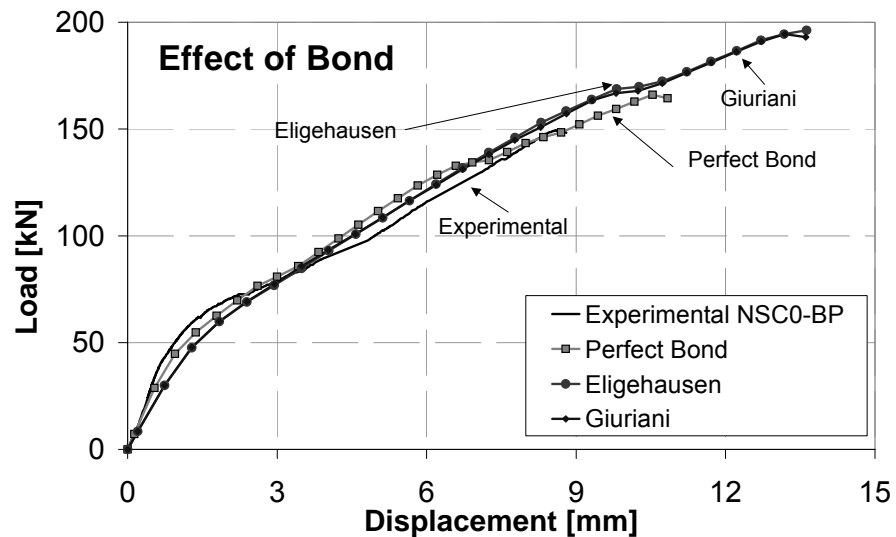
Figure 6.22: Comparison among the experimental results and some bond models, specimen NSC0-BP.

No significant difference can be reported between the two models, which means that only small slippages were numerically calculated, as one would have expected. Figure 6.23 presents the crack patterns at failure of the experiment and of the three numerical analyses. As already mentioned in Chapter 5, the FE program tends not to model the sub-horizontal second branch of the shear-critical crack. The cracking phenomenon develops along a strut connecting the load point to the bottom layer of reinforcement with an inclination of around 45°. In other words, the shear-critical crack locates in a portion of the beam that, in the numerical model, is closer to the point load than it was observed in the experiment.

No significant difference can be reported among the three numerical patterns.

More interesting is the case of unbonded rebars. Figure 6.24 shows the comparisons among the experimental results of specimen NSC0-UP and the numerical curves of three specimens having different bond-slip relationships (no bond, 1.50 MPa and 3.0 MPa).

Experimental crack pattern at failure. Specimen NSC0-BP

Perfect Bond

Eligehausen's Model

Giuriani's Model
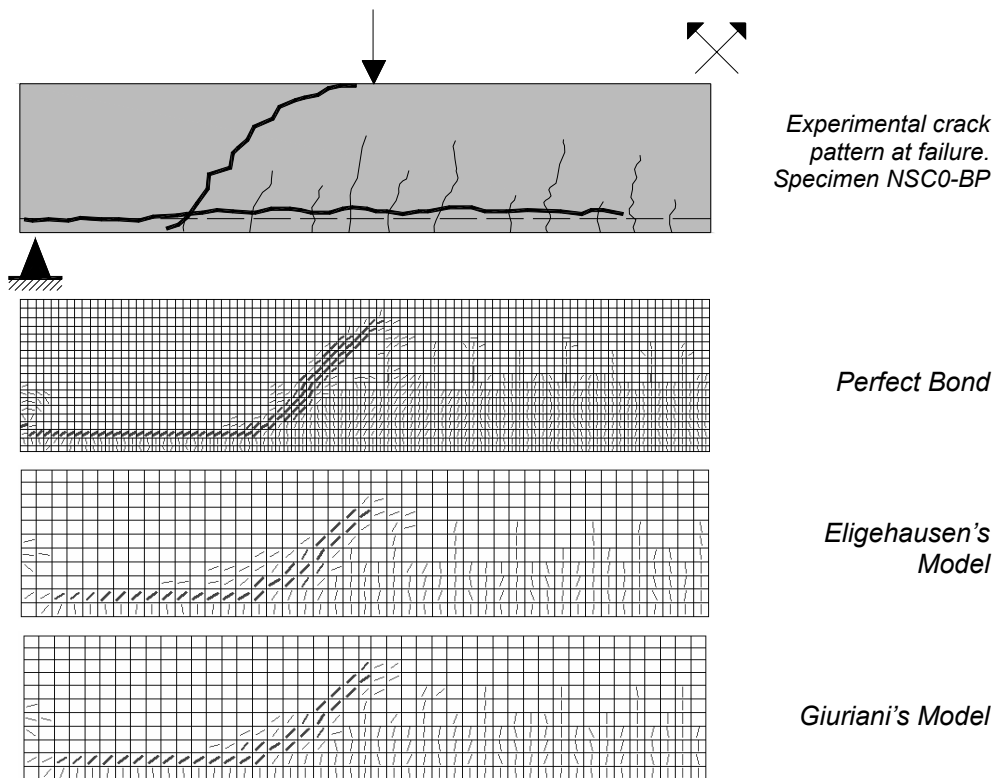
Figure 6.23: Crack patterns at failure with changing of bond-slip relationships: comparison with specimen NSC0-BP.

The scope of this plot is not related to the optimization of the fitting between the experimental results and the numerical analyses. Conversely, the evaluation of different bond characteristics can determine different responses.

One can recognize that the analysis with no bond, as expected, determines the achievement of the full flexural capacity of the member, accompanied to a consistent ductility. The fitting of the experimental data is also satisfactory, as already mentioned in Chapter 5, Section 5.4.2.1.

According to Figure 6.25, which deals with the crack patterns of the experiment and numerical analyses, in the numerical test with no bond there is no cracking at all in the shear span, and that is totally in agreement with the experimental evidence.

With increasing bond (from a plateau of 1.5 MPa to a plateau of 3.0 MPa, which anyway are values really small if compared to those of regular deformed bars), cracking in the shear span greatly influences the overall behavior, determining a premature collapse of the member, under a combination of flexure and shear. Moreover, in the central part of the beam a more diffused crack pattern develops without the formation of wide cracks only (compare, with this regard, the numerical pattern between no bond and 3.0 MPa plateau).
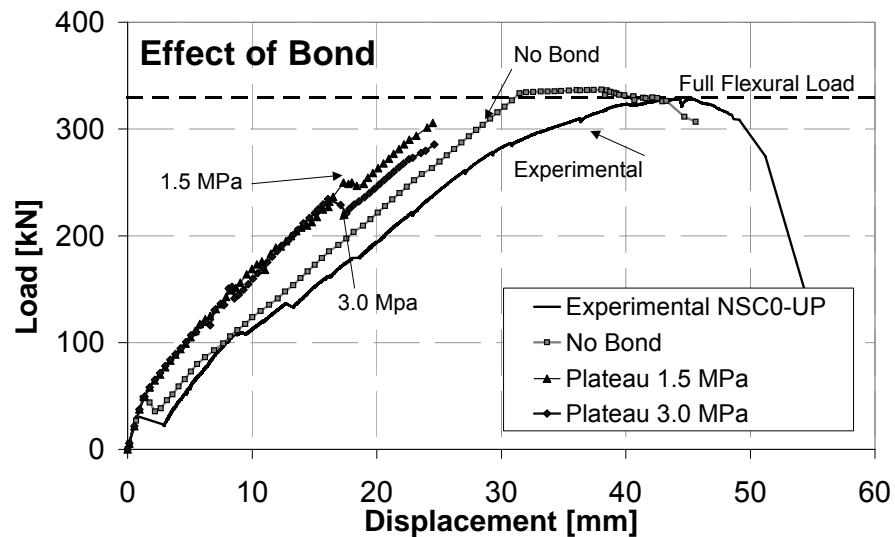
Figure 6.24: Comparison among the experimental results and some bond models, specimen NSC0-UP.

In all cases, however, the response and the crack patterns are mainly governed by flexure.

It is worth emphasizing that at the first cracking point, for a total load of about 30 kN (see Figure 6.24), the experiment and the analysis with no bond exhibited a big concentrated crack, which dramatically increased the overall displacements. Conversely, a more diffused cracking within the two point loads arose at early crack stages, in the two cases with plateaus of 1.5 MPa and 3.0 MPa.

Moreover, the post-cracking stiffness of the two latter models proved to be almost similar to that observed for the bonded experiments. This is particular important because a little bond, more than preventing from a brittle shear collapse, allows the beam to maintain a satisfactory post-cracking stiffness and to exhibit, only at early stages of deformations, a diffused crack pattern.

This can be really useful for design purposes as, with little bond, both cracking control and sufficient bearing capacity can be combined to achieve a suitable performance of the structure.

Experimental crack pattern at failure. Specimen NSC0-UP

No Bond

Plateau 1.5 MPa

Plateau 3.0 MPa
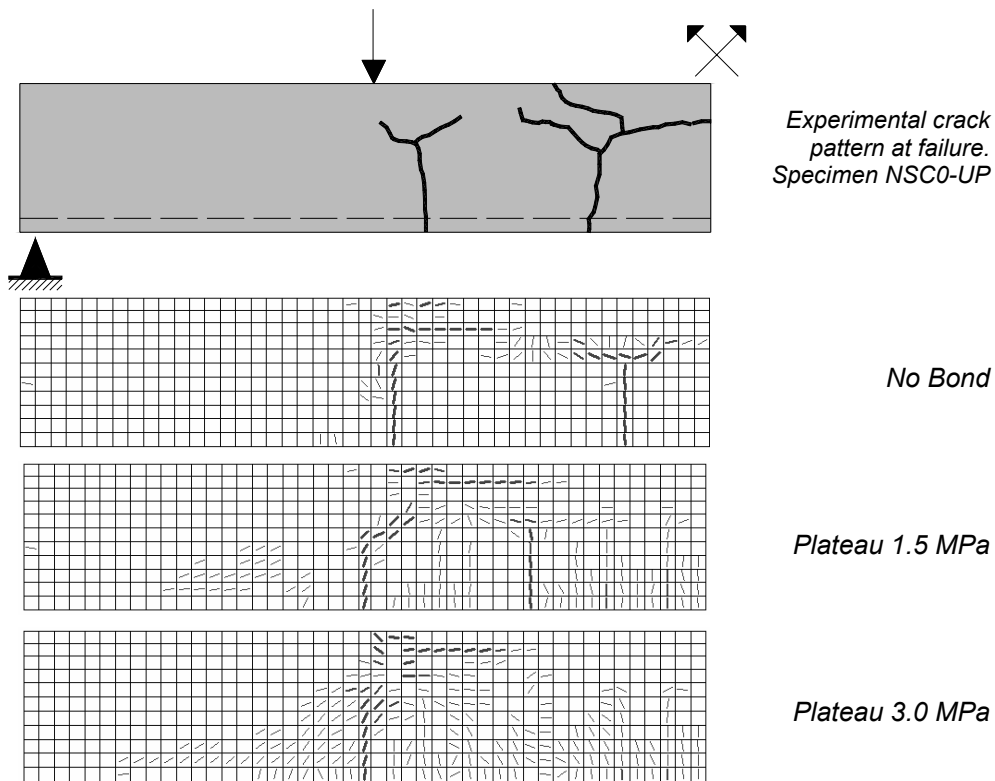
Figure 6.25: Crack patterns at failure with changing of bond-slip relationships: comparison with specimen NSC0-UP.

Table 6.6 reports the main quantities monitored in the numerical analyses, against the experimental results. Eligehausen's model and Giuriani's models overestimated the experimental ultimate shear of about 25%. Once again, the case of little bond is the most interesting, showing that the ratio between the moment from analysis and the flexural ultimate moment is nearby 1.0 in these two cases.

	Maximum Load	Midspan Displacement	$V_{u,exp}/V_{u,num}$	$M_{u,analysis}/M_{u,Flex.failure}$
	[KN]	[mm]	[-]	[-]
Experimental bonded NSC0-BP	149	8.8	-	0.45
Perfect Bond	166	10.5	0.90	0.50
Eligehausen's Model	196	13.6	0.76	0.59
Giuriani's Model	194	13.6	0.77	0.59
	Maximum Load	Midspan Displacement	$M_{u,analysis}/M_{u,Flex.failure}$	
	[KN]	[mm]	[-]	
Experimental unbonded NSC0-UP	329	49.2	1.00	
No Bond	337	38.0	1.02	
Plateau 1.5 MPa	306	24.5	0.93	
Plateau 3.0 MPa	285	24.6	0.87	

Table 6.6: Summary of the main results of numerical analyses.

6.5 Discussion on the Effect of Fibers as Web Reinforcement: a Parametric Study.

Fibers proved to be highly effective in diminishing the domain of a/d ratios among which brittle shear failure occurs. This experimental evidence can be numerically proved and extended to similar structures having different parameters.

The following section will provide a discussion on the effect of fibers on the valley of diagonal shear failure, investigated for:

- Two typologies of concrete, one having high strength concrete and the other of normal strength. The first resembles the concrete utilized for specimen of series I-Beam whereas the second is similar to specimens of series NSC2. Acronyms HSC and NSC2 will be utilized in the following for the two set of numerical models. A concrete cylinder compressive strength of 70 MPa was assumed for model HSC while 35 MPa for model NSC2;

- Three different reinforcement percentages, namely 0.72%, 1.04% and 1.42%. All three reinforcement ratios reflect reliable practical situations, even though the first one is the most representative case for members cast without web reinforcement (plates, secondary beams...);
- Two typologies of fibers, having different toughness, for each concrete considered. FRC composites were actually the same as those experimentally tested for both HSC and NSC2 series. The same acronyms will be therefore used, namely HSC-FRC1, HSC-FRC2, NSC2-FRC1 and NSC2-FRC2.

Table 6.7 summarizes the main material properties and fibers adopted for the four models adopted. Note that perfect steel-to-concrete bond was assumed in all analyses.

Specimen	Transverse Reinforcement	f'_c [MPa]	f_{ct} [MPa]	E_c [MPa]	$f_{sy, Rebar}$ [MPa]	a_g [mm]
HSC-FRC1	50 kg/m^3 Fibers 45/30	70.0	2.75	46000	512	15
HSC-FRC2	50 kg/m^3 Fibers 80/30	70.0	2.75	46000	512	15
NSC2-FRC1	30 kg/m^3 Fibers 50/1.0	35.0	1.95	32500	512	20
NSC2-FRC2	30 kg/m^3 Fibers 50/1.0 + 15 kg/m^3 Fibers 12/0.18	35.0	1.95	32500	512	20

Table 6.7: Summary of material properties of numerical models.

Toughness of fibers were included in the program through suitable tension softening laws calibrated in the same way as the ones reported and discussed in Section 5.3.1 for the shear-critical beams numerically tested.

All other details, concerning material modeling, mesh adopted and assumption in the mode are identical to those discussed and presented in Chapter 5.

A number of 3D plots of the valley of shear diagonal failure ($M_u/M_{u,fl}$ versus a/d ratio), as a function of the reinforcement ratio, or of the equivalent stress $f_{eq(0.6-3)}$ according to the Italian Standard [2.125] will be discussed in the following.

It should be recognized first that numerical results, in case of a/d ratios lower than 2.5, should be carefully evaluated as in those situations the effect of bearing steel plates, placed at supports and load points, might significantly affect the results in terms of bearing capacity as well as of ductility and failure mechanism.

In this parametric study, three plates 100 mm long, 200 mm wide and 30 mm thick were placed at the anchor of bars, at support and at the load location. By changing

the dimension of the plates, different values of load were obtained, especially when dealing with *a/d*=1 and *a/d*=1.5.

However, this is not the main point of the present investigation, which aims at determining the effect of fibers on the diagonal shear behavior; this phenomenon typically arises for *a/d* ratios greater than 2.5 under the hypothesis of "beam behavior".

Not much emphasis will therefore be devoted to results obtained for *a/d* ratios lower than 2.5, even though a considerable effect of fibers was noticed.

The ratio between the ultimate moment M_u (the moment at which the collapse of the structure occurred, whether under shear or flexure), numerically obtained, and the moment due to flexural failure, $M_{u,fl}$, was performed with a number of assumptions in calculating the latter. For members made of plain concrete, the ultimate flexural moment $M_{u,fl}$ was calculated by assuming the yielding of rebars and a classical stress-block approach. For members containing fibers, even though no big changes would be expected, the ultimate moment was calculated according to the formulation of Imam [2.158] reported in Equation (2.279) (Section 2.8.9.3 of Chapter 2). This formulation proved to be in agreement with the experimental results of HSC-FRC2 and NSC1-FRC2, which both exhibited a flexure failure. Note that the increase in flexural ultimate moment due to the presence of fibers was in all cases lower than 10%, if compared to that of plain concrete elements. As an example, the ultimate moment for the high strength concrete shear-critical beams having a reinforcement ratio of 1.04% was calculated as 192 kN m (with a classical approach), while Imam' formula gave 205 kN m and 213 kN m as the flexural moment respectively for HSC-FRC1 and HSC-FRC2 models. Therefore, the effect of fibers in improving the flexural strength is not crucial in beams containing conventional reinforcement.

Figure 6.26-Figure 6.28 show the Kani's valley as a function of the equivalent post-cracking strength (evaluated according to the Italian Standard), which is representative of the fiber contribution. Each figure refers to one of the three reinforcement percentages selected.

Linear interpolation of results was chosen among the values numerically obtained.

In the first plot, the highly relevant effect of 50 kg/m^3 of hooked steel fibers in a high strength concrete with a low reinforcement ratio is shown. According to Table 6.7, in this matrix whether fiber 45/30 (having a equivalent strength of 3.12 MPa, determined from 4PBTs) or fibers 80/30 (in which $f_{eq(0.6-3)}$=*5.99 MPa*) were utilized.
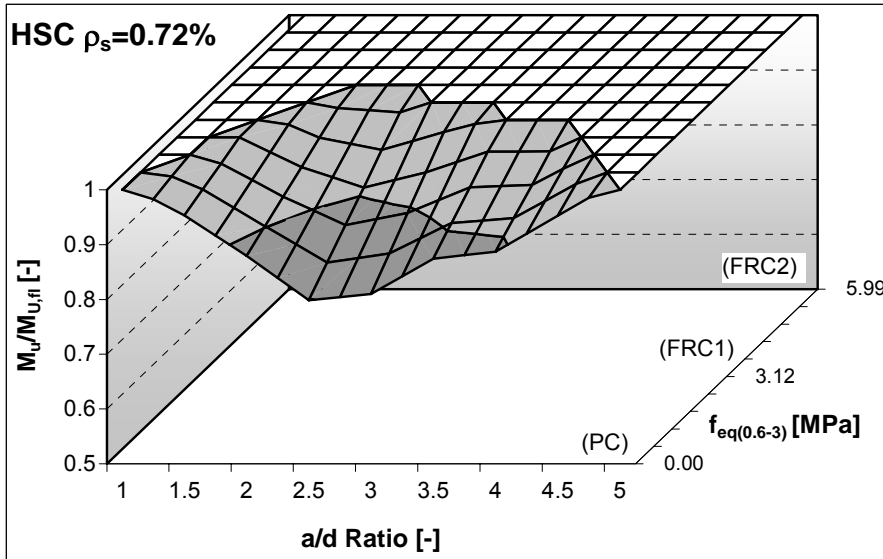
Figure 6.26: Influence of the fiber toughness on the valley of shear failure, high strength concrete, ρ_s=0.72%.

In one hand, plain concrete shows a domain of shear failure for all range of *a/d* ratios plotted (with a minimum, as expected for *a/d=2.5*, where $M_u/M_{u,fl}$=0.8), while HSC-FRC1 model shows a very limited domain of shear failure, only for *a/d* ratios between 1.75 and 2.75, with ratio of $M_u/M_{u,fl}$ just below one (the minimum value of $M_u/M_{u,fl}$ was, again for a/d=2.5, equal to 0.98). The valley of shear diagonal failure disappears completely for the high strength fibers, in the model HSC-FRC2.

With increasing reinforcing ratio (Figure 6.27 and Figure 6.28) the valley of diagonal shear failure tends to become deeper and, moreover, to expand even in region with relatively high equivalent post-cracking strength. In case of ρ_s=*1.04%* (equal to the experimental value of all shear-critical beams), the minimum value of the ultimate moment occurs for *a/d=2.5* both for plain concrete and for HSC-FRC1 model, the first having the ratio $M_u/M_{u,fl}$=*0.69*, and the second $M_u/M_{u,fl}$=*0.87.* Model HSC-FRC2 does not exhibit any shear failure for any range of *a/d* ratio.

When dealing with ρ_s=*1.42%* (Figure 6.28), the shear diagonal failure slightly also affects model HSC-FRC2 (in the range of *a/d=2.5*). The ratio $M_u/M_{u,fl}$ turned out to be equal to 0.98 and 0.99 respectively for *a/d* of 2 and 2.5. The failure mechanism was under a combination of flexure and shear, since big cracks were noticed both within the two load points and in the shear span. It is worthy noticing that the choice of the ultimate flexural moment influences the ratio $M_u/M_{u,fl}$, which can be just below or above one.

402

A higher reinforcement ratio would certainly determine a clear appearance of the domain of shear diagonal failure even in the model with high strength fibers (HSC-FRC2). However, reinforcement ratios higher than 1.5% are generally not usual in practical applications.
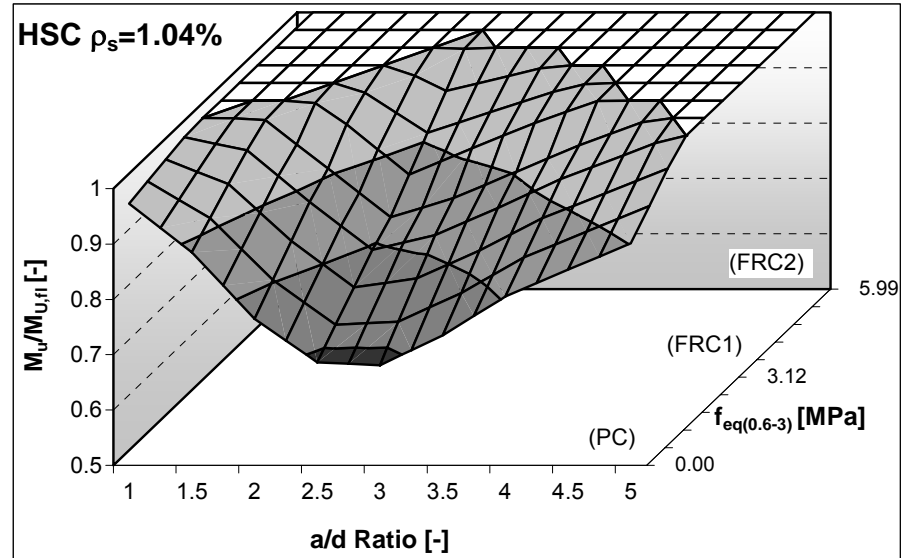
Figure 6.27: Influence of the fiber toughness on the valley of shear failure, high strength concrete, ρ_s=1.04%.

From these three plots, the effect of fibers in reducing the brittleness of members by forcing a flexural failure rather than an early shear failure is extremely clear.
Differently from Imam et al. [2.158] and Russo et al. [2.103] who, with analytical approaches, predicted a critical *a/d* ratio inversely dependent on the compressive strength (so that the critical *a/d* ratio for members having a compressive strength of 70 MPa was predicted to be around 1.9), this numerical investigation confirms that *a/d=2.5* is still the critical ratio, for which the minimum ultimate moment is attained.
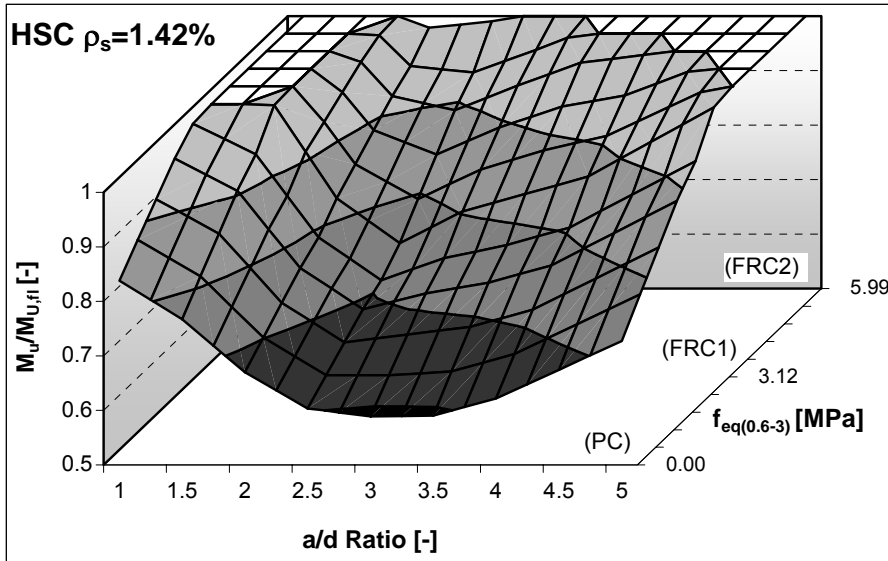
Figure 6.28: Influence of the fiber toughness on the valley of shear failure, high strength concrete, ρ_s=1.42%.

Figure 6.29-Figure 6.31 illustrate the Kani's valley of the same numerical models above discussed, as a function of the reinforcing ratio. The first plot concerns model HSC-PC, the second HSC-FRC1 and the last refers to model HSC-FRC2.

As already diffusely reported in the literature, the valley of shear diagonal failure deepens with increasing longitudinal reinforcing ratio. This is confirmed even for high strength concrete and in presence of fibers. If for plain concrete all points of the domain are below the flexural moment, in model HSC-FRC1 shear failure occurs for all values of a/d only with the highest reinforcement ratio, while it disappears completely in case of ρ_s=0.72%.

For model HSC-FRC2, no shear failure is reported anywhere, for any value of a/d and reinforcement ratio. Only two situations might be critical under shear (*a/d=2* and *a/d=2.5* for ρ_s=1.42%), as already remarked.
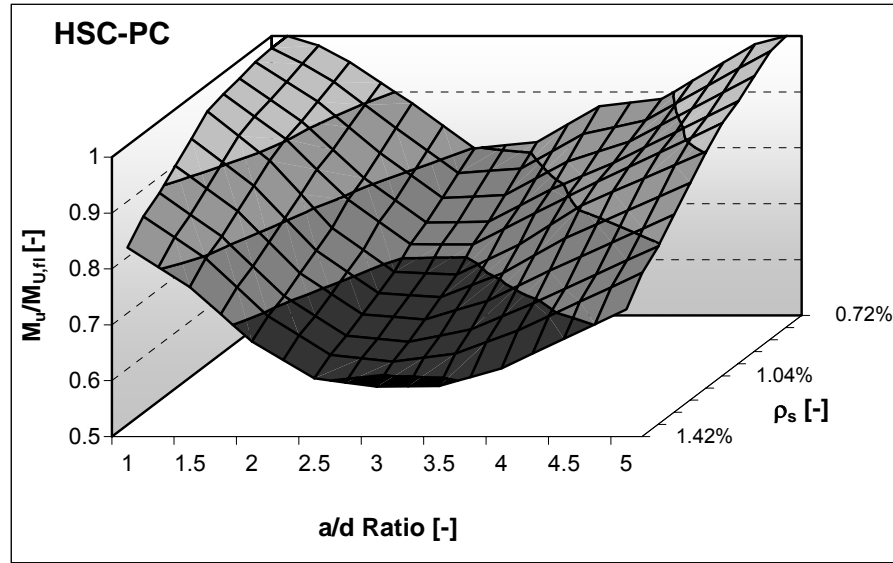
Figure 6.29: Influence of the longitudinal reinforcement ratio on the valley of shear failure, high strength plain concrete.
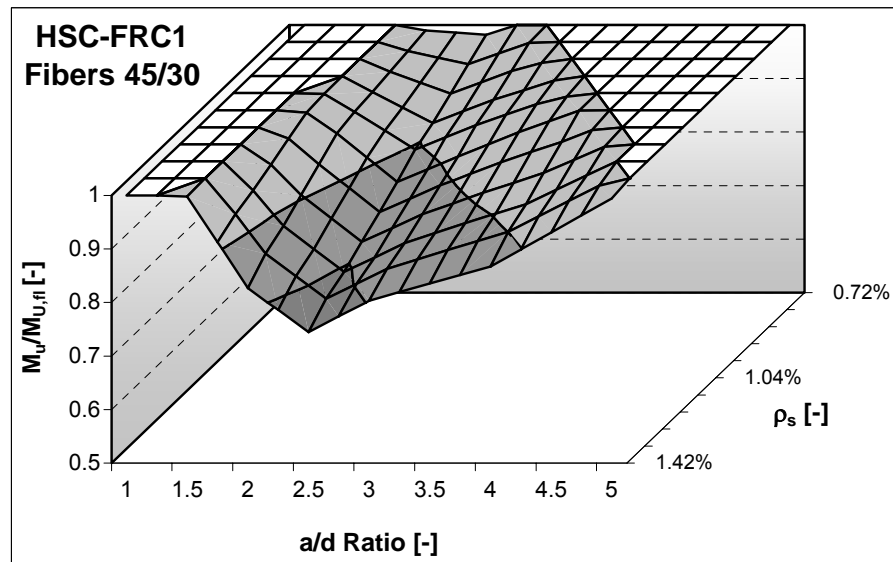
Figure 6.30: Influence of the longitudinal reinforcement ratio on the valley of shear failure, high strength concrete with fibers 45/30.
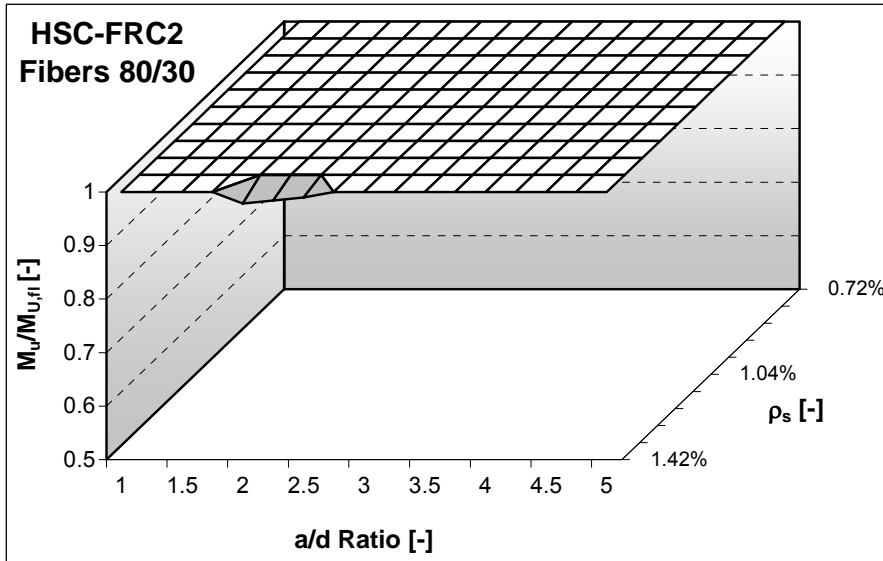
Figure 6.31: Influence of the longitudinal reinforcement ratio on the valley of shear failure, high strength concrete with fibers 80/30.

Table 6.8 summarizes the values of $M_u/M_{u,fl}$ obtained from the set of numerical analyses performed on model of series HSC.

a/d	ρs=0.72%			ρs=1.04%			ρs=1.42%		
	HSC-PC	HSC-FRC1	HSC-FRC2	HSC-PC	HSC-FRC1	HSC-FRC2	HSC-PC	HSC-FRC1	HSC-FRC2
1.0	1.00	1.00	1.00	0.97	1.00	1.00	0.84	1.00	1.00
1.5	0.95	1.00	1.00	0.89	1.00	1.00	0.77	1.00	1.00
2.0	0.88	0.99	1.00	0.76	0.96	1.00	0.67	0.83	0.98
2.5	0.80	0.98	1.00	0.69	0.87	1.00	0.60	0.74	0.99
3.0	0.81	1.00	1.00	0.68	0.91	1.00	0.59	0.80	1.00
3.5	0.87	1.00	1.00	0.73	0.96	1.00	0.59	0.84	1.00
4.0	0.89	1.00	1.00	0.81	1.00	1.00	0.62	0.87	1.00
5.0	1.00	1.00	1.00	0.90	1.00	1.00	0.73	0.99	1.00
M*u,fl* [kN m]	136	149	158	192	205	213	258	270	277

Table 6.8: Values of $M_u/M_{u,fl}$ obtained from the numerical analyses of models of HSC series.

Similar results were obtained for models of series NSC2, as presented in Figure 6.32-Figure 6.37. Concerning plain concrete, the valley of shear diagonal failure is herein deeper than the model simulating high strength concrete, as the ultimate

shear strength of members decays much more rapidly than the ultimate flexural moment with decreasing compressive strength. The ultimate flexural moment for members without fibers, as an example, was estimated as 182 kN m versus 193 kN m, in case of ρ_s=1.04%, respectively for specimen NSC2-PC and HSC-PC. Conversely, the ultimate moment due to shear turned out to be quite different, namely 110 kN m and 132 kN m for the normal and high strength concrete model, respectively. This explains the greater deepness of the Kani's valley for normal strength concrete.

Some differences are also due to the amount of fibers added to the matrixes. While both models of HSC series simulated *50 kg/m³* of fibers (in one case they had normal strength whereas in the second fibers had high strength), NSC2-FRC1 modeled only *30 kg/m³* of normal strength fibers while NSC2-FRC2 simulated a total of *45 kg/m³* of fibers, with *15 kg/m³* of micro fibers and *30 kg/m³* of the same macro fibers included in NSC2-FRC1 model (see Table 4.6). For this reason, model NSC2-FRC1 did not show the same ability (as the HSC-FRC1 did) in limiting the effect of the shear diagonal failure, even though a clear enhancement is noticed, compared to the plain concrete model.
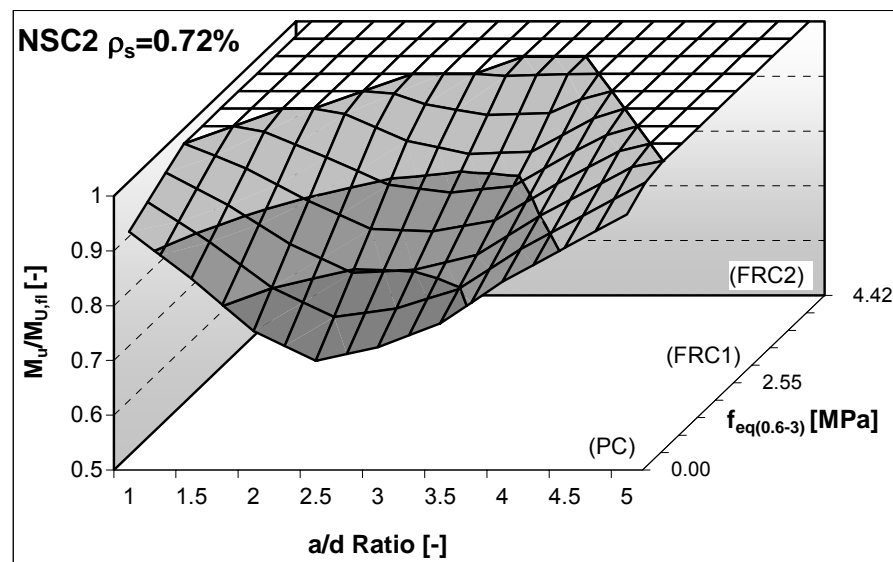
Figure 6.32: Influence of the fiber toughness on the valley of shear failure, normal strength concrete, ρ_s=0.72%.

The poor strengths obtained for *a/d* ratios less than 2.5, in certain cases much lower than the full flexural capacity, are also clear. This is due to two main factors:

the first is related to the dimension of the bearing plates chosen, which were actually selected too small for bringing the member up to its flexural capacity. The other is due to the modeling of concrete in compression in presence of fibers. No model is at the moment available in the FE Program VecTor2 that could simulate the enhanced ductility and residual strength provided by fibers in compression. However, the FE routine implicitly recognizes a certain contribution of fibers in compression, since they allow a lower decay in the residual compression strength by limiting cracking in tension. This is certainly correct, even though this phenomenon was included in the program only for plain concrete matrixes, in which the reduction of compressive strength due to cracking in concrete is much higher. Refinements for taking into account a lower decay of the residual compressive strength due to fibers should be included in the program, in order to address some improvements in results. This means that further experimental investigations should be done to properly model the enhanced capacity of struts made of FRC.
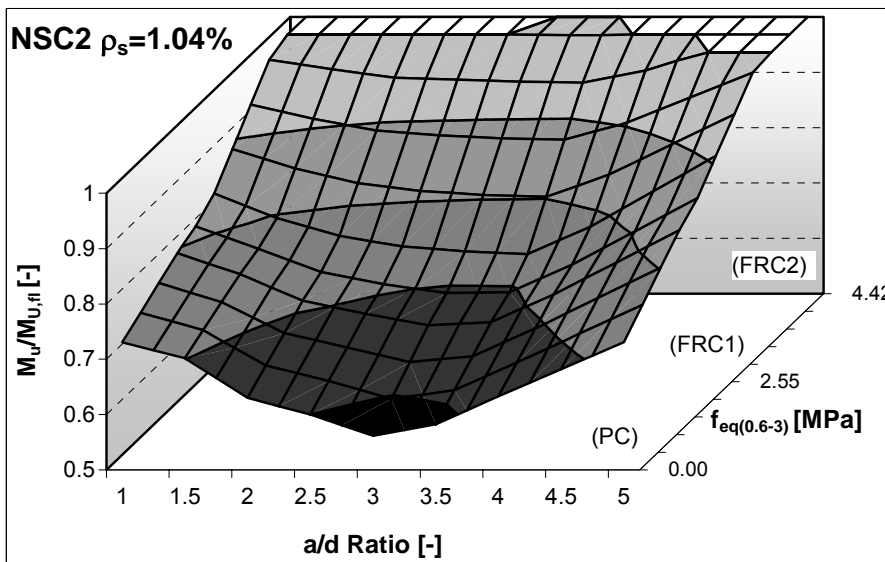
Figure 6.33: Influence of the fiber toughness on the valley of shear failure, normal strength concrete, ρ_s=1.04%.

With the highest reinforcement ratio (ρ_s=1.42%, Figure 6.34), the domain of shear failure extends for around all over the cases investigated, with the exception of model NSC2-FRC2, which seems to have fibers with the minimum toughness able to bring the member up to it flexural capacity.

Figure 6.35-Figure 6.37 illustrates the plot of the Kani's valley for each single model, as a function of the reinforcement percentage. Note that while models NSC2-PC and NSC2-FRC1 are in the domain of shear failure for all situations considered, model NSC2-FRC2 exhibits the ability to attain the full flexural capacities in most of cases.
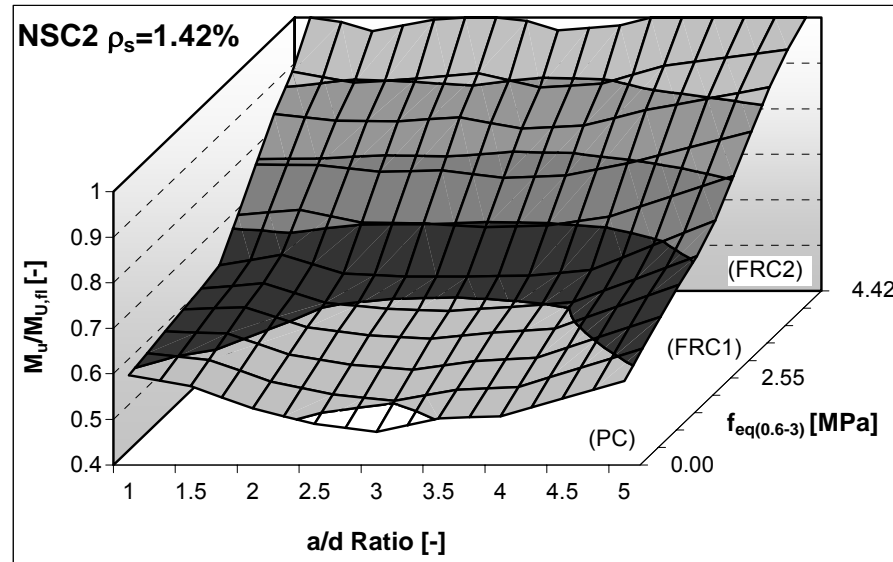
Figure 6.34: Influence of the fiber toughness on the valley of shear failure, normal strength concrete, ρ_s=1.42%.

This is certainly due to the higher fiber content, but also to the combination of fibers having different geometry. The hybrid fiber composite likely determined high toughness properties [11], which were transferred in the FE program as a more performing tension softening law.

The considerable scatter between results obtained from models NSC2-FRC1 and NSC2-FRC2 can make the linear interpolation of results among them not very refined. An intermediate case study should be numerically performed to obtain a more reliable interpolation. This would involve an experimental campaign for finding an intermediate tension softening between the two FRC models herein investigated.
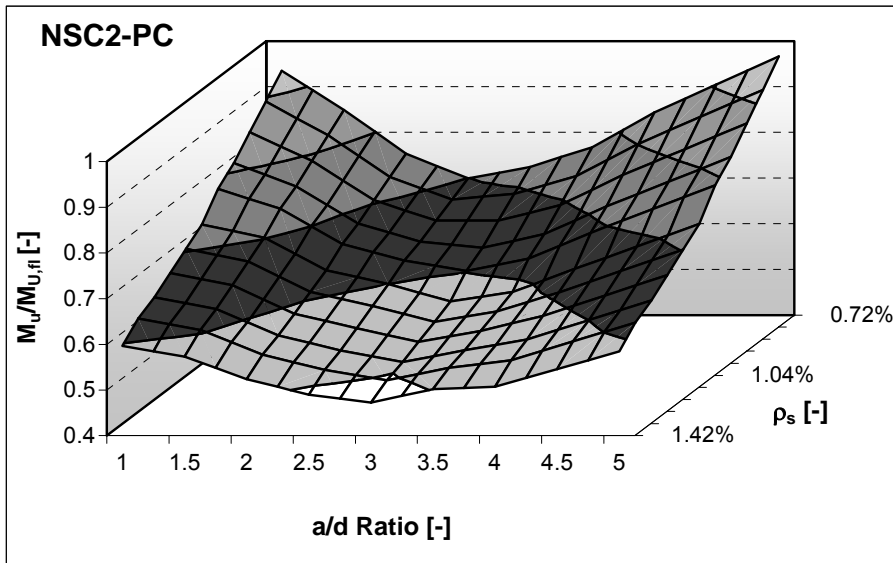
Figure 6.35: Influence of the longitudinal reinforcement ratio on the valley of shear failure, normal strength plain concrete.
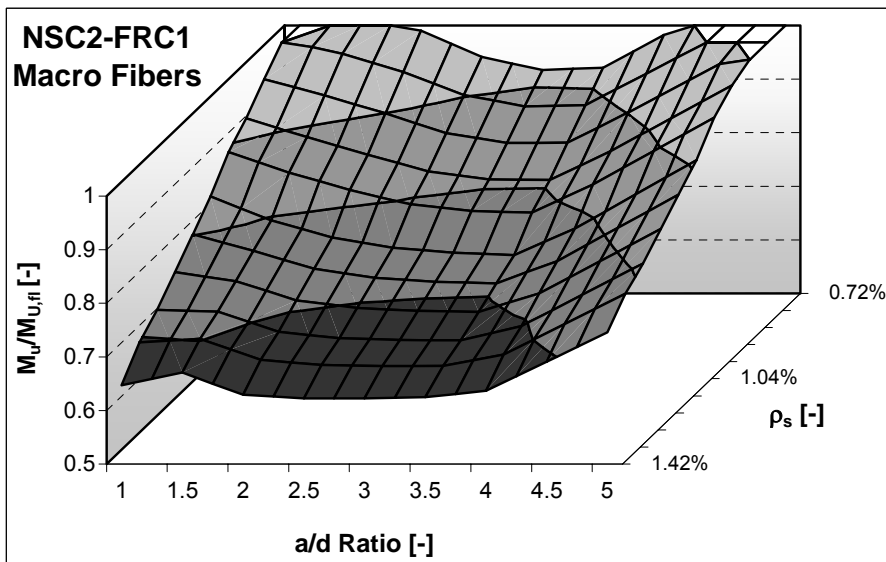
Figure 6.36: Influence of the longitudinal reinforcement ratio on the valley of shear failure, normal strength concrete with macro fibers.
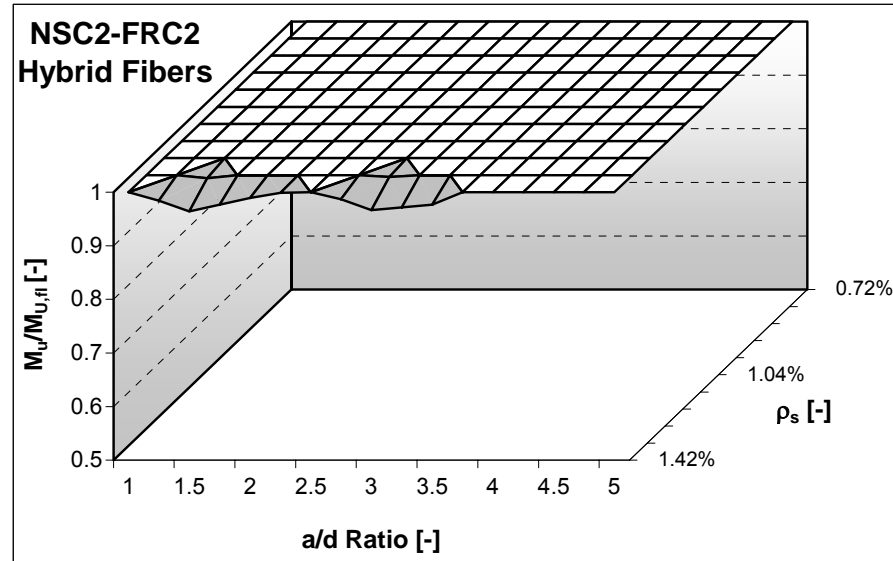
Figure 6.37: Influence of the longitudinal reinforcement ratio on the valley of shear failure, normal strength concrete with hybrid fibers.

Table 6.9 summarizes all values of the ratio $M_u/M_{u,fl}$ obtained for models of series NSC2. Note, once again, the huge scatter between model NSC2-FRC1 and model NSC2-FRC2.

a/d	$\rho_s=0.72\%$			$\rho_s=1.04\%$			$\rho_s=1.42\%$		
	NSC2-PC	NSC2-FRC1	NSC2-FRC2	NSC2-PC	NSC2-FRC1	NSC2-FRC2	NSC2-PC	NSC2-FRC1	NSC2-FRC2
1.0	0.93	1.00	1.00	0.73	0.84	1.00	0.60	0.65	1.00
1.5	0.85	1.00	1.00	0.70	0.80	1.00	0.57	0.67	0.96
2.0	0.75	0.99	1.00	0.63	0.76	1.00	0.52	0.63	0.99
2.5	0.70	0.94	1.00	0.60	0.74	1.00	0.49	0.62	1.00
3.0	0.72	0.92	1.00	0.56	0.74	1.00	0.47	0.62	0.97
3.5	0.77	0.92	1.00	0.58	0.73	1.00	0.50	0.62	0.98
4.0	0.84	0.98	1.00	0.63	0.78	1.00	0.51	0.64	1.00
5.0	0.97	1.00	1.00	0.73	0.91	1.00	0.58	0.75	1.00
M*u,fl* [kN m]	131	139	143	183	190	194	241	247	250

Table 6.9: Values of $M_u/M_{u,fl}$ obtained from the numerical analyses of models of NSC2 series.

6.6 Discussion on Available Models for Shear Strength of SFRC Members without Web Reinforcement.

This section mainly deals with a critical review of the available models predicting the shear strength of SFRC members without traditional web reinforcement.

It should be recognized first that the knowledge of shear in FRC beams is much lower than that in beams made of plain concrete. The available analytical models for FRC reflect that: most of those presented in Section 2.8.9 of Chapter 2 can not be considered rational models since they were extrapolated for a limited series of experimental tests, which did not take into account all parameters influencing shear behavior. As a result, some of these formulations can not be used for a wide range of structural elements or material properties, which are too different from the ones that form the basis of the model.

Moreover, the comparison of these models gives a huge scatter, which means that some formulas are unsafe whereas some other are too conservative.

The important issue of size effect is not properly considered, or even neglected, by many proposals.

The majority of formulations refers to the fiber factor F for including the effect of fibers in the shear strength. This can be considered as a very convenient way to account for fibers. As F is a function only of the aspect ratio, the volume fraction and the shape of fibers, no special tests are required to determine the shear strength.

As a first attempt to model the contribution of fibers in shear, this can be considered acceptable. However, it is crucial to emphasize that the effect of identical fibers in different concrete matrixes can be considerably disparate, as the bond properties and the interaction between fiber and concrete can determine various situations.

Moreover, fibers having the same aspect ratio and added in equal amount (so having the same value of fiber factor F) might determine a quite different effect on the concrete matrix. As an exemplification, short and thin fibers in general provide a higher performance than larger and thicker fibers (the two types having the same aspect ratio and added to the matrix in the same amount) for small values of cracking. Conversely, when the crack process is advanced, longer fibers are able to resist more load, as most of short fibers are already debonded or broken.

The two latter important aspects can not be modeled at all by using the fiber factor F, which therefore is an inadequate parameter for a comprehensive modeling of the effect of FRC in shear.

Rather than considering *F*, one should take into account the effect of fibers by means of a quantity related to the fiber reinforced concrete composite.

In this research, this will be done by considering the equivalent post-cracking strength $f_{eq(0.6-3)}$ according to the Italian Standard ([2.125], see also Chapter 2, Section 2.8.4). This parameter includes the interaction between concrete and fibers. Furthermore, this procedure allows the definition of a post-cracking strength in the most convenient range of admissible cracks, which the designer can define according to the importance of the structural element. More details will be provided in next section.

Another concern has to be expressed with regard to the available models of Table 2.4 and Section 2.8.9 of Chapter 2. Some of them include the contribution of fibers as a separate addendum, to be added to that of concrete and, where provided, to that of web reinforcement.

Once again, fibers give considerably different performance as the concrete matrix changes, leading to the argument that the contribution of fibers is to be included in the concrete contribution.

RILEM formulation [2.157], even though it includes the fiber contribution as a separate addendum, it is the only one that defines it through a residual post-peak strength. As already mentioned in Chapter 3 (Section 3.6), no fracture mechanics tests according to RILEM were carried out for the FRC materials studied herein. However, similar tests, according to the Italian Standard, were performed and adopted for predicting the ultimate strength of shear-critical beams in accordance with the RILEM Final Recommendation [2.157].

An ongoing research at the University of Brescia is currently looking for a correlation between the different post-cracking toughness parameters contained in the two provisions (RILEM and Italian). Results are not available yet, even though not big differences between the parameters calculated by the two Standards were noticed. It should therefore be correct using the equivalent strength of the Italian Standard.

Table 6.10 reports the comparison between the experimental shear strength and the analytical ultimate shear predicted by five different available formulations:

- RILEM [2.157];
- Ashour et al. [2.171];
- Imam [2.158] ;
- Narayanan [2.175] ;
- Khuntia [2.162].

413

A very huge scatter can be highlighted among the predictions of the five formulations. Especially Ashour's and Khuntia's formulations, respectively the most unconservative and conservative, give very different predictions, so that the Ashour's relation estimates almost a double ultimate shear, in comparison with Khuntia' model. Ashour's formulation is totally unsafe: it overestimates also the response of the specimen made of plain concrete. It is therefore not recommended for design purposes. Khuntia's model is even too conservative since it predicts, especially with normal strength concrete, ultimate shear capacity 80% lower than the experimental.

Designation	$P_{u,exp}$	$V_{u,exp}$	$V_{u,exp}/V_{u,an}$ RILEM	$V_{u,exp}/V_{u,an}$ ASHOUR	$V_{u,exp}/V_{u,an}$ IMAM	$V_{u,exp}/V_{u,an}$ NARAYANAN	$V_{u,exp}/V_{u,an}$ KHUNTIA
NSC1-FRC1	258	134	1.15	0.77	1.13	1.12	1.44
NSC1-FRC2	349	180	1.48	0.96	1.40	1.37	1.81
NSC2-FRC1	229	120	0.99	0.62	0.94	0.92	1.11
NSC2-FRC2	273	142	0.91	0.68	1.03	1.00	1.23
NSC3-FRC	272	141	1.05	0.69	1.06	1.03	1.22
HSC-FRC1	372	191	1.37	0.72	1.17	1.05	1.18
HSC-FRC2	435	223	1.16	0.70	1.15	1.01	1.14

Table 6.10: Prediction of several analytical models against the experimental results of shear-critical beams presented in Chapter 4.

The other three formulations (RILEM, Imam and Narayanan) are characterized by fairly similar results: all of them are a little unconservative in case of NSC2 specimens while in the other cases they provide accurate estimations. Narayanan's model shows the best fitting of the experimental results, even though the formulation does not come from a rational model and it includes the fiber factor *F*.
Figure 6.38 plots the ratio between the experimental and the predicted shear force for the five models above discussed. The same considerations can be reaffirmed. Note especially the upper and lower bound (Khuntia and Ashour respectively) and the other three formulations, whose predictions quite resemble to each other.
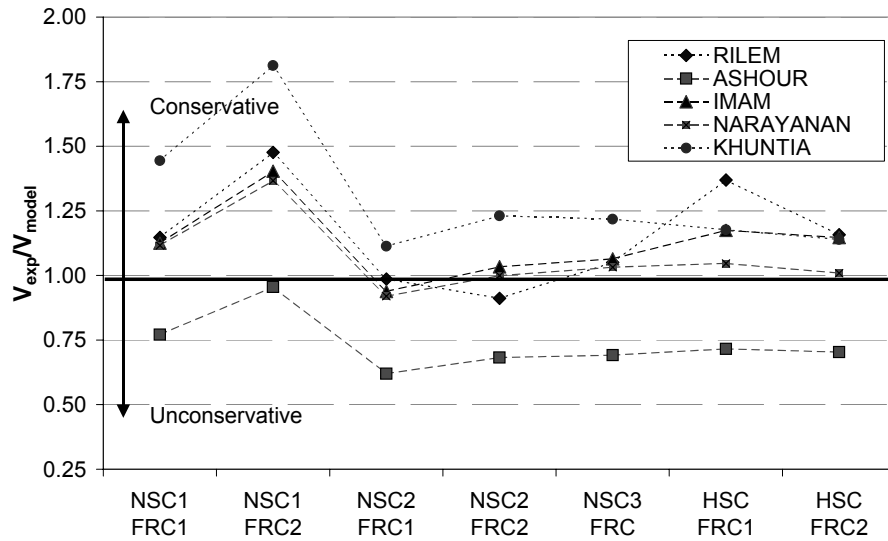
Figure 6.38: Ratio between the predicted and experimental shear force, for the 5 models discussed.

6.7 The Eurocode Provisions for Shear in presence of Fibers: an Adaptation.

As mentioned in the previous section, an attempt to model the current formula for shear of member without web reinforcement contained in the current EC2 [3.3] for FRC beams will be herein discussed and corroborated against all experiments presented in Chapter 3 and Chapter 4.

The main idea is to include the contribution of fibers by using the provisions of the Italian Standard ([2.125] and Section 2.8.4).

In doing so, a designer should perform a number of fracture mechanics tests on notched small beams, for the determination of the equivalent stresses, which reflect the toughness provided by fibers to the concrete mixture.

Note that the Italian Standard defines two equivalent post-cracking strengths, one related to the Serviceability Limit State, while the other correlated to the Ultimate Limit State, as herein recalled (Figure 2.145):

$$f_{eq,(0-0.6)} = \frac{l}{b(h-a_0)^2} \cdot \frac{U_1}{0.6} \tag{2.245}$$

$$f_{eq,(0.6-3)} = \frac{l}{b(h-a_0)^2} \cdot \frac{U_2}{2.4} \tag{2.246}$$

415

$f_{eq(0-0.6)}$ and $f_{eq(0.6-3)}$ are respectively the equivalent stress in the CTOD ranges of 0 - 0.6mm (typical for SLS) and 0.6-3 mm (typical for ULS).

The equivalent strength related to the ultimate limit state will be considered in this research project since shear cracking in SFRC members proved to develop in a quite stable fashion, even for crack widths of 3 mm (See Table 4.8).

Furthermore, the ability of fibers in controlling the second branch of the shear-critical crack even for big crack widths is due to their capability of bridging the two faces of a crack by means of their toughness. By keeping cracks stable, the bearing capacity of members considerably increases till, eventually, the full flexural capacity is attained. Therefore, it is definitely more correct to relate the experimental behavior with a quantity that is relevant for the ultimate limit state.

The issue is now how to include this parameter. Fibers act as a randomly distributed reinforcement, bridging the cracks and allowing the transmission of significant stresses even with considerable crack widths. Especially the presence of fibers all over the depth is relevant for the shear behavior, in the same way as placing longitudinal rebars at certain spacing along the depth of a member proved to be highly beneficial in terms of bearing capacity and overall ductility. Kuchma et al. ([2.26]; see Chapter 2, Section 2.5.6.3) demonstrated that adding three layers of relatively low diameter bars over the depth of a specimen 1000 mm deep (this additional reinforcement did not significantly change the reinforcement ratio) increased the shear strength of about 50%, doubled the ductility and made possible the formation of a distributed crack pattern, without an early localization of any shear-critical crack.

Fibers act in providing a member with exactly the same effect, as it has been shown many times in Chapter 3 and Chapter 4. It is hence correct modeling the shear contribution of fibers as a modifier of the longitudinal reinforcement ratio (as previously done, see i.e. Imam [2.158]) throughout a factor that includes the toughness properties of fibers, namely, the equivalent strength relevant for the ultimate limit state.

From the equation available in the current EC2 [3.3] for members without web reinforcement, herein recalled as:

$$V_{Rd,ct} = \left[C_{Rd,c} \cdot k \cdot (100 \cdot \rho_1 \cdot f_{ck})^{1/3} + k_1 \cdot \sigma_{CP} \right] \cdot b_w \cdot d \tag{2.212}$$

the equivalent strength $f_{eq(0.6-3)}$ can be included so that the following relationship can be written:

416

$$V_{Rd,ct} = \left[C_{Rd,c} \cdot k \cdot (100 \cdot \rho_1 \cdot (1 + \frac{a}{d} \cdot \frac{f_{eq(0.6-3)}}{f_{ct}}) \cdot f_{ck})^{\frac{1}{3}} + k_1 \cdot \sigma_{CP} \right] \cdot b_w \cdot d \qquad (6.35)$$

Equation (6.35), by substituting the two coefficients $C_{Rd,c}$ and k_l, assumes its final shape as:

$$V_{Rd,ct} = \left[0.18 \cdot k \cdot (100 \cdot \rho_1 \cdot (1 + \frac{a}{d} \cdot \frac{f_{eq(0.6-3)}}{f_{ct}}) \cdot f_{ck})^{\frac{1}{3}} + 0.15 \cdot \sigma_{CP} \right] \cdot b_w \cdot d \qquad (6.36)$$

where all coefficients and notations were defined in Section 2.7.1.

Equation (6.36) can be generalized by introducing a factor C_F, so that the formulation becomes:

$$V_{Rd,ct} = \left[0.18 \cdot k \cdot \left\{ 100 \, \rho_1 \cdot \left[1 + C_F (\frac{a}{2.5 \cdot d} \cdot \frac{f_{eq(0.6-3)}}{f_{ct}}) \right] \cdot f_{ck} \right\}^{\frac{1}{3}} + 0.15 \cdot \sigma_{CP} \right] \cdot b_w \cdot d \qquad (6.37)$$

where C_F should be determined with an extensive corroboration against test data. At the moment, C_F should be taken equal to 2.5.

Equation (6.36) is a very simple relationship. It is well known and already diffusely utilized in practice for members made of plain concrete. It should hence be easily applied for design purposes.

Equation (6.36) could be considered as a design formulation by providing all materials coefficients, as stated by EC2. A safer estimation would be obtained by dividing the characteristics values of the ratio $f_{eq(0.6-3)}/f_{ct}$ by the partial safety factor for SFRC that, as a first approximation, can be assumed as $\gamma_c=1.6$, typical for plain concrete (situ-cast) in Italy.

In addition to the equivalent strength, two other factors were included in the proposal, the a/d ratio and the tensile strength of concrete. The first parameter could be a little annoying in practice, as in many situations the combinations of loads do not allow a quick selection of the proper a/d ratio. For members loaded under a uniformly distributed load, there is an easy procedure for determining an equivalent a/d ratio (See Section 2.5.6.1); in more complicated cases, the value $a/d=2.5$ is to be assumed.

The second parameter is the concrete tensile strength f_{ct}. If missing or not properly evaluated, the corresponding expressions as a function of the cylinder compressive strength, provided by EC2, should be utilized (See Equation (6.30) in Section 6.3.2). Note that Equation (6.36) is valid in presence of shear diagonal failure ("beam behavior"), namely for a/d ratios greater than 2.5. In case of failure due to arch

417

action, further studies have to be carried out (with this respect, a research team is currently working on that at the University of Brescia). The key point of this procedure is the evaluation of parameter v in the current formula of EC2, which is a reduction factor for the compressive strength of concrete cracked in shear. A formulation less restrictive for this factor is expected in FRC, as fibers increase the area of the resisting strut and determine crack widths much smaller than those in plain concrete, for the same load intensity (some experimental evidences were outlined in Chapter 3).

Table 6.11 reports the main characteristics of all specimens, with fibers and without stirrups, tested in the present thesis. It also provides the equivalent post cracking strength according to the Italian Standard and the ultimate shear strength attained. The latter is compared with the new model herein discussed.

Designation	f_{cm}	f_{ct}	$f_{eq(0.6-3)}$	$V_{u,exp}$	$V_{u,NEW\ MODEL}$	$V_{u,exp}/V_{u,NEW\ MODEL}$
	[MPa]	[MPa]	[MPa]	[kN]	[kN]	[-]
Shear-Critical Beams						
NSC1-PC	24.8	2.3	0	69	78	0.89
NSC1-FRC1	24.8	2.3	2.67	134	122	1.10
NSC1-FRC2	24.8	2.3	3.06	180	127	1.42
NSC2-PC	33.5	3.15	0.00	84	86	0.98
NSC2-FRC1	33.5	3.15	2.55	120	124	0.97
NSC2-FRC2	33.5	3.15	4.42	142	142	1.00
NSC3-PC	38.6	2.6	0.00	83	90	0.92
NSC3-FRC	38.6	2.6	3.03	141	142	0.99
HSC-PC	60.5	3.15	0	113	105	1.08
HSC-FRC1	61.1	3.48	3.12	191	155	1.23
HSC-FRC2	58.3	3.2	5.99	223	184	1.21
Prestressed I-Beams						
I-Beam 3, DZ	68.3	4.65	3.18	587	370	1.59
I-Beam 4, DZ	77.0	5.18	8.61	722	433	1.67
I-Beam 5 I, DZ	69.4	4.43	3.18	579	373	1.55
I-Beam 5 II, DZ	69.9	4.72	3.18	555	370	1.50
I-Beam 6 I, DZ	69.9	4.72	8.61	586	432	1.36
I-Beam 6 II, DZ	69.9	4.72	8.61	620	432	1.44

Table 6.11: Predictions of all FRC tests discussed in this thesis obtained by the new formulation proposed.

418

Note that the current EC2 tends to be a little unconservative in predicting the ultimate shear strength of members made of plain concrete (all calculations were performed assuming all material factors equal to one), with a difference that is at most of around 10%.

Predictions with the new formulation are quite satisfactory for all shear-critical beams, even though values obtained for the two high strength concrete beams are a little low, determining a quite conservative estimation. Worse estimations are obtained for the prestressed I-Beams, as expected. In fact, pretty low predictions were already reported in Section 3.6, where it was concluded that the current EC2, the RILEM and other analytical formulations are very conservative. The effect of the two huge flanges and the particular geometry chosen can in part explain the relatively poor estimations.

Figure 6.39 reports a plot of the V_{exp}/V_{model} ratio of the proposed equation, in comparison with 4 of the 5 formulations above reviewed. The Ashour's relationships is no longer discussed, as it proved to be very unsuccessful in predicting reliable shear capacities. The proposed model provides good estimations of the experiments, especially for shear-critical beams. Note, once again, that all models really underestimate the shear capacity of the experiments of the prestressed I-Beams, with the exception of the Imam's formulation, which was developed for high strength concrete members.
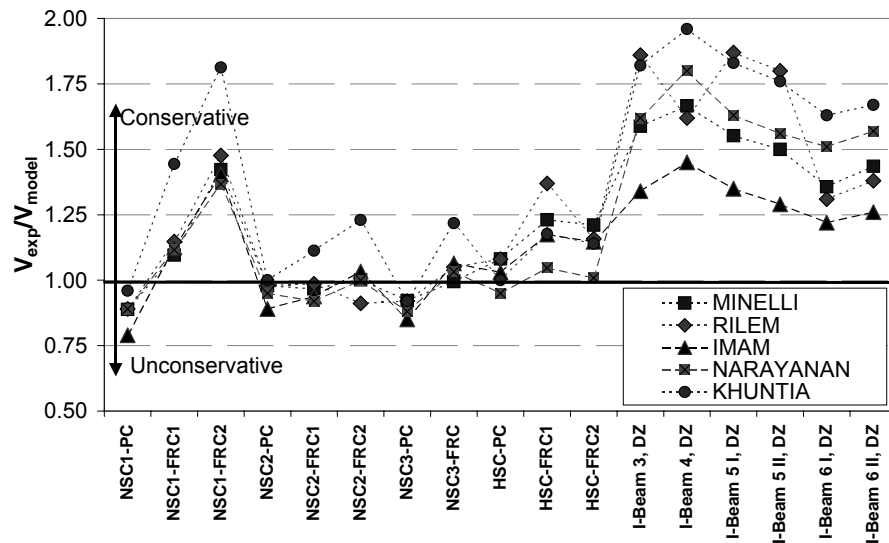
Figure 6.39: Comparison between the predictions of available models and the new model herein proposed.

Figure 6.40 illustrates only the comparison between the model herein developed and the RILEM formulation. They both result from an adaptation of the EC2 current design equation, and therefore give similar results. The model herein proposed slightly improves the fitting of experimental results, especially for members made of high strength concrete and in the experiments of I-Beam series. It should be recognized that the calculation of the residual strength $f_{R,4}$ (as indicated by RILEM) from notched specimens tested in accordance with the Italian Standard could generate some small inconsistencies in values. As already noticed in Section 3.6, especially the contribution of fibers 45/30 is underestimated by the RILEM formulation. This generates a considerable difference between the two models (see specimen HSC-FRC1, I-Beam 3-DZ, I-Beam 5I-DZ and I-Beam 5II-DZ. All of them were cast with fibers 45/30).
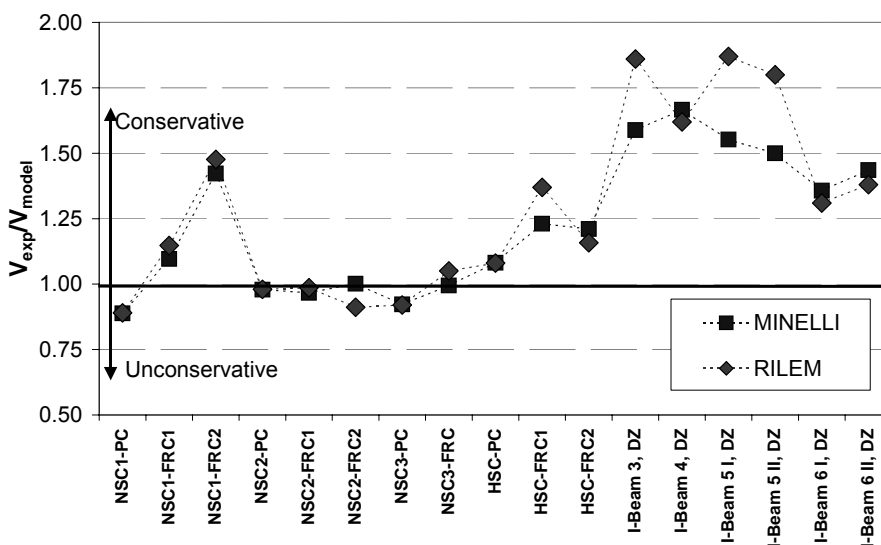
Figure 6.40: Comparison between the predictions of RILEM model and the new model herein proposed.

In conclusion, the proposal above presented seems to be fairly successful and, moreover, includes fibers in a rational and consistent way. An engineer can easily utilize this formula: he only needs to know the equivalent post-cracking strength, which, if unknown, is to be calculated by performing fracture mechanics tests, in the same way as the compressive strength is to be checked through tests on cylinders or cubes. The procedure of performing 4PBTs for the determination of the equivalent stresses is quite easy, and most of laboratories already have the

necessary equipment. Therefore, transferring this calculation into the practice would allow engineers to incorporate fibers in their design procedures in an easy way.

In presence both of stirrups and fibers, the truss model provided by EC2 should be investigated and adapted for including the contribution of steel fibers. The key point is the evaluation of the inclination of the strut θ with emphasis on its range of variation, feasible of eventual adaptations in presence of fibers. However, further studies are needed with this respect.

6.8 Concluding Remarks.

A broad and critical discussion of experimental results outlined in this thesis and an attempt to analytically model shear in beams without web reinforcement have been presented in this Chapter.

Several analytical models published in the scientific literature were evaluated and compared with the experimental results of the present research. Some of them proved to be quite effective both in giving good predictions and in accurately modeling the shear mechanism at failure.

A new model for predicting the shear strength of beams without web reinforcement, limited to plain concrete, was presented, based on the assumption that shear failure occurs through a sudden and brittle critical crack, having two branches: the second branch develops in an unstable way once the tensile strength of concrete is reached.

To explain this phenomenon, a practical distribution of shear stresses in the critical cross-section was assumed: this distribution was intended to increase the shear flow above the neutral axis and to decrease the shear stresses below it, compared to the shear stresses predicted by the "beam theory".

By analyzing the effect of this adjunctive distribution of stresses, an analytical formulation for predicting the shear strength of members was suggested, as a function mainly of the tensile strength of concrete and of factor χ, representing the ratio between the maximum shear stress of the new distribution assumed and the shear stress according to Jourawski. A corroboration of this relation was performed against more than 50 experiments on shear.

A number of considerations for the extension of this formula to a wide range of beams were also outlined, by concluding that some further considerations on the factor χ have to be done, based on the study of the development of the first branch of the shear-critical crack as a function of the main parameters influencing the shear response of a member under shear loading.

The effect of steel-to-concrete bond was in depth evaluated and correlated to the occurrence of shear failure. The total absence of bond is actually favorable with this respect, as it allows the formation of the arch action, with the attainment of the full-flexural capacity of a member. Conversely, the presence of bond generates a crack pattern (due to the compatibility between steel and concrete) which does not allow the formation of the arch mechanism and determines an early shear failure.

Several intermediate bond-slip relationships were numerically examined, confirming that, with decreasing bond, the bearing capacity augments until the ultimate flexural moment is attained, the cracking process tends to appear only in the region of the specimen within the two point loads and localizes in a few macro cracks, allowing the formation of the resisting arch.

Concerning fibers, a review of the available models for shear strength of beams without web reinforcement highlighted that many formulas are empirical and based on a limited set of experiments. Moreover, the effect of fibers is taken into account through the fiber factor, which is not a comprehensive parameter and cannot properly model the concrete-fiber interaction, which is crucial.

Furthermore, some formulations include fibers as a separate addendum, to be added to that of plain concrete and stirrups, not recognizing that identical fibers in different concrete matrixes might provide considerably diverse performances.

Based on these observations, an adaptation of the current equation of EC2 for shear in members without transverse reinforcement was proposed as a function of a parameter related to the toughness provided by fibers to the concrete matrix.

The fiber contribution was included into that of concrete as a modifier of the longitudinal reinforcement ratio, since fibers can be considered as an additional randomly distributed reinforcement all over the depth of a beam.

The proposal proved to be fairly accurate and gave satisfactory predictions of all specimens made of FRC tested in the present research.

Finally, a numerical study showing the extremely relevant effect of fibers in reducing the domain of shear diagonal failure, by varying the toughness of fibers and the longitudinal reinforcement, was presented, both for a normal and a high strength concrete model.

6.9 REFERENCES.

[1]   **Boussinesq and Flamant, A.**, *"Notice sur la vie et les travaux de M de Saint-Venant" ("Report on the life and work of de Saint Venant"), Annales des ponts et chaussées 12, 1886, pp. 557-595.*

[2]   **Adami, P., Giuriani, E., Minelli, F., and Pozzani, G.**, *"Resistenza a taglio di travi in c.a."; ("Shear strength of r.c. beams"), Tecnical Report n° 3; Department of Civil Engineering, University of Brescia-Italy. June 2003, pp.294. Only available in Italian.*

[3]   **Jourawski, D. J.**, *"Sur la résistance d'un corps prismatique et d'une pièce composées en bois ou en tôle de fer à une force perpendiculaire à leur longueur" . , ("On the resistance of a prismatic member…")Annales des Ponts et Chaussées, Mémoires et Documents, 3rd Series, vol. 12, Part 2,1856, pp. 328-351.*

[4]   **Timoshenko, S. P.**, *"History of Strength of Materials", 1953.*

[5]   **Giuriani, E., and Riva, E.**, *"The Method of Scalar and Vector Potentials of the Displacements applied to Beam and Plate Structures", Costruzuioni in Cemento Armato - Studi e Rendiconti, Vol 14, pp. 147-157, 1977.*

[6]   **Bottazzi, M., and Zanaglio, L.**, *"Studi sul Comportamento di Travi non Armate a Taglio" ("Some Studies on the Behavior of Beams without Web Reinforcement"), B.Sc Thesis Supervised by Giuriani E. and Marini A., University of Brescia, 2003/2004, pp. 243. Only available in Italian.*

[7]   **Kuchma, D.**, *http://www.ce.uiuc.edu/kuchma/sheardatabank.*

[8]   **Eligehausen, R., Popov, E. P., and Bertero, V.V.**, *"Local bond stress-slip relations of deformed bars under generalized excitations", Report UCB/EERC-83/23, University of California, Berkley, CA, 1983.*

[9]   **Giuriani, E.**, *"On the Effective Axial Stiffness of a Bar in Cracked Concrete" Contribution to "Bond in Concrete", Edited by P. Bartos- Department of Civil Engineering, Paisley College of Technology, Scotland, pp. 107-126, 1982.*

[10]   **Cairns J., and Plizzari, G.A.**, *"Towards a Harmonised European Bond Test", RILEM Material and structures, Vol. 36, 2003, pp. 498-506.*

[11]   **Meda, A., Plizzari, G.A., Sorelli, L., and Banthia, N.**, *"Uni-axial and bending tests on hybrid fibre reinforced concrete", in Proceedings of the international symposium Role of concrete in sustainable development, Dhir K., Newlands, M.D. and Paine K.A. Eds., Dundee (UK), September 3-4, 2003, pp. 709-718.*

424

7. CONCLUSIONS

This thesis meanly dealt with the study of shear behavior of beams without web reinforcement and cast whether with plain concrete of fiber reinforced concrete.
Main scope of the research carried out was the evaluation of the shear mechanism, both in member with plain concrete and in beams with fiber reinforced concrete, toward a rational analytical model predicting the shear strength.

A first detailed review of the state of the art on shear was reported, with particular emphasis on the mechanisms of shear transfer and the analytical models available.
A critical discussion of the most interesting and known formulations was also done, in light of the huge experimental campaign performed.
A total number of twenty-seven experiments on full scale elements was performed.
Twelve tests concerned prestressed I-Beams, whose main scope was the evaluation of the possibility of substituting or integrating the transverse reinforcement with steel fibers.
Fifteen experiments were carried out on shear-critical beams having different concrete strength, fiber content (where provided), and steel-to-concrete bond characteristics.

The main conclusions that can be highlighted are reported in the following.
Concerning the experiments on I-Beams, presented in Chapter 3, the experimental results showed that beams reinforced only with steel fibers had a similar, or even better, post-cracking behavior than beams with the minimum amount of transverse reinforcement. In prefabrication, this is particularly appealing for facilitating the industrialization of the production and introducing an improvement in the overall characteristics and durability of the products. Moreover, reducing in handling and placing of rebars, with a consequent possibility of saving labor and money, should be considered.
When fibers were used in addition to conventional transverse reinforcement, the shear strength significantly increased. Steel fibers also determined a reduction of the width of shear cracks, thus improving also durability.
Steel fibers turned out to be really effective in increasing also the residual compressive stress, which governed the experimental behavior when arch action occurred.

Regarding the fifteen experiments on shear-critical beams, diffusely examined in Chapter 4, a first series of four experiments made of normal strength plain concrete demonstrated the crucial effect of steel-to-concrete bond in determining the collapse mode as well as in influencing the post-cracking behavior and the crack formation and evolution. Steel-to-concrete bond tends to anticipate the collapse by determining a critical shear failure at load and displacement levels very low. This is due to the cracking process governed by the compatibility between steel and concrete. The lack of bond, on the other hand, determines a flexural behavior, even though under considerable deflections and localizations of cracks, which might be unacceptable under a design point of view.

The second series of experiments concerned the comparison of identical beams with different amount of steel fibers, used as the only shear reinforcement in the concrete matrix. Both normal strength and high strength concrete were investigated, whereas only bonded specimens were considered.

Fibers, even though in relatively low amount (30-50 kg/m^3), turned out to extremely influence the shear behavior of beams, basically by delaying the occurrence of the block mechanism, and eventually by altering the collapse from shear to flexure, with increasing bearing capacity and, especially, ductility.

A series of numerical analyses were then reported in Chapter 5, in which a validation of the MCFT and the DSFM, through a comparison between numerical analyses and shear experiments on both series of structures experimented in the thesis was presented.

Numerical analyses were performed by using the FE program VecTor2, suitably adapted to fiber reinforced concrete in terms of different post-cracking behavior and local conditions at cracks.

The adopted model accurately predicted the post-cracking response of the members in terms of strength, stiffness, ductility, crack patterns and failure modes. It was also able to simulate the post-peak behavior up to failure and to accurately predict the different collapse modes that occurred in the experiments.

The numerical results were accurate in every case, particularly in presence of transverse reinforcing steel or when dealing with specimens which failed under bending.

The rotating crack model proved to be effective in simulating the final collapse mechanism of the I-Beam specimens, which related to arch action, involving crack re-orientation and merging.

426

The shear contribution due to fibers and regular reinforcement was also modeled with good accuracy.

Chapter 6 mainly dealt with the discussion of results and modeling of shear.
A new model for predicting the shear strength of beams without web reinforcement, limited to plain concrete, was presented, based on the assumption that shear failure occurs through a sudden and brittle critical crack, having two branches: the second branch develops in an unstable way once the tensile strength of concrete is reached.
To explain this phenomenon, a distribution of shear stresses, in the critical cross-section, was assumed, so that it increased the shear flow above the neutral axis and decreased the shear stresses below it, in comparison to the classical shear stress distribution predicted by the "beam theory". The adjunctive distribution of shear stresses determines the occurrence of significant transverse tensile stresses on the section that, by reaching the tensile strength of concrete, make possible the formation of the block mechanism.
Based on this interpretation, an analytical formulation for predicting the shear strength of members was suggested, function mainly of the tensile strength of concrete and of factor χ, representing the ratio between the maximum shear stress of the new distribution and the shear stress at the neutral axis location, according to Jourawski.

The effect of steel-to-concrete bond was in depth evaluated in relation to the occurrence of shear failure. The total absence of bond is positive with this respect, as it allows the formation of the arch action. Conversely, the presence of bond generates a crack pattern, due to the compatibility between steel and concrete, which determines an early shear failure.
Several intermediate bond-slip relationships (between no bond and perfect bond) were numerically examined, confirming that, with decreasing bond, the bearing capacity becomes higher until the ultimate flexural moment is attained. Moreover, the cracking process tends to appear only in the region of the specimen within the two point loads and localizes in a few macro cracks, allowing the formation of the resisting arch.

Concerning fibers, a review of the available models for shear strength of beams without web reinforcement highlighted that many formulas are empirical and based on a limited set of experiments.

427

An adaptation of the current equation of EC2 for shear in members without transverse reinforcement was proposed as a function of a parameter related to the toughness of FRC, namely the equivalent post-cracking strength relevant for the ultimate limit state. The tensile strength of concrete and a factor related to the *a/d* ratio were also added into the formula.

The fiber contribution was included into that of concrete as a modifier of the longitudinal reinforcement ratio, since fibers can be considered as an additional randomly distributed reinforcement all over the depth of a beam.

The proposal proved to be fairly accurate and gave satisfactory predictions of all specimens made of FRC tested in the present research. Compared to other available formulations, the proposed model exhibited one of the best fitting of the experiments considered.

7.1 Recommendation for future research

This thesis investigated a consistent number of scientific aspects. Some of them should be investigated in depth with a number of refinements, as summarized in the following.

Concerning the model predicting the ultimate shear for members cast with plain concrete and without web reinforcement, a number of considerations on factor χ have to be done, based on the study of the development of the first branch of the shear-critical crack as a function of the main parameters influencing the shear response of a member under shear loading. This factor should mainly include the reinforcement ratio, the concrete grade and the size effect.

The model presented should also be extended to prestressed members as well as to elements subjected to axial force.

Furthermore, an extension of the model to FRC beams should be investigated. In doing so, one should consider the eventuality of using a fracture mechanics approach for predicting the tensile stresses generates by the adjunctive distribution of shear stresses assumed. In fact, in FRC members the second branch proved to steadily develop, due to the significant effect of residual tensile strength provided by fibers.

With regard to the adaptation of the current formula of EC2 for fibers, some refinements should be considered, in terms of the *a/d* ratio (not always easy to define) and on the definition of post-cracking tensile strength. Further experimental

results are available and should be checked with the new proposals. A proper definition of equivalent post-cracking strength in those cases, where no fracture mechanics test on notched beams (or different test) was performed has to be studied. Aiming at that, an experimental and numerical comparisons of different tests characterizing FRC materials should be preformed, in order to come up with suitable relations between the parameters defined by each Standard. This procedure would allow the application of the proposed formula to many other experiments, with eventual refinements.

Fibers increase the ultimate strength of the compression strut (see I-Beam model and NSC1 series), which is critical in some structures. With this respect, the corresponding check formula, prescribed by many building Codes, should be adapted to FRC structures. Regarding the formulation included by EC2, this could be done by basically reconsidering factor v, which reduces the compressive residual strength of concrete since it takes into account cracking due to shear. This goal should be attained with an experimental campaigns on FRC members having a/d ratios lower than 2.5.

Steel-to-concrete bond is crucial in guiding the failure mechanism. An experimental campaign would be recommended for confirming the numerical results outlined in Chapter 6, with emphasis on the bond characteristics that could allow a great bearing capacity accompanied by an acceptable stiffness and a limited deformability.

Finally, some refinements in the numerical model adopted (VecTor2) should be studied, with two respects: the first concerns a proper definition of the characteristic length, with a possible formulation related to the fracture energy of fibers, especially when dealing with members with little or no shear reinforcement, for which the tension softening of concrete is crucial. The second regards the compressive stress-strain relationships of concrete, which do not take into account the presence of fibers. Including suitable relations that could model the enhanced ductility offered by fibers in compression should allow some improvements toward a more refined simulation of members in which the residual compressive strength plays a considerable role.